Mapping Voids, Debonding, Delaminations, Moisture, and Other Defects Behind or Within Tunnel Linings

PREPUBLICATION DRAFT • NOT EDITED

SHRP 2
STRATEGIC HIGHWAY RESEARCH PROGRAM
Accelerating solutions for highway safety, renewal, reliability, and capacity

TRANSPORTATION RESEARCH BOARD
OF THE NATIONAL ACADEMIES

NOTICE

The project that is the subject of this document was a part of the second Strategic Highway Research Program, conducted by the Transportation Research Board with the approval of the Governing Board of the National Research Council.

The members of the technical committee selected to monitor this project and to review this document were chosen for their special competencies and with regard for appropriate balance. The document was reviewed by the technical committee and accepted for publication according to procedures established and overseen by the Transportation Research Board and approved by the Governing Board of the National Research Council.

The opinions and conclusions expressed or implied in this document are those of the researchers who performed the research. They are not necessarily those of the second Strategic Highway Research Program, the Transportation Research Board, the National Research Council, or the program sponsors.

The information contained in this document was taken directly from the submission of the authors. This document has not been edited by the Transportation Research Board.

Authors herein are responsible for the authenticity of their materials and for obtaining written permissions from publishers or persons who own the copyright to any previously published or copyrighted material used herein.

The Transportation Research Board of the National Academies, the National Research Council, and the sponsors of the second Strategic Highway Research Program do not endorse products or manufacturers. Trade or manufacturers' names appear herein solely because they are considered essential to the object of the report.

THE NATIONAL ACADEMIES
Advisers to the Nation on Science, Engineering, and Medicine

The **National Academy of Sciences** is a private, nonprofit, self-perpetuating society of distinguished scholars engaged in scientific and engineering research, dedicated to the furtherance of science and technology and to their use for the general welfare. On the authority of the charter granted to it by Congress in 1863, the Academy has a mandate that requires it to advise the federal government on scientific and technical matters. Dr. Ralph J. Cicerone is president of the National Academy of Sciences.

The **National Academy of Engineering** was established in 1964, under the charter of the National Academy of Sciences, as a parallel organization of outstanding engineers. It is autonomous in its administration and in the selection of its members, sharing with the National Academy of Sciences the responsibility for advising the federal government. The National Academy of Engineering also sponsors engineering programs aimed at meeting national needs, encourages education and research, and recognizes the superior achievements of engineers. Dr. Charles M. Vest is president of the National Academy of Engineering.

The **Institute of Medicine** was established in 1970 by the National Academy of Sciences to secure the services of eminent members of appropriate professions in the examination of policy matters pertaining to the health of the public. The Institute acts under the responsibility given to the National Academy of Sciences by its congressional charter to be an adviser to the federal government and, upon its own initiative, to identify issues of medical care, research, and education. Dr. Harvey V. Fineberg is president of the Institute of Medicine.

The **National Research Council** was organized by the National Academy of Sciences in 1916 to associate the broad community of science and technology with the Academy's purposes of furthering knowledge and advising the federal government. Functioning in accordance with general policies determined by the Academy, the Council has become the principal operating agency of both the National Academy of Sciences and the National Academy of Engineering in providing services to the government, the public, and the scientific and engineering communities. The Council is administered jointly by both Academies and the Institute of Medicine. Dr. Ralph J. Cicerone and Dr. Charles M. Vest are chair and vice chair, respectively, of the National Research Council.

The **Transportation Research Board** is one of six major divisions of the National Research Council. The mission of the Transportation Research Board is to provide leadership in transportation innovation and progress through research and information exchange, conducted within a setting that is objective, interdisciplinary, and multimodal. The Board's varied activities annually engage about 7,000 engineers, scientists, and other transportation researchers and practitioners from the public and private sectors and academia, all of whom contribute their expertise in the public interest. The program is supported by state transportation departments, federal agencies including the component administrations of the U.S. Department of Transportation, and other organizations and individuals interested in the development of transportation. **www.TRB.org**

www.national-academies.org

MAPPING VOIDS, DEBONDING, DELAMINATIONS, MOISTURE, AND OTHER DEFECTS BEHIND OR WITHIN TUNNEL LININGS

PRELIMINARY REVISED DRAFT
FINAL REPORT

Prepared for
The Strategic Highway Research Program 2
Transportation Research Board
of
The National Academies

Andrew Wimsatt, Joshua White, Chin Leung, and Tom Scullion
Texas A&M Transportation Institute

Stefan Hurlebaus, Dan Zollinger, and Zachary Grasley
Texas A&M University

Soheil Nazarian, Hoda Azari, and Deren Yuan
The University of Texas at El Paso

Parisa Shokouhi
The German Federal Institute for Materials Research and Testing

Timo Saarenketo
Roadscanners Oy

and

Fulvio Tonon
The University of Texas at Austin

College Station, Texas
December 2012

MAPPING VOIDS, DEBONDING, DELAMINATIONS, MOISTURE, AND OTHER DEFECTS BEHIND OR WITHIN TUNNEL LININGS

PRELIMINARY DRAFT
FINAL REPORT

Prepared for
The Strategic Highway Research Program 2
Transportation Research Board
of
The National Academies

Andrew Wimsatt, Joshua White, Chin Leung, and Tom Scullion
Texas A&M Transportation Institute

Stefan Hurlebaus, Dan Zollinger, and Zachary Grasley
Texas A&M University

Soheil Nazarian, Hoda Azari, and Deren Yuan
The University of Texas at El Paso

Parisa Shokouhi
The German Federal Institute for Materials Research and Testing

and

Timo Saarenketo
Roadscanners Oy

College Station, Texas
October 2012

CONTENTS

LIST OF FIGURES

LIST OF TABLES

ACKNOWLEDGMENTS

ABSTRACT

This report documents the work conducted under Phase II of SHRP 2 Project R06(G), Mapping Voids, Debonding, Delaminations, Moisture, and Other Defects behind or within Tunnel Linings. Based on the results of this study, the following techniques are able to detect defects with minimum surface areas of 1 ft^2 up to 4 inches deep (and in some cases even deeper):

- Air-coupled ground-penetrating radar (GPR).
- Thermography (handheld thermal camera).
- SPACETEC scanner.
- Ground-coupled GPR.
- Ultrasonic tomography.
- Ultrasonic echo.
- Portable seismic property analyzer (PSPA) ultrasonic surface waves and impact echo.

They appear to provide useful information for evaluating tunnel linings and should be considered for implementation, but the limitations outlined in the appropriate appendix for each technology need to be considered.

EXECUTIVE SUMMARY

This final report documents the work conducted under Phase II of Strategic Highway Research Program (SHRP 2) Project R06(G), Mapping Voids, Debonding, Delaminations, Moisture, and Other Defects behind or within Tunnel Linings.

The objectives of the proposed research are as follows:

- Identify nondestructive testing (NDT) technologies for evaluating the condition (e.g., moisture, voids, and corrosion) of various types of tunnel linings (e.g., unreinforced concrete, reinforced concrete, shotcrete, and steel) and tunnel lining finishes such as tile. The techniques must be capable of analyzing conditions within the tunnel lining and the surrounding substrate.
- Evaluate the applicability, accuracy, precision, repeatability, ease of use, capacity to minimize disruption to vehicular traffic, and implementation and production costs of the identified technologies.
- Conduct the required development in hardware or software for those techniques that show potential for technological improvement within the time limitations of this project.
- Prove the validity of the selected technologies/techniques to detect flaws within or verify conditions of the targeted tunnel components.
- Recommend test procedures and protocols to successfully implement these techniques.

Evaluation, in the context of this project, is defined as both a rapid screening of the testing area and as an in-depth, although slower, assessment of an area deemed problematic during screening. In both cases, and based on SHRP 2 priorities, dependable NDT techniques that minimize disruption to traffic are sought under this project.

The following is a summary of the conclusions and recommendations.

As stated in Chapter 2 of this report, in terms of performance criteria, the expert panel indicated that NDT should detect any defect within or immediately behind tunnel linings that have a minimum surface area of 1 ft^2, and any defect needs to be located within 1 ft of the actual location on the tunnel lining. The panel also indicated that NDT should identify delaminated areas and voids up to 4 inches deep as measured from the lining surface with an accuracy of within 0.25 inches.

Based on the results in Chapter 3, the following techniques are able to detect defects with minimum surface areas of 1 ft^2 up to 4 inches deep (and in some cases even deeper):

- Air-coupled ground-penetrating radar (GPR).
- Thermography (handheld thermal camera).
- SPACETEC scanner.
- Ground-coupled GPR.
- Ultrasonic tomography.
- Ultrasonic echo.
- Portable seismic property analyzer (PSPA) ultrasonic surface waves and impact echo.

They appear to provide useful information for evaluating tunnel linings and should be considered for implementation, but the limitations outlined in the appropriate appendix for each technology need to be considered. In addition, none of the devices are able to detect a 1-square-foot void in a steel lining behind concrete. In addition, the 0.25-inch accuracy criterion for defects up to 4 inches deep can be problematic for the in-depth devices. It appears that a 0.5-inch accuracy is more realistic for these devices.

The following table summarizes the accuracy, detection depth, deterioriation mechanisms detected, tunnel lining types, and other information for these technologies.

Table. Summary of NDT Devices.

Device	Accuracy	Detection Depth	Deterioriation Mechanisms Detected	Tunnel Lining Types	Other information
Air-coupled ground-penetrating radar (GPR)	Locates defects within 1 foot of its actual location	Does not measure depth, but indicates areas of high moisture or low density (high air voids). Such areas may represent problems within or behind the tunnel lining	Tile debonding, delaminations, air filled voids, water filled voids, moisture intrusion	Concrete, Tile-lined Concrete, and Shotcrete	This is a scanning tool that can indicate where to conduct testing with in depth devices
Thermography (handheld thermal camera)	Locates defects within 1 foot of its actual location	Does not measure depth, but can indicate tile debonding, delaminations up to 1 inch, voids up to 3 inches.	Tile debonding, delaminations, air filled voids, water filled voids, moisture intrusion	Concrete, Tile-lined Concrete, and Shotcrete	This is a scanning tool that can indicate where to conduct testing with in depth devices
SPACETEC scanner	Locates defects within 1 foot of its actual location	Does not measure depth, but can indicate tile debonding, possibly delaminations up to 1 inch, and possibly voids up to 3 inches.	Tile debonding, delaminations, air filled voids, water filled voids, moisture intrusion	Concrete, Tile-lined Concrete, and Shotcrete	This is a scanning tool that can indicate where to conduct testing with in depth devices. Testing can only be conducted through a service contract.
Ground-coupled GPR	Can determine defect depth within 10% of the actual depth without reference cores, 5% if cores are available	The device can possibly detect defects at any depth within or immediately behind tunnel linings. However, specimen testing indicates it cannot locate 1 square foot voids in steel plates behind tunnel linings	Delaminations, air filled voids, water filled voids, moisture intrusion	Concrete, Tile-lined Concrete, and Shotcrete	Experienced personnel are needed to intepret defect locations and depths from the GPR scans. Specimen testing indicates it cannot locate 1 square foot voids in steel plates behind tunnel linings

Table (continued). Summary of NDT Devices.

Device	Accuracy	Detection Depth	Deterioriaton Mechanisms Detected	Tunnel Lining Types	Other information
Ultrasonic tomography	Concrete: voids within 0.5 inch, shallow delaminations within 0.75 inch. Shotcrete:air filled voids within 0.7 inch, water filled voids within 1.21 inch, shallow delaminations within 1.88 inch	Can detect defects up to 8 inches deep based on specimen tests. Tunnel tests indicate it can detect possible defects up to 20 inches deep.	Delaminations and voids	Concrete, Tile-lined Concrete, and Shotcrete	May not be effective for measuring defects that are 2 inches or less from the lining surface. May not be accurate enough for measuring defect depths in shotcrete.
Ultrasonic echo	Comparable to the ultrasonic tomography system based on tunnel testing with both devices. Past experience indicates also it can measure tunnel lining thickness within 3% of the actual thickness	Comparable to the ultrasonic tomography system based on tunnel testing with both devices.	Delaminations and voids	Concrete and shotcrete	May not be effective for measuring defects that are 2 inches or less from the lining surface. May not be accurate enough for measuring defect depths in shotcrete. Tunnel tests indicated problems with using this device on tiles.
Portable seismic property analyzer (PSPA) ultrasonic surface waves and impact echo	Ultrasonic Surface Waves: about 15% of the actual depth for defects up to 6 inches deep. Impact Echo: 10% for deep delaminations greater than 6 inches deep.	Ultrasonic Surface Waves: up to 6 inches deep. Impact Echo: up to 18 inches deep	Delaminations and voids	Concrete, Shotcrete, and Tile-lined Concrete	May be difficult to quantify the depth of defects that are shallow or extensive. May not get good results when testing on very rough concrete surfaces, oily surfaces, and severely curved surfaces

The following sequence of testing is suggested for evaluating tunnel linings based on the research conducted under this study:

- o Collect thermal images and air coupled GPR data on the tunnel lining. Air coupled GPR data should be collected every foot along the tunnel lining. Thermal images can be collected every foot as well; however, the equipment covered in this report can collect data at a spacing determined by the camera operator or tunnel inspector. This data should be collected ideally on the same day; however, it can be collected separately. The thermal images should be collected when the air temperature is rising or falling; areas of possible defects may show up better in the thermal images. The data from any of these devices can be obtained at a walking pace (around 1 mph or 1.61 kmh). Air coupled GPR data can be obtained at much higher speeds, but the geometry and features in tunnels may make it difficult to operate the equipment at speeds much greater than 1 mph.

- o Analyze the data from the scanning devices above.   Select areas for in depth testing based on the GPR surface dielectric results, thermal images, and observed surface distresses that are of concern to tunnel inspectors.

- o Conduct in depth testing with the ground coupled GPR and either the ultrasonic tomography, ultrasonic echo, or portable seismic property analyzer device. The choice of equipment could be based on the cost and the type of defect to be detected (tile debonding, delamination, and voids) The ultrasonic tomography and ultrasonic echo devices may be more appropriate for measuring and mapping defects greater than two inches from the tunnel lining surface. The ultrasonic tomography device is more expensive than the other two devices; however, it has the capability to provide more information in the field about such defects.   The portable seismic property analyzer may be more appropriate for determining the limits of shallow defects.

- o Evaluate the data collected from these devices.

The SPACETEC Scanner is only available through a service provider. Service providers can also perform NDT using the actual or similar devices or techniques described in this report. However, all but the SPACETEC equipment could be operated by tunnel owner personnel. The equipment and essential data processing software used is commercially available. To implement each of these methods, however, the personnel in charge need to be sufficiently trained for data collection, reduction and interpretation.

The handheld thermal cameras appear to be the easiest to use of the devices tested under this study and can be effectively used by tunnel owner personnel. Data collection and analysis of the images can be conducted in the field.   On the other hand, the air coupled and ground coupled GPR equipment will require considerably more training and experience than the other devices for data collection and operation. These devices involve the use of integrated systems containing a data collection module, computer, antenna, and distance measuring indicator.   Data analysis of the air coupled GPR data will generally be simpler than that from ground coupled GPR data,

however. The researchers recommend that the surface dielectric data from the air coupled GPR be used for determining where to conduct more in depth tests; this data is easily generated by GPR analysis programs. The training and experience needed to effectively collect and analyze data from ultrasonic tomography, ultrasonic echo, and portable seismic property analyzer equipment is expected to be less than that for the GPR equipment.

For rapid scanning of tunnel linings, data from the SPACETEC scanner, the air-coupled GPR, and thermal camera images can indicate areas where further inspection by tunnel personnel may be warranted. All devices were able to detect problems within 1 ft of the actual location on the tunnel lining. However, the SPACETEC scanner is not for sale; data collection and analysis are provided by SPACETEC through a service contract.

The 1-GHz ACGPR antennas such as the one used in this study are no longer for sale in the United States due to FCC regulations; several service providers still own these antennas, however. In any case, antennas for sale in the United States should be effective for collecting data if they meet the radar specifications contained in Appendix T.

Thermal cameras have the ability to detect 1-ft^2 voids 3 inches deep when significant concrete thermal gradients exist according to this study, and the literature suggests they can detect even deeper voids. However, the team believes that vehicle-mounted thermal camera systems are not quite ready for implementation; further software development is needed.

Ground-coupled GPR, ultrasonic tomography, ultrasonic echo, and the PSPA are all able to detect defects up to 4 inches in depth. However, for GCGPR, the defects can only be detected if they contain significant air pockets or significant moisture. Ultrasonic Tomography can detect even deeper defects, but cannot directly detect defects if they are less than 2 inches away from the surface.

As for implementation, all of these devices will require a combination of classroom and hands-on training for collecting and/or analyzing data.

Although beyond the scope of this study, the Laser scanning and digital photogrammetry techniques can also provide information about tunnel lining profile and surface distress that may be useful to tunnel inspectors.

Finally, service providers can collect and analyze data for clients using the devices listed above. However, clients should consider the limitations for each device before selecting a service provider.

6

CHAPTER 1
BACKGROUND

SHRP 2 BACKGROUND

To address the challenges of moving people and goods efficiently and safely on the nation's highways, Congress has created the second Strategic Highway Research Program (SHRP 2). SHRP 2 is a targeted, short-term research program carried out through competitively awarded contracts to qualified researchers in the academic, private, and public sectors. SHRP 2 addresses four strategic focus areas:

- Safety: the role of human behavior in highway safety.
- Renewal: rapid highway renewal.
- Reliability: congestion reduction through improved travel time reliability.
- Capacity: transportation planning that better integrates community, economic, and environmental considerations into new highway capacity.

Under current legislative provisions, SHRP 2 will receive approximately $232 million over a total program duration of 9 years.

The U.S. highway system is aging and must be rebuilt while we are driving on it and living next to it. Research in the SHRP 2 Renewal focus area therefore addresses the need to develop a consistent, systematic approach to completing highway projects quickly, with minimal disruption to the community, and producing facilities that are long lasting. Identifying new technologies for locating underground utilities; developing procedures to speed the evaluation of designs and the inspection of construction; and applying new methods and materials for preserving, rehabilitating, and reconstructing roadways and bridges are among the goals for this focus area. Alternative strategies for contracting, financing and managing projects, and mitigating institutional barriers also are part of the emphasis on rapid renewal. The renewal scope applies to all classes of roads.

PROBLEM STATEMENT

Periodic inspection of highway tunnels to assess changes in structural condition over time is critical to timely detection and remediation of problems to ensure road user safety. Tunnel structural problems that are considered widespread and potentially serious are tunnel leaks, concrete cracking, concrete spalling, concrete delamination, debonding, steel corrosion, and improper drainage. Monitoring of tunnel condition and deterioration rate is key to determining the appropriate schedule of maintenance and/or rehabilitation activities to remedy structural and safety problems that might lead to accelerated deterioration and sudden tunnel failures that could cause serious injury and even fatalities.

Tunnel inspection is a challenging problem. Tunnels typically service high-volume traffic and operate in aggressive environments. Keeping tunnels open during inspection and minimizing tunnel closures and user delays must be carefully balanced with the need to conduct detailed inspections to ensure the safety of drivers. Consequently, nondestructive testing (NDT) methods

that are automated, quantitative, and rapid, and that provide complete coverage compared to conventional visual inspections need to be identified and evaluated. However, there does not appear to be any high-speed NDT method for assessing the condition of tunnel linings that would minimize the disruption of ongoing traffic.

RESEARCH OBJECTIVES

The objectives of the proposed research are to:

- Identify NDT technologies for evaluating the condition (e.g., moisture, voids, and corrosion) of various types of tunnel linings (e.g., unreinforced concrete, reinforced concrete, shotcrete, and steel) and tunnel lining finishes such as tile. The techniques must be capable of analyzing conditions within the tunnel lining and the surrounding substrate.
- Evaluate the applicability, accuracy, precision, repeatability, ease of use, capacity to minimize disruption to vehicular traffic, and implementation and production costs of the identified technologies.
- Conduct the required development in hardware or software for those techniques that show potential for technological improvement within the time limitations of this project.
- Prove the validity of the selected technologies/techniques to detect flaws within or verify conditions of the targeted tunnel components.
- Recommend test procedures and protocols to successfully implement these techniques.

Evaluation, in the context of this project, is defined as both a rapid screening of the testing area and as an in-depth, although slower, assessment of an area deemed problematic during screening. In both cases, and based on SHRP 2 priorities, dependable NDT techniques that minimize disruption to traffic are sought under this project.

CHAPTER 2
RESEARCH APPROACH

INTRODUCTION

According to data provided by the Federal Highway Administration, the vast majority of tunnel linings in the United States use cast-in-place (CIP) reinforced concrete, with a significant number using CIP unreinforced concrete, steel/iron liner plate, or shotcrete. In addition, a significant number of tunnels use CIP concrete and a steel/iron liner plate behind the concrete.

According to the expert panel for this project, the following major problems exist with tunnel linings where NDT methods are needed to assess the extent of such problems:

- Water leakage.
- Delaminations and spalling of concrete liners due to reinforcing steel corrosion.
- Voids behind and within tunnel linings.
- Concrete permeability.
- Tiles separating from the tunnel liner.
- Detecting integrity of steel liners underneath concrete linings.
- Problems with integrity of ceiling systems and connections to the tunnel lining.

In terms of performance criteria, the expert panel indicated that NDT should detect any defect within or immediately behind tunnel linings that have a minimum surface area of 1 ft^2, and any defect needs to be located within 1 ft of the actual location on the tunnel lining. The panel also indicated that NDT should identify delaminated areas and voids up to 4 inches deep as measured from the lining surface with an accuracy of within 0.25 inches.

The expert panel stated that NDT hardware developed for in-depth assessment of tunnel linings be handheld devices that are easy to use and that can rapidly detect, locate, and report tunnel lining defects; there was a need to develop a simple tunnel lining screening tool that inspectors can use; and NDT should make it easier for users to locate and calculate quantities for areas to be repaired.

RESEARCH AND DEVELOPMENT PLAN

Based on the findings indicated above, the team produced a research and development plan as follows:

- An investigation for detecting delaminations, voids, and water intrusion with NDT: This investigation involved the use of concrete, shotcrete, and steel test specimens constructed at the Texas A&M Transportation Institute (TTI) Riverside Annex. The NDT techniques used in this investigation are ultrasonic tomography, impact echo, ultrasonic surface waves, air-coupled ground-penetrating radar (GPR), ground-coupled GPR, and thermography. The investigation involved 11 concrete and 13 shotcrete specimens constructed by TTI personnel. To simulate delaminations, the team placed plastic sheets

in the concrete specimens and thin cloth sheets in the shotcrete specimens. To simulate air voids, the team placed 1-inch-thick styrofoam wrapped in plastic in the specimens. To simulate water-filled voids, the team placed water-filled plastic bags approximately 1 inch thick. Each slab was 6 ft by 6 ft. The first set of specimens included six intact concrete slabs with thicknesses of 12, 15, 18, and 24 inches, and three defective 15 inch thick slabs with embedded 1 ft by 1 ft delaminated zones in the center of the slabs. The last three slabs contained defects at depths of 1, 2, and 3 inches from the top surface. Two other concrete slabs in this set were 15 inches thick with embedded air voids and water voids at a depth of 8 inches. The second set of slabs used shotcrete and included four intact slabs with thicknesses of 4, 6, 8, and 12 inches, and five 12 inch-thick delaminated slabs. The 1 ft by 1 ft delaminated areas were embedded at the center of each slab at depths of 1, 2, 3, 4, and 8 inches from the top surface. Four other shotcrete slabs contained air voids and water voids with different sizes at different depths. The team also used specimens containing clay lumps constructed under another TTI study, a concrete bridge deck constructed by the University of Texas at El Paso (UTEP) for another SHRP 2 study, a continuously reinforced concrete pavement section on IH 20 in Fort Worth, and an airport runway section at the George Bush Intercontinental Airport.

- Field validation testing of NDT devices using actual tunnels: A pilot project for the SPACETEC equipment was conducted for the Chesapeake Bay tunnel in April 2011. In addition, initial tests with air-coupled GPR and thermal cameras were conducted using two tunnels in Helsinki, Finland. Finally, the team conducted tunnel testing in Colorado, Texas, and Virginia.

- An investigation for detecting loose tiles and moisture underneath tiles using NDT: The NDT techniques to be used in this investigation are the air-coupled GPR, thermal cameras, and sounding. The team used a tiled surface in an actual tunnel for this ongoing investigation.

- Developing NDT for measuring concrete permeability: This involved a laboratory study to correlate NDT measurements with concrete specimens that have different permeabilities, and field verification using existing concrete tunnel linings. The NDT techniques to be used in this investigation are the dielectric probe, air-coupled GPR, resistivity, and ultrasonic surface waves. As shown in this report, concrete permeability cannot be measured directly in the field using air-coupled GPR; however, the team did generate recommendations that relate potential for corrosion to GPR dielectric measurements. In addition, the report indicates how permeability could be estimated if future NDT can measure certain properties.

TEST SPECIMENS

Concrete and Shotcrete Specimens with Simulated Delaminations and Voids

Eleven normal-weight concrete slabs and 13 shotcrete slabs were constructed to mock various defects. The concrete slabs were used to mimic typical concrete tunnel linings with and without reinforcing steel. The shotcrete slabs were constructed to mimic applications in which shotcrete is sprayed on as a finished layer, as typically found in tunnel linings. A specially designed lattice girder, also typical in tunnel wall construction, was used as reinforcement in the shotcrete slabs (Figure 1, bottom right).

Figure 1. Construction of slabs with simulated defects.

The simulated delaminations in these slabs were constructed from three types of material. Delaminations were imitated by using 0.05 mm (0.002-inch) plastic square sheets and 0.25 mm (0.01-inch) cloth squares (Figure 1, top right). Air-filled voids (Figure 1, top left) were constructed by inserting 13 mm (0.5-inch) thick foam squares in vacuum-sealed plastic bags. Water-filled voids (Figure 1, bottom left) were constructed in a similar manner by placing water-filled Ziploc bags within vacuum-sealed plastic bags and carefully padding the defect with concrete/shotcrete during construction so as not to puncture the plastic. Table 1 is a summary of the specimen details.

Table 1. Summary of concrete/shotcrete slab specimens with simulated defects (all slab specimens are nominally 1.83 m x 1.83 m).

SPECIMEN NAME	SPECIMEN DEPTH (mm)	MATERIAL	REINF. DETAIL	DEFECTS	TRUE DEPTH OF DEFECTS (mm)
Alpha	305	Concrete	None	None	N/A
Beta	457	Concrete	* d = 127 mm	Natural crack	N/A
Gamma	305	Concrete	* d = 127 mm	None	N/A
Delta	610	Concrete	None	None	N/A
Epsilon	610	Concrete	* d = 127 mm	None	N/A
Zeta	381	Concrete	* d = 127 mm	None	N/A
Eta	381	Concrete	* d = 127 mm	0.05 mm thin plastic	51 from top
Theta	381	Concrete	* d = 127 mm	0.05 mm thin plastic	76 from top
Iota	381	Concrete	* d = 127 mm	0.05 mm thin plastic	25 from top
Kappa	381	Concrete	* d = 127 mm	Air-filled void (13 mm foam)	203 from top
Lambda	381	Concrete	* d = 127 mm	Water-filled void (Ziploc bag)	203 from top
A	102	Shotcrete	None	None	N/A
B	152	Shotcrete	None	None	N/A
C	203	Shotcrete	None	None	N/A
D	305	Shotcrete	**	Air-filled void (13 mm foam)	193 from top
E	305	Shotcrete	**	Water-filled void (Ziploc bag)	191 from top
F	305	Shotcrete	**	Air-filled void (13 mm foam)	76 from top
G	305	Shotcrete	**	Water-filled void (Ziploc bag)	76 from top
H	305	Shotcrete	**	0.25 mm thin cloth	203 from top
I	305	Shotcrete	**	0.25 mm thin cloth	102 from top
J	305	Shotcrete	**	0.25 mm thin cloth	76 from top
K	305	Shotcrete	**	0.25 mm thin cloth	51 from top
L	305	Shotcrete	**	0.25 mm thin cloth	25 from top
M	305	Shotcrete	**	None	N/A

*Two mats of No. 5 Rebar, at depth "d" from top and bottom, 203 mm on center.
**One lattice girder in center of slab, sitting on bottom form.

Concrete Specimens with Simulated Clay Lumps

In addition to the concrete and shotcrete slabs, six concrete slabs were tested that were constructed in the 1990s by the Texas Transportation Institute as part of a previous research project. These slabs contain manufactured clay lumps of different diameters. The clay lumps are a high-plasticity clay, classified as Burleson Clay CH (American Association of State Highway and Transportation Officials [AASHTO] A-7-6) with a plasticity index (PI) range of 35-45. The slabs and lumps are shown in Figure 2 and are summarized in Table 2 (Specimens A2-F2). These six specimens consist of two sets of three slabs: one set with steel reinforcement and one set without. In each set, one slab was designated as the control with no clay lump contaminations. The remaining two had various levels of lumps of documented sizes corresponding to three regions of interest: (1) lumps below the reinforcement that represent typical lumps dense enough not to be quickly displaced toward the surface via vibration, (2) those that are caught in the reinforcing steel layer on their path toward the surface, and (3) those that are dispersed between the reinforcement and the top surface. The depth of the slabs is nominally 305 mm (12 inches), but all measurements are taken as approximate since neither ground truth data were retrieved nor any accurate pictures were taken to confidently support documented placement.

Figure 2. Clay lump slab construction.

Table 2. Summary of concrete specimens with simulated clay lumps

SPECIMEN NAME	SPECIMEN DEPTH (mm)	MATERIAL	REINF. DETAIL	DEFECTS	TRUE DEPTH OF DEFECTS (mm)
A2	305	Concrete	* d = 152 mm	None	N/A
B2	305	Concrete	* d = 152 mm	Large (152 mm ⌀) clay lumps	152 from top
C2	305	Concrete	* d = 152 mm	Med. (102 mm ⌀) clay lumps	76, 152, 229 from top
D2	305	Concrete	* d = 152 mm	None	N/A
E2	305	Concrete	* d = 152 mm	Large (152 mm ⌀) clay lumps	152 from top
F2	305	Concrete	* d = 152 mm	Med. (102 mm ⌀) clay lumps	76, 152, 229 from top

Concrete Bridge Deck with Simulated Defects

In addition to the above-mentioned slabs, a bridge deck constructed by the University of Texas at El Paso (UTEP) was available for blind testing. The bridge deck was constructed with known artificial delaminations, cracks, and corroded reinforcement. Several parameters were considered in the construction of the artificial delaminations including stacked delaminations, delaminations of various thicknesses (ranging from 0.3 mm [0.01-inch] to 2.0 mm [0.08-inch] thickness), sizes (ranging from 305 mm x 305 mm to 610 mm x 1220 mm [12 inch x 12 inch to 24 inch x 48 inch]), depths (above reinforcing steel at 64 mm [2.5 inches] below surface, and below two layers of reinforcing steel at 152 mm [6 inches]), with some located above prestressed girders supporting the slab. The deck, pictured in Figures 3 and 4, measures 2.4 m x 6.1 m x 0.2 m (8 ft x 20 ft x 8-3/4 inches), and rests on three prestressed concrete girders. Simulated defects constructed in the deck consist of nine artificial delaminations, five cracks, and two corroded reinforcement mats, which are all summarized in Table 3.

In constructing the deck, 27.6 MPa (4000 psi) concrete was used, and two layers of No. 5 longitudinal and transverse steel were placed at 254 mm and 203 mm (10 inches and 8 inches) on center, respectively, at centroid depths of 83 mm and 184 mm (3.25 inches and 7.25 inches) from the surface. The 28-day strength and modulus exceeded 34.5 MPa (5000 psi) and 27.6 MPa (4000 ksi), respectively. A 0.25 mm (0.01-inch) polyester fabric was used to mock an ultra-thin horizontal delamination. The vertical cracks were constructed from both thick and thin cardboard sheets. The No. 5 corroded steel mats were electrically merged and attached to the normal reinforcement. The corrosion depth was measured to be 1-2 mm (0.04-0.08 inch) prior to pouring the concrete.

Figure 3. Simulated bridge deck at UTEP in El Paso, Texas.
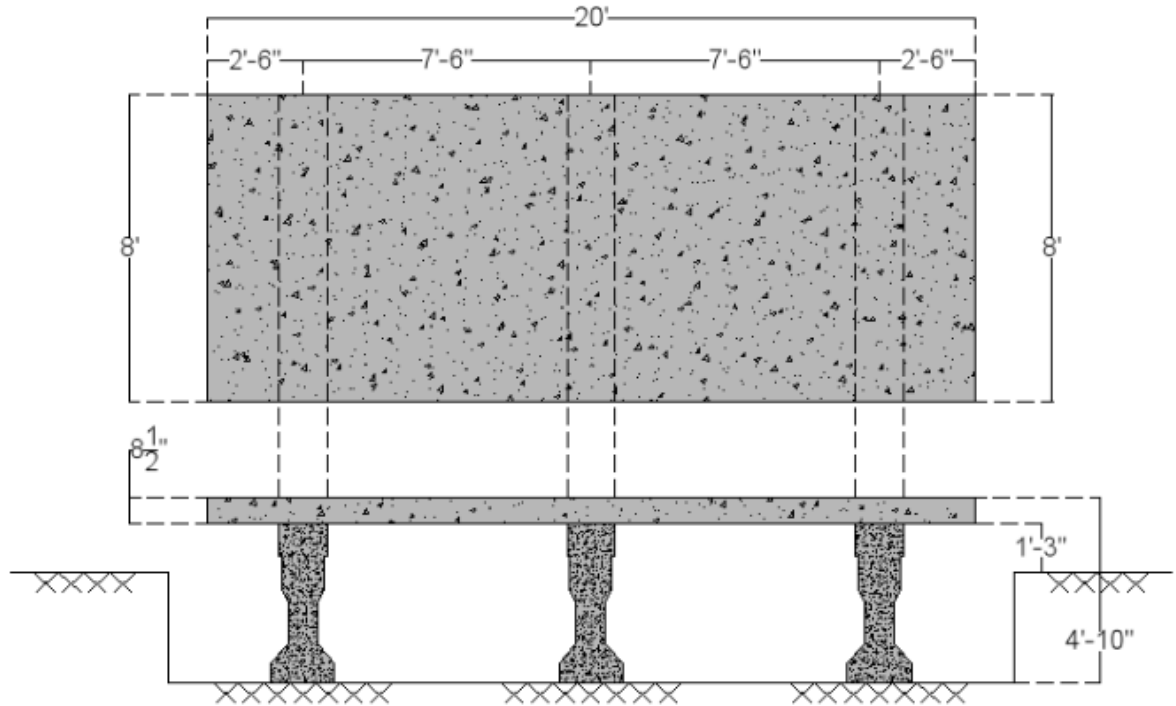
Figure 4. Layout of constructed bridge deck.

Table 3. Summary of simulated defects in the concrete bridge deck.

Simulated Defect	Defect Material	Actual Dimension (mm)	Actual Depth (mm)
Delamination (DL 1)	Soft, high strength 1 mm foam	305 x 305	64
Delamination (DL 2)	Soft, high strength 1 mm foam	610 x 610	64
Delamination (DL 3)	Soft, high strength 1 mm foam	610 x 610	64
Delamination (DL 4)	Soft, high strength 2 mm foam	305 x 305	64
Delamination (DL 5)	Soft, high strength 2 mm foam	610 x 610	64
Delamination (DL 6)	Soft, high strength 2 mm foam	610 x 610	64
Delamination (DL 7)	Soft, high strength 1 mm foam	610 x 610	152
Delamination (DL 8)	Soft, high strength 1 mm foam	610 x 1219	152
Delamination (DL 9)	Soft, 0.25 mm polyester fabric	305 x 610	64
Vertical Crack (CK 1)	Soft, thin cardboard	305 long	64
Vertical Crack (CK 2)	Soft, thin cardboard	305 long	64
Vertical Crack (CK 3)	Soft, thick cardboard	305 long	76
Vertical Crack (CK 4)	Soft, thick cardboard	305 long	152
Vertical Crack (CK 5)	Natural crack (observed after construction)	330 long	64
Corroded Reinforcement (CR 1)	1-2 mm deep corrosion, #5 bars	762 x 762	76
Corroded Reinforcement (CR 2)	1-2 mm deep corrosion, #5 bars	762 x 762	165

TUNNELS TESTED IN THE STUDY

Chesapeake Channel Tunnel, Virginia

The Chesapeake Channel Tunnel (Figure 5) is one of two tunnels that comprise the Chesapeake Bay Bridge Tunnel system, joining southeastern Virginia to the Delmarva Peninsula. Hailed worldwide as a modern engineering wonder, the 37 km (23-mi) long system includes 3.2 km (2 mi) of causeway, four manmade islands, 8.9 km (5.5 mi) of approach roads, 19.3 km (12 mi) of low-level trestle, two 1.6 km (1-mi) steel tunnels, and two bridges. The Chesapeake Channel Tunnel (during construction and briefly afterward it was called the Baltimore Channel Tunnel) was constructed using a cut-and-cover method. Precast steel tubes, fabricated and assembled in Orange, Texas, were floated to a shipyard in Norfolk, Virginia, where the reinforced concrete linings and roadway were constructed. The sections were floated to the site before being sunk into a trench. Each steel tube, 483 km (300 ft) in length and 60 km (37 ft) in diameter, was joined to the other, sealed, and connected to its adjoining section. As each steel section was welded together, patches between the 483 km (300 ft) sections had to be formed with concrete to make an overlapping seal.

Figure 5. Chesapeake Channel Tunnel: entrance (left) and interior view (right).

Eisenhower Memorial Tunnel, Colorado

The Eisenhower Memorial Tunnel, located approximately 97 km (60 mi) west of Denver, Colorado, is one of a 2.7 km (1.7-mi) dual bore project started in 1968. Shown in Figure 6, Eisenhower Memorial, which carries Interstate 70 west, is paired with the Edwin C. Johnson Memorial Tunnel, which carries Eastbound I-70. Although the eastbound bore was not completed until almost 1980, construction on the Eisenhower bore was completed by 1973. Built using drill and blast methods through a mountain with a maximum overburden of 448 m (1470 ft), the average tunnel dimensions were 14.6 m in height (48 ft) and 12.2 m (40 ft) in width. In 2011, the average daily traffic was 28,155 vehicles. All areas of interest evaluated within the tunnel were tested from inside the plenum (above the traffic, Figure 7)

Figure 6. Eisenhower Memorial Tunnel, Colorado.
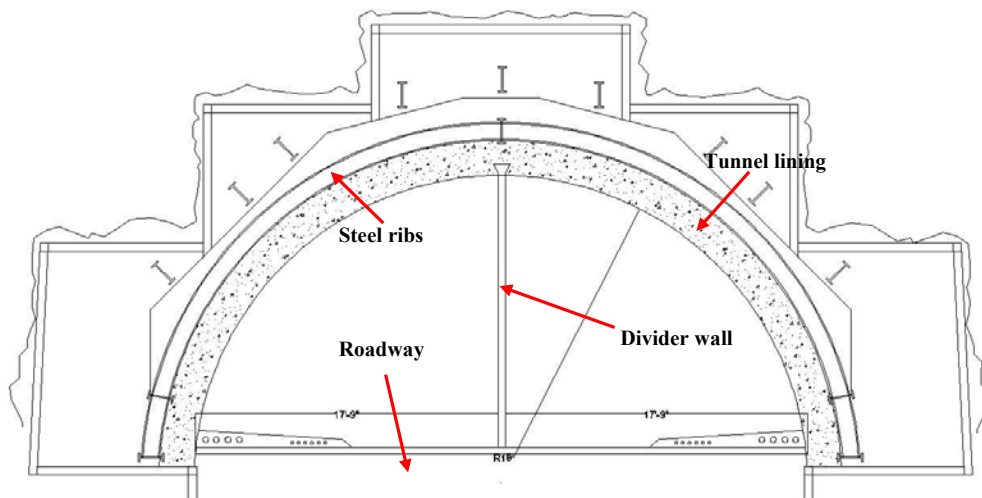
Figure 7. Eisenhower Tunnel plenum view.

Hanging Lake Tunnel, Colorado

Completed in 1992 with a maximum length of 1219 m (4000 ft) through the southern wall of Glenwood Canyon, Hanging Lake Tunnel (Figure 8) was the last link to the Interstate Highway System. Both bores of the tunnel were built using multiple-face drill and blast methods. Between the west and eastbound bores, a four-story control center monitors traffic along I-70, fully equipped with emergency response vehicles and trained staff.
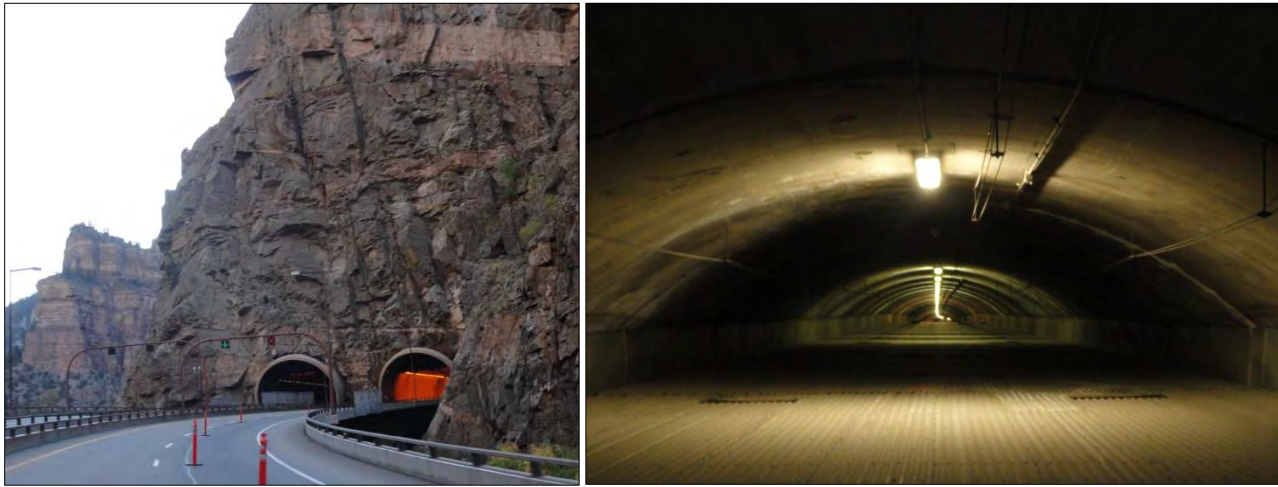
Figure 8. Hanging Lake Tunnel: exterior (left) and interior plenum view (right).

No Name Tunnel, Colorado

The No Name tunnel was constructed in 1965 and is located approximately 7.5 miles west of the Hanging Lake Tunnel. The team collected air coupled ground penetrating radar data and infrared images only in the westbound bore, which is approximately 1,000 feet long. The upper portion of this tunnel consists of a concrete surface; the sides are tiled. Figure 9shows the TTI air coupled GPR system collecting data in this tunnel. Plan sets were not available for this tunnel.

Figure 9. TTI air-coupled GPR system collecting data in the No Name Tunnel.

Washburn Tunnel, Texas

The Washburn Tunnel (Figure 10), the only underwater vehicle tunnel in operation in Texas, was completed in 1950 and carries Federal Road beneath the Houston Ship Channel joining two Houston suburbs. The tunnel was constructed via the immersed tube method, with sections joined together in a prepared trench, 26 m (85 ft) below water. The entire inner wall is tiled with 110 mm by 110 mm (4.3 inches by 4.3 inches) ceramic tiles.
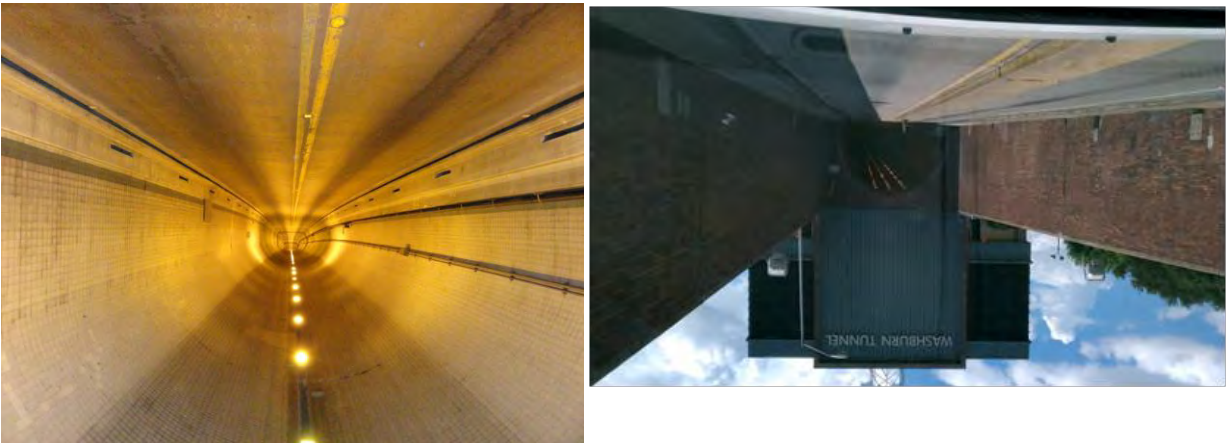
Figure 10. Washburn Tunnel: entrance (left) and interior view (right).

NDT DEVICES AND TECHNIQUES USED IN THIS STUDY

Air-Coupled Ground-Penetrating Radar

Ground-penetrating radar sends discrete electromagnetic pulses into a structure and then captures the reflections from layer interfaces in the structure. Radar is an electro-magnetic (e-m) wave and therefore obeys the laws governing reflection and transmission of e-m waves in layered media. At each interface within a structure, a part of the incident energy will be reflected, and a part will be transmitted.

The amplitude of radar reflections and the time delay between reflections are used to calculate layer thicknesses and layer dielectrics. For purposes of this study, the surface layer dielectric is of most interest. This value is calculated as follows:

$$\varepsilon_a = \left[\frac{1 + \left(\frac{A_1}{A_m} \right)}{1 - \left(\frac{A_1}{A_m} \right)} \right]^2$$

where:

ε_a = the dielectric of the lining surface.

A_1 = the amplitude of reflection from the surface in volts.

A_m =   the amplitude of reflection from a large metal plate in volts (this represents the 100 percent reflection case).

Since such air-coupled systems (Figures 10 and 11) are not in contact with the structure, data collection can theoretically happen at full traffic speeds, although this is not practical for tunnel lining data collection. Currently, air-coupled antenna systems are manufactured by GSSI, Penetradar, Pulse Radar, and Wavebounce, all from the United States; butterfly dipole systems are manufactured by Radar Team Sweden Ab.

Figure 11. TTI air-coupled GPR system collecting tunnel roof lining data in Colorado.

The system used by TTI in collecting tunnel lining data includes a Wavebounce 1-GHz central frequency GPR antenna with distance measuring indicator (DMI) equipment. The system uses data collection software developed by TTI. Researchers used the Pavecheck and Colormap programs, also developed by TTI, to analyze the data. The researchers slightly modified Pavecheck and renamed it Tunnelcheck. This software is available for free download; the user's manual is provided in a separate publication. The researchers also mounted a FLIR T-300 camera on the GPR boom; the TTI data collection system collected images from this camera along with the GPR data.

The penetration depth of air-coupled ground-penetrating radar (ACGPR) is usually around 24 inches for a 1-GHz system. It cannot detect defects in concrete unless there are significant air pockets or significant moisture within the defects. ACGPR can detect reinforcing steel. However, the research team believes that the surface dielectric can be used to determine where to conduct testing with in-depth nondestructive testing devices and techniques.

Appendix A contains the ACGPR testing criteria. Appendix K contains data analysis results from the ACGPR tunnel and specimen testing conducted under this study.

Ground-Coupled Ground-Penetrating Radar

Ground-coupled ground-penetrating radar (GCGPR) needs to be either in contact or very close to the lining surface when collecting data (Figure 12). The operating principles are the same as ACGPR; GCGPR cannot detect defects in concrete unless significant air pockets or significant moisture is within the defects. However, GCGPR can detect defects that ACGPR cannot. GCGPR can also detect reinforcing steel. Researchers used the GSSI 1.5-GHz central frequency GPR antenna during the tunnel tests because shallow defects were found during those tests; researchers used a 900-MHz central frequency GPR antenna during the TTI specimen tests since the researchers were trying to determine if GCGPR can detect deep defects.

Appendix B contains the GCGPR testing criteria. Appendix Q contains data analysis results from the GCGPR testing conducted under this study.

Figure 12. GCGPR equipment.

Handheld Thermal Camera

Handheld thermal cameras (Figure 13) have improved significantly over the past decade, with consistently higher image resolutions and improved temperature accuracy occurring over time. The research team used the FLIR T-300 thermal camera for this study. The researchers analyzed the images for changes in tunnel lining temperature, which could indicate possible defects within or behind the lining. The research team believes that the images from such cameras can be used to determine where to conduct testing with in-depth nondestructive testing devices and techniques.

Figure 13. FLIR T300 thermal camera used in the study.

Appendix C contains the handheld infrared camera testing criteria. Appendix L contains selected images from tunnels and TTI test specimens.

Ultrasonic Tomography

The ultrasonic tomography (UST) system used in this study is a device that uses an array of ultrasonic transducers to transmit and receive acoustic stress waves for the inspection of concrete structures. The system used here, the A1040 MIRA, is produced by Acoustic Control Systems (Figure 14).

Figure 14. The A1040 M IRA system (left) and the transmission/reception of acoustic waves and corresponding echo intensity (right)

The tomograph, shown in Figure 14 (left), uses a 4 by 12 grid of mechanically isolated and dampened transducers that can fit the profile of a rough concrete testing surface with a variance of approximately 10 mm (0.4 inches). Each row of four transducers transmits stress waves sequentially while the remaining rows act as receivers. In this manner, there is a wide

coverage of shear wave pulses that reflect at internal interfaces where the material impedance changes.

With the help of a digitally focused algorithm, a three-dimensional (3D) volume is presented with each point of possible reflection in half-space represented by a color scheme, scaled according to reflecting power. This 3D image can also be dissected into each of the three planes representing its volume: the B-scan, C-scan, and D-scan (Figure 15). The B-scan is an image slice showing the depth of the specimen on the vertical (or z) axis versus the width of scan on the horizontal (or x) axis. This slice is a plane perpendicular to the scanning surface and parallel to the length of the device. The C-scan is an image slice showing the plan view of the tested area, with the vertical (or y) axis of the scan depicting the width parallel to the scanning direction and the horizontal (or x) axis of the scan representing the length perpendicular to the scanning direction. Note that the scanning direction is always defined as the y-axis as seen in Figure 6. The D-scan is like the B-scan in that it images a plane perpendicular to the testing surface, but it is oriented parallel to the scanning direction. On each of the scans, the various intensities reported by the returned waves are color-coded from light blue to deep red, representing low reflectivity (typically sound concrete) and high reflectivity (any type of impedance), respectively. With this intensity scaling, it is easy to see any discontinuities with distinctly different wave speeds, such as voids, delaminations, cracks, and other abnormalities..
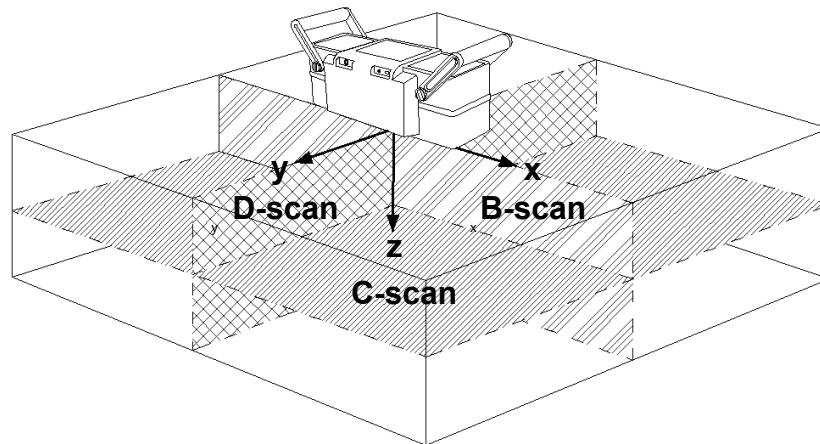

Figure 15. B-scan, C-scan, and D-scan relative to the tomograph

This UST system has had limited exposure to industrial applications but is quickly becoming recognized as a powerful NDT method.

Appendix D contains the ultrasonic tomography testing criteria. Appendix M and Appendix N contain the testing results from tunnel linings and test specimens.

Ultrasonic Echo

An ultrasonic transducer is used to generate and/or receive ultrasonic waves in/from a test medium. Ultrasonic echo technique involves sending and receiving the ultrasonic pulses from the same side of the test object, by the same or two separate transducers. The ultrasonic pulse velocity (UPV) is correlated to material strength or quality. The measurement of propagation

time is used to localize cracks, voids, and delamination and/or to estimate the thickness of a structure. Large enough defects (with respect to the ultrasonic wavelength) and structural boundaries induce a high contrast in acoustic impedance and result in the reflection of ultrasonic waves. The reflected waves are detected in ultrasonic scans, and the two-way travel time is used to estimate the reflector location (assuming or knowing the ultrasonic wave velocity in the test medium).

The handheld ultrasonic transducer used by the German Federal Institute for Materials Research and Testing (BAM) for field testing together with the corresponding data acquisition/analyzer unit is shown in Figure 16. In tunnel testing applications, the ultrasonic echo technique can be used to estimate the thickness of the tunnel lining and to detect delamination and voids within the lining.

Figure 16. Ultrasonic echo equipment A1220 Monolith by ACSYS.

Appendix E contains the ultrasonic echo test criteria. Appendix Q contains data analysis results from the ultrasonic echo testing conducted under this study.

Ultrasonic Surface Waves and Impact Echo Methods with the Portable Seismic Property Analyzer (PSPA)

Ultrasonic Surface Wave (USW) Method

The USW method is used to estimate the average velocity of propagation of surface waves in a medium, based on the time at which different types of energy arrive at each sensor (Figure 17a). The velocity of propagation, V_R, is typically determined by dividing the distance between two receivers, ΔX, by the difference in the arrival time of a specific wave, Δt. Knowing the wave velocity, E, the modulus can be determined from shear modulus, G, through Poisson's ratio (ν) using:

$$E = 2(1+\nu)G$$

Shear modulus can be determined from shear wave velocity, V_S, using:

$$G = \frac{\gamma}{g}V_S^{\ 2}$$

25

To obtain the modulus from surface wave velocity, V_R is first converted to shear wave velocity:

$$V_S = V_R(1.13 - 0.16\nu)$$

In the USW method, the variation in velocity with wavelength is measured to generate a dispersion curve. For a uniform or intact tunnel lining, the dispersion curve shows more or less a constant velocity within the wavelengths no greater than the thickness of the slab. When a delamination or void is present in a concrete slab or the concrete is deteriorated, the average surface wave velocity (or modulus) becomes less than the actual one due to the interference caused by the defect. In this case, the velocity or modulus obtained may be called an apparent velocity or modulus.
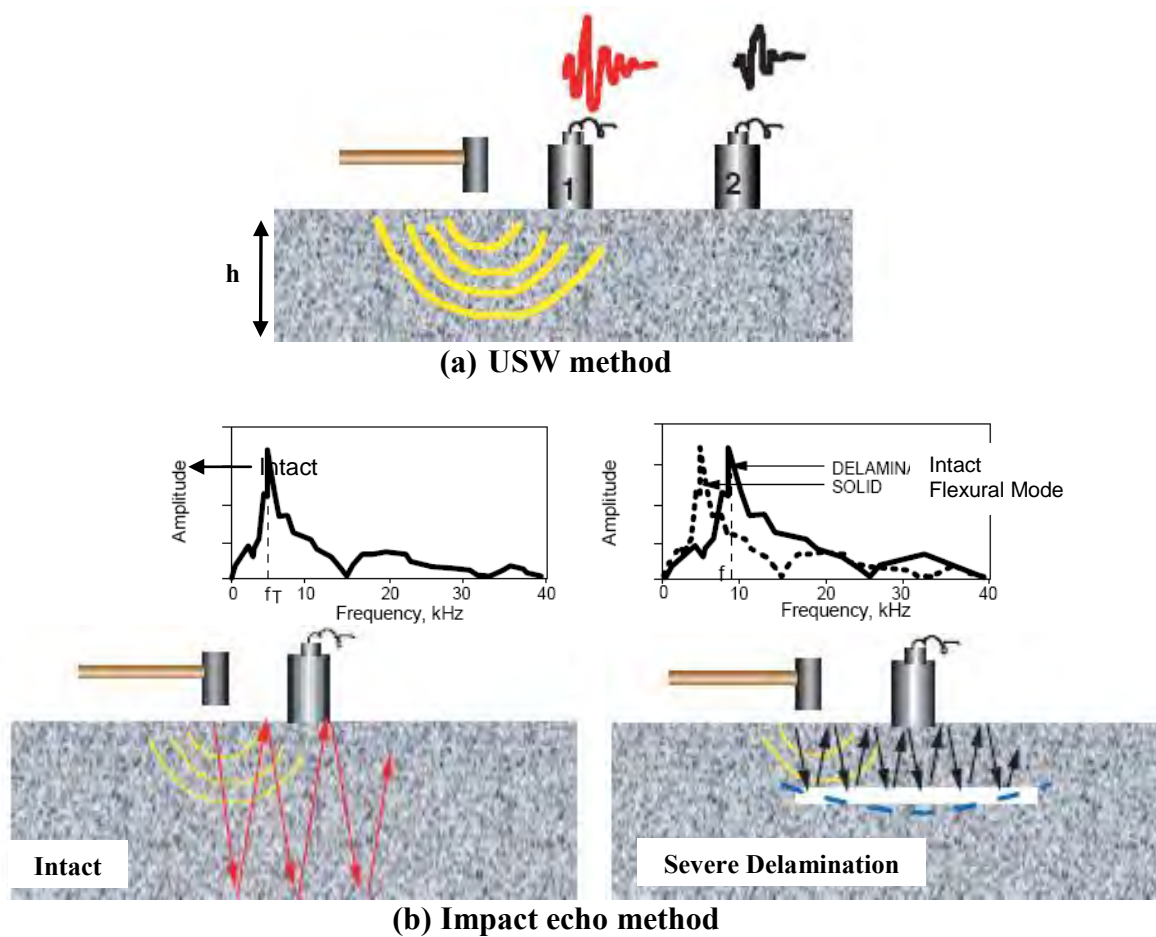

(a) USW method

(b) Impact echo method

Figure 17. Schematic illustration of the test methods (Gucunski and Maher, 1998).

Impact Echo (IE) Method

The IE method is one of the most commonly used NDT methods in detecting delamination in concrete. This method is based on impacting a plate-like object such as a tunnel lining with an impactor that generates stress waves at frequencies of up to 20 to 30 kHz, and collecting signals by a receiver (Figure 17b). By using a fast Fourier transform (FFT) algorithm,

26

the recorded time domain signal is converted into a frequency domain function (amplitude spectrum), and the peak frequency is monitored. For an intact point on a slab, the thickness (h) is then determined from the compression wave velocity (V_p) and the return frequency (f):

$$h = \alpha \frac{V_p}{2f}$$

where α is about 0.96 for concrete slabs.

For a deep and relatively small delaminated location in a tunnel lining, the return frequency may shift to a higher frequency corresponding to the depth of the delamination. As shown in Figure 16b, a shallow or a deep but extensive and severe delaminated area is usually manifested by a low peak frequency, indicating that little or no energy propagates toward the bottom of the deck, and a flexural mode dominates the frequency response. In this case, the equation is not applicable to measure the depth of delamination since it is influenced by several factors.

Description of the PSPA

USW and IE measurements can be performed with these two methods simultaneously with the PSPA shown in Figure 18. The traditional PSPA is a box containing a solenoid-type impact hammer and two high-frequency accelerometers (Figure 18a). All controls and data acquisition are in a computer that is connected to the box. The two receivers allow the calculation V_p using the USW method. The test at a single point is simple and takes less than 30 s. The impact duration (contact time) is about 60 μs, and the data acquisition system has a sampling frequency of 390 kHz.

(a) Traditional device

(b) New version

Figure 18. PSPA.

As shown in Figure 18b, the PSPA has been redesigned to make it more user friendly and compact for tunnel work. The new PSPA is self-contained, and there is no need for an external computer to collect data. The waveforms collected in the field are stored in a removable flash memory. The new PSPA is also lighter as compared with the traditional PSPA (8 lb versus 16 lb). Data collection with the new PSPA is a two-hand operation, which can accommodate the curvature within the tunnel more easily. Data acquisition with the new PSPA is on average two to three times faster than the traditional one. Also the new PSPA is equipped with three receivers to better optimize the data collection for the combined IE-USW methods. The power source for the device is six AAA battery placed in a container that can be carried by the operator on her or his belt. Typical signals collected with the PSPA are shown in Figure 19. These signals are used to develop USW dispersion curves and the IE amplitude spectra. The advantage of combining USW and IE methods in a single device is that once the test is performed, the variations in the modulus (an indication of the quality of concrete) and return resonance frequency (an indication of the full thickness or depth of delamination) of a slab can be assessed concurrently.
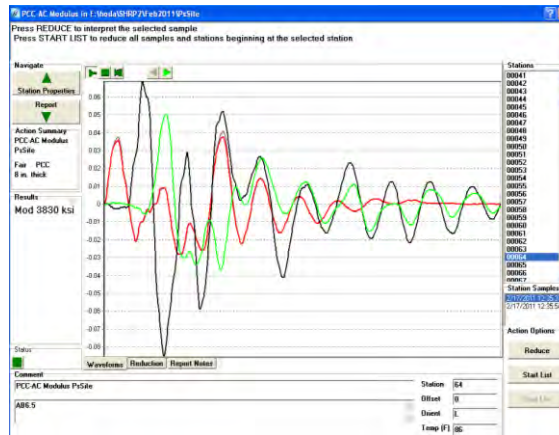

Figure 19. PSPA sample test results.

Figure 20 compares typical USW dispersion curves from an intact area and a defective area. The dispersion curve shifts to lower moduli in defective areas. The amplitude spectra for typical intact and defective points are shown in Figure 21. Based on an average compression wave velocity of about 14,000 ft/s measured for the concrete, the dominant frequency corresponding to the tunnel thickness (15 inches) is around 5.4 kHz. As compared to the intact point, higher peak frequencies mostly control the response at the defective points.
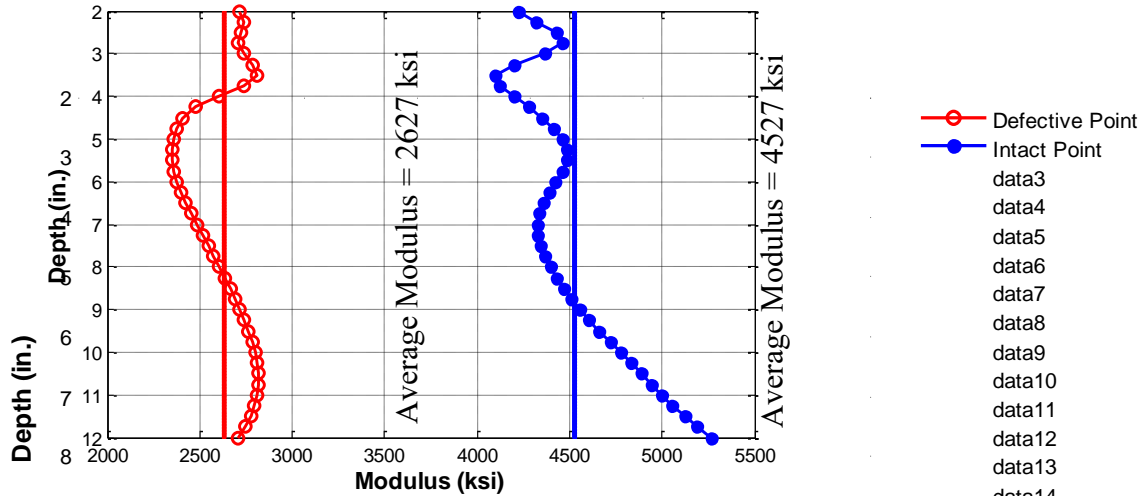
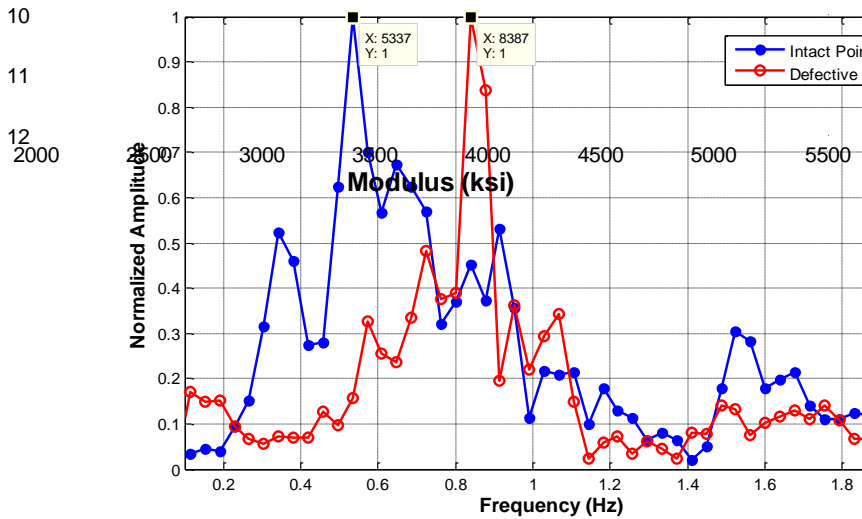**Figure 20. Typical dispersion curves for intact and defecti**

Figure 21. Typical amplitude spectra for intact and defecti

SPACETEC Scanner

The SPACETEC scanner (Figure 22) is a mature system developed
inspection of railway and roadway tunnels. Therefore, employing this tech   ose
of this project requires no additional hardware/software development. The
been already used to survey many miles of railway and roadway tunnels (n
different countries, but it has never been used in the United States prior to

The SPACETEC TS3 scanner records three different measurement

- Surveying the cross-sectional tunnel profile.
- Full-surface visual recording of the tunnel lining.
- Full-surface thermographic recording (thermal imaging) of the tunnel surface.

Figure 22. SPACETEC scanner in the Chesapeake Bay Tunnel.

The measurements are processed and can be viewed individually or together to detect and locate tunnel surface and near-surface anomalies. The high-resolution visual recording allows a thorough inspection of the tunnel surface and, combined with the profiling, the location of surface defects. The cold spots in the thermal images are usually indications of near-surface moisture. Superimposing the thermal images on the visual recordings allows such moist zones to be easily identified. Monitoring the changes in the tunnel profile over time presents another potential application of this system.

Appendix I contains results of the SPACETEC testing in the Chesapeake Bay Tunnel.

Other NDT Devices and Techniques Used in the Study

The research team used resistivity and dielectric probe devices during this research. However, the devices were only useful in a laboratory environment and are not recommended for use in tunnel lining field tests. Appendix L contains the results of a laboratory study that attempted to correlate dielectric (or permittivity) measurements to concrete permeability. Researchers used resistivity and dielectric probe equipment during this laboratory study.

Researchers also attempted to develop an acoustic sounding technique for detecting delaminated tiles. Appendix O contains a description of the technique and the results obtained so far. This technique is still under development; thus, it is not ready for implementation at this time.

The team did collect thermal data in Finland and U.S. tunnels with a vehicle-mounted system. Researchers used the FLIR A325 thermal camera for this system. This camera has the same thermal measurement specifications as the FLIR T300 handheld thermal camera. Roadscanners developed commercial software before this SHRP 2 study began that collects and helps analyze such data for the FLIR A325 camera. Although the results from the testing are promising, the team does not recommend implementation of the system at this time. Further

software refinements are needed before this system can be implemented effectively. Appendix H contains the system's testing criteria. Appendix L contains images from this system.

As described later in this report, the research work in Finland also involved the use of laser scanning systems. Although the data analysis results and images from these systems did not apply directly to the goals of this project, the testing results in Finland indicated that the system provided interesting and useful data relating to the shape (or profile) and the surface condition of the tunnel lining. Appendix J more information about the results of testing with these systems.

Finally, Dr. Fulvio Tonon conducted digital photogrammetry work in three tunnels during the course of this project. Although the data analysis results and images from this technique did not apply directly to the project, the results may be of interest to the reader. Appendix X contains a description of and results from this technique.

CHAPTER 3
FINDINGS AND APPLICATIONS

AN INVESTIGATION FOR DETECTING DELAMINATIONS, VOIDS, AND WATER INTRUSION

Introduction

As indicated in the previous chapter, this investigation involves the use of concrete, shotcrete, and steel test specimens. The NDT techniques used in this investigation are the ultrasonic linear array system, air-coupled GPR , ground-coupled GPR , thermal camera, and the portable seismic property analyzer.

Ultrasonic Tomography

The results of the ultrasonic tomography testing are contained in Appendix M and Appendix N.

As indicated in Appendix D and Appendix M, the team concluded that the system is effective in detecting defects but with the following limitations:

- Speed of data acquisition is low (0.8 to 2.3 min/ft^2).
- There is no phase change information to infer defect type.
- No information deeper than initial air interfaces is discernible.
- The system has difficulty detecting reinforcement below two layers of reinforcement mesh.
- For a 50-kHz use, defects under 2 inches from the surface are not directly detected.
- For a 50-kHz use, reinforcement under #5 (0.625-inch diameter) is not typically detected.

Air-Coupled GPR

TTI personnel used the specimens described previously for this investigation. Details of the results are in Appendix K of this report. The team used a 1-GHz central frequency device owned by TTI.

The TTI team determined that the equipment could only detect three simulated voids, all of them located in the shotcrete sections. Those specimens are:

- Specimen D (air-filled void placed 7.625 inches from the surface).
- Specimen F (air-filled void placed 3 inches from the surface).
- Specimen G (water-filled void placed 3 inches from the surface).

The equipment could not detect delaminations or voids in the other specimens. The delaminations in the specimens did not contain significant air pockets or moisture, so GPR would not be effective in any case.

The team estimated the depth to the defect using air-coupled GPR analysis software developed by TTI. For specimen D, the estimated depth is 7.7 inches. For specimen F, the estimated depth is 2.6 inches. For specimen G, the estimated depth is 2.7 inches.

The team also collected ACGPR data on a 12-inch-thick plain concrete specimen placed on top of a steel plate with a 1-ft^2 void in the center of the plate. The team determined that the equipment could not locate this defect. The team repeated the test with a 15-inch-thick specimen with two layers of reinforcement. Again, the team determined that the equipment could not locate the defect.

Although layer depth information, areas of moisture, and areas of low material density can possibly be measured with air-coupled GPR, the team recommends using surface dielectric measurements from this device to determine areas to test with other devices. Normal concrete has a dielectric value usually between 8 and 12. Values above this range indicate excessive moisture; values below this range indicate lower than normal material density (i.e., more air voids). Air has a dielectric value of 1; water has a dielectric value of 81.

Ground-Coupled GPR

The team has collected data using a 900-MHz GCGPR on five reinforced concrete specimens. Three specimens had simulated 1-ft^2 delaminations, one specimen had a simulated 1-ft^2 air-filled void placed 8 inches from the surface, and the final specimen had a 1-ft^2 water-filled void placed 8 inches from the surface. The team determined that the equipment could not locate the defects. The delaminations in the three specimens did not contain significant air pockets or moisture, so GPR would not be effective in any case. The voids in the other two specimens were located under a layer of reinforcement that consisted of Number 9 rebar placed at an 8-inch spacing in both directions. As a result, the GCGPR could not see through this layer of reinforcement However, as documented in the literature, ground-coupled GPR is effective in detecting voids and significant delaminations in concrete, provided the correct device is used.

The team also collected GCGPR data on a 12-inch-thick plain concrete specimen placed on top of a steel plate with a 1-ft^2 void in the center of the plate. The team determined that the equipment could not locate this defect. The team repeated the test with a 15-inch-thick specimen with two layers of reinforcement. Again, the team determined that the equipment could not locate the defect.

However, as described in Appendix Q, the GCGPR data showed defects in tunnel linings relatively near the tunnel lining surface.

Thermal Camera

In this investigation, the TTI team used a FLIR T-300 infrared camera owned by TTI. The team collected infrared images on the specimens during the daytime and nighttime. Details of the results are in Appendix L of this report.

The camera images indicated defects in three shotcrete specimens: the 3-inch-deep air-filled void (specimen F), the 3-inch-deep water-filled void (specimen G), and the 1-inch-deep delamination (specimen L). The image for specimen F was the most distinct. The images did not indicate the defects in the other specimens. The team noted that surface texture did influence the surface temperature measured by the camera.

Portable Seismic Property Analyzer (Impact Echo and Ultrasonic Surface Waves)

The IE and USW results on the TTI specimens are shown in Appendix U. As an example, a USW planar contour map and an IE spectral B-scan on selected intact concrete and shotcrete slabs are shown in Figure 23. In spite of the heterogeneity of shotcrete slabs, the contour maps of the variations in average USW modulus and dominant IE frequency exhibited reasonable uniformity for intact slabs (both concrete and shotcrete). In most cases the variation in modulus with depth was quite small. The reported thicknesses from spectral B-scan agreed well with the actual slab thicknesses. However, the peak frequency along the centerline of shotcrete slab varies more significantly than the concrete slab, mostly due to the heterogeneity of shotcrete. In spite of the effectiveness of the IE method in estimating the slab thickness, this method, as configured in the PSPA, cannot estimate the thickness of slabs that are thicker than 18 inches or thinner than 6 inches.
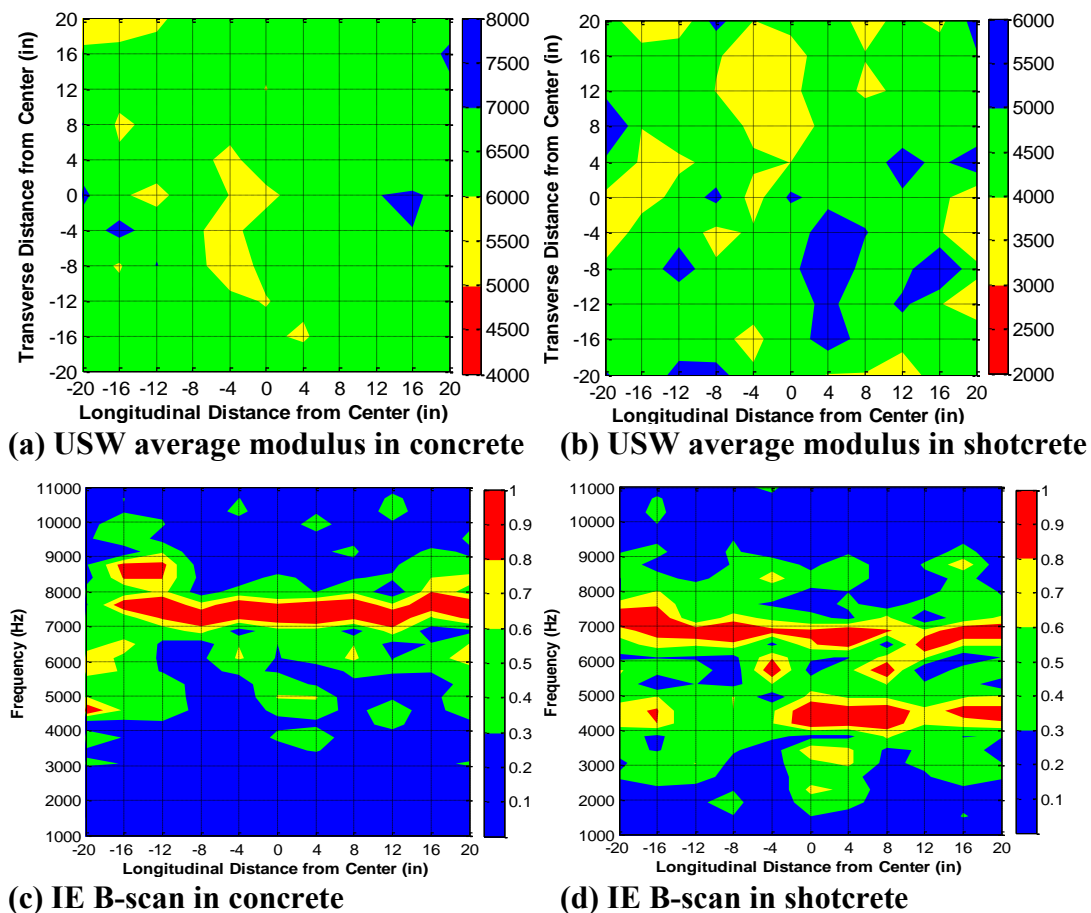

(a) USW average modulus in concrete   (b) USW average modulus in shotcrete

(c) IE B-scan in concrete   (d) IE B-scan in shotcrete

Figure 23. PSPA results on 12-inch-thick intact concrete and shotcrete slabs.

The manifestations of shallow delaminated zones or voids were quite apparent on the time records collected by the device. USW and IE contour maps on selected defective concrete and shotcrete slabs are shown in Figure 24. Both methods provided confirmatory planar maps of shallow (3-inch) defects. As the defects became deeper, the USW average modulus became less sensitive to the presence of defects, while the thickness mode (as opposed to the flexural mode) of the IE method became more effective. This occurs because surface waves propagate along a cylindrical front, and thus they became less sensitive to horizontal discontinuities with depth. Deep defects (deeper than 6 inches) were not readily detectable from the USW results. However, they could be readily identified through the IE results.

Due to the size of the specimens, reflections from the vertical boundaries sometimes affect the frequency content of the signal. The PSPA software contains appropriate filters to minimize the impact of these reflections as long as the slab is not very thick and the PSPA is located at an adequate distance from the boundary.

(a) USW results in 15-inch-thick concrete   (b) USW results in 12-inch-thick shotcrete

(c) IE results in 15-inch-thick concrete   (d) IE results in 12-inch-thick shotcrete
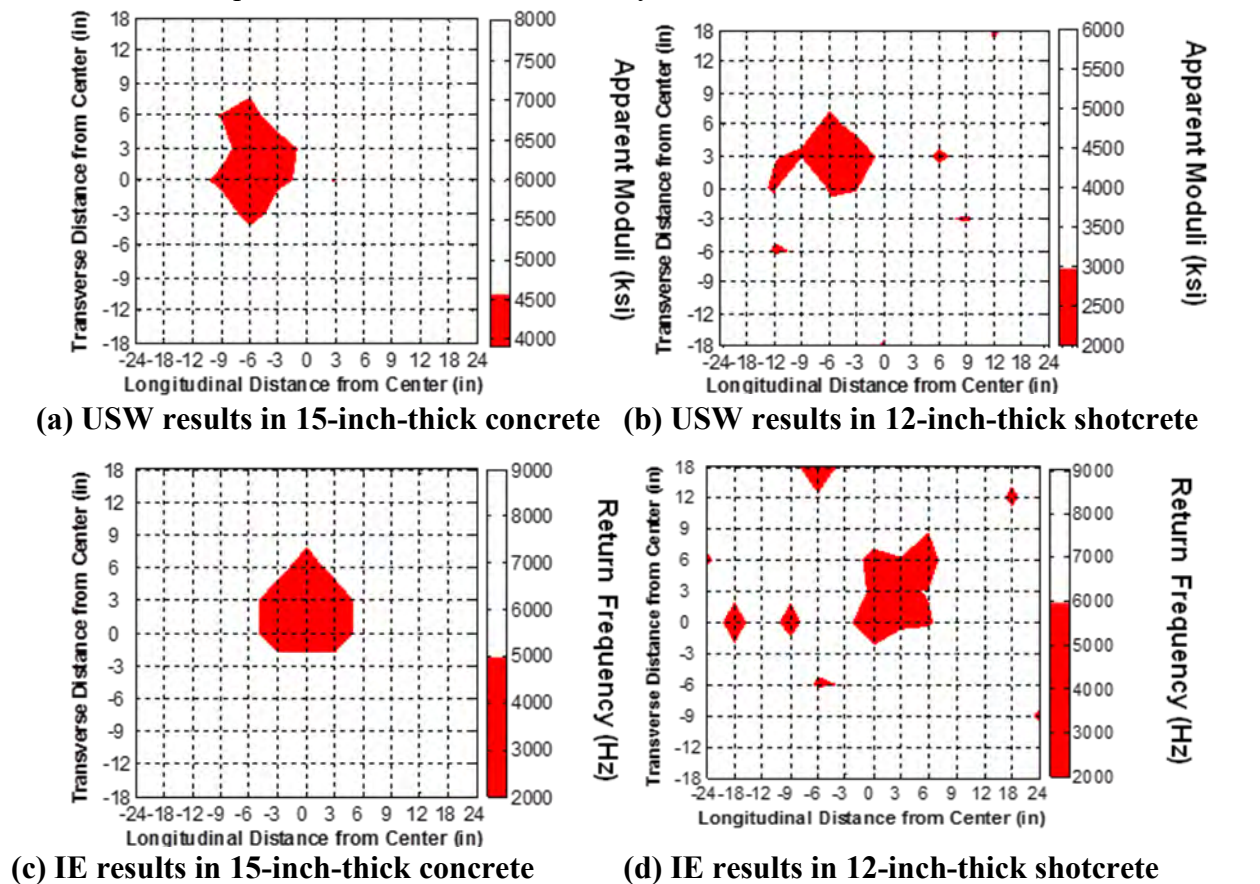
Figure 24. Contour maps of USW average modulus and IE dominant frequency in concrete and shotcrete slabs with embedded delamination at 3 inches from top surface.

35

FIELD VALIDATION TESTING OF NDT DEVICES USING ACTUAL TUNNELS

Introduction

This section summarizes the results of the following:

- A pilot project for the SPACETEC equipment.
- Initial tests with air-coupled GPR and thermal cameras in Finland.
- Tunnel testing in Texas, Virginia, and Colorado.

SPACETEC Pilot Project

The research team conducted the SPACETEC pilot project during the night between April 11 and 12, 2011. The TS3 scanner was installed on the roof in the rear part of the inspection vehicle . This provided an undisturbed 360-degree measurement. The highest resolution of 10,000 pixels was used for an appropriate imaging of fine-scale features.

A full traffic closure was not possible; thus, the recording was performed twice: in the north-south direction of the lane to Virginia Beach and vice versa on the opposite lane toward the eastern shore of Virginia. The traffic could pass the inspection vehicle, as is visible in the recordings.

Appendix I contains a report from SPACETEC concerning the testing in the Chesapeake Bay Tunnel in April 2011. SPACETEC provided a copy of the TuView software that is used to analyze the data from this equipment. SPACETEC personnel indicated areas of concern in the data files that are displayed by the software. The team was interested in the infrared images from this equipment (this SHRP 2 study does not involve evaluating profile or visual images).

The team discussed the results of this testing in person with Chesapeake Bay Bridge and Tunnel (CBBT) personnel using the TuView software. CBBT personnel and the team compared SPACETEC infrared images to CBBT construction plans for a tunnel tile replacement project.

In addition, the SPACETEC equipment operator reviewed the infrared images immediately after data collection in April 2011. He noticed an area on the tunnel wall that appeared to have a defect according to the infrared image. This image is shown in Figure 25.
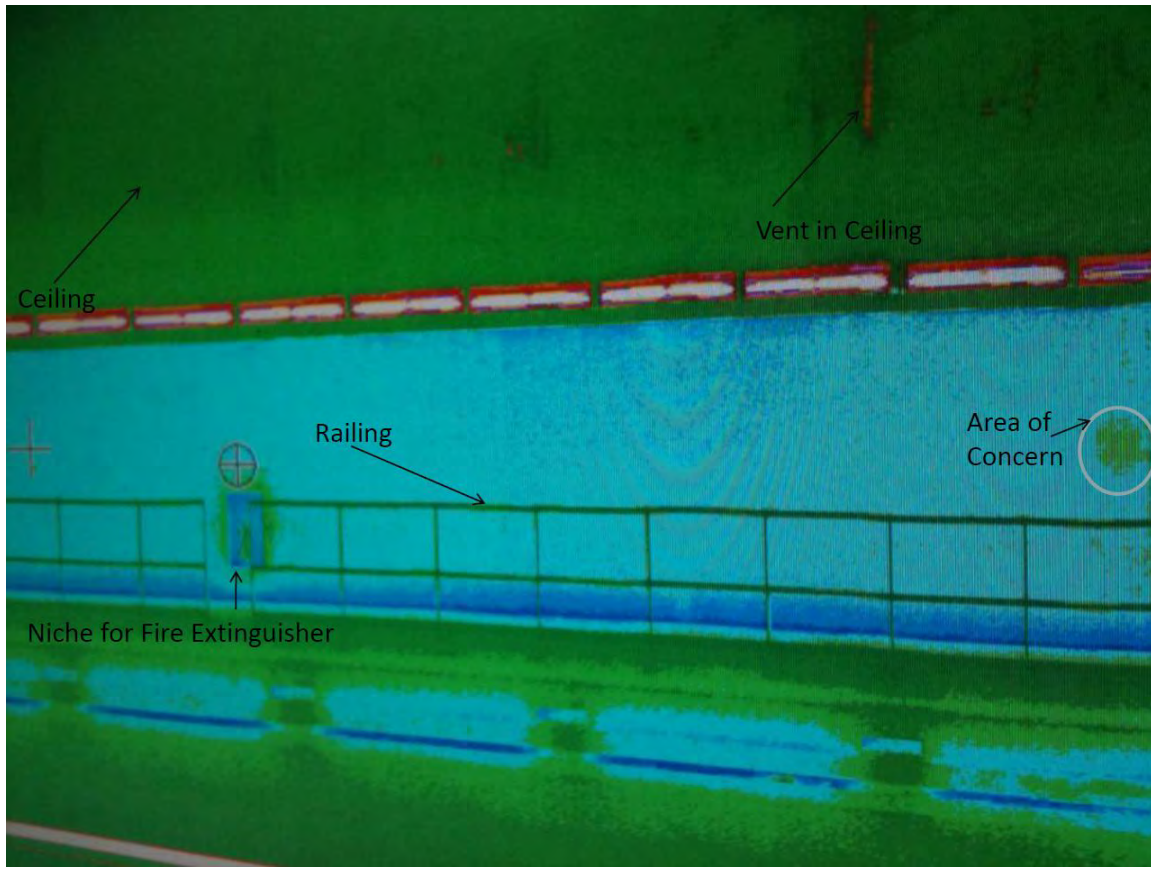
Figure 25. Infrared image from SPACETEC indicating an area of concern.

The team evaluated this area using impact echo and determined that there did appear to be a problem in this area.

The team compared the SPACETEC thermal images to the hammer sounding results. 97% of areas including more than 50 tiles could be detected, compared to 55% for areas covering less than 50 tiles. An additional analysis was performed to investigate why some of the debonded areas were not detected in Spacetec data. Very small debonded areas covering less than 20 tiles seem not to be always detectable in thermal images obtained during this particular survey. Reflection of light from the surface of tiles (at certain scanning angles) and the interference with the temperature gradient in front of the air vents were found to be the top two factors why larger debonded areas were not detected. In any case, the great advantage of such scanning operations becomes obvious considering the speed of the SPACETEC survey (about one hour at 1.5 km/h or 1 mph) in comparison to that of the tedious hammer sounding (one man-month). Appendix V contains the results of this analysis.

To summarize, the team's analysis suggests that a combination of thermal and visual imaging offers an alternative to the tedious practice of hammer sounding on individual tiles to determine tile debonding.

Initial Tests with Air-Coupled GPR, Thermal Cameras, and Laser Scanners in Finland

The tests in Finland concentrated on research of the technical feasibility of air-coupled GPR systems, thermal cameras, and laser scanners, as well as their integrated analysis, for tunnel lining condition monitoring. The idea was to test whether these systems can provide reliable and repeatable data and to collect information concerning the potential sources of error in these techniques. Another goal for these tests is to provide basic information on the potential defects, such as moisture problems close to the surface of tunnel lining structures. These tests were carried out in two tunnels in the Helsinki area in Finland. The first tunnel was a concrete tunnel, and the other lining was made of shotcrete.

The two tunnels described above were used to determine if air-coupled GPR can be used in different types of tunnel lining measurements, Air-coupled GPR data collection settings were the same as used normally in pavement thickness and quality control surveys. The collected data preprocessing was done using standard methods, including automatic air-coupled elevation and amplitude correction, background removal, and vertical time domain filtering. The standard GPR data analysis consisted of reflection amplitude and dielectric value calculations and their analysis.

The same two tunnels were also used to determine how well digital thermal cameras can detect thermal anomalies from tunnel linings, pointing out areas of moisture anomalies, voids, or cracks. In addition, different kinds of data collection and analysis techniques were used to find an optimal survey method.

The goal in the laser scanner tunnel tests was to test if the method could provide valuable information concerning the tunnel lining condition and shape. Although laser scanning is beyond the scope of this project, the results were of interest to the team.

The following findings are of particular interest for this study:

- GPR horn antenna data provided good quality structural information from the concrete tunnel but could not be used in the shotcrete tunnel where steel fibers were used in the shotcrete. The GPR data provided useful information on structures behind the tunnel linings.
- The optimum distance from the air-coupled GPR antenna to a tunnel lining surface is 0.5 m (or 19.7 inches).
- The thermal camera gave excellent results on a shotcrete tunnel. However, in a new concrete tunnel, hardly any anomalies could be detected with the system. One reason for this may be there were no problems close to the surface.
- The thermal camera results are repeatable, but it has to be taken into account that tunnel wall surface temperature can change during the day.
- Thermal anomalies can be seen in different ways when the surveys are conducted in summer, fall, and winter. The best time for surveys is early summer. However, results, surprisingly, showed that moisture anomalies could always be seen as colder areas.

- The thermal camera is sensitive to the survey direction to the tunnel wall and roof, and focusing the camera on white tiles can be difficult. Also, the survey van can cause unwanted thermal reflections.
- Laser scanning systems provided very useful data of the shape and condition of the tunnel linings. The results were excellent, especially in the shotcrete tunnel, but interesting and valuable info was also detected in the concrete tunnel.

Although layer depth information, areas of moisture, and areas of low material density can possibly be measured with air-coupled GPR, the researchers used surface dielectric measurements from this device to determine areas to test with in-depth devices. Normal concrete has a dielectric value usually between 8 and 12. Air has a dielectric value of 1; water has a dielectric value of 81. Values above this range indicate excessive moisture; values below this range indicate lower than normal material density (i.e., more air voids).

Appendix J contains a report concerning tunnel testing in Finland.

Tunnel Testing in Texas, Virginia, and Colorado

The team conducted nondestructive testing in the following tunnels:

- Washburn Tunnel, located under the Ship Channel east of Houston, TX: The TTI team collected air-coupled GPR, ultrasonic tomography, and acoustic sounding data in this tunnel in September 2011..
- Chesapeake Bay Tunnel, located east of Norfolk, VA: The team collected nondestructive testing data in this tunnel in September and October 2011.
- Hanging Lake Tunnel, located on IH 70 west of Denver, CO: The team collected nondestructive testing data in this tunnel in October 2011.
- No Name Tunnel, located on IH 70 west of Denver, CO: The TTI team collected air-coupled GPR data in this tunnel in October 2011.

The following is a summary of the results from the tunnel testing.

Air-Coupled GPR

The team used the TTI 1 GHZ air coupled GPR system for collecting data in the tunnels described earlier. In particular, the team collected data at a one foot spacing in the plenums of the Chesapeake Bay, Eisenhower, and Hanging Lake tunnels; and along the tiled roadway sections in the Chesapeake Bay, Hanging Lake, and No Name tunnels. As mentioned earlier, the research team was most interested in the surface dielectric measurements from this device. The team mounted the equipment on a cart for testing in the plenums, and on a vehicle with a crane for testing in the roadway.

Figure 26 shows results from testing on the Chesapeake Bay Tunnel roof. As shown in the figure, the surface dielectric varies, with significant peaks occurring in several areas. The research team was not able to test all areas due to time constraints. However, one high dielectric

area selected for testing did contain a shallow delamination, but no visual distress was present. Researchers could only collect ACGPR data along the top of the tunnel roof. The presence of cables and conduits on the sides of the tunnel roof made it impossible to collect GPR data in those areas.
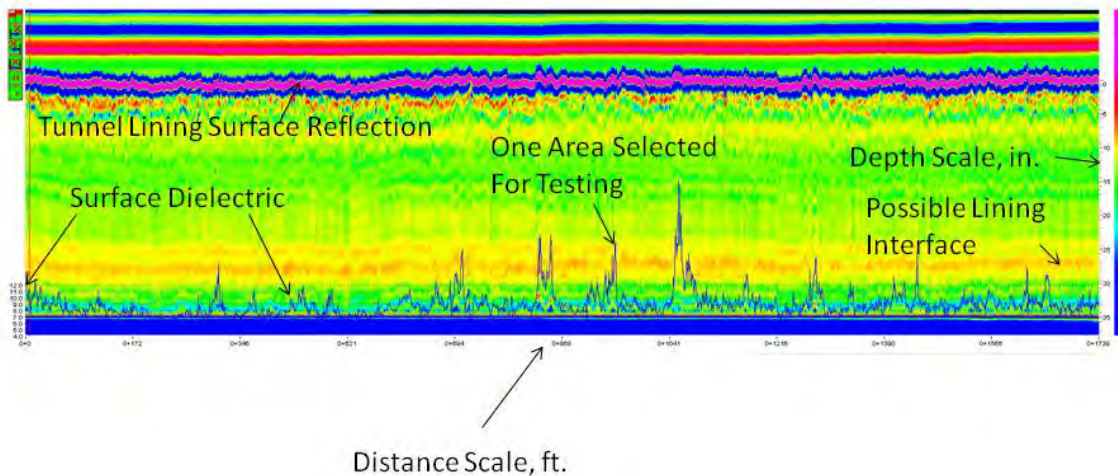

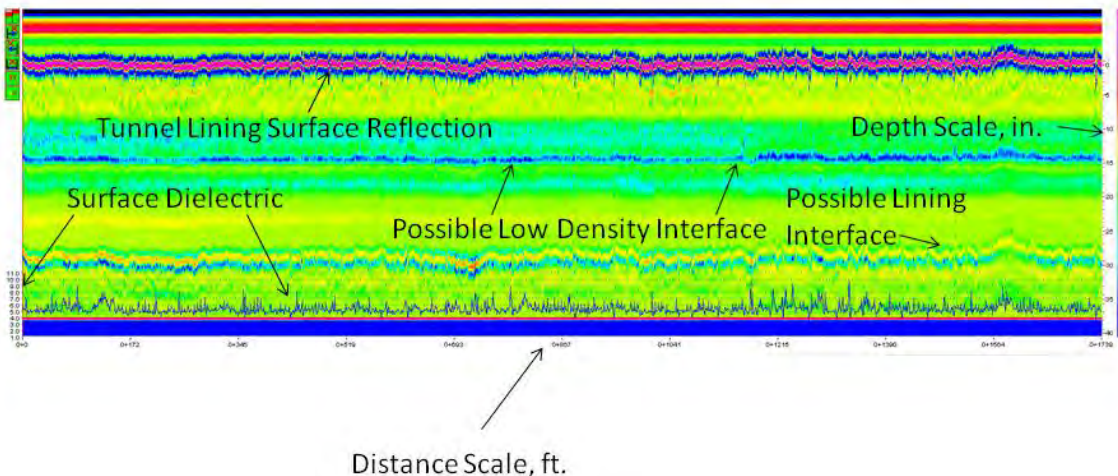**Figure 26. Air-coupled GPR data for the Chesapeake Bay Tunnel roof.**

Figure 27 shows results from testing on the Hanging Lake Tunnel roof. In this case, none of the surface dielectric values exceed 11. However, there are peaks in the values at several locations; these areas should be inspected more closely. This tunnel roof contained many cracks with moisture; however, the moisture usually was outside of the GPR testing area. Again, the presence of cables and conduits on the sides of the tunnel roof made it impossible to collect GPR data in those areas.

Figure 27. Air-coupled GPR data for the Hanging Lake Tunnel roof.

To summarize, the team recommends that the surface dielectric measurements from air coupled GPR be used for scanning purposes in order to determine where more in depth inspection and testing may be desired. The team noted surface dielectric changes in both

concrete and tile lined tunnels. In general, the researchers recommend inspecting areas where the surface dielectric is greater than 11 or if significant peaks or troughs in the dielectric value are observed. The team did note that the data analysis could indicate lining interfaces and lining thickness estimates; however, actual defects within or behind the tunnel lining could not be readily determined from the analysis. In addition, more work is needed to keep the antenna at a relatively constant distance between it and the lining in order to calculate reasonable surface dielectric values; ideally, ideally the variation in this distance should not be more than four inches from the recommended distance (usually 19.7 inches). Appendix K contains the data analysis of ACGPR data collected in tunnels.

Thermal Cameras

The team collected thermal images using both handheld and vehicle-mounted thermal cameras in all of the tunnels tested in this project . Both cameras were able to detect significant thermal changes that indicate possible problems at those locations, both on concrete surfaces and tile lined surfaces. Figure 28 shows a thermal camera image from the top of the Eisenhower Memorial Tunnel. Cracks and stalactites containing moisture are indicated in light blue. The team recommends that the handheld thermal camera be used for scanning purposes where more in depth inspection and testing may be desired. In particular, areas with images that contain significant thermal differences from the surrounding lining should be investigated. Appendix L contains more images from these devices.
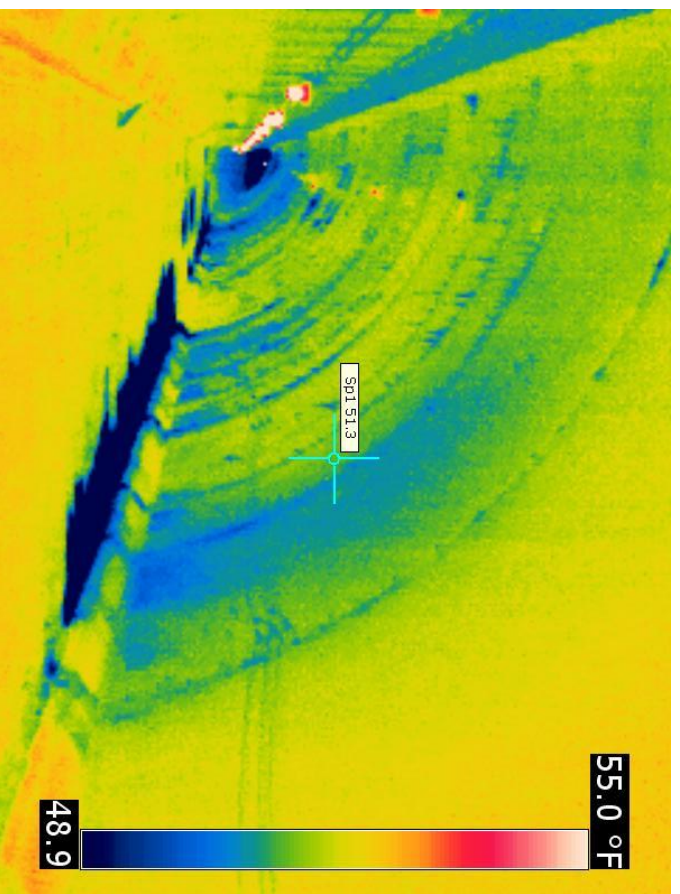
Figure 28. FLIR T300 infrared image of the top of the Eisenhower Memorial Tunnel.

Ultrasonic Tomography

Field evaluations of four public tunnels were conducted using the ultrasonic tomography (UST) technique to evaluate natural structural defects within actual tunnel linings. The tunnels tested consisted of the Eisenhower Memorial Tunnel; Hanging Lake Tunnel; Chesapeake Bay Tunnel; and Washburn Tunnel. Because the UST technique does not currently have a testing methodology that is field ready, the system was first evaluated based on its ability to detect simulated defects in specimens with simulated defects as well as other available sites (pavements, airport runways, bridge decks) where ground truth validation was available. After such testing, the system was then taken to the field to evaluate natural structural defects within actual tunnel linings

The conclusions of the tunnel testing are as follows:

- The UST system is exceptional at locating horizontal delaminations ranging in thickness from 0.05-2.0 mm (0.002-0.079 inches) and is able to differentiate between fully debonded and partially bonded areas within a single map based on the color distribution. It is not, however, able to directly measure the thickness of delaminations.
- Cracks were only clearly characterized when they formed non-perpendicular to the testing surface; however, the presence of perpendicular cracks could be assumed by the omission of surface detail. It should be noted that no crack depths were confirmed by ground truth validation, and this should be a focus of further research.
- Backwall surfaces up to a depth of 965 mm (38 inches) were successfully and accurately determined. Assuming the plan details were correct (no ground truth validation was available), the UST system predicted this depth within an accuracy of 5 mm (0.3 inch).
- Both air- and water-filled voids ranging from 76-203 mm (3-8 inches) in depth could be detected, but differentiation between the two was difficult due to the fact that shear waves are not supported by air or water, and almost all of the acoustic energy is reflected by these types of voids. Further study could be conducted to analyze the difference between phase changes involving these two types of voids.
- Reinforcement layout and depth, as long as the device is polarized in the correct direction, was also successfully determined, with the only exception being in some shotcrete applications. When potentially porous materials such as the shotcrete specimens were evaluated, the presence of very small air voids made internal inspection very difficult.
- With the exception of some medium-sized clay lumps (with a diameter of approximately 102 mm, or 4 inches) surrounding reinforcement, all clay lumps tested were also highly successful.
- Two MIRA systems were used to compare the system's abilities to reproduce the same wave speed. For a test involving 16 specimens, a strong positive correlation existed (with a coefficient of determination of 0.952), with a standard error of approximately 33 m/s (108 ft/s).

- Precision for detecting the depth of delaminations using the same device with the same testing procedures and input parameters (wave speed, frequency, gain selection, etc.) was typically on the order of 1-3 mm (0.04-0.12 inch) and is more likely to be explained by user error/interpretation rather than device error. This is the same for water- and air-filled voids.
- The minimum area able to be tested with the MIRA system is merely tied to the size of the device: 370 mm x 170 mm (14.6 inches x 6.7 inches).

Figure 29 shows an example of a scan from the Hanging Lake Tunnel.
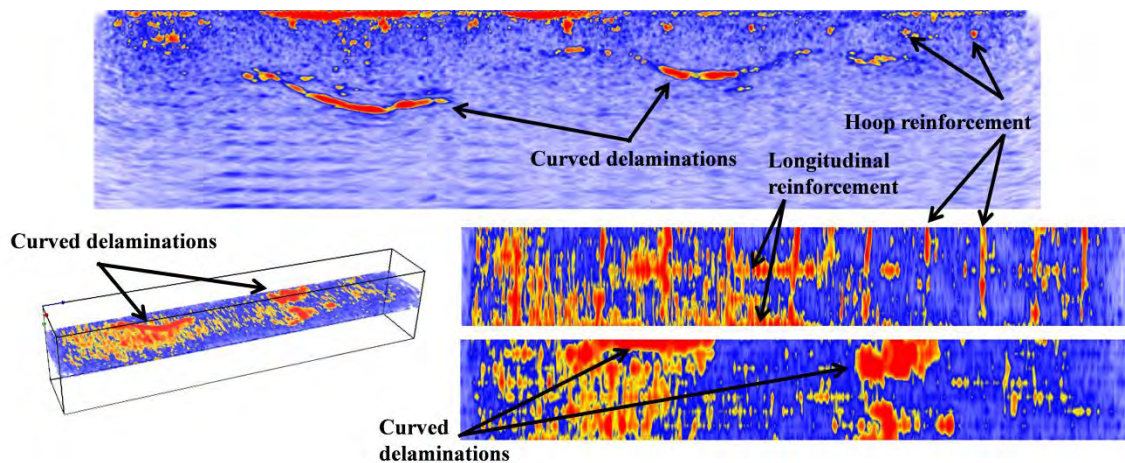
Figure 29. Ultrasonic tomography scan from the Hanging Lake Tunnel.

The researchers believe that this device is especially effective for mapping deeper defect and is recommended for situations where such deep defects are suspected. Results of tunnel testing using ultrasonic tomography are contained in Appendix M and Appendix N.

Portable Seismic Property Analyzer (Impact Echo and Ultrasonic Surface Waves)

The UTEP team used the PSPA, which can perform IE and USW tests simultaneously.

USW Method (PSPA). After testing each tunnel point by point by PSPA, the cross-sections of variation of modulus with wavelength (or depth) were obtained for each tested section. As shown in Figure 30a, intact areas exhibit more or less constant modulus with depth. The average modulus is around 4500 ksi. Figure 31a shows an example of USW results in a defective area of one of the tested tunnels. In this figure, the problematic areas manifested themselves as areas with lower average moduli. The depth of delamination could be approximated through the B-scan in Figure 31a. In Figure 32a, the crack was recognized through high average moduli in the USW B-scan, when the crack was placed between the source and the first receiver (because of the travel path of the wave). On the other hand, when the crack was between the two receivers, the reported USW modulus was lower than normal. The results for these points agreed well with the actual condition that was documented during visual inspection. The rest of the USW results for the tested tunnels are shown in Appendix P.

(a) USW dispersion curve   **b) IE frequency spectrum**
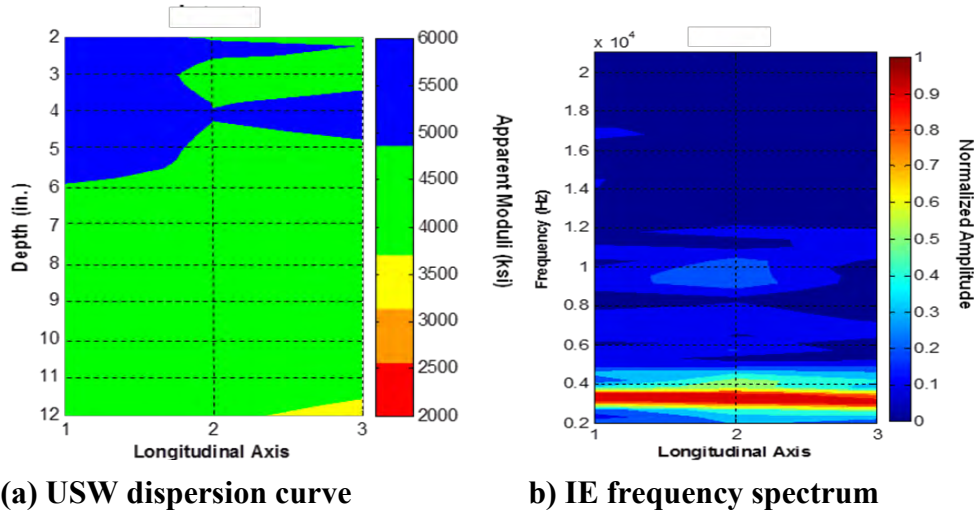
Figure 30. PSPA results on an intact area in Chesapeake Tunnel.

(a) USW dispersion curve

(b) IE frequency spectrum
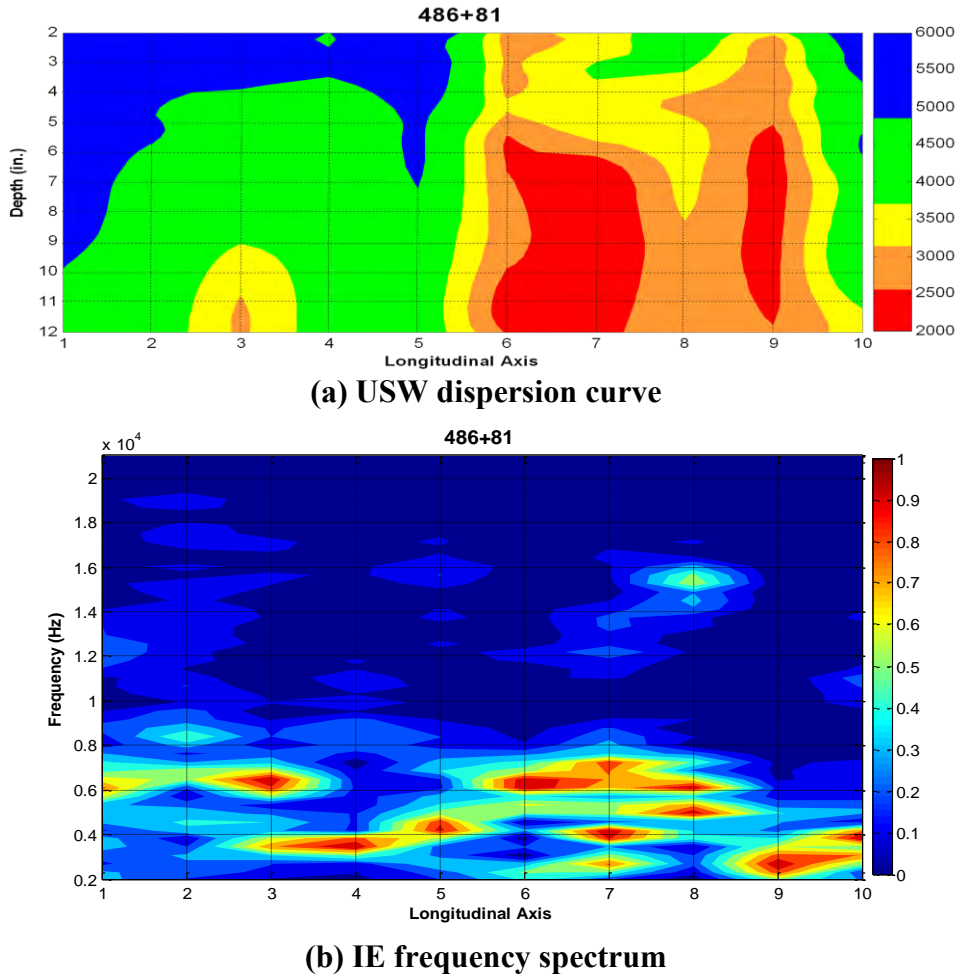
Figure 31. PSPA results on a defective area in the Chesapeake Tunnel.

(a) USW dispersion curve   (b) IE frequency spectrum
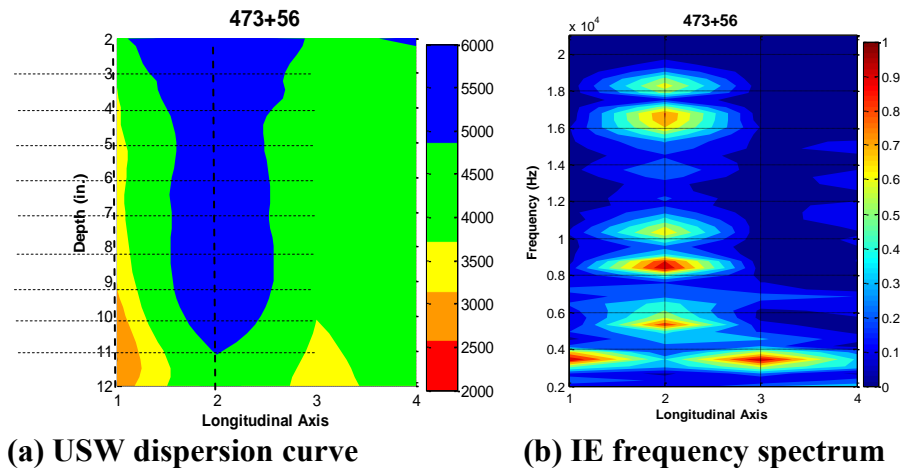
Figure 32. PSPA results on a cracked area in the Chesapeake Tunnel.

IE Method (PSPA). Similar to the USW method, the IE results in the form of a spectral B-scan were visualized in contour maps. As shown in Figures 30b and 31b, a thickness frequency (around 3 kHz) governed the response of intact test points. Other points in Figure 31b exhibit either a lower or higher dominant frequency. The low-frequency flexural mode is due to a shallow or a deep but an extensive delamination. Thus, its peak frequency does not correspond to any thickness measurement, and the depth of defect can be estimated from a USW B-scan (Figure 31a). On the other hand, the high frequency response could be attributed to the onset of delamination. In this case, the depth of delamination is estimated and confirmed with the USW B-scan. In the presence of a crack, data analysis was more complicated. As shown in Figure 32b, multiple frequencies were present in the response when a crack was between the source and receiver in an IE B-scan.

The remaining IE results are shown in Appendix P. In most cases, the calculated depth and location of delamination agreed well with the USW results. Some exceptions happened, where the IE and USW analyses were not consistent. The reason for this can be attributed to the edge effect near a crack and placement of the current PSPA sensor unit relative to the crack.

The description and results of this testing are contained in Appendix P.

Ultrasonic Echo, Ground-Coupled GPR, and Impact Echo Testing

Field testing using three nondestructive testing techniques was carried out between October 3, 2011, and October 12, 2011, in three tunnels in the United States: two in Colorado (Eisenhower Memorial Tunnel and Hanging Lake Tunnel) and one in Virginia (Chesapeake Bay Bridge-Tunnel). In each tunnel, selected areas were tested using three nondestructive testing (NDT) techniques: ground penetrating radar (GPR), ultrasonic echo (US), and impact echo (IE). The allocated testing time in each tunnel was limited. The number and location of the test areas were selected based on either pre-analysis or the existence of visual distress. The on-site working conditions were also taken into account.

The different measurement techniques used by BAM for this project were mounted on an automated scanning device developed by BAM. Figure 33 shows the BAM scanner with the ultrasonic echo device. It can be carried in a relatively light and small package. Its size allows the scanner to be transported in cars and carried through small openings to reach difficult-to-access areas such as the vents above tunnels. The commonly used equipment for NDT of structures, including GPR, US and IE devices, can be easily attached to the scanner for testing and detached after the completion of the measurements. The scanning and NDT data acquisition are controlled by a single notebook. This simplifies the control and reduces the equipment and weight of the measurement system.
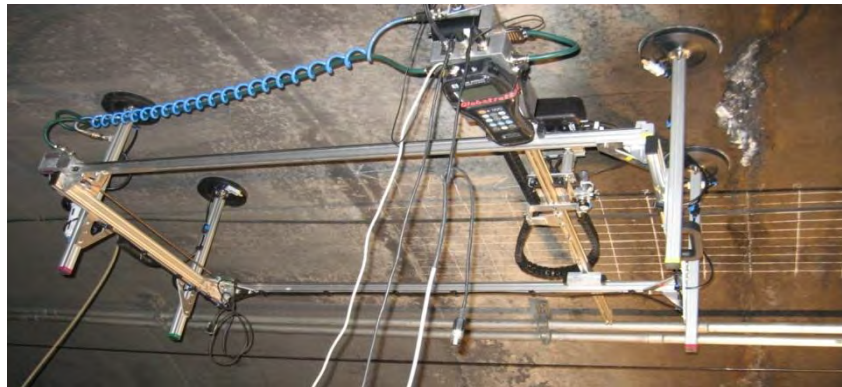
Figure 33. BAM scanner with the ultrasonic echo device.

For the Eisenhower tunnel plenum, the ground coupled GPR proved to be the best tool in identifying and locating the reinforcement. The ultrasonic echo device could, on the other hand, locate an anomaly of unknown origin more clearly than the ground coupled GPR . A combination of the two result sets would provide the most detailed and reliable results. Both methods detected the reinforcement and an unknown anomaly. GPR was more effective in detecting the former, and US in detecting the latter. The backwall couldn't be seen with any of the employed techniques here. However, the impact echo technique could not register either reinforcement or the anomaly detected by the other two techniques.

For the Hanging Lake tunnel plenum, the ground coupled GPR proved to be the only method to identify the reinforcement mesh and the reinforcing elements. The fine measurement grid and three-dimensional data collection allowed detection of reinforcing elements overlapping each other in some views. The ultrasonic echo technique was on the other hand, able to detect a deeper anomaly and establishing that the anomaly under the test area is located at different depths. No reliable information could be extracted from the impact echo data. Again, combining the results of the ground coupled GPR and ultrasonic echo is desirable. It should be noted that none of the utilized NDT techniques were able to reliably identify the extent of the Hanging Lake tunnel lining .

For the Chesapeake Bay tunnel plenum, the ground coupled GPR proved to be the most reliable NDT method for detecting and identifying reinforcement bars. However, it couldn't detect a 15-inch-deep localized anomaly. The ultrasonic echo technique, however, wasn't as

clear in detecting the steel bars but indicated the presence of an anomaly. Both the ultrasonic echo and impact echo could yield the thickness of the tunnel lining. A more clear picture of the geometry and condition of the tunnel emerged using all three techniques.

For the Chesapeake Bay roadway section that was lined with tiles, the ground coupled GPR signals were not disturbed by the presence of the tiles and could image the reinforcement mesh behind the lining. The impact echo signals carried useful information about the bonding condition at tile-concrete interface and occasionally about the lining itself. The ultrasonic echo device, however, could provide no useful information about the condition of the lining . The ultrasonic echo transducer was too large (4 inches x 3 inches) compared to the size of the tiles (2 inches x 2 inches). The grid location and spacing had to be adjusted such that meaningful data could be obtained. However, the measurements were interrupted due to an unforeseen weather condition, and no further measurements could be obtained with the ultrasonic echo device.

To summarize, the automated scanning device used by BAM in this project was effectively used for collecting nondestructive testing data in the tunnels with the three techniques. The team recommends that data from both the ground coupled GPR and the ultrasonic echo devices be collected when conducting in depth evaluations directly on concrete surfaces. However, for tiled surfaces, data from the ground coupled GPR and impact echo should be collected together, since the ultrasonic echo device may not work on tiled surfaces due to the tile dimensions. These devices should also be effective in collecting data on shotcrete linings as well.

Appendix Q contains more information on the tunnel testing with these devices.

Other Information

Appendix R contains depth measurement estimates of apparent defects as indicated by the in-depth evaluation devices used in this portion of the research. The appendix also contains estimated depth measurements to reinforcing steel or the backwall of the tunnel lining if they were detected.

AN INVESTIGATION FOR DETECTING LOOSE TILES AND MOISTURE UNDERNEATH TILES

As mentioned earlier in this report, air-coupled GPR data on tiled linings in the Chesapeake Bay and Hanging Lake Tunnels indicated high surface dielectric areas (greater than 11) as indicated in Appendix K. Researchers tested some of these areas with ultrasonic tomography, impact echo and hammer sounding. The researchers found debonded tiles and delaminations in those areas. Thus, the team concluded that high surface dielectric measurements on tiled linings can indicate areas of debonded tiles or delaminations, as well as areas of high moisture behind tiles.

Also, as described earlier in this report, , the SPACETEC thermal imaging data can be useful for locating loose tiles. In addition, thermal cameras can also indicate areas of loose tiles.

As indicated in Appendix G, the TTI team is developing an acoustic sounding test to detect loose tiles. However, this method is still under development and is not recommended for implementation at this time.

To summarize, the team suggests that air coupled GPR, thermal cameras, and the SPACETEC system's thermal images can be effective scanning devices to locate loose tiles and moisture underneath tiles.

DEVELOPING NDT FOR MEASURING CONCRETE PERMEABILITY

Appendix S contains the results of a laboratory study that attempted to correlate dielectric (or permittivity) measurements to concrete permeability. As indicated in Appendix S, the team determined that the air-coupled GPR cannot measure permeability directly in the field. However, Appendix S does contain information that can be used in the future for NDT development. In addition, the TTI team developed Tables 1 and 2 for the real portion of the permittivity measurement for cement paste based on the results in Appendix L. These can be related to the dielectric measurements made with the air-coupled GPR. Table 4 is for a 1-GHz frequency. Table 5 is for a 2-GHz frequency.

Table 4. Permittivity values (real portion) for a 1-GHz frequency.

Water to Cement Ratio	Relative Humidity, %				
	100	85	75	63	43
0.4	17	16	15.5	14.5	12.5
0.5	15	12.7	12	11.8	9.9
0.6	20	15	10.9	10	8.5

Table 5. Permittivity values (real portion) for a 2-GHz frequency.

Water to Cement Ratio	Relative Humidity, %				
	100	85	75	63	43
0.4	15.5	15	14.5	13.5	12
0.5	14.5	13.5	11.5	11	9
0.6	18	14.9	10.2	9.8	7.5

The values above can be used as a general guide. Although the measurements were made on cement paste, the team believes that the moisture content in the paste would have the greatest effect on dielectric readings with the GPR. Essentially, the tables suggest that air-coupled GPR dielectric readings above 11 may indicate a potential problem, and readings above 15 would indicate excessive moisture present in the concrete.

The team also attempted to measure resistivity on the concrete and shotcrete specimens. However, the measured values varied widely. The team concluded that the concrete resistivity device was suitable only for controlled laboratory testing purposes.

Based on the observed distress in the Chesapeake Bay Tunnel, the team developed the relationship in Figure 34 that relates surface dielectric values measured in the tunnel to surface distress that is assumed to be caused by excessive moisture, leading to reinforcing steel corrosion and further distress. Admittedly there is significant scatter in the data shown in Figure 34. However, this figure could be useful in interpreting surface dielectric data for concrete.
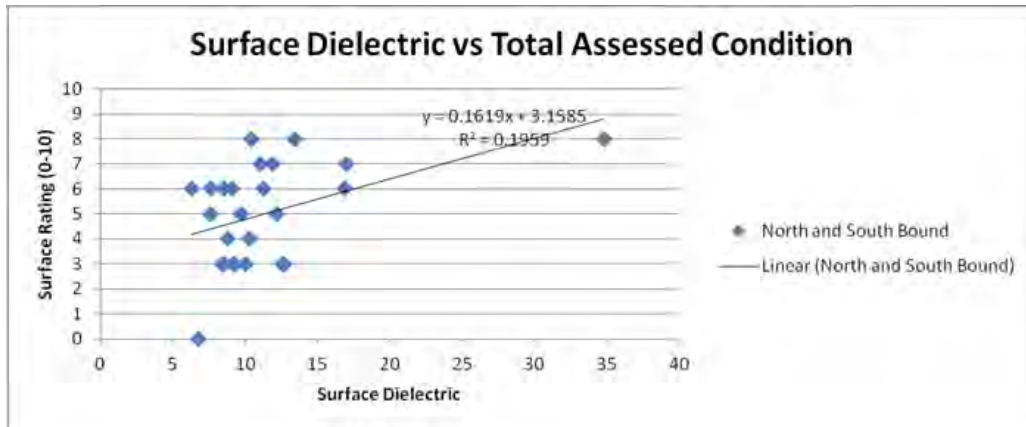
Figure 34. Surface dielectric versus surface rating (using Chesapeake Bay results).

The surface rating is defined in Table 6.

Table 6. Surface rating based on distress observed.

Distress Observed	Surface Rating
Cracks, No Staining	0
Cracks, Light Staining	1
Cracks, Light Staining and Light calcium carbonate deposits	2
Cracks, moderate calcium carbonate deposits and staining	3
Cracks, moderate calcium carbonate deposits and staining, potential spalling (< 2")	4
Cracks, moderate calcium carbonate deposits and staining, potential spalling (2"-6")	5
Cracks, moderate calcium carbonate deposits and staining, potential spalling (6"-10")	6
Cracks, moderate-heavy calcium carbonate deposits and staining, spalling (< 2")	7
Cracks, moderate-heavy calcium carbonate deposits and staining, spalling (2"-6")	8
Cracks, moderate-heavy calcium carbonate deposits and staining, spalling (6"-10")	9
Cracks, moderate-heavy calcium carbonate deposits and staining, spalling (>10")	10

CHAPTER 4
CONCLUSIONS AND RECOMMENDED RESEARCH

As stated in Chapter 2 of this report, in terms of performance criteria, the expert panel indicated that NDT should detect any defect within or immediately behind tunnel linings that have a minimum surface area of 1 ft^2, and any defect needs to be located within 1 ft of the actual location on the tunnel lining. The panel also indicated that NDT should identify delaminated areas and voids up to 4 inches deep as measured from the lining surface with an accuracy of within 0.25 inches.

Based on the results in Chapter 3, the following techniques are able to detect defects with minimum surface areas of 1 ft^2 up to 4 inches deep (and in some cases even deeper):

- Air-coupled GPR.
- Thermography (handheld thermal camera).
- SPACETEC scanner.
- Ground-coupled GPR.
- Ultrasonic tomography.
- Ultrasonic echo.
- PSPA ultrasonic surface waves and impact echo.

They appear to provide useful information for evaluating tunnel linings and should be considered for implementation, but the limitations outlined in the appropriate appendix for each technology need to be considered. In addition, none of the devices are able to detect a 1-ft^2 void in a steel lining behind concrete. In addition, the 0.25-inch accuracy criterion for defects up to 4 inches deep can be problematic for the in-depth devices. It appears that a 0.5-inch accuracy is more realistic for these devices. Table 7 summarizes the accuracy, detection depth, deterioriation mechanisms detected, tunnel lining types, and other information for these technologies.

Table 7. Summary of NDT Devices.

Device	Accuracy	Detection Depth	Deterioriation Mechanisms Detected	Tunnel Lining Types	Other information
Air-coupled ground-penetrating radar (GPR)	Locates defects within 1 foot of its actual location	Does not measure depth, but indicates areas of high moisture or low density (high air voids). Such areas may represent problems within or behind the tunnel lining	Tile debonding, delaminations, air filled voids, water filled voids, moisture intrusion	Concrete, Tile-lined Concrete, and Shotcrete	This is a scanning tool that can indicate where to conduct testing with in depth devices
Thermography (handheld thermal camera)	Locates defects within 1 foot of its actual location	Does not measure depth, but can indicate tile debonding, delaminations up to 1 inch, voids up to 3 inches.	Tile debonding, delaminations, air filled voids, water filled voids, moisture intrusion	Concrete, Tile-lined Concrete, and Shotcrete	This is a scanning tool that can indicate where to conduct testing with in depth devices
SPACETEC scanner	Locates defects within 1 foot of its actual location	Does not measure depth, but can indicate tile debonding, possibly delaminations up to 1 inch, and possibly voids up to 3 inches.	Tile debonding, delaminations, air filled voids, water filled voids, moisture intrusion	Concrete, Tile-lined Concrete, and Shotcrete	This is a scanning tool that can indicate where to conduct testing with in depth devices. Testing can only be conducted through a service contract.
Ground-coupled GPR	Can determine defect depth within 10% of the actual depth without reference cores, 5% if cores are available	The device can possibly detect defects at any depth within or immediately behind tunnel linings. However, specimen testing indicates it cannot locate 1 square foot voids in steel plates behind tunnel linings	Delaminations, air filled voids, water filled voids, moisture intrusion	Concrete, Tile-lined Concrete, and Shotcrete	Experienced personnel are needed to intepret defect locations and depths from the GPR scans. Specimen testing indicates it cannot locate 1 square foot voids in steel plates behind tunnel linings

Table 7 (continued). Summary of NDT Devices.

Device	Accuracy	Detection Depth	Deterioriaton Mechanisms Detected	Tunnel Lining Types	Other information
Ultrasonic tomography	Concrete: voids within 0.5 inch, shallow delaminations within 0.75 inch. Shotcrete:air filled voids within 0.7 inch, water filled voids within 1.21 inch, shallow delaminations within 1.88 inch	Can detect defects up to 8 inches deep based on specimen tests. Tunnel tests indicate it can detect possible defects up to 20 inches deep.	Delaminations and voids	Concrete, Tile-lined Concrete, and Shotcrete	May not be effective for measuring defects that are 2 inches or less from the lining surface. May not be accurate enough for measuring defect depths in shotcrete.
Ultrasonic echo	Comparable to the ultrasonic tomography system based on tunnel testing with both devices. Past experience indicates also it can measure tunnel lining thickness within 3% of the actual thickness	Comparable to the ultrasonic tomography system based on tunnel testing with both devices.	Delaminations and voids	Concrete and shotcrete	May not be effective for measuring defects that are 2 inches or less from the lining surface. May not be accurate enough for measuring defect depths in shotcrete. Tunnel tests indicated problems with using this device on tiles.
Portable seismic property analyzer (PSPA) ultrasonic surface waves and impact echo	Ultrasonic Surface Waves: about 15% of the actual depth for defects up to 6 inches deep. Impact Echo: 10% for deep delaminations greater than 6 inches deep.	Ultrasonic Surface Waves: up to 6 inches deep. Impact Echo: up to 18 inches deep	Delaminations and voids	Concrete, Shotcrete, and Tile-lined Concrete	May be difficult to quantify the depth of defects that are shallow or extensive. May not get good results when testing on very rough concrete surfaces, oily surfaces, and severely curved surfaces

The following sequence of testing is suggested for evaluating tunnel linings based on the research conducted under this study:

o Collect thermal images and air coupled GPR data on the tunnel lining. Air coupled GPR data should be collected every foot along the tunnel lining. Thermal images can be collected every foot as well; however, the equipment covered in this report can collect data at a spacing determined by the camera operator or tunnel inspector. This data should be collected ideally on the same day; however, it can be collected separately. The thermal images should be collected when the air temperature is rising or falling; areas of possible defects may show up better in the thermal images. The data from any of these devices can be obtained at a walking pace (around 1 mph or 1.61 kmh). Air coupled GPR data can be obtained at much higher speeds, but the geometry and features in tunnels may make it difficult to operate the equipment at speeds much greater than 1 mph.

o Analyze the data from the scanning devices above. Select areas for in depth testing based on the GPR surface dielectric results, thermal images, and observed surface distresses that are of concern to tunnel inspectors.

o Conduct in depth testing with the ground coupled GPR and either the ultrasonic tomography, ultrasonic echo, or portable seismic property analyzer device. The choice of equipment could be based on the cost and the type of defect to be detected (tile debonding, delamination, and voids) The ultrasonic tomography and ultrasonic echo devices may be more appropriate for measuring and mapping defects greater than two inches from the tunnel lining surface. The ultrasonic tomography device is more expensive than the other two devices; however, it has the capability to provide more information in the field about such defects. The portable seismic property analyzer may be more appropriate for determining the limits of shallow defects.

o Evaluate the data collected from these devices.

The SPACETEC Scanner is only available through a service provider. Service providers can also perform NDT using the actual or similar devices or techniques described in this report. However, all but the SPACETEC equipment could be operated by tunnel owner personnel. The equipment and essential data processing software used is commercially available. To implement each of these methods, however, the personnel in charge need to be sufficiently trained for data collection, reduction and interpretation.

The handheld thermal cameras appear to be the easiest to use of the devices tested under this study and can be effectively used by tunnel owner personnel. Data collection and analysis of the images can be conducted in the field. On the other hand, the air coupled and ground coupled GPR equipment will require considerably more training and experience than the other devices for data collection and operation. These devices involve the use of integrated systems containing a data collection module, computer, antenna, and distance measuring indicator. Data analysis of the air coupled GPR data will generally be simpler than that from ground coupled GPR data,

however. The researchers recommend that the surface dielectric data from the air coupled GPR be used for determining where to conduct more in depth tests; this data is easily generated by GPR analysis programs. The training and experience needed to effectively collect and analyze data from ultrasonic tomography, ultrasonic echo, and portable seismic property analyzer equipment is expected to be less than that for the GPR equipment.

For rapid scanning of tunnel linings, data from the SPACETEC scanner, the air-coupled GPR, and thermal camera images can indicate areas where further inspection by tunnel personnel may be warranted. All devices were able to detect problems within 1 ft of the actual location on the tunnel lining. However, the SPACETEC scanner is not for sale; data collection and analysis are provided by SPACETEC through a service contract.

The 1-GHz ACGPR antennas such as the one used in this study are no longer for sale in the United States due to FCC regulations; several service providers still own these antennas, however. In any case, antennas for sale in the United States should be effective for collecting data if they meet the radar specifications contained in Appendix T.

Thermal cameras have the ability to detect 1-ft^2 voids 3 inches deep when significant concrete thermal gradients exist according to this study, and the literature suggests they can detect even deeper voids. However, the team believes that vehicle-mounted thermal camera systems are not quite ready for implementation; further software development is needed.

Ground-coupled GPR, ultrasonic tomography, ultrasonic echo, and the PSPA are all able to detect defects up to 4 inches in depth. However, for GCGPR, the defects can only be detected if they contain significant air pockets or significant moisture. Ultrasonic Tomography can detect even deeper defects, but cannot directly detect defects if they are less than 2 inches away from the surface.

As for implementation, all of these devices will require a combination of classroom and hands-on training for collecting and/or analyzing data.

Although beyond the scope of this study, the Laser scanning and digital photogrammetry techniques can also provide information about tunnel lining profile and surface distress that may be useful to tunnel inspectors.

Finally, service providers can collect and analyze data for clients using the devices listed above. However, clients should consider the limitations for each device before selecting a service provider.

REFERENCES

Gucunski, N., and A. Maher. 1998. Bridge Deck Condition Monitoring by Impact Echo Method. *Proceedings of International Conference MATEST '98—Life Extension*, Brijuni, Croatia, pp. 39–45.

APPENDIX A
AIR-COUPLED GROUND-PENETRATING RADAR (GPR)
TESTING CRITERIA

ACCURACY

The surface dielectric values calculated from the air-coupled ground-penetrating radar (ACGPR) data are used to determine where to test with in-depth nondestructive testing devices. The surface dielectric is calculated as follows:

$$\varepsilon_a = \left[\frac{1 + \left(\dfrac{A_l}{A_m}\right)}{1 - \left(\dfrac{A_l}{A_m}\right)} \right]^2$$

where:

ε_a = the dielectric of the lining surface.

A_l = the amplitude of reflection from the surface in volts.

A_m = the amplitude of reflection from a large metal plate in volts (this represents the 100 percent reflection case).

The accuracy of these amplitudes is critical in calculating the surface dielectric.

The Texas A&M Transportation Institute (TTI) developed an ACGPR hardware specification (see Appendix T) that contains the requirements for such systems. This specification addresses the accuracy of the system.

The distance measuring indicator (DMI) used with the ACGPR system used in this study is accurate within 1 ft.

ACGPR data should not be relied on to accurately measure the depths of defects in tunnel linings. The researchers believe that the surface dielectric value can indicate where such defects could possibly be located. Testing conducted during this study indicated that the ACGPR data could indicate 1-ft^2 air voids (1 inch thick) up to 3 inches from the lining surface for reinforced linings; and 7.625 inches from the lining surface for plain unreinforced linings. The calculated depths of these defects from the TTI ACGPR data analysis software was 2.6 inches and 7.7 inches, respectively. Therefore, the system was accurate within 0.4 inches for the shallow void and approximately 0.1 inches for the deeper void.

The testing indicated that the ACGPR data could indicate a 1-ft^2 water-filled void at 3 inches from the lining surface. The calculated depth of this defect from the TTI ACGPR data analysis software was 2.7 inches. Therefore, the system was accurate with 0.3 inches for this water-filled void.

PRECISION

The ACGPR hardware specification (Appendix T) also addresses the precision of the system in order to ensure that the surface dielectric measurement is precise.

The measurement results of the DMI used with the TTI ACGPR system are repeatable and reproducible within 1 ft.

CALIBRATION PROCEDURES

The ACGPR hardware specification (Appendix T) is also used for calibrating the system.

The DMI should be calibrated every 3 months. This is done by traveling over a known distance (minimum 500 ft) and comparing the DMI measurement to the known distance measurement.

TESTING PROCEDURES

ACGPR antenna manufacturers have their own GPR-system-specific user manual that should be followed when collecting data.

Before collecting data on a tunnel lining, personnel should collect at least 50 ACGPR waveform traces over a minimum 16-ft^2 metal plate (4 ft long by 4 ft wide) at the operating height of the antenna (between 12 and 18 inches). These data will be used to calculate the surface dielectric. During data collection on the tunnel lining, the ACGPR data should be collected at 1-ft spacing or less.

COST

A price for a complete system with survey van and mounting is usually between $180,000 and $200,000.

LIMITATIONS

The ACGPR surface dielectric is recommended for use in determining where to test tunnel linings with in-depth nondestructive testing devices.

At the time of this report, only one company manufactures Federal Communications Commission (FCC)–compliant ACGPR systems for sale in the United States. However, several ACGPR service providers in the United States provide data collection and interpretation services. They may use the FCC-compliant systems or grandfathered systems similar to the 1-GHz system used by TTI in this study.

ACGPR data should not be relied on to accurately measure the depths of defects in tunnel linings. ACGPR can detect 1-ft^2 defects up to a depth of 3 inches for reinforced linings and 7 inches for plain unreinforced linings if they contain a significant amount of air (such as a 1-inch-deep air gap) or a significant amount of moisture (such as a 1-inch-deep water-filled void).

External electromagnetic radiation such as cellphone antennas, radio antennas, and television station antennas can cause signal degradation.

Salts (either from deicing operations or from seawater) in the concrete may result in signal penetration problems.

Steel fibers in shotcrete prevent ACGPR signal penetration. Concrete containing steel slag can also prevent ACGPR signal penetration

DATA MANAGEMENT

Commercially available ACGPR systems (such as the FCC-compliant system described at the webpage http://www.geophysical.com/antennas.htm) come with data collection and management software. ACGPR service providers can also have their own data management software.

DATA ANALYSIS AND INTERPRETATION

Data analysis software is provided by the manufacturer of such systems. ACGPR service providers can also provide data analysis and interpretation services.

The surface dielectric data are easy to calculate using available software. However, data interpretation for locating subsurface defects can only be done by experienced, trained users and usually demands engineering judgment.

APPENDIX B
GROUND-COUPLED GROUND-PENETRATING RADAR (GPR) TESTING CRITERIA

ACCURACY

The accuracy of determining depths to defects depends on the experience of the data interpreter—in general, the depth accuracy is +/−10 percent without reference cores and 5 percent if cores are available.

PRECISION

The precision is generally dependent on the hardware, but in general all ground-coupled systems are precise enough for tunnel surveys (repeatable and reproducible) as long as there are no significant changes in moisture content or material properties in the area being measured. Such changes can have a complex effect on coupling and thus antenna performance. But in general, ground-coupled ground-penetrating radar (GCGPR) shows anomalies on the same location.

CALIBRATION PROCEDURES

There is no special calibration with such antennas. The important issue is to use a gain level that does not cause a signal clipping effect.

TESTING PROCEDURES

GCGPR antenna manufacturers have their own GPR-system-specific user manual that should be followed when collecting data. For example, GSSI provides a handbook for concrete inspection on its website (http://www.geophysical.com/Documentation/Manuals/MN72367D1%20Concrete%20Handbook.pdf).

COST

The price for a complete system starts around $50,000. Antennas with different central frequencies are available (usually from 100 MHz to 1.5 GHz). The researchers used GSSI 900-MHz and 1.5-GHz antennas.

LIMITATIONS

Data collection can be slow since the antenna needs to be either in contact or very close to the lining surface during data collection.

Data interpretation requires educated and experienced personnel.

External electromagnetic radiation such as cellphone antennas, radio antennas, and television station antennas could cause signal degradation, although it is not usually observed with such antennas.

Salts (either from deicing operations or from seawater) in the concrete may result in signal penetration problems.

Steel fibers in shotcrete prevent GCGPR signal penetration. Concrete containing steel slag can also prevent GCGPR signal penetration

DATA MANAGEMENT

Commercially available GCGPR systems (such as the systems described on the webpage http://www.geophysical.com/antennas.htm) come with data collection and management software. GCGPR service providers can also have their own data management software.

DATA ANALYSIS AND INTERPRETATION

Data analysis software is provided by the manufacturer of such systems. GCGPR service providers can also provide data analysis and interpretation services.

However, data interpretation for locating subsurface defects can only be done by experienced, trained users and usually demands engineering judgment.

APPENDIX C
HANDHELD THERMAL CAMERA TESTING CRITERIA

ACCURACY

The handheld thermal camera system used in this study is described in Appendix L. A commercially available FLIR T300 camera was used in this study. The specifications for this camera can be found at http://support.flir.com/DsDownload/Assets/45305-0201_en_41.pdf.

According to FLIR, the accuracy of the temperature readings is $+/-3.6$ °F or $+/-2$ percent of the reading.

Images from this system do not indicate depths of defects. However, the images can indicate possible tile debonding, delaminations up to one inch deep with a minimum surface area of 1 square foot, and voids up to 3 inches deep with a minimum surface area of one square foot, based on specimen testing. These defects can be located within one foot of their actual location with this system.

PRECISION

According to FLIR, the precision of the system is less than 0.09 °F (0.05 °C). The areas of possible defects can be located within one foot of the actual defects with any system as long as the thermal contrast of the area of interest has not changed and the systems are properly calibrated.

CALIBRATION PROCEDURES

Each thermal camera manufacturer publishes its own calibration procedures (if needed). The user cannot make this calibration; the camera has to be sent to the manufacturer or authorized reseller.

TESTING PROCEDURES

The operator needs to ensure that the camera is properly focused before data collection. No other special testing procedures are needed.

The process used by the researchers when testing in tunnels was as follows:

1. Turn on the camera.
2. Aim the camera at a tunnel lining. Observe the temperature of the lining in the center of the display.
3. Manually set the temperature range to a range of around 5 °F (for example, 60 to 65 °F if the tunnel lining temperature at the center is 62 °F).
4. Adjust the range so that a color spectrum appears on the camera display.
5. Aim the camera down the tunnel. Point out areas with the laser pointer (mounted on the camera) to personnel where it appears that the temperature is higher or lower than usual based on the camera display.

6. Have the personnel inspect the area and determine if the area should be investigated. This can be done by hammer tapping, or visual observations of distress or moisture. Mark the area if further investigation is needed.

COST

The thermal camera is approximately $9,000.

LIMITATIONS

The equipment is not accurate for temperatures below −4 °F (−20 °C) and over 248 °F (120 °C). This is according to the FLIR A325 camera default calibration. The normal operating temperature is between 5 °F (−15 °C) and 122 °F (50 °C).

DATA MANAGEMENT

Thermal cameras contain data collection/management software. The images are stored on a secure digital (SD) card with the image number and date. This SD card can be removed so the images can be transferred to a computer.

DATA ANALYSIS AND INTERPRETATION

Thermal camera manufacturers provide data analysis and interpretation software with which the images can be further refined and inspected. For example, FLIR provides free software for data analysis and interpretation of images taken with its equipment. This software is described and can be downloaded at http://www.flir.com/cs/emea/en/view/?id=42406.

APPENDIX D
ULTRASONIC TOMOGRAPHY TESTING CRITERIA

ACCURACY

Concrete Slabs with Blind Calibration

Blind calibration is the typical field approach for ultrasonic tomography testing (UST). This means the wave speed used in collecting data (the parameter that mostly affects the depth readings of anomalies) is calculated by averaging wave speeds from eight initial calculations (see "Section 3: Test Procedures" in the *Users Manual*). The resulting average may vary from location to location, giving an inaccurate depth reading. Even so, the UST system has been demonstrated to locate 8-inch-deep air-filled voids with 0.44-inch depth accuracy, 8-inch-deep water-filled voids with 0.50-inch depth accuracy, and 2- to 3-inch-deep delaminations with 0.74-inch depth accuracy. Backwall reflections for specimens from 12 to 24 inches can be located with a 2.00-inch accuracy.

Shotcrete Slabs with Blind Calibration

The UST system has been demonstrated to locate 3- to 8-inch-deep air-filled voids with a 0.70-inch accuracy, 3- to 8-inch-deep water-filled voids with a 1.21-inch accuracy, and 2- to 8-inch-deep delamination with a 1.88-inch accuracy. Backwall reflections for specimens as deep as 12 inches can be located with a 1.53-inch accuracy.

Note that under 2 inches (at 50 kHz), defects are typically only seen by the shadowing effect. Occasionally, the nature of the defect allows detection from 1 to 2 inches in depth.

PRECISION

Three cases for precision are presented: *repeatability of one device*, in which the same device is used with the same settings on the same specimen; *reproducibility with the same settings*, in which two separate but identical devices are used with the same settings on the same specimens; and *reproducibility with blind testing*, in which two separate but identical devices are used to individually calculate wave speed but are used on the same specimens.

Repeatability of One Device

In repeatability tests using the same device with exactly the same settings and parameters, air- and water-filled voids, delamination, and backwall reflections are detected with a precision of 0.16 inches.

Reproducibility with the Same Settings

In reproducibility tests with two separate but identical systems compared side by side with exactly the same settings and parameters, air- and water-filled voids, delamination, and backwall reflections are detected with a precision of 0.51 inches.

Note that the two separate systems did not have the exact same version of firmware, and the system used for the comparison consistently predicted the features 0.51 inches deeper than the Texas A&M Transportation Institute's (TTI's) system. It is therefore not expected that every system differs this much when using the same version of firmware.

Reproducibility with Blind Testing

The following are results from reproducibility tests using two systems following similar blind calibration procedures.

Concrete Slabs with Blind Calibration

The two UST systems have been demonstrated to locate 8-inch-deep air- and water-filled voids with a 0.51-inch precision and 2- to 3-inch-deep delamination with a 0.55-inch precision. Backwall reflections for specimens as deep as 12 to 24 inches can be located with a 0.70-inch precision.

Shotcrete Slabs with Blind Calibration

The two UST systems have been demonstrated to locate 3- to 8-inch-deep air-filled voids with a 0.51-inch precision, 3- to 8-inch-deep water-filled voids with a 0.70-inch precision, and 2- to 8-inch-deep delamination with a 0.35-inch precision. Backwall reflections for specimens as deep as 12 inches can be located with a 0.70-inch precision.

Reproducibility of Wave Speed

Two MIRA UST systems were used to compare the system's abilities to reproduce the same wave speed. For a test involving 16 specimens, a strong positive correlation exists (with a coefficient of determination of 0.952), as shown in Figure D-1, with a standard error of approximately 33 m/s (108 ft/s).

Wave Speed Calculated by Two Systems
(in m/s)

$$y = 0.9939x + 3.2208$$
$$R^2 = 0.952$$
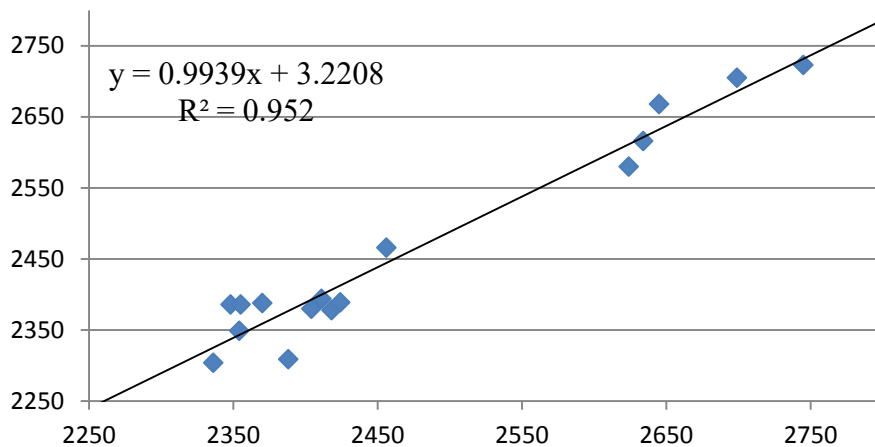
Figure D-1. R^2 for reproducibility of wave speed calculation (two separate MIRA systems).

REPEATABILITY

Repeatability measurements were performed using the same system on the same day with the exact same settings, and the precision results are given above in "Repeatability of One Device." Reproducibility measurements were performed using the same day with the exact same settings, and the precision results are given above in "Reproducability with Same Settings" and "Reproducability with Blind Testing."

CALIBRATION PROCEDURES

Blind Calibration Procedures

Blind calibration is performed when ground truth is not available for the type of concrete under inspection. This is the typical field condition. The system is calibrated by using an average wave speed calculated from eight randomly oriented collection points. Calibration procedures can be found in "Section 3: Test Procedures" in the *Users Manual* or Sections 1.3 and 1.4 in the manufacturer's *User Manual*.

Ground Truth Calibration Procedures

When ground truth is available to fine-tune the system, the wave speed should first be estimated by the procedure outlined in "Section 3: Test Procedures" in the *Ultrasonic Tomography Field Manual*. If the determined wave speed does not accurately produce the same results as the ground truth information, the user should adjust the wave speed in order for the displayed defect to match ground truth information.

TESTING PROCEDURES

Testing procedures are given in "Section 3: Test Procedures" in the *Ultrasonic Tomography Field Manual* and in Section 2 in the manufacturer's *User Manual*.

COST

The cost of the A1040 MIRA UST system is approximately $58,000, which includes the A1040 unit, a removable battery, analysis software on a laptop, a USB cable for data transfer, a user manual, and a transportation case.

LIMITATIONS

The limitations of the system are given in detail in "Section 8: Limitations" in the *Ultrasonic Tomography Field Manual.* The limitations include the following:

The speed of data acquisition is low (0.8 to 2.3 min/ft^2).
There is no phase change information to infer defect type.
No information deeper than initial air interfaces is discernible.
The system has difficulty detecting reinforcement below two layers of reinforcement mesh.
For a 50-kHz use, defects under 2 inches from the surface are not directly detected.
For a 50-kHz use, reinforcement under #5 (0.625-inch diameter) are not typically detected.

DATA MANAGEMENT

Data files for typical grid spacings (50 to 200 mm by 50 to 200 mm) for comprehensive maps range from 12 to 35 kb/ft^2. It is recommended that all data be stored on a remote hard drive.

DATA ANALYSIS AND INTERPRETATION

Data reconstruction and imaging are performed automatically by the system for two-dimensional review mode, and data reconstruction and imaging are performed automatically by the accompanied IDEALViewer software for three-dimensional map mode. Raw data files are generated as *.lbv, *.bin, *.bmp, and *.cfg files.

Data interpretation is manually performed by an experienced operator for both the map and review modes of operation. Interpretive guidelines are given in "Section 7: Interpretation Guidelines" in the *Ultrasonic Tomography Field Manual*.

APPENDIX E
ULTRASONIC ECHO TESTING CRITERIA

ACCURACY

The ultrasonic echo equipment used in this research study is commercially available. It is the A1220 Monolith developed by ACSYS in cooperation with the German Federal Institute for Materials Testing and Research (BAM). The accuracy depends mainly on the data acquisition hardware; however, with the A1220, the tunnel thickness can be estimated within an accuracy of +/−3 percent of the actual thickness. This system and the ultrasonic tomography testing system (discussed in Appendix D) measured comparable depths to defects in tunnel linings.

PRECISION (REPEATABILITY AND REPRODUCIBILITY)

The A1220 measurements are highly reproducible (i.e., the precision is very good) when no coupling agent is used. Using a scanning system enhances the reproducibility of the measurements because the pressing pressure on the transducer and its location can be accurately controlled.

CALIBRATION PROCEDURES

There are no standard calibration procedures to be performed before the start of measurements.

TESTING PROCEDURES

When using dry-point contact probes, no coupling liquids need to be applied on the surface. However, it is necessary to clean the surface of dust and sand, and remove all the materials from the surface that could prevent the penetration of low-frequency ultrasonic energy in the material.

The location of the test site and its dimensions should be marked and noted in order to reproduce measurements if necessary and locate the detected features. For scanner testing, the location of the scanner feet and the dimension of the scanner aperture need to be carefully noted. It is equally important to record the orientation of the probe (i.e., its polarization) with respect to the test area or scanner opening.

The technical passport of the hardware includes information about the center frequency of the probe, the delay time, and the voltage level. These constitute all the parameters to be set before starting with the measurements. The choice of parameters depends on the particular application: i.e., the test material and the required penetration depth. For testing of concrete tunnel linings of up to 3 ft thick, a center frequency of 55 KHz could be used.

The number of test points and grid spacing depend highly on the required resolution (i.e., the minimum size of sought defects) and the allocated time for field investigations. In this project, a spacing of 1 inch in each direction was chosen, allowing the scanning operation at about 11 ft^2/h (or 1 m^2/h) for acoustic testing. Investigations revealed that doubling the grid

spacing to 2 inches would not compromise the accuracy of the test results. Reconstruction algorithms used for post-processing the data (e.g., Synthetic Aperture Focusing Technique) are most effective for grid spacing of 2 inches or less. To achieve the maximum accuracy, it might be necessary to do the measurements with two polarizations.

COST

A handheld unit with one transducer can be purchased for less than $10,000. The cost of a scanning system with the control unit is about $100,000.

LIMITATIONS

The main limitation of conventional ultrasonic techniques is that the sensors have to be in contact with the structure during the measurements. This leads to several issues such as poor repeatability and/or inconsistency of measurements, as well as delays in displacing and reinstalling the transducers. Mounting the ultrasonic device on a scanning system accelerates the measurements and greatly enhances the repeatability and consistency of the measurement results. However, in comparison to contact-free measurement systems, conventional ultrasonic testing (even with dry-contact transducers like A1220) is relatively slow. Therefore, it is suitable for the assessment of areas deemed problematic during screening. Other limitations of this technique include the following:

- At (or near) block joints or other structural boundaries, the signals suffer great disturbance due to the reflection of surface waves. This makes the reliable evaluation of measurements difficult.
- The acoustic waves reflect partially at the interface between the inner shell concrete and roof gap backfill material. If these two materials are well bonded, the reflection is very small or may not be identified. However, there is often a separation between these two materials. A gap of a few hundredths of a millimeter is sometimes enough to completely reflect the sound waves. In such cases, only the thickness of the inner shell is measured (excluding the backfill material).
- Generally speaking, even with the phase evaluation, it is not always possible to establish the difference between certain types of defects, e.g., a flaw and an excessively thin cross-section of lower acoustic impedance.
- In the case of air-entrained concrete or fiber reinforced concrete (FRC), the range of thickness measurements was reportedly reduced, or carrying out the measurements was more difficult.

DATA MANAGEMENT

The collected data are downloaded from the ultrasonic hardware and saved on an external hard disk for safekeeping. Depending on the amount of data acquired, downloading might be necessary in between a measurement cycle, or an external hard disk can be hooked up to the instrument. Using the A1220 device on a 1 inch by 1 inch grid of size 48 inches by 24 inches (1,225 data points, 1,024 samples per signal, and a sampling frequency of 1 MHz) produces a 16-bit binary file of 2.39 MB. The analysis software delivered with the hardware is able to read

the binary data format in which the information is saved. With other analysis software, data transformation into a different file format might be needed.

DATA ANALYSIS AND INTERPRETATION

Basic data analysis software is provided by the manufacturer. Other standard data analysis software can be used to post-process the experimental data.

Interpretation depends on the mode of testing (one point [A-scan], linear [B-scan], or surface measurements [D- and C-scans]) and may be enhanced using advanced analysis and visualization tools. For example, applying the SAFT (Synthetic Aperture Focusing Technique) to the data improves the signal-to-noise ratio. Phase analysis, on the other hand, makes it possible to distinguish between features and anomalies of different constituents, e.g., steel or air void. Built-in plans or other information about the test area may greatly facilitate the interpretation of the results.

Data interpretation can be done by experienced trained users and usually demands engineering judgment.

APPENDIX F
ULTRASONIC SURFACE WAVES AND IMPACT ECHO (PSPA) TESTING CRITERIA

ACCURACY

Based on results obtained in Strategic Highway Research Program (SHRP 2) Project R06A, the measurement spacing should be equal to or less than the smallest delaminated area to be detected by either the ultrasonic surface waves (USW) or impact echo (IE) method. To map the area of the delaminated area accurately, the measurement spacing should be half the desired smallest dimension of the area that is of practical value.

Figure F-1 represents the USW and IE results of the old PSPA, along with the approximate horizontal distribution of the defects from SHRP 2 Project R06A. Based on an objective criterion defined by Azari et al. (2012), the accuracy of the USW and IE methods in detecting the defects was estimated at about 83 percent and 85 percent of the points tested, respectively. The detectability of the combined USW and IE results in locating the defects improved slightly at 86 percent.

The new PSPA results are similar to the old PSPA results. The amplitude and dominant frequency spectra are shown in Figure F-2. The defective areas are indicated by high amplitude and low frequency.

The USW method is about 15 percent accurate in approximating the depth of defects. It becomes less effective as the delamination gets deeper than 6 inches. On the other hand, the IE method is more effective in locating deep delamination. The accuracy of the IE method in estimating the depth of delamination is about 10 percent.
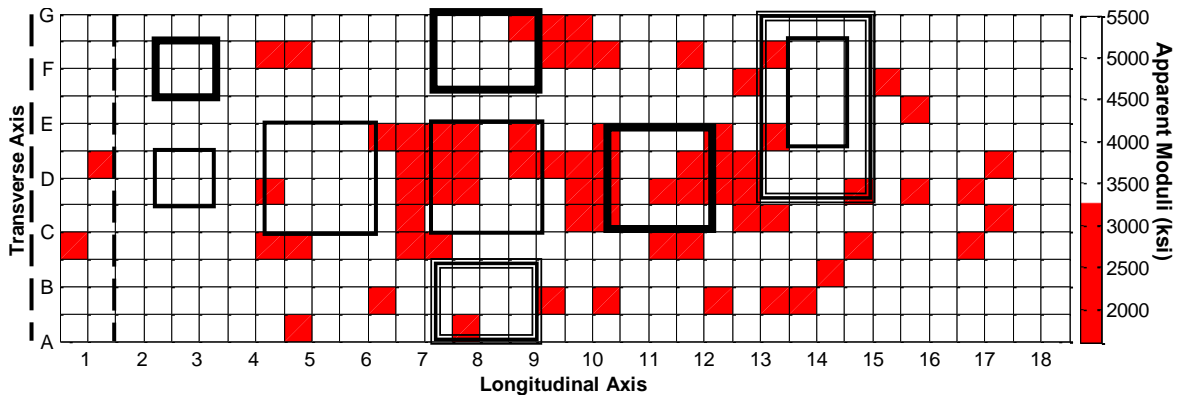
a) **Average apparent modulus obtained by USW method**
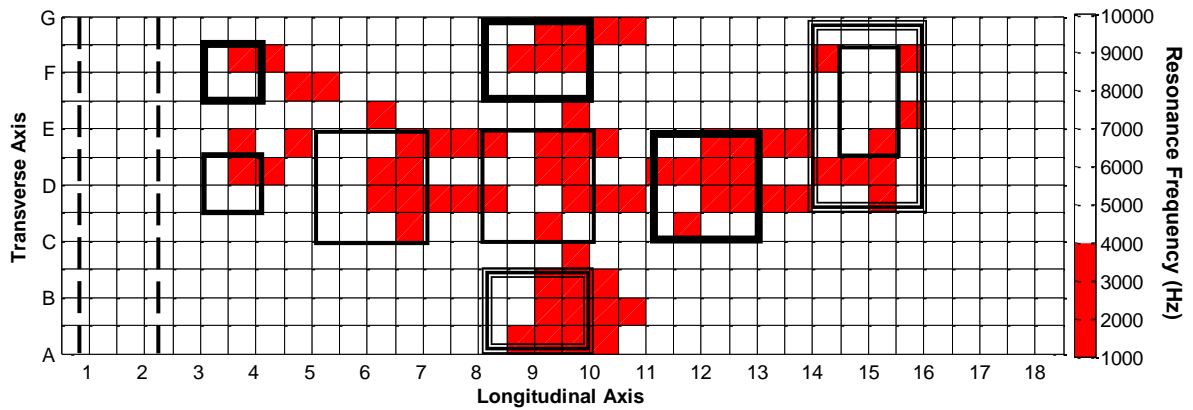
b) **Dominant frequency obtained by IE method**

Figure F-1. USW and IE contour maps.

Amplitudes: red high, blue low
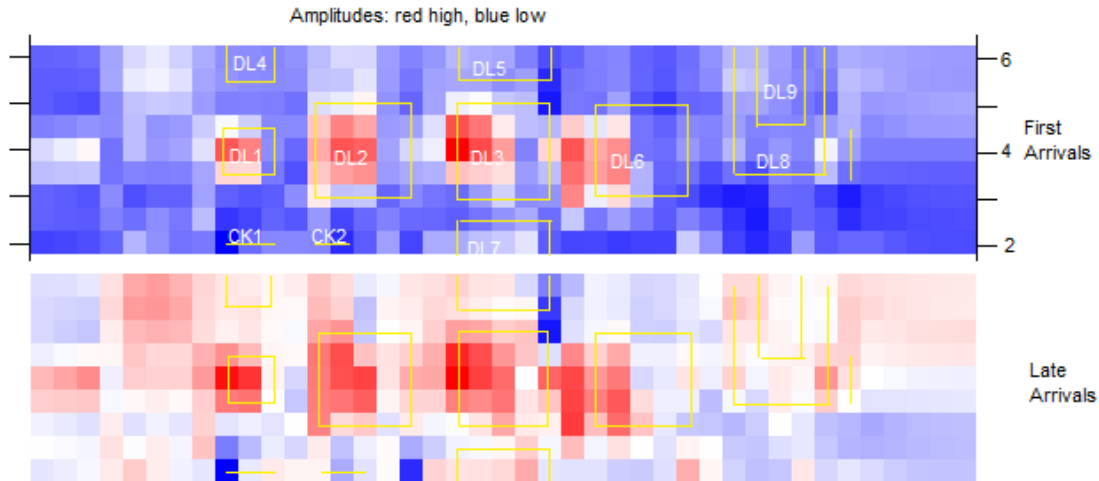
a) Planar contour map of amplitude of waveforms

Frequency: red high, blue low
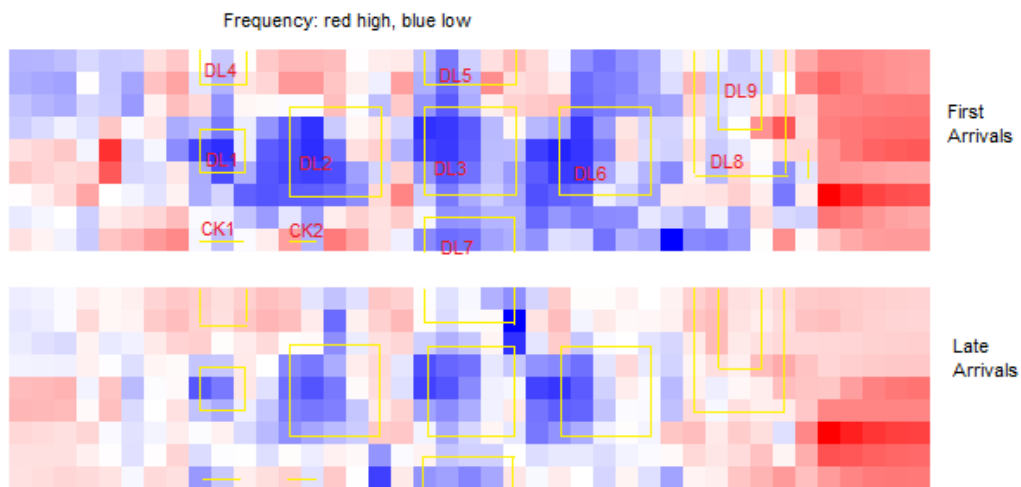
b) Planar contour map of dominant frequency

Figure F-2. New PSPA defect maps on the bridge deck.

PRECISION

Precision was evaluated through statistical analyses of the three sets of data from the three runs of the USW and IE methods on the centerline of the specimen. The USW method's repeatability results from SHRP 2 Project R06A are shown in Figure F-3a. The upper and lower bounds were calculated for each test by adding/subtracting one standard deviation σ of the three runs to/from the mean modulus of three runs. The coefficient of variation (COV) was used as a measure of repeatability, which was obtained by calculating σ of the three runs divided by their corresponding mean value μ (COV=σ/ μ). As shown in Figure F-3b, the average COV was about 12 percent. The repeatability of IE test results was also evaluated in terms of estimating the thickness of the slabs. The main points contributing to the higher standard deviation are the severely deteriorated points where slight spatial variation may cause differences in the values. Nazarian et al. (2006) have shown that for new construction, the average COV is less than 7 percent.

The thickness is calculated based on the dominant frequency and compression wave velocity of each slab. The average COV of thickness was about 6 percent. These values correspond well with the anticipated uncertainty of 5 percent to 10 percent reported in the literature for the IE method. As recommended by a number of researchers (Nazarian et al., 2006), the evaluative power of the thickness estimation with the IE method can be improved through a calibration process using one or two cores.
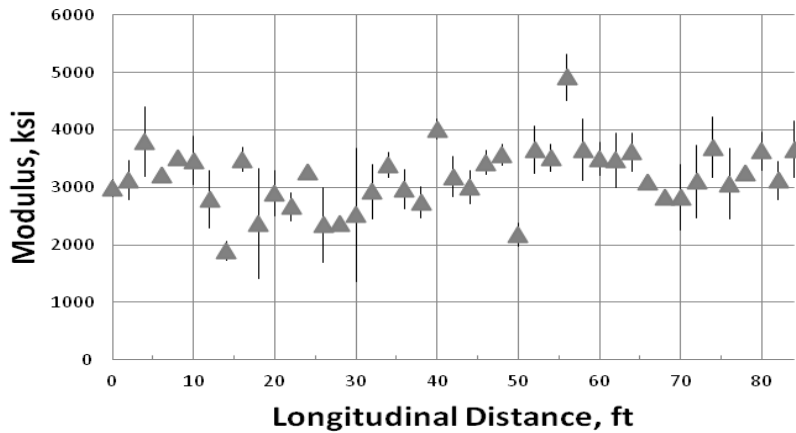
a) **Average, upper, and lower bound of modulus for each run**
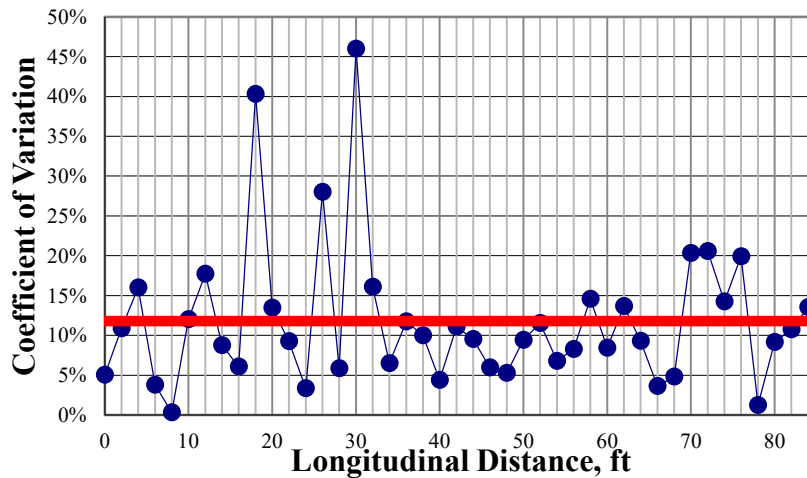
b) **Coefficient of variation of modulus**

Figure F-3. Precision of the USW method.

CALIBRATION PROCEDURES

After initial calibration by the manufacturer, a rigorous calibration is not necessary unless the sensors are replaced.

TESTING PROCEDURES

Test procedures are documented at http://www.geomedia.us/. To collect data with the PSPA, the user initiates the testing sequence through the computer. The high-frequency source is activated four to six times. The outputs of the two transducers from the last three impacts are saved and averaged (stacked). The other (pre-recording) impacts are used to adjust the gains of the pre-amplifiers. The gains are set in a manner that optimizes the dynamic range.

COST

The PSPA costs around $25,000. The speed of data collection can also be considered in the cost category because of the cost of traffic control and losses associated with traffic interruptions. Although the PSPA collects data point by point, the PSPA is a relatively rapid testing device. The data collection speed of the PSPA is about 30 s/point.

LIMITATIONS

Although the USW and IE methods are shown to be successful in detecting internal defects, there are some apparent disadvantages to consider. They are localized testing methods, and testing a long tunnel may take a lot of resources and time. Although the IE method does have the ability to show the existence of a defect, it is difficult to quantify the depth of defects that are shallow or extensive. Inadequate contact will result in inaccurate and false measurements, especially for very rough concrete surfaces and oily and curved surfaces such as tunnel linings, which cause occasional slips of the device during testing. The new PSPA has resolved some of these issues.

DATA MANAGEMENT

The PSPA saves the raw data from each test point with appropriate meta-data indicating the time and information about the test parameters. The collected data can be reanalyzed readily with new algorithms if necessary. Upon initiation of a project, the user identifies the location where the data will be stored.

DATA ANALYSIS AND INTERPRETATION

The data analysis is defined as the processing of the raw data collected by the PSPA and includes preprocessing, data analysis and presentation, and data interpretation. In the preprocessing phase of the IE method, using a time window to remove the surface wave energy from the time records provides a more robust and accurate thickness measurement as compared to when the entire waveform is used. On the other hand, in the USW method, the surface wave energy should be reinforced by implementing proper filters to minimize the reflection and body wave energy.

The graphical output of the USW and IE methods are color contour maps, namely traditional with unlimited-color index, traditional with two-color index, and checkerboard (Azari et al., 2012). The traditional contouring uses a smoothing algorithm to ensure that the displayed contour lines change gradually and incrementally from a minimum value to a maximum value. A large number of shades of primary colors are used in the smoothing algorithm when the

unlimited-color index approach is selected. The two-color index contours contain only two colors delineated by a threshold value. However, a smoothing algorithm is still used to depict the results. The checkerboard algorithm plots a rectangular array of cells. The value for each cell is determined by smoothing the results using the values of that cell and the four adjacent cells to define a surface rectangle. Recent studies have shown that representing the data in a checkerboard format enhances the evaluative power of the results (Azari et al., 2012).

To interpret the results, it is necessary to define the modulus and frequency threshold to delineate between the intact and delaminated areas. In the USW results, the target modulus was set at 0.86 to ensure that the delaminated areas are selected with a level of confidence of about 95 percent (Nazarian et al., 2006). The test points with a modulus less than 0.86 are demonstrated in red, indicating that they are defective. The threshold in IE contour maps was selected based on the thickness of the slab and the depth and extent of delamination. The test points with dominant frequency less than thickness frequency are marked as red (defective).

REFERENCES

Azari, H., D. Yuan, S. Nazarian, and N. Gucunski. 2012. Impact of Testing Configuration and Data Analysis Approach on Detection of Delamination in Concrete Bridge Deck with Sonic Methods. *Transportation Research Record*, forthcoming.

Nazarian, S., D. Yuan, K. Smith, F. Ansari, and C. Gonzalez. 2006. *Acceptance Criteria of Airfield Concrete Pavement Using Seismic and Maturity Concepts.* Report IPRF-01-G-002-02-2. Innovative Pavement Research Foundation, Airport Concrete Pavement Technology Program.

APPENDIX G
FIELD TESTING WITH ACOUSTIC SOUNDING

INTRODUCTION

This appendix describes the progress of a particular nondestructive testing (NDT) technique known as acoustic sounding, and outlines how this system will work within the framework of the Strategic Highway Research Program (SHRP 2) Project R06(G), High-Speed Nondestructive Testing Methods for Mapping Voids, Debonding, Delaminations, Moisture, and Other Defects behind or within Tunnel Linings.

This system is in its final stages of development, and has shown to be a promising technique capable of quickly determining the stage of tile debonding in tunnel linings. Since the system remains under development, this appendix discusses how the system will be used in inspection procedures and provides an idea of the end product. An evaluation of public tunnels and a series of test specimens will still be conducted for this research and will be discussed in the final report.

ACOUSTIC SOUNDING TECHNIQUE

When debonding occurs on tiled surfaces, hammer sounding by ear or by microphone can readily differentiate bonded from debonded tile. This is determined by the characteristic lower frequency pinging that occurs on debonded areas relative to fully bonded tiles. The goal of the system devised here is to provide a quick and efficient way for inspectors to characterize the condition of tile bonding in a less subjective method.

Technical Needs

In general, debonded tile can occur for two reasons: improper installation or external influences. Improper installation commonly includes the following:

- Improper use of bonding agent (e.g., mixing ratios or using the wrong type).
- Improper tile spacing.
- Excessive open time.
- A low standard of workmanship (e.g., not backbuttering the tile).

External influences can include the following:

- Environmental conditions (e.g., thermal expansion).
- Excessive tunnel lining forces (e.g., damaged lining due to voids, cracks, delamination, and debonding).

In either case, debonding of the tile can occur and pose a danger to the public. Many NDT techniques are used in this SHRP 2 project to determine the onset of damage behind the tiled wall lining prior to tile debonding, but there is a need to quickly and efficiently determine regions of tile that need immediate attention after this debonding occurs.

Research Approach

The system under development is used with a laptop computer capable of recording audio signals and installed with a version of MATLAB, and an impact source (preferably a ball-peen hammer). As the centers of tile are lightly tapped with the hammer, the laptop's internal microphone records the audio signal. MATLAB software performs a fast Fourier transform (FFT) on the data set and uses pattern recognition techniques to monitor the fundamental frequencies of flexural vibration for each individual tile. The modes of vibration frequencies in a voided tile can be predicted using acoustic theory for a rectangular plate with simply supported edges (Rossing and Fletcher, 2003):

$$f_{mn} = 0.453 c_L h \left[(\frac{m+1}{L_x})^2 + (\frac{n+1}{L_y})^2 \right]$$

where c_L is the longitudinal wave speed, h is the thickness of the tile, m and n are the integers describing the current mode of excitation ($m = n = 0$ for the fundamental frequency of flexural vibration), and L_x and L_y are the respective side lengths of the tile. The vibration frequencies increase as the voided sections of tile decrease (Liu et al., 2011). Therefore, it is theoretically possible to relate the fundamental frequency to the approximate area of debonding.

This technique can be incorporated into a program that assigns a color scale to the frequency spectrum of a tile wall under inspection. It is envisioned that the final result can operate in two methods. The first method is for near-real-time inspection. In this mode of operation, a threshold frequency from an expected frequency band representing sound concrete is established and used to make a pass-fail decision telling the operator whether the tile is most likely bonded or debonded. The second method is intended to be used in mapping a large region of tile, and the final result is a map of the tiles showing the degree of expected bond. As in the first mode of operation, the operator will select a section of tile representing a fully bonded state for the program to determine the fundamental frequencies associated with bonded sections. The user will then tap each tile in a predetermined order. For instance, the section might consist of an area 13 tiles high and 40 tiles wide. The program will prompt the user to select the layout desired, and after the user taps each tile in the given order, the program will output a plot showing the frequency spectrum.

FIELD APPLICATION IN THE WASHBURN TUNNEL

A rudimentary version of this technique was used for a proof-of-concept test in Washburn Tunnel in Houston, TX. Washburn Tunnel is the only underwater vehicle tunnel in operation in Texas and was completed in 1950. It carries a Federal road beneath the Houston Ship Channel, joining two Houston suburbs.

The tunnel was constructed via the immersed tube method, with sections joined together in a prepared trench, 26 m (85 ft) below water. The entire inner wall is tiled with 110 mm by 110 mm (4.3 inches by 4.3 inches) ceramic tiles. Like many underwater tunnels with tiled walls, this one is experiencing debonding of tile in various areas. Three sections of tile were chosen that contained debonded regions (as determined by an inspector performing hammer sounding by

ear). The regions, shown on the left side of Figure G-1, show the area under consideration outlined with blue painter's tape. The debonded section (determined by human ear) is also outlined with blue painter's tape with an X on the debonded section. On the right side of Figure G-1, scans made via ultrasonic tomography (UST) are shown with each of the three regions. The depths of the C-scans (or plan views) in Figure G-1 range from 16 mm to 103 mm (0.63 inches to 4.1 inches). One of the areas investigated (Figure G-1, middle) was evaluated using a rudimentary version of the acoustic sounding technique and is shown in Figure G-2. This example shows a strong correlation between hammer sounding by ear and the automated version.
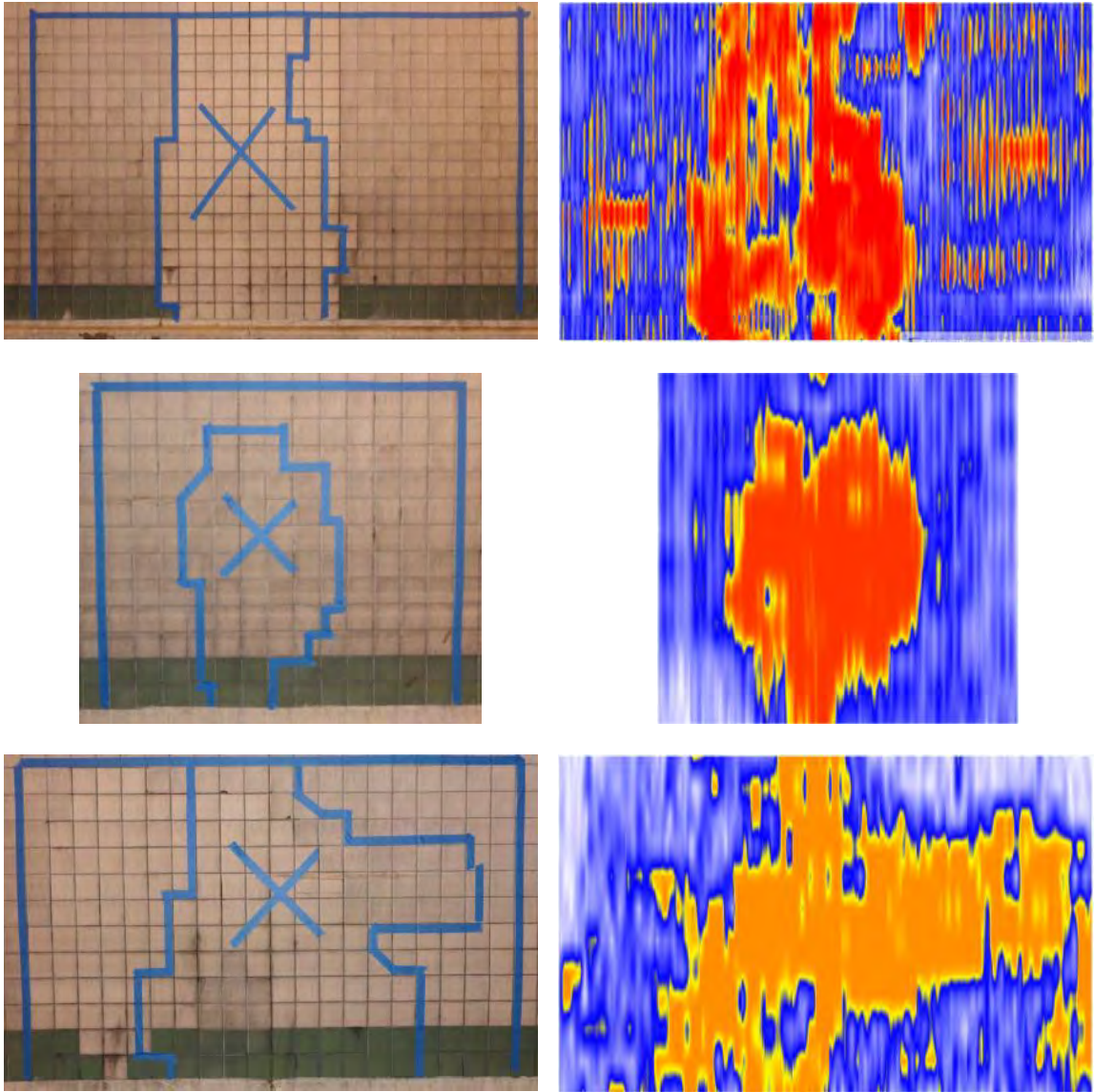
Figure G-1. Debonded regions of tile (left) paired with the associated UST C-scans (right).
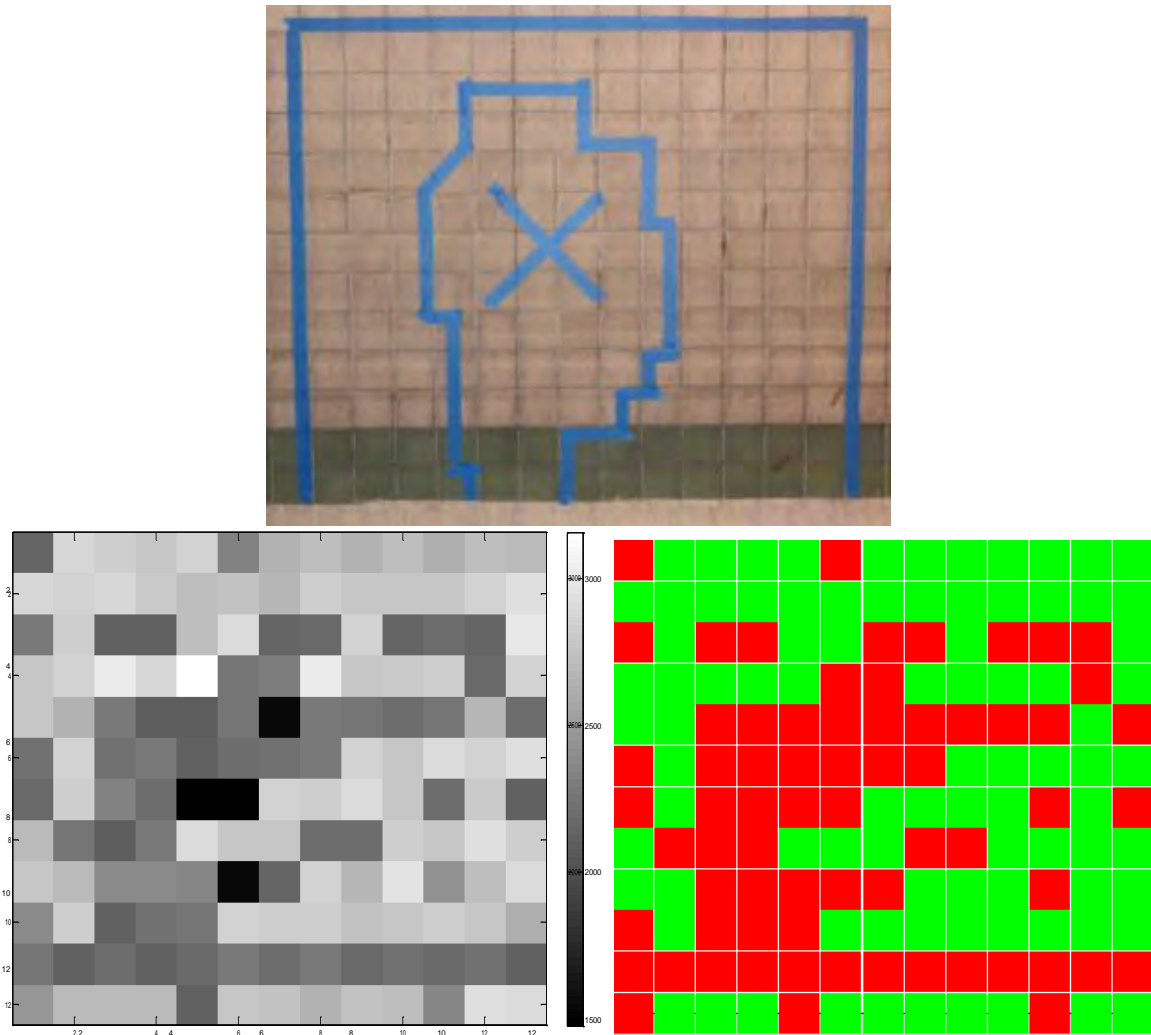
Figure G-2. Debonded regions of tile (top) paired with the acoustic sounding results (bottom).

In Figure G-2, the bottom left plot depicts the tiles color coded in grayscale, with the higher frequencies (predicting a fully bonded state) as white and the lower frequencies (predicting a debonded state) as black. As previously discussed, the lower frequencies observed should theoretically correspond to larger voided areas behind the tile. The bottom right plot in Figure G-2 shows the output with a pass-fail algorithm denoting tiles that fall below the expected fully bonded state (red is the expected debonded state, and green is the expected fully bonded state).

TESTING CRITERIA

For the automated acoustic sounding device discussed here, no system is commercially available. The following testing criteria are given to estimate the usefulness in designing/implementing this technique.

Precision, Accuracy, and Repeatability

Precision and accuracy criteria would need to be determined based on ground truth data (which were not available for the tunnel lining under inspection) of actual debonded tiles. Technological difficulties prevented the research team from completing a system for validation on test specimens within the time constraints of this project. The system described in the section "Field Application in the Washburn Tunnel" is only compared to hammer sounding (by ear) and UST, which should not be used in place of ground truth data.

Since the detection of debonded tiles depends on the frequency band chosen to represent bonded tile, the threshold value for a pass-fail decision will vary. The researchers recommend rating the failures (debonded tiles) by color-coded signals based on the proximity of the fundamental frequency response to the chosen threshold. After this is experimentally tried, it will be possible to estimate the precision and accuracy of this technique.

Repeatability will depend on the precise location of impact. It is possible to have a great deal of variance depending on how far the point of impact is from the center of the tile.

Calibration Procedures

Calibration will have to be made on a section of tile evaluated by other NDT devices or otherwise assured to be sound. The researchers recommend determining a band from several sample locations of bonded tiles. After this frequency band is determined, it can be used as a threshold value for determining debonded tiles.

Testing Procedures

It is envisioned that a developed automated sounding method will be able to operate in two modes. The first mode is for near-real-time inspection, where the threshold frequency from an expected frequency band representing bonded tile is established and used to make a pass-fail decision telling the operator whether the tile is most likely bonded or debonded. The second mode is intended to be used in mapping a large region of tile, and the final result is a map of the tiles showing the degree of expected bond. This pass-fail decision will be based on how close the fundamental frequency of the tile is compared to the threshold value. As in the first mode of operation, the operator will select a section of tile representing a fully bonded state for the program to determine the fundamental frequencies associated with bonded sections. The user will then tap each tile in a predetermined order.

Another recommendation of this technique is to develop an application for a smart phone to signal whether a tile is suspected to be debonded or bonded. In this application, a threshold value can be chosen to represent bonded tile, and significant deviations from this threshold will result in a pass-fail (green or red, respectively) screen.

Cost

The research team attempted to construct a viable prototype, but this is in progress and not yet ready for field application. It is expected that a final and proven technique would be inexpensive.

Limitations

The limitations of this device are as follows:

- *Battery power*. Any remote device will rely on battery-powered operation for long periods of analysis.
- *Consistent impact location.* Repeatability of impact can play a huge role in precision and accuracy. The operator's point of impact should not deviate significantly from the center of the tile.
- *Microphone quality.* It is uncertain at this time whether the microphone quality from a typical smart phone or laptop computer is sensitive enough for distinguishing fundamental frequencies from the ambient noises present in a tunnel. The proof-of-concept method presented above used recordings from a smart phone video recorder and post-processed with MATLAB code. When used in the field, the laptop computer had trouble recording usable data.

Data Analysis and Interpretation

The purpose of the automated acoustic sounding technique is to remove the subjective component from the operator by allowing the software to make a pass-fail decision. Further analysis and decision making would involve other NDT techniques.

Equipment and Systems Integration Requirements

It is recommended that devices use MATLAB software (http://www.mathworks.com/products/matlab/) on any platform compatible with the version purchased.

CONCLUSIONS

This automated sounding technique is still under development. Many factors influence the peak frequencies observed in the frequency spectrum from a single tile tap, including the size of the void, whether or not the hammer tap was directly in the center of the tile, and multiple-mode interference. Preliminary results indicate that this technique, although basic in its approach, could offer the tunnel inspector a quick, efficient, inexpensive, and objective technique that provides sufficient information for repair procedures or further investigation.

REFERENCES

Liu, S., F. Tong, B. Luk, and K. Liu. 2011. Fuzzy Pattern Recognition of Impact Acoustic Signals for Nondestructive Evaluation. *Sensors and Actuators: A. Physical,* Vol. 167, No. 2, pp. 588–593.

Rossing, T., and N. Fletcher. 2003. *Principles of Vibration and Sound*, 2nd ed. Springer, New York, NY.

APPENDIX H
VEHICLE-MOUNTED THERMAL CAMERA TESTING CRITERIA

ACCURACY

The vehicle-mounted thermal camera system used in this study is described in Appendix J. A commercially available FLIR A325 camera was used. The accuracy of the temperature readings is according to FLIR +/−3.6 °F (+/- 2 °C) or +/−2 percent of the reading.

Images from this system do not indicate depths of defects. However, the images can indicate possible tile debonding, delaminations up to one inch deep with a minimum surface area of 1 square foot, and voids up to 3 inches deep with a minimum surface area of one square foot, based on specimen testing. These defects can be located within one foot of their actual location with this system.

PRECISION

The precision of the system according to FLIR is less than 0.09 °F (0.05 °C). The areas of possible defects can be located within one foot of the actual defects with any system as long as the thermal contrast of the area of interest has not changed and the systems are properly calibrated.

CALIBRATION PROCEDURES

Each thermal camera manufacturer has published its own calibration procedures (if needed). With the FLIR cameras used in Finnish tests, the manufacturer recommends calibration every year. The user cannot make this calibration; the camera has to be sent to the manufacturer or authorized reseller.

Calibration is also needed for the distance measurement indicator (DMI). This usually involves driving the vehicle over a known distance (usually 1,000 ft) and checking the DMI reading against that known distance.

TESTING PROCEDURES

The operator needs to ensure that the camera is properly focused before data collection. No other special testing procedures are needed.

COST

The thermal camera itself is approximately $15,000, which includes a 90-degree wide-angle lens. The price for a complete package with racks, software, and positioning system is approximately $30,000.

LIMITATIONS

The equipment is not accurate for temperatures below −4 °F (−20 °C) and over 248 °F (120 °C). This is according to the FLIR A325 camera default calibration. The normal operating temperatures are between 5 °F (−15 °C) and 122 °F (50 °C).

DATA MANAGEMENT

Data management consists of thermal camera data and positioning data collection and storage. The data management under this study was with the Road Doctor CamLink software with the Road Doctor TD Module

DATA ANALYSIS AND INTERPRETATION

Data analysis requires specialized software that allows the viewing of thermal camera image data as a video image. The software also needs to prepare a thermal color map from the tunnel wall or roof that can be used for monitoring real changes in temperature and detecting anomalies. In addition, the software should be able to filter unwanted external noise from the thermal data.

APPENDIX I
SURVEY OF THE CHESAPEAKE TUNNEL

INTRODUCTION

Since 1982, SPACETEC has offered a scanner system to monitor disruptions and conditions of tunnel linings (Figure I-1). With this tool, it is possible to validate the effects of degradation, like crack developments, cavities beneath the surface, changes in material composition, and water intrusions, over time.

Figure I-1. **TS3 scanner.**

The scanner is able to record high-precision surface, thermographic, and three-dimensional (3D) images simultaneously with a resolution of 10,000 pixels and a recording angle of 360 degrees (Figure I-2). The SPACETEC scanner is capable of identifying cracks as small as 0.3 mm in width. The rotating mirror speed of up to 300 Hz is one of the crucial features for the measuring speed. It determines a fast and nondestructive measurement with only a short period of traffic disruption. The compact scanner can be installed in almost every road vehicle that offers enough space for the scanner head and the operator console, such as a minivan.
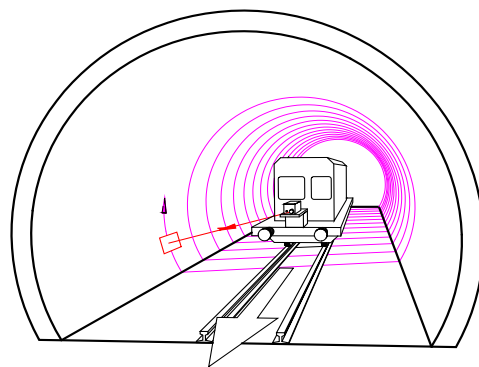
Figure I-2. Scanning principle.

The data are visualized with an easy-to-use, powerful software package to display all three channels (visual, thermal, and 3D) simultaneously. The software allows for a tunnel inspection on the screen, with a pixel-by-pixel synchronism of the recordings. This helps to analyze and identify suspicious anomalies and compare them on all three channels.

Image manipulation like adjusting the contrast and brightness of the display is also possible, as is creating 3D presentations and performing a 3D zoom of image details. In many

cases, long-term monitoring supports the observation of the tunnel degradation over time with multiple measurements and a recording interval of at least 1 year.

A survey of the Chesapeake Tunnel in Virginia was performed in April 2011. The survey was conducted according to the subcontract agreement with the Federal Institute for Materials Research and Testing (BAM).

The Chesapeake Bay Bridge Tunnel is a 37-km-long link crossing the mouth of the Chesapeake Bay and connecting the Delmarva Peninsula's Eastern Shore of Virginia with Virginia Beach and the metropolitan area of Hampton Roads. The bridge tunnel system combines bridges via four artificial islands with the Timble Shoal Tunnel (the western side of the bay) and the Chesapeake Tunnel. The Chesapeake Tunnel is one of two immersed-type (sunken-tube) tunnels constructed under the ship channels of Chesapeake Bay in the approximately east-west direction and was opened in 1964. Since it opened, the tunnel has been exposed to extreme environmental conditions. Water intrusion and corrosion have been reported during visual inspections.

The portal-to-portal length is 1661 m, with a roadway (two-lane) width of 7.3 m plus a sidewalk on one side. The tunnel interior is faced with ceramic tiles, which is uncommon for non-U.S. tunnels. Therefore, the surface of the concrete lining underneath is inaccessible.

This appendix describes the methods and results of the survey and is divided into the following parts:

- Available data channels.
- The recording process, including scanner measurements and scanning parameters.
- A description of results, including a brief introduction to data processing and a detailed description of the data.
- Working with the data.

The corresponding datasets, including the analysis software package, were shipped with an external hard drive to BAM on January 6, 2011.

AVAILABLE DATA CHANNELS

Visual Images

Visual images (Figure I-3) are most frequently used for general documentation and maintenance purposes. They show the condition of the lining as far as visible phenomena are concerned. At any time, later data may be consulted to look for changes in these conditions.

Figure I-3. Visual image showing the conditions of a shotcrete lining in a motorway tunnel.

Profile Data

Profile data (Figures I-4 and I-5) show the dimensions of the tubes and are used to consider and solve clearance problems.

In the small range, the presence of distance measurements at high density allows for finding and identifying surface defects (for instance, a chip-off or spalling) of the lining.
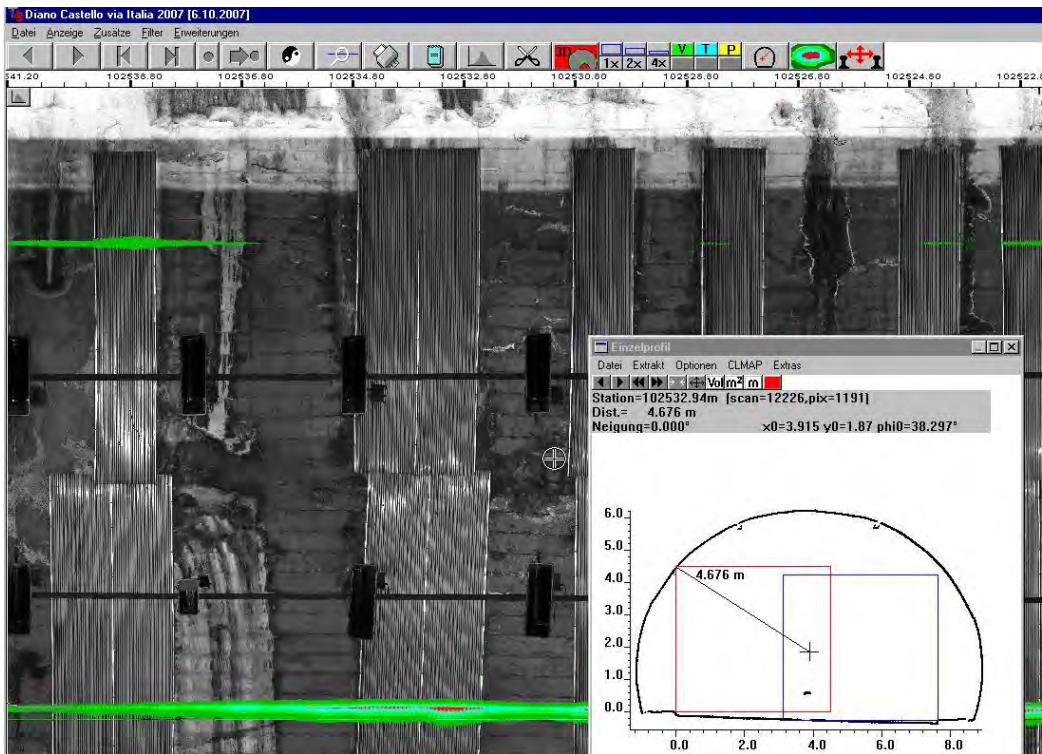
Figure I-4. Structural gauge investigation in a motorway tunnel. Red spots indicate obstructions to the given clearance profile. The user may determine cut volume and the affected area immediately at the screen.
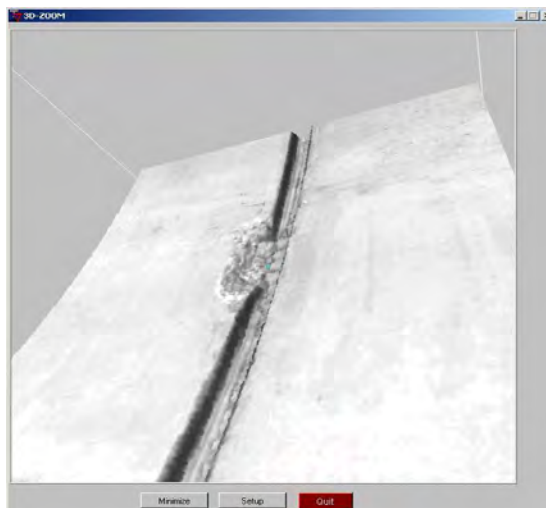
Figure I-5. 3D view of the concrete surface in a tunnel with damage (chip-off) near the joint of two sections.

Thermal imaging (Figure I-6) results in a measurement of the surface temperature in the tunnel interior.
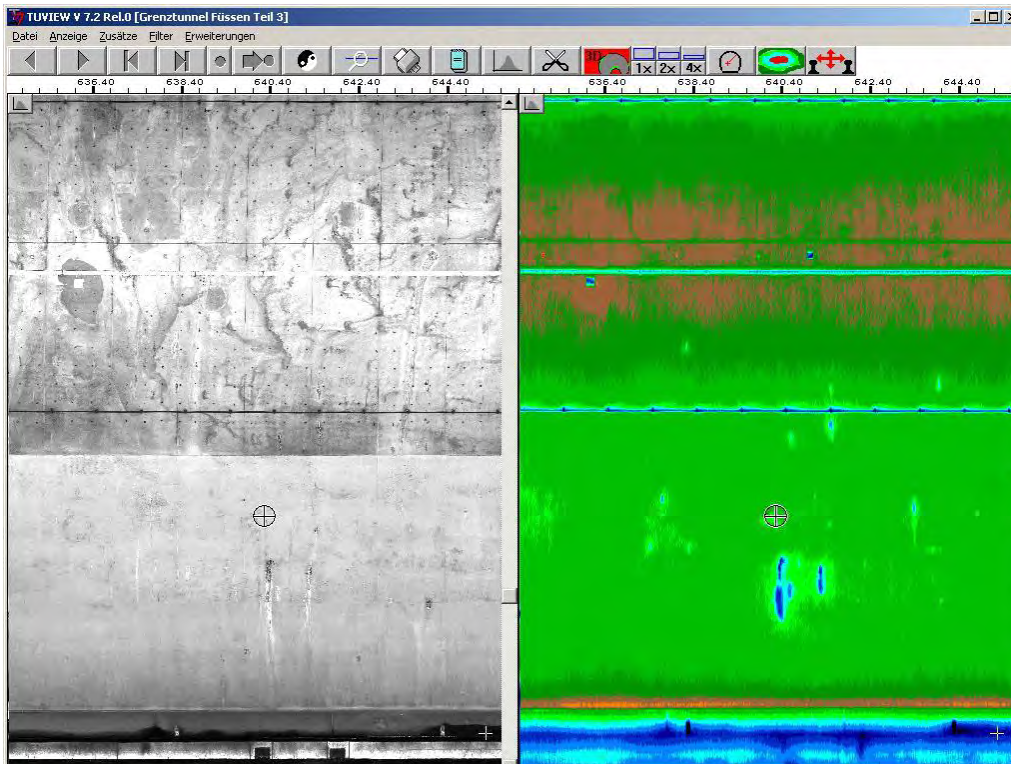
Figure I-6. Example of a thermal image showing water infiltration. Due to the evaporation of water on the surface, a clear cold signal is obtained. This marks even smaller spots with water very clearly.

Temperature differences determine information about the state of the lining and are the result of interacting processes between the surface of the lining and the air in the tunnel, such as:

- Cooling due to evaporation of water from the surface.
- The reaction of the lining material during cooling or heating.
- The influence of cold and warm temperatures, respectively, at the surface.
- Surface roughness.
- Cavities (gravel nests below the surface, bad contact of the lining to the rock, and gravel rock material).
- Non-homogeneous material composition.

Using detailed known measuring conditions, certain thermal interactions can be excluded, and a correct interpretation of the thermal imaging is ensured. A quasi-stationary heat flow between the air in the tunnel and the rock behind the lining determines suitable measuring conditions. In the case of unknown heat-flow conditions, certain features cannot be clearly identified. However, the thermographic image displays signals that offer supplemental information to the visual image (Figure I-6). This can be used to highlight some effects, like the evaporation of water.

The pre-measurement program used in this project was part of the thermographic survey and evinced proper conditions for the recording. The temperature survey had to be done in a short period due to permanently changing temperatures in the Chesapeake Tunnel. The TS3 scanner system by SPACETEC was able to perform such a fast and reliable measurement.

RECORDING PROCESS

Table I-1 provides a data summary of the Chesapeake Tunnel.

Table I-1 Data summary of the Chesapeake Tunnel.

Time of measurement	April 11–12, 2011
Scanning length	1680 m
Vehicle speed	approx. 1.5 km/h
Recording channels	infrared (8–12 µm) 10,000 px/scan visual 10,000 px/scan profile..
Mirror speed	160 Hz
Temperature resolution	approx. 0.1 °C
Spatial resolution	3 mm × 3 mm at the surface

With the inspection vehicle used for this survey (Fig. I-8), it was not always possible to keep the intended driving speed of 1.5 km/h constant (the speeds were as high as 3.5 km/h). Therefore some pixels are stretched in the driving direction. Driving too fast may cause gaps of the laserscan lines at the tunnel wall, which influences in some cases visibility of the cracks. To avoid such problems, it is necessary to maintain a nearly constant speed during the survey.

The survey was performed during the night between April 11 and 12, 2011. During the measurement, a sufficient temperature difference for a quasi-stationary heat flow was obtained. The TS3 scanner was installed on the roof in the rear part of the inspection vehicle (Figure I-7). This provided an undisturbed 360-degree measurement. The highest resolution of 10,000 pixels was used for an appropriate imaging of fine-scale features.

A full traffic closure was not possible; thus, the recording was performed twice: in the north-south direction of the lane to Virginia Beach and vice versa on the opposite lane toward the eastern shore of Virginia. The traffic could pass the inspection vehicle, as is visible in the recordings.

Figure I-7. Inspection vehicle in the Chesapeake Tunnel.

DESCRIPTION OF RESULTS

Data Processing

The recorded data were geometry corrected, and the 360-degree display of the tunnel was projected with a defined scale onto a plane surface (Figure I-8) for a synchronous display of all three channels.
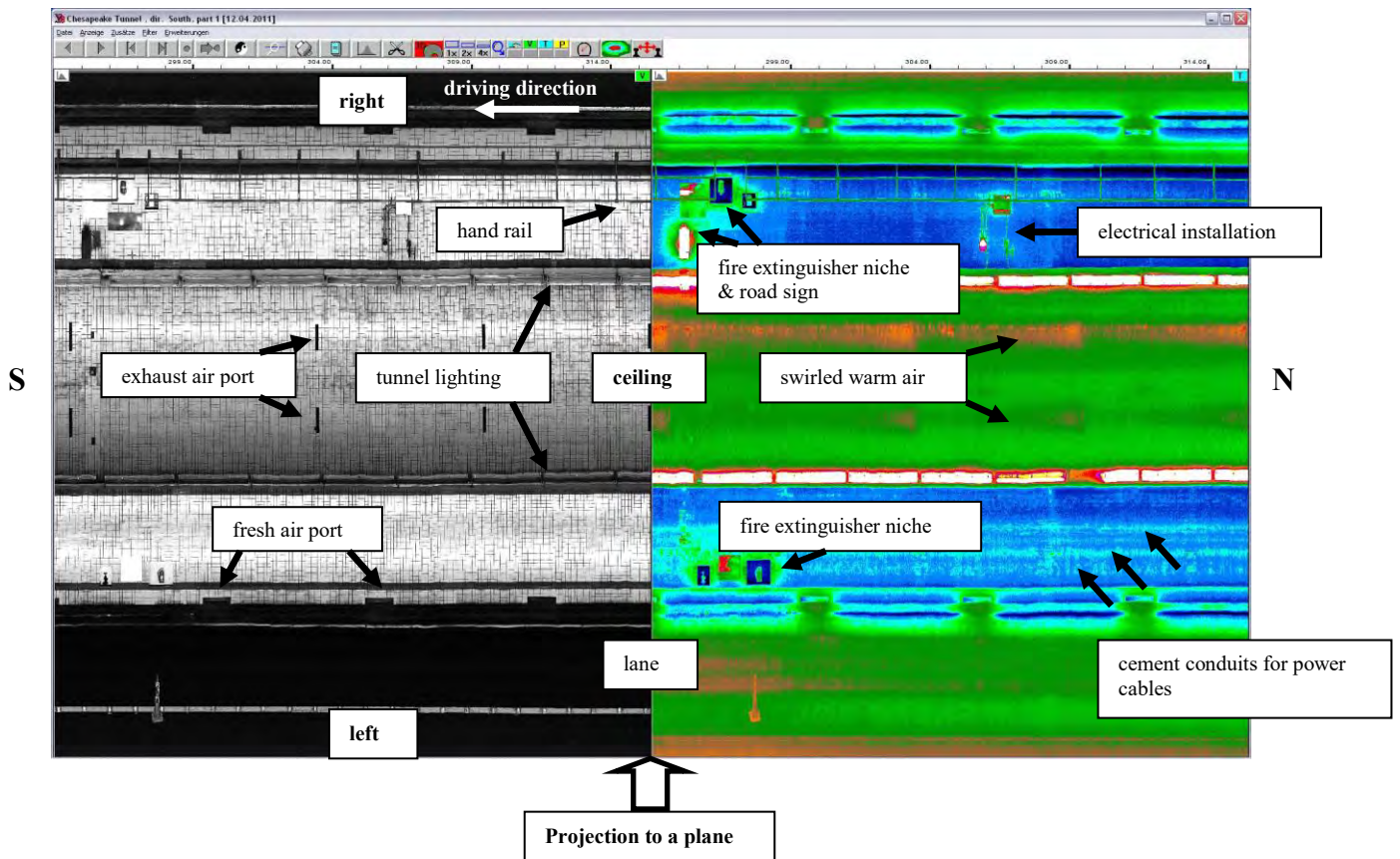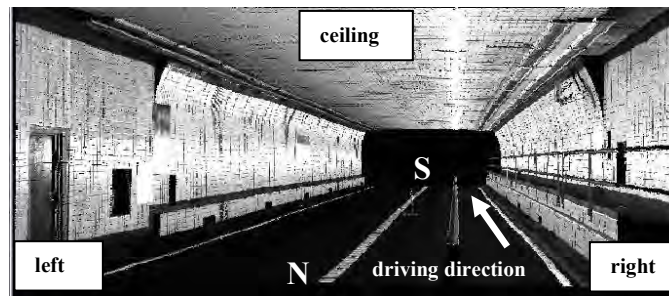
Figure I-8. A perspective view (bottom) demonstrates the projection of the cylindrical-shaped tunnel onto a plane (top). The top panel displays the true-scale projected tunnel with a visual (left) and thermal (right) channel from an interior view. Both synchronized channels show the same location and the same content with different datasets.

One lane was recorded in the north-south driving direction, and the second lane was recorded in the opposite (south-north) direction. Figure I-8 is labeled with the corresponding driving direction (south or north) and with an absolute true-scale location in meters. Common artificial installations like hand rails, air ports, and electrical and maintenance installations are highlighted. They are clearly visible in both data channels. The cement conduits behind the ceramic tiles are only visible in the thermal image and correlate with information from the construction plans of the tunnel.

A full dataset consisted of a visual, thermal, and three-dimensional channel that was formatted and edited to evince a true-to-scale display, labeled with a meter range (a change in feet was also possible, if needed).

The thermal data were corrected by the commonly existing air temperature drift along the tunnel axis. After leveling, thermal data were displayed with a constant air temperature. Therefore, the same phenomena were displayed with the same colors. The data interpretation was based on local temperature differences (anomalies); thus, an absolute temperature was not needed.

Every thermographic surface point corresponded to a color-coded temperature interval with a temperature resolution of 0.1 °C (Figure I-9) and 16 colors from black, blue, green, red, yellow, and white. This color palette gave an intuitive physiological impression of cold (dark to blue) and warm (red to white) temperatures.

Figure I-9. Color scale for thermographic images.

Figure I-8 highlights the most common installations in the dataset, which could mainly be ascribed to artificial origins, like the following:

- Fresh and exhaust air ports and corresponding swirled air.
- Hand railings, niches, and supply boxes installed in the lining wall.
- Traffic lightings and signs.
- Tubes behind the lining, visible in the thermal image.

Visual Results and Distance Measurements

Since opening in 1964, the tunnel has been exposed to a strong environmental impact through exhaust gases from traffic, corrosion, and water intrusion. In general, the visual damages are easy to identify and self-explanatory. Figure I-10 displays split and dirty ceramic tiles, which are the main concern of disruption.
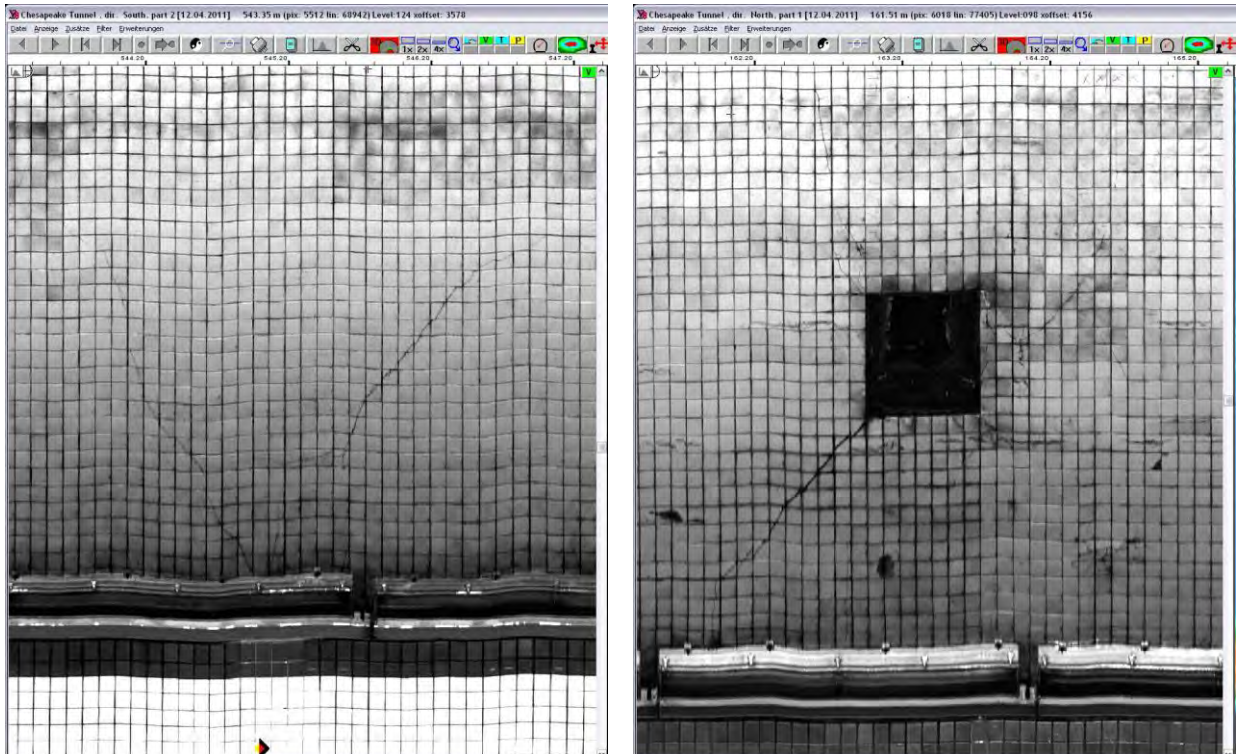
Figure I-10. Development of split ceramic tiles (south, 544 m; north, 163 m).

Besides the importance of profiles for clearance considerations in the railway sector, the distance measurements can be used for damage characterization. The dimensions of the damaged areas can be easily worked out.

Figure I-11 shows one of the common types of damage, broken or missing tiles, which are clearly visible in the visual channel (upper left). A perspective view of this area (A) (lower right) displays more details and is useful for damage assessment. A distance profile (middle) helps to estimate the dimensions of these disruptions or highlight artificial installations like emergency lighting (B). The thermal image usually shows a clear cut in the outer rim of disruptions. The right side is positioned in the wind shadow and is cooler (darker blue), and the left side is exposed to the warm, lighter air flow coming from the right side of the image. In the area directly ahead and in 90 degrees beside the detector, the sensor is over-modulated, and the intensities of the reflected signal are very high, which is highlighted by an intense horizontal stripe in both channels.

The loose and broken tiles are mainly located on the ceiling of the tunnel (Figures I-10 and I-11).
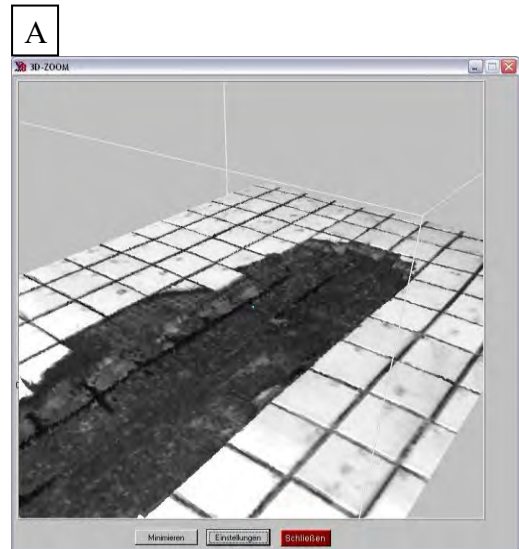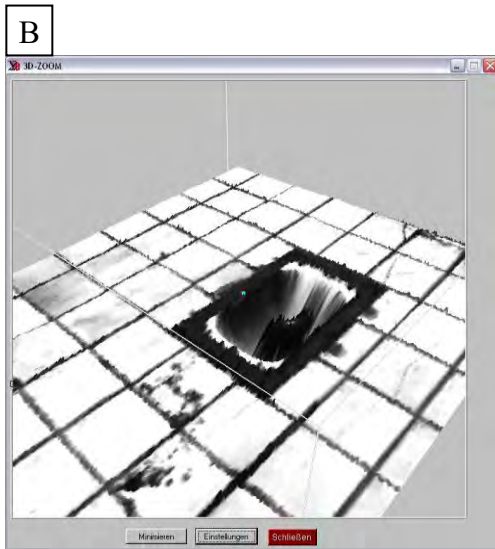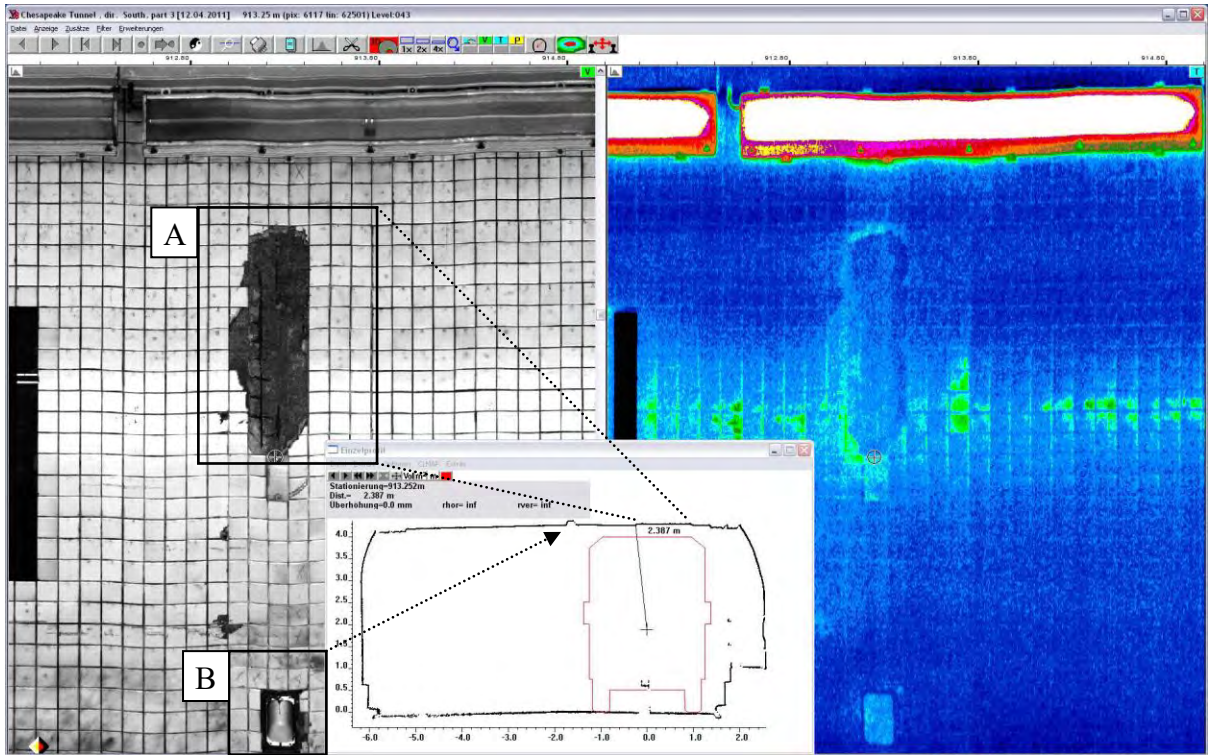
Figure I-11. Views of broken or missing tiles.

Classification of Thermal Anomalies

Thermal images consist of a thermal conduction from the tunnel interior into the rock. This determines the qualitative correspondence to the nature of the heat source, as shown in Table I-2.

Table I-1. Dependency between temperature anomaly and heat conduction.

Anomaly	Thermal conduction	Possible reasons
cold	better	Good thermal contact between rock and lining: • water in lining • higher density of the material
warm	worse	Bad thermal contact between rock and lining: • loose, less lithified rock • lower density of the material • higher porosity, hollow spaces

Some local temperature anomalies could be explained by construction factors, for example, air swirls due to obstacles (road signs and traffic lights), niches (which could be recognized in the visual images), and tubes behind the linings.

Detailed analysis and interpretation of the data were applied interactively on the screen. Visual and thermal images were analyzed simultaneously to figure out some correspondences between temperature-related patterns and visible constructions. The color-coded temperatures and the color resolution were adjusted to the specific temperature anomaly to improve the visibility of the objects.

The Pre-measuring Program

A pre-testing unit was installed in a fire extinguisher niche 250 m away from the western portal (Virginia Beach). The unit could not be installed at the place with the worst-case conditions for thermal measurements in the middle of the tunnel because the distance for data transfer through a cable to the next telephone plug would have been too long.

The pre-measurement program was used before and during the recording of the thermal image. It allowed for advanced determination of the time and weather conditions that would be favorable for the purpose of the survey. It documented the required heat flow conditions during the thermal measurement between the lining and the rock to resolve and interpret patterns of heat anomalies.

Temperature sensors were placed in the target structure. One sensor measured the air temperature, the second sensor measured the material temperature near the surface at a depth of 0.075 m, and the third sensor measured deeper depths of 0.3 m. The data logger (master) read and stored the temperature recordings (usually one record per hour) permanently from the sensors (Table I-3). The data could be accessed via telephone line and displayed on the screen (Figure I-12).

Table I-2. Pre-measurement program of the Chesapeake Tunnel.

Location in the tunnel	Sensor depth	Remarks
250 m from the east (to Virginia Beach)	at the front of the lining 0.075 m in the lining 0.3 m in the lining	air temperature temperature differences
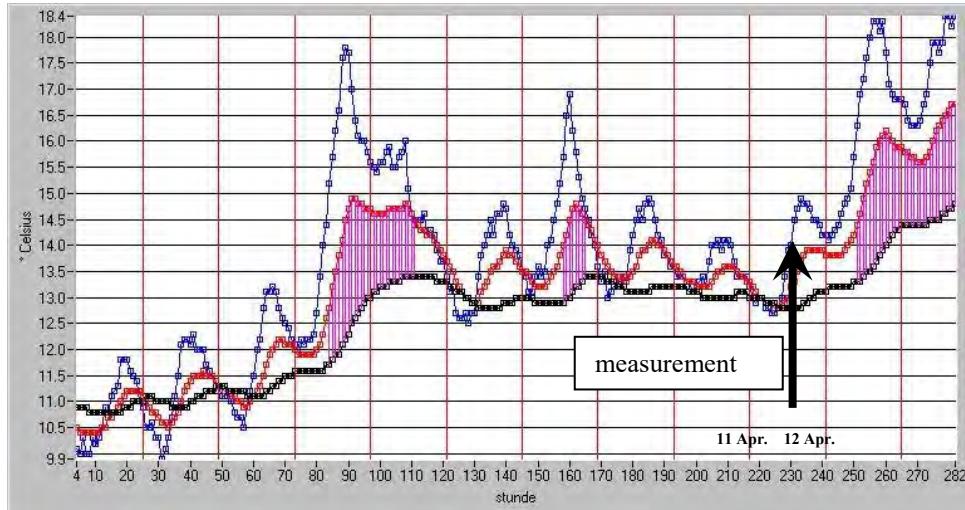
Figure I-12. Temperature alignment prior to the thermographic survey.

Thermal Results

The temperature at the tunnel surface reflected the heat conduction of the lining below the surface. Figure I-13 displays an example of a heat flow under different material conditions with a cavity or wet spots (which are not visible at the surface). The displayed situation is typical for warmer seasons: the air temperature in the tunnel is higher than the rock temperature.

The stationary heat flow between the air temperature and the rock resulted in a surface temperature that was dependent on the heat conductivity of the lining. A cavity reduced the heat conductivity and resulted in a higher surface temperature. Therefore, the tunnel thermography revealed damages in the lining when they influenced the conductivity.

The quasi-stationary measuring conditions were adjusted naturally with the corresponding weather conditions and the air temperature when the tunnel had proper air convection due to a chimney effect caused by different air pressures between the tunnel portals or due to steady traffic. Long-term surveys of other tunnels revealed a number of good measuring conditions during a period of several months.

Figure I-14 displays the effect of the thermal reflections of the installed constructions on the bended corners of the tube. The ceramic tiles seemed to have a higher reflectivity in the infrared spectrum. This is uncommon for concrete or brickwork tunnel linings.
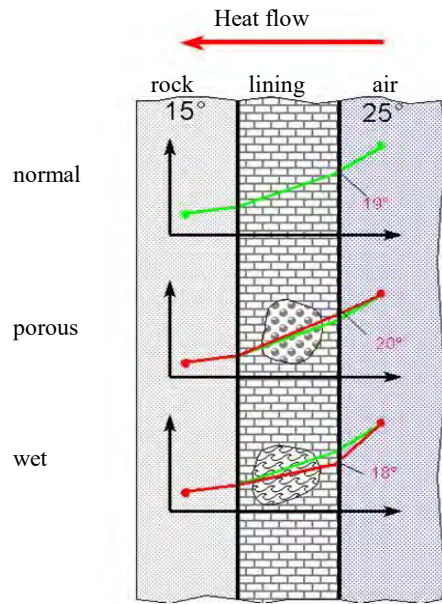
Figure I-13. Dependency of the surface temperature on the heat conduction of the lining material.
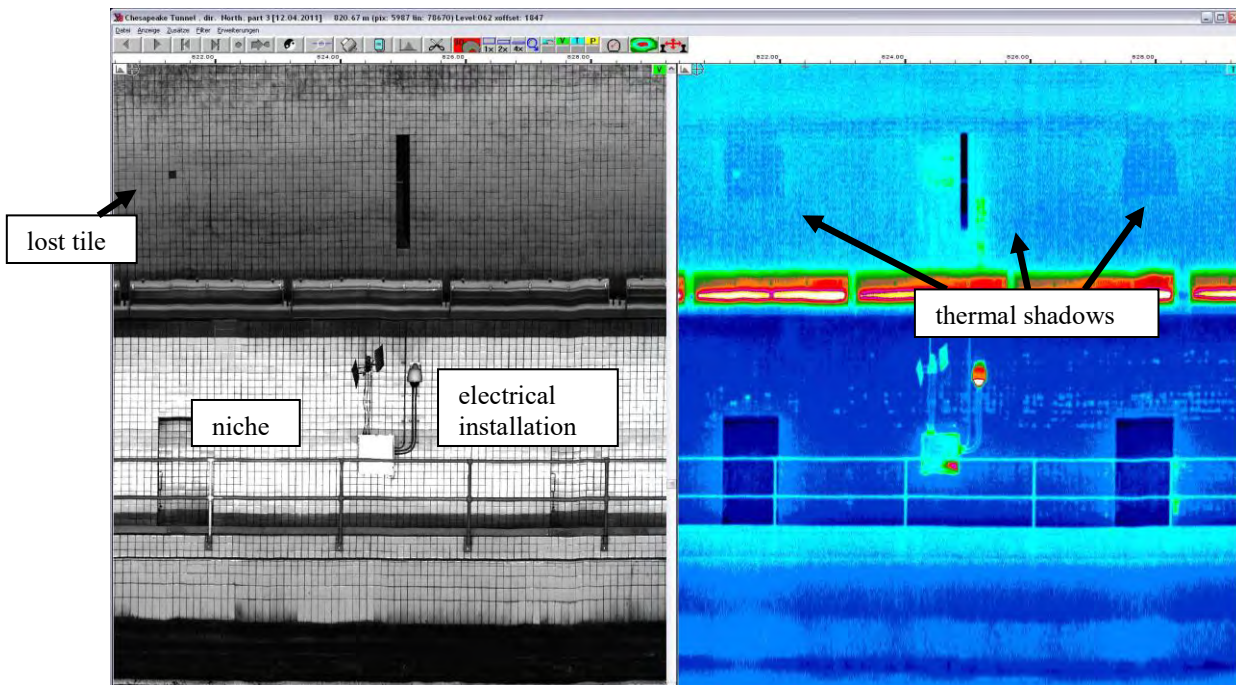
Figure I-14. Thermal shadows of the installation. The ceramic tiles have a higher reflectivity in the infrared spectrum (north, around 825 m).
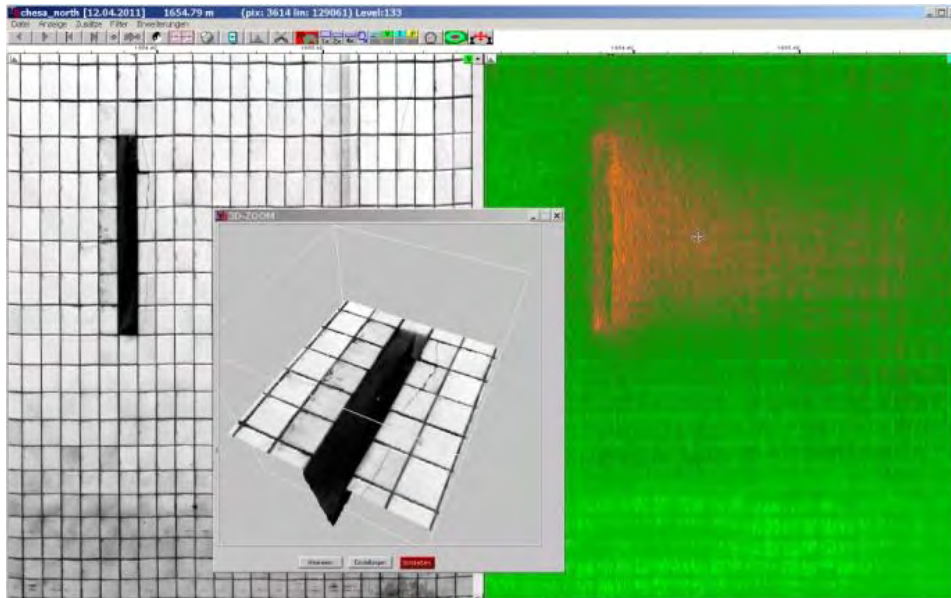
Figure I-15. Air flow from a port in the ceiling of the tunnel. The warmer air flows in the right-hand side direction and is clearly visible in the thermal image (north, 1654 m).

Figure I-16 reveals some linear structures behind the lining of a side wall, which is referred to as drainage channels with a lower heat conductivity and higher temperatures. This indicates that the building documentation needs to be reviewed before further investigations.

In the overall length of the tunnel, some temperature-related anomalies were detected (Figure I-17). Some larger temperature anomalies that could not be ascribed to artificial sources were revealed. The thermography displayed a center with lower temperatures (higher heat conductivity) surrounded by a rim of higher temperatures (lower heat conductivity). The origin of these anomalies was unknown. Figure I-18 displays a common feature that was visible in both the visual and the thermal datasets: joints between the tiles showed a different reflectivity, which seemed to indicate renewed ceramic tiles.

The main findings in the thermographic dataset were:

- Cable channels and drainage tubes behind the linings with lower heat conduction.
- Areas with lighter tile joints, maybe renewed or repaired tiles, with different materials and lower heat flow at the side walls.
- Areas with larger anomalies behind the ceiling walls.

Concerning the interpretation of the thermographic images, it was not always possible to make exact determinations of what was behind a surface. Therefore, it was necessary to conduct further investigations on the reasons for the weak points in the lining.
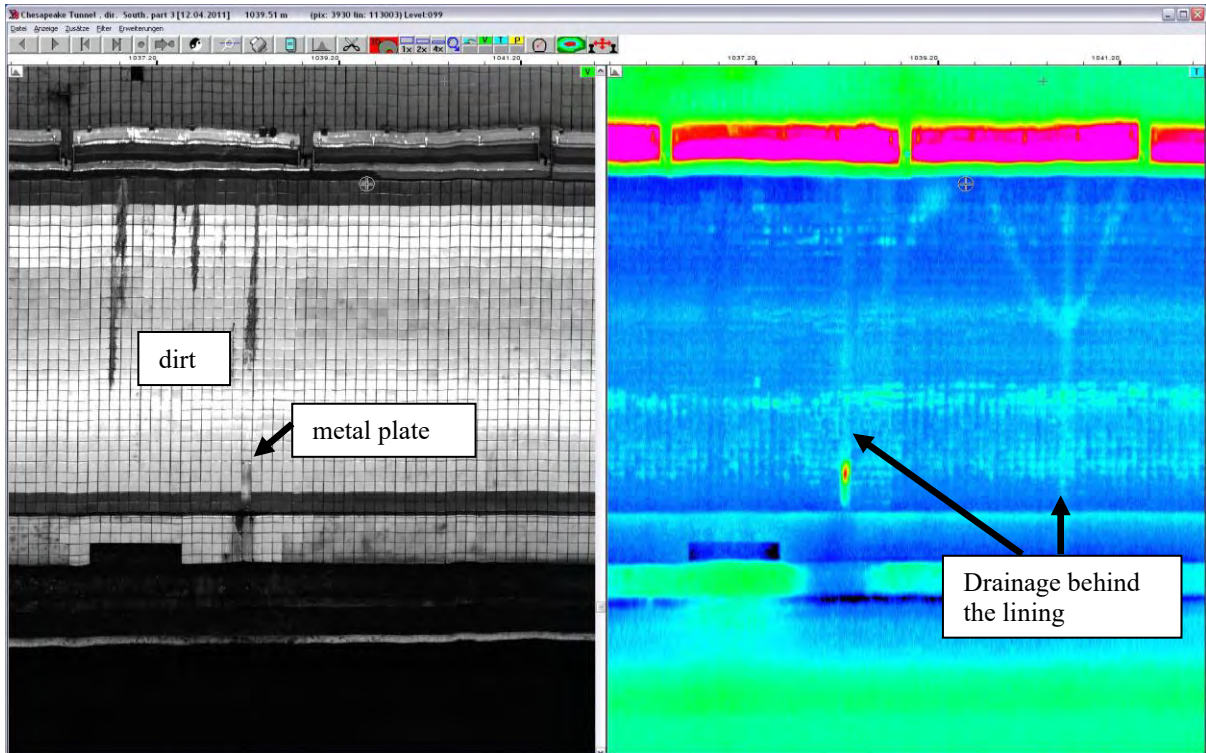
Figure I-16. Visible structures at the surface and drainage behind the lining surface (south, 1038 m).
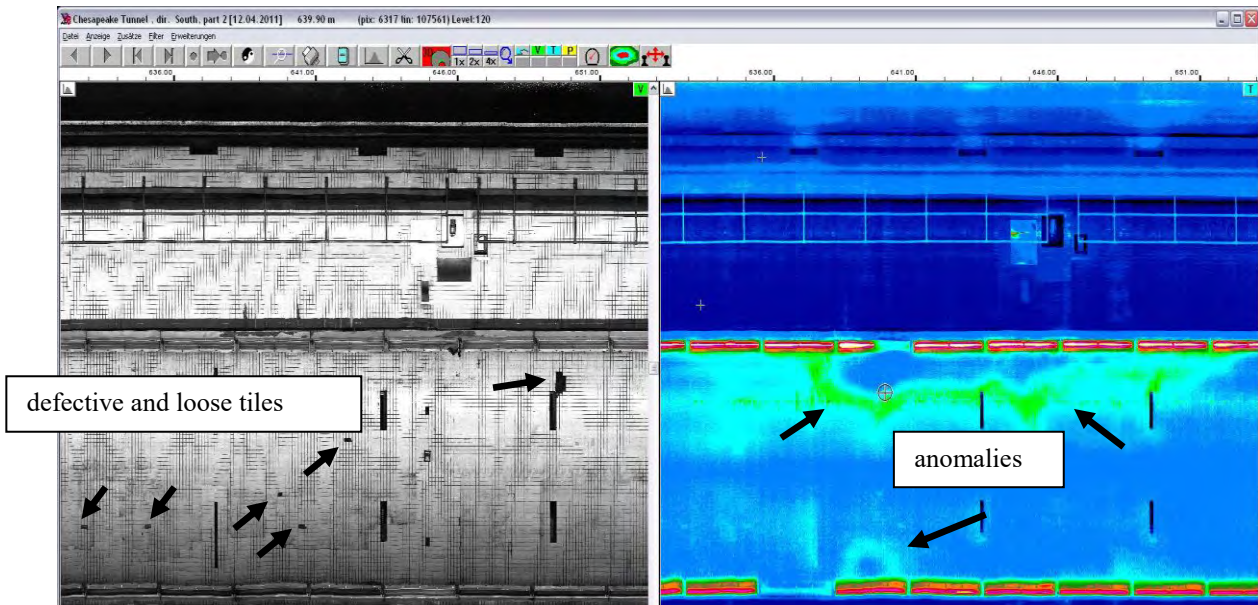
Figure I-17. Loose tiles (left) and warmer temperature anomalies in the ceiling area (south, 636–652 m).
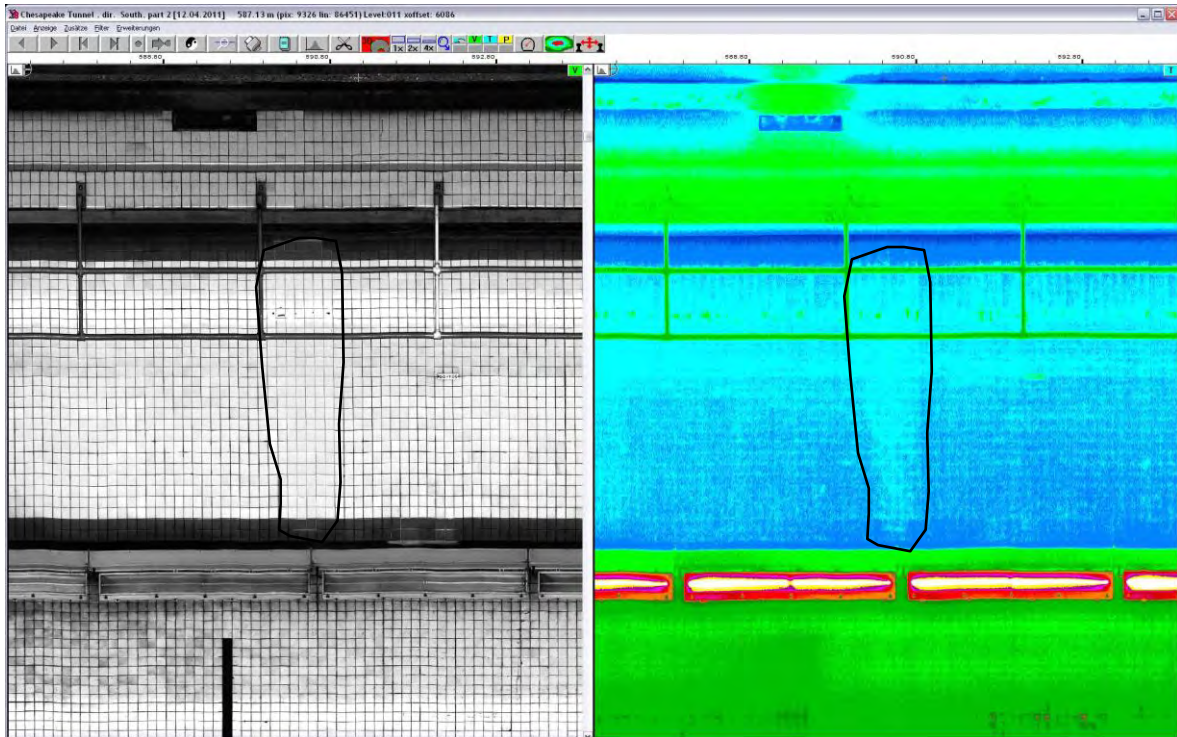
Figure I-18. Renewed tiles with different, compacted material (south, around 675 m).

WORKING WITH THE DATA

TuView was the software package used to analyze and display the datasets of the corresponding three channels. Data access was provided by information files containing the specifications for the image files and the true-scale information.

TuView offered the ability to highlight zones of interest with different color codes. The information was saved in notebook files, which were delivered with this report. The notebook files were separated into the following categories: blue indicating artificial installations like road signs or traffic lights, red indicating damaged areas (loose and broken tiles), and green indicating anomalies of unknown origin.

APPENDIX J
TUNNEL TESTS IN FINLAND 2010-2011

INTRODUCTION

The second Strategic Highway Research Program (SHRP2) is a 7-year program that started in 2005 and is managed by the Transportation Research Board (TRB). A significant component of the program is research and development of innovative, high-speed, nondestructive testing and evaluation technologies that promise to accelerate design evaluations and construction inspection for highway renewal projects. One of these research and development projects has been focusing on the field of nondestructive testing (NDT) of highway tunnels (SHRP2 Project R06-G).

Tests in Finland have been concentrating on research of the technical feasibility of ground penetrating radar (GPR) air-coupled antenna (horn antenna) systems, thermal cameras, and laser scanners, as well as their integrated analysis, for tunnel lining condition monitoring. The idea is to test whether these systems can provide reliable and repeatable data and to collect information concerning the potential sources of error in these techniques. Another goal for these tests is to provide basic information on the potential defects, such as moisture problems close to the surface of tunnel lining structures. Since all the basic test instruments (GPR, thermal cameras, laser scanners) and survey vans that can be used for the tests are located in Finland, these tests were be carried out in two tunnels in the Helsinki area in Finland. The tests were done for the SHRP2 R06(G) project by Roadscanners Oy in cooperation with the Finnish Transport Agency.

TESTED TECHNIQUES

Ground Penetrating Radar Technology

The ground penetrating radar method is based on the use of radiofrequency electromagnetic (EM) waves with a frequency range from 100-5000 MHz. Physical parameters of the medium affecting the GPR waves are conductivity, dielectricity, and magnetic susceptibility.

The impulse radar is the most popular ground penetrating radar type. Its working principles are as follows. A short electromagnetic pulse, generated in a transmitter antenna, is sent into the medium. The length of the pulse ranges from under a nanosecond to tens of nanoseconds, depending on the frequency. Part of the pulse energy is then reflected from different structural surfaces with different electrical properties, and part of the energy is propagating through the interface and is reflected from interfaces beneath. The signal attenuation depends on the geometric attenuation, signal scattering, reflections, and thermal losses. The two-way travel time and reflection amplitudes are recorded with a receiver antenna. When the measurements are made rapidly over sequential survey points, it can be viewed as a GPR profile.

The depth penetration of ground penetrating radar depends on the antenna frequency, i.e., the signal wavelength. The signal attenuation is greater with higher frequencies, and the signal depth penetration is smaller. On the other hand, the resolution improves.

Ground penetrating radar antennas can be divided roughly into two categories: air-coupled antennas (see data example, Figure J-1) and ground-coupled antennas. These in turn

can be either monostatic, where the same antenna acts as a transmitter and a receiver, or bistatic, where transmitter and receiver units are different antennas. Most of the pulse radar antennas are bistatic, but the antenna elements are contained in a single box. The frequency of the ground-coupled antennas differs from 80 MHz to 2500 MHz. Their advantage compared to air-coupled antennas is better depth penetration. Ground-coupled antennas have better resolution of the individual objects than the air-coupled antennas, but with the ground-coupled antennas, surveys are done considerably slower.
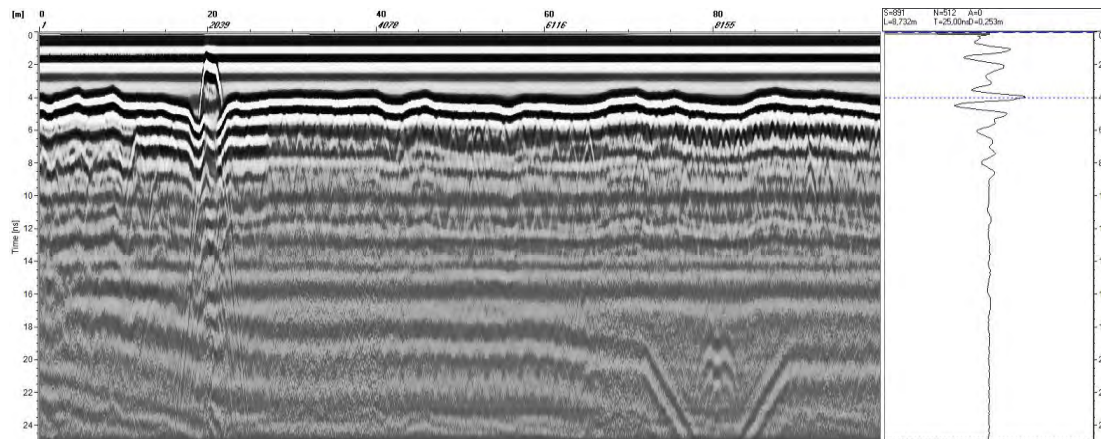
Figure J-1. An example of an unprocessed GPR data profile from a concrete tunnel wall presented with a single scan alongside. Data were collected using a GSSI 1.0 GHz horn antenna.

The goal of the tests in Finnish road tunnels was to test if air-coupled GPR can be used in different types of tunnel lining measurements. Two test tunnels were selected to represent different road tunnel types. The first tunnel was a concrete tunnel, and the other lining was made of a shotcrete. The air-coupled GPR system used in these tests was an SIR-20 mainframe with an air-coupled 1 GHz horn antenna, model 4108, manufactured by Geophysical Survey Systems Inc, USA (GSSI) (Figure J-2).

Air-coupled GPR data collection settings were the same as used normally in pavement thickness and quality control surveys. Collected data consisted of 100 scans per meter, 16 bits, and 512 samples per scan. A time window of 30 ns was slightly longer than that normally used in pavement surveys. All GPR data processing and analysis were done using Road Doctor™ (RD) Pro software by Roadscanners Oy. The collected data preprocessing was done using standard methods, including automatic air-coupled elevation and amplitude correction, background removal, and vertical time domain filtering. The standard GPR data analysis consisted of reflection amplitude and dielectric value calculations and their analysis.
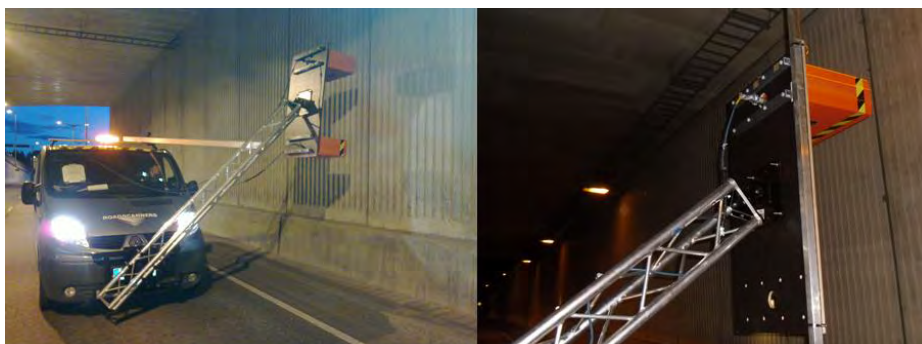
Figure J-2. The survey van equipped with GSSI horn 1.0 GHz antennas.

Thermal Camera (TC) Technology

The thermal camera method is based on the use of electromagnetic infrared (IR) waves, which means that the TC wavelength is located between GPR waves and visual light. Thermal cameras are built to receive and record infrared waves reflected and emitted by objects, thus thermal camera surveys are classified as a nondestructive survey method. Thermal cameras have been used in traffic infrastructure surveys for several decades, but recently the quality of new digital thermal cameras has increased so much that interest in this technology has started to grow. Currently, new high-precision thermal cameras can measure small changes in surface temperatures, even at the range of 0.05 $^{\circ}$C. The camera measures infrared radiation with a wavelength of 8-12 μm.

In the SHRP2 tunnel project, the goal was to test if and how well digital thermal cameras can detect thermal anomalies from tunnel linings, pointing out areas of moisture anomalies, voids, or cracks. The other goal was to test different kinds of data collection and analysis techniques to find an optimal survey method. Tests were done in both a concrete tunnel and a shotcrete tunnel. In this project, the data were collected using a FLIR A325 digital thermal camera made by Flir Systems Inc, USA. All thermal data processing and analysis were done using Road Doctor™ Pro software with the Road Doctor™ Thermal Diagnostics (RDTD) module. Figure J-3 presents a screen capture from the Vuosaari Tunnel roof raw (unprocessed) thermal video data. The video screen capture is taken from the RDTD video viewing tool.
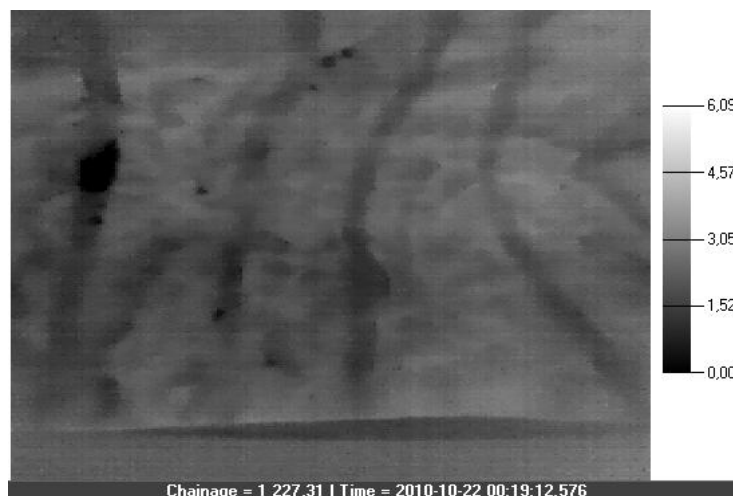
Figure J-3. Thermal video screenshot from Vuosaari Tunnel roof with thermal scale. Darker lines present the location of drainage pipes beneath shotcrete. Black spots are locations of excess moisture.

The thermal videos were collected using Road Doctor™ CamLink video equipment by Roadscanners Oy. In addition to the digital thermal videos, normal digital videos were also recorded. All the collected data were linked to the distance information using CamLink's software synchronization file. In the collected thermal video, the resolution was 320 x 240, and thermal videos were collected using a 60 Hz image frame rate. The device manufacturer declares a ± 2 $^{\circ}$C or ± 2 percent accuracy for the thermal camera. Figures J-4 and J-5 present examples of FLIR thermal camera mounting systems used on the survey van. The mounting system presented in Figure J-5 was judged to be better because an analysis of the data indicated that it reduced the thermal reflection of the van, which was causing noise in the data.

Figure J-4. Thermal camera installed on the roof of the van in the first measurement.

Figure J-5. Thermal camera installed on the end of the beam behind the van.

Laser Scanner Technology

As with GPR and thermal camera techniques, laser scanner techniques also apply electromagnetic waves. Laser scanning is a technique where the distance measurement is based on the laser beam travel time from the laser scanner to the target and back. In recent years, the greatest advancements in all of the NDT techniques used in infrastructure surveys have been made in the field of laser scanner techniques. It is inevitable that these systems will become standard tools used in a variety of tasks in traffic infrastructure condition management systems.

A laser scanner is composed of three parts: a laser canon, a scanner, and a detector. The laser canon produces a laser beam, the scanner circulates the laser beam, and the detector measures the reflected signal and defines the distance to the target. The distance measurement is based on the travel time of light or phase shift or a combination of these. The quality and price of mobile laser scanner survey systems vary, but they can be roughly classified into two categories: effective high accuracy systems (Category A), and cheaper laser scanner systems with reduced distance measurement capability and accuracy (Category B).

The goal in the laser scanner tunnel tests was to test if the method could provide valuable information concerning the tunnel lining condition and shape. The Category A laser scanner data were collected by GEOVAP Ltd, from the Czech Republic, using their quantum three-dimensional technique based on Lynx laser scanner hardware. The GEOVAP survey vehicle is presented in Figure J-6. Data analysis and all the presentations were made by GEOVAP using their software packages. The Category B laser scanner data were collected by Roadscanners Oy using a model SICK LMS151 laser scanner. The survey van is presented in Figure J-7. The data analysis was made with a new Road Doctor™ Laser Scanner (R LS) module, which is an additional module for the Road Doctor™ Pro software. The module facilitates integrated analysis of the laser scanner data and other survey data in Road Doctor™ Pro software.

When the laser beam angle is known, as in the setups shown above, and beams are sent in different directions from a moving vehicle with a known position, it is possible to make a three-dimensional surface image—a point cloud—of the road and its surroundings. A point cloud can have billions of points with accurate x, y, z coordinates and reflection or remission characteristics. Since all points have coordinates, it is possible to measure distances between points and changes between these distances. This gives extra value to tunnel management tasks, for instance, changes in the position of a tunnel lining after an earthquake. For these high-accuracy x, y, z tasks, Category A laser scanner systems are needed. An example of a point cloud view of the Vuosaari Tunnel mouth area is shown in Figure J-8. The accuracy of the laser scanner survey can be reduced by different factors that affect visibility, such as dust, rain, fog, or snow.

Figure J-6. Category A laser scanner survey system used in this research.

J-7. Category B laser scanner mounting systems used in the trials.

SICK laser scanners measure the distance to a reflective objective, as well as the amplitude of reflection, i.e., remission. This reflection is different for different materials, textures, and colors; for instance, changes in moisture content in a shotcrete tunnel wall could be detected using the laser scanner remission analysis method. This information was analyzed from the Category B laser scanner data collected in this study. Figure J-9 presents a reflectivity image produced from the Vuosaari Tunnel roof.
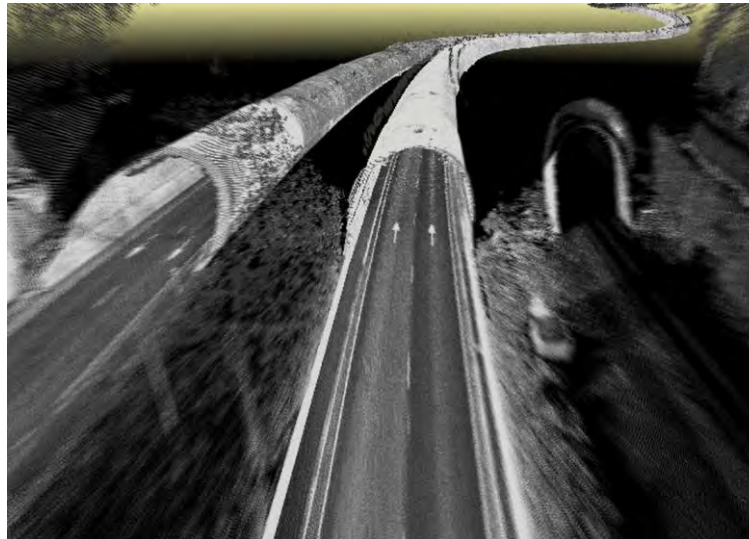
Figure J-8. Three-dimensional surface image of road tunnel produced from Category A laser scanner data (Vuosaari Tunnel mainland opening).
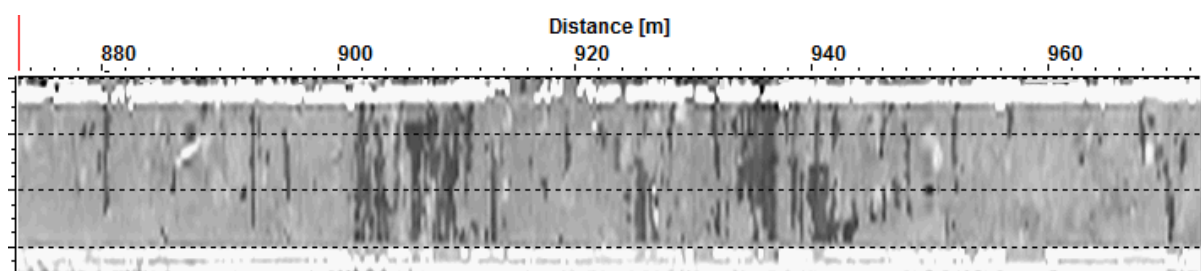
Figure J-9. Remission (reflectivity) surface image from Vuosaari Tunnel roof produced from Category B laser scanner data. Black areas present areas with higher moisture content in shotcrete surface.

FINNISH TEST TUNNELS

Two test tunnels were chosen for this research project in cooperation with Roadscanners and the Finnish Transport Agency. The selected tunnels represent common types of tunnels in Finland and are also very common tunnel types in the United States (US). Both tunnels are located in the Helsinki area of southern Finland. The first test tunnel, called Hakamäentie Tunnel, is a concrete tunnel, and the second test tunnel, the Vuosaari Tunnel, is built in igneous bedrock under a sea bay and has a shotcrete surface structure. The tunnels are part of the Finnish public road network and are owned and maintained by the Finnish Transport Agency.

Hakamäentie Tunnel

The Hakamäentie Tunnel is located in the Helsinki City area of Kivihaka. The 320 m long tunnel was built to alleviate traffic jams on the Hakamäki road and consists of two tubes,

both with two lanes of traffic in opposite directions (Figure J-10). Most of the traffic consists of private cars and inner-city heavy traffic. The tunnel is modern and was opened in 2009. Tunnel walls and ceiling consist of casted concrete block elements (Figure J-11). The tunnel is in good condition, and moisture-related problems have not been detected.

All the data collection was done in the southbound tunnel, with most of it on the right wall. Due to traffic volumes through the tunnel, all the measurements were done in a closed lane during the night.

Figure J-10. Hakamäentie Tunnel opening and GPR measurement van in the tunnel.

Figure J-11. Hakamäentie Tunnel structure.

Vuosaari Tunnel

The 1520 m long Vuosaari undersea tunnel is located in the eastern Helsinki area leading from the mainland to the new Vuosaari port. The tunnel consists of three tunnels—one railway tunnel and two road tunnels—both with two lanes (Figure J-12). The tunnel was excavated through bedrock, and the rock surface was covered using 80 mm of shotcrete with steel fibers. Drainage pipes were installed behind the shotcrete. Between the shotcrete and bedrock, there is also 50 + 50 mm of frost insulation (Figure J-13). The greatest part of the traffic consists of heavy trucks heading to and from the Vuosaari port. This tunnel is also new and was opened in 2007. The tunnel is mainly in good condition, but some water leakage has been detected recently, especially in the roof.

All the data collection was done in tube A along the right wall leading south. Due to traffic in the tunnel, all the measurements were done in a closed lane using an automatic lane control system.
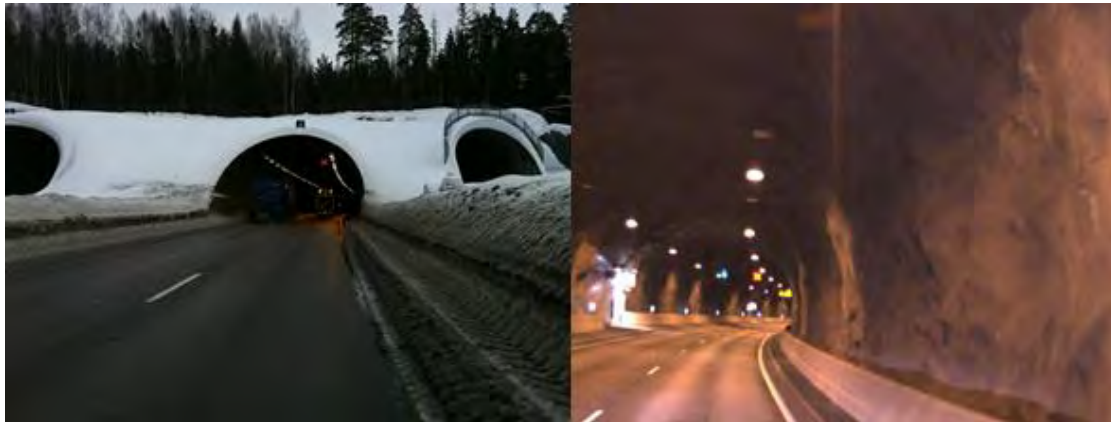
Figure J-12. Vuosaari test tunnel. The A-tunnel opening is on the mainland, the railway tunnel is on the right, and the B-tunnel is on the left.
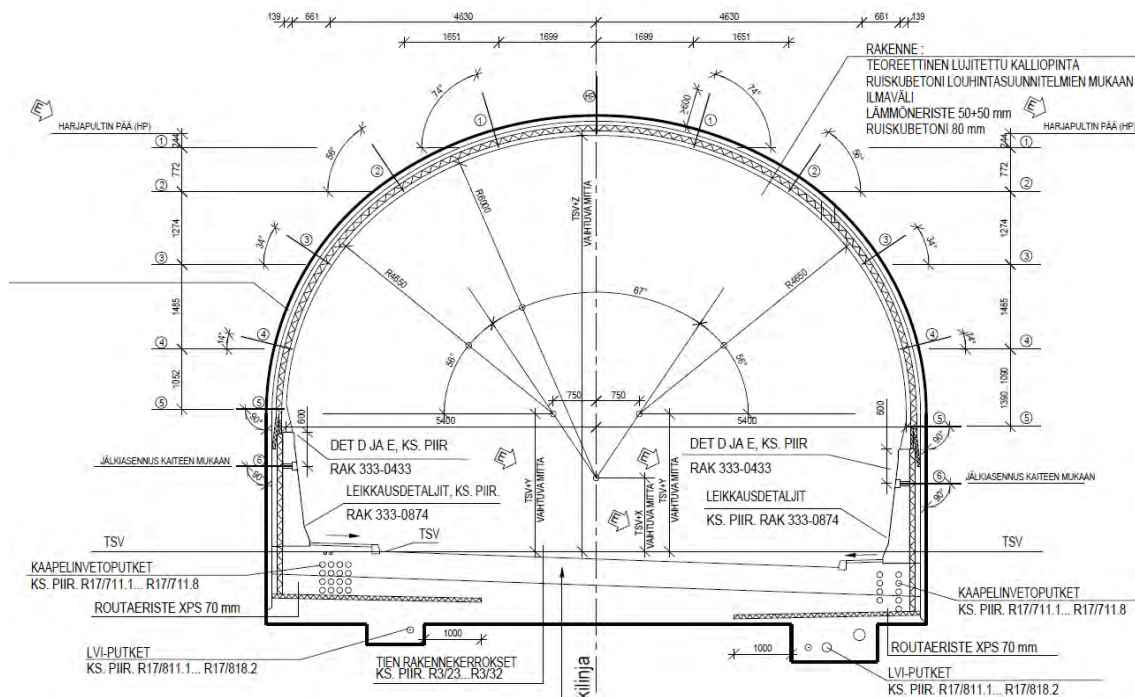
Figure J-13. Vuosaari Tunnel structure.

SURVEYS CONDUCTED

The survey program consisted of four test trials. The first trial was done to test the data collection technique and procedure in both tunnels, and actual data collection was done in the other three trials. Based on the experience of the previous trials, the data collection practice was further developed in each trial. Measurements performed and developments in the data collection practice are described below.

Technical Test, June 2010

Technical tests took place in the Hakamäentie southbound road tunnel in June 2010. The primary goal in these tests was to develop GPR measurement techniques and rack systems for air-coupled GPR tunnel measurements (see Figure J-10). The GPR measurements, using two GSSI air-coupled 1 GHz horn antennas, were performed on the Hakamäentie concrete tunnel walls and roof. Altogether seven survey lines were measured. GPR tests with GSSI 2.2 GHz antennas were also done, but the results were quite poor due to the high amount of noise in the survey data close to tunnel mouths caused by a TV station nearby. In addition to GPR tests, short and simple thermal imaging system and laser scanner tests were also performed. The results of these tests provided important knowledge of measurements, and both data collection hardware and software were improved based on the experience.

Fall Tests, October 2010

The second part of the tunnel tests with GPR were performed in the Hakamäentie Tunnel, and the Vuosaari Tunnel was also surveyed. Trials took place in October (week 42) in 2010. These tests represented data collection in the fall when air temperature and tunnel wall temperature are most likely on the same level. The right-hand wall in both research tunnels was selected for further measurements and analysis.

On the technical side of the data collection, the crew tested the new GPR rack system. The system was modified based on the experiences from the first technical tests in June. The new system solved problems with the antenna height adjustments. To make the GPR rack system lighter, the second horn antenna was removed. A rolling beam receiving support from the pavement surface was added. The new system was more rigid but a bit more difficult to use. With the new rack system antenna, it was easier to maintain a constant distance between the wall and the antenna. The GPR measurements in the Hakamäentie Tunnel were made along seven parallel lines on the right-hand wall in the southbound tunnel. Data were collected using a single 1.0 GHz horn antenna. Measurements were started at a height of 1.4 m, and the lines had a 0.3 m offset. The GPR survey in the Vuosaari Tunnel consisted of six parallel lines on the right-hand wall in the southbound tunnel. The 1.0 GHz horn antenna was also used. The respective heights of the survey lines were 1.0, 1.5, 2.0, 2.5, 3.0, and 4.0 m.

Thermal camera measurements were also conducted in both test tunnels. Data were collected at nighttime to minimize the warming effect of the sun at the tunnel ends. Digital thermal videos were recorded in the Hakamäentie Tunnel on the right-hand wall of the southbound tunnel. In the Vuosaari Tunnel, thermal data were recorded from the right-side wall and roof in the southbound tunnel. Different data collection speeds were also tested with a thermal camera.

Laser scanner measurements were conducted in both tunnels. The laser scanner was positioned as low as possible to obtain as wide a coverage as possible. One laser scanner data collection run covered both tunnel walls and the roof. Different data collection speeds were also tested with the laser scanner.

Winter Tests, February 2011

The third part of the tunnel measurements was done in the beginning of February (week 5) in 2011. Both the Hakamäentie and Vuosaari Tunnels were tested. Surveys consisted of GPR, thermal camera, and laser scanner measurements. Data collection was done using the same technique and procedure as in the previous trial of fall 2010, but in addition, some new ideas concerning measurement practice were also tested. Some improvements were made to the antenna rack supporting beams and thermal camera and laser scanner positioning. The main goal of the measurements was to collect data in the winter with air temperatures below 0 ^{o}C and compare the results to the previously collected fall data.

The GPR measurements in the Vuosaari Tunnel consisted of seven parallel lines on the right-side wall in the southbound tunnel. The first measurement line was at a height of 1.6 m. The second line was at a height of 1.8 m, and the next lines were spaced 0.30 m apart up to 3.3 m. Due to snow and ice on the tunnel mouth, the first section of the tunnel was excluded from the data collection. The GPR measurements in the Hakamäentie Tunnel consisted of four parallel lines on the right-hand wall in the southbound tunnel. Measured heights were 1.5 m, 2.0 m, 2.5 m, and 3.0 m. Here, snow and ice, packed against tunnel wall and road edges, also caused problems for data collection. Due to these problems, some survey lines measured in the fall tests could not be repeated.

Thermal camera measurements were repeated in the Vuosaari and Hakamäentie Tunnels. Thermal videos were recorded in both tunnels on the right-hand wall in the southbound tunnels. Some problems were encountered with the distance measurement instrument (DMI) due to really slow van speed. This problem was solved before the fourth measurement session. In the early phase of the thermal data analysis, it was discovered that the thermal emission image of the van reflected from the tunnel wall to the video. To avoid this, the thermal camera was mounted on the end of the beam behind the van in the Vuosaari Tunnel.

Laser scanner tests were also improved. Earlier laser scanner measurements provided good results from the tunnel ceiling, but information from the walls' reflection features was limited. To get a better image of the tunnel wall reflectivity, the laser scanner was oriented toward the Vuosaari Tunnel southbound right wall. Basic laser scanner measurements were also repeated in both tunnels. Repeated measurements covered the tunnel walls and ceiling with a single measurement.

Summer Tests, June 2011

The fourth and last road tunnel trials were done in mid-June (week 24) in 2011. These surveys consisted of GPR and thermal camera measurements. Measurements were carried out using the same techniques and data collection procedures as in previous measurements. The goal of the measurements was to collect data during the summer when air temperature is high and compare the results to the previously collected fall and winter data. In this survey, tests were also conducted concerning the effect that data collection speed has on the GPR and thermal data quality. A third goal in the summer tests was to collect GPR horn antenna data at different distances from the tunnel wall to find out possible effects on the data.

The GPR measurements in the Vuosaari Tunnel consisted of four parallel lines on the right-side wall in the southbound tunnel. Measurement lines were at heights of 1.6 m, 2.1 m, 2.4 m, and 3.1 m. The GPR measurements in the Hakamäentie Tunnel consisted of basic

measurement lines at heights of 1.5 m, 2.0 m, 2.5 m, and 3.0 m. Additionally, GPR measurement repeatability, measurement speed, and GPR antenna distance from the wall were tested on the tunnel wall at a height of 2 m. Data collection speed tests were conducted using the following speeds: 6 km/h, 20 km/h, and 30 km/h. Antenna distance to the tunnel wall in the speed tests was approximately 80 cm. The effect of GPR antenna distance to the tunnel wall was tested at distances around 0.5 m, 1.0 m, and 1.5 m.

Thermal camera surveys were repeated in the Vuosaari and Hakamäentie Tunnels in the summer tests. Thermal videos were recorded in both tunnels on the right wall of the southbound tunnels. Additionally, the effect of using different measurement speeds was tested in the Vuosaari Tunnel. The tunnel was thermal videoed using van speeds of 20 km/h, 40 km/h, and 60 km/h.

Later in the summer, data were collected from the Vuosaari Tunnel using a quantum three-dimensional laser scanner technique developed by GEOVAP from the Czech Republic.

Data Collection Practice, Lessons Learned

The experience of the data collection tests was that the GPR antenna rack system used in the Finnish tests was difficult to use. This rack system (Figure J-10) was cheap to build, but the measurement practice was slow and laborious. The height of the antenna using this rack system is adjustable, but the system is not able to reach higher than 4 m without special modification. The problem was that the rack became unstable at heights higher than 3 m. The beam support wheels rolling on the pavement also caused some problems, and all objects on the pavement on the road side needed to be cleared before measurement. Manholes and curb stones also caused problems. Compared to the Finnish system, the Texas A&M Transportation Institute (TTI) GPR mounting system used in the US tests was obviously a better solution. This TTI system uses a special truck with an electric crane, allowing adjustment of antenna height, angle, and distance to wall (Figure J-14).
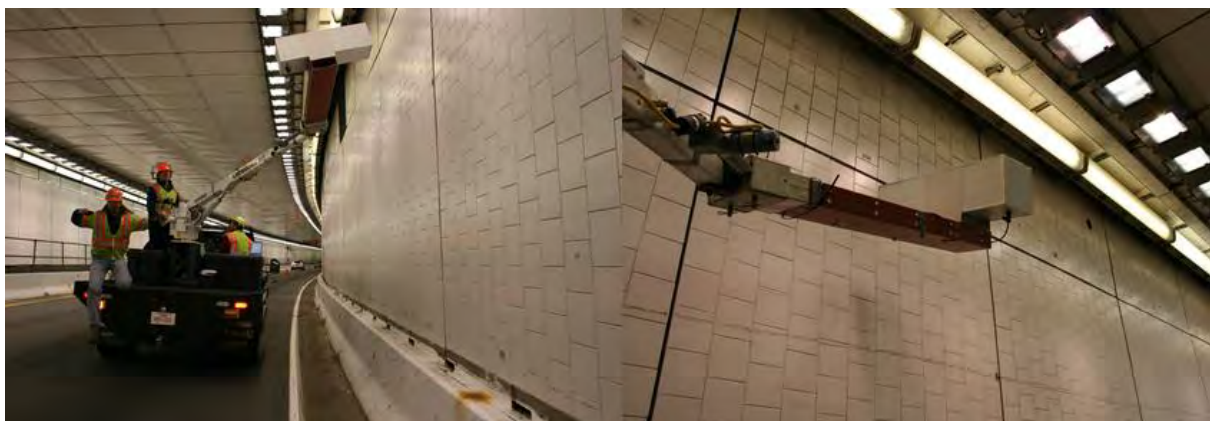
Figure J-14. GPR antenna mounted on a crane. This system, developed and used by the Texas A&M Transportation Institute, was used in SHRP2 tunnel tests in the US.

In the thermal video-logging data analysis, it was observed that thermal camera position and angle has a great effect on video quality. Thermal noise produced by the vehicle is lower when the camera is placed farther away from the survey van. The thermal camera needs to be installed either in front of or behind the vehicle. The camera also needs to be aimed in such a way that only the area of interest is visible; this way, the most accurate and informative thermal data can be collected. For thermal video logging in the US, the thermal

camera was also installed on the end of the beam of the crane. It was easy to get the thermal camera to the correct position, especially in high and wide tunnels (Figure J-15).
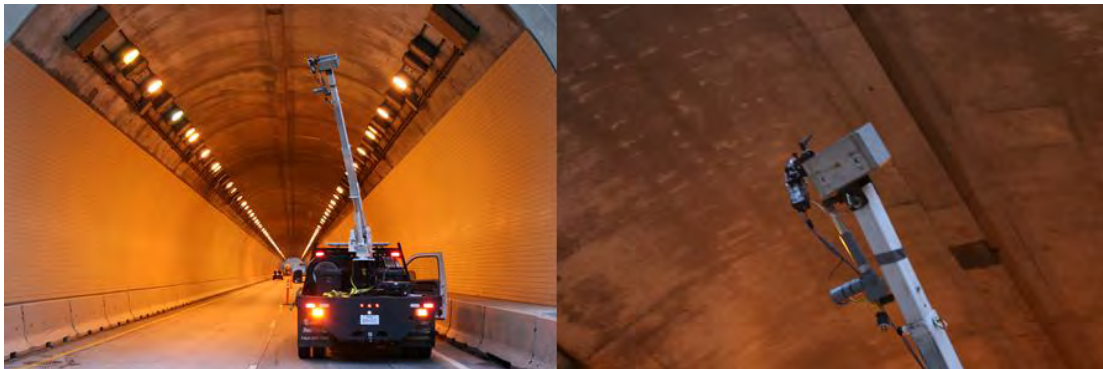
Figure J-15. Thermal video camera mounting used in tunnel surveys in the US.

Thermal video collection can also be done without a vehicle, and all the required devices can be installed on a cart. Part of the thermal video collection in the US was done in tunnel air ducts, which were not accessible by vehicles. A thermal video-logging cart consisted of a thermal video camera, normal video camera, DMI kit, control laptop, and battery. The developed system can also be used when measuring road tunnels and difficult-to-reached locations. Two different carts used in air duct measurements are shown in Figure J-16.
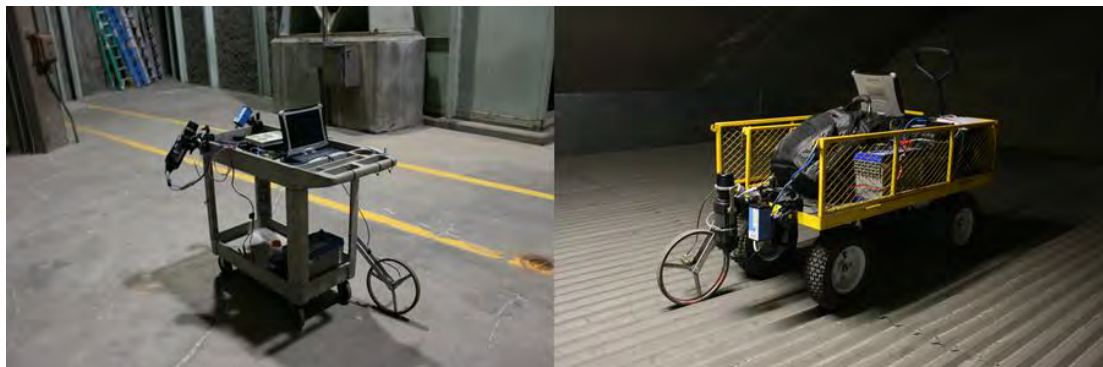
Figure J-16. Thermal video collection carts used in tunnel air duct measurements in the US.

For future surveys, Roadscanners has been developing a new rack system for thermal cameras and laser scanners. This new rack system is mounted on a van roof. The rotating rack system can be slid back and forth on the roof. Device angles can be modified to be optimal for different tasks. These rack features make measurement practice easier and thus improve data quality. The rack system is presented in Figure J-17.

Figure J-17. New Roadscanners van roof-mounted rack system for laser scanner and thermal camera data collection.

PROCESSING AND INTERPRETATION OF DATA SETS

GPR Data Processing, Interpretation, and Outputs

All GPR data preprocessing, processing, and interpretations were done using Road Doctor™ Pro analysis software and a Road Doctor™ three-dimensional module. Preprocessing means operations that do not change the signal content of the original data. Such operations used in this project were GPR data channel splitting, GPR data scaling, GPR data reversing, and zero-level correction. The GPR data processing operations consist mainly of different filtering operations and amplitude and dielectric value calculations. These operations are fully reversible and changeable. The main target of processing is to make GPR data more informative so that it will be easy to interpret. Figure J-18 presents examples of how different processing operations affected the GPR data collected from the Hakamäentie Tunnel.
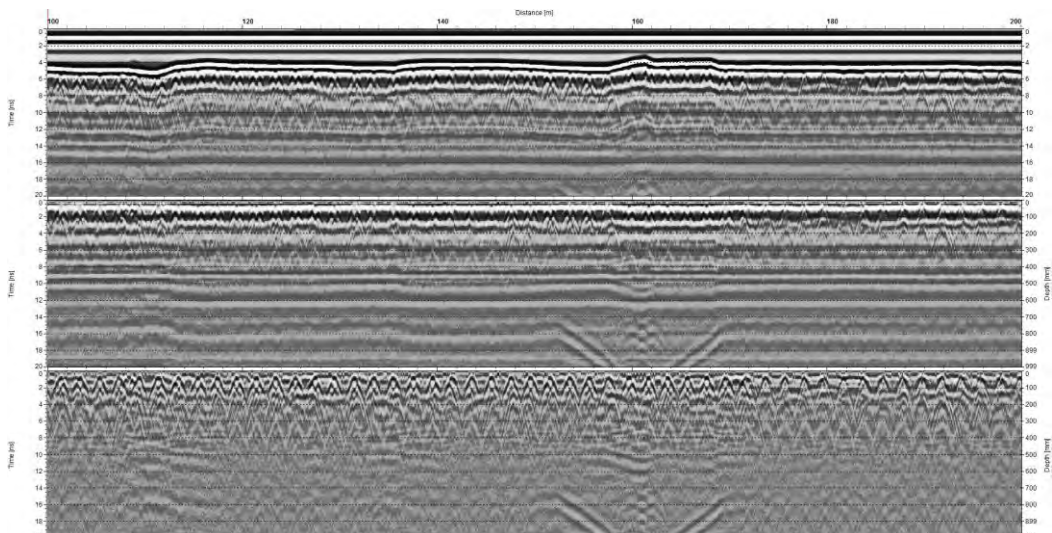
Figure J-18. Raw (top), preprocessed (middle), and processed (bottom) GPR data from Hakamäentie Tunnel right wall.

The GPR data interpretations were done using the Road Doctor™ Data Interpretation Mode. Figure J-19 presents a Road Doctor™ view of processed data with two-layer interpretation, calculated layer depths, and reflection amplitude of surface, as well as first interpreted (concrete surface) and second interpreted layer (reinforcement level).
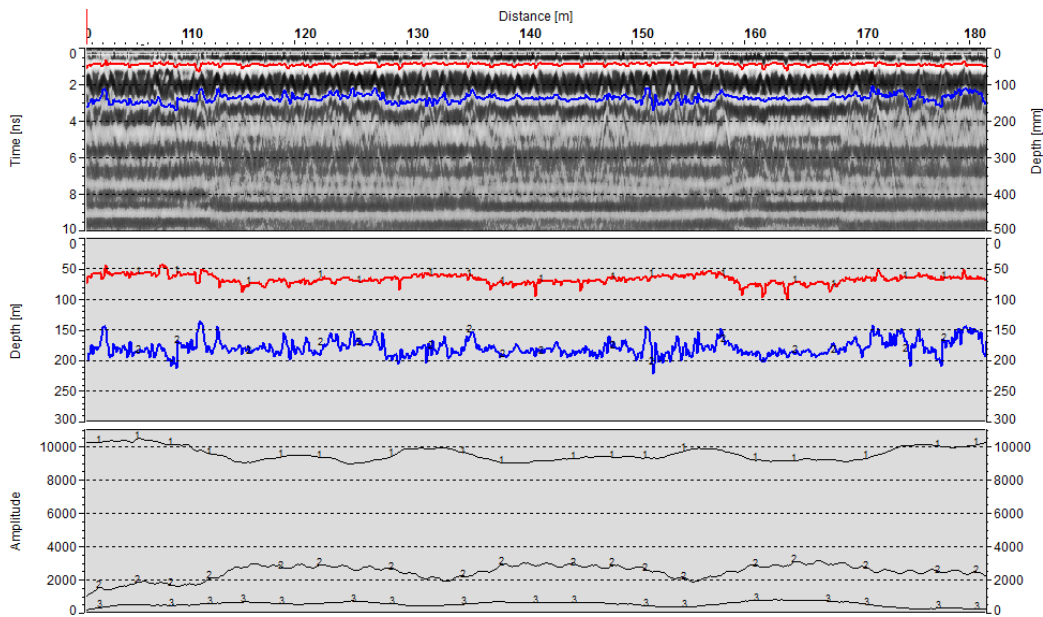
Figure J-19. Processed air-coupled GPR data with two-layer interpretation (top), calculated layer depths (middle), and bottom field presents reflection amplitudes of tunnel wall surface (1), first interpreted layer (2), and second interpreted layer (3).

Thermal Data Processing and Outputs

Thermal videos were collected using the Road Doctor™ CamLink (RDCL) video-logging package with the RDTD additional module. The following data were collected in each survey run: thermal video (*.SEQ), digital video (*.AVI), and synchronization file (*.SYNC) including distance information. In addition, audio comments were made using RDCL software.

Thermal data processing starts with the thermal video data convert operation to an RD-compatible format. This operation is executed with RDTD Converter software, which converts the collected *.SEQ raw thermal file to a *.RDTD RD-compatible thermal file. The convert operation also links thermal video frames to *.SYNC file distance and coordinate information. The final operation is to link the thermal video to the RD project. Figure J-20 presents an example of RDTD Converter and *.RDTD file creation. The RDTD Converter software and the same initial measurement files can then be used to create thermal color-scale maps. Figure J-21 presents an example of a thermal color-scale map made using RDTD Converter software.

The RDTD module allows analysis of the thermal data directly from the thermal video. For that, the supported data type is converted into *.RDTD format. Compared to thermal maps, thermal video analysis is also recommended because thermal video analysis gives even more detailed information concerning thermal anomalies (Figures J-21 and J-22). A maximum of four thermal videos can be analyzed in the same view at once.
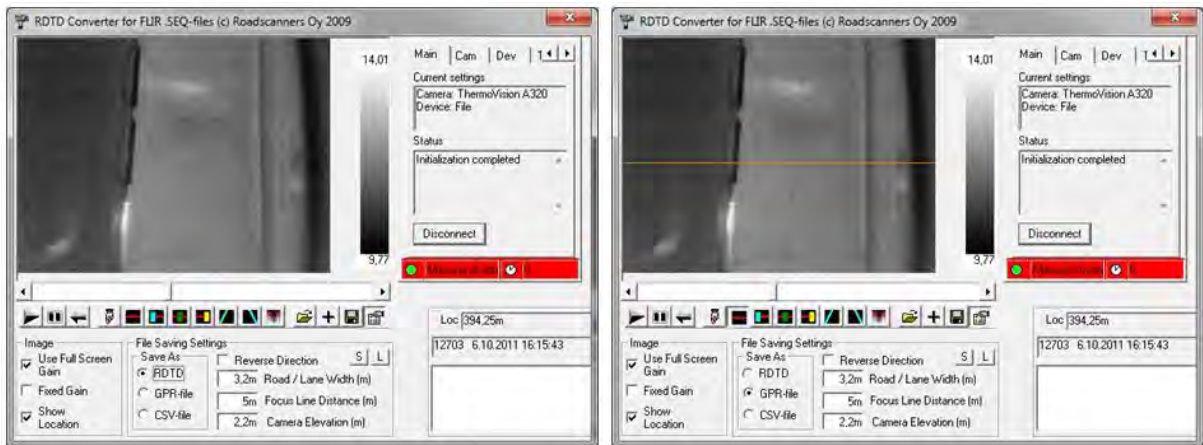
Figure J-20. Left: Road Doctor™ digital thermal video file creation. Right: thermal color-scale map creation. Red line presents the position where the map database is calculated.
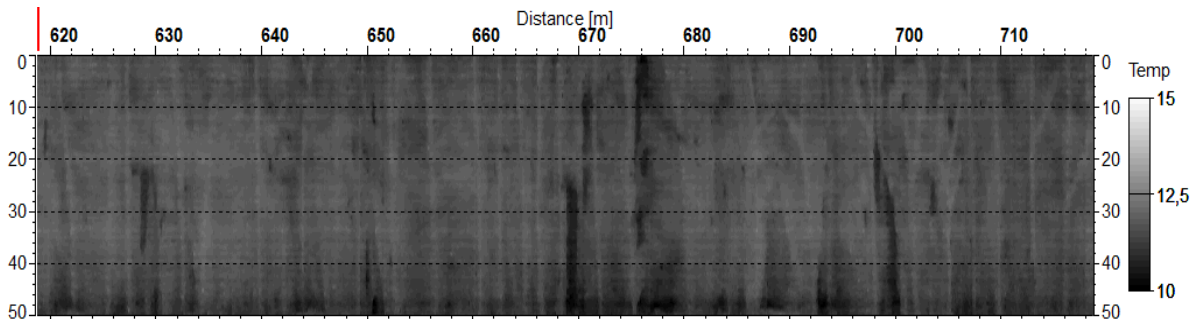
Figure J-21. Thermal color-scale map with temperature scale in Celsius degrees.
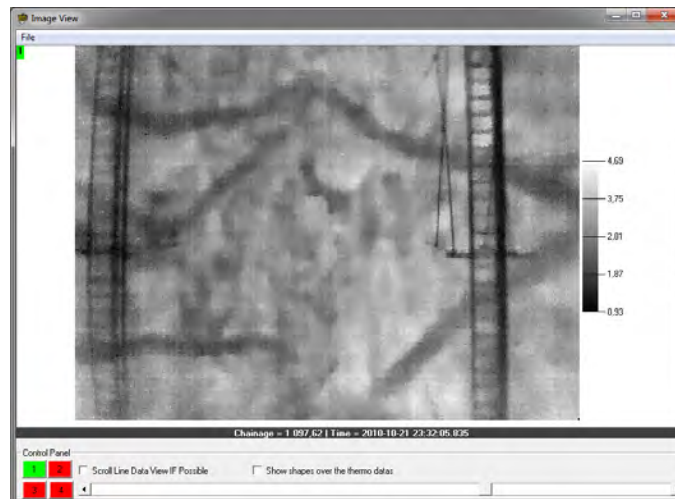
Figure J-22. Thermal video view in Road Doctor™ software display using an example from Vuosaari Tunnel roof.

Laser Scanner Data Processing and Outputs

Category B laser scanner data were collected using the RD CamLink data collection package. Data were collected along with digital video and distance information, and collected data were saved in an RD-compatible format (*.RDLS). This text file was then opened with Road Doctor™ using the Road Doctor™ Laser Scanner (RDLS) module. In this phase, the

operator needs to select whether distance (shape) or remission information will be written to the new file. The final data file also includes distance information for each laser scan point.

Laser scanner surface shape information can be displayed in Road Doctor™ in two ways. Data can be viewed as a cross-section view, which gives information of the shape and dimensions of the tunnel, i.e., the cross section (Figure J-23). Surface shape data can also be displayed as a contour map (Figure J-24). Contour maps give more definite information from the chosen tunnel plane. The relationship between the tunnel wall shape with detected water leakages can be analyzed from laser scanner information. Bedrock fracture zones in particular can be identified from this view.
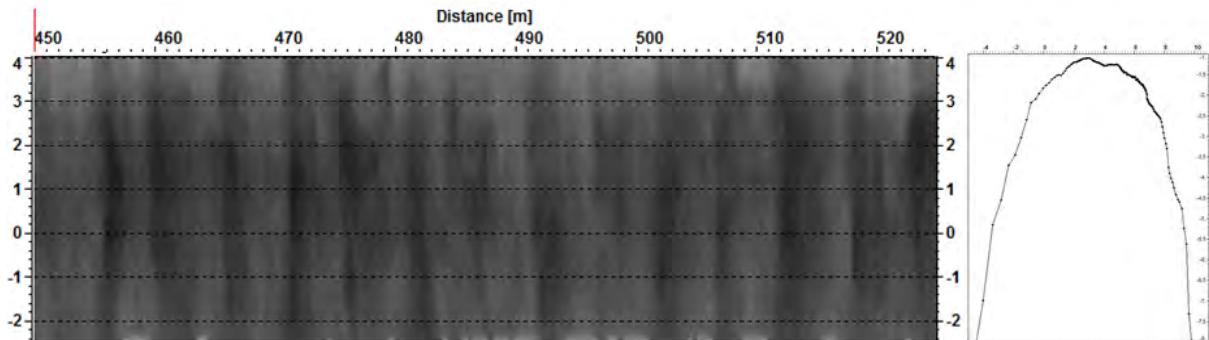
Figure J-23. A cross-section presentation of tunnel shape (right) and a contour map of Vuosaari Tunnel right wall shape change information (darker colors = longer distance).

In this project, laser scanner remission information was also analyzed using RD software. Data were viewed as a color-scale map based on the amplitude of the reflected laser signal. This amplitude depends on the optical reflectivity of the laser beam from the tunnel wall and roof surface and can be used to locate and analyze surface anomalies. In the Vuosaari Tunnel, moist areas could be seen as darker spots;, however, detailed reference surveys could not be done. Digital videos provide valuable supporting information. An example of a Vuosaari roof remission color-scale map is presented in Figure J-24.
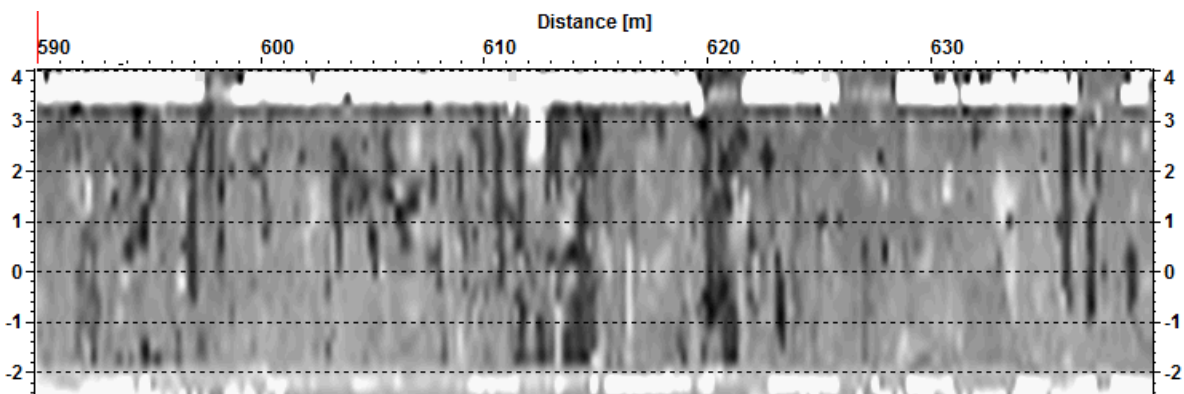
Figure J-24. RD grayscale emission map of Vuosaari Tunnel roof. Darker areas present potential moist areas.

Category A laser scanner data were collected and processed by GeoVap using their quantum three-dimensional system. After data preprocessing, the laser scanner data (lidar) were analyzed further using Terrasolid and Point Tools™ software packages. In this research, only videos produced from point clouds were analyzed. Two grayscale remission videos were created from the Vuosaari Tunnel: a whole-view video and a video toward the right wall (Figure J-25). Videos were linked to RD projects for comparison with other collected data

types. The data were measured in a single run through the tunnel. The data collection procedure was fast, and speed of the survey truck could be as high as 50 km/h. However, in order to get accurate coordinates from the tunnel, measured reference points were needed from certain intervals.
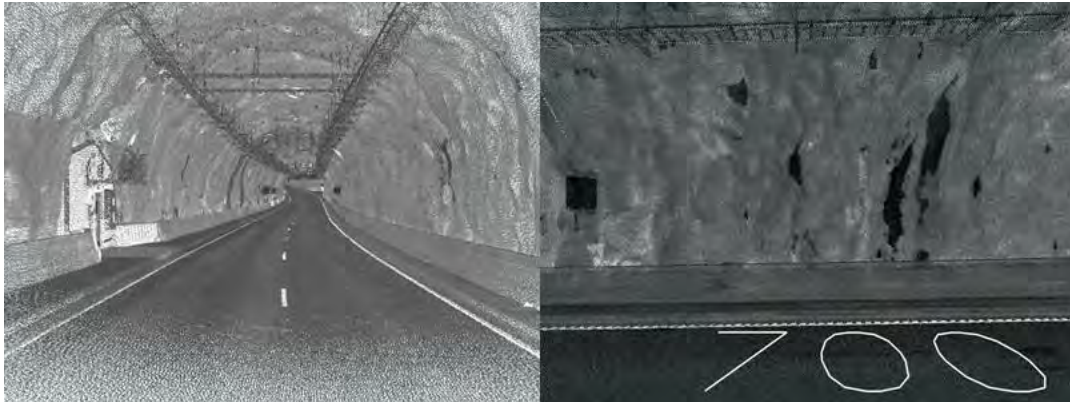
Figure J-25. Screen shots from Vuosaari point cloud videos. On the left is the overall view, and on the right is the targeted view toward the right wall.

Later, in winter 2011, a new analysis was made with Category A laser scanner point cloud data in order to try to find more detailed information from the Vuosaari Tunnel roof, where it was difficult to collect data. At that time, the selected view type, from the top down toward the tunnel roof, proved to be successful, and these data provided valuable information about cracks and water leakage in the tunnel roof (Figure J-26).
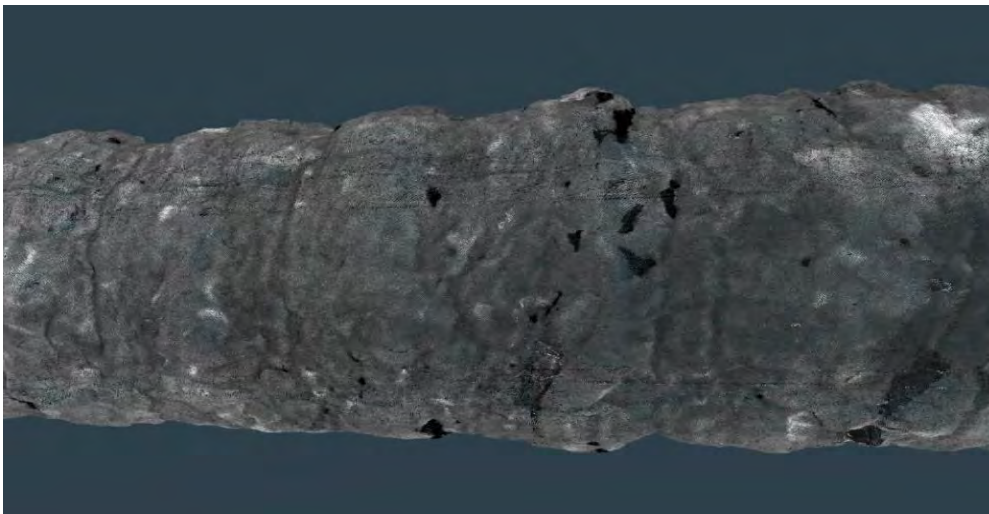
Figure J-26. Point cloud video view from top down for Vuosaari Tunnel roof. Black areas have problems with water leakage.

RESULTS

General

The Vuosaari and Hakamäentie Tunnel structures are quite different, and that is why results are presented here separately. The quality and information value of the tested NDT methods also varied in the different test tunnels. The GPR method did not give satisfactory results in the Vuosaari Tunnel due to the steel fibers in shotcrete, but the thermal camera data provided very good information on the drainage pipes and their condition behind the

shotcrete as well as areas of higher moisture content. On the contrary, in the Hakamäentie Tunnel, the GPR method gave very good results, and the value of the thermal camera survey data was inadequate. The Category A laser scanner was tested only in the Vuosaari Tunnel, and the results were very promising. Data can be used in multiple ways, but in this study, only remission and tunnel shape information was used in the analysis. Category B laser scanner data were also good, and the collected data provided similar information concerning the tunnel surfaces as the Category A laser scanner data did. Data accuracy was not as high, though.

GPR Test Results

The general goal of the GPR tests was to test the suitability of GPR air-coupled antennas in routine tunnel surveys. In addition to structural evaluation, tests were also conducted to survey data collection repeatability, antenna-to-wall distance, and speed effect, as well as the effects of seasonal changes on the survey results. The results of these tests are presented in the following sections.

Vuosaari Tunnel

Vuosaari Tunnel air-coupled GPR data processing proved to be much more difficult than expected, and results were not satisfactory, mainly due to two reasons. The first reason was that the amplitude analysis showed to be sensitive to major antenna-to-wall distance changes. Due to the shotcrete structure, the Vuosaari Tunnel wall and roof surface is uneven, and antenna-to-wall distance varied along the measurement line. Moderate antenna distance changes can be taken into account, but the correction methods used are not reliable when such a big distance change is encountered. RD software automatic surface lever detection were not capable of handling changes, which were as high as 1.5 m. The other reason was that the Vuosaari Tunnel is surfaced with shotcrete (sprayed concrete), and to improve its technical properties, steel fibers were added. This steel-fiber-strengthened shotcrete reflected the GPR signal so effectively that the detected amplitude values were too high to be used in dielectric analysis. The detected amplitude values were also changing along the measurement line depending on the density and position of iron fibers in the shotcrete. As a result, the GPR reflection amplitude did not provide reliable information concerning moisture conditions. Figure J-27 presents an example of the shotcrete surface amplitude value along a 50 m long section. The amplitude data show major variation, partly as a function of antenna distance to the wall, but bigger changes were cause by steel fibers.
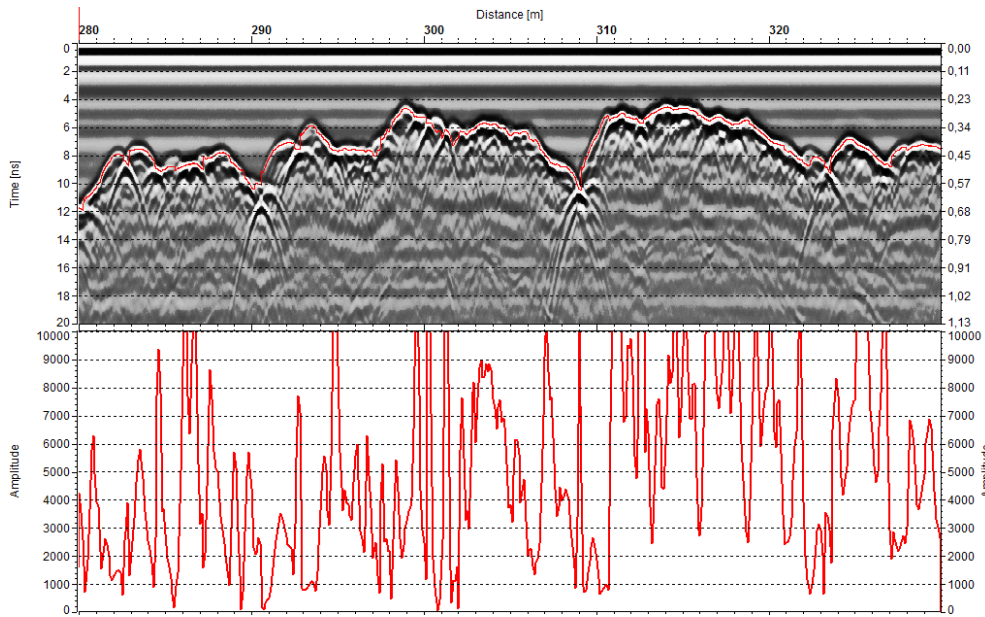
Figure J-27. Interpreted surface reflection of air-coupled 1 GHz horn data and amplitude of interpreted surface reflection (Vuosaari). Y-axis in GPR data (right) presents distance to the wall (calculated with Er:1).

Hakamäentie Tunnel

Hakamäentie Tunnel air-coupled GPR results were better than the Vuosaari data. Due to the relatively even surface of the concrete tunnel walls, it was possible to conduct the amplitude and dielectric analyses. Even though the GPR data were sensitive to major antenna-wall distance changes, it was not a major problem in the Hakamäentie Tunnel, and Road Doctor™ software was able to analyze the collected GPR data without problems. Because the Hakamäentie Tunnel is new, only a few and weak anomalies could be detected. The concrete wall elements were in good condition, and visible damages were rare. Dielectric values higher than 10, indicating major water leakage, were not encountered, but small anomalies were found. Wavy concrete block surface texture had an effect on the measured surface dielectric value, which was lower than predicted. Normally, concrete dielectric value varies between 8 and 12. In this study, average dielectric value was around 5.

In order to collect information concerning the effect of different seasons on the GPR data results, GPR data were collected in summer, winter, and autumn. Then the surface dielectric values were compared to one another. The comparison data are presented in Figure J-28. The dielectric maps were similar in each season, but the most detailed information could be collected in early summer.
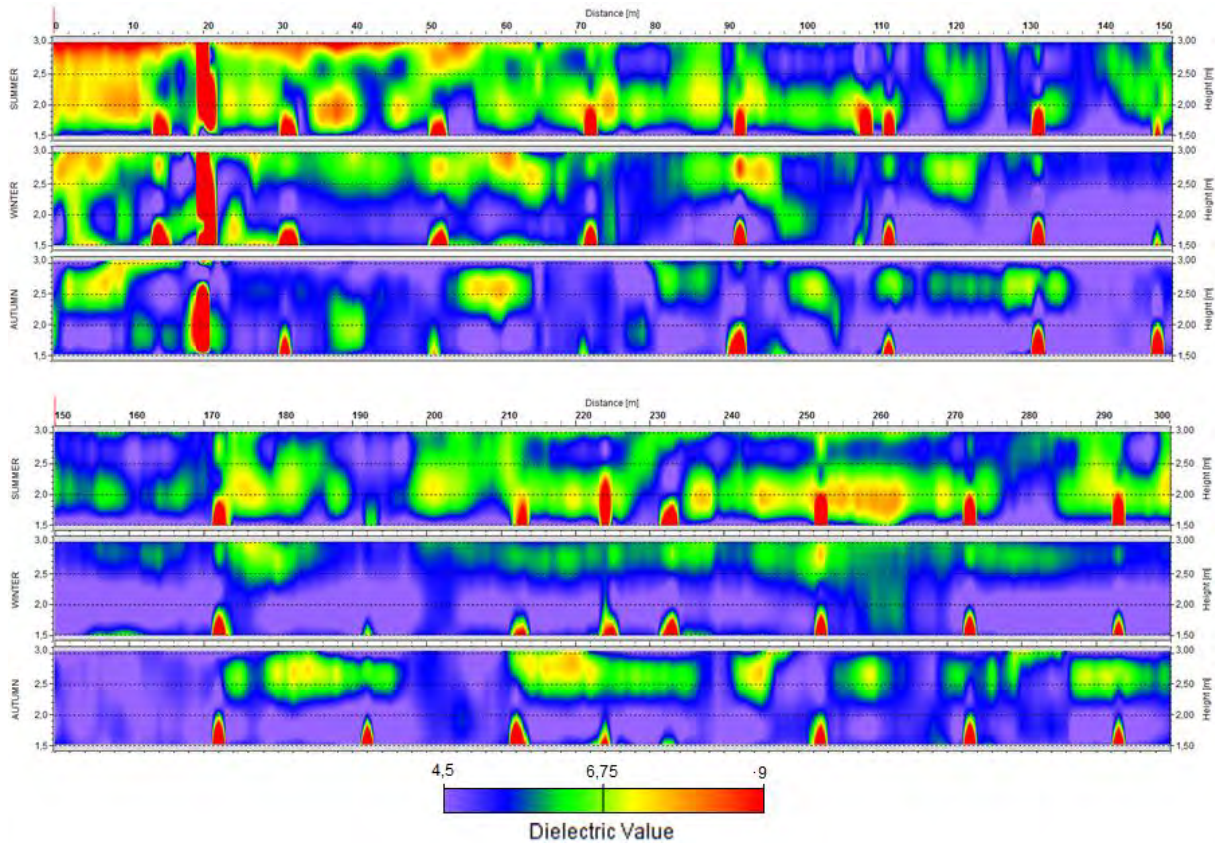
Figure J-28. Dielectric surface maps of Hakamäentie right wall (summer, winter, and autumn; above 0-150 m and below 150-300 m).

Repeatability, Antenna-Wall Distance Effect, and Data Collection Speed Tests

Repeatability tests were made by taking two measurements along the same line and using the same antenna-to-wall distance, and the results are shown in Figure J-29. In this figure, measured dielectric (Er) is displayed in the graph above, and the corresponding antenna-wall distance is in the graph below. Test graphs show that results were quite repeatable and areas of higher moisture content could be detected even though the value was not exactly the same.
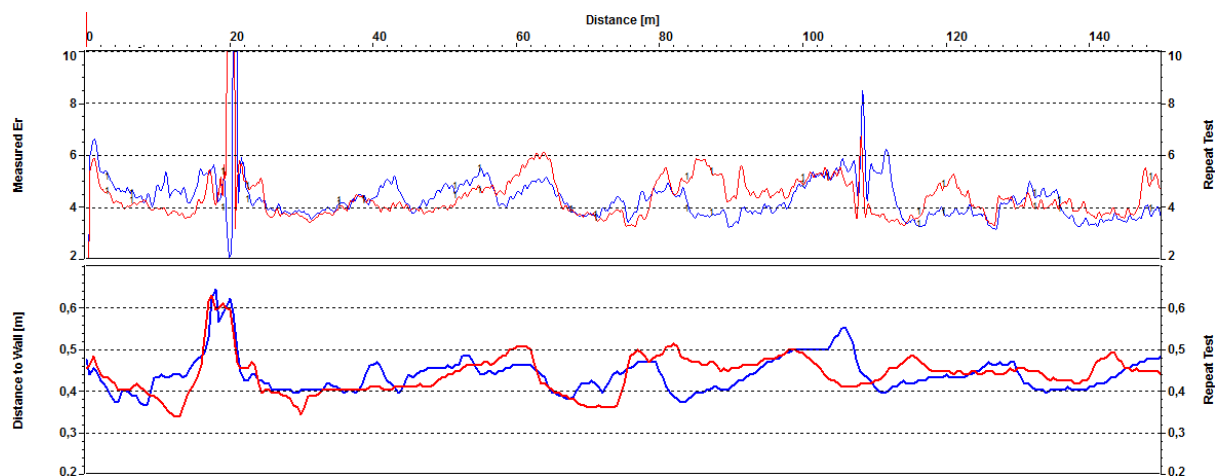
Figure J-29. Results of surface dielectric values repeatability tests (above) and the antenna distance to wall (below).

Based on the repeatability test results, antenna-wall distance seemed to have an effect on the measured dielectric value, and increased antenna-wall distance seemed to have an increasing effect on dielectric value even though the antenna-wall distance variation between the two test measurements was quite small (see Figure J-29). When the distance difference is low, about 2 to 3 cm, dielectric results correlate. This means that the elevation correction algorithm used in the analysis was not working as expected (Figure J-30). However, when better taking antenna-wall distance changes into account, GPR measurements are repeatable.
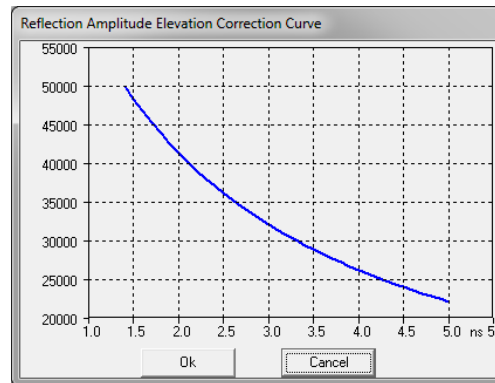
Figure J-30. Reflection amplitude elevation correction curve used in Road Doctor™.

Antenna-wall distance effect was analyzed from data sets measured from three different distances: 0.5 m, 1.0 m, and 1.5 m (Figure J-31). Dielectric values were calculated using metal reflection measured on 0.5 m antenna-plate distance. Performed antenna-wall distance tests gave complex results, and results showed that measured surface dielectric value was not acting linearly when antenna-wall distance changes were large. This can be explained by geometrical signal attenuation when an antenna is moved farther from the wall. Current amplitude correction algorithms are not able to handle these critical distance changes. Figure J-31 also shows that when measuring farther away from the wall (1.0 m and 1.5 m), the general level of the dielectric value was reduced compared to the 0.5 m survey distance. This could be explained by the fact that wall shape starts to have an effect at longer distances. However, results from the 1.0 and 1.5 m distances show similar trends and anomalies.

In further tests, metal plate reflections were also measured using two other test distances, but the size, 1 m by 1 m, of the metal plate was observed to be too small at distances of 1 and 1.5 m (Figure J-32). The GPR signal did not reflect from the metal as expected, and signal loss was too high. From a distance of 1.0 m, the signal was 20 percent weaker, and from a distance of 1.5 m, it was 50 percent weaker compared to the signal received from the 0.5 m distance.
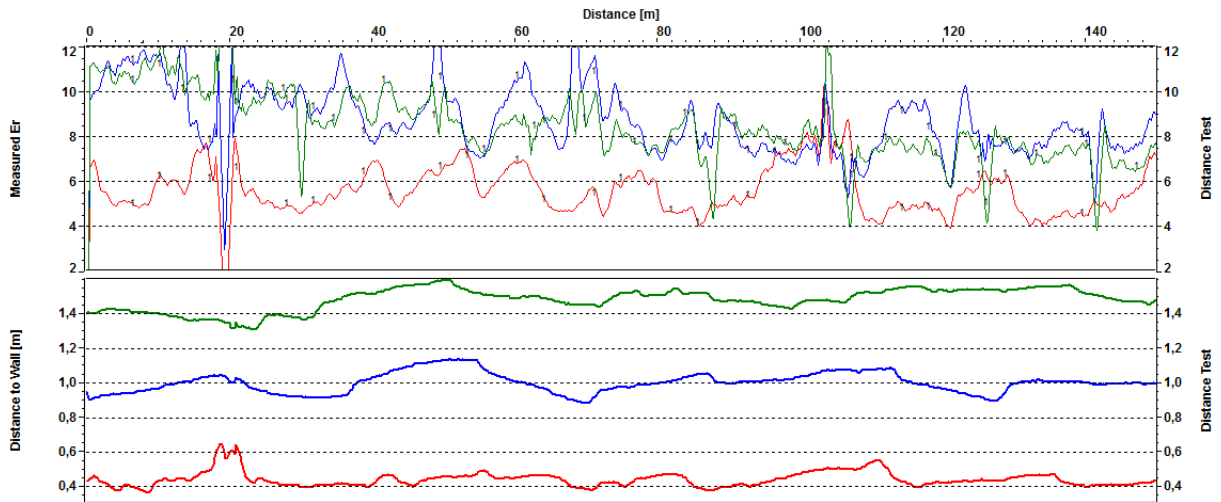
Figure J-31. Above-surface dielectric values in antenna distance-to-wall tests and below antenna distance to wall (red: 0.5 m; blue: 1.0 m; green: 1.5 m).

Figure J-32. GPR metal reflection data collection during winter tests in 2011.

In addition, GPR tests were also conducted at different data collection speeds in order to collect information on the effect of the survey van speed on the GPR data. These measurements were performed on three different speeds: 6, 20, and 30 km/h. Higher speeds than 30 km/h were impossible for testing due to problems with the antenna support system. The GPR itself has no limits with higher data collections speed; for instance, the maximum speed using a SIR-20 GPR unit and one air-coupled horn antenna would be around 70 to 80 km/h. The most critical speed-reducing factor was the antenna-wall distance, which had to stay roughly the same between measurements, and when the van speed increased, it was more difficult to observe and adjust the antenna-wall distance. Test results are presented in Figure J.33, which shows that after 20 km/h, the distance to the wall changed more and had an effect on the measured dielectric value.
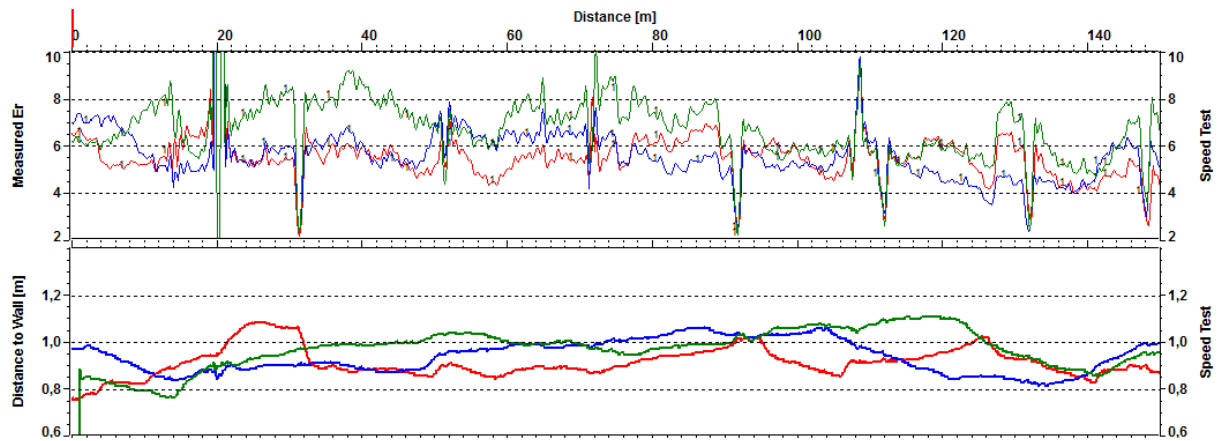
Figure J-33. Above-surface dielectric values in speed tests along the antenna distance to wall (red: 6 km/h; blue: 20 km/h; green: 30 km/h).

All the test results presented above show that horn antennas should be kept at a relatively close distance to the wall if the current algorithms will be used. Surveys with longer distances and higher speed have given interesting and promising results, but if such will be used, there is a need to develop new calibration methods for accurate dielectric value calculations. It must also be kept in mind that at longer distances, the footprint area from the reflection will be much larger, which means that the GPR survey results will be less detailed.

Finally, when the GPR tests were performed with two antennas side by side (see Figure J-2, left photo), it was noticed that the performance of the two antennas was not similar.

Other Observations with the GPR Tests—Positioning

The positioning of the GPR data and other data collection is more complex in underground tunnel surveys without the possibility to use global positioning system (GPS) techniques. In detailed tunnel surveys, it is possible to use expensive robot tachymeters, but their use is expensive and time consuming, which is why in this study, positioning was done using a survey wheel. All the data points were stored as a function of a distance from the start point of the measurement line. A survey wheel is really a simple tool to get positioning for the data, but accuracy is limited.

Thermal Camera Test Results

Thermal camera tests gave promising results, especially from the Vuosaari shotcrete tunnel, but some anomalies could be detected in the Hakamäentie Tunnel. The main findings of the thermal camera test are given in the following sections.

Vuosaari Tunnel

The Vuosaari Tunnel proved to be ideal for the thermal analysis. Water seeping from the bedrock and infiltrating through the shotcrete was causing strong thermal anomalies, which were detected by the thermal camera. Leaking and blocked water seem to cause cold thermal anomalies in all outside air weather conditions. Other visible thermal differences are caused by water drains. These thermal anomalies can be cold or warm, depending on the outside air temperature. In warm conditions, drains can be seen as warm anomalies due to warm air inside the drains. The Vuosaari Tunnel was opened for use in 2007, and as a

recently built tunnel, it is in good condition. Similar studies of older tunnels would reveal more anomalies.

Figure J-34 presents thermal data sets from the Vuosaari Tunnel collected in different seasons. The figure shows that the best and most detailed data could be collected in the summer when moisture anomalies (black areas), in particular, are very visible and results show where drain pipes are not collecting all the water. In the fall, many of the summer anomalies could also be seen, but in the winter, when the wall was frozen (at the time of the data collection air temperature was from -4 to 2 °C), only small indications of the problem sections could be seen, and data were more blurry.

Thermal data collected in summer 2011 from the Vuosaari roof also had good quality (Figure J-35). Because the Vuosaari Tunnel is an undersea tunnel, most of the water tries to leak through the roof, and that is why the roof data had more thermal anomalies compared to the thermal data from the wall. Temperature differences between anomalous and other areas, however, were low, as can be seen in Figure J-35 where the relative temperature difference is 2 °C.
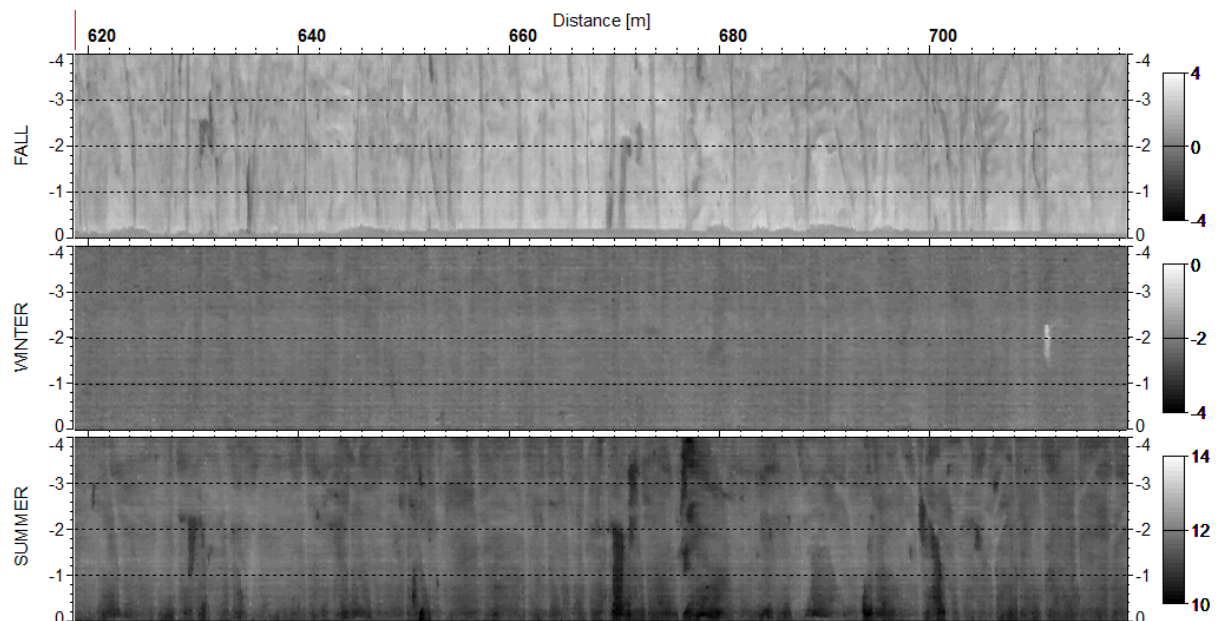
Figure J-34. Comparison of thermal data collected in different times of year (fall, winter, and summer; temperature scale in Celsius degrees).
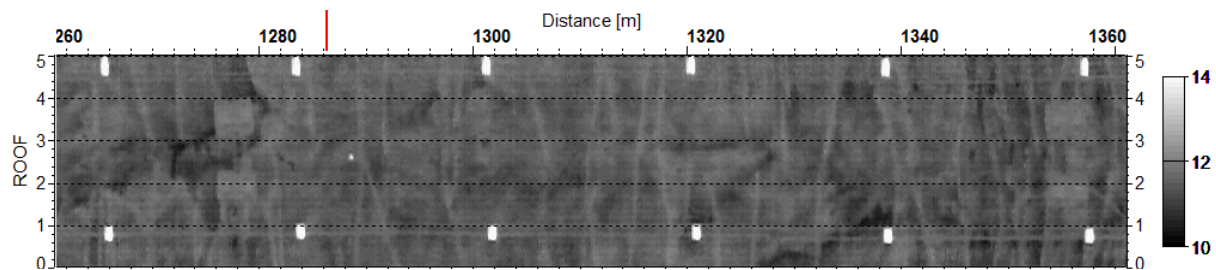
Figure J-35. Thermal color-scale map of Vuosaari roof (temperature scale in Celsius degrees). White spots are lamps.

Hakamäentie Tunnel

In the Hakamäentie Tunnel, southbound tunnel right wall thermal camera data collection was made in summer, autumn, and winter. Wall temperatures were noted to be constant in every survey season, and thermal anomalies were rare. All spotted anomalies were caused by tunnel technology, water spatters on the wall, and snow. Wall temperature variation, regardless the time of the year, was less than 1 °C. Compared to the Vuosaari Tunnel, thermal variation was really low. Figure J-36 presents the thermal color-scale map from the right wall summer data.
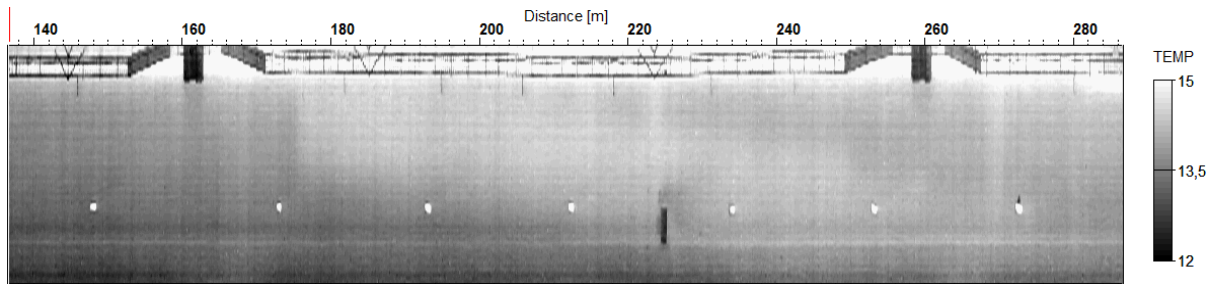
Figure J-36. Thermal color-scale map from Hakamäentie southbound tunnel right wall.

Data Collection Speed Tests

Thermal camera data collection speed tests consisted of three measurements on the Vuosaari Tunnel right wall on the same camera-wall distance. Measurements were performed using van speeds of 20 km/h, 45 km/h, and 60 km/h. Figure J-37 shows an example of test results, which proved that measurements were repeatable on all the three tested data collection speeds. The same features can be spotted in all the data sets. Differences in data sets were caused mainly by increased speed of the van. When the camera was moving faster by the objects, the anomalies started to fade and blur. Still, up to a speed of 60 km/h, anomalies did not disappear. Greater water leak areas could be still detected at speeds of 60 km/h.
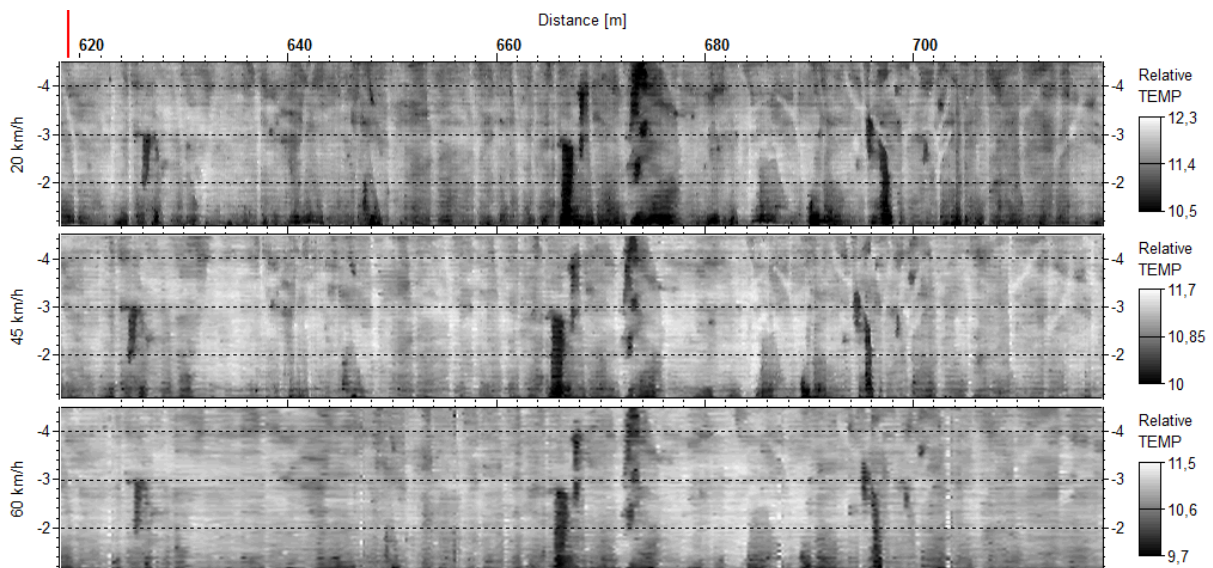
Figure J-37. Repeat-speed test result example from Vuosaari Tunnel (data collected in summer).

Laser Scanner Test Results

Laser scanning was performed in the Vuosaari Tunnel using two different laser scanner types: effective high-accuracy systems (Category A), cheaper lower-accuracy systems (Category B). The Hakamäentie Tunnel was measured using the Category B laser scanner only. The key findings are presented in the following sections.

Vuosaari Tunnel

Tests results in the Vuosaari Tunnel with both tested laser scanner systems gave very promising results. Both systems provided information about the tunnel wall surface shape, and remission data provided information about the water leakage areas. Figure J-38 presents an example of the Category B laser scanner shape data where a tunnel cross section can be seen on the right. Figure J-39 presents an example of the detailed information provided by the Category A laser scanner, which shows points/areas where salty water was leaching through the shotcrete. Figure J-40 presents a comparison of Category A and B laser scanner data in the tunnel roof surveys. It shows that the cheaper Category B laser scanner can be used to detect anomalous areas. The detailed analysis of the high-precision Category A laser scanner data even revealed cracking in the tunnel roof, as Figure J-41 shows.
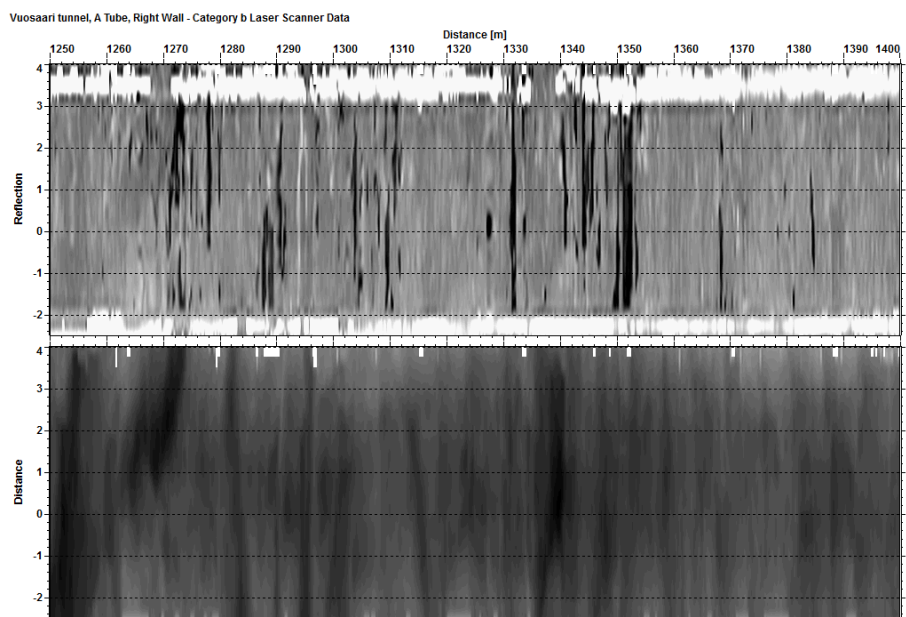
Figure J-38. Category B laser scanner data from Vuosaari Tunnel A (tube right wall at 1250-1300 m). The top data field presents remission data where darker areas present potential moisture anomalies. The lower data field presents wall shape information where darker areas are farther away from the road.

Figure J-39. Category A laser scanner detailed view from the side wall at 1350 m (also see Figure J-38). See the small wet spots on the right side of the figure and white areas beneath them indicating salt.
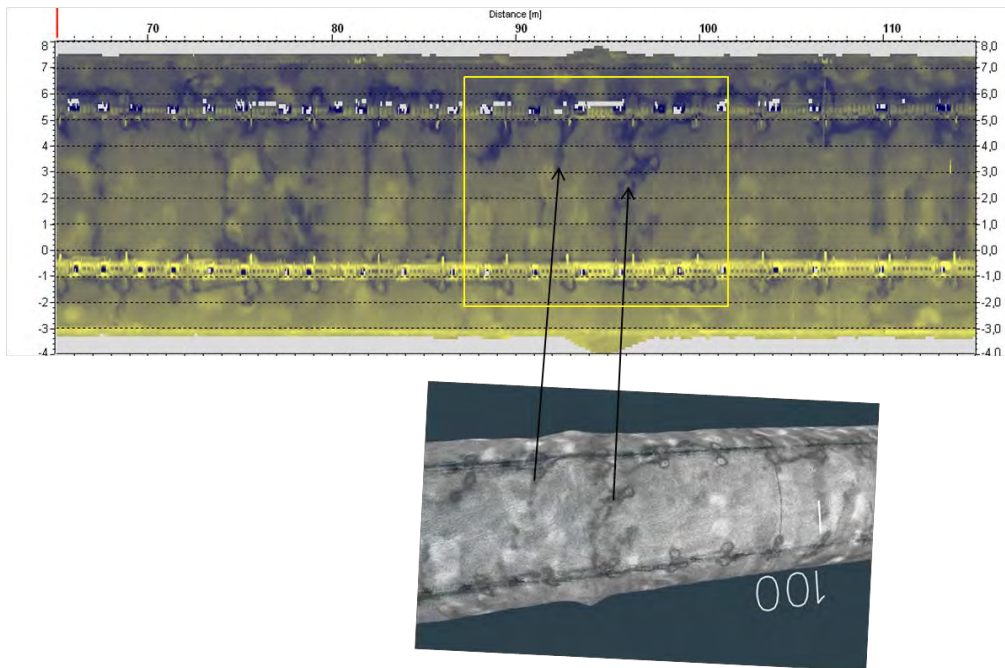
Figure J-40. Comparison of Category B laser scanner data (above) and Category A laser scanner data (below) from the tunnel roof around 100 m at the tunnel roof. The same anomalies can be seen in both data sets.
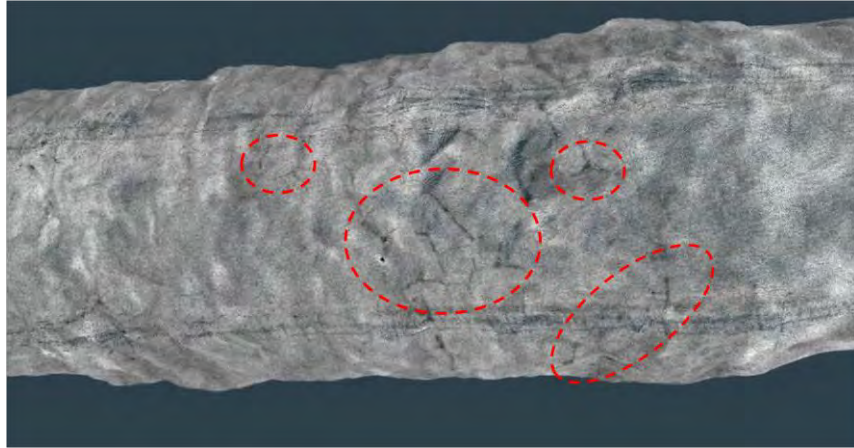
Figure J-41. Example of Category A laser scanner data from Vuosaari Tunnel roof. Areas with cracks in shotcrete are shown with red circles.

Laser scanner data are very repeatable, and data collection can be carried out in tunnels with speeds of 30-40 km/h. Even higher speeds can be used, but there can be problems with accurate positioning when doing so. In order to get really reliable x, y, z position data reference points that can be detected from laser scanner data, collection should be made in the tunnel at 200 m intervals.

Hakamäentie Tunnel

The results of the laser scanner tests from the Hakamäentie Tunnel did not reveal any major problem areas. Figure J-42 presents an example of Category B laser scanning data from the Hakamäentie Tunnel roof. Results showed small anomalies in concrete block joints and from the joints where the roof meets the wall. Thermal camera data did not show any major thermal anomalies on these locations.
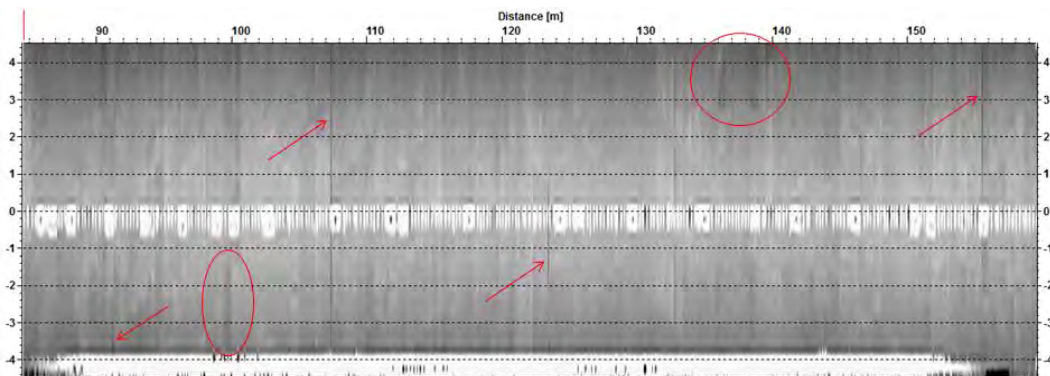
Figure J-42. Category B laser scanner reflection amplitude data from the Hakamäentie Tunnel roof. Red markings point out detected anomalies.

Integrated Analysis of Different Methods

In this work, a comparison of the different data types could be made only with the thermal camera and laser scanner data because GPR data were not usable for data analysis due to steel fibers. Figure J-43 presents a comparison of the thermal data (in the center) with the point cloud videos (in the corners) in the Vuosaari Tunnel. The connection between the anomalies detected is clear. When water entered the shotcrete-surfaced tunnel, surface leakages could be seen as darker areas in the laser scanner remission data. On the thermal

data, these areas with higher water content could be seen as colder anomalies and, with proper color scale, as dark spots. In both data sets, the darkest areas indicated water existence in the tunnel structure. Analysis of multiple points showed that the correlation between these points was really good.
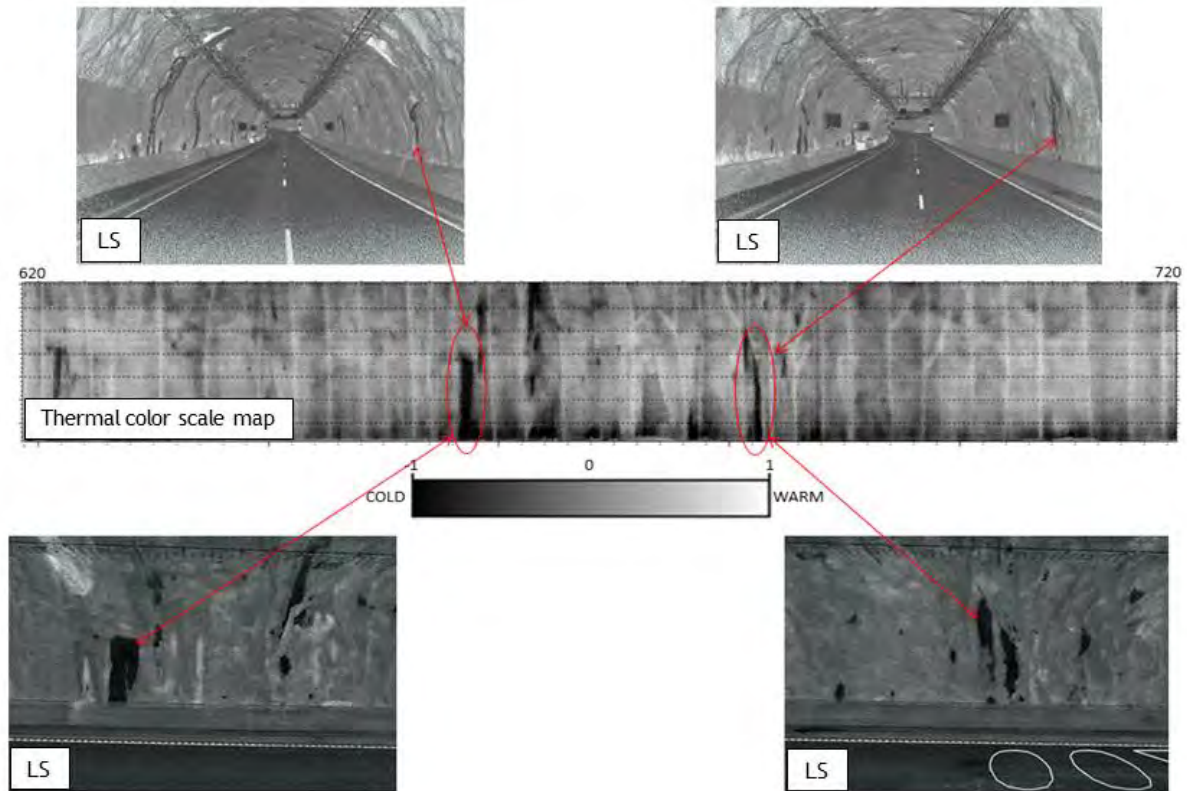
Figure J-43. Thermal color-scale map anomalies' connection to the Category A laser scanning video results on Vuosaari Tunnel right wall.

CONCLUSIONS

The results of the tunnel tests showed that all the three systems are potential tools to be used in the surveys of the conditions of tunnel linings. However, there are some shortcomings for each system based on the type of tunnel structure, and these need to be known before the survey method can be selected for each tunnel. The key conclusions for each tested tunnel survey method are presented in the following sections.

GPR Analysis

The key conclusions for the GPR analysis survey method are as follows:

1. GPR horn antenna data provided good quality structural information from the concrete tunnel but could not be used in the shotcrete tunnel where steel fibers were used in the shotcrete. The GPR data provided useful information on structures behind the tunnel linings.

2. Research still needs to be done before surface dielectric information can be reliably used in finding moisture anomalies on the lining structure. The distance from the antenna to the wall should be kept constant, and better calibration files need to be made. An optimal distance is 0.5 m, which allows for safe measurement and is close

enough for reliable dielectric value calculation. However, this might exclude the horn antenna technique in the use of surveys of tunnel roofs. Also, surface texture of the wall can have an effect on the results, but if the surface is smooth, data collection can be done and results will be reliable.

3. Data collection speed can be increased by building better mounting systems for horn antennas that protect the antennas in case they hit obstacles.

4. Different GPR horn antennas gave slightly different results, and at this time, only one antenna is recommended to be used in one survey.

5. The GPR system is relatively expensive. The price estimate for a complete horn antenna tunnel survey system can be $150,000 to $200,000 USD.

6. GPR horn antenna data collection and data analysis requires well-trained and experienced personnel.

Thermal Camera Surveys

The key conclusions for the thermal camera survey method are as follows:

1. Thermal cameras gave excellent results on the shotcrete tunnel, but in the new Hakamäentie concrete tunnel, hardly any anomalies could be detected with the system. One reason for this may be that there were not any problems close to the surface.

2. The thermal camera is a fast method for tunnel surveys, and first results can be seen during the data collection. In higher speeds, data will be slightly blurred, but bigger anomalies can be reliably detected.

3. Results are repeatable, but it must be taken into account that tunnel wall surface temperature can change during the day.

4. Anomalies can be seen in different ways when the surveys are conducted in summer, fall, and winter. The best time for surveys is early summer. However, results surprisingly showed that moisture anomalies could always be seen as colder areas.

5. The thermal camera is sensitive to the survey direction toward the tunnel wall and roof, and focusing the camera on white tiles can be difficult. Also, the survey van can cause unwanted IR reflections.

6. Survey equipment is relatively cheap. The price range estimate for the complete hardware package to conduct a thermal camera survey in a tunnel can be $40,000 to $60,000 USD (excluding the survey van).

7. Thermal cameras are easy to use, and data collection and analysis can be started after 1 to 2 days of training.

Laser Scanning Analysis

The key conclusions for the laser scanning analysis survey method are as follows:

1. Laser scanning systems provided very useful data of the shape and condition of the tunnel linings. The results were excellent, especially in the shotcrete Vuosaari Tunnel, but interesting and valuable info was also detected in the concrete Hakamäentie Tunnel.

2. The Category A laser scanner (lidar) provides very accurate information of the tunnel shape and changes in the shape, especially if there are good x, y, z reference points available in the tunnel. The accuracy of the Category B laser scanner is only good enough for rough surface shape analysis.

3. Both systems provided detailed enough remission results to detect moisture anomalies in the tunnel linings. Software plays a key role in presenting the results in the optimal way.

4. The Category A laser scanner (lidar) showed cracking in shotcrete concrete.

5. Laser scanning is repeatable, and surveys can be performed at relatively high speeds.

6. The price range of the system varies. The price for a good Category A laser scanning system can be up to $1 million USD, while price estimate for a Category B laser scanner complete hardware system is around $50,000 to $70,000 USD.

7. Category A laser scanning system data collection and analysis requires very experienced personnel with a good background on geodesy, but training for Category B laser scanning system data collection and analysis only takes roughly 1-2 weeks.

Other Instruments Used in the Survey

In addition to the performance of the tested equipment, the tunnel tests in Finland provided useful information on other instruments used in the surveys:

1. The quality of digital videos used in the surveys was not good; thus, video cameras with good luminous power are recommended to be used in future surveys.

2. Because GPS does not work in tunnels, the quality requirements for encoders are very high, and there cannot be any shift even at very low speeds.

3. Because survey cars cannot always drive at exactly the same survey line, the survey tunnels should have referencing systems at about 200 m intervals that could be detected in all survey data (for instance, metallic tapes) and that could be used in scaling the data.

APPENDIX K
FIELD TESTING WITH THE AIR-COUPLED GPR

AIR-COUPLED GPR—OPERATING PRINCIPLES

The Texas A&M Transportation Institute (TTI) air-coupled ground-penetrating radar (GPR) antenna transmits pulses of radar energy, with a central frequency of 1 GHz, into a tunnel lining. These waves are reflected at significant layer interfaces in the lining. The reflected waves are captured by the system and displayed as a plot of reflection amplitude (voltage) versus arrival time. As shown in Figure K-1, the largest peak is the reflection from the surface. The amplitudes before the surface reflection are internally generated noise, and if they are significant, they should be removed from the trace prior to signal processing. The reflections that can also be of significance to tunnel personnel are those that occur after the surface echo. These represent significant interfaces within the lining, and the measured travel time is related to the depth to another layer or to a defect. For example, the time between the surface echo A1 and A2 is related to the depth to another layer or to a defect.
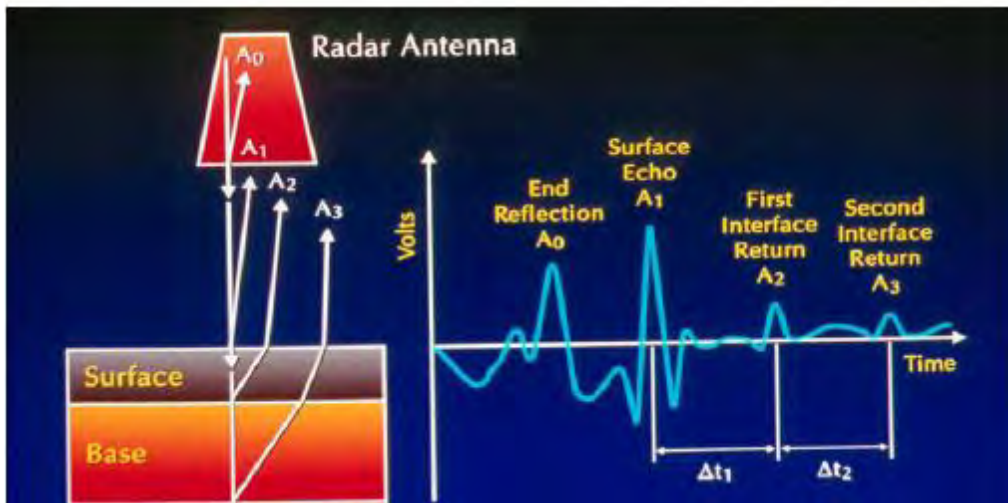
Figure K-1. Air-coupled GPR operation.

The software developed at TTI automatically measures the amplitudes of reflection and time delays between peaks. Using these measurements, it is possible to calculate layer dielectrics and depths to another layer or defect. The equations used are summarized below:

$$\varepsilon_a = \left[\frac{1 + \left(\dfrac{A_1}{A_m} \right)}{1 - \left(\dfrac{A_1}{A_m} \right)} \right]^2$$

(Equation K.1)

where:

ε_a = the dielectric of the lining surface.
A_1 = the amplitude of reflection from the surface in volts (peak A1 in Figure K-1).
A_m = the amplitude of reflection from a large metal plate in volts (this represents the 100 percent reflection case).

$$h1 = \frac{c \cdot \Delta t1}{\sqrt{\varepsilon_a}}$$

(Equation K.2)

where:

$h1$ = the depth to another interface (such as to another layer, void, or other defect).
c = a constant (speed of the radar wave in air as measured by the system).
$\Delta t1$ = the time delay between peaks A1 and A2 of Figure K-1.

$$\sqrt{\varepsilon_b} = \sqrt{\varepsilon_a} \left[\frac{\left(1 - \left\{\frac{A_1}{A_m}\right\}^2 + \left\{\frac{A_2}{A_m}\right\} \right)}{\left(1 - \left\{\frac{A_1}{A_m}\right\}^2 - \left\{\frac{A_2}{A_m}\right\} \right)} \right]$$

(Equation K.3)

where:

ε_b = the dielectric of the lower layer, void, or other defect.
A_2 = the amplitude of reflection from the top of the lower layer or defect in volts (peak A2 in Figure K-1).

Dielectric values and depths can be readily determined from two software packages developed by TTI—COLORMAP and Pavecheck. Both software packages are relatively easy to use for production-level purposes.

AIR-COUPLED GPR RESULTS FOR THE TTI TEST SPECIMENS

TTI personnel collected air-coupled GPR data on concrete and shotcrete specimens that contained delaminations or voids. The TTI team determined that the equipment could only detect three simulated voids, all located in the shotcrete sections. Those specimens were:

- Specimen D (air-filled void placed at 7.625 inches from the surface).
- Specimen F (air-filled void placed at 3 inches from the surface).
- Specimen G (water-filled void placed 3 inches from the surface).

The equipment could not detect delaminations or voids in the other sections.

Figure K-2 shows the analysis of the GPR data on specimen D using the COLORMAP program. The program indicated that the depth to the defect was 7.7 inches. The program calculated a surface dielectric of 8.2 and a void dielectric of 6.6. If an air-filled void exists, the calculated dielectric of the void is less than the surface dielectric.
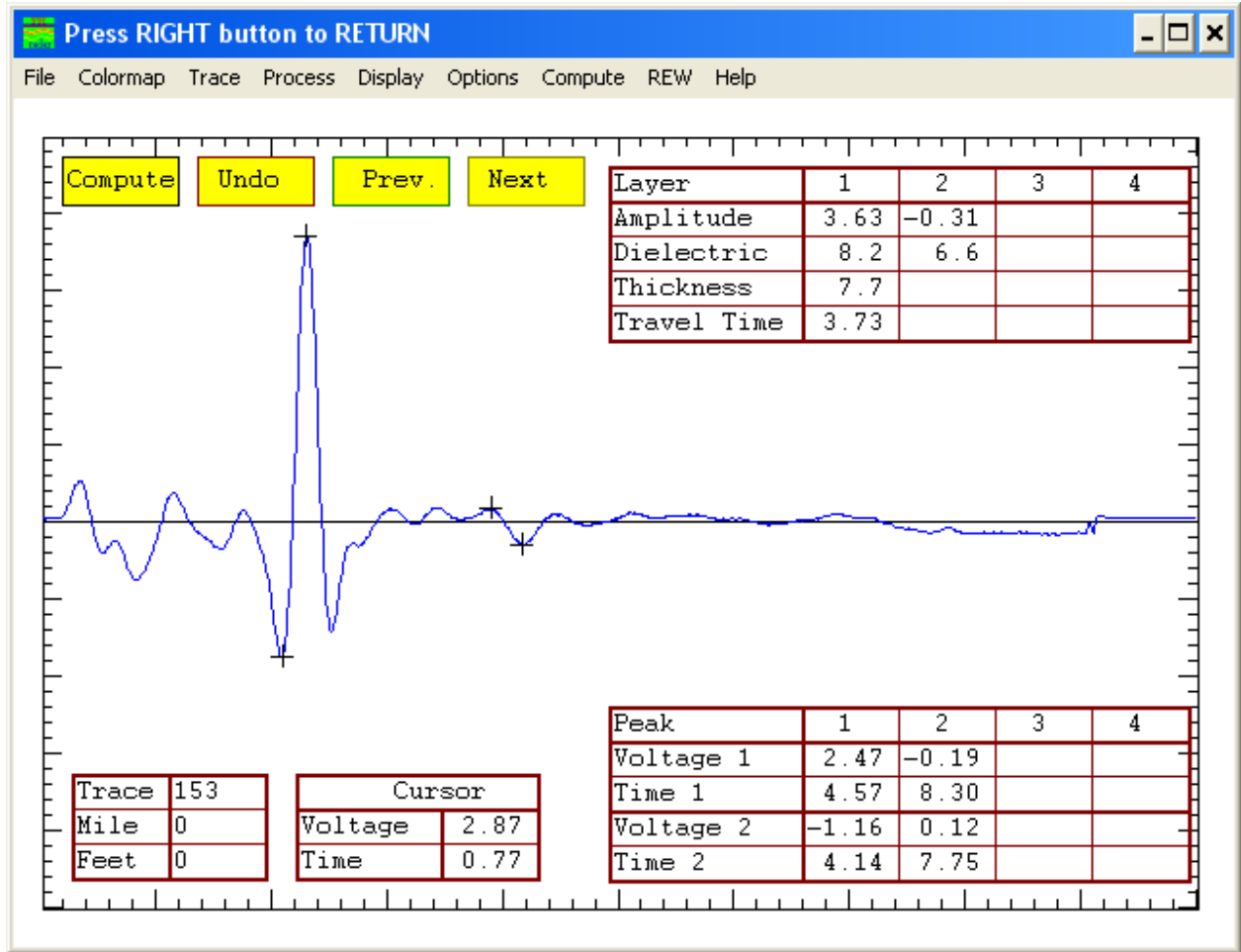
Figure K-2. Air-coupled GPR data on specimen D.

Figure K-3 shows the analysis of the GPR data on specimen F using the COLORMAP program. The program indicated that the depth to the defect was 2.6 inches. The program calculated a surface dielectric of 9.1 and a void dielectric of 7.3. If an air-filled void exists, the calculated dielectric of the void is less than the surface dielectric.
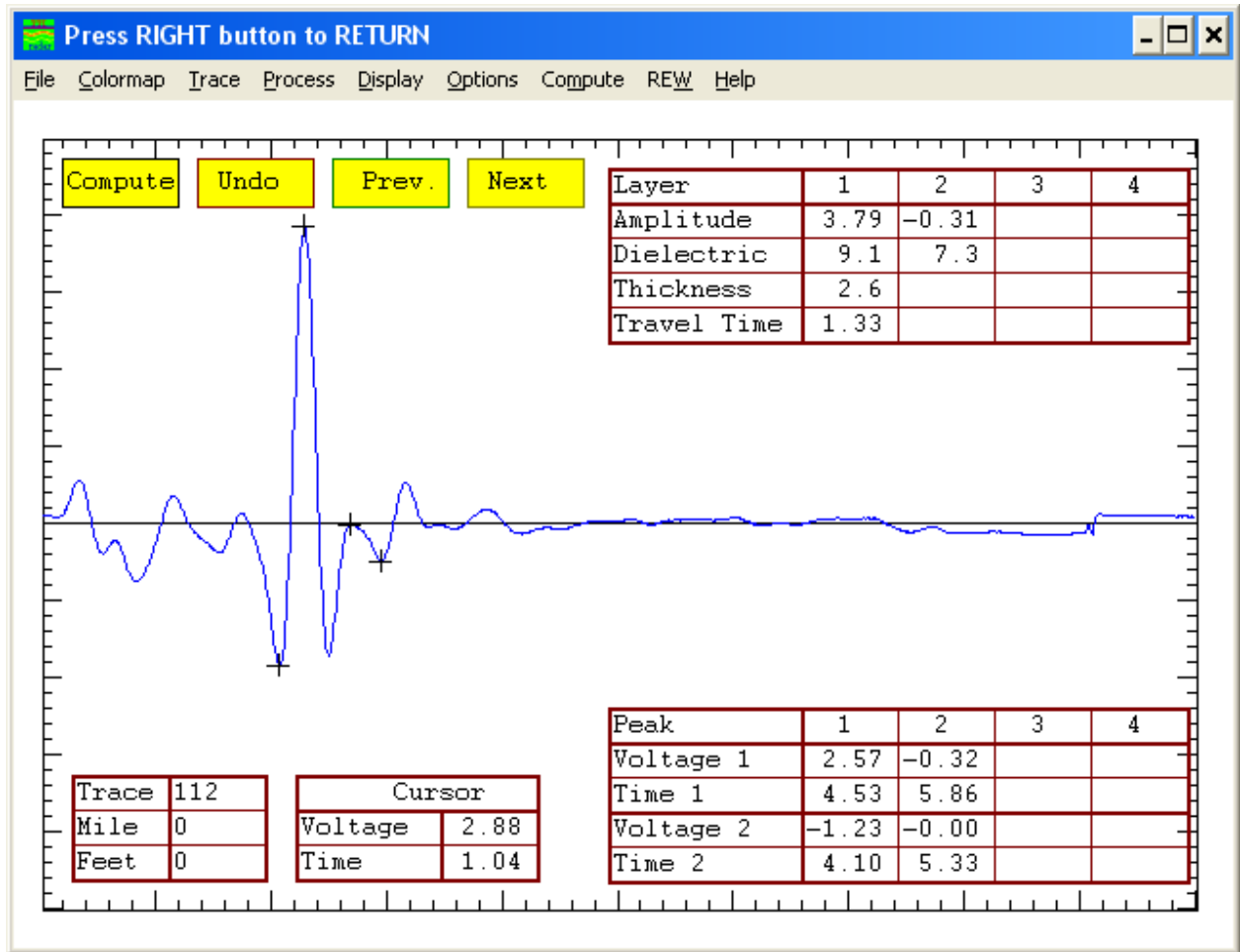
Figure K-3. Air-coupled GPR data on specimen F.

Figure K-4 shows the analysis of the GPR data on specimen G using the COLORMAP program. The program indicated that the depth to the defect was 2.7 inches. The program calculated a surface dielectric of 8.5 and a void dielectric of 12.4. If a water-filled void exists, the calculated dielectric of the void is greater than the surface dielectric.

File Colormap Trace Process Display Options Compute REW Help

Compute   Undo   Prev.   Next

Layer	1	2	3	4
Amplitude	3.70	0.54		
Dielectric	8.5	12.4		
Thickness	2.7			
Travel Time	1.33			

Trace	189
Mile	0
Feet	1

Cursor	
Voltage	2.83
Time	1.27

Peak	1	2	3	4
Voltage 1	2.49	0.34		
Time 1	4.55	5.88		
Voltage 2	-1.21	-0.20		
Time 2	4.12	6.45		
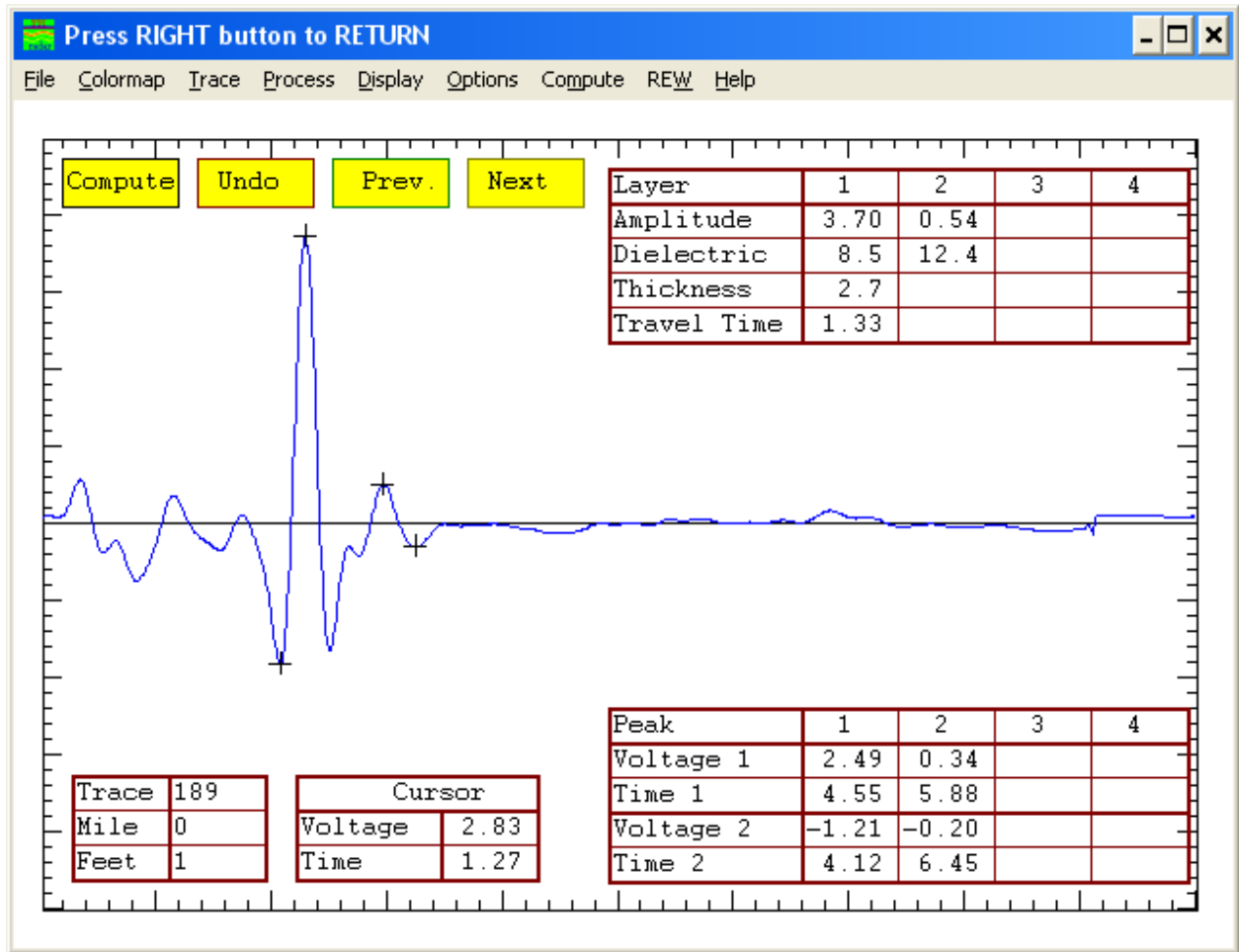
Figure K-4. Air-coupled GPR data on specimen G.

AIR-COUPLED GPR RESULTS FROM TUNNEL TESTING

Washburn Tunnel

In the Washburn Tunnel, which is completely lined with tiles, the air-coupled GPR data were collected every foot and indicated changes in the surface dielectric along the length of the tunnel. An example of air-coupled GPR data collected in the Washburn Tunnel is shown in Figure K-5. This figure was generated by the Pavecheck program developed by TTI to analyze air-coupled GPR data. The dielectric values shown in Figure K-5 have not been corrected for changes in the distance between the antenna and the tunnel lining. As can be inferred in Figure K-5, the distance between the antenna and the tunnel surface did vary because it was difficult to keep the vehicle traveling in a straight line. However, the TTI team believes the data are useful in their current form. The unusually large peak on the left-hand side of the figure is associated with a steel plate installed in the tunnel lining.
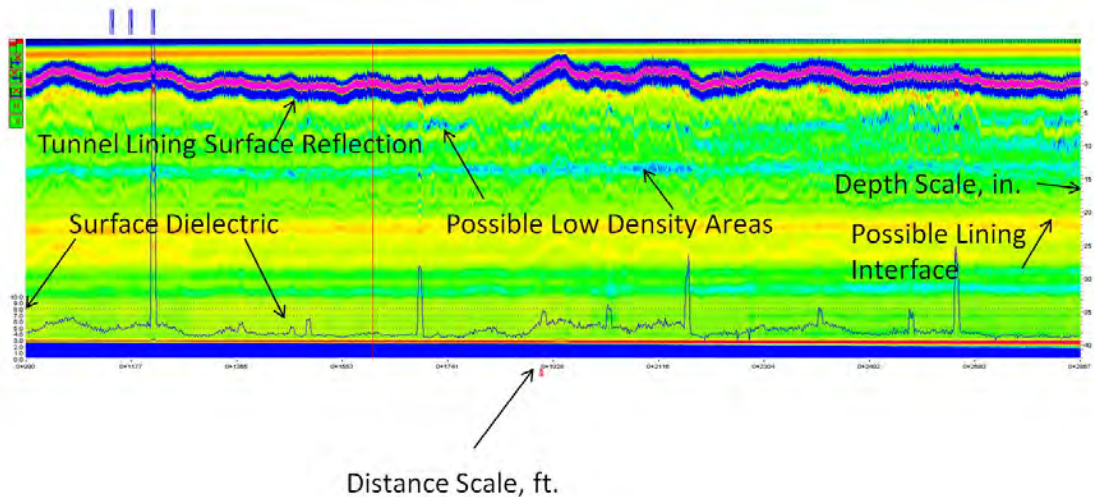
Figure K-5. Air-coupled GPR data for the Washburn Tunnel.

Chesapeake Bay Tunnel

At the top of the Chesapeake Bay Tunnel lining, the team used air-coupled GPR data to locate one area with no surface distress for in-depth testing. The data were collected every foot with the antenna directly aimed at the top of the tunnel lining. Data could not be collected on the top sides of the tunnel due to the cables and utilities installed. The area chosen for testing had a surface dielectric value of 18.7, which is unusually high for concrete, at Station 486+67. Figure K-6 shows the air-coupled GPR data for this area. As can be inferred from Figure K-6, the distance between the antenna and the tunnel lining surface was kept relatively constant (the antenna was mounted on a pushcart and pointed directly at the top of the tunnel lining). The results of the in-depth testing in this area showed that a shallow delamination existed at that location. The team tested other locations at the top of the tunnel and on the tiled tunnel wall.

The team used infrared data from the SPACETEC equipment to determine testing locations on the tiled tunnel wall at Chesapeake Bay. The team could not collect air-coupled GPR data at that location because of construction equipment blocking access to the wall at the time of the air-coupled GPR data collection. The in-depth evaluation devices were able to detect defects in the areas tested.

The TTI team also collected handheld infrared camera images in the Chesapeake Tunnel roof and roadway; selected images are shown in Appendix L. The team found very few changes in temperature in the tunnel roof. The team found that collecting images on tiled tunnel linings with this equipment was problematic since the tile reflected heat from any heat-generating source, such as construction equipment, lights, and people. In addition, the team was not able to effectively compare the SPACETEC results along the area tested by the team because it would require a lane closure on the other side to effectively obtain images with the handheld device. The vehicle-mounted thermal camera scans were also affected by construction equipment operations during the scans, thus

making it impossible to generate comparisons between the SPACETEC results and that device.
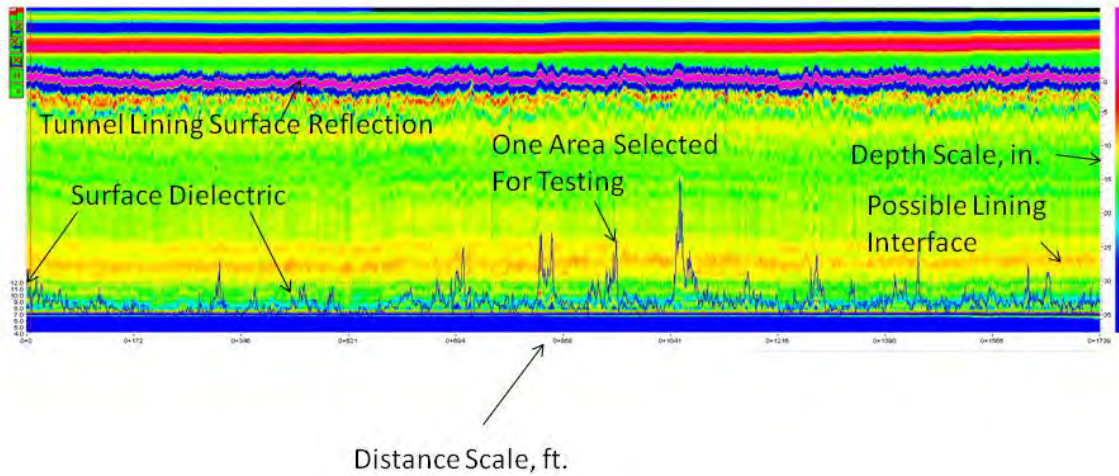
Figure K-6. Air-coupled GPR data for the Chesapeake Bay Tunnel roof.

Figure K-7 shows an example of the air-coupled GPR data taken along the tiled tunnel wall. The dielectric values shown in Figure K-7 have not been corrected for changes in the distance between the antenna and the tunnel lining (a version of this software will be developed soon with this capability). However, the TTI team believes the data are useful in their current form. The unusually large peaks are associated with steel plates or fixtures installed on the tunnel surface.
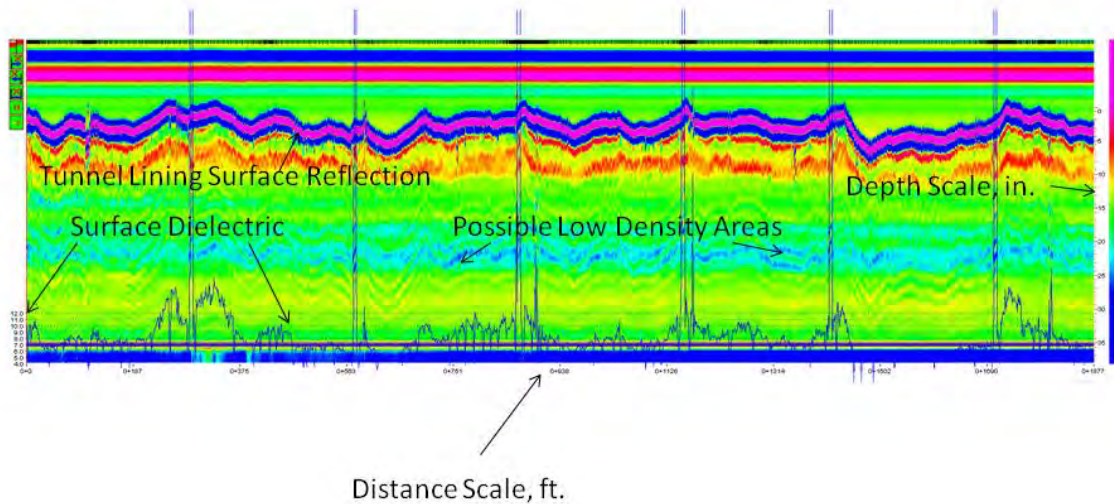
Figure K-7. Air-coupled GPR data for the Chesapeake Bay Tunnel tiled wall.

Eisenhower Tunnel

In the Eisenhower Tunnel, the in-depth evaluation devices were able to detect defects in the areas tested. The locations selected for testing with the in-depth devices were based on observed surface distress and feedback from the tunnel operator.

The team encountered problems with collecting air-coupled GPR in the top portion of the Eisenhower Tunnel with an exposed concrete surface, mainly due to cables and other obstructions in the way. In addition, the team could not collect such data at the top of the tunnel due to the distance between the ceiling and the roof. Figure K-8 shows an example of the data collected (the antenna was mounted on a pushcart). The antenna was pointed at the side of the tunnel; it was difficult to keep the pushcart traveling in a straight line, so the distance between the antenna and the lining surface varied.

Although GPR data were collected on the tiled roadway section, the data proved not to be useable since the tiles were mounted on steel panels, and the panels were apparently not attached directly to the concrete.

The TTI team also collected handheld infrared camera images in the top section of the Eisenhower Tunnel and found significant temperature changes. Appendix L contains selected images from the handheld device and the thermal scan.
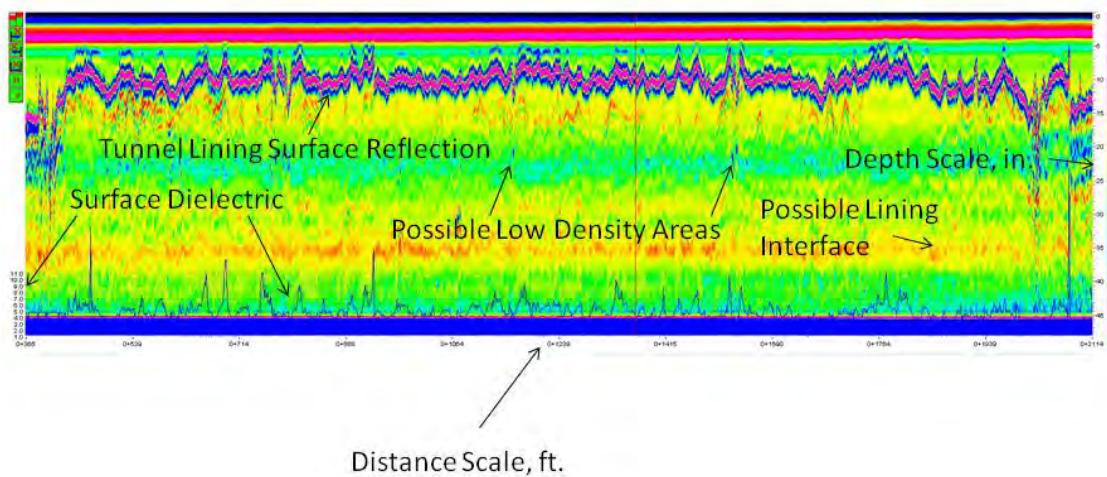
Figure K-8. Air-coupled GPR data for the Eisenhower Tunnel, top portion.

Hanging Lake Tunnel

In the Hanging Lake Tunnel, the in-depth evaluation devices were able to detect defects in the areas tested on the tunnel roof. The locations selected for testing with the in-depth devices were requested by the tunnel operator.

Figure K-9 shows an example of the air-coupled data taken on the Hanging Lake Tunnel roof (the antenna was mounted on a pushcart and pointed directly at the top of the lining). As can be inferred from Figure K-9, the distance between the antenna and the tunnel lining surface was kept relatively constant. Also, Figure K-9 shows two distinct interfaces.
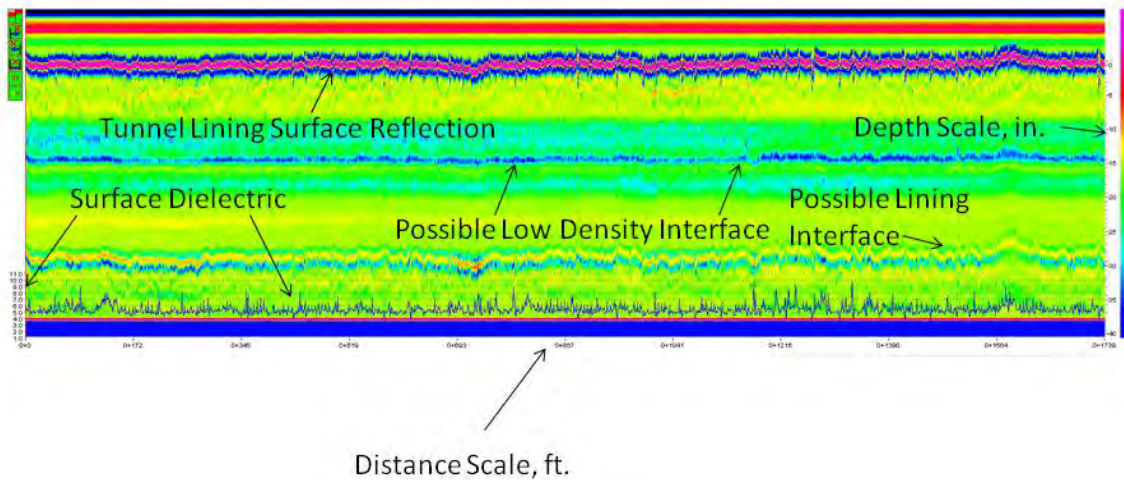
Figure K-9. Air-coupled GPR data for the Hanging Lake Tunnel roof.

Figure K-10 shows an example of the air-coupled GPR data taken on the Hanging Lake Tunnel tiled wall. The dielectric values shown in Figure K-10 have not been corrected for changes in the distance between the antenna and the tunnel lining. However, the TTI team believes the data are useful in their current form. The unusually large peaks are associated with steel plates or fixtures installed on the tunnel surface.
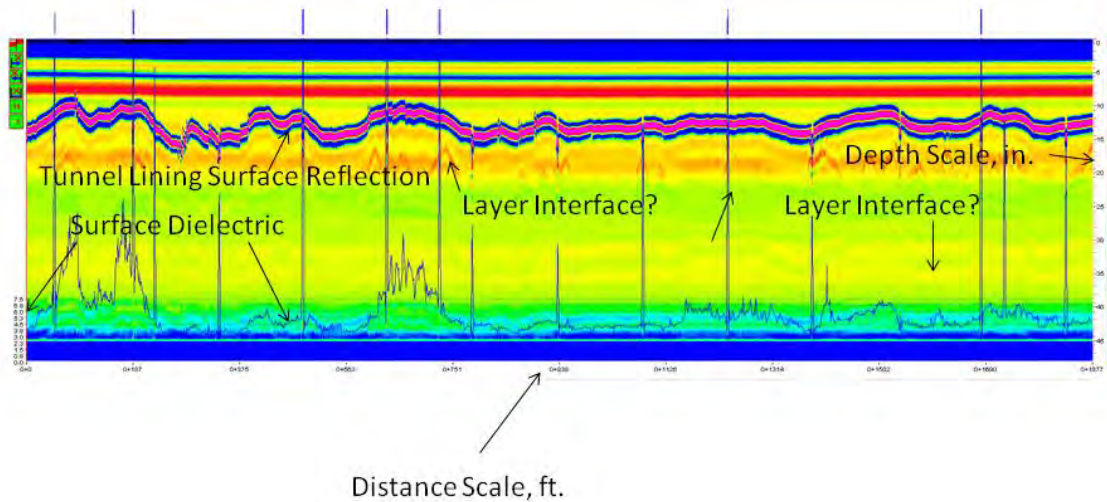
Figure K-10. Air-coupled GPR data for the Hanging Lake Tunnel tiled wall.

No Name Tunnel

In the No Name Tunnel, the team collected only air-coupled GPR data. Figure K-11 shows an example of the air-coupled GPR data taken in that tunnel. As can be seen in Figure K-11, the dielectric values are unusually low. The team did not encounter this issue in the other tunnels tested. One explanation is that the antenna was inadvertently set into a lower power output mode, which resulted in lower reflection amplitudes from the

tunnel lining. In any case, the air-coupled GPR data indicated possible layer interfaces in this tunnel.
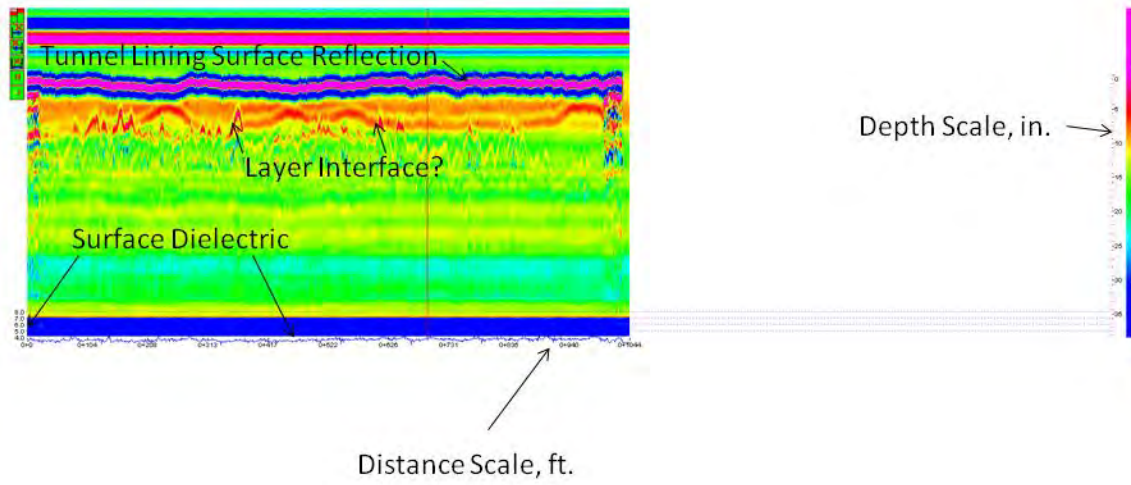
Figure K-11. Air-coupled GPR data for the No Name Tunnel.

APPENDIX L
EVALUATION OF TEXAS A&M TRANSPORTATION INSTITUTE TEST SPECIMENS WITH THE HANDHELD INFRARED CAMERA

HANDHELD INFRARED CAMERA

The Texas A&M Transportation Institute (TTI) purchased a FLIR T-300 handheld infrared camera for this project. The cost of the camera was approximately $9,000. Figure L-1 is a photo of this camera.

Figure L-1. FLIR T-300 infrared camera.

INFRARED CAMERA IMAGES FOR THE TTI TEST SPECIMENS

As described in Chapter 3 of the main body of this report, TTI personnel collected infrared camera images of ground penetrating radar (GPR) data on concrete and shotcrete specimens that contained simulated delaminations and voids. The TTI team determined that the equipment could only detect three simulated voids, all of which were located in the shotcrete sections. Those specimens were:

- Specimen F (air-filled void placed at 3 inches from the surface).
- Specimen G (water-filled void placed 3 inches from the surface).
- Specimen L (delamination placed 1 inch from the surface).

Specimen F had the most distinct thermal image.

The following images were taken at night. Figure L-2 shows the infrared image for Specimen F. The blue grid lines are chalk marks placed on the specimen. The spacing between the chalk marks is 50 mm (or approximately 2 inches).
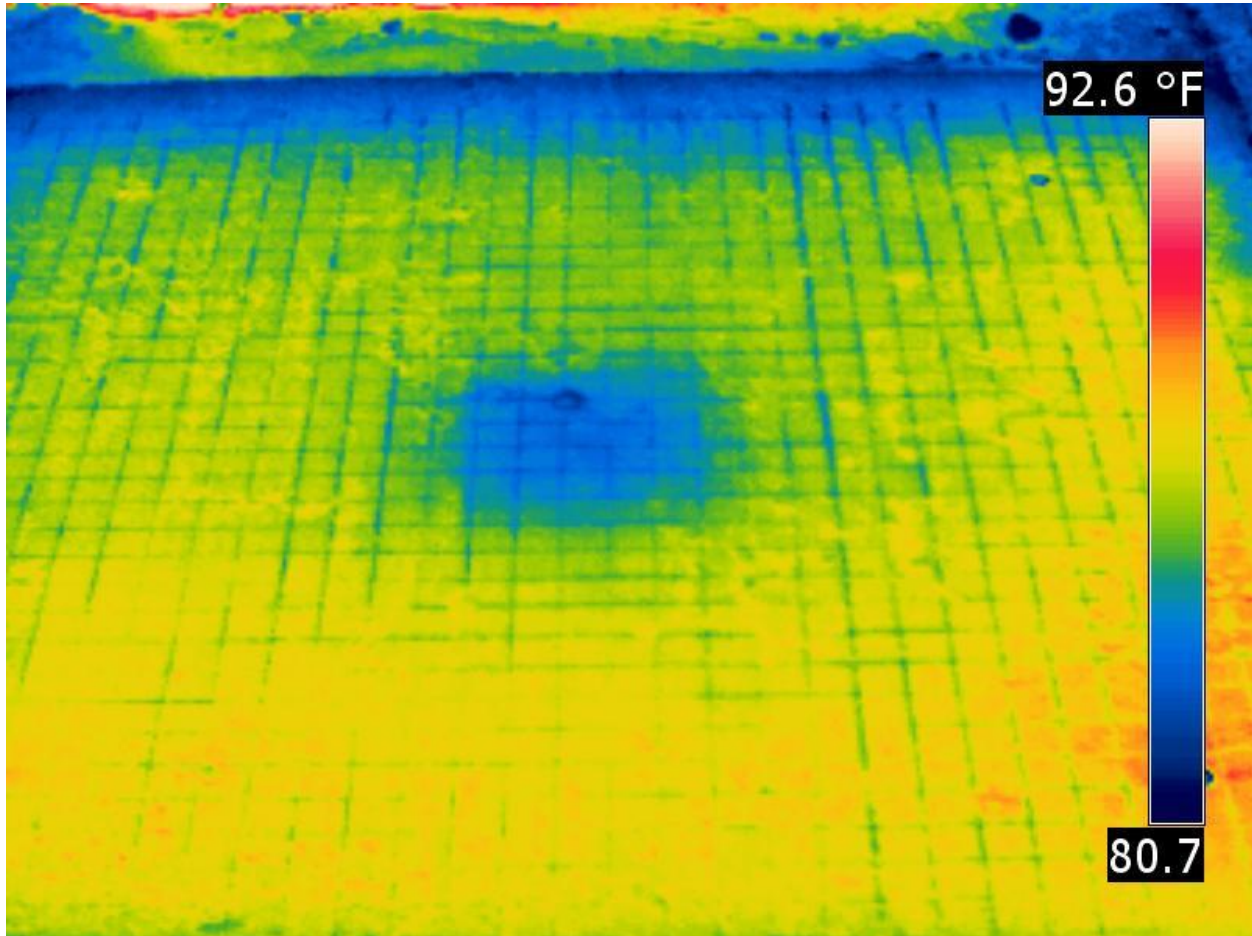
Figure L-2. Infrared camera image for Specimen F.

Figure L-3 shows the infrared image for Specimen G. As shown in Figure L-3, the thermal image is less distinct. The blue grid lines are chalk marks placed on the specimen. The spacing between the chalk marks is 50 mm.
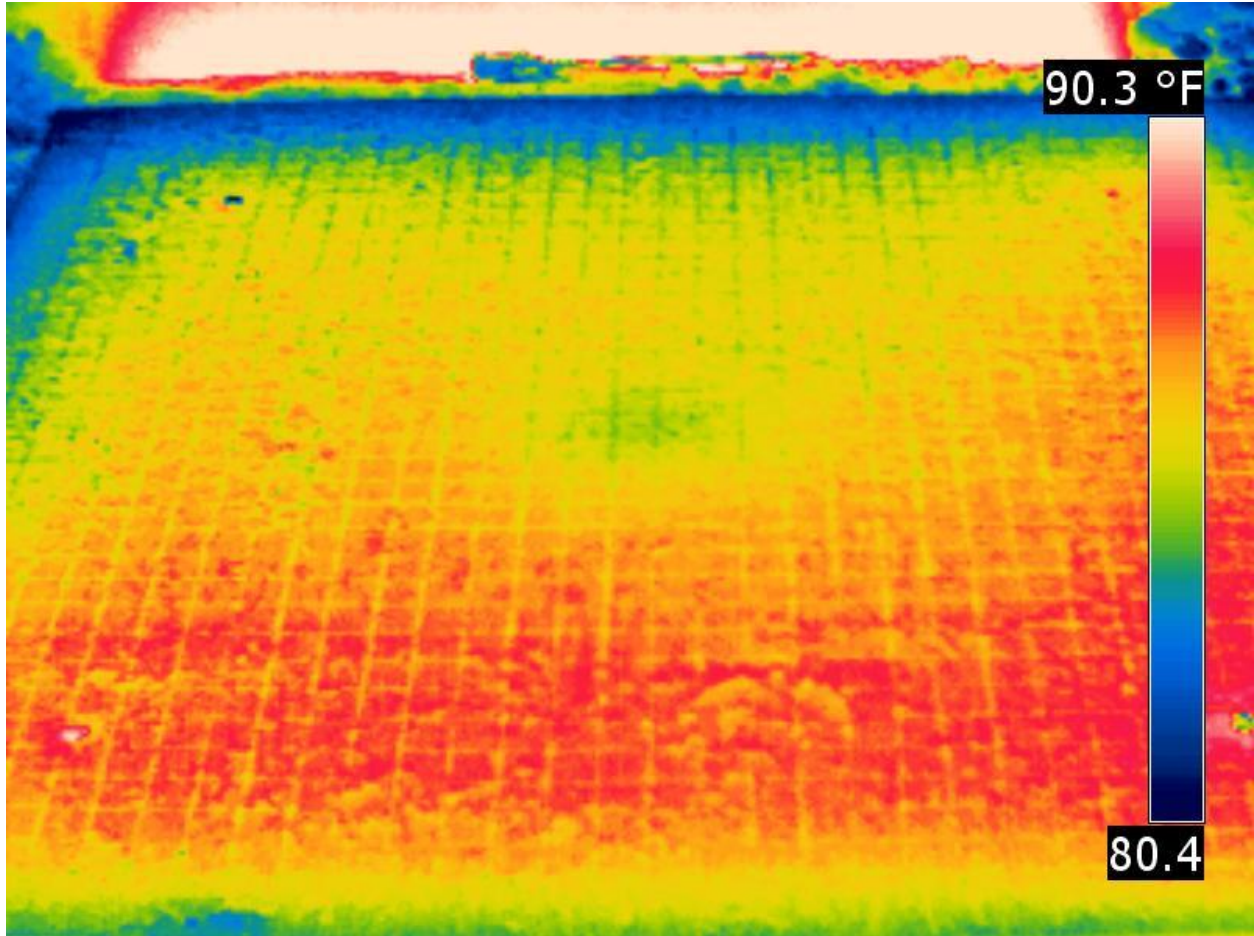
Figure L-3. Infrared camera image for Specimen G.

Figure L-4 shows the infrared image for Specimen L. As shown in Figure L-4, the thermal image is less distinct than the image in Figure L-2. The blue grid lines are chalk marks placed on the specimen. The spacing between the chalk marks is 50 mm.
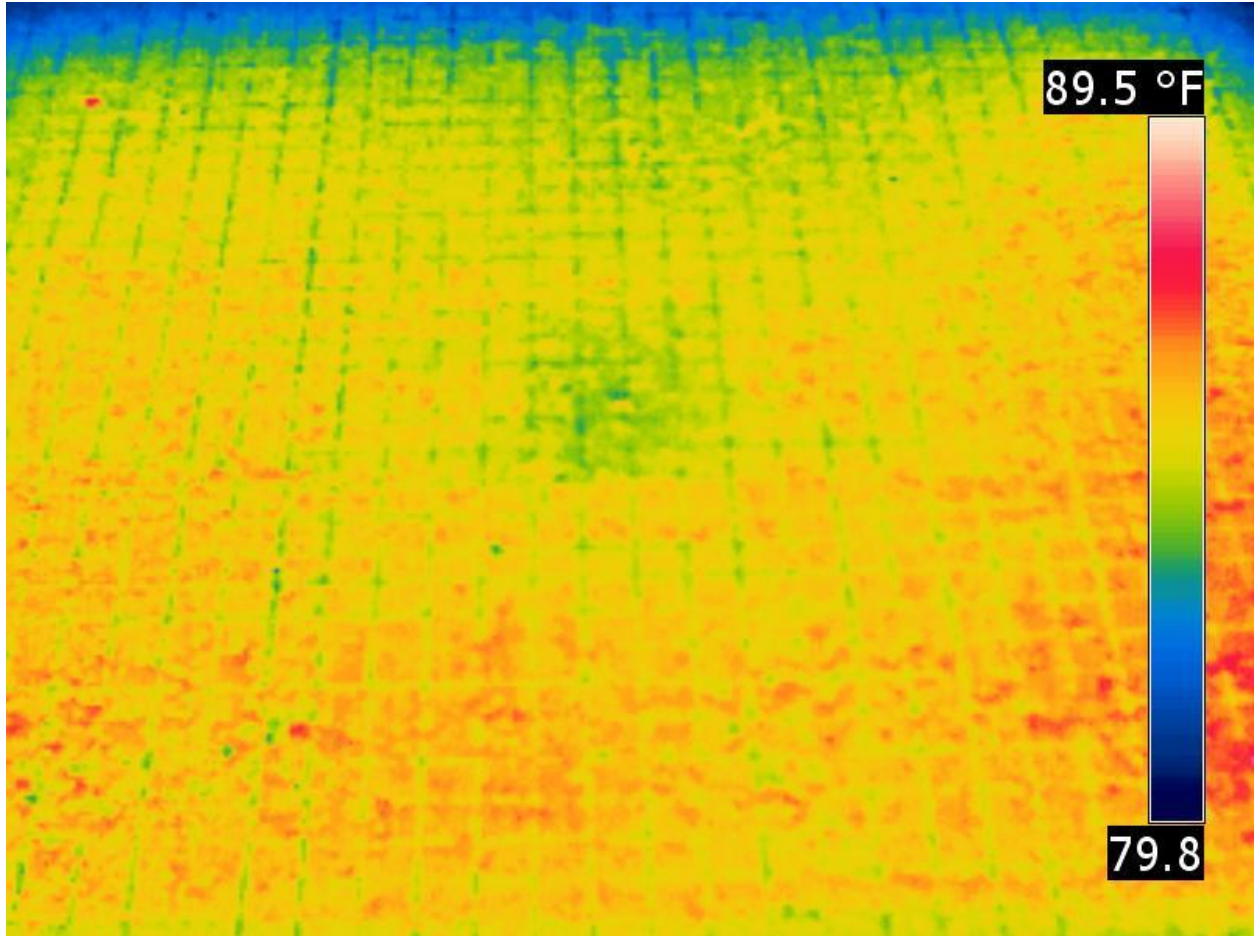
Figure L-4. Infrared camera image for Specimen L.

SELECTED INFRARED IMAGES

Introduction

This section contains selected infrared images from the FLIR T-300 infrared camera and the FLIR A325 vehicle-mounted infrared camera. TTI personnel obtained the FLIR T-300 images. Roadscanners personnel obtained and analyzed the images from the FLIR A325.

Chesapeake Bay Tunnel Images

Figures L-5 through L-14 show the images obtained in the Chesapeake Bay Tunnel.

Figure L-5. FLIR T-300 infrared image of the top of the Chesapeake Bay Tunnel. The areas in red are air vents.

Figure L-6. Visual image of the top of the Chesapeake Bay Tunnel.
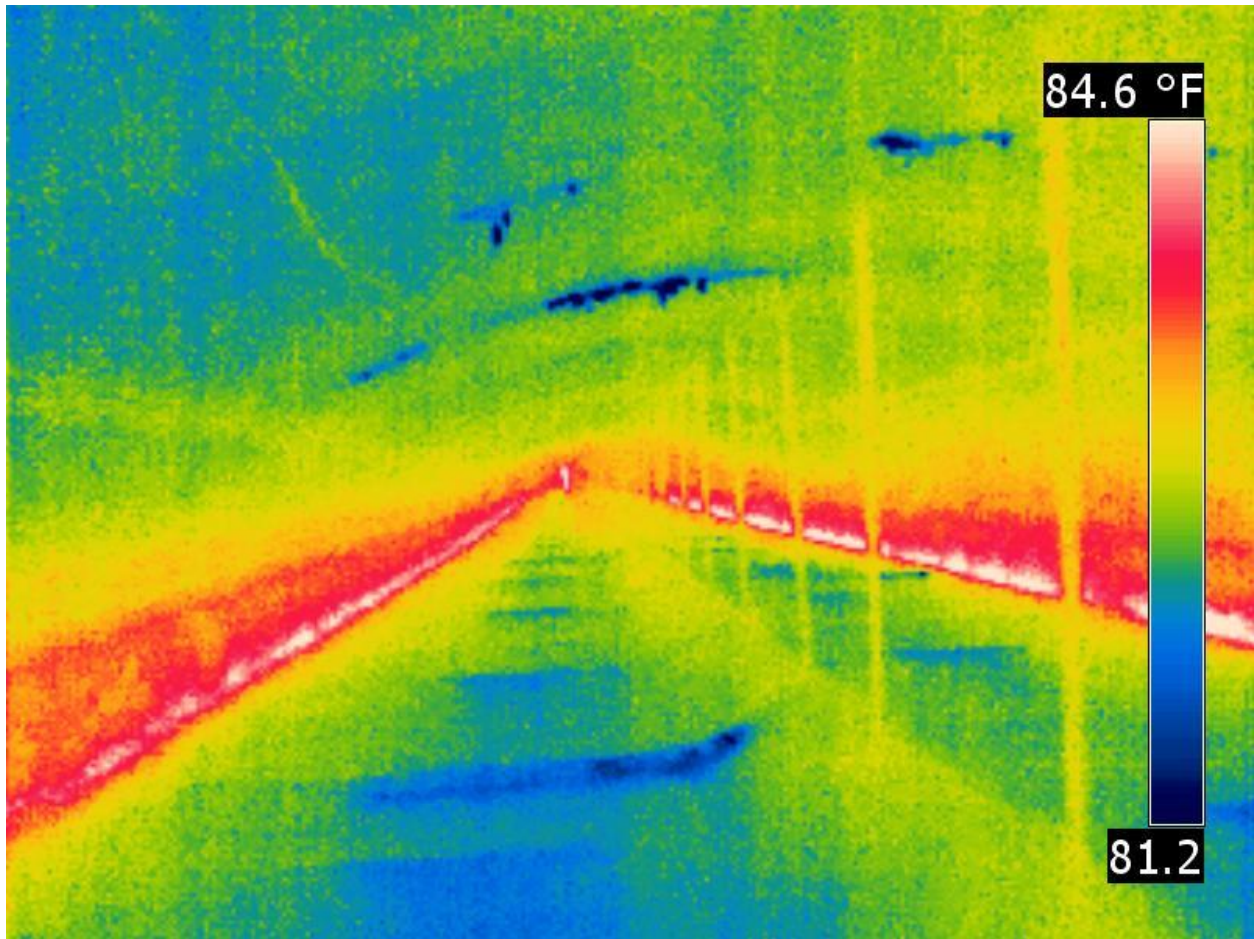
Figure L-7. FLIR T-300 infrared image of the top of the Chesapeake Bay Tunnel. The areas in blue at the top of the tunnel are cracks with moisture.

The infrared image color scale ranges from 84.6 °F (top) to 81.2 °F (bottom).
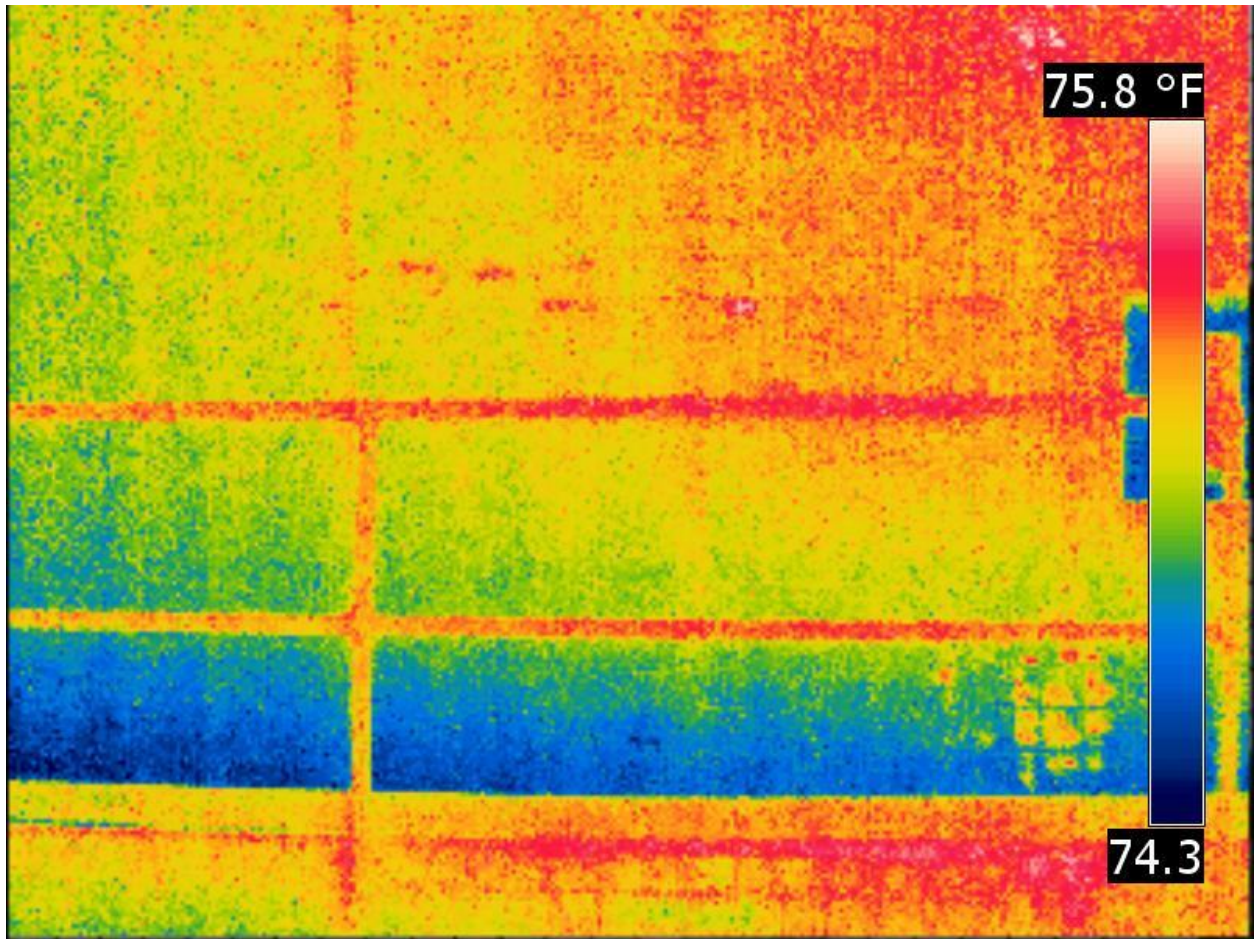
Figure L-8. FLIR T-300 infrared image of the tiled lining in the Chesapeake Bay Tunnel.

Figure L-9. FLIR T-300 visual image of Figure L-3.
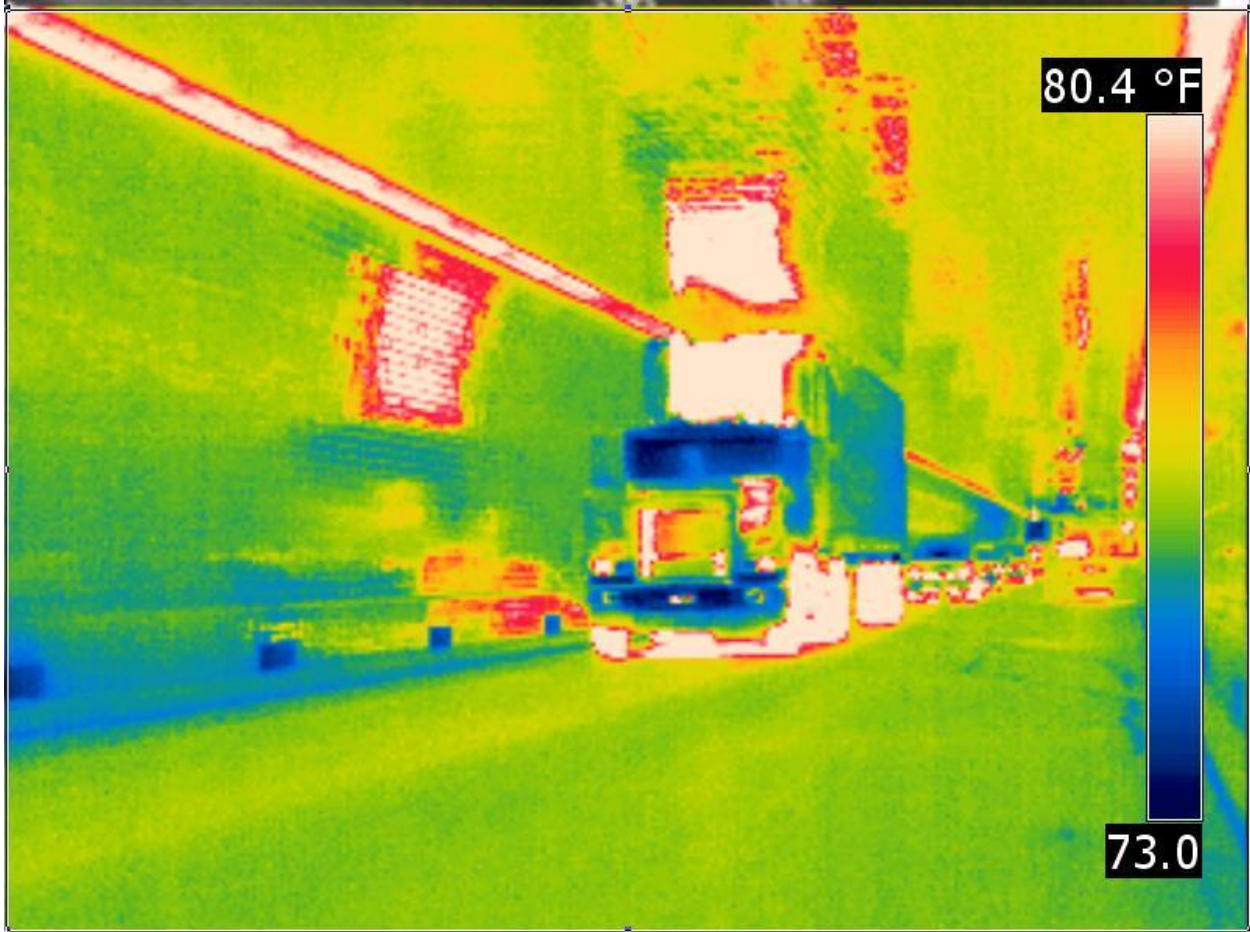
Figure L-10. FLIR T-300 infrared image of the tiled lining in the Chesapeake Bay Tunnel. Notice the thermal reflection of the vehicles.

Figure L-11. FLIR T-300 visual image of Figure L-5.
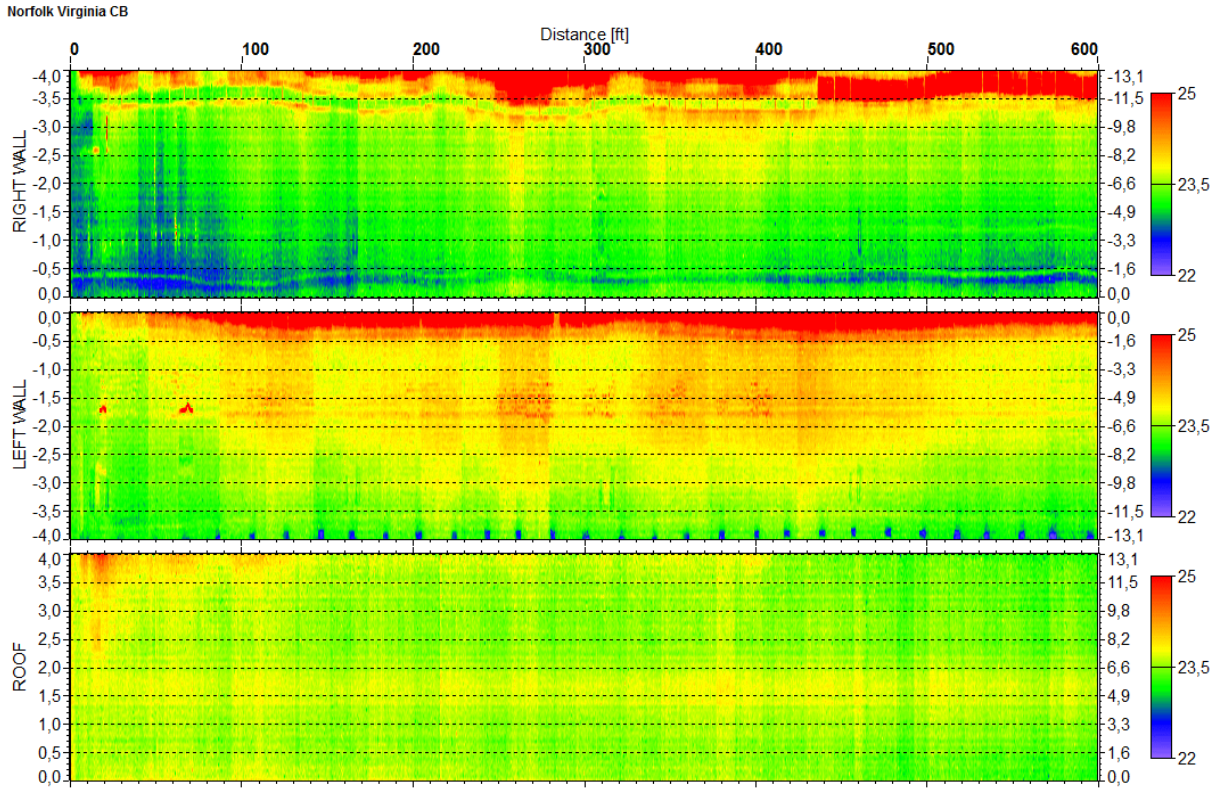
Figure L-12. FLIR A325 scan of the tiled roadway section in the Chesapeake Bay Tunnel. The temperature range is in centigrade (0-600 feet).
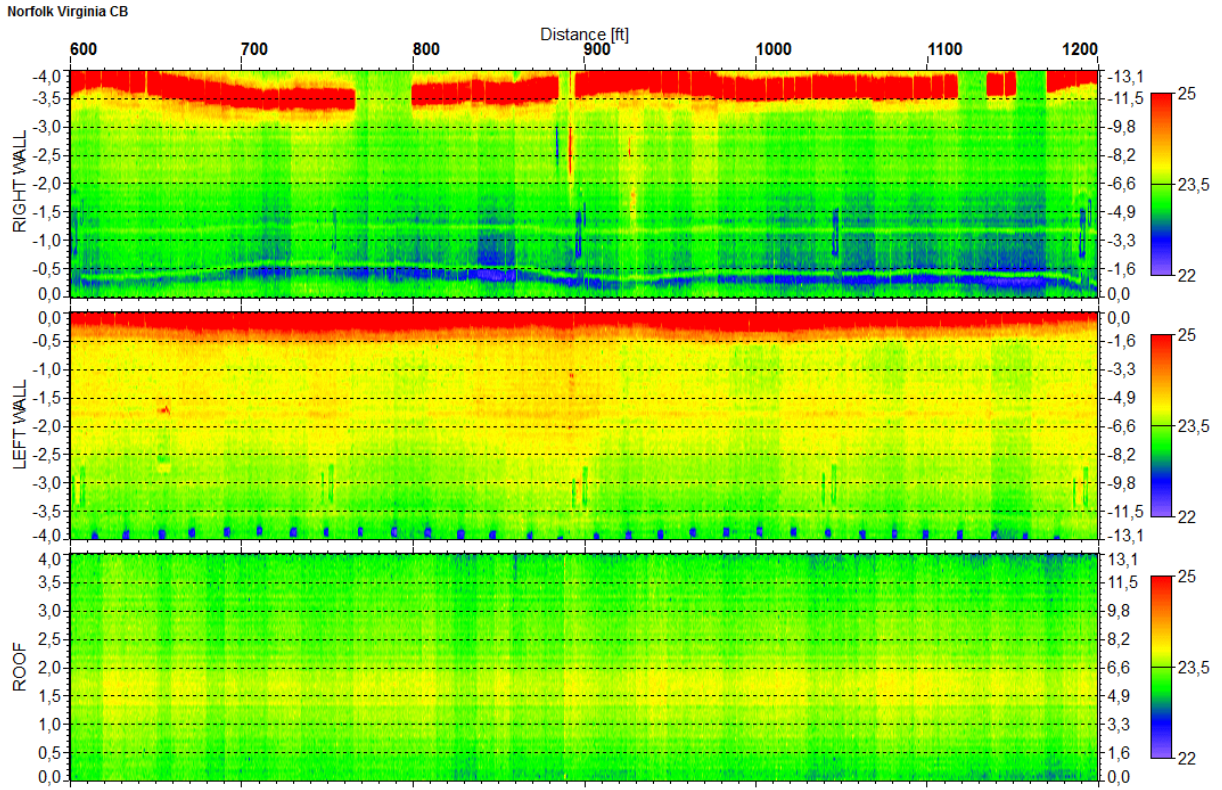
Figure L-13. FLIR A325 scan of the tiled roadway section in the Chesapeake Bay Tunnel. The temperature range is in centigrade (600-1200 ft).
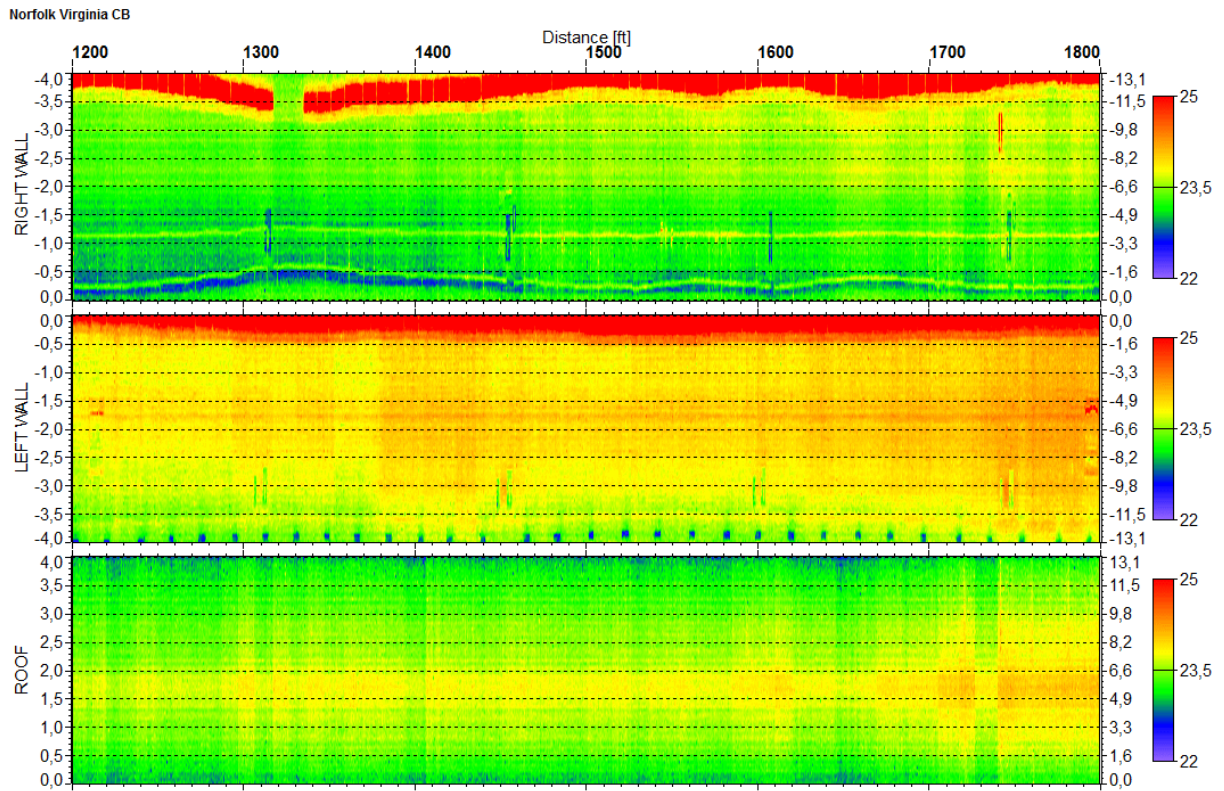
Figure L-14. FLIR A325 scan of the tiled roadway section in the Chesapeake Bay Tunnel. The temperature range is in centigrade (1200-1800 ft).

Eisenhower Memorial Tunnel Images

Figures L-15 through L-23 show the images obtained from the Eisenhower Memorial Tunnel.
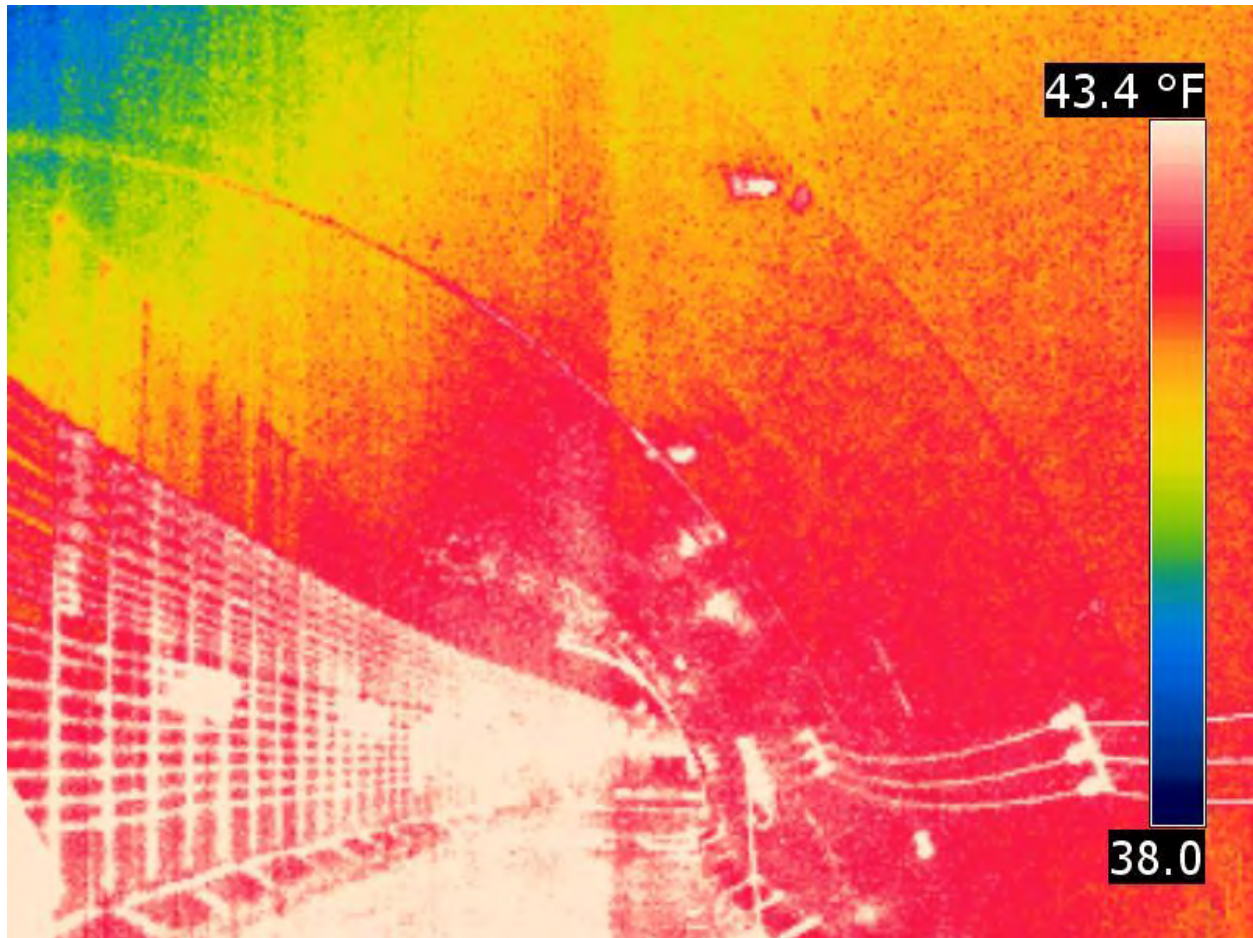
Figure L-15. FLIR T-300 infrared image of the top of the Eisenhower Memorial Tunnel. The areas in white are cables.
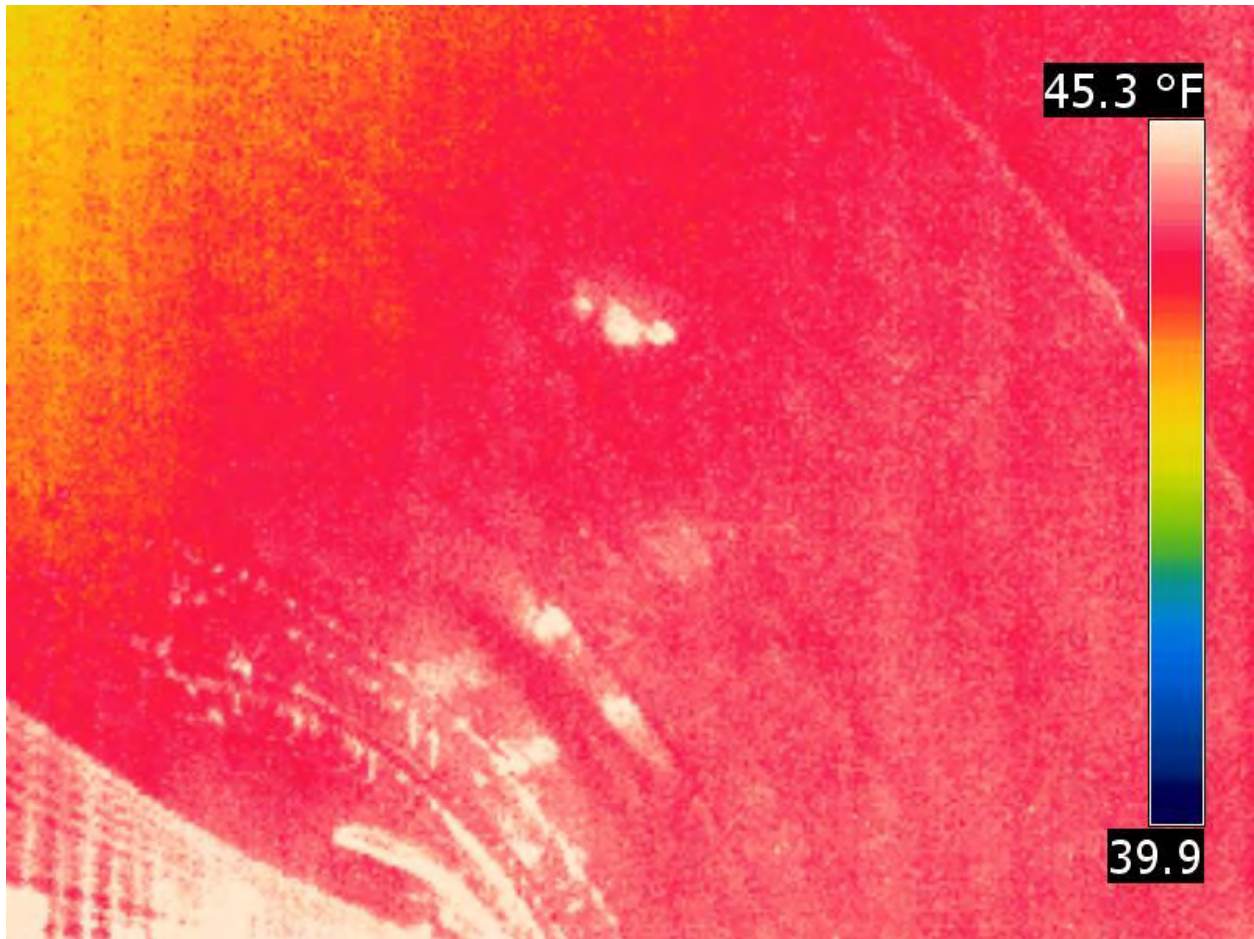
Figure L-16. FLIR T-300 infrared image of the top of the Eisenhower Memorial Tunnel.

Figure L-17. Visual image of the top of the Eisenhower Memorial Tunnel.
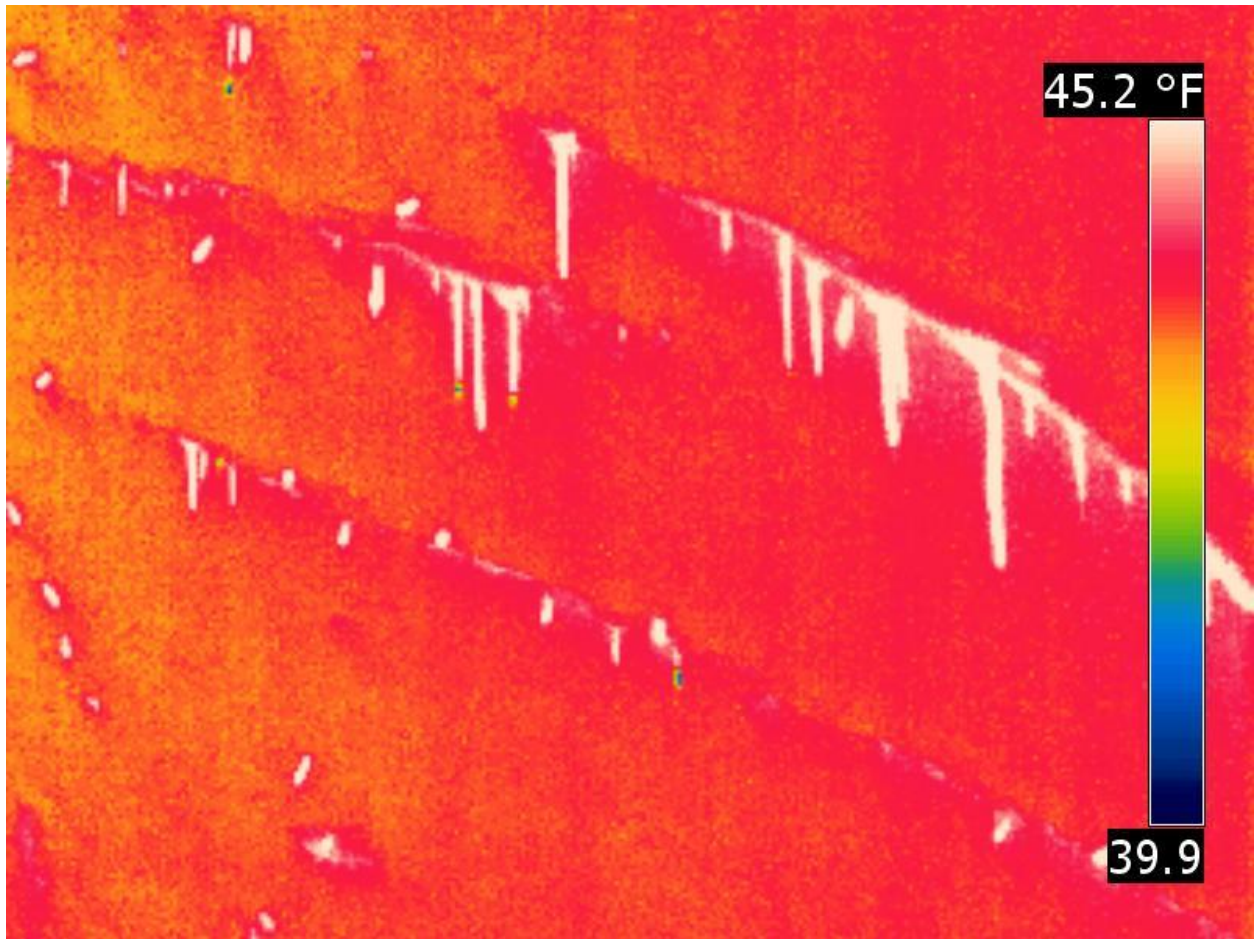
Figure L-18. FLIR T-300 infrared image of the top of the Eisenhower Memorial Tunnel. Stalagmites are shown in white.
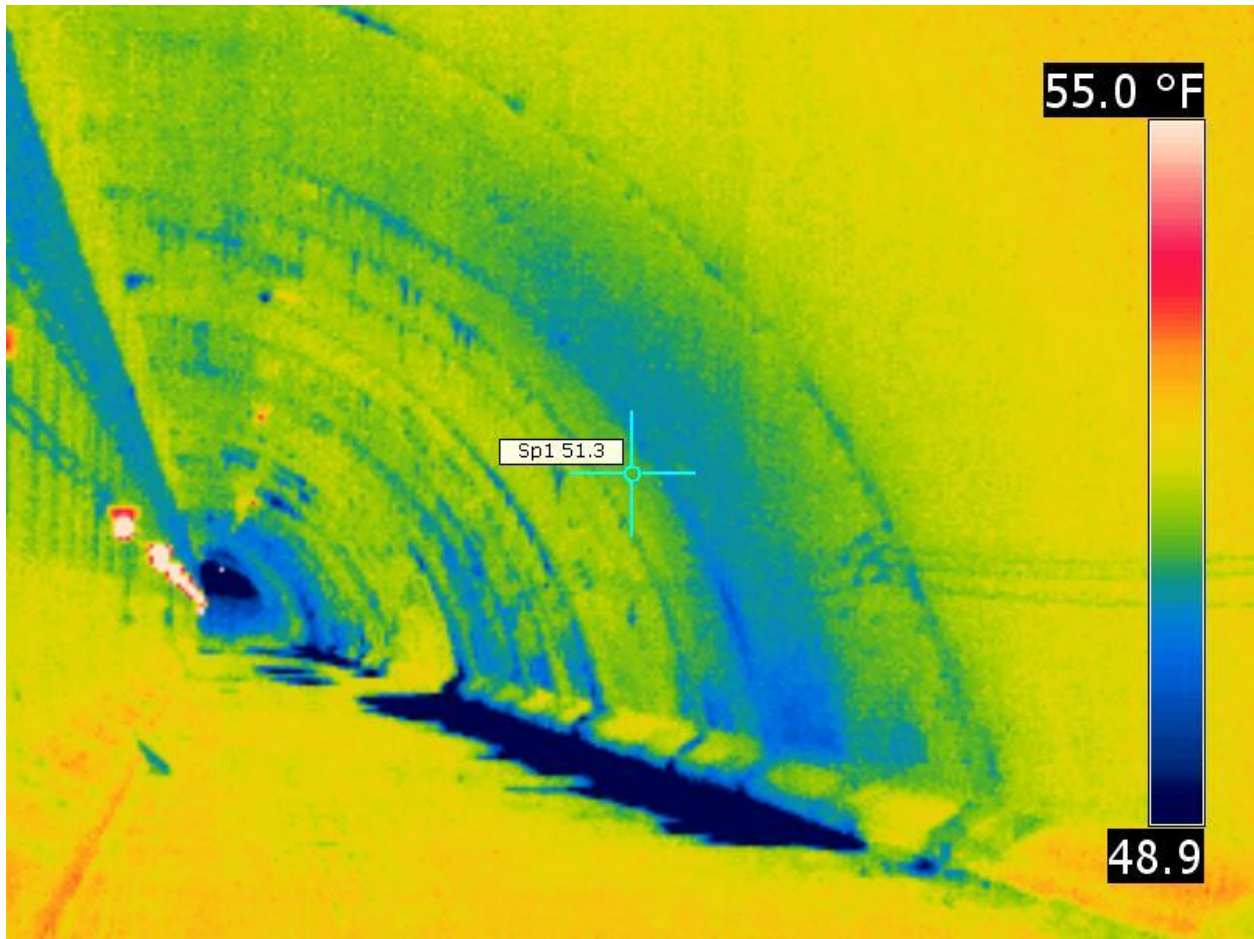
Figure L-19. FLIR T-300 infrared image of the top of the Eisenhower Memorial Tunnel.
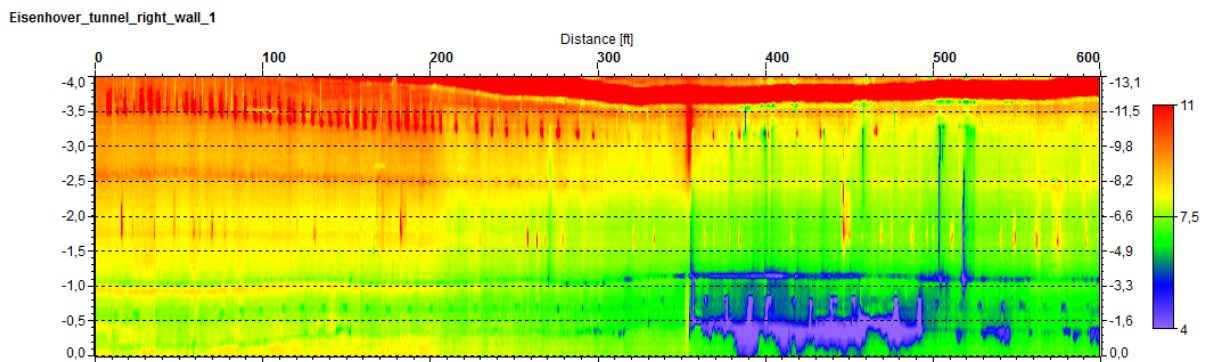
Figure L-20. FLIR A325 scan of the tiled roadway section in the Eisenhower Tunnel. The temperature range is in centigrade (0-600 ft).
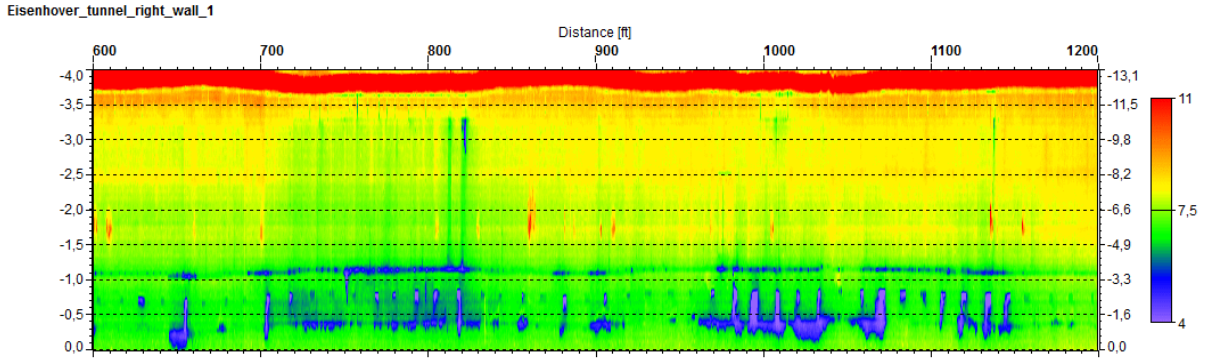
Figure L-21. FLIR A325 scan of the tiled roadway section in the Eisenhower Tunnel. The temperature range is in centigrade (600-1200 ft).
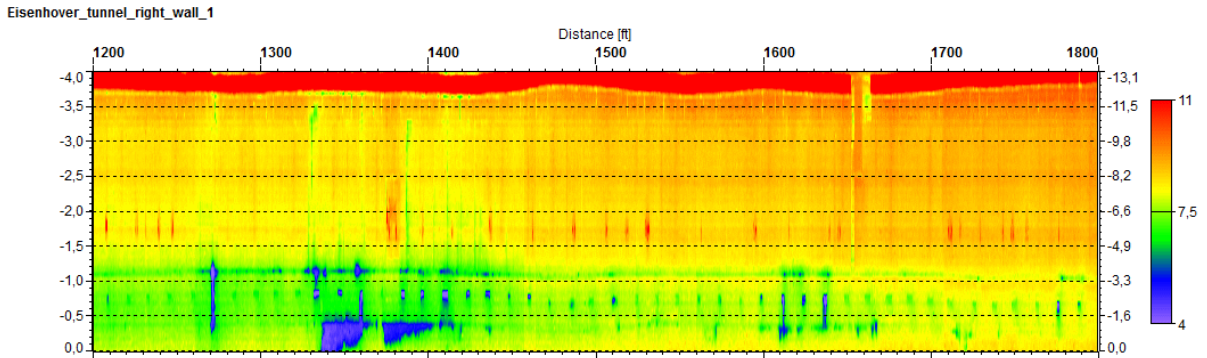
Figure L-22. FLIR A325 scan of the tiled roadway section in the Eisenhower Tunnel. The temperature range is in centigrade (1200-1800 ft).
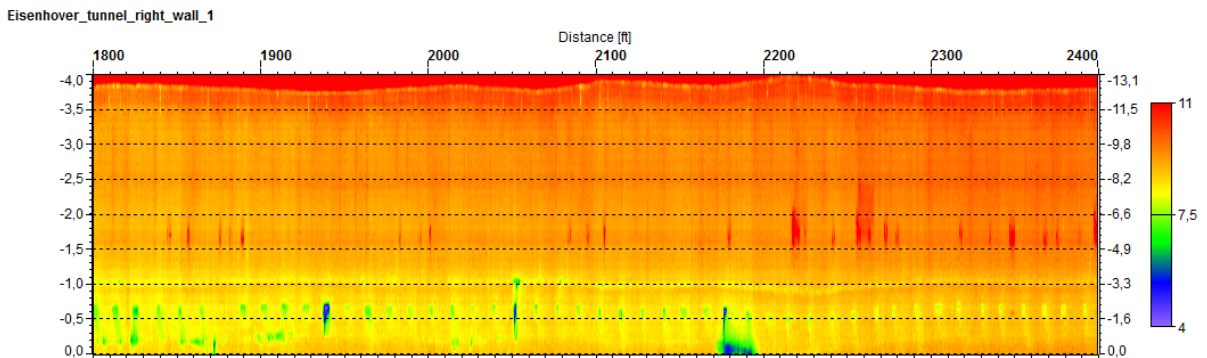
Figure L-23. FLIR A325 scan of the tiled roadway section in the Eisenhower Tunnel. The temperature range is in centigrade (1800-2400 ft).

Hanging Lake Tunnel Images

Figure L-24 through Figure L-35 show the images taken in the Hanging Lake Tunnel.
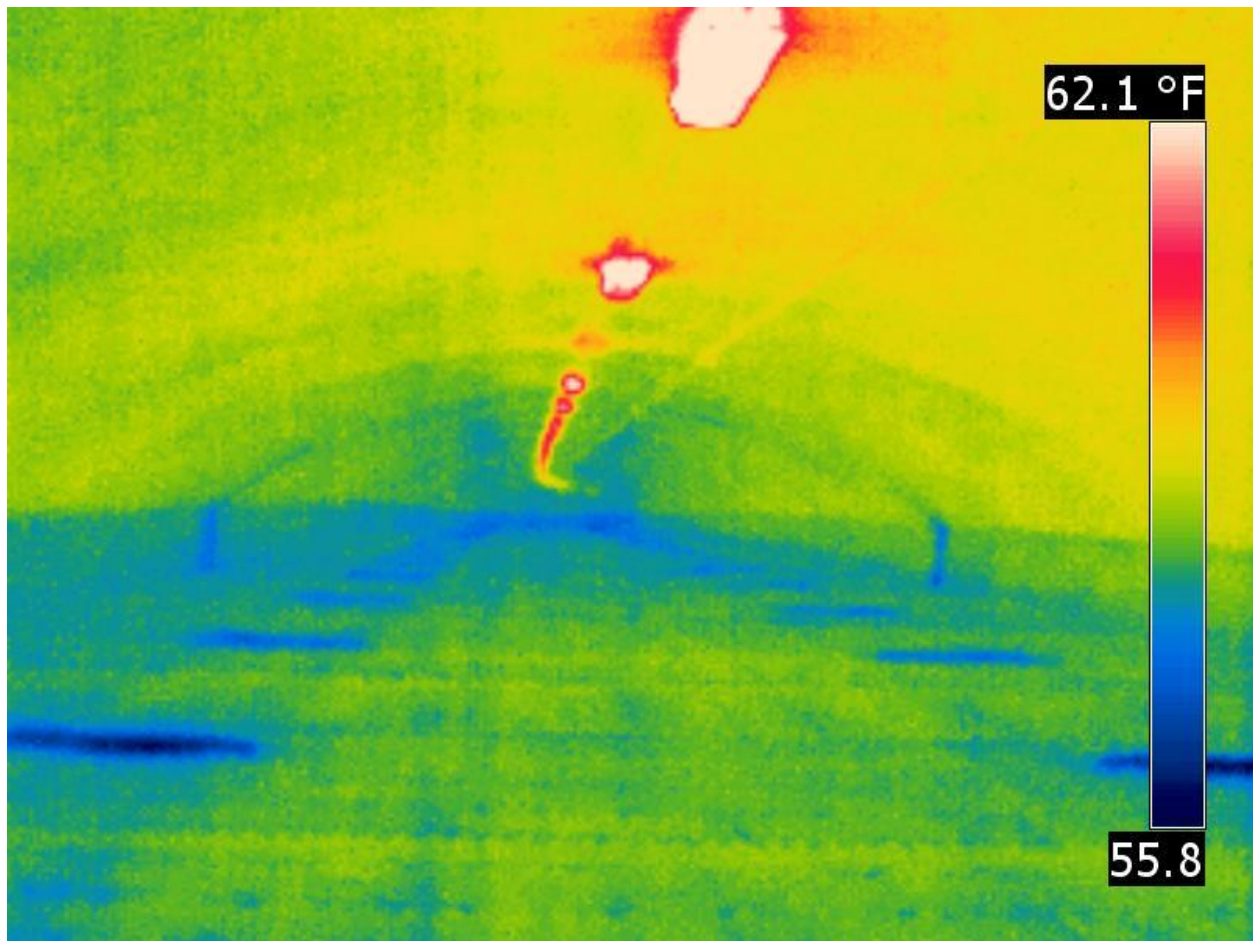
Figure L-24. FLIR T-300 infrared image of the top of the Hanging Lake Tunnel.

Figure L-25. Visual image of the top of the Hanging Lake Tunnel. Notice the staining around cracks.
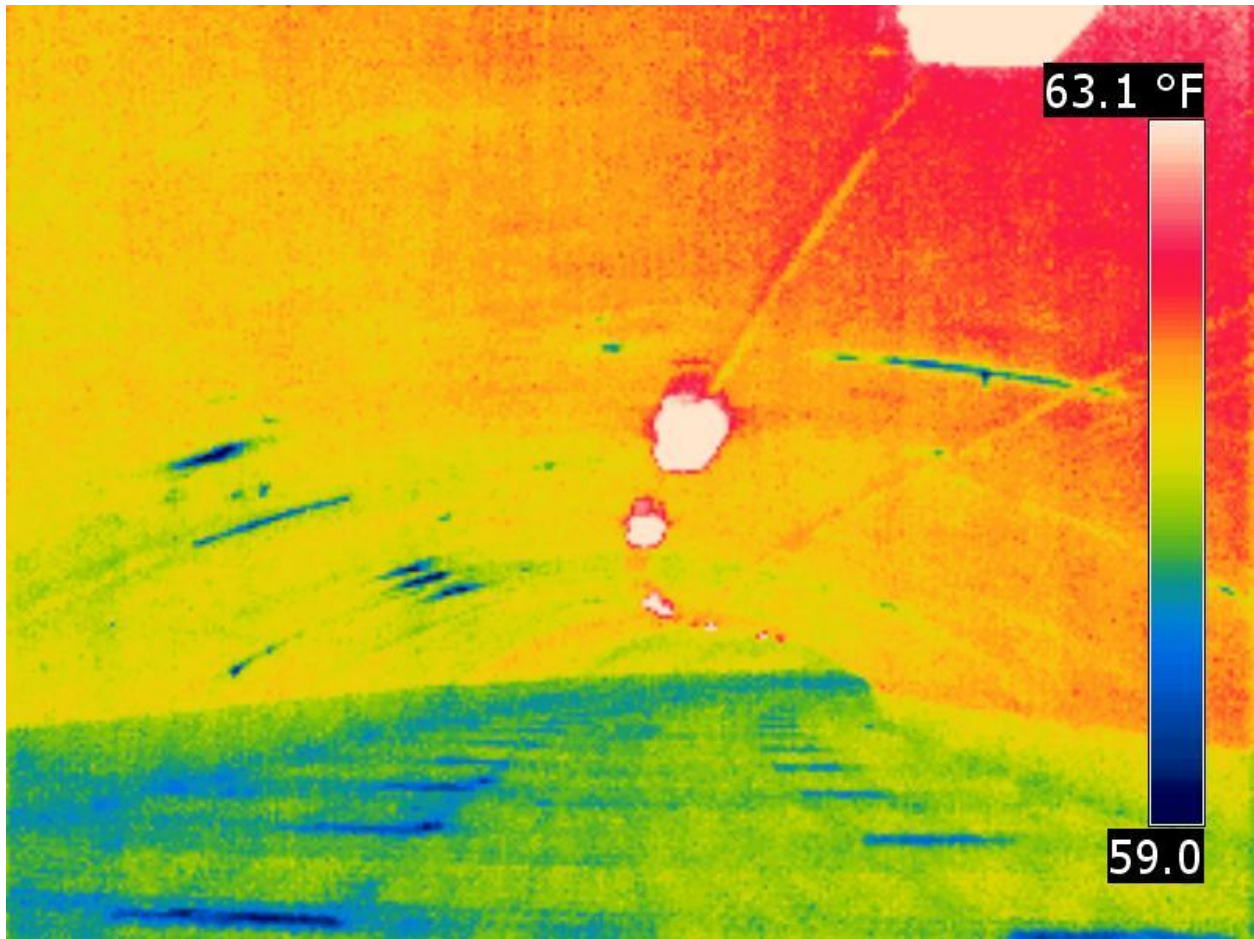
Figure L-26. FLIR T-300 infrared image of the top of the Hanging Lake Tunnel. The areas in blue along the tunnel ceiling are cracks with moisture according to visual observations. The areas in blue at the bottom are air vents.
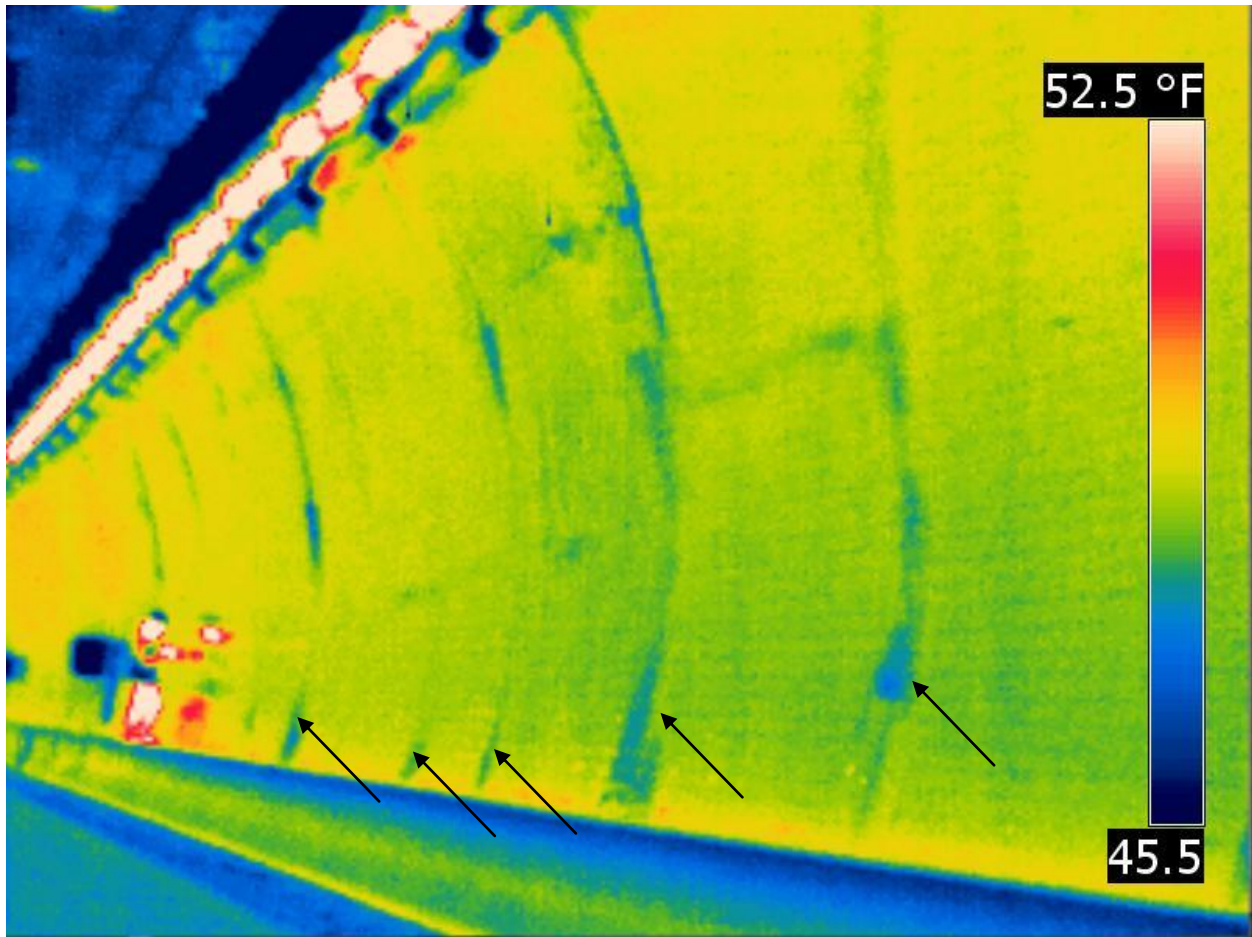
Figure L-27. FLIR T-300 infrared image of the tiled tunnel wall in the roadway section (eastbound). The areas in blue appear to be areas of debonded tiles according to limited sounding tests.
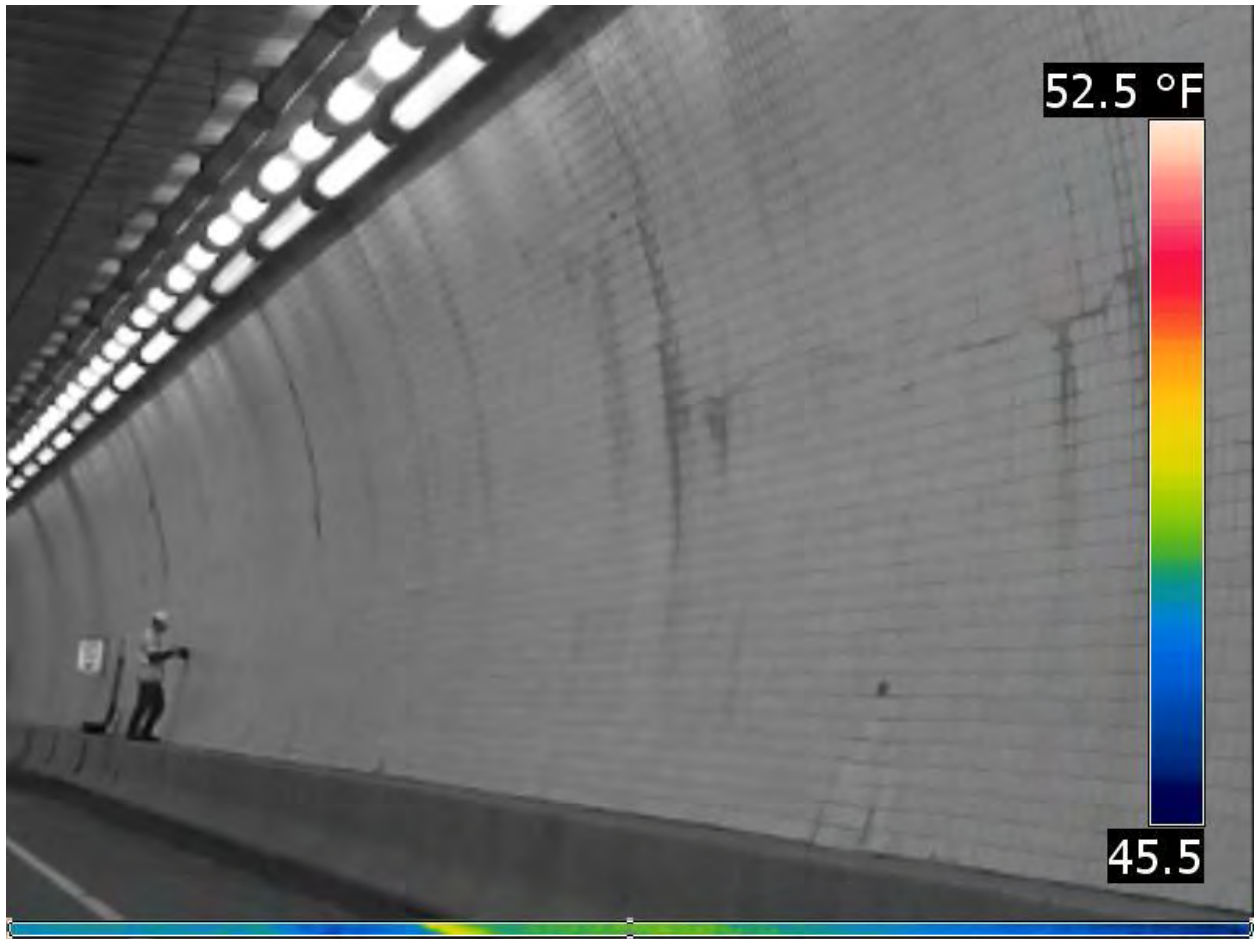
Figure L-28. FLIR T-300 visual image of Figure L-21.

Figure L-29. Visual image of the Hanging Lake Tunnel roadway section.
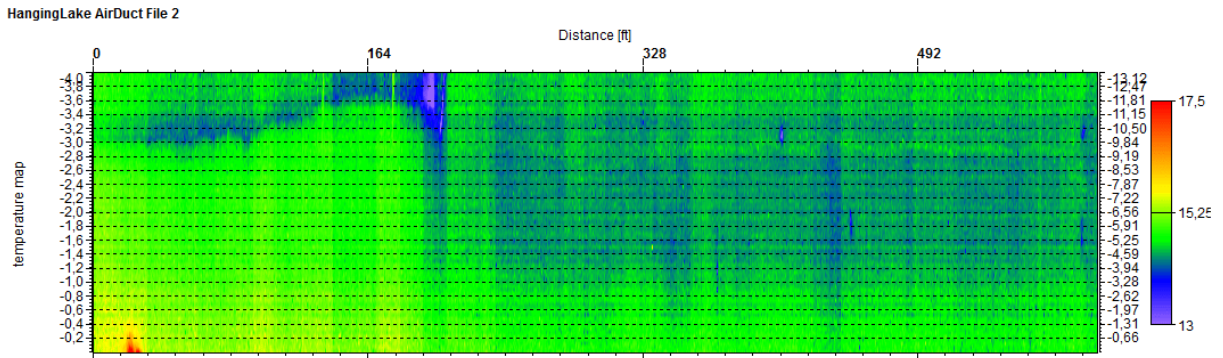
Figure L-30. FLIR A325 scan of the top of the Hanging Lake Tunnel. The temperature range is in centigrade (0-600 ft).
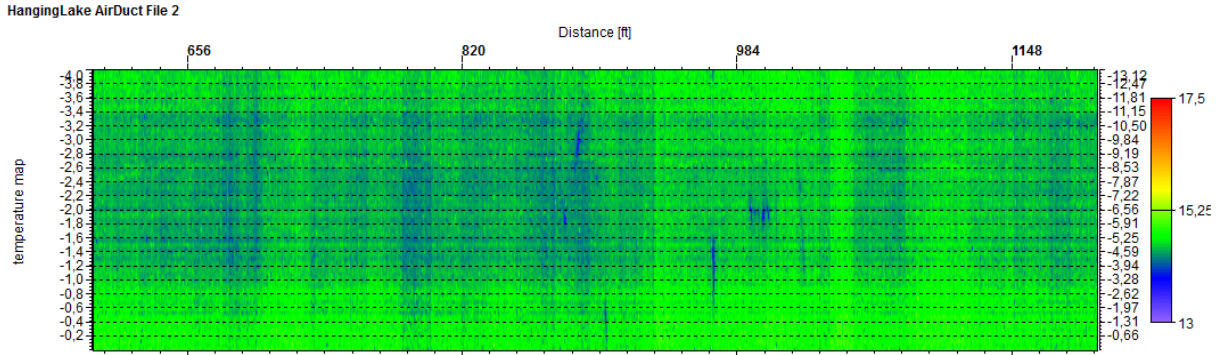
Figure L-31. FLIR A325 scan of the top of the Hanging Lake Tunnel. The temperature range is in centigrade (600-1200 ft).
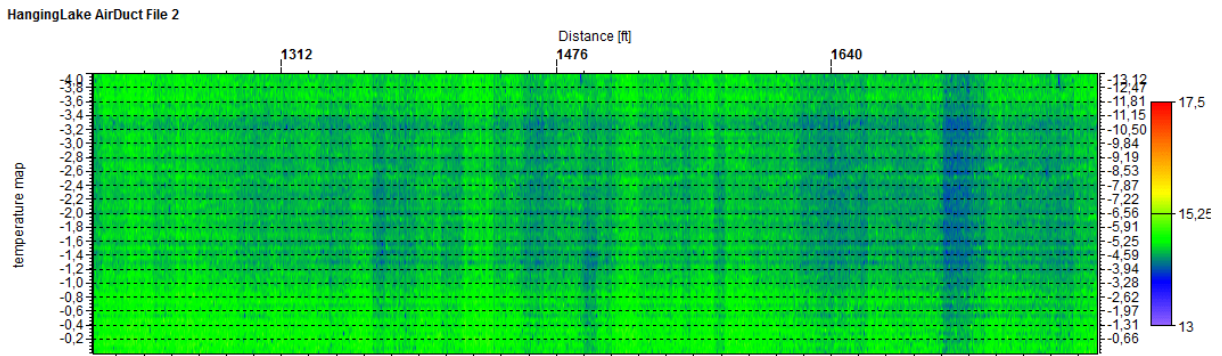
Figure L-32. FLIR A325 scan of the top of the Hanging Lake Tunnel. The temperature range is in centigrade (1200-1800 ft).
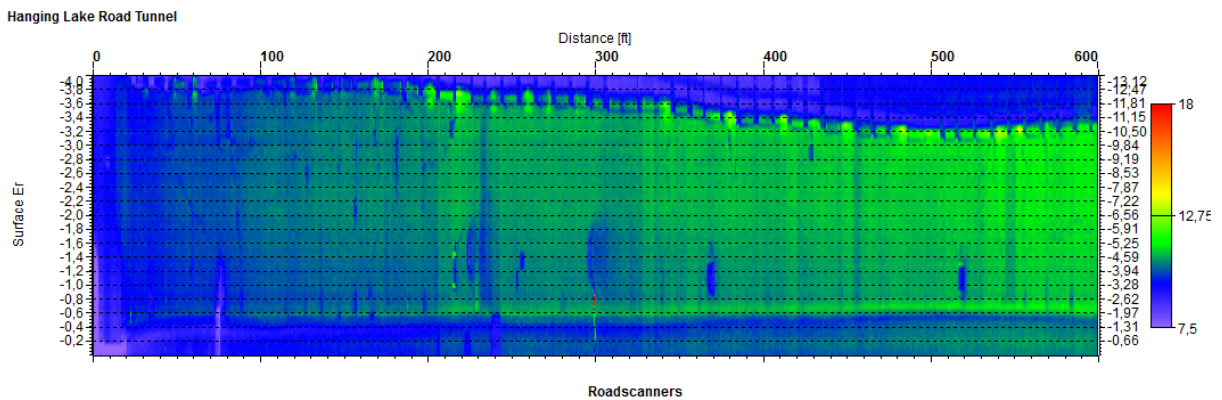
Figure L-33. FLIR A325 scan of the tiled roadway section in the Hanging Lake Tunnel. The temperature range is in centigrade (0-600 ft).
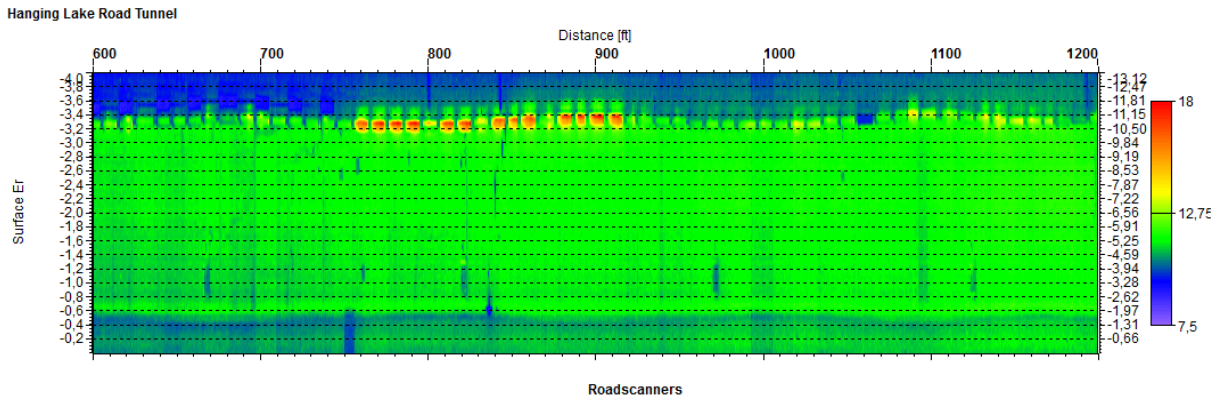
Figure L-34. FLIR A325 scan of the tiled roadway section in the Hanging Lake Tunnel. The temperature range is in centigrade (600-1200 ft).
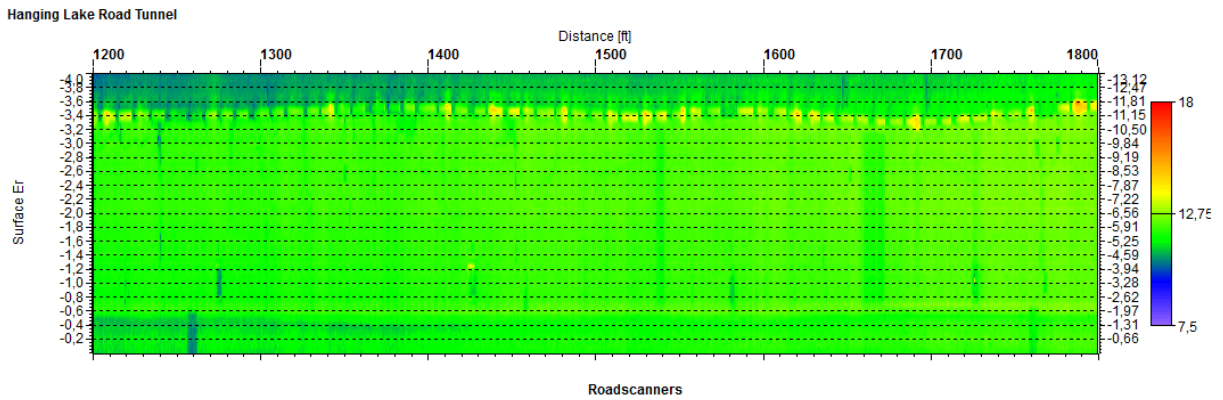
Figure L-35. FLIR A325 scan of the tiled roadway section in the Hanging Lake Tunnel. The temperature range is in centigrade (1200-1800 ft).

APPENDIX M
FIELD TESTING WITH ULTRASONIC TOMOGRAPHY (MIRA) IN THE US

INTRODUCTION

Field evaluations of four public tunnels and a series of test specimens were conducted for this research. Because the UST technique does not currently have a testing methodology that is field ready, the system was first evaluated based on its ability to detect simulated defects in laboratory specimens with simulated defects as well as other available sites (pavements, airport runways, bridge decks) where ground truth validation was available. After such testing, the system was then taken to the field to evaluate natural structural defects within actual tunnel linings. The tunnels tested consisted of the Eisenhower Memorial Tunnel near Dillon, Colorado; Hanging Lake Tunnel near Glenwood Springs, Colorado; Chesapeake Bay Tunnel near Norfolk, Virginia; and Washburn Tunnel in Houston, Texas. Types of concrete defects the system is used to detect and localize include air- and water-filled voids, vertical cracks, horizontal delaminations, tile debonding, and abnormalities such as clay lumps. The device is also used to determine reinforcement depth and spacing as well as concrete thickness measurements.

This testing concluded that the UST system is effective in locating horizontal delaminations ranging in thickness from 0.05-2.0 mm (0.002-0.079 inch) and is able to differentiate between fully debonded and partially bonded areas. Vertical cracks were only clearly characterized when the polarization of the shear waves was nonparallel with the direction of the crack; however, the presence of cracks often resulted in the omission of surface detail in the scanned images since shear waves could not be supported by air. Backwall surfaces up to a depth of 965 mm (38 inches) were successfully and accurately determined. Air- and water-filled voids ranging from 76-203 mm (3-8 inches) in depth, as well as reinforcement details such as layout and depth, were also successfully determined and located. With the exception of some medium-sized clay lumps (with a diameter of approximately 102 mm, or 4 inches) surrounding reinforcement, all clay lumps tested were successfully located.

A summary of the ultrasonic tomography technique and field-testing results in the US are provided in this report.

ULTRASONIC TOMOGRAPHY TECHNIQUE

The ultrasonic tomography system used in this study is a device that utilizes an array of ultrasonic transducers to transmit and receive acoustic stress waves for the inspection of concrete structures. The system used here, the A1040 MIRA, is produced by Acoustic Control Systems.

Figure M-1. The A1040 M IRA system (left), and the transmission/reception of acoustic waves (right).

The tomograph, shown in Figure M-1 (left), uses a 4 x 12 grid of mechanically isolated and dampened transducers that can fit the profile of a rough concrete testing surface with a variance of approximately 10 mm (0.4 inch). Each row of four transducers transmits stress waves sequentially while the remaining rows act as receivers. In this manner, there is a wide coverage of shear wave pulses that reflect at internal interfaces where the material impedance changes (Figure M-1, right). With the help of a digitally focused algorithm (an alteration of the Synthetic Aperture Focusing Technique (SAFT; Schickert 1995 and Schickert et al. 2003), a three-dimensional volume is presented with each point of possible reflection in half-space represented by a color scheme, scaled according to reflecting power. This three-dimensional image can also be dissected into each of the three planes representing its volume: the B-scan, C-scan, and D-scan (Figure M-2). The B-scan is an image slice showing the depth of the specimen on the vertical (or   ) axis versus the width of the scan on the horizontal (or   ) axis. This slice is a plane perpendicular to the scanning surface and parallel to the length of the device. The C-scan is an image slice showing the plan view of the tested area, with the vertical (or   ) axis of the scan depicting width parallel to the scanning direction and the horizontal (or   ) axis of the scan representing the length perpendicular to the scanning direction. The scanning direction is always defined as the   -axis, as seen in Figure M-2. The D-scan is like the B-scan in that it images a plane perpendicular to the testing surface, but it is oriented parallel to the scanning direction. On each of the scans, the various intensities reported by the returned waves are color coded, from light blue to deep red, representing low reflectivity (typically sound concrete) and high reflectivity (any type of impedance), respectively. With this intensity scaling, it is easy to see any discontinuities with distinctly different wave speeds, such as voids, delaminations, cracks, and other abnormalities.
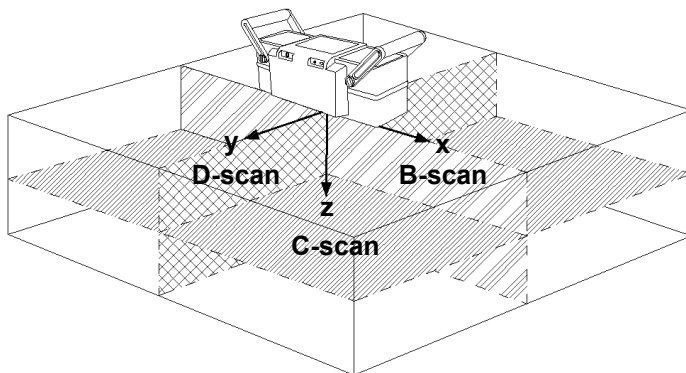
Figure M-2. B-, C-, and D-scans relative to tomograph.

This UST system has had limited exposure to industrial applications but is quickly becoming recognized as a powerful NDT method. The ultrasonic technique in general has

been used in concrete structures to identify concrete thickness and elastic modulus, as well as to detect grouting conditions of internal ducts in prestressed structures (Im et al. 2010; De La Haza et al. n.d.). Previous uses of the ultrasonic tomograph technique have largely been conducted by the Federal Institute for Materials Research and Testing (BAM) in Germany. BAM collaborated with Acoustic Control Systems (ACS) in the development of the MIRA system and has successfully detected delaminations at 203 mm, or 8 inches, below the surface (Shokouhi et al. 2011). This study was conducted on a demolished bridge deck and was limited to delaminations ranging from 76-203 mm (3-8 inches) in depth. This study also used a previous version of the UST device (with a 4 x 10 transducer array). Another study conducted by BAM indicated the UST technique could detect grouting conditions in post-tensioned concrete elements (Krause et al. 2009). Overall, the studies conducted by BAM have raised awareness of the abilities of the UST device and encourage more research discovering its capabilities and limitations.

PRELIMINARY EVALUATION OF THE UST SYSTEM

Because the A1040 MIRA device has had limited exposure to industrial applications, the system was first used on a variety of test specimens prior to taking the system into the field. The test specimens included mock-up slabs built specifically to mimic defects common in tunnel linings, as well as certain structural applications exhibiting the types of defects of interest. These other sites (highways, bridge decks, airport runways) were made available to the research team and were capable of providing ground truth validation.

The process used for the following evaluations was experimentally determined. It was necessary to experiment with scanning increments, grid locations, device orientations, and other types of configurations to help develop a reliable methodology. The evaluation procedure discussed later reflects the insights gained from scanning the following simulated specimens.

Fabrication, Testing, and Validation of Concrete/Shotcrete Specimens with Simulated Delaminations and Voids

Eleven normal-weight concrete slabs and 13 shotcrete slabs were constructed to mock various defects. The concrete slabs were used to mimic typical concrete tunnel linings with and without reinforcing steel. The shotcrete slabs were constructed to mimic applications in which shotcrete is sprayed on as a finished layer, as typically found in tunnel linings. A specially designed lattice girder, also typical in tunnel wall construction, was used as reinforcement in the shotcrete slabs (Figure M-3, bottom right).

Figure M-3. Construction of slabs with simulated defects.

The simulated delaminations in these slabs were constructed from three types of material. Delaminations were imitated by using 0.05 mm (0.002-inch) plastic square sheets and 0.25 mm (0.01-inch) cloth squares (Figure M-3, top right). Air-filled voids (Figure M-3, top left) were constructed by inserting 13 mm (0.5-inch) thick foam squares in vacuum-sealed plastic bags. Water-filled voids (Figure M-3, bottom left) were constructed in a similar manner by placing water-filled Ziploc bags within vacuum-sealed plastic bags and carefully padding the defect with concrete/shotcrete during construction so as not to puncture the plastic.

The simulated specimens were tested by first placing a 50 mm x 150 mm (2 inch x 6 inch in a -increment vs. -increment) grid on the surface. This grid increment was determined experimentally and is shown to provide optimal resolution for the types of defects under inspection in these slabs. After constructing the grid, the UST device is manually placed along each marked increment, taking 3-5 s per increment to automatically scan and store the gathered data. At the 50 mm x 150 mm (2 inch x 6 inch) spacing, this process takes approximately 13.5 min/m^2 (1.25 min/ft^2).

Some of these specimens were fully measured twice in opposing directions. This was done for two reasons. First, it is necessary to show the reproducibility of the ultrasonic tomography technique when scanned in different directions. Second, since the device is polarized in the sense that the shear waves are transmitted and received in one direction only (the -axis), scanning in two orthogonal directions allows objects to be more accurately dimensioned.
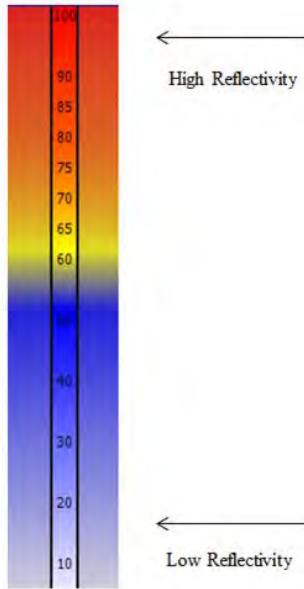
Figure M-4. Scale of reflectivity (or acoustic impedance).

After constructing a grid on the specimens and gathering the data, the images produced by the A1040 MIRA proprietary software were analyzed for regions of high reflectivity, which are denoted by the red regions in the UST images. Since the software output is a color scheme that depicts intensity of reflectivity (low reflectivity or impedance is coded as light blue, while high reflectivity or impedance is coded as red, as shown in Figure M-4), great care has to be taken when determining the type of discontinuity under inspection. The software used in this research does not display a waveform in the time domain; therefore, phase changes, which would be directly related to the density of the discontinuity, cannot be determined without additional features or post-processing. Also, since for these specimens the grid increment in the direction normal to the B-scans was 50 mm (2 inches), the B-scans in the inspection software are in 50 mm (2 inch) increments.

With the firmware used for this research, 50 mm (2 inches) is the minimum scanning increment available. Toward the end of this project, a firmware update (3.0-9.1.22) was available for the A1040 MIRA system, which added the ability to scan as closely as 10 mm (0.4 inch). The C- and D-scans, on the other hand, can be viewed in very small increments (on the order of 1-2 mm, or 0.04-0.08 inch) that are associated with the geometry of the transducer spacing and depth of scan and are values that are preset by the device manufacturer.

For most concrete structures, a backwall reflection is the first discontinuity that is expected to be readily visible since backwall surfaces are usually exposed to air, causing almost complete reflection of the sound waves. This is not the case in instances where there is full bonding of a layer to a sublayer. When a visible backwall reflection readily correlates with the expected concrete depth, inspection of the area between the testing surface and backwall reflection can take place. As each B-, C-, and D-scan is fully investigated, regions of high reflectivity that appear to be damage are catalogued by the judgment of the operator. If details such as concrete cover and reinforcement direction and spacing are desired, these can be catalogued as well.

C-scans, which offer the most comprehensive visual dimensioning of the simulated delaminations, are shown in Figures M-5 and M-6. The images in these figures are representative of defect visualization for the simulated concrete and shotcrete slabs. Figures M-5 and M-6 depict typical C-scans showing a simulated delamination (top left), an air-filled void (top right), a water-filled void (bottom left), and a slab with only reinforcement (bottom right). A summary of all simulated defects and specimen characteristics for the concrete/shotcrete slabs with simulated defects (in addition to the simulated concrete specimens with clay lumps discussed in the next section) is provided in Table M-1. These images demonstrate that the discontinuities in normal-strength concrete are more clearly detectable than in the shotcrete specimens. One explanation is that the shotcrete application, perhaps when misapplied, can be more porous than

typical concrete; within the shotcrete are numerous micro voids that more quickly attenuate the acoustic waves. Even so, delaminations can still be detected. When the system is applied in the
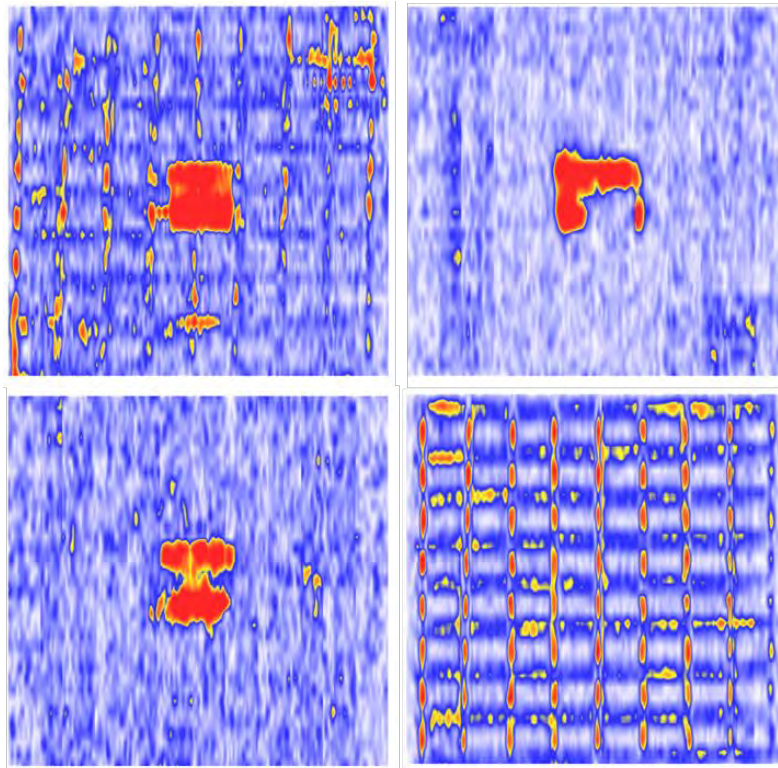
Figure M-5. Typical C-scans for simulated defects in concrete slabs: Specimens Theta (top left), Lambda (top right), Kappa (bottom left), and Gamma (bottom right).

field on shotcrete applications, the images are not significantly different than typical cast concrete.

Fabrication, Testing, and Validation of Specimens with Simulated Clay Lumps

In addition to the concrete and shotcrete slabs, six concrete slabs were tested that were constructed in the 1990s by the Texas Transportation Institute as part of a previous research project. These slabs contain manufactured clay lumps of different diameters. The clay lumps are a high-plasticity clay, classified as Burleson Clay CH (American Association of State Highway and Transportation Officials [AASHTO] A-7-6) with a plasticity index (PI) range of 35-45. The slabs and lumps are shown in Figure M-7 and are summarized in Table M-1 (Specimens A2-F2). These six specimens consist of two sets of three slabs: one set with steel reinforcement and one set without. In each set, one slab was designated as the control with no clay lump contaminations. The remaining two had various levels of lumps of documented sizes corresponding to three regions of interest: (1) lumps below the reinforcement that represent typical lumps dense enough not to be quickly displaced toward the surface via vibration, (2) those that are caught in the reinforcing steel layer on their path toward the surface, and (3) those that are dispersed between the reinforcement and the top surface. The depth of the slabs is nominally 305 mm (12 inches), but all measurements are taken as approximate since neither

ground truth data were retrieved nor any accurate pictures were taken to confidently support documented placement.

Figure M-6. Typical C-scans for simulated defects in shotcrete slabs: Specimens D (top left), E (top right), I (bottom left), and M (bottom right).

Similar to the concrete and shotcrete slab specimens discussed previously, the simulated specimens with clay lumps were tested using a 50 mm x 150 mm (2 inch x 6 inch) scanning grid. Since the type of discontinuity under inspection was known beforehand, scanning only took place in one direction, although all of these specimens were fully scanned twice to judge repeatability. The scans took place in only one direction because the objects under inspection had a cross-sectional surface area (parallel to the scanning surface) greater than 50 mm (2 inches) in the -scanning direction (more on the topic of device polarity and increment sizes can be found in the Conclusions section). Repeatability was necessary in order to confirm the detection of each lump. In both sets of measurements taken for repeatability, the clay lumps found in all slabs were precisely in the same location, indicating remarkable repeatability.

Figure M-7. Clay lump slab construction.

It is important to note that the depths of the clay lumps were easily determined from either a single scanned image on the device screen or a more detailed analysis on the computer model. This indicates that it is possible to assess the general condition of the structure both in the field and in the laboratory. Measurements to the centroid of high reflectivity regions, which denote any sort of discontinuity, represent the depth of these anomalies. Keys are provided alongside each ultrasonic image, Figures M-8 and M-9, detailing the intended location of the lumps. It should be understood that during concrete pouring and vibrating, the lumps will inevitably be displaced from side to side (e.g., the inward movement of the two center lumps in Figure M-9, left) and upwards (e.g., the upward displacement of the lump in Figure M-8, right). The C- and B-scans from Figures M-8 and M-9 show both the large and medium lumps were highly detectable, both in slabs with no reinforcement and in slabs that include reinforcement. However, with lumps that are exactly at the layer of reinforcement (Figure M-8, right, and the middle set of lumps in Figure M-9, right), it is clear that lumps surrounding reinforcement are highly improbable of detection. It would be difficult or highly improbable to know these areas had clay lumps if the system were to be applied in a field application with lumps caught in the reinforcement. At these levels within a specimen, it may be inferred that a lump is present, but the clarity is not as persuasive as in the detection of lumps located farther from the reinforcement.

Table M-1. Summary of concrete/shotcrete slab specimens with simulated defects (all slab specimens are nominally 1.83 m x 1.83 m).

SPECIMEN NAME	SPECIMEN DEPTH (mm)	MATERIAL	REINF. DETAIL	DEFECTS	TRUE DEPTH OF DEFECTS (mm)	UST DEPTH OF DEFECTS (mm)
Alpha	305	Concrete	None	None	N/A	N/A
Beta	457	Concrete	* d = 127 mm	Natural crack	N/A	N/A
Gamma	305	Concrete	* d = 127 mm	None	N/A	N/A
Delta	610	Concrete	None	None	N/A	N/A
Epsilon	610	Concrete	* d = 127 mm	None	N/A	N/A
Zeta	381	Concrete	* d = 127 mm	None	N/A	N/A
Eta	381	Concrete	* d = 127 mm	0.05 mm thin plastic	51 from top	58 from top
Theta	381	Concrete	* d = 127 mm	0.05 mm thin plastic	76 from top	89 from top
Iota	381	Concrete	* d = 127 mm	0.05 mm thin plastic	25 from top	43 from top
Kappa	381	Concrete	* d = 127 mm	Air-filled void (13 mm foam)	203 from top	203 from top
Lambda	381	Concrete	* d = 127 mm	Water-filled void (Ziploc bag)	203 from top	196 from top
A	102	Shotcrete	None	None	N/A	N/A
B	152	Shotcrete	None	None	N/A	N/A
C	203	Shotcrete	None	None	N/A	N/A
D	305	Shotcrete	**	Air-filled void (13 mm foam)	193 from top	193 from top
E	305	Shotcrete	**	Water-filled void (Ziploc bag)	191 from top	193 from top
F	305	Shotcrete	**	Air-filled void (13 mm foam)	76 from top	89 from top
G	305	Shotcrete	**	Water-filled void (Ziploc bag)	76 from top	107 from top
H	305	Shotcrete	**	0.25 mm thin cloth	203 from top	183 from top
I	305	Shotcrete	**	0.25 mm thin cloth	102 from top	99 from top
J	305	Shotcrete	**	0.25 mm thin cloth	76 from top	74 from top
K	305	Shotcrete	**	0.25 mm thin cloth	51 from top	79 from top
L	305	Shotcrete	**	0.25 mm thin cloth	25 from top	*only shadow*
M	305	Shotcrete	**	None	N/A	N/A
A2	305	Concrete	* d = 152 mm	None	N/A	N/A
B2	305	Concrete	* d = 152 mm	Large (152 mm ⌀) clay lumps	152 from top	160 from top
C2	305	Concrete	* d = 152 mm	Med. (102 mm ⌀) clay lumps	76, 152, 229 from top	69, 137, 216 from top
D2	305	Concrete	* d = 152 mm	None	N/A	N/A
E2	305	Concrete	* d = 152 mm	Large (152 mm ⌀) clay lumps	152 from top	107 from top
F2	305	Concrete	* d = 152 mm	Med. (102 mm ⌀) clay lumps	76, 152, 229 from top	61, 137, 198 from top

*Two mats of No. 5 Rebar, at depth "d" from top and bottom, 203 mm on center.

**One lattice girder in center of slab, sitting on bottom form.
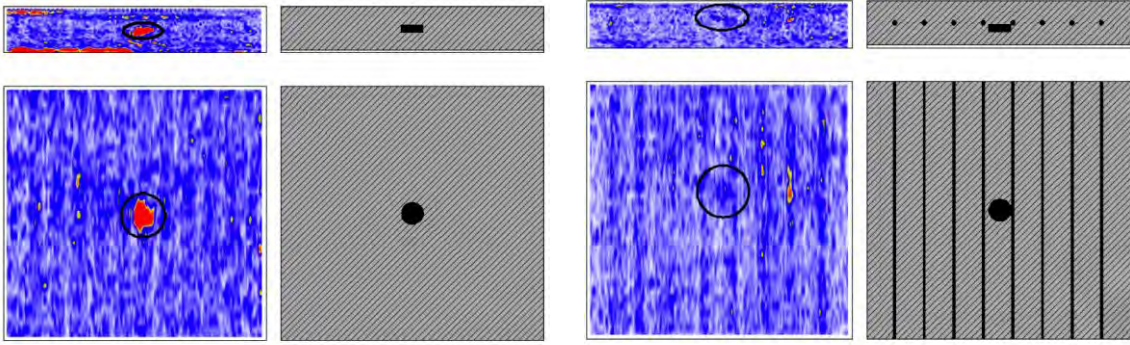
Figure M-8. Large clay lump slabs: (left) without reinforcement, and (right) with reinforcement.
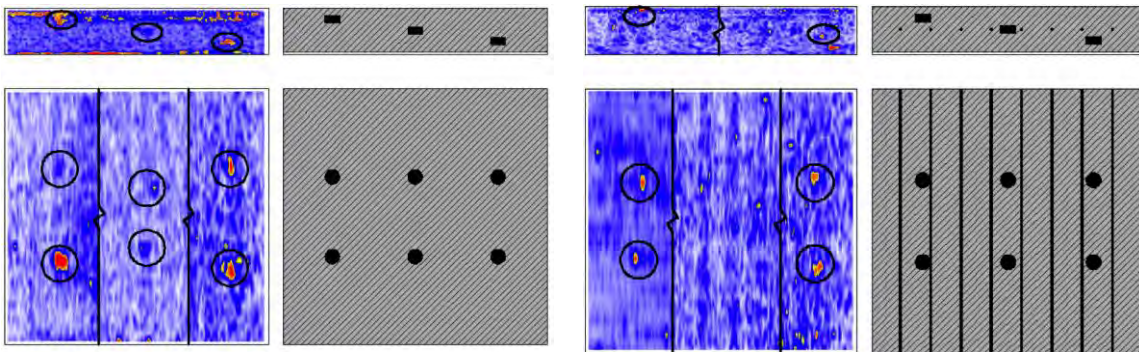
Figure M-9. Medium clay lump slabs: (left) without reinforcement, and (right) with reinforcement.

Fabrication, Testing, and Validation of Concrete Bridge Deck with Simulated Defects

In addition to the above-mentioned slabs, a bridge deck constructed by the University of Texas at El Paso (UTEP) was available for blind testing. The bridge deck was constructed with known artificial delaminations, cracks, and corroded reinforcement. Several parameters were considered in the construction of the artificial delaminations including stacked delaminations, delaminations of various thicknesses (ranging from 0.3 mm [0.01-inch] to 2.0 mm [0.08-inch] thickness), sizes (ranging from 305 mm x 305 mm to 610 mm x 1220 mm [12 inch x 12 inch to 24 inch x 48 inch]), depths (above reinforcing steel at 64 mm [2.5 inches] below surface, and below two layers of reinforcing steel at 152 mm [6 inches]), with some located above prestressed girders supporting the slab. The deck, pictured in Figures M-10 and M-11, measures 2.4 m x 6.1 m x 0.2 m (8 ft x 20 ft x 8-3/4 inches), and rests on three prestressed concrete girders. Simulated defects constructed in the deck consist of nine artificial delaminations, five cracks, and two corroded reinforcement mats, which are all summarized in Table M-2.

In constructing the deck, 27.6 MPa (4000 psi) concrete was used, and two layers of No. 5 longitudinal and transverse steel were placed at 254 mm and 203 mm (10 inches and 8 inches) on center, respectively, at centroid depths of 83 mm and 184 mm (3.25 inches and 7.25 inches) from the surface. The 28-day strength and modulus exceeded 34.5 MPa (5000 psi) and 27.6 MPa (4000 ksi), respectively. A 0.25 mm (0.01-inch) polyester fabric was used to mock an ultra-thin horizontal delamination. The vertical cracks were constructed from both thick and thin cardboard sheets. The No. 5 corroded steel mats were electrically merged and attached to the normal reinforcement. The corrosion depth was measured to be 1-2 mm (0.04-0.08 inch) prior to pouring the concrete.

For the UST analysis, the grid increment used on the bridge deck (100 mm x 100 mm, or 4 inches x 4 inches) was greater in the -scanning direction than the previously evaluated

Figure M-10. Simulated bridge deck at UTEP in El Paso, Texas.

specimens since this deck was actually the first specimen to be tested and an optimal increment was not yet established. In retrospect, this is a contributing factor for the defects in this specimen to be less defined than in the previous cases. Figure M-12 shows the defects present at 64 mm (2.5 inches) deep, and Figure M-13 shows the defects present at 152 mm (6 inches) deep. As can be seen from the UST results, six of the seven defects were detected. The one defect undetected was the 0.25 mm (0.01-inch) thin polyester fabric at 64 mm (2.5 inches) below the surface (DL 9), as well as details of the various cracks. This scan was not particularly useful for examining cracks, as the data set for the entire scan was too massive for careful evaluations via D-scans, and the B-scans were spaced too far apart for careful analysis. Nevertheless, a sample crack (CK1) is shown in Figure M-14. The B-scans with their associated end-view keys are shown in Figures M-14 through M-20.
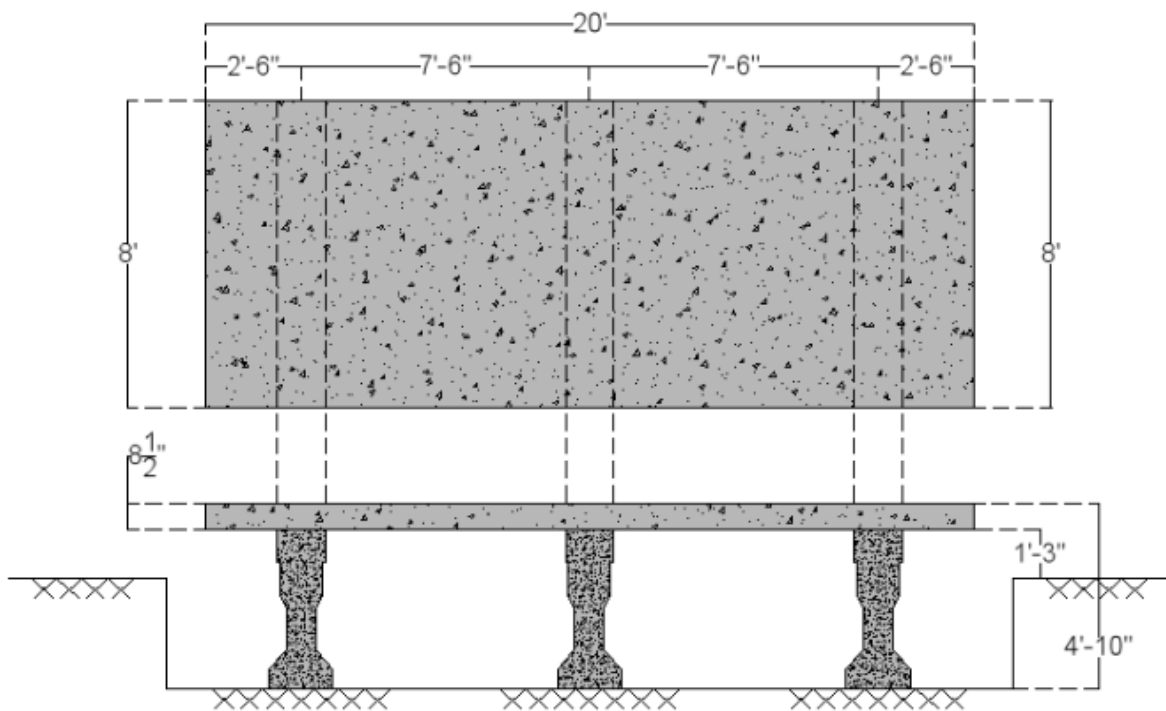
Figure M-11. Layout of constructed bridge deck.

Table M-2. Summary of simulated defects in the concrete bridge deck.

Simulated Defect	Defect Material	Key Legend	Actual Dimension (mm)	Actual Depth (mm)	UST Measured Dimension (mm)	UST Measured Depth (mm)
Delamination (DL 1)	Soft, high strength 1 mm foam		305 x 305	64	301 x 341	65
Delamination (DL 2)	Soft, high strength 1 mm foam		610 x 610	64	578 x 642	71
Delamination (DL 3)	Soft, high strength 1 mm foam		610 x 610	64	603 x 651	81
Delamination (DL 4)	Soft, high strength 2 mm foam		305 x 305	64	333 x 390	69
Delamination (DL 5)	Soft, high strength 2 mm foam		610 x 610	64	587 x 650	81
Delamination (DL 6)	Soft, high strength 2 mm foam		610 x 610	64	587 x 650	54-116
Delamination (DL 7)	Soft, high strength 1 mm foam		610 x 610	152	562 x 667	136
Delamination (DL 8)	Soft, high strength 1 mm foam		610 x 1219	152	667 x 1197	150-177
Delamination (DL 9)	Soft, 0.25 mm polyester fabric		305 x 610	64	N/A*	N/A*
Vertical Crack (CK 1)	Soft, thin cardboard		305 long	64	N/A**	N/A**
Vertical Crack (CK 2)	Soft, thin cardboard		305 long	64	N/A**	N/A**
Vertical Crack (CK 3)	Soft, thick cardboard		305 long	76	N/A**	N/A**
Vertical Crack (CK 4)	Soft, thick cardboard		305 long	152	N/A**	N/A**
Vertical Crack (CK 5)	Natural crack (observed after construction)		330 long	64	N/A**	N/A**
Corroded Reinforcement (CR 1)	1-2 mm deep corrosion, #5 bars		762 x 762	76	Identified ***	Identified ***
Corroded Reinforcement (CR 2)	1-2 mm deep corrosion, #5 bars		762 x 762	165	Identified ***	Identified ***

* Not available. Indiscernible due to surface noise and upper transverse reinforcement.

**Not available. Unable to analyze crack details.

***The corroded steel mats were identified, but the map taken did not completely cover the end of the slab, so dimensions could not be verified.
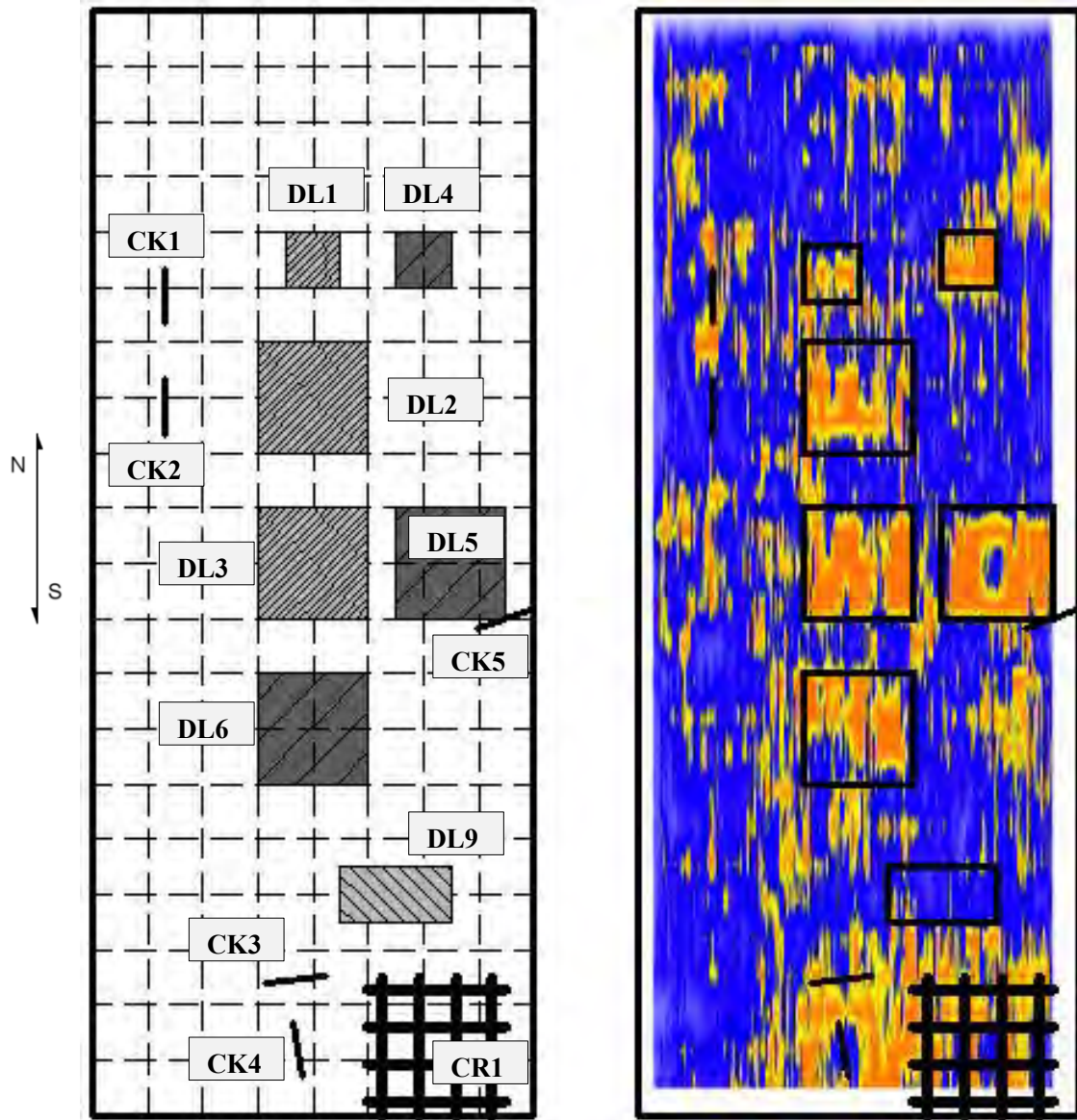
Figure M-1. C-scan at 2.5-inch depth: construction key (left) and UST results (right).
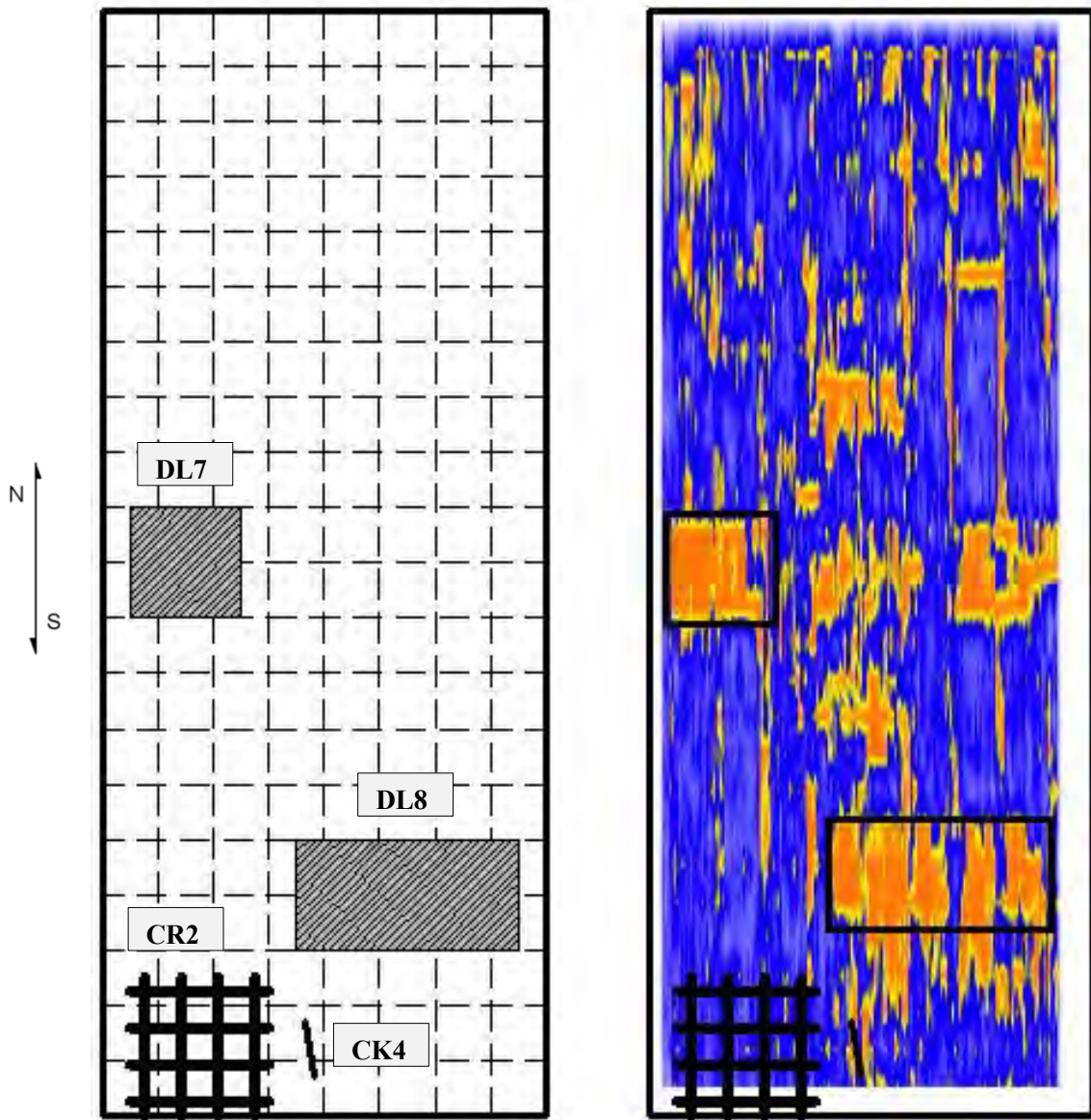
Figure M-2. C-scan at 6-inch depth: construction key (left) and UST results (right).
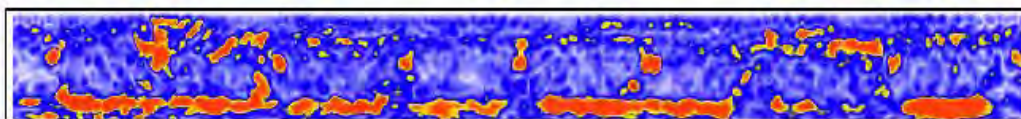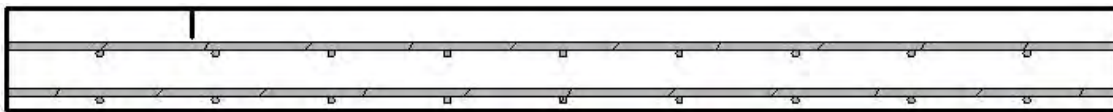
Figure M-3. B-scan showing CK 1: construction key (above) and UST results (below).
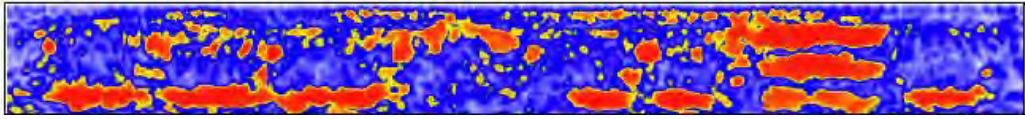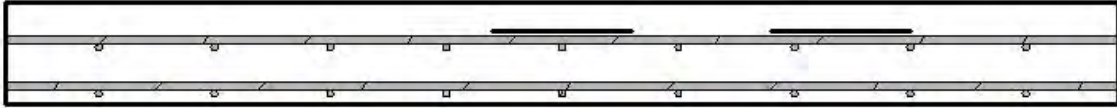
Figure M-4. B-scan showing DL 1 and 4 (l-r): construction key (above) and UST results (below).
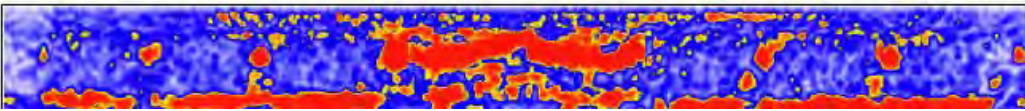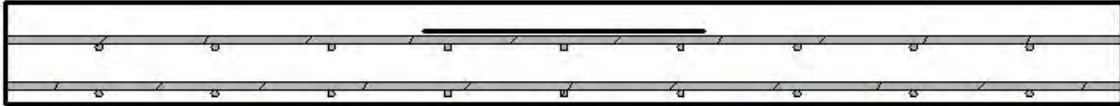
Figure M-5. B-scan showing DL 2: construction key (above) and UST results (below).
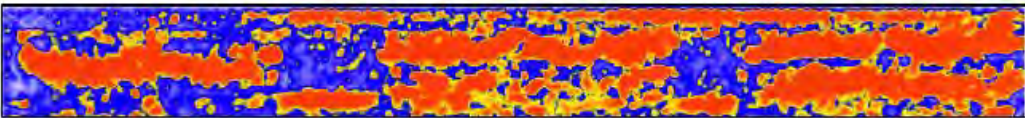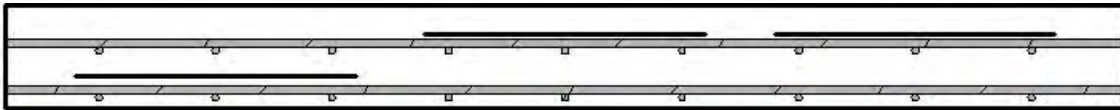
Figure M-6. B-scan showing DL 7, 3, and 5 (l-r): construction key (above) and UST results (below).
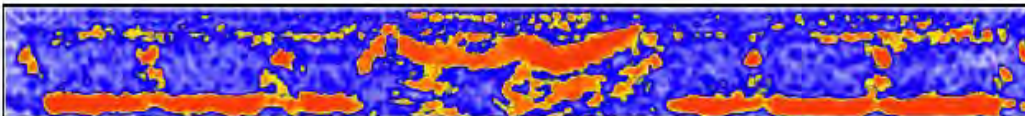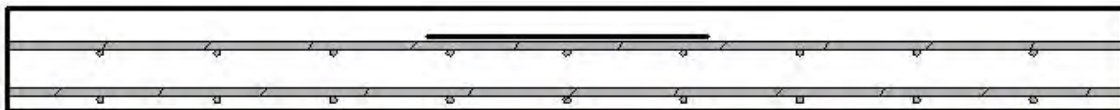
Figure M-7. B-scan showing DL 6: construction key (above) and UST results (below).
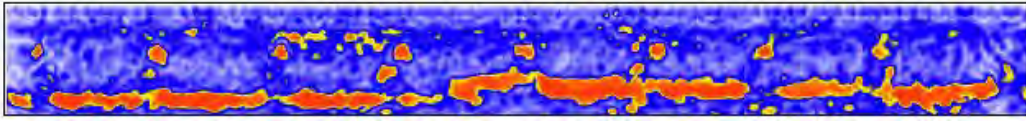
Figure M-8. B-scan showing DL 8: construction key (above) and UST results (below).
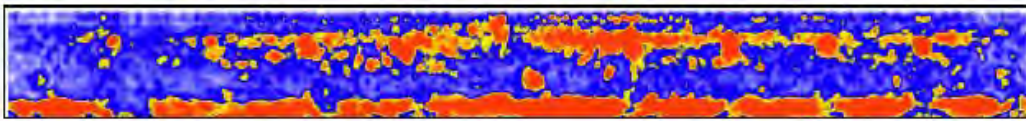
Figure M-20. B-scan showing CR 1: construction key (above) and UST results (below).

Continuously Reinforced Concrete Pavement (CRCP) on Interstate 20 in Ft. Worth, Texas

In the past few decades, Interstate 20 (Figure M-21) has had numerous repairs and overlays, including a section of continuously reinforced concrete pavement (CRCP) in Ft. Worth, Texas, west of RM 2871 (~ MP 426 + 0.5). A nominal 254 mm (10-inch) thick CRCP was constructed over a two-lift pavement, which consisted of a top layer of a 51 mm (2-inch) asphalt base. Over a period of time, significant signs of distress began to appear. The ultrasonic tomography method was used to evaluate transverse surface cracks on the CRCP and determine the existence of any delamination within the overlay. The four areas tested are shown in Figure M-22. Each area was tested using a 50 mm x 150 mm (2 inch x 6 inch) grid. After scanning the section, cores were taken to verify the predicted overlay depth, reinforcement cover, and delamination depth.

The UST results of the first area tested (Figure M-22, top left) are shown in Figure M-23. These are typical B-, C-, and Volume-scans that are seen in the other scanned areas. The two B-scans in Figure M-23 (left) show an area with delamination at the level of longitudinal reinforcement (top B-scan) and an area with no delamination, but a backwall reflection at the top layer interface (bottom B-scan). The C-scan (Figure M-23, center) shows the width of the delamination at the level of reinforcement. Figure M-24 shows all four areas scanned with their appropriate C-scans overlaid on the image. All delaminations in these figures are at the level of reinforcement (see Tables M-3 through M-6 for details).

Figure M-21. I-20 in Ft. Worth, Texas.

Figure M-9. Four areas tested on I-20 in Ft. Worth, Texas.
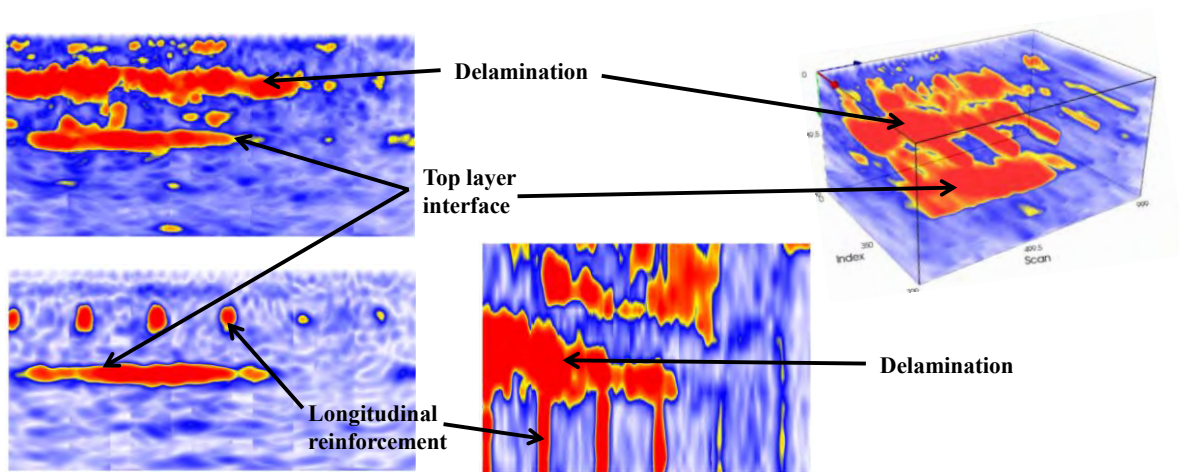
Figure M-10. Typical UST results for I-20 scanning.
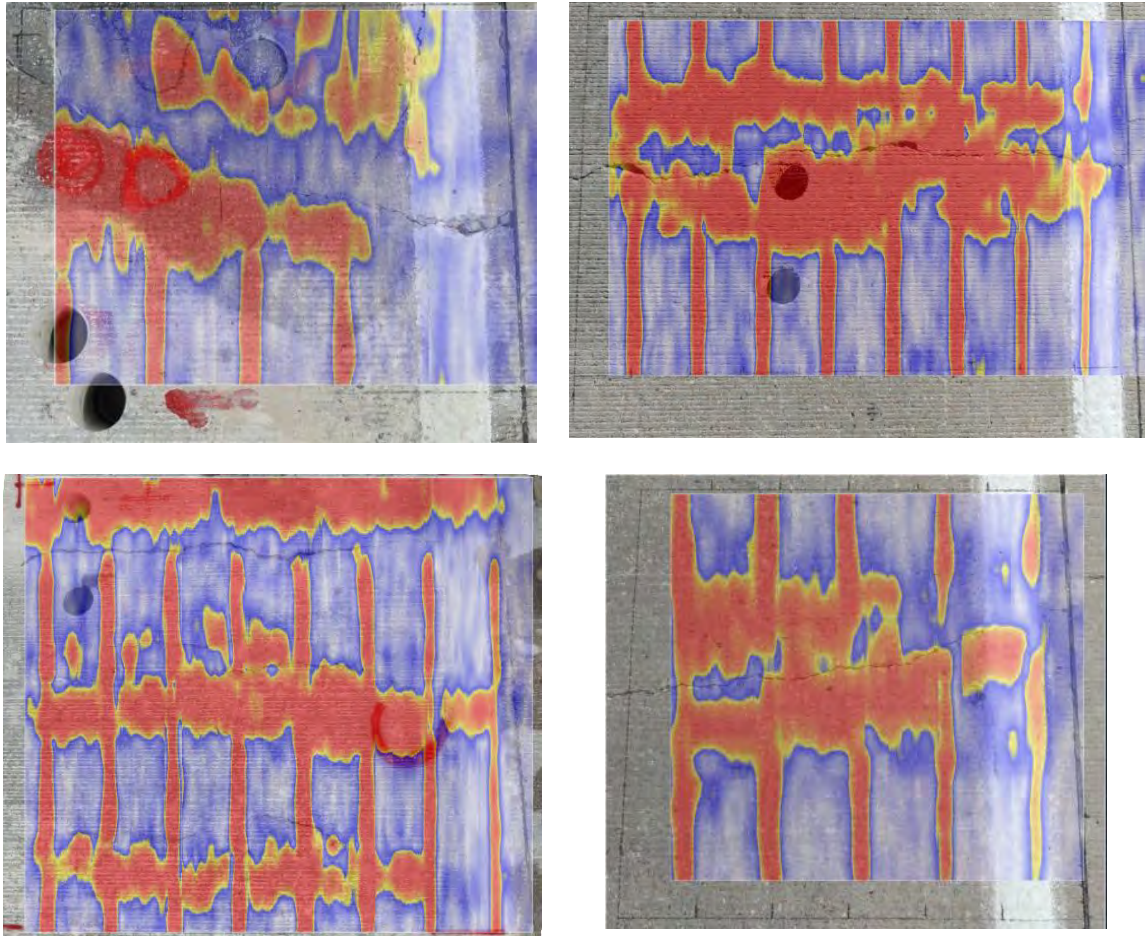
Figure M-11. UST C-scans overlaid on I-20 images: Section A (top left), Section B (top right), Section C (bottom left), and Section D (bottom right).

Table M-3. Section A, I-20 evaluations.

Overlay		
	Tomograph	
Depth to delamination	Varies: 107 – 127 mm	
Depth to reinforcement	Varies: 117 – 127 mm	
Core 1		
	Tomograph	Core Results
Depth to asphalt sub-layer	264 mm	259 mm
Depth to delamination	None	None
Depth to reinforcement	127 mm	127 mm
Core 2		
	Tomograph	Core Results
Depth to asphalt sub-layer	254 mm	259 mm
Depth to delamination	None	None
Depth to reinforcement	None	None

Table M-4. Section B, I-20 evaluations.

Overlay		
	Tomograph	
Depth to delamination	Varies: 114 – 135 mm	
Depth to reinforcement	Varies: 114 – 132 mm	
Core 3		
	Tomograph	Core Results
Depth to asphalt sub-layer	257 mm	264 mm
Depth to delamination	None	None
Depth to reinforcement	None	None
Core 4		
	Tomograph	Core Results
Depth to asphalt sub-layer	N/A	239 mm
Depth to delamination	117 mm	119 mm
Depth to reinforcement	None	None

Table M-5. Section C, I-20 evaluations.

Overlay	
	Tomograph
Depth to delamination	Varies: 117 – 130 mm
Depth to reinforcement	Varies: 122 – 127 mm
Core 5	
	Tomograph	Core Results
Depth to asphalt sub-layer	257 mm	259 mm
Depth to delamination	None	None
Depth to reinforcement	None	None
Core 6	
	Tomograph	Core Results
Depth to asphalt sub-layer	259 mm	259 mm
Depth to delamination	104 – 135 mm	137 mm
Depth to reinforcement	None	None

Table M-6. Section D, I-20 evaluations.

Overlay	
	Tomograph
Depth to delamination	Varies: 119 – 140 mm
Depth to reinforcement	Varies: 122 – 130 mm

George Bush Intercontinental Airport, Houston, Texas

A recent construction project at the George Bush Intercontinental Airport (IAH) in Houston, Texas, entailed overlaying existing runways with a nominal 203 mm (8-inch) jointed plain concrete pavement (Figure M-25). The existing runways were 762 mm (30-inch) sections of concrete pavement: a 457 mm (18-inch) Portland cement concrete (PCC) layer over a 305 mm (12-inch) PCC layer. Within a period of 3 months, significant surface cracks on the bonded concrete overlay (BCO) instigated an evaluation on the source of these cracks. Using a grid spacing of 100 mm x 200 mm (4 inches x 7.9 inches), UST was used to completely scan two entire sections of the runway (two 7.6 m x 7.6 m, or 25 ft x 25 ft slabs) to evaluate the extent of damage present. The

Figure M-12. Airport runway at IAH.

UST results are shown in Figures M-26 and M-27. The first runway tested showed over 70 percent of the area delaminated at the first layer interface (Figure M-26, C-scan at bottom right, Volume-scan at top right). The B-scans on the left of this figure show the first layer interface at 193-206 mm (7.6-8.1 inches) deep, the second layer interface at 683 mm (26.9 inches) deep, and the third layer interface at 958 mm (37.7 inches) deep. The second area tested showed approximately 15 percent of the total area debonded at the first layer interface (Figure M-27, C-scans at bottom right, Volume-scan at top right). It was also easy to see the partially bonded region at the second layer interface.

Cores were taken in both runway sections to verify the degree of bonding based on three locations: where the UST results indicated (a) full bonding, (b) full debonding, and (c) an area in between. Three core strength testing locations within location 1 (predicted full bond) indicated tensile strengths ranged from 1230 Pa to 1500 Pa (178 psi to 219 psi). A core in location 2 (predicted partial bond) indicated a tensile strength of 131 Pa (19 psi). Finally, a couple of cores in location 3 (predicted full debond) confirmed delamination at the first layer interface.
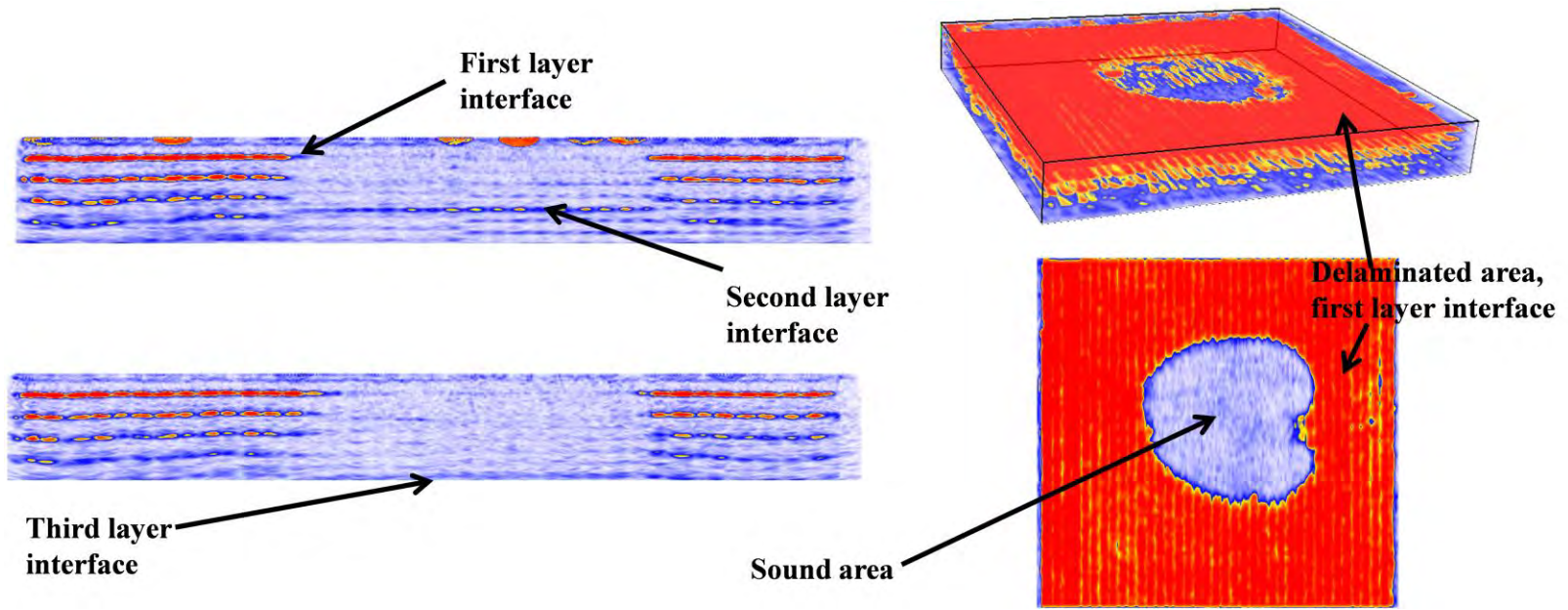
Figure M-13. First segment tested at IAH: B-scans (left), Volume-scan (top right), and C-scan (bottom right).
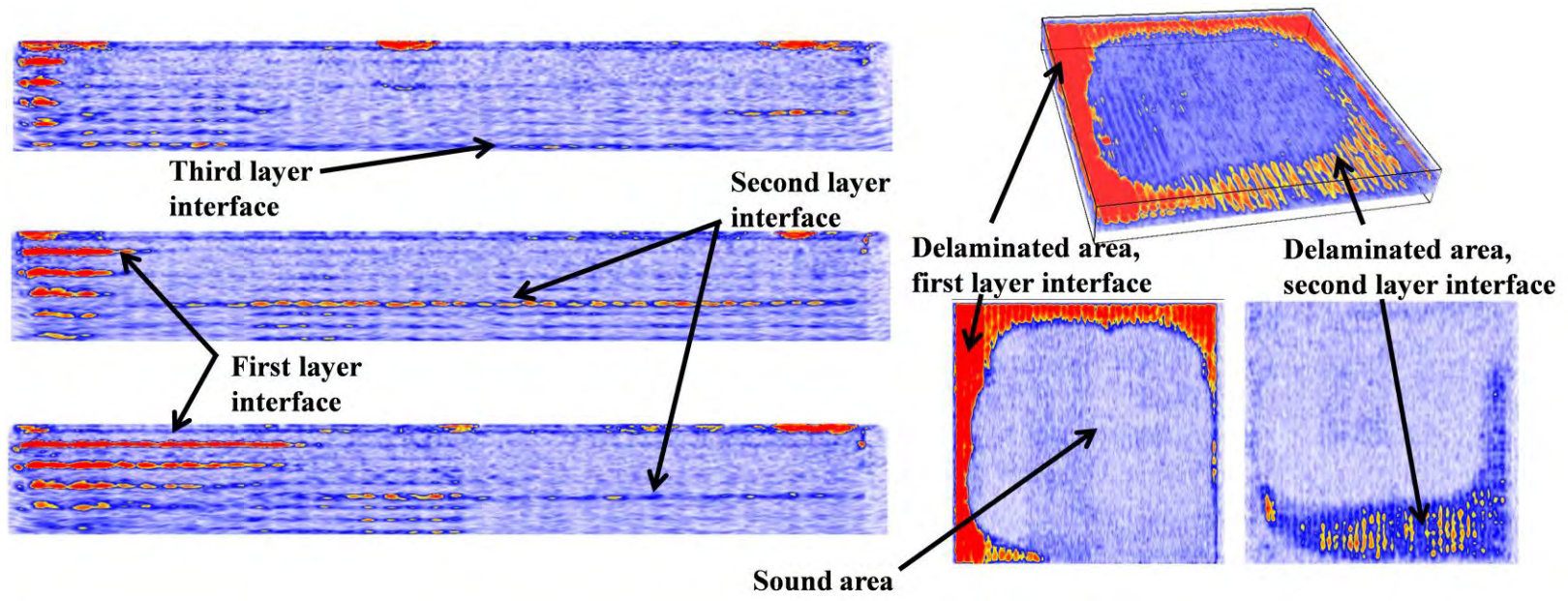
Figure M-14. Second segment tested at IAH: B-scans (left), Volume-scan (top right), and C-scans (bottom right).

Assessment for Preliminary Defect Evaluation Using UST

A summary of all simulated defects and specimen characteristics for all specimens tested can be found in Tables M-1 and M-2. After scanning each of the concrete/shotcrete slabs, the measurements indicated by UST inspection versus the actual measurement from ground truth data were plotted. A linear regression model was fitted to the data (Figure M-28). The types of discontinuities plotted in this manner were:

- Defect depth.
- Defect length (parallel to B-scans, or the -scanning direction).
- Defect width (parallel to D-scans, or the -scanning direction).
- Shotcrete specimen thickness.
- Concrete specimen thickness.
- Reinforcement cover.

The coefficient of determination shows strong agreement between actual discontinuity measurements and measurements taken by ultrasonic tomography. It should be noted that defect width and length are characteristics that should be determined after scanning the region in more than one scanning direction. This is due to the fact that the phased-array tomograph is polarized, in the sense that shear waves are emitted and received in one direction, the -scanning direction (or direction normal to the D-scans). Objects (such as reinforcement) can therefore appear wider (measured in the -scanning direction) than they are in reality since the B-scan is an average over a row of four transducers.

The defect location and dimensions as well as other useful parameters were plotted against the measurements taken from UST. Linear regression analysis indicated that the coefficient of determination (R^2) varied between 0.82-0.98, indicating that 82-98 percent of the variability in defect dimensions (depth from surface, length, and width) or specimen characteristics (thickness, reinforcement cover, and spacing) measured by the UST device was directly related to the variability in the actual defect dimensions or specimen characteristics. These evaluations on simulated specimens were invaluable for two reasons. Primarily, it instilled confidence that the method of data collection would be reliable for inspection of existing structures, particularly since coring or any type of physical validation may not be allowed. The high values for R^2 translate into a reliability threshold of the system by which we can confidently map real-life structures. It is understood that further testing needs to be completed in order to have a statistical analysis that predicts confidence levels and meaningful probability of
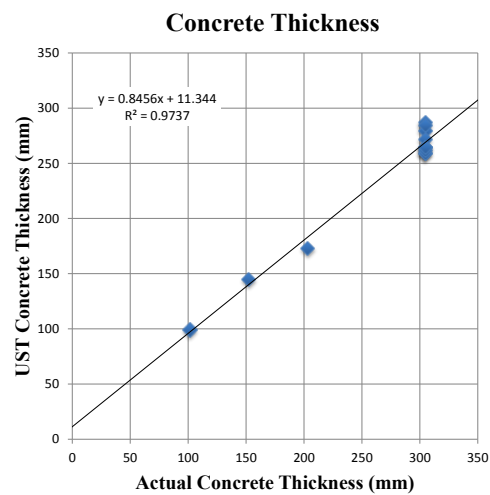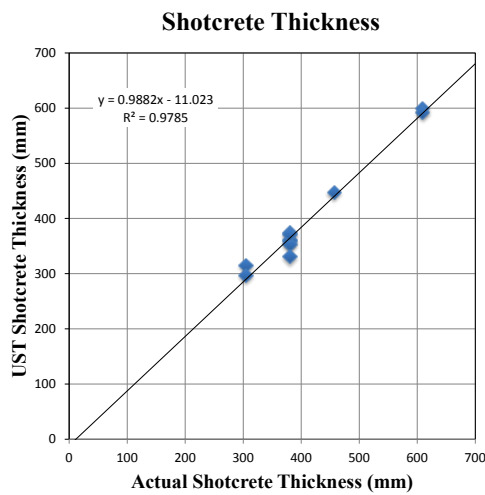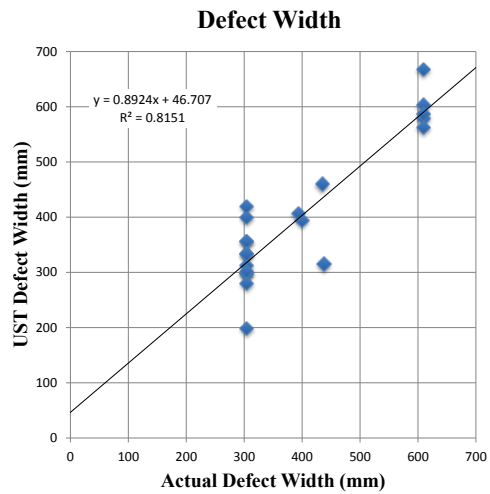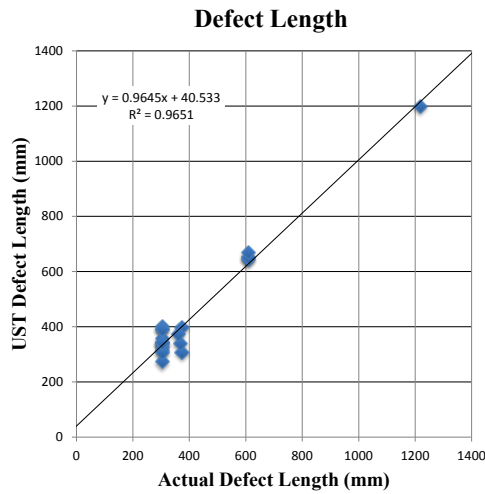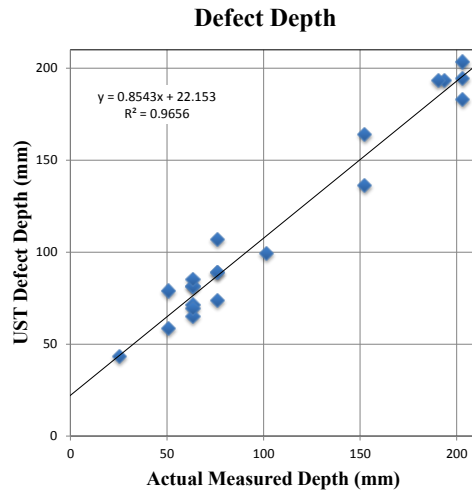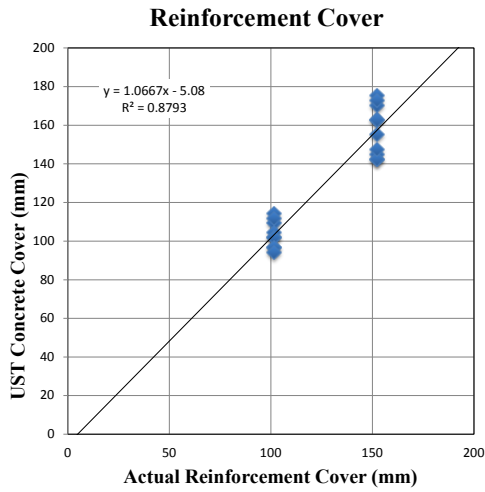
Figure M-15. R^2 for various defect detection parameters in the concrete/shotcrete slabs.

detection (POD) curves. A limitation of the research performed here is the lack of numerous constructed specimens with similar or repeated defect evaluations.

There are many variables that can be adjusted when calibrating the tomograph that will improve the accuracy of the device, including period of impulse, time-corrected gain, firing impulse pause, and wave velocity. Determination of wave velocity can be accurately estimated by averaging between eight to 10 random readings at different positions on the concrete surface. If physical validation is possible, the wave speed and other variables can be adjusted so that the tomograph is calibrated by a known measurement, such as reinforcement depth or backwall reflection. Since these measurements are rarely known in existing structures to a high level of precision without destructive validation, the accuracy of the device can be difficult to fine tune prior to testing. For this reason, most of the simulated specimens were tested blindly by an operator who was not familiar with the location or type of defects to accurately mimic field-testing conditions. For all simulated specimens, a wave velocity was calculated by averaging eight to 10 evaluations, and no other parameters (period of impulse, time-corrected gain, firing impulse pause) were changed from default settings. In this manner, the accuracy of the device could be predicted in preparation for testing existing structures.

The second reason these evaluations were invaluable was the ability to try many variations of grid size, location, and creation for future use on existing structures. It was critical to learn how to relate a defect found in the three-dimensional image reconstruction with the actual grid established on the specimen.

FIELD EVALUATION OF THE UST SYSTEM

For the following six test sites, limited ground truth data were available for confirmation of UST defect locations. The descriptions of the test sites, including interpretation of UST evaluations, were made using engineering judgment.

Eisenhower Memorial Tunnel, Colorado

The Eisenhower Memorial Tunnel, located approximately 97 km (60 mi) west of Denver, Colorado, is one of a 2.7 km (1.7-mi) dual bore project started in 1968. Shown in Figure M-29, Eisenhower Memorial, which carries Interstate 70 west, is paired with the Edwin C. Johnson Memorial Tunnel, which carries Eastbound I-70. Although the eastbound bore was not completed until almost 1980, construction on the Eisenhower bore was completed by 1973. Built using drill and blast methods through a mountain with a maximum overburden of 448 m (1470 ft), the average tunnel dimensions were 14.6 m in height (48 ft) and 12.2 m (40 ft) in width. In 2011, the average daily traffic was 28,155 vehicles.

All areas of interest evaluated within the tunnel were tested from inside the plenum (above the traffic), and evaluations were conducted on the precast concrete divider wall separating the intake and exhaust portions of the plenum and on the lining itself (Figure M-30). Areas tested on the lining included representative locations of relatively sound (uncracked) concrete (Figure M-31a), areas with particularly extensive surface cracks and crazing near a joint in the tunnel lining (Figure M-31b), and near severe vertical cracks with stalactite formations (Figure M-31c).

Figure M-16. Eisenhower Memorial Tunnel, Colorado.

As would be expected, the sound concrete area (Map ET 10.4-1, 2 in Appendix N: Ultrasonic Tomography Test Summaries) showed no signs of significant delamination, but a clear interface was observed approximately 411 mm (16.2 inches) below the surface (~239 mm, or 9.4 inches wide).

This interface was consistently seen at every testing location between Segments 8-10 within the Eisenhower Tunnel lining and is surmised to be part of the structural reinforcement that was in place prior to the placing of the tunnel lining. Detailed tunnel blueprints for verification at this location were not available for confirmation. The scans in Figure M-32 correspond to typical B-, C-, and Volume-scans at this location. In the B-scan, the hoop (or circumferential) reinforcement is clearly observable at approximately 107 mm (4.2 inches) in depth and at 251 mm (9.9 inches) on center. A single rebar as part of the longitudinal reinforcement is seen in the B-scan and Volume-scan as well.
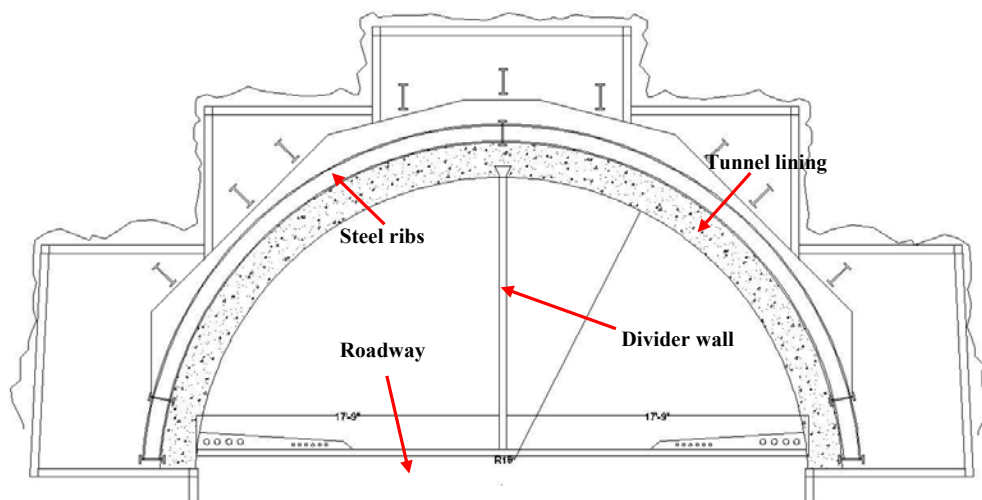
Figure M-30. Eisenhower Tunnel plenum view indicating the interior precast divider wall, structural steel ribs, roadway, and concrete tunnel lining.
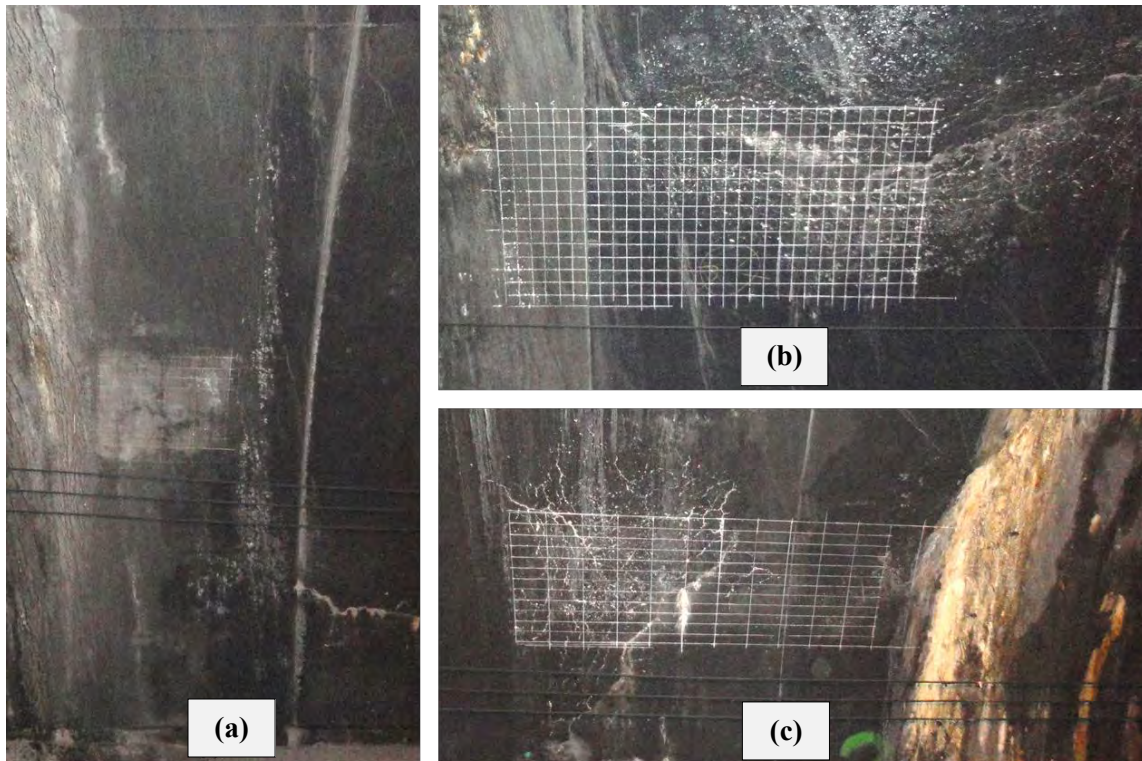
Figure M-31. Scanned areas within Eisenhower Tunnel: (a) sound concrete, (b) surface cracking and crazing near joint, and (c) surface cracking and crazing near joint and crack with stalactite formation.
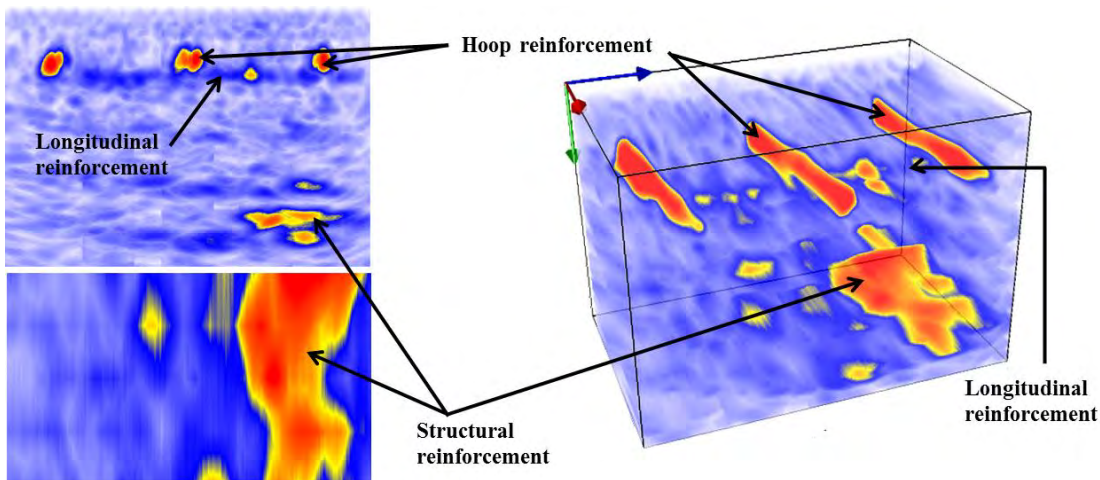
Figure M-32. UST images of sound area: B-scan (top left), C-scan (bottom left), and Volume-scan (right).

As noted earlier, one of the two areas tested that displayed significant surface cracking and crazing occurred near a joint (Map ET 10.4-4, 5 in Appendix N: Ultrasonic Tomography Test Summaries). At this location, the structural reinforcement is again located approximately 409 mm (16.1 inches) below the surface (~343 mm, or 13.5 inches wide). B-, C-, and Volume-scans are shown in Figure M-33. In the B-scan, the longitudinal reinforcement is seen directly

under the hoop reinforcement with multiple echoes observed in increments approximately the same as the depth of the longitudinal and hoop reinforcement. These echoes are suspected to be the effect of debonding of the longitudinal and hoop reinforcement. Interestingly, this supposed debonding also occurs directly below the lining joint. This may indicate moisture intrusion has corroded the reinforcement, causing debonding. Unfortunately, no ground truth data have confirmed this observation.
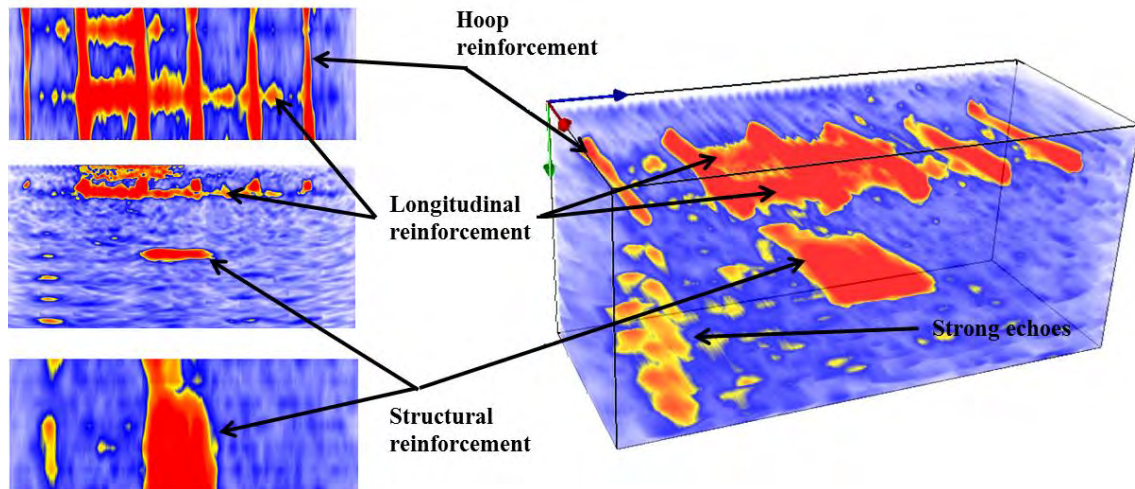
Figure M-33. UST images of surface cracking/crazing area: B-scan (center left), C-scans (top and bottom left), and Volume-scan (right).
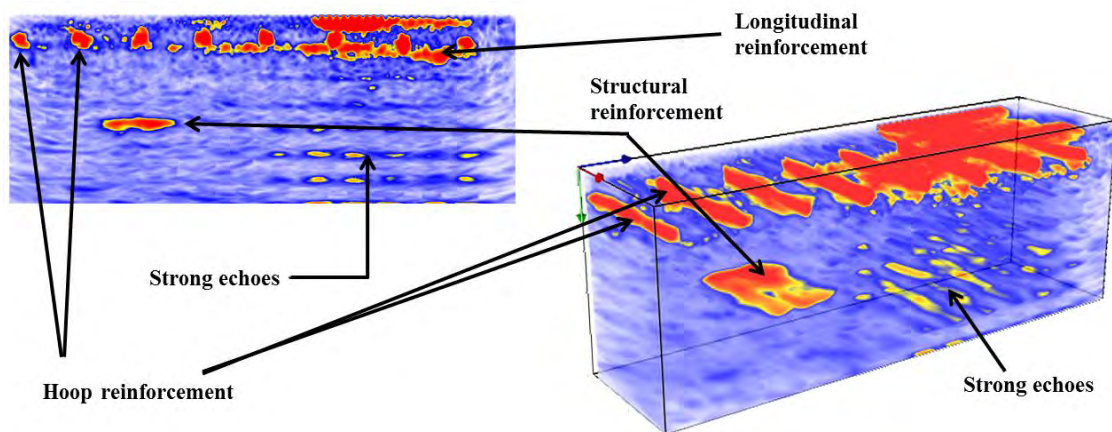
Figure M-34. UST images of surface cracking/crazing area near stalactite formation: B-scan (left) and Volume-scan (right).
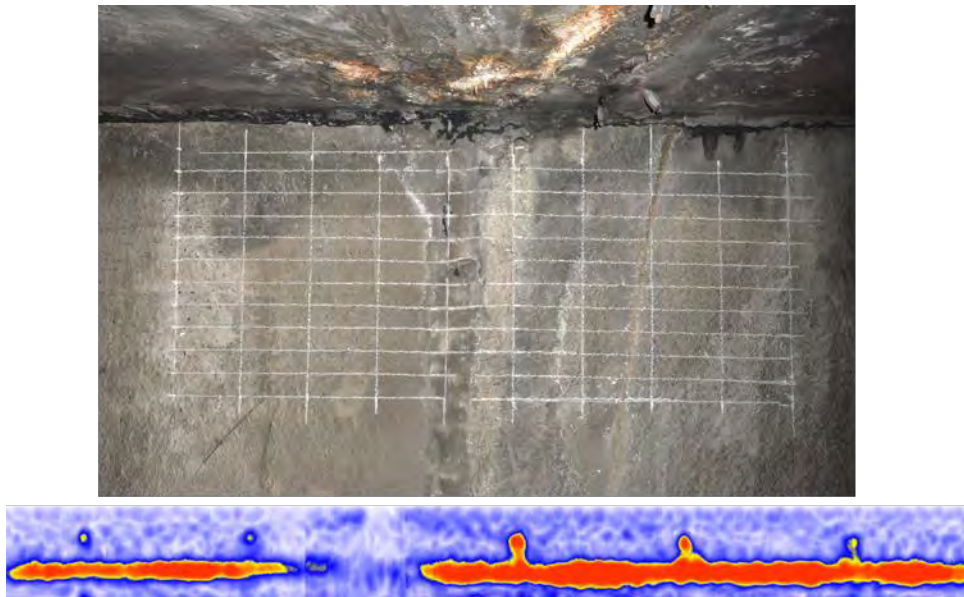
Figure M-35. B-scan of precast divider panel showing backwall reflection and reinforcement.

In the second area that displayed significant surface cracking and crazing near a joint (Map ET 10.4-3 in Appendix N: Ultrasonic Tomography Test Summaries), a severe crack running vertically down the tunnel lining is present. The map was built to the side of this crack (Figure M-31c) but due to the stalactite formation and grout fittings could not extend over the crack. The same structural reinforcement (here approximately 437 mm [17.2 inches] deep and 310 mm [12.2 inches] wide) is present in both the B- and Volume-scans (Figure M-34). Also at this location, strong echoes under the region nearest the stalactite formation and crack indicate possible debonding of the hoop and longitudinal reinforcement. The last areas tested at the Eisenhower Tunnel were on the interior precast divider wall (particularly surrounding joints) even though significant distress was not visible. Figure M-35 shows the typical B-scan, with the region surrounding the crack completely lacking in any reflection. It is typical for large cracks (here filled with a caulking sealant) to completely attenuate all of the sound waves emitted, making it difficult to assess the presence of nearby distress. This phenomenon surrounding cracks leads to an important clue in analyzing concrete ultrasound images; the lack of reflection around an area can be indicative of an unusual amount of air, making it impossible for the shear wave to be transmitted across the boundary since gases and fluids do not support shear wave propagation.

Overall testing at the Eisenhower Tunnel concluded that the UST system could consistently detect some type of structural reinforcement (other than steel rebars), although the type of reinforcement was not determined. The UST evaluation also revealed possible areas of debonding that occur near severe cracks and joints. The reinforcement cover and spacing were also detectable.

Hanging Lake Tunnel, Colorado

Completed in 1992 with a maximum length of 1219 m (4000 ft) through the southern wall of Glenwood Canyon, Hanging Lake Tunnel (Figure M-36) was the last link to the Interstate Highway System. Both bores of the tunnel were built using multiple-face drill and blast methods. Between the west and eastbound bores, a four-story control center monitors traffic along I-70, fully equipped with emergency response vehicles and trained staff.

Figure M-17. Hanging Lake Tunnel: exterior (left) and interior plenum view (right).
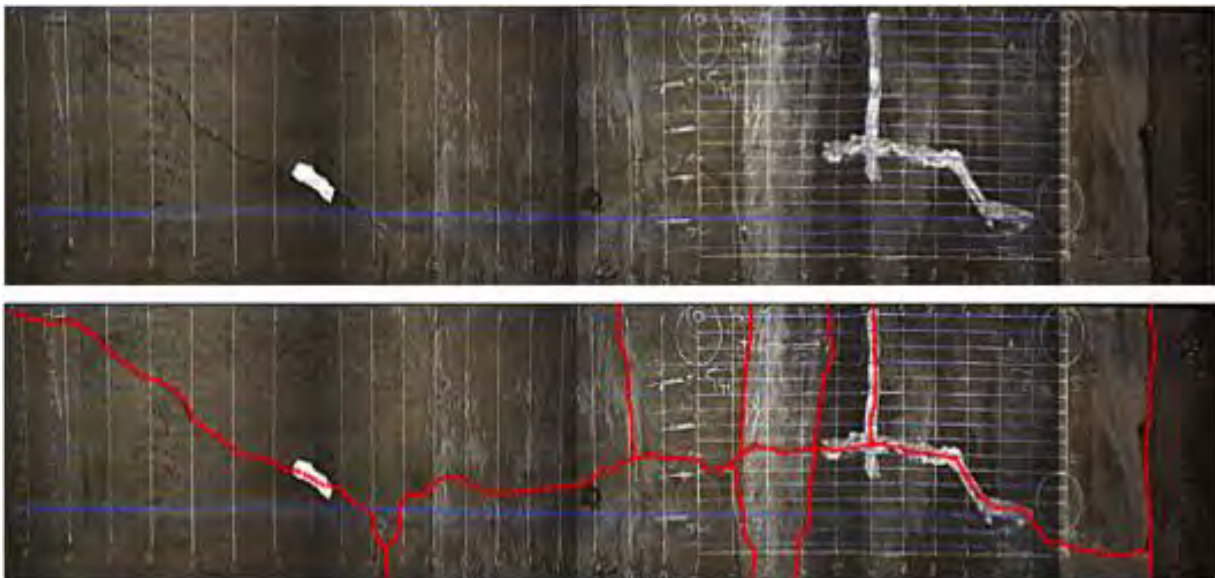
Figure M-18. Image collage of extensive map with cracks (shown in red).

Areas of interest within the tunnel include a number of significant surface cracks (Figure M-37, as well as Figure M-38, a and b), some of which had been partially patched with a skim coat of some type of grout. Other areas include a standard sound concrete region

(Figure M-38c), regions surrounding joints (Figure M-38d), and a region of tiled lining in the eastbound lane (Figure M-39).

The sound concrete region (Figure M-38c, as well as Map HLT 10.5-5, 6, 7 in Appendix N: Ultrasonic Tomography Test Summaries) shows that the backwall reflection varies from 752-823 mm (29.6-32.4 inches) in depth, with the hoop reinforcement at 109-130 mm (4.3-5.1 inches) in depth and a longitudinal rebar on top of the hoop reinforcement.
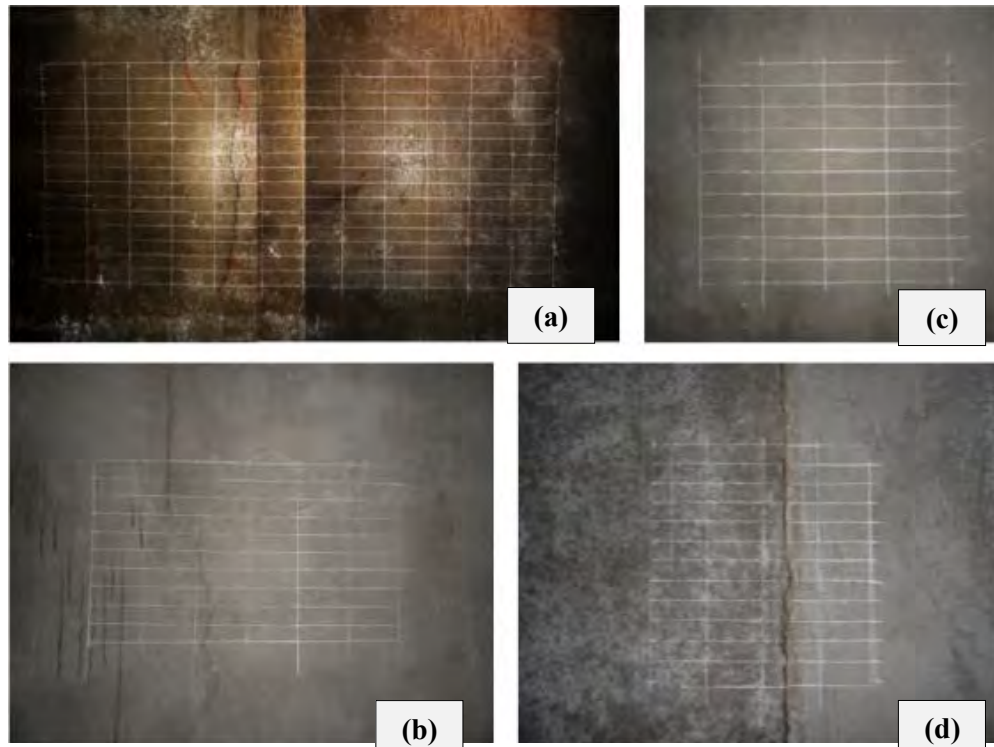
Figure M-19. Images of areas tested at Hanging Lake Tunnel: (a-b) severe vertical cracks, (c) sound concrete, and (d) lining joint.

Figure M-20. Image of tile surface that was evaluated.

One area with significant surface cracks revealed shallow delaminations emanating from the surface cracks (Map HLT 10.5-1, 2, 3 in Appendix N: Ultrasonic Tomography Test
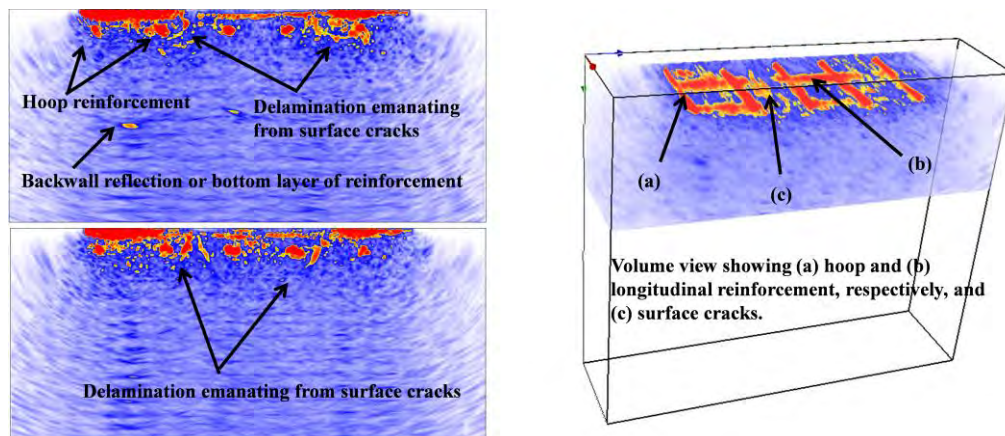
Figure M-40. UST images showing surface cracks and delamination: B-scans (left) and Volume-scan (right).

Summaries). These cracks (Figure M-40, top and bottom left) show what looks to be the beginning stages of spalling, with the curved cracks penetrating approximately 312 mm (12.3 inches) in depth and closing toward each other. This map also revealed a backwall surface at 701 mm (27.6 inches). The hoop and longitudinal reinforcement can be seen in all scans.

Another area with significant cracking (Map HLT 10.5-8, 9 in Appendix N: Ultrasonic Tomography Test Summaries) did not show any sign of delamination; the surface crack appeared only to follow a single hoop reinforcing rebar. The backwall, however, was clearly distinguished at approximately 752 mm (29.6 inches) in depth (Figure M-41). Above this backwall reflection is an area of high reflectivity that either corresponds to shallow (51-76 mm, or 2-3 inches) backwall delamination or the lower layer of reinforcing steel.
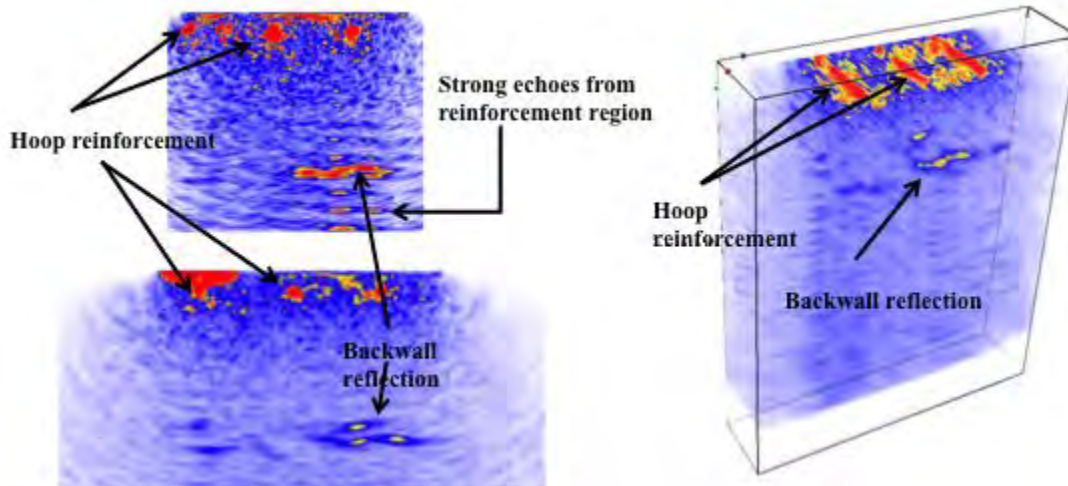
Figure M-41. UST images showing possible deep delamination: B-scans (left) and Volume-scan (right).

Another area showing significant cracking was originally mapped to cover a small area (~1.2 m, or 4 ft wide). After collecting the data, however, it was noticed that a delamination appeared around the boundary of this grid. The grid was extended to cover as much of the delamination as possible, eventually reaching over 4.9 m (16 ft). This map (HLT 10.5-10, 11, 12 in Appendix N: Ultrasonic Tomography Test Summaries) is shown as a collage of photos in Figure M-37. The B-scan shown in Figure M-42 (top) reveals an extensive delamination ranging from 203-508 mm (8-20 inches) below the surface and stretching over 3.4 m (11 ft) in length. The C-scans in Figure M-42 (bottom right) show the hoop and longitudinal reinforcement, as well as a plan view of the curved delamination's planar spread. Because of the significant reflection from the delamination's boundaries, the backwall reflection is not detectable.

The map tested over a joint (Figure M-38d, as well as Map HLT 10.5-4 in Appendix N: Ultrasonic Tomography Test Summaries) showed possible signs of debonding or the presence of voids and/or shallow delaminations at a maximum depth of 229 mm, or 9 inches (Figure M-43). Also, similar to the suspected debonding at the Eisenhower Tunnel locations in Figures M-33 and M-34, multiple reflections are seen at increments corresponding to the reinforcing steel depth. As noted before, these characteristic echoes are suspected to be present when debonding of the reinforcement occurs due to corrosion.

The last area tested at the Hanging Lake Tunnel was a section of tile inside the eastbound lane along the outer wall (refer back to Figure M-39, as well as HLT 10.5-13 in Appendix N: Ultrasonic Tomography Test Summaries). Although no backwall surface was detectable, all reinforcement could be clearly seen.

Overall, testing at this tunnel indicated shallow delaminations emanating from surface cracks (approximately 312 mm [12.3 inches] in depth), as well as severe delaminations at an approximate depth of 508 mm (20 inches). The UST evaluation also revealed possible areas of debonding near severe cracks and joints. The reinforcement cover and spacing were also detectable. Unfortunately, validation of delamination and crack depth was not available at this tunnel.
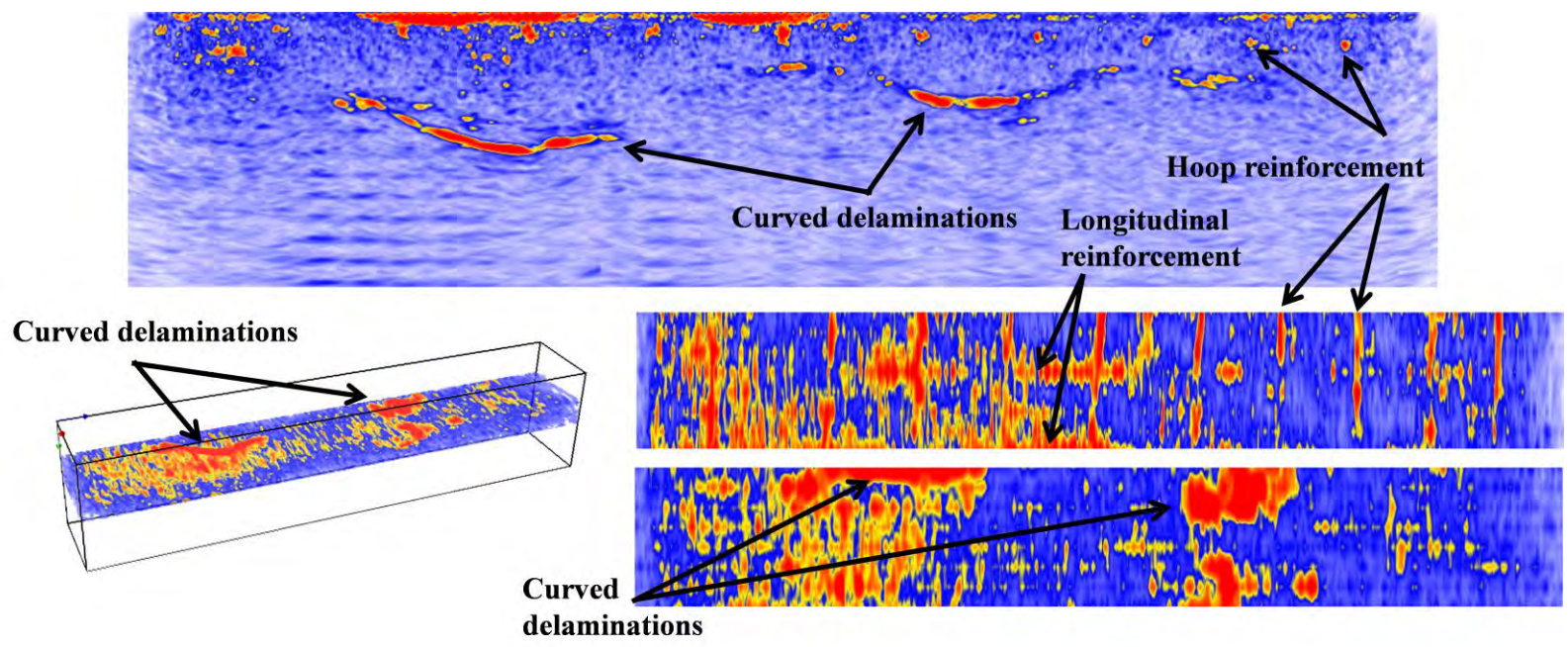
Figure M-42. UST images showing significant deep delamination: Volume-scan (bottom left), B-scan (top), and C-scans (bottom right).
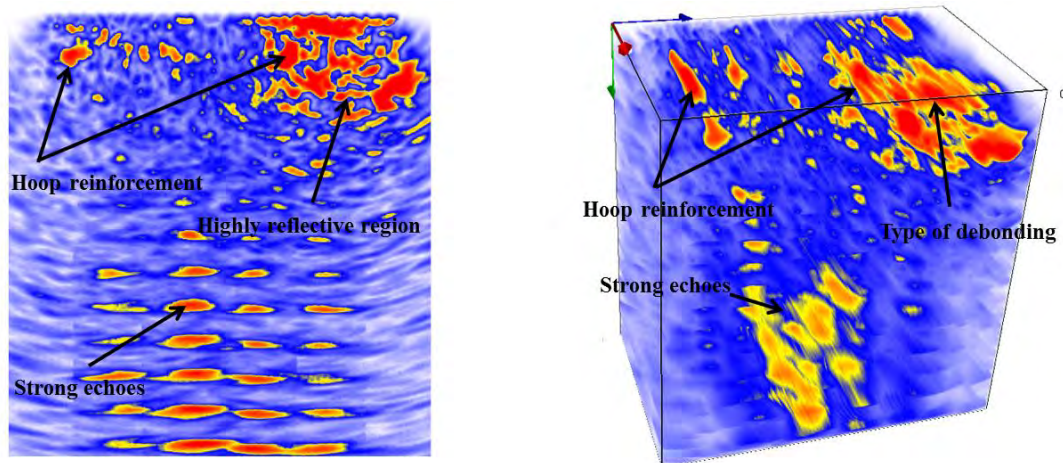
Figure M-43. UST images over lining joint: B-scan (left) and Volume-scan (right).

Chesapeake Channel Tunnel, Virginia

The Chesapeake Channel Tunnel (Figure M-44) is one of two tunnels that comprise the Chesapeake Bay Bridge Tunnel system, joining southeastern Virginia to the Delmarva Peninsula. Hailed worldwide as a modern engineering wonder, the 37 km (23-mi) long system includes 3.2 km (2 mi) of causeway, four manmade islands, 8.9 km (5.5 mi) of approach roads, 19.3 km (12 mi) of low-level trestle, two 1.6 km (1-mi) steel tunnels, and two bridges. The Chesapeake Channel Tunnel (during construction and briefly afterward it was called the Baltimore Channel Tunnel) was constructed using a cut-and-cover method. Precast steel tubes, fabricated and assembled in Orange, Texas, were floated to a shipyard in Norfolk, Virginia, where the reinforced concrete linings and roadway were constructed. The sections were floated to the site before being sunk into a trench. Each steel tube, 483 km (300 ft) in length and 60 km (37 ft) in diameter, was joined to the other, sealed, and connected to its adjoining section. As each steel section was welded together, patches between the 483 km (300 ft) sections had to be formed with concrete to make an overlapping seal.

Figure M-44. Chesapeake Channel Tunnel: entrance (left) and interior view (right).

As testing for this SHRP 2 project began, a cart with an attached ground penetrating radar (GPR) antennae was wheeled throughout the entire length of the 1.6 km (1-mi) tunnel in various configurations. The data from the GPR evaluations revealed two significant features. The first was a change in steel layout. Within two segments of the entrance to the tunnel, the layer of reinforcement in the GPR scan showed a change, although specifics of the change were indiscernible. Two maps were built on what appeared to be a representation of sound concrete: one before the change shown in the GPR, and one after the change (Maps CBBT 10.11-1 through 4 in Appendix N: Ultrasonic Tomography Test Summaries). The first area, shown in Figure M-45a, revealed that the hoop reinforcement was approximately 61 mm (2.4 inches) in depth and 112 mm (4.4 inches) on center with the longitudinal reinforcement located directly beneath it. The backwall at this location was identified to be 627 mm (24.7 inches) from the surface. The second area, shown in Figure M-45b, revealed the hoop reinforcement to be 58 mm (2.3 inches) in depth and 300 mm (11.8 inches) on center, with the longitudinal reinforcement located directly beneath it. The backwall at this location was 620 mm (24.4 inches) from the surface. After consulting the blueprints for these two areas, it was verified that the first bridge section on both ends was constructed with the hoop reinforcement at 114 mm (4.5 inches) on center, and the rest of the sections were constructed with the increase to 305 mm (12 inches) on center. The plans also indicate all wall thicknesses are a nominal 610 mm (24 inches) in depth. Comparison of the two B-scans showing the difference in hoop rebar layout is shown in Figure M-46.

The second significant feature of the GPR data was the frequent spike in dielectric. Almost every noticed spike in dielectric corresponded to a lining seam or crack and was marked for ultrasonic inspection.

Spalling and corrosion are the two predominant damages this tunnel is facing (see Figure M-47 for typical spalling and corrosion damage); therefore, the areas of greatest interest were identified to be cracks through which water seeps, or live cracks. The primary objective was to cover as much of a variety of cracking conditions located by the GPR dielectric as possible. The most significant live cracks, shown in Figure M-45 (c-d), were evaluated by building a map that spanned across the crack in such a way as to capture the origin of the crack. This would theoretically cover the entire surface area of the visible crack for detailed analysis. Due to time constraints, this was not practiced at every location. It should be noted that these maps, though large, took from 30 min to 1.5 hr for data collection.
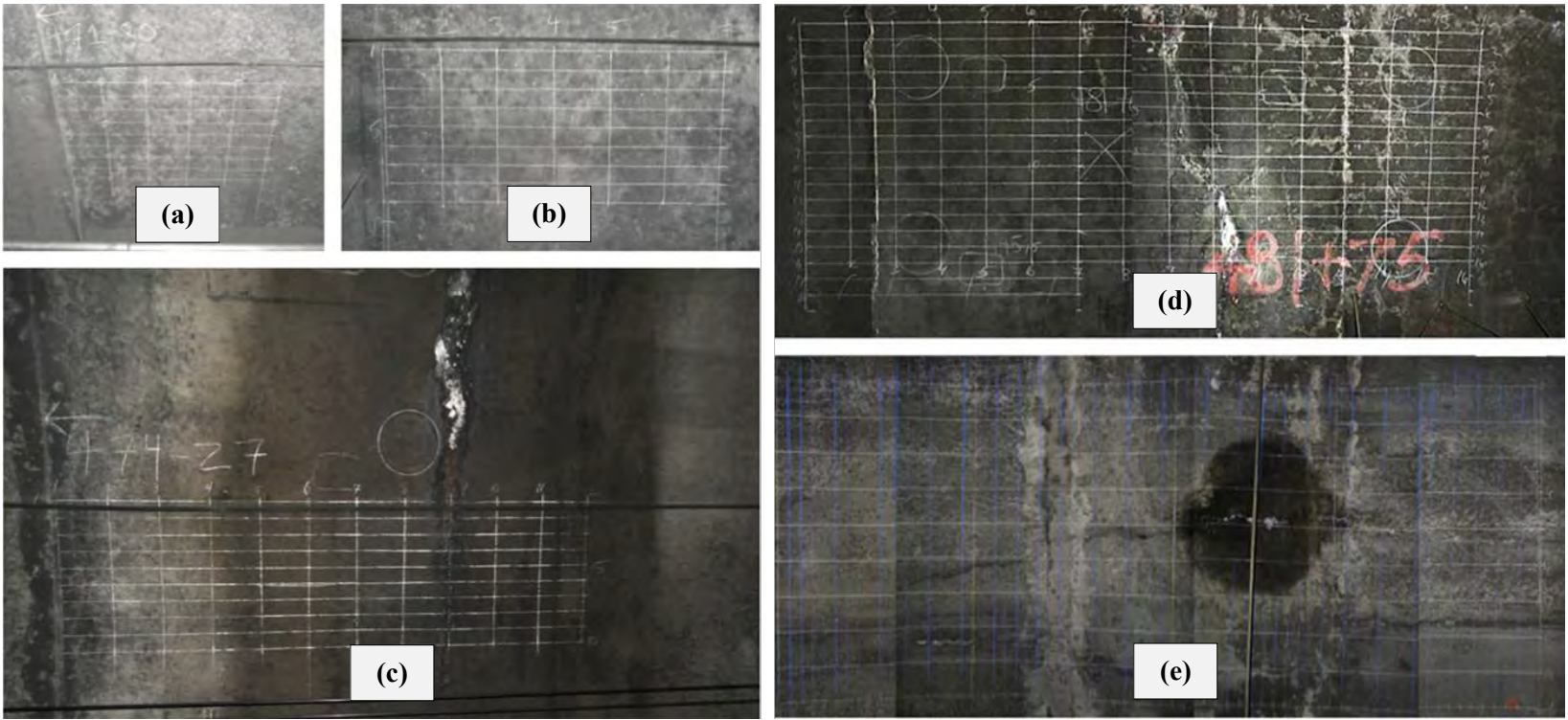
Figure M-45. Areas tested at Chesapeake Bay Tunnel.
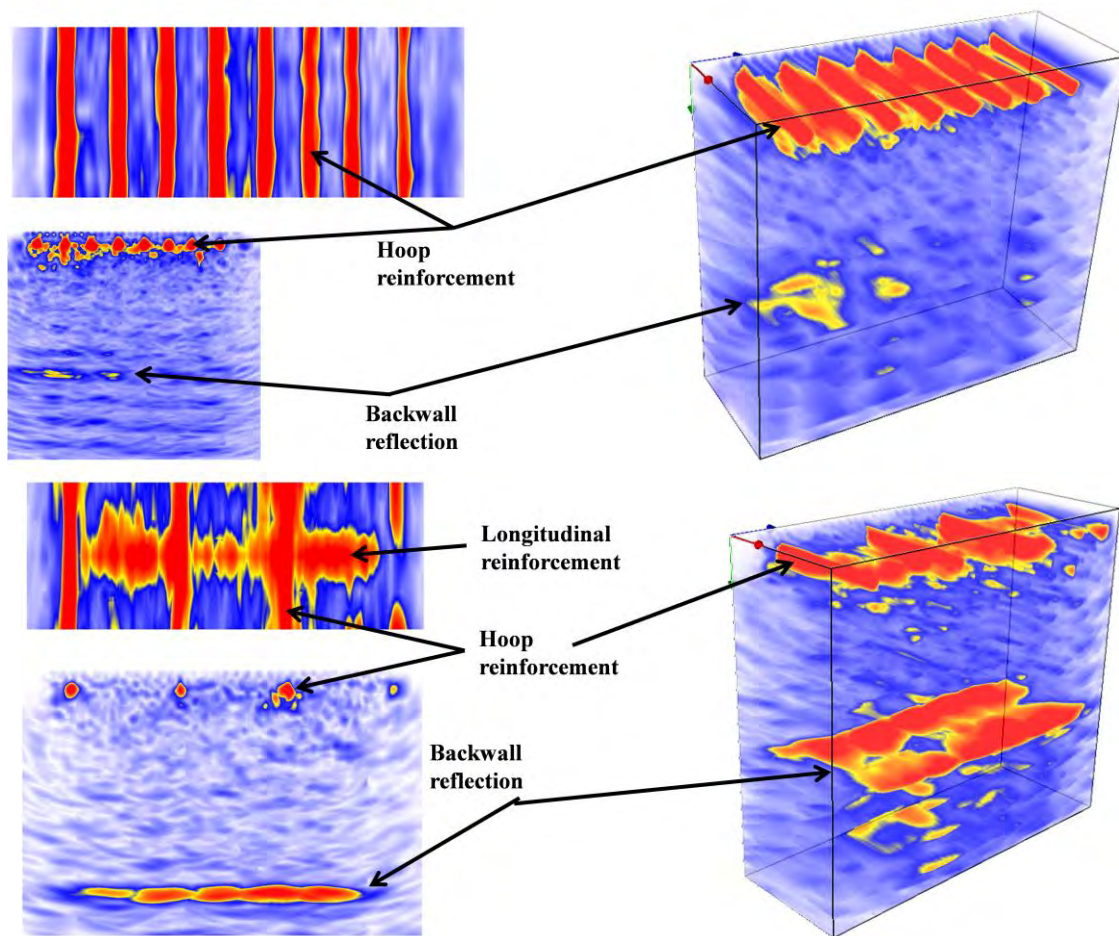
Figure M-46. Comparison of steel layout differences.

Figure M-48 displays the scanning results of a live crack at Sta. 474+27 ft (Figure M-45c, as well as Map CBBT 10.11-5 in Appendix N: Ultrasonic Tomography Test Summaries). The backwall surface, clearly located at 612 mm (24.1 inches) below the surface, is consistent with tunnel blueprints that depict the lining to be approximately 610 (24 inches) in depth. Also in line with the tunnel blueprints for this section of tunnel is the reinforcement spacing. The tomograms indicate the hoop reinforcement to be located at approximately 305 mm (12.0 inches) on center, at a depth of 51-66 mm (2.0-2.6 inches), along with longitudinal reinforcement located directly beneath. The blueprints for this section indicate the hoop reinforcement to be 305 mm (12 inches) on center, with the longitudinal reinforcement directly underneath.

Surrounding the surface cracks, the tomograms also indicate severe shallow defects, including cracks as deep as 229 mm (9 inches) and possibly shallow delaminations approximately 51 mm (2 inches) below the surface. The heavy ringing surrounding the cracked region (Figure M-48, top left and both bottom images) indicates discontinuities that are suspected to have occurred surrounding the reinforcement. This is presumed to be due to corrosion of the top layer of reinforcement.

Figure M-47. Typical spalling and corrosion.
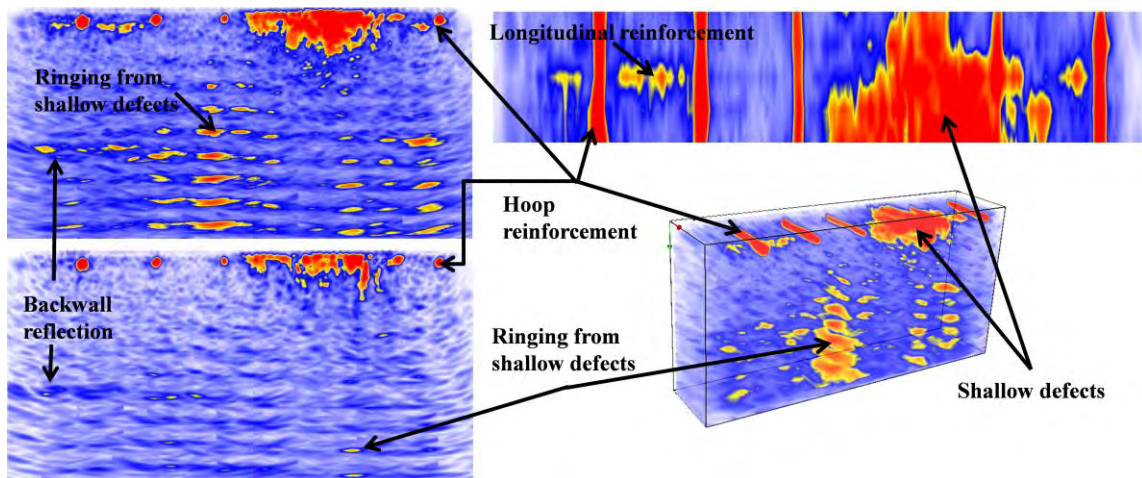
Figure M-48. Area surrounding live crack.
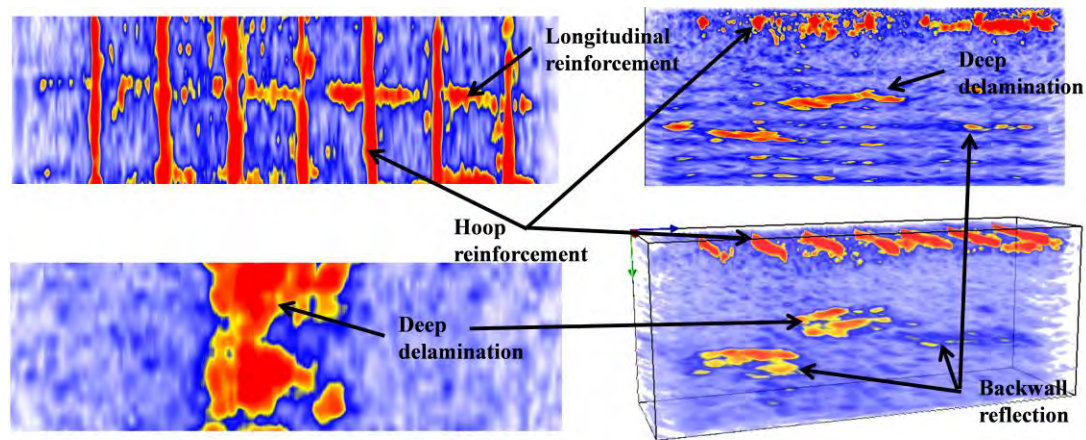
Figure M-49. UST images at Sta. 481+76 showing deep delamination.

Another map covering a severe crack, located at Sta. 481+76 (Map CBBT 10.11-13 in Appendix N: Ultrasonic Tomography Test Summaries) was built to completely capture the width of a delamination less than 102 mm (4 inches) below the bottom surface (from the steel plate). Shown in Figure M-49, this delamination may originate from the layer of hoop reinforcement nearest the steel skin. The backwall surface, a little more than the typical 610 mm (24 inches) in depth, was measured to vary between 676-721 mm (26.6-28.4 inches). The delamination was approximately 513 mm (20.2 inches) below the surface and approximately 696 mm (27.4 inches) in width. The hoop reinforcement is located approximately 307 mm (12.1 inches) on center, at a depth of 51-91 mm (2.0-3.6 inches), along with longitudinal reinforcement located directly beneath. The blueprints for this section indicate the hoop reinforcement to be 305 mm (12 inches) on center with the longitudinal reinforcement directly underneath.

Another area of interest involved a circumferential crack that had only just begun to indicate signs of moisture intrusion (Figure M-45e, and Map CBBT 10.11-10 in Appendix N: Ultrasonic Tomography Test Summaries). A map was built around this crack, attempting to cover as much of the length of the crack as was possible from inside the plenum. Another feature that made this crack interesting was the presence of a longitudinal crack in that area between the stainless steel ceiling hangers (visible in Figure M-45e approximately one-third the distance from the left side of the image). The backwall surface was clearly distinguishable and ranged from 577-658 mm (22.7-25.9 inches) below the surface (Figure M-50). The hoop reinforcement measured to be 69-81 mm (2.7-3.2 inches) in depth and 307 mm (12.1 inches) on center, and the longitudinal reinforcement measured 434 mm (17.1 inches) on center. This matches with the blueprint's details of 305 mm (12.0 inches) on center for the hoop reinforcement, but the plans do not indicate spacing for the longitudinal. As seen in Figure M-50 (top left B-scan), there appears to be two layers of hoop reinforcement, but as this is not indicated in the blueprints, it is possible that this could be an area of a splice. Light reflections, or echoes, are seen throughout the entire region of the crack, specifically surrounding the reinforcement nearest the moisture. Debonding of the reinforcement is suspected here due to corrosion.
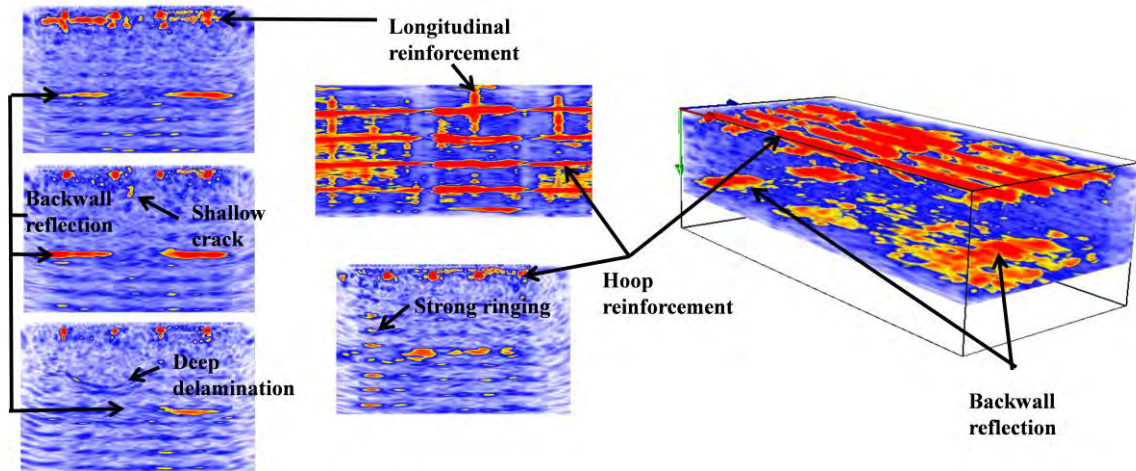
Figure M-50. UST images surrounding circumferential crack.

The gap in the backwall reflection (Figure M-50, B-scans on left) and the omission of some of the hoop reinforcement (Figure M-50, Volume-scan on right and C-scan top center) indicate the presence of a crack. When cracks are present, the ultrasonic waves are strongly attenuated, causing the reception of the signals to be scarce if not completely absent. The other noticeable feature in this map is the possibility of a curved delamination approximately 450 mm (17.7 inches) in depth and up to 483 mm (19 inches) wide (Figure M-50 bottom left). It is also apparent from Figure M-50 (center left B-scan) that surface cracks appear to extend a maximum of 249 mm (9.8 inches) in depth.

The last section tested within the plenum was a location detected by a high spike in GPR dielectric. Upon investigation, no live crack was found, but rather a dry seam. Although no visible signs of distress were apparent, hammer tapping revealed an extremely shallow delamination that appeared close to separating and falling. A grid was applied to this region surrounding the seam and shallow delamination and the area broken up into two sections, Region I (Map CBBT 10.11-9 in Appendix N: Ultrasonic Tomography Test Summaries) and Region II (Map CBBT 10.11-7, 8 in Appendix N: Ultrasonic Tomography Test Summaries), as shown in Figure M-51. Both regions showed strong ringing emanating from the layer of reinforcement, indicating potential reinforcement debonding.

Region I UST evaluations revealed significant cracks and/or voids as deep as 218 mm, or 8.6 inches (Figure M-52, bottom left). The hoop reinforcement was shown to vary between 51-76 mm (2.0-3.0 inches) in depth at approximately 310 mm (12.2 inches) on center, with the longitudinal reinforcement located directly beneath at 503 mm (19.8 inches) on center. The backwall in this section varied from 617-660 mm (24.3-26.0 inches).

Region II UST evaluations, shown in Figure M-53, showed the delaminated region (marked as "shallow delamination") and also showed the presence of cupped delaminations as deep as 488 mm (19.2 inches) below the surface, or approximately the same depth as the lower reinforcement closest to the tube skin. The backwall in this area ranged from 612-660 mm (24.1-26.0 inches). The hoop reinforcement at 56 mm (2.2 inches) deep was found to be 307 mm

(12.1 inches) on center, with the longitudinal rebars underneath at 411 mm (16.2 inches) on center.

The last two areas tested within the Chesapeake Bay Tunnel were both located in the driving lane, along the tiled wall lining. One of these areas with potential deterioration was discovered by using data from SPACETEC, a German company that utilizes a contact-free scanning system that provides detailed images, profiles, and thermal data for tunnel linings (http://www.spacetec.de). After evaluating the Chesapeake Bay Tunnel, SPACETEC's analysis report revealed an area detected by the infrared scan, indicating possible debonding. When debonding occurs beneath tile, hammer sounding by ear or by microphone can readily differentiate bonded from debonded tile. Debonded tile can occur for two reasons: (1) improper installation (wrong type of thinset, disproportionate water ratios, improper mixing, and/or low standard of workmanship, i.e., not backbuttering the tile); or (2) presence of degrading agent (typically water) behind the tile lining. If the debonding occurs for the first reason, reapplication of the tile lining can solve the problem. However, when debonding occurs due to cracks that facilitate the degradation of the thinset by moisture entrainment, NDT techniques can hopefully be used to determine the source of such moisture. Therefore, it became a goal to search for a damaged area that was not verifiable by sounding techniques. In other words, we wanted to determine the beginning stages of tile debonding before the tile debonding actually occurred to a noticeable extent. SPACETEC's data served this purpose very well by determining an area (Figure M-54, left) that showed signs of possible delamination but was not detectable via hammer sounding. Figure M-54, right, details a damaged area that includes debonded tile detectable by hammer sounding. The UST results from scanning the area determined by SPACETEC's data are shown in Figure M-55. The three B-scans (Figure M-55, left images) indicate the backwall reflection varies between 714-787 mm (28.1-31.0 inches). This variance can be seen in the D-scan in Figure M-55 (far right image, the dark blue curved strip on the right of the figure), which shows the curvature of the tube's skin. Also in the same figure is a C-scan image of the area tested at a depth of 102 mm (4 inches) directly beneath the reinforcement. When compared to SPACETEC's infrared analysis, this outline correlates strongly with the infrared image. It appears that there is significant delamination at the level of reinforcement and above, and this has yet to cause significant debonding of the tile. The top left image in Figure M-55 shows much of the shallow surface cracks and possible shallow delaminations above the reinforcement, and the center left image depicts a deep crack (directly left of the last hoop rebar on the right). Notice the hoop and longitudinal reinforcement are both detectable at 122-239 mm (4.8-9.4 inches) below the surface at 297 mm (11.7 inches) on center (again, refer to the D-scan in Figure M-55 and the hoop reinforcement profile). The longitudinal reinforcement is seen, but it is hard to differentiate between the actual longitudinal rebars and 51 mm (2-inch) diameter electrical ducts that are present. If the scanning direction were oriented perpendicular to the rebar/ducts, this distinction could be made.

The UST results from the second area tested (Figure M-54, right) are shown in Figure M-56. The region of debonded tile correlated greatly with a joint in the tube lining, as can
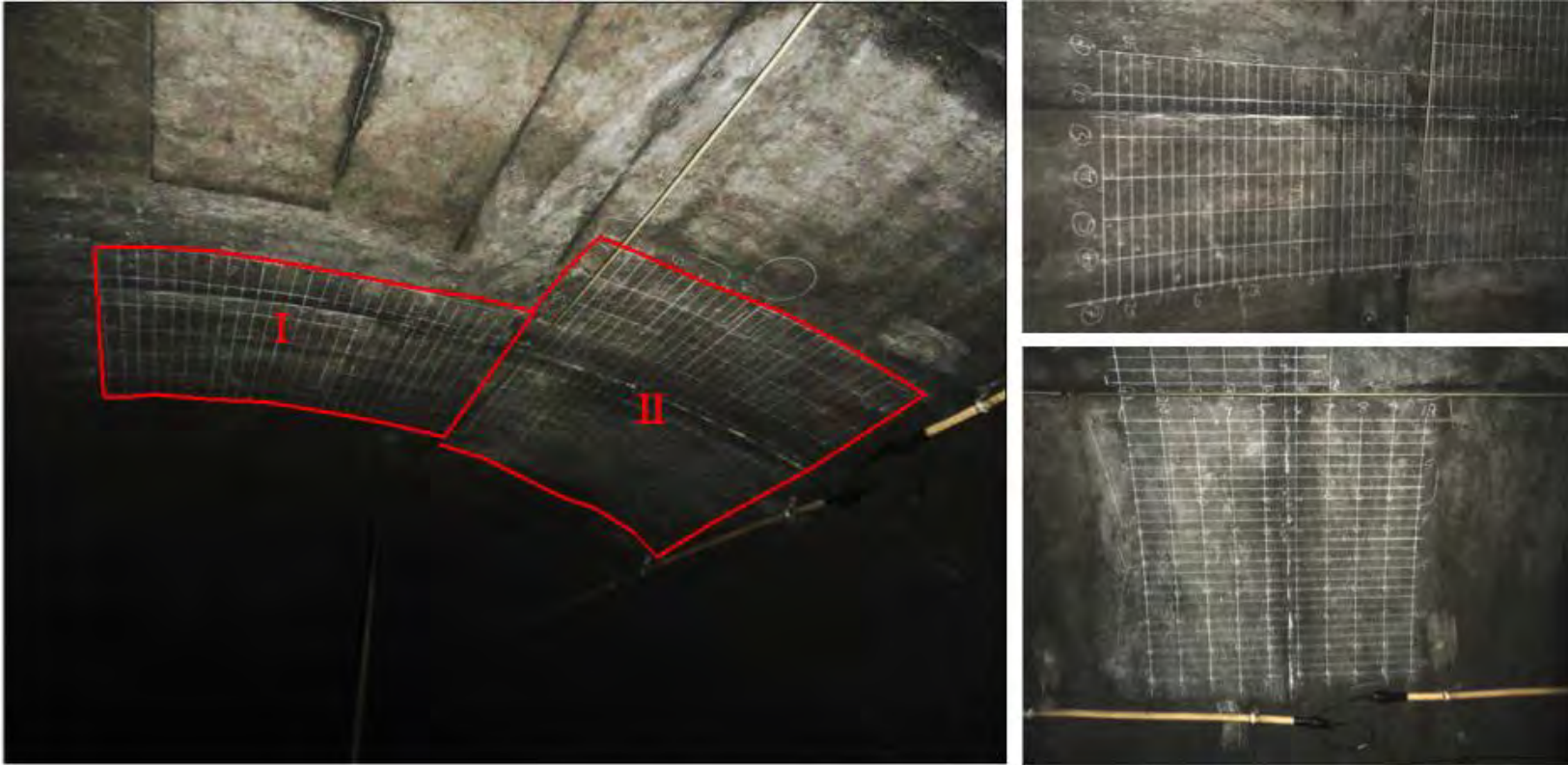
Figure M-51. Images depicting Region I (top right) and Region II (bottom right).
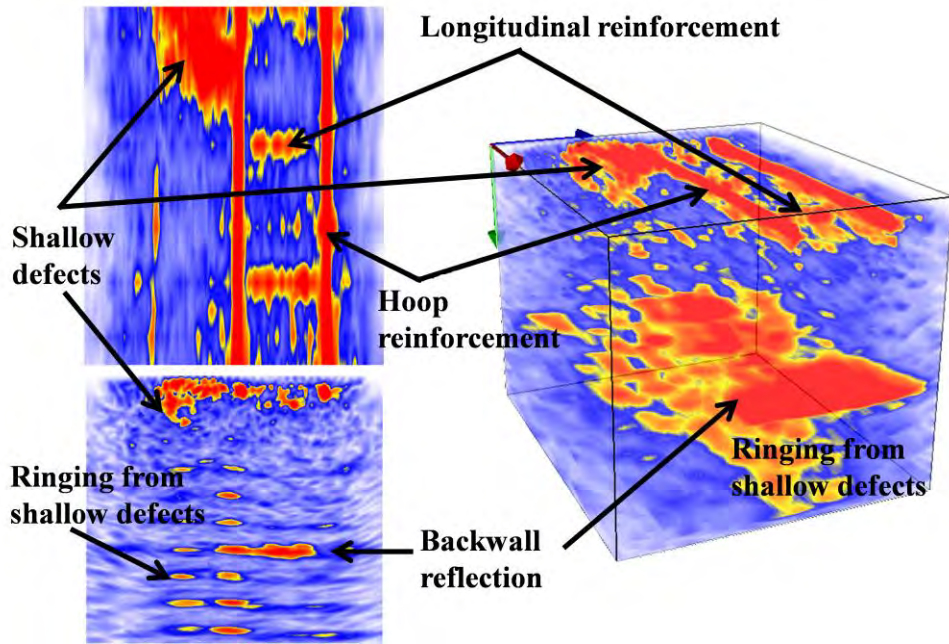
Figure M-52. Region I UST images.
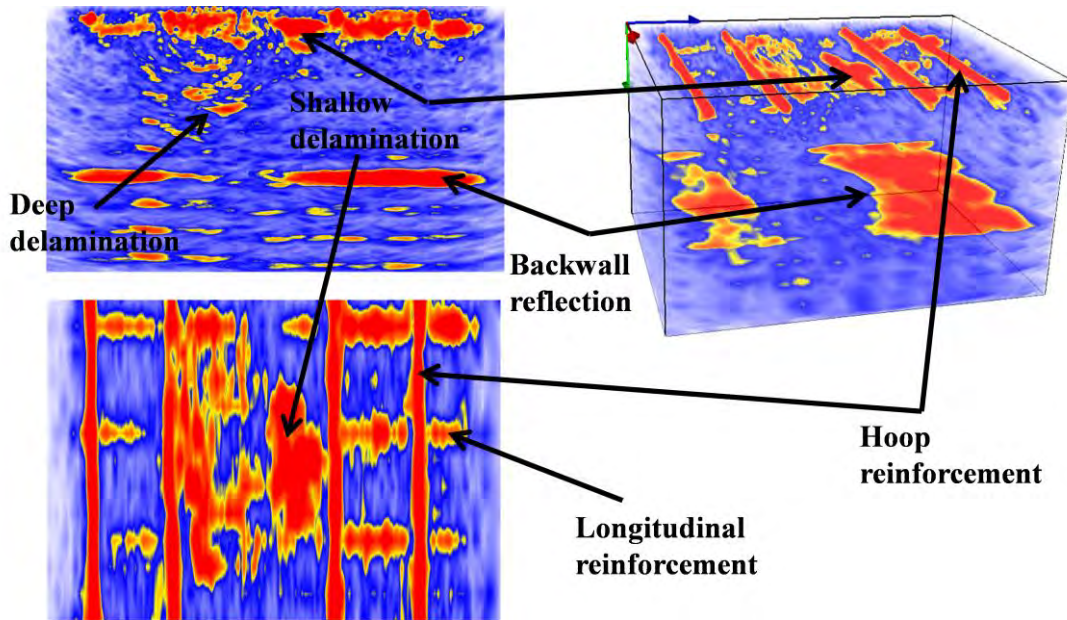
Figure M-53. Region II UST images.
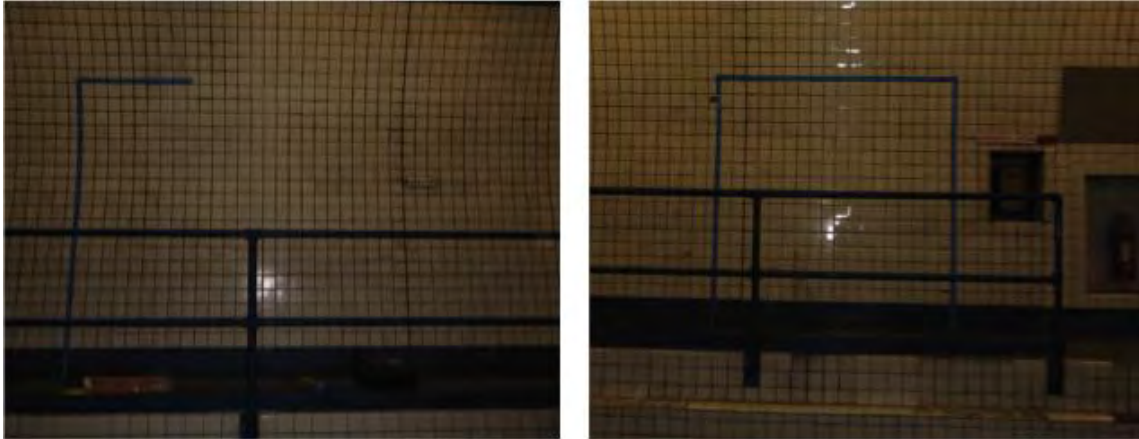
Figure M-54. Tile lining sections in Chesapeake Bay Tunnel.
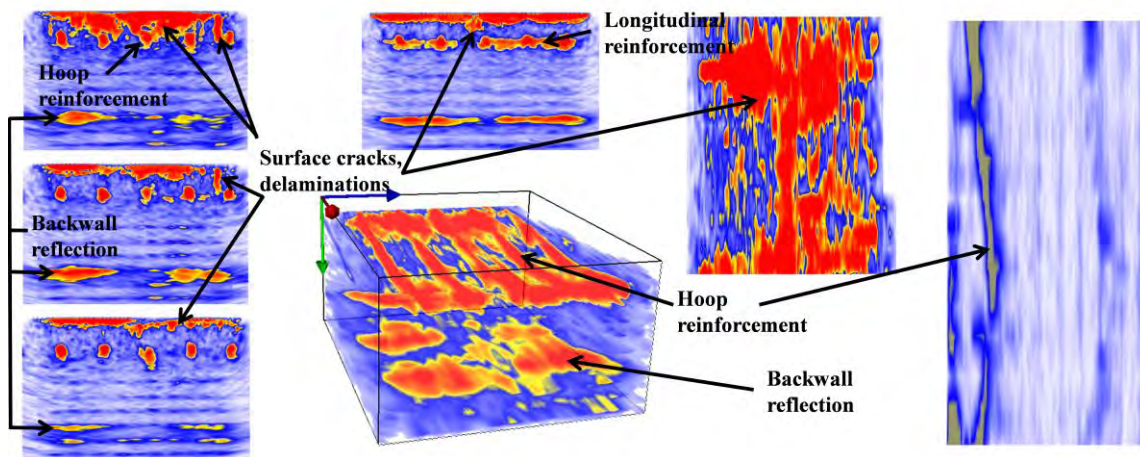
Figure M-55. First tile lining area tested, discovered by SPACETEC scanning.

as can also be supported by the extensive delamination noted mid-image in the B-scans (Figure M-56, left images). The backwall in this region varied from 635-762 mm (25-30 inches), due to the same reasons of tube curvature discussed in the previous map. The hoop reinforcement was 109-196 mm (4.3-7.7 inches) in depth and approximately 307 mm (12.1 inches) on center. As in the previous map, the longitudinal reinforcement is hard to distinguish from the 51 mm (2-inch) diameter electrical ducts present. It is suspected that the top left image is evidence of a lap splice (notice two distinct layers of steel rebar to the right of the joint, where different tube sections could have different splice locations). During the assembly of the tubes underwater, as noted beforehand, steel skins were connected by bolting and welding overlapped hoods. After this mechanical lock connection was complete, concrete was poured surrounding the joint location to make the interior steel-reinforced concrete continuous and waterproof. Although no detailed plans show the width of this scratch joint, it remains a question as to whether the deep delaminations seen in the B-scans could be a result of degrading concrete joints.
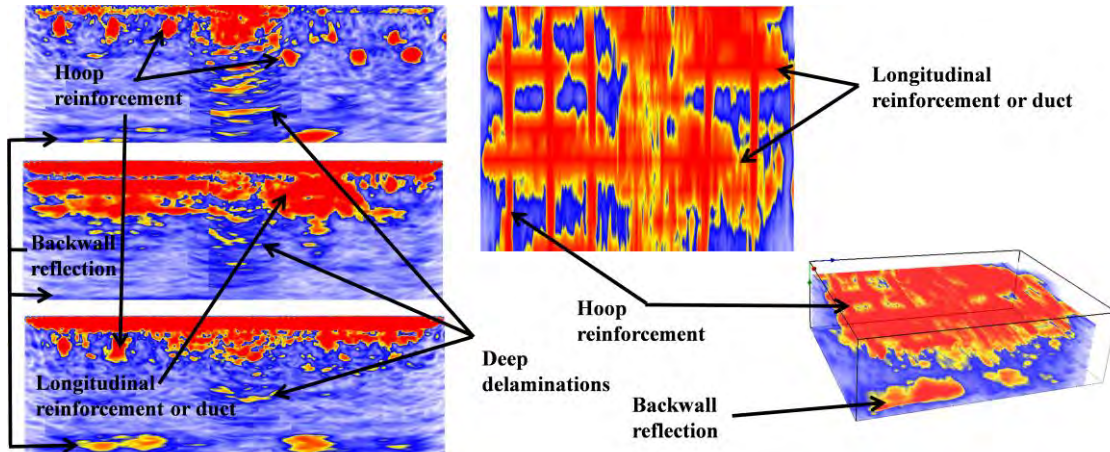
Figure M-56. Second tile lining area tested.

Washburn Tunnel, Texas

The Washburn Tunnel (Figure M-57), the only underwater vehicle tunnel in operation in Texas, was completed in 1950 and carries Federal Road beneath the Houston Ship Channel joining two Houston suburbs. The tunnel was constructed via the immersed tube method, with sections joined together in a prepared trench, 26 m (85 ft) below water.

A specific area of interest in this tunnel was tile debonding. As noted earlier, in tile-lined tunnels such as these, acoustic sounding via hammer tapping can quickly reveal debonded tiles. As an object such as a hammer is lightly tapped (or even dragged) along the surface, the lower frequencies perceived by the ear as pinging is a typical indication of debonding. Most debonding of tiles happens as water infiltrates the lining, deteriorating the mortar that holds the tile. However, trouble arises when trying to locate the source of the water infiltration; while hammer sounding is effective in locating debonded tiles, it does not necessarily locate the source of the water. In this tunnel, four areas were evaluated that indicated debonding through hammer sounding. Blue painter's tape was used to outline both the grid and the outside perimeter of the
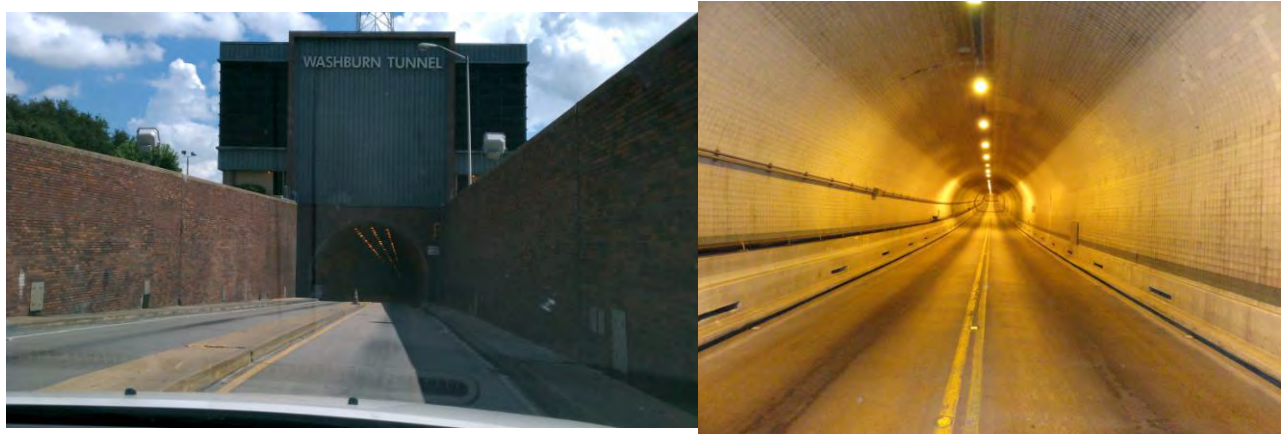
Figure M-57. Washburn Tunnel: entrance (left) and interior view (right).

area that the human ear perceived as a debonded section.
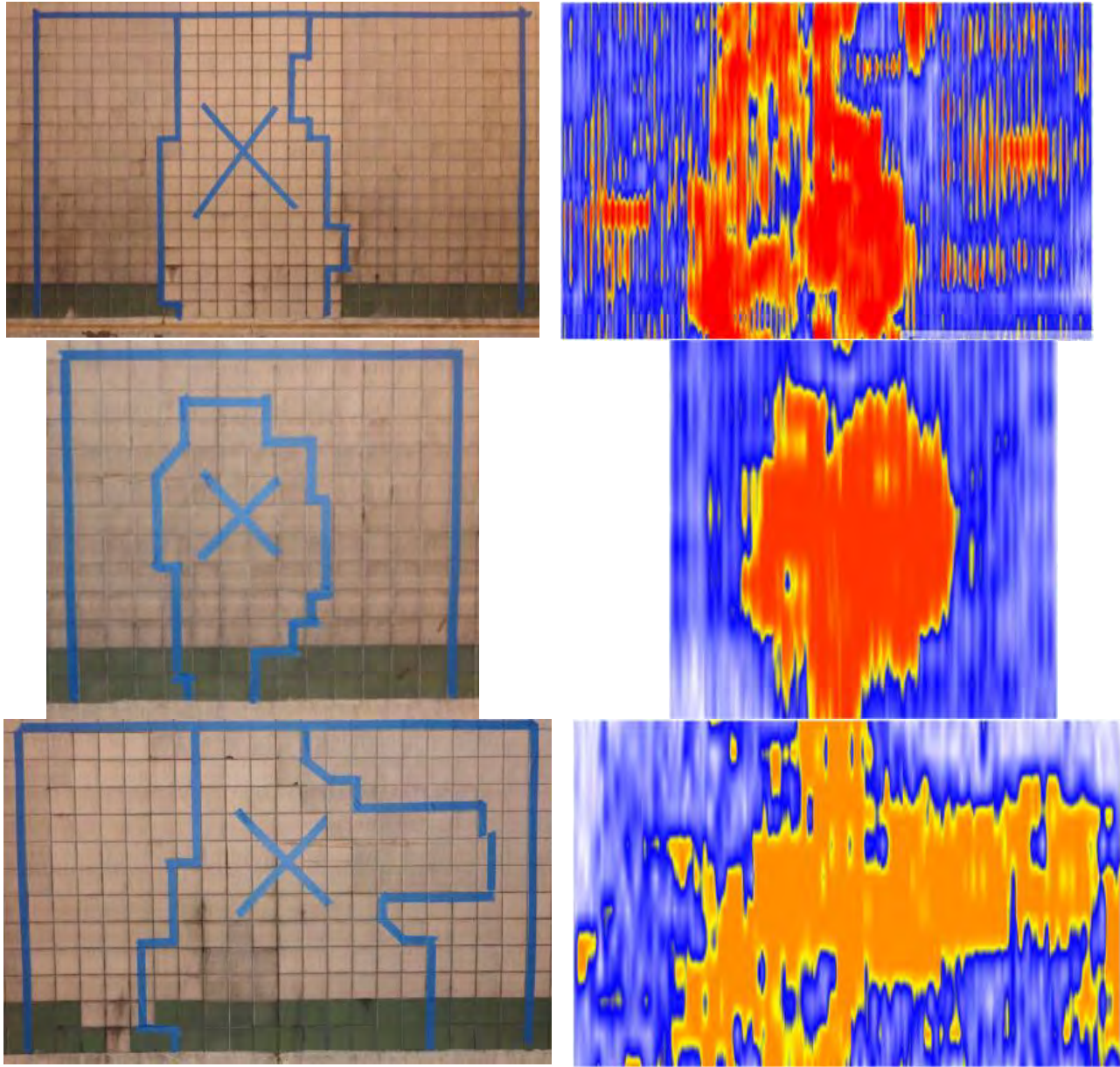
Figure M-58. Tile linings via UST (left) paired with the associated C-scans (right).

The first three sections are shown in Figure M-58. The images shown have blue painter's tape outlining debonded areas (detected by hammer sounding) and are paired with the associated C-scans that show shallow delaminations ranging from 16-103 mm (0.63-4.1 inches) deep. It can be seen that the area marked off by hammer sounding closely matches the region of shallow debonding.

Representations of typical B-, C-, and Volume-scans for the three regions in Figure M-58 are shown below in Figure M-59. Again, large areas depicting shallow debonding are visible, as well as regions of delamination surrounding the reinforcement. It is clear from the B-scans that

there exists significant damage that penetrates as deep as 457 mm (18 inches). These B- and C-scans are representative of the other areas tested in the Washburn Tunnel.

The last section tested, depicted in Figure M-60, reveals shallow debonding (note the C-scan image of the debonded area 16 mm, 0.63 inches below the surface in Figure M-60, bottom center). The B-scan (Figure M-60, bottom left) shows areas suspected to have deep delamination. This delamination is also seen in the Volume-scan on the right.

Overall, testing at the Washburn Tunnel showed significant damage behind debonded tile that lead to the conclusion that the debonding was due to lining stresses (i.e., not due to tile workmanship).
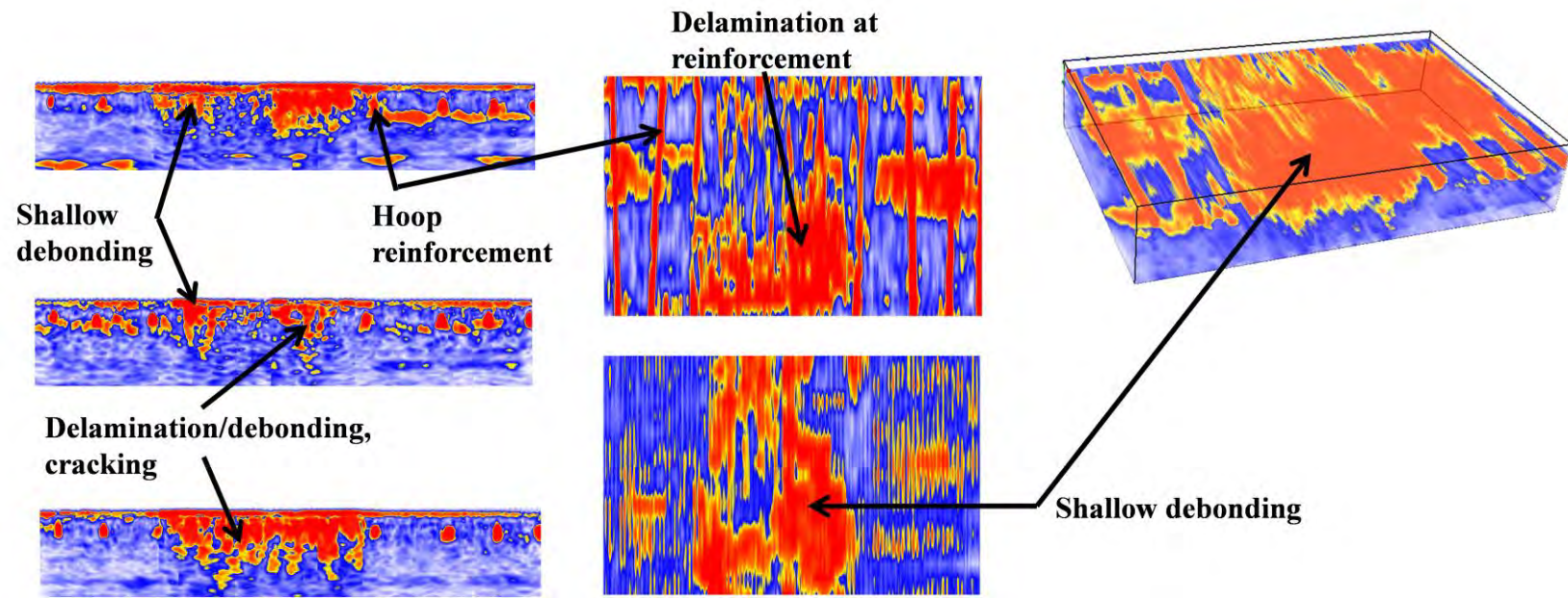
Figure M-59. Area tested surrounding debonded tiled: B-scans (left), C-scans (center), and Volume-scans (right).
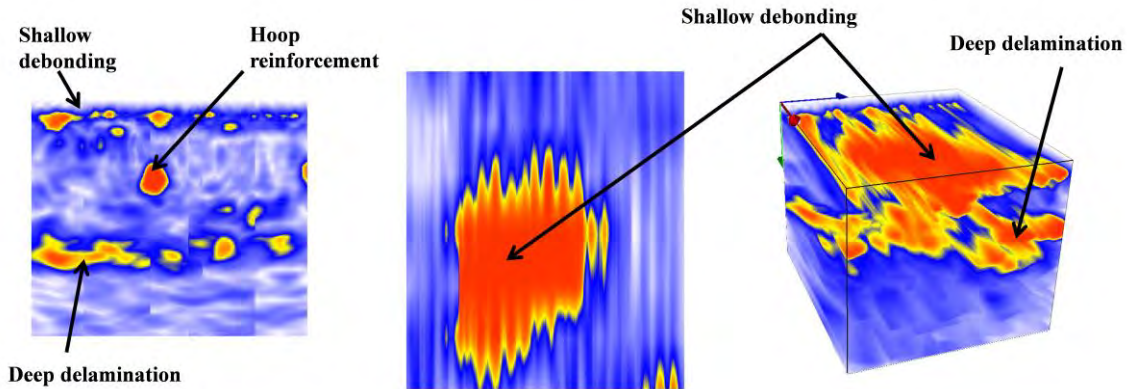
Figure M-60. Tile lining tested at Washburn Tunnel.

CONCLUSIONS

The UST system was used to perform evaluations on over 30 concrete and shotcrete specimens containing simulated defects, numerous concrete pavements, airport runways, and bridge decks. These defects included air- and water-filled voids, vertical cracks, horizontal delaminations, and abnormalities such as clay lumps. The device was also used to determine specimen characteristics such as reinforcement depth and spacing, as well as concrete thickness measurements. After evaluating the system's capabilities and establishing confidence in the used methodology, the system was used on four existing tunnels. Where able, ground truth data were further used to determine the precision and accuracy of the system with various types of defects. Table M-7 shows the maximum and minimum features detected by this research. Note that these values do not necessarily express the limits of the device but the limits of the performed research. Further research needs include expanding the variety of structural defects (both size and location) to determine maximum and minimum detectable features along with confidence levels for each type of defect.

Table M-7. Maximum and minimum detected features tested by the A1040 MIRA system. Note that all testing here reported with 50 kHz scanning frequency.

Component Detected	Component Extremes	Minimum Depth Detected	Maximum Depth Detected
Reinf. diameter	Min. diameter: #5	83 mm (to center)	184 mm (to center)
	Max. diameter: #11	51 mm (to center)	196 mm (to center)
Reinf. cover	N/A	#11 @ 33 mm	#9 @ 377 mm
Secondary reinf. layer	Min. diameter: #5	184 mm (to center)	184 mm (to center)
	Max. diameter: #9	210 mm (to center)	377 mm (to center)
Delamination thickness	Min. thickness: 0.05 mm	43 mm (to center)	89 mm (to center)
	Max. thickness: 2.0 mm	69 mm (to center)	69 mm (to center)
Delamination depth	N/A	0.05 mm thickness @ 43 mm depth (to center)	0.25 mm thickness @ 183 mm depth (to center)
Clay lump diameter (all 51 mm thick)	Min. diameter: 102 mm	61 mm (to center)	216 mm (to center)
	Max. diameter: 152 mm	107 mm (to center)	160 mm (to center)
Specimen thickness (structural depth)	N/A	102 mm	711 mm
Air-filled voids	Only thickness tested: 13 mm	76 mm (to center)	203 mm (to center)
Water-filled voids	Water-filled Ziploc bag: ~ 13 mm	76 mm (to center)	203 mm (to center)

*Size only verified by ground truth data; feature not detectable by the A1040 MIRA system.

Limitations of the UST System

The limitations of the device are as follows:

- *Speed of data acquisition.* If the system is used for detailed mapping in the Map Mode, the user should expect the scanning process to take between 9-25 min/m^2 (0.8-2.3 min/ft^2). The Review Mode can be used for single-point evaluations at much faster rates of inspection (3-5 s per scan), but only limited-width B-scans are available for evaluation in this mode.
- *No indication of phase change.* The color palette response represents quantity of reflectivity regions and is a measurement relative to the medium (in which there should ideally exist zero reflectivity, the blue spectrum). As such, the type of defect is largely guesswork on the end of the user and requires greater skill and knowledge of ultrasonics to interpret these signals.
- *Detection of layered defects.* If defects are stacked, particularly in such a manner that air gaps are located above other types of defects, then the device can rarely determine anything below the initial air-filled gaps. This is due to ultrasonic pulse attenuation at air boundaries. If pulses are capable of being transmitted past air interfaces, then the received signal is extremely weak and should be examined to be certain it is not a multiple or echo of the initial flaw.
- *Shallow defects.* Due to the spacing of the transducer array and the beam spread of the individual transducers, defects that exist approximately 25 mm (1 inch) from the surface cannot be expected to be received by other transducers and carry any accurate

information regarding the depth and lateral dimensions of the shallow defects. However, near-surface defects can leave a shadow on the data collected below the near-surface defects. An example of this is the shotcrete Specimen L and concrete Specimen Iota, where the defect leaves a shadow beneath its presence. Though it is too shallow to reflect the actual boundary, its presence inhibits ultrasonic pulses to be transmitted (or received) beyond it.

Conclusions of Tunnel Testing

The conclusions of the tunnel testing are as follows:

- The UST system is exceptional at locating horizontal delaminations ranging in thickness from 0.05-2.0 mm (0.002-0.079 inches) and is able to differentiate between fully debonded and partially bonded areas within a single map based on the color distribution. It is not, however, able to directly measure the thickness of delaminations.
- Cracks were only clearly characterized when they formed non-perpendicular to the testing surface; however, the presence of perpendicular cracks could be assumed by the omission of surface detail. It should be noted that no crack depths were confirmed by ground truth validation, and this should be a focus of further research.
- Backwall surfaces up to a depth of 965 mm (38 inches) were successfully and accurately determined. Assuming the plan details were correct (no ground truth validation was available), the UST system predicted this depth within an accuracy of 5 mm (0.3 inch).
- Both air- and water-filled voids ranging from 76-203 mm (3-8 inches) in depth could be detected, but differentiation between the two was difficult due to the fact that shear waves are not supported by air or water, and almost all of the acoustic energy is reflected by these types of voids. Further study could be conducted to analyze the difference between phase changes involving these two types of voids.
- Reinforcement layout and depth, as long as the device is polarized in the correct direction, was also successfully determined, with the only exception being in some shotcrete applications. When potentially porous materials such as the shotcrete specimens were evaluated, the presence of very small air voids made internal inspection very difficult.
- With the exception of some medium-sized clay lumps (with a diameter of approximately 102 mm, or 4 inches) surrounding reinforcement, all clay lumps tested were also highly successful.
- Two MIRA systems were used to compare the system's abilities to reproduce the same wave speed. For a test involving 16 specimens, a strong positive correlation existed (with a coefficient of determination of 0.952), with a standard error of approximately 33 m/s (108 ft/s).
- Precision for detecting the depth of delaminations using the same device with the same testing procedures and input parameters (wave speed, frequency, gain selection, etc.) was typically on the order of 1-3 mm (0.04-0.12 inch) and is more likely to be explained by user error/interpretation rather than device error. This is the same for water- and air-filled voids.
- Reproducibility, using separate devices with the same testing procedures and input parameters (wave speed, frequency, gain selection, etc.), indicated a consistent offset of

9-13 mm (0.35-0.51 inch) between the two systems, with a single system always revealing the deeper measurement. The research team is pursuing an explanation for this offset with the device's manufacturer. Reproducibility using separate devices with the same testing procedures and an individual calculation of wave speed (with all other parameters equal) indicated a strong positive correlation between defect depths (coefficient of determination of 0.9965) with a standard error of 3.85 mm.

- The minimum area able to be tested with the MIRA system is merely tied to the size of the device: 370 mm x 170 mm (14.6 inches x 6.7 inches).

REFERENCES

De La Haza, A., Peterson, C., and Samokrutov, A. (n.d.). "Three Dimensional Imaging of Concrete Structures Using Ultrasonic Shear Waves." *ACS <http://acsys.ru/eng/article/files/Imaging_of_concrete_structures.pdf>* (December, 2011).

Im, S., Hurlebaus, S., and Trejo, D. (2010). "Inspection of Voids in External Tendons of Posttensioned Bridges*." Transportation Research Record: Journal of the Transportation Research Board*, Transportation Research Board of the National Academies, Washington, DC, 2172, 115-122.

Krause, M., Gräfe, B., Mielentz, F., Milmann, B., Friese, M., and Wiggenhauser, H. (2009). "Ultrasonic imaging of post-tensioned concrete elements: New techniques for reliable localization of grouting defects*." Proc., 2nd International Conference on Concrete Repair, Rehabilitation and Retrofitting,* Concrete Repair, Rehabilitation, and Retrofitting II, Cape Town, South Africa, 215-216.

Schickert, M. (1995). "Towards SAFT-Imaging in Ultrasonic Inspection of Concrete." *Proc., International Symposium on Non-destructive Testing in Civil Engineering,* NDT-CE, Berlin, Germany, 1, 411-418.

Schickert, M., Krause, M., and Muller, W. (2003). "Ultrasonic Imaging of Concrete Elements Using Reconstruction by Synthetic Aperture Focusing Technique*." J. Mater. Civ. Eng.,* 15(3), 235-246.

Shokouhi, P., Wöstmann, J., Schneider, G., Milmann, B., Taffe, A., and Wiggenhauser, H. (2011). "Nondestructive Detection of Delamination in Concrete Slabs." *Transportation Research Record: Journal of the Transportation Research Board*, Transportation Research Board of the National Academies, Washington, DC, 2252, 103.

APPENDIX N
ULTRASONIC TOMOGRAPHY TEST SUMMARIES

INTRODUCTION

This appendix describes the test summaries of field evaluations for a particular nondestructive testing (NDT) technique known as ultrasonic tomography (UST). This testing is performed within the framework of the second Strategic Highway Research Program (SHRP2) Project R06(G), "High-Speed Nondestructive Testing Methods for Mapping Voids, Debonding, Delaminations, Moisture, and Other Defects Behind or Within Tunnel Linings." The objectives of this project were:

- To identify NDT technologies for evaluating the condition of various types of tunnel linings and tunnel lining finishes such as tile. The techniques had to be capable of analyzing conditions within the tunnel lining and the surrounding substrate.
- To evaluate the applicability, accuracy, precision, repeatability, ease of use, capacity to minimize disruption to vehicular traffic, and implementation and production costs of the identified technologies.
- To conduct the required development in hardware or software for those techniques that showed potential for technological improvement within the time limitations of the project.
- To prove the validity of the selected technologies/techniques to detect flaws within or verify conditions of the targeted tunnel components.
- To recommend test procedures and protocols to successfully implement these techniques.

The following represents evaluation summaries of sites located at Eisenhower Memorial Tunnel near Dillon, Colorado; Hanging Lake Tunnel near Glenwood Springs, Colorado; Chesapeake Bay Tunnel near Norfolk, Virginia; Washburn Tunnel in Houston, Texas; continuously reinforced concrete pavement (CRCP) on I-20 in Ft. Worth, Texas; and bonded concrete overlays (BCOs) at the George Bush International Airport in Houston, Texas.

Table N-1. Detailed defect dimensions (dim.), depth, and cover and spacing (C & S). All units in inches.

Note. C = concrete; SC = shotcrete; WF = water-filled; AF = air-filled.
*Two mats of No. 5 Rebar, 4 inches from top and bottom, 8 inches on center.

SPECIMEN NAME & MATERIAL	ACTUAL REINF. C & S	MEASURED REINF. C & S	TYPE OF DEFECT	ACTUAL DIM. OF DEFECT	ACTUAL DEPTH OF DEFECT	MEASURED DIM. OF DEFECT	MEASURED DEPTH OF DEFECT	ACTUAL SPECIMEN DEPTH	MEASURED SPECIMEN DEPTH
Alpha, C	None	N/A	None	N/A	N/A	N/A	N/A	12	12.4
Beta, C	*	4.0 @ 8.0 OC	None	N/A	N/A	N/A	N/A	18	17.6
Gamma, C	*	4.3 @ 7.9 OC	None	N/A	N/A	N/A	N/A	12	11.7
Delta, C	None	N/A	None	N/A	N/A	N/A	N/A	24	23.6
Epsilon, C	*	4.1 @ 8 OC	None	N/A	N/A	N/A	N/A	24	23.3
Zeta, C	*	3.8 @ 7.9 OC	None	N/A	N/A	N/A	N/A	15	14.1
Eta, C	*	4.5 @ 7.9 OC	plastic	12 x 12 x 1	2	11.7 x 12.8	2.3	15	14.2
Theta, C	*	4.4 @ 8.0 OC	plastic	12 x 12 x 1	3	11.7 x 13.5	3.5	15	13.9
Iota, C	*	4.0 @ 8.0 OC	plastic	12 x 12 x 1	1	7.8 x 12.3	1.7	15	13.0
Kappa, C	*	3.8 @ 8.0 OC	Styrofoam	12 x 12 x 1	8	15.7 x 15.7	8.0	15	14.7
Lambda, C	*	3.7 @ 8.1 OC	WF void	12 x 12	8	16.5 x 15.4	6.5-8.8	15	14.6
A, SC	None	N/A	None	N/A	N/A	N/A	N/A	4	3.9
B, SC	None	N/A	None	N/A	N/A	N/A	N/A	6	5.7
C, SC	None	N/A	None	N/A	N/A	N/A	N/A	8	6.8
D, SC	**	6.9	AF void	17.25 x 14.75	7-5/8	12.4 x 12.1	7.6	12	11.3
E, SC	**	6.4	WF void	15.75x 14.5	7-1/2	15.5 x 13.3	7.6	12	11.0
F, SC	**	6.7	AF void	17.125 x14.75	3	18.1 x 15.6	3.5	12	11.2
G, SC	**	6.8	WF void	15.5 x 14.25	3	16.0 x 14.7	4.2	12	10.7
H, SC	**	6.4	Thin cloth	12 x 12	8	14.0 x 10.7	7.2	12	10.2
I, SC	**	5.7	Thin cloth	12 x 12	4	11.0 x 14.0	3.9	12	10.4
J, SC	**	6.1	Thin cloth	12 x 12	3	13.1 x 12.0	2.9	12	10.4
K, SC	**	5.6	Thin cloth	12 x 12	2	12.3 x 13.4	3.1	12	10.2
L, SC	**	5.6	Thin cloth	12 x 12	1	14.0 x 13.3	Very shallow	12	10.3
M, SC	**	5.8	None	N/A	N/A	N/A	N/A	12	10.4
A2, C	***	N/A	None	N/A	N/A	N/A	N/A	N/A	N/A
B2, C	***	N/A	1 clay lump	6-ø x 2	~ 6	6.1	6.3	N/A	N/A
C2, C	***	N/A	6 clay lumps	4-ø x 2	~3, 6, 9	3.1-4.1	2.7, 5.4, 8.5	N/A	N/A
D2, C	***	6.0 @ 8.0 OC	None	N/A	N/A	N/A	N/A	N/A	N/A
E2, C	***	6.0 @ 8.0 OC	1 clay lump	6-ø x 2	~ 6	4.2	4.6	N/A	N/A
F2, C	***	6.0 @ 8.0 OC	6 clay lumps	4-ø x 2	~3, 6, 9	2.9-3.9	2.4, 5.4, 7.8	N/A	N/A

**One lattice girder in center of slab, sitting on bottom form, centroid of upper bar 5.25 inches from bottom, or ~6.25 inches from top.
***One mat of No. 5 Rebar, 6 inches from top, 8 inches on center.

	Eisenhower Memorial Tunnel, Dillon, CO		Texas A&M Transportation Institute

Defects	Notes	Reinf. Detail	V_{shear} = 2751 m/s
No significant defect noticed, except for strip of area (~9.4" wide, 16.2" deep) consistently found in other maps. Possibly structural steel reinforcement.	Backsurface not discernible. Area tested as representative of sound concrete.	Hoop reinf: ~4.2" deep @ ~9.9" on center. Longitudinal reinf: below hoop reinforcement.	X-step: 150 mm Y-step: 50 mm Max Depth: 1000 mm Frequency: 50 kHz
			Dillon, CO Eisenhower Tunnel ET 10.4-1, 2 Segment 8 TAMU/TTI 10/2011

Figure N-1. Images of test site ET 10.4-1, 2.

Eisenhower Memorial Tunnel, Dillon, CO			Texas A&M Transportation Institute

Defects	Notes	Reinf. Detail	
No significant defect noticed, except for strip of area (~9.4" wide, 16.2" deep) consistently found in other maps. Possibly structural steel reinforcement.	Backsurface not discernible. Area tested as representative of sound concrete.	Hoop reinf: ~4.2" deep @ ~9.9" on center. Longitudinal reinf: below hoop reinforcement.	V_{shear} = 2751 m/s X-step: 150 mm Y-step: 50 mm Max Depth: 1000 mm Frequency: 50 kHz
			Dillon, CO Eisenhower Tunnel ET 10.4-1, 2 Segment 8 TAMU/TTI 10/2011

Figure N-2. UST images of test site ET 10.4-1, 2.

Eisenhower Memorial Tunnel, Dillon, CO			Texas A&M Transportation Institute

Defects	Notes	Reinf. Detail	
No significant defect noticed, except for strip of area (~12.2" wide, 17.2" deep) consistently found in other maps. Possibly steel structural reinforcement.	Backsurface not discernible. Area tested because of surface cracking and crazing, nearby stalactite formation. Could not test over stalactite crack due to obtrusions.	Hoop reinf: ~3.7"-5.1" deep @ ~10.1" on center. Longitudinal reinf: below hoop reinforcement.	V_{shear} = 2751 m/s X-step: 150 mm Y-step: 50 mm Max Depth: 750 mm Frequency: 50 kHz
			Dillon, CO Eisenhower Tunnel ET 10.4-3 Segment 8 TAMU/TTI 10/2011

Figure N-3. Image of test site 10.4-3.

Eisenhower Memorial Tunnel, Dillon, CO

Texas A&M Transportation Institute

Defects	Notes	Reinf. Detail	
No significant defect noticed, except for strip of area (~12.2" wide, 17.2" deep) consistently found in other maps. Possibly steel structural reinforcement.	Backsurface not discernible. Area tested because of surface cracking and crazing, nearby stalactite formation. Could not test over stalactite crack due to obtrusions.	Hoop reinf: ~3.7"-5.1" deep @ ~10.1" on center. Longitudinal reinf: below hoop reinforcement.	V_{shear} = 2751 m/s X-step: 150 mm Y-step: 50 mm Max Depth: 750 mm Frequency: 50 kHz
			Dillon, CO Eisenhower Tunnel ET 10.4-3 Segment 8 TAMU/TTI 10/2011

Figure N-4. UST images of test site 10.4-3.

Eisenhower Memorial Tunnel, Dillon, CO			Texas A&M Transportation Institute

Defects	Notes	Reinf. Detail	V_{shear} = 2751 m/s
No significant defect noticed, except for strip of area (~13.5" wide, 16.1" deep) consistently found in other maps. Possibly steel structural reinforcement.	Backsurface not discernible. Area tested because of surface cracking and crazing and nearby joint.	Hoop reinf: ~4.1" deep @ ~10.1" on center. Longitudinal reinf: below hoop reinforcement.	X-step: 150 mm Y-step: 50 mm Max Depth: 750 mm Frequency: 50 kHz
			Dillon, CO Eisenhower Tunnel ET 10.4-4, 5 Segment 10 TAMU/TTI 10/2011

Figure N-5. Image of test site ET 10.4-4, 5.

| | Eisenhower Memorial Tunnel, Dillon, CO | | Texas A&M Transportation Institute |

Defects	Notes	Reinf. Detail	
No significant defect noticed, except for strip of area (~13.5" wide, 16.1" deep) consistently found in other maps. Possibly steel structural reinforcement.	Backsurface not discernible. Area tested because of surface cracking and crazing and nearby joint.	Hoop reinf: ~4.1" deep @ ~10.1" on center. Longitudinal reinf: below hoop reinforcement.	V_{shear} = 2751 m/s X-step: 150 mm Y-step: 50 mm Max Depth: 750 mm Frequency: 50 kHz
			Dillon, CO Eisenhower Tunnel ET 10.4-4, 5 Segment 10 TAMU/TTI 10/2011

Figure N-6. UST images of test site ET 10.4-4, 5.

	Hanging Lake Tunnel, Glenwood Springs, CO		Texas A&M Transportation Institute
Defects	Notes	Reinf. Detail	Vshear = 2159 m/s
Apparent delamination extending 12.3" deep, originating from surface crack; possibly connecting to another crack located approximately 35" to the right of surface crack	Backsurface possibly seen at 27.6" in depth. Severe cracking. Area also tested by BAM.	Hoop reinf: 4.6"- 6.2" deep @ 15.7" on center. Longitudinal reinf: above and possibly below hoop reinforcement @ 14.1" on center.	X-step: 150 mm Y-step: 50 mm Max Depth: 2500 mm Frequency: 50 kHz
			Glenwood Springs, CO Hanging Lake Tunnel HLT 10.5-1, 2, 3 Segment 57 + 3.4 TAMU/TTI 10/2011

Figure N-7. Image of test site HLT 10.5-1, 2, 3.

Hanging Lake Tunnel, Glenwood Springs, CO

Texas A&M Transportation Institute

Defects	Notes	Reinf. Detail	
Apparent delamination extending 12.3" deep, originating from surface crack; possibly connecting to another crack located approximately 35" to the right of surface crack	Backsurface possibly seen at 27.6" in depth. Severe cracking. Area also tested by BAM.	Hoop reinf: 4.6"- 6.2" deep @ 15.7" on center. Longitudinal reinf: above and possibly below hoop reinforcement @ 14.1" on center.	Vshear = 2159 m/s X-step: 150 mm Y-step: 50 mm Max Depth: 2500 mm Frequency: 50 kHz Glenwood Springs, CO Hanging Lake Tunnel HLT 10.5-1, 2, 3 Segment 57 + 3.4 TAMU/TTI 10/2011

Delamination emanating from surface
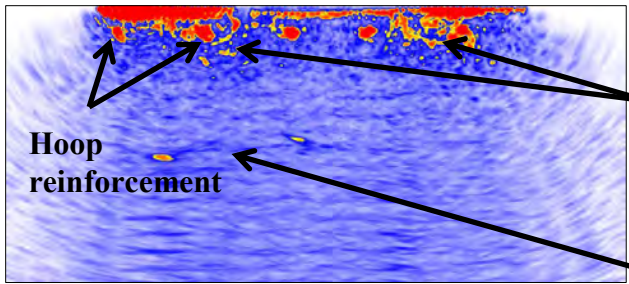
Hoop reinforcement

Backwall reflection or bottom layer of reinforcement

B-Scan
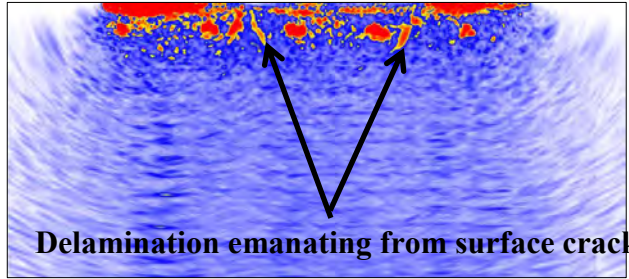
Delamination emanating from surface cracks

B-Scan

(a)

(b)

(c)
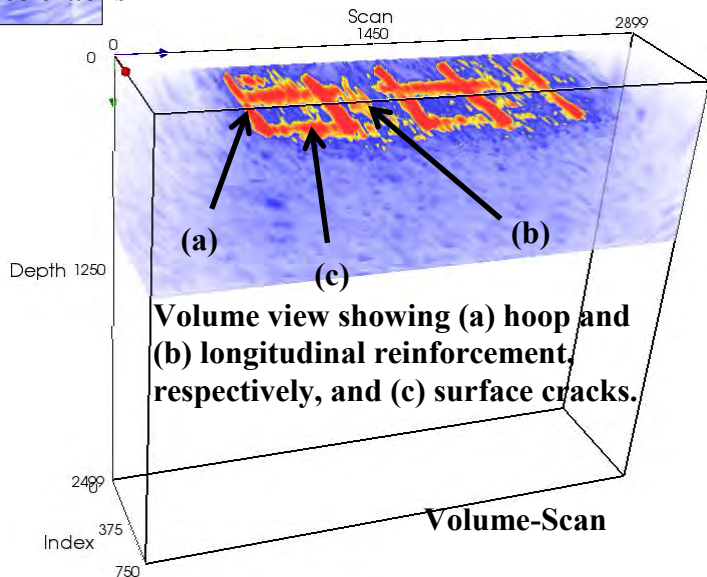
Volume view showing (a) hoop and (b) longitudinal reinforcement, respectively, and (c) surface cracks.

Volume-Scan

Figure N-8. UST images of test site HLT 10.5-1, 2, 3.

Hanging Lake Tunnel, Glenwood Springs, CO

Texas A&M Transportation Institute

Defects	Notes	Reinf. Detail	
Suspected debonding around east (right) side of joint. Surface crack around area might support this. Suspected debonding extends a maximum of 9" deep.	Backsurface not detected. Area tested because of natural joint. This map should be extended east to detail more of possible debonding.	Hoop reinf: ~3.6" deep on center.	Vshear = 2159 m/s X-step: 150 mm Y-step: 50 mm Max Depth: 1000 mm Frequency: 50 kHz Glenwood Springs, CO Hanging Lake Tunnel HLT 10.5-4 Segments 54/55 Joint TAMU/TTI 10/2011

Figure N-9. Images of test site HLT 10.5-4.

Hanging Lake Tunnel, Glenwood Springs, CO

Texas A&M Transportation Institute

Defects	Notes	Reinf. Detail	
Suspected debonding around east (right) side of joint. Surface crack around area might support this. Suspected debonding extends a maximum of 9" deep.	Backsurface not detected. Area tested because of natural joint. This map should be extended east to detail more of possible debonding.	Hoop reinf: ~3.6" deep on center.	Vshear = 2159 m/s X-step: 150 mm Y-step: 50 mm Max Depth: 1000 mm Frequency: 50 kHz Glenwood Springs, CO Hanging Lake Tunnel HLT 10.5-4 Segments 54/55 Joint TAMU/TTI 10/2011

Figure N-10. UST images of test site HLT 10.5-4.

Hanging Lake Tunnel, Glenwood Springs, CO

Texas A&M Transportation Institute

Defects	Notes	Reinf. Detail	
No significant defect noticeable. Backwall reflection varies 2-3" in depth. This may be lower reinforcement reflection or backwall delamination (see HLT 10.5-8,9).	Backsurface possibly 29.6"-32.4" deep. Area tested as a representation of sound cocnrete-no apparent cracks or defects.	Hoop reinf: ~4.3"-5.1" deep @ 16.6" on center. Longitudinal reinf: above hoop reinforcement.	Vshear = 2159 m/s X-step: 150 mm Y-step: 50 mm Max Depth: 2500 mm Frequency: 50 kHz
			Glenwood Springs, CO Hanging Lake Tunnel HLT 10.5-5, 6, 7 Segments 49 TAMU/TTI 10/2011

Figure N-11. Images of test site HLT 10.5-5, 6, 7.

Hanging Lake Tunnel, Glenwood Springs, CO

Texas A&M Transportation Institute

Defects	Notes	Reinf. Detail	
No significant defect noticeable. Backwall reflection varies 2-3" in depth. This may be lower reinforcement reflection or backwall delamination (see HLT 10.5-8,9).	Backsurface possibly 29.6"-32.4" deep. Area tested as a representation of sound cocnrete-no apparent cracks or defects.	Hoop reinf: ~4.3"-5.1" deep @ 16.6" on center. Longitudinal reinf: above hoop reinforcement.	Vshear = 2159 m/s X-step: 150 mm Y-step: 50 mm Max Depth: 2500 mm Frequency: 50 kHz
			Glenwood Springs, CO Hanging Lake Tunnel HLT 10.5-5, 6, 7 Segments 49 TAMU/TTI 10/2011

Very shallow, highly reflective region

Hoop reinforcement

Backwall

B-Scan

Hoop reinforcement

Backwall reflection

Volume-Scan

Figure N-12. UST images of test site HLT 10.5-5, 6, 7.

Hanging Lake Tunnel, Glenwood Springs, CO

Texas A&M Transportation Institute

Defects	Notes	Reinf. Detail	
No significant defect noticeable. Backwall reflection varies 2-3" in depth. This may be lower reinforcement reflection or backwall delamination (see HLT 10.5-8,9).	Backsurface possibly 24.5"- 29.6" deep. Area tested because of single surface crack. Note strong echoes emanating from region of reinforcement. This is possible sign of debonding.	Hoop reinf: ~3.7" deep @ 15.9" on center. Longitudinal reinf: below hoop reinforcement. .	Vshear = 2159 m/s X-step: 150 mm Y-step: 50 mm Max Depth: 2500 mm Frequency: 50 kHz
			Glenwood Springs, CO Hanging Lake Tunnel HLT 10.5-8, 9 Segments 49 TAMU/TTI 10/2011

Figure N-13. Image of test site HLT 10.5-8. 9.

Hanging Lake Tunnel, Glenwood Springs, CO

Texas A&M Transportation Institute

Defects	Notes	Reinf. Detail	
No significant defect noticeable. Backwall reflection varies 2-3" in depth. This may be lower reinforcement reflection or backwall delamination (see HLT 10.5-8,9).	Backsurface possibly 24.5"-29.6" deep. Area tested because of single surface crack. Note strong echoes emanating from region of reinforcement. This is possible sign of debonding.	Hoop reinf: ~3.7" deep @ 15.9" on center. Longitudinal reinf: below hoop reinforcement. .	Vshear = 2159 m/s X-step: 150 mm Y-step: 50 mm Max Depth: 2500 mm Frequency: 50 kHz
			Glenwood Springs, CO Hanging Lake Tunnel HLT 10.5-8, 9 Segments 49 TAMU/TTI 10/2011

Figure N-14. UST images of test site HLT 10.5-8, 9.

	Hanging Lake Tunnel, Glenwood Springs, CO		Texas A&M Transportation Institute

Defects	Notes	Reinf. Detail	Vshear = 2159 m/s
Significant delamination/debonding discovered which stretched over 11', ranging from 8"-20" below the surface.	Backsurface not discernible due to high presence of delamination/debonding. Area tested because of severe surface cracking.	Hoop reinf: ~2.9"-5.1" deep @ ~16.4" on center. Longitudinal reinf: above hoop reinforcement.	X-step: 150 mm Y-step: 50 mm Max Depth: 1000 mm Frequency: 50 kHz Glenwood Springs, CO Hanging Lake Tunnel HLT 10.5-10, 11, 12 Segment 55 TAMU/TTI 10/2011
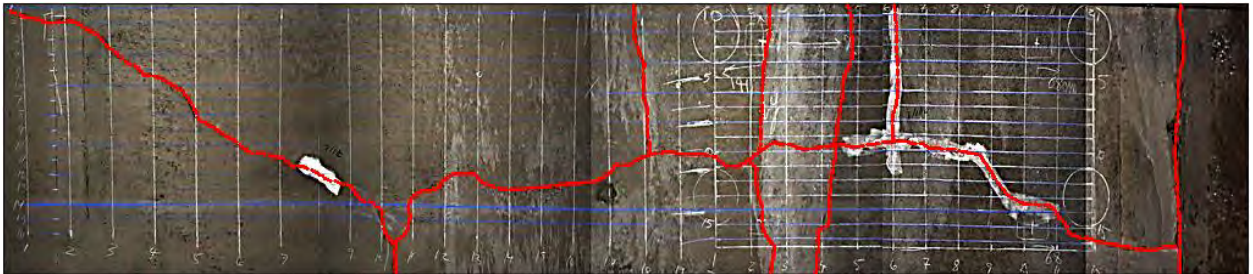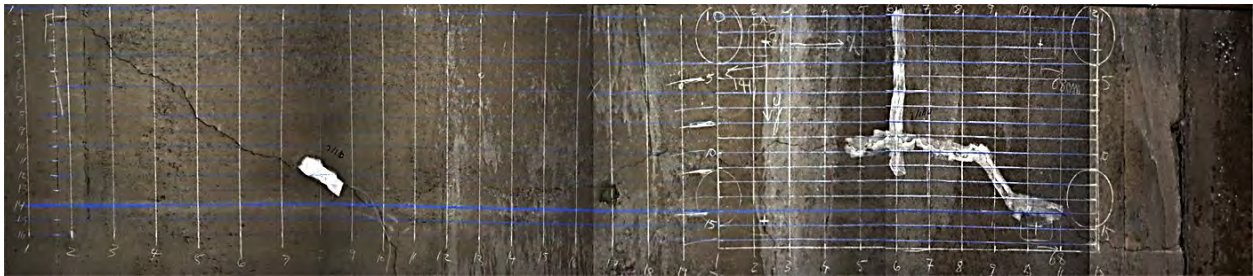
Figure N-15. Images of test site HLT 10.5-10, 11, 12.

Hanging Lake Tunnel, Glenwood Springs, CO			Texas A&M Transportation Institute

Defects	Notes	Reinf. Detail	Vshear = 2159 m/s
Significant delamination/debonding discovered which stretched over 11', ranging from 8"-20" below the surface.	Backsurface not discernible due to high presence of delamination/debonding. The B-scan below shows variance in depth and the C-scans show the horizontal spread of the delamination/debonding.	Hoop reinf: ~2.9"-5.1" deep @ ~16.4" on center. Longitudinal reinf: above hoop reinforcement.	X-step: 150 mm Y-step: 50 mm Max Depth: 1000 mm Frequency: 50 kHz
			Glenwood Springs, CO Hanging Lake Tunnel HLT 10.5-10, 11, 12 Segment 55 TAMU/TTI 10/2011

Figure N-16. UST images of test site HLT 10.5-10, 11, 12.

Hanging Lake Tunnel, Glenwood Springs, CO			Texas A&M Transportation Institute

Defects	Notes	Reinf. Detail	
No significant defect noticed.	Backsurface not discernible. Area tested on surface of tile. Hair-line crack present.	Hoop reinf: ~5.1" deep @ ~16.3" on center. Longitudinal reinf: below and possible above hoop reinforcement @ ~14.0" on center.	Vshear = 2159 m/s X-step: 150 mm Y-step: 50 mm Max Depth: 1000 mm Frequency: 50 kHz
			Glenwood Springs, CO Hanging Lake Tunnel HLT 10.5-13 Interior Tile Lining TAMU/TTI 10/2011

Figure N-17. Images of test site HLT 10.5-13.

Hanging Lake Tunnel, Glenwood Springs, CO			Texas A&M Transportation Institute

Defects	Notes	Reinf. Detail	Vshear = 2159 m/s
No significant defect noticed.	Backsurface not discernible. Area tested on surface of tile. Hair-line crack present.	Hoop reinf: ~5.1" deep @ ~16.3" on center. Longitudinal reinf: below and possible above hoop reinforcement @ ~14.0" on center.	X-step: 150 mm Y-step: 50 mm Max Depth: 1000 mm Frequency: 50 kHz
			Glenwood Springs, CO Hanging Lake Tunnel HLT 10.5-13 Interior Tile Lining TAMU/TTI 10/2011

Longitudinal reinforcement

Hoop reinforcement

B-Scan

C-Scan

Longitudinal reinforcement

Volume-Scan

Figure N-18. UST images of test site HLT 10.5-13.

Chesapeake Channel Tunnel, Norfolk, VA			Texas A&M Transportation Institute

Defects	Notes	Reinf. Detail	
No significant defect noticed.	Backsurface at ~24.7" deep. Area tested as representative of sound concrete. Also tested because GPR data revealed different steel detail (c.f. with CBBT 10.11-3,4).	Hoop reinf: ~2.4" deep @ ~4.4" on center. Longitudinal reinf: below hoop reinforcement.	Vshear = 2710 m/s X-step: 150 mm Y-step: 50 mm Max Depth: 1000 mm Frequency: 50 kHz
			Norfolk, VA Chesapeake Tunnel CBBT 10.11-1, 2 Sta. 471+80 TAMU/TTI 10/2011

Figure N-19. Images of test site CBBT 10.11-1, 2.

Chesapeake Channel Tunnel, Norfolk, VA

Texas A&M
Transportation
Institute

Defects	Notes	Reinf. Detail	
No significant defect noticed.	Backsurface at ~24.7" deep. Area tested as representative of sound concrete. Also tested because GPR data revealed different steel detail (c.f. with CBBT 10.11-3,4).	Hoop reinf: ~2.4" deep @ ~4.4" on center. Longitudinal reinf: below hoop reinforcement.	Vshear = 2710 m/s X-step: 150 mm Y-step: 50 mm Max Depth: 1000 mm Frequency: 50 kHz
			Norfolk, VA Chesapeake Tunnel CBBT 10.11-1, 2 Sta. 471+80 TAMU/TTI 10/2011

C-Scan

Hoop reinforcement

B-Scan

Backwall reflection

Volume-Scan

Figure N-20. UST images of test site CBBT 10.11-1, 2.

Chesapeake Channel Tunnel, Norfolk, VA			Texas A&M Transportation Institute
Defects	Notes	Reinf. Detail	Vshear = 2710 m/s
No significant defect noticed.	Backsurface at ~24.4" deep. Area tested as representative of sound concrete. Also tested because GPR data revealed different steel detail (c.f. with CBBT 10.11-1,2).	Hoop reinf: ~2.3" deep @ ~11.8" on center. Longitudinal reinf: below hoop reinforcement.	X-step: 150 mm Y-step: 50 mm Max Depth: 1000 mm Frequency: 50 kHz
			Norfolk, VA Chesapeake Tunnel CBBT 10.11-3, 4 Sta. 473+56 TAMU/TTI 10/2011

Figure N-21. Images of test site CBBT 10.11-3, 4.

Chesapeake Channel Tunnel, Norfolk, VA

Texas A&M Transportation Institute

Defects	Notes	Reinf. Detail	
No significant defect noticed.	Backsurface at ~24.4" deep. Area tested as representative of sound concrete. Also tested because GPR data revealed different steel detail (c.f. with CBBT 10.11-1,2).	Hoop reinf: ~2.3" deep @ ~11.8" on center. Longitudinal reinf: below hoop reinforcement.	Vshear = 2710 m/s X-step: 150 mm Y-step: 50 mm Max Depth: 1000 mm Frequency: 50 kHz
			Norfolk, VA Chesapeake Tunnel CBBT 10.11-3, 4 Sta. 473+56 TAMU/TTI 10/2011

C-Scan

Longitudinal reinforcement

Hoop reinforcement

B-Scan

Backwall reflection

Volume-Scan

Figure N-22. UST images of test site CBBT 10.11-3, 4.

Chesapeake Channel Tunnel, Norfolk, VA			Texas A&M Transportation Institute

Defects	Notes	Reinf. Detail	Vshear = 2710 m/s
Significant shallow defects, such as shallow cracks (~9" deep) and possibly shallow delaminations (~2" deep), which seem to produce the ringing.	Backsurface at ~24.1" deep. Area tested because of live crack. Significant ringing may suggest debonding of longitudinal reinforcement.	Hoop reinf: ~2.0"-2.6" deep @ ~12.0" on center. Longitudinal reinf: below hoop reinforcement.	X-step: 150 mm Y-step: 50 mm Max Depth: 1000 mm Frequency: 50 kHz
			Norfolk, VA Chesapeake Tunnel CBBT 10.11-5 Sta. 474+27 TAMU/TTI 10/2011

Figure N-23. Images of test site CBBT 10.11-5.

N-25

Chesapeake Channel Tunnel, Norfolk, VA			Texas A&M Transportation Institute

Defects	Notes	Reinf. Detail	
Significant shallow defects, such as shallow cracks (~9" deep) and possibly shallow delaminations (~2" deep), which seem to produce the ringing.	Backsurface at ~24.1" deep. Area tested because of live crack. Significant ringing may suggest debonding of longitudinal reinforcement.	Hoop reinf: ~2.0"-2.6" deep @ ~12.0" on center. Longitudinal reinf: below hoop reinforcement.	Vshear = 2710 m/s X-step: 150 mm Y-step: 50 mm Max Depth: 1000 mm Frequency: 50 kHz
			Norfolk, VA Chesapeake Tunnel CBBT 10.11-5 Sta. 474+27 TAMU/TTI 10/2011

Figure N-24. UST images of test site CBBT 10.11-5.

Chesapeake Channel Tunnel, Norfolk, VA			Texas A&M Transportation Institute

Defects	Notes	Reinf. Detail	
Hammer tapping revealed hollow region as shown by shallow reflective region in the C- and B-scans. Significant cupped-shaped delaminations as deep as 19.2"	Backsurface at 24.1"-26.0" deep. Area tested because of high dielectric reading from GPR scan. No significant visual distress noticeable, but hammer sounding revealed shallow delamination in Region II.	Hoop reinf: ~2.2" deep @ ~12.1" on center. Longitudinal reinf: below hoop reinforcement @ 16.2" on center.	Vshear = 2710 m/s X-step: 150 mm Y-step: 50 mm Max Depth: 1000 mm Frequency: 50 kHz
			Norfolk, VA Chesapeake Tunnel CBBT 10.11-7, 8 (Region II) Sta. 486+67 TAMU/TTI 10/2011

Figure N-25. Images of test site CBBT 10.11-7, 8.

Chesapeake Channel Tunnel, Norfolk, VA

Texas A&M Transportation Institute

Defects	Notes	Reinf. Detail	
Hammer tapping revealed hollow region as shown by shallow reflective region in the C- and B-scans. Significant cupped-shaped delaminations as deep as 19.2"	Backsurface at 24.1"-26.0" deep. Area tested because of high dielectric reading from GPR scan. No significant visual distress noticeable, but hammer sounding revealed shallow delamination in Region II.	Hoop reinf: ~2.2" deep @ ~12.1" on center. Longitudinal reinf: below hoop reinforcement @ 16.2" on center.	Vshear = 2710 m/s X-step: 150 mm Y-step: 50 mm Max Depth: 1000 mm Frequency: 50 kHz
			Norfolk, VA Chesapeake Tunnel CBBT 10.11-7, 8 (Region II) Sta. 486+67 TAMU/TTI 10/2011

B-Scan

C-Scan

Deep delamination

Shallow delamination

Hoop reinforcement

Longitudinal reinforcement

Volume-Scan

Backwall reflection

Volume-Scan (Isosurface rendering)

Figure N-26. UST images of test site CBBT 10.11-7, 8.

Chesapeake Channel Tunnel, Norfolk, VA			Texas A&M Transportation Institute

Defects	Notes	Reinf. Detail	
Significant cracks up to 8.6" deep.	Backsurface at 24.3"-26.0" deep. Area tested because of high dielectric reading from GPR scan. No significant visual distress noticeable.	Hoop reinf: ~2.0"-3.0" deep @ ~12.2" on center. Longitudinal reinf: below hoop reinforcement @ 19.8" on center.	Vshear = 2710 m/s X-step: 150 mm Y-step: 50 mm Max Depth: 1000 mm Frequency: 50 kHz
			Norfolk, VA Chesapeake Tunnel CBBT 10.11-9 (Region I) Sta. 486+67 TAMU/TTI 10/2011

Figure N-27. Images of test site CBBT 10.11-9.

Chesapeake Channel Tunnel, Norfolk, VA

Texas A&M
Transportation
Institute

Defects	Notes	Reinf. Detail	
Significant cracks up to 8.6" deep.	Backsurface at 24.3"-26.0" deep. Area tested because of high dielectric reading from GPR scan. No significant visual distress noticeable.	Hoop reinf: ~2.0"-3.0" deep @ ~12.2" on center. Longitudinal reinf: below hoop reinforcement @ 19.8" on center.	Vshear = 2710 m/s X-step: 150 mm Y-step: 50 mm Max Depth: 1000 mm Frequency: 50 kHz
			Norfolk, VA Chesapeake Tunnel CBBT 10.11-9 (Region I) Sta. 486+67 TAMU/TTI 10/2011

Shallow defects

Longitudinal reinforcement

Ringing from shallow defects

Backwall reflection

B-Scan

C-Scan

Shallow defects

Hoop reinforcement

Volume-Scan

Volume-Scan (Isosurface rendering)

Figure N-28. UST images of test site CBBT 10.11-9.

N-30

Chesapeake Channel Tunnel, Norfolk, VA			Texas A&M Transportation Institute

Defects	Notes	Reinf. Detail	
Heavy ringing made internal inspection difficult. Possible deep delamination (~17.7" deep and possibly 19" wide) and evidence of surface crack extending ~9.8" deep.	Backsurface at 22.7"-25.9" deep. Area tested because of large surface crack and small area of water intrusion.	Hoop reinf: ~2.7"-3.2" deep @ ~11.7"-12.4" on center. Second layer of hoop reinf. directly beneath top layer. Longitudinal reinf. below first layer of hoop reinforcement @ ~17.1" on center.	Vshear = 2710 m/s X-step: 150 mm Y-step: 50 mm Max Depth: 1000 mm Frequency: 50 kHz
			Norfolk, VA Chesapeake Tunnel CBBT 10.11-10 Sta. 491+25 TAMU/TTI 10/2011

Figure N-29. Images of test site CBBT 10.11-10.

Chesapeake Channel Tunnel, Norfolk, VA			Texas A&M Transportation Institute

Defects	Notes	Reinf. Detail	
Heavy ringing made internal inspection difficult. Possible deep delamination (~17.7" deep and possibly 19" wide) and evidence of surface crack extending ~9.8" deep.	Backsurface at 22.7"-25.9" deep. Area tested because of large surface crack and small area of water intrusion.	Hoop reinf: ~2.7"-3.2" deep @ ~11.7"-12.4" on center. Second layer of hoop reinf. directly beneath top layer. Longitudinal reinf. below first layer of hoop reinforcement @ ~17.1" on center.	Vshear = 2710 m/s X-step: 150 mm Y-step: 50 mm Max Depth: 1000 mm Frequency: 50 kHz
			Norfolk, VA Chesapeake Tunnel CBBT 10.11-10 Sta. 491+25 TAMU/TTI 10/2011

Figure N-30. UST images of test site CBBT 10.11-10.

Chesapeake Channel Tunnel, Norfolk, VA			Texas A&M Transportation Institute
Defects	Notes	Reinf. Detail	Vshear = 2710 m/s
Heavy ringing made internal inspection difficult. Possible deep delamination (~15.7" deep and 20.3" wide).	Backsurface at 25.0"-30.0" deep. Area tested was tiled lining over a joint where tile has debonded. Determined area via hammer sounding.	Hoop reinf: ~4.3"-7.7" deep @ ~12.1" on center. Second layer of hoop reinf. seen beneath top layer in one location-possibly splice area. Longitudinal reinf. below hoop reinforcement @ ~13.0" on center.	X-step: 110 mm Y-step: 110 mm Max Depth: 750 mm Frequency: 50 kHz
			Norfolk, VA Chesapeake Tunnel CBBT TILE 10.11-11 Approx. Sta. 488 TAMU/TTI 10/2011

Figure N-31. Images of test site CBBT TILE 10.11-11.

Chesapeake Channel Tunnel, Norfolk, VA			Texas A&M Transportation Institute

Defects	Notes	Reinf. Detail	
Heavy ringing made internal inspection difficult. Possible deep delamination (~15.7" deep and 20.3" wide).	Backsurface at 25.0"-30.0" deep. Area tested was tiled lining over a joint where tile has debonded. Determined area via hammer sounding.	Hoop reinf: ~4.3"-7.7" deep @ ~12.1" on center. Second layer of hoop reinf. seen beneath top layer in one location-possibly splice area. Longitudinal reinf: below hoop reinforcement @ ~13.0" on center.	Vshear = 2710 m/s X-step: 110 mm Y-step: 110 mm Max Depth: 750 mm Frequency: 50 kHz Norfolk, VA Chesapeake Tunnel CBBT TILE 10.11-11 Approx. Sta. 488 TAMU/TTI 10/2011

Hoop reinforcement

B-Scan

Backwall reflection

B-Scan

Longitudinal reinforcement or duct

B-Scan

C-Scan

Longitudinal reinforcement or duct

Deep delaminations

Hoop reinforcement

Backwall reflection

Volume-Scan
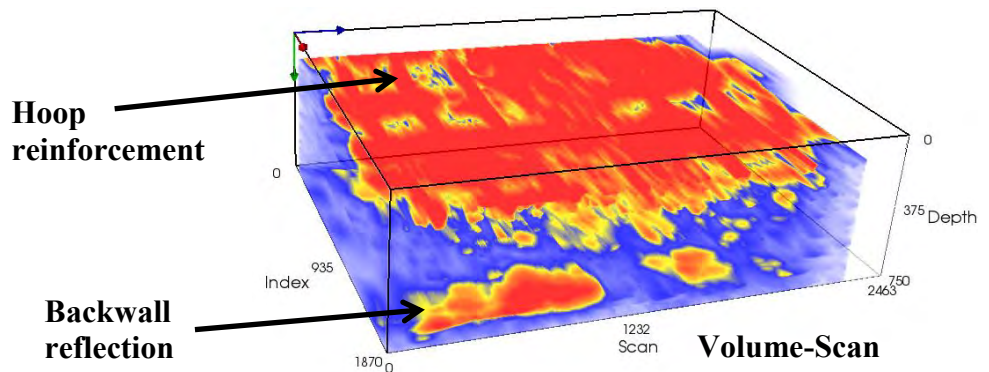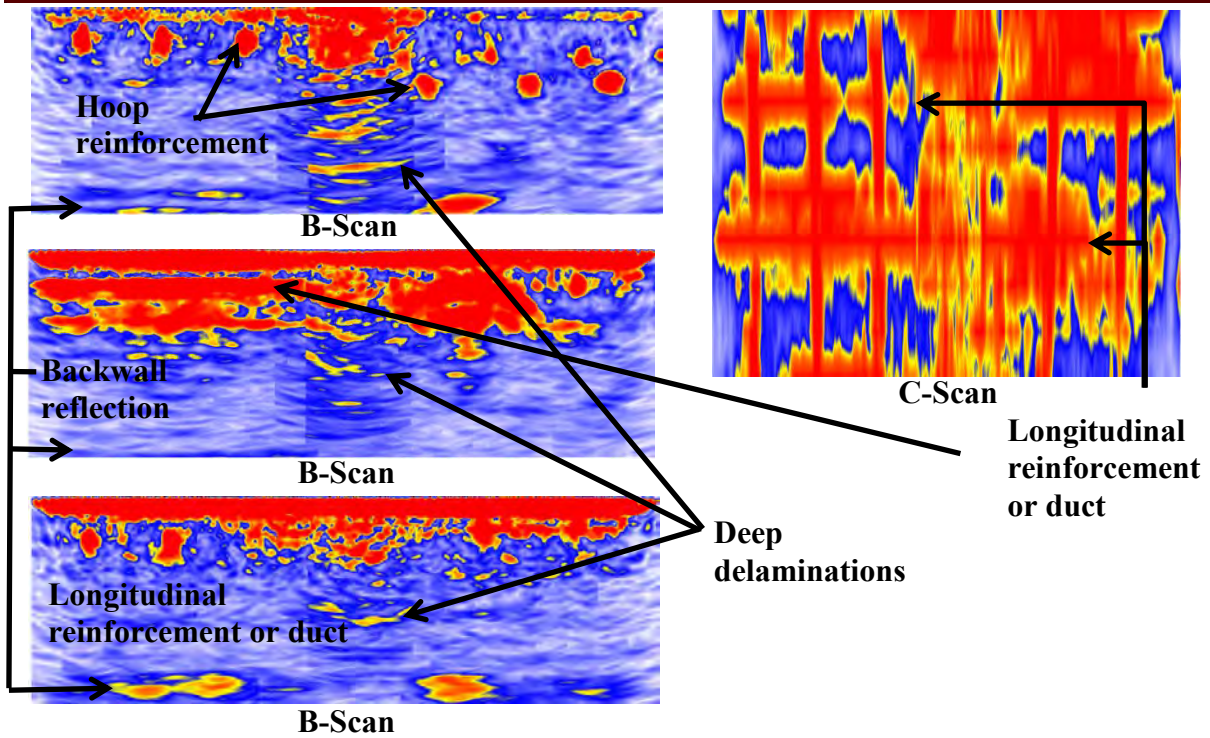
Figure N-32. UST images of test site CBBT TILE 10.11-11.

Chesapeake Channel Tunnel, Norfolk, VA			Texas A&M Transportation Institute

Defects	Notes	Reinf. Detail	Vshear = 2710 m/s
Heavy ringing made internal inspection difficult. Possibly multiple cracks as deep as 8.6".	Backsurface at 28.1"-31.0" deep. Area tested was tiled lining. Hammer sounding did not indicate debonding, but SPACETEC infrared scans showed area of question..	Hoop reinf: ~4.8"-9.4" deep @ ~11.7" on center. Longitudinal reinf: below and possibly above hoop reinforcement.	X-step: 110 mm Y-step: 110 mm Max Depth: 1000 mm Frequency: 50 kHz
			Norfolk, VA Chesapeake Tunnel CBBT TILE 10.11-12 Sta. 486-09 TAMU/TTI 10/2011

Figure N-33. Images of test site CBBT TILE 10.11-12.

Chesapeake Channel Tunnel, Norfolk, VA

Texas A&M Transportation Institute

Defects	Notes	Reinf. Detail	
Heavy ringing made internal inspection difficult. Possibly multiple cracks as deep as 8.6".	Backsurface at 28.1"-31.0" deep. Area tested was tiled lining. Hammer sounding did not indicate debonding, but SPACETEC infrared scans showed area of question..	Hoop reinf: ~4.8"-9.4" deep @ ~11.7" on center. Longitudinal reinf: below and possibly above hoop reinforcement.	Vshear = 2710 m/s X-step: 110 mm Y-step: 110 mm Max Depth: 1000 mm Frequency: 50 kHz Norfolk, VA Chesapeake Tunnel CBBT TILE 10.11-12 Sta. 486-09 TAMU/TTI 10/2011

Figure N-34. UST images of test site CBBT TILE 10.11-12.

Chesapeake Channel Tunnel, Norfolk, VA

Texas A&M Transportation Institute

Defects	Notes	Reinf. Detail	
Apparent delamination 20.2" deep and 27.4" wide.	Backsurface at 26.6"-28.4" deep. Area tested because of surface crack and varying backwall reflections from single-point evaluations.	Hoop reinf: ~2.0"-3.6" deep @ 12.1" on center. Longitudinal reinf: below hoop reinforcment.	Vshear = 2710 m/s X-step: 150 mm Y-step: 50 mm Max Depth: 1000 mm Frequency: 50 kHz
			Norfolk, VA Chesapeake Tunnel CBBT 10.13 Sta. 481+76 TAMU/TTI 10/2011

Figure N-35. Images of test site CBBT 10.11-13.

Chesapeake Channel Tunnel, Norfolk, VA

Texas A&M Transportation Institute

Defects	Notes	Reinf. Detail	
Apparent delamination 20.2" deep and 27.4" wide.	Backsurface at 26.6"-28.4" deep. Area tested because of surface crack and varying backwall reflections from single-point evaluations.	Hoop reinf: ~2.0"-3.6" deep @ 12.1" on center. Longitudinal reinf: below hoop reinforcment.	Vshear = 2710 m/s X-step: 150 mm Y-step: 50 mm Max Depth: 1000 mm Frequency: 50 kHz
			Norfolk, VA Chesapeake Tunnel CBBT 10.13 Sta. 481+76 TAMU/TTI 10/2011

C-Scan

Longitudinal reinforcement

Hoop reinforcement

C-Scan

Deep delamination

B-Scan

Volume-Scan

Backwall reflection

Figure N-36. UST images of test site CBBT 10.11-13.

Washburn Tunnel, Houston, TX			Texas A&M Transportation Institute
Defects	Notes	Reinf. Detail	Vshear = 2710 m/s
Significant shallow debonding/delamination. Deep delamination approximately 13" deep (B-scan image).	Backsurface not discernible. Area tested because of debonding located via hammer sounding.	Hoop reinf: ~6.8" deep.	X-step: 110 mm Y-step: 110 mm Max Depth: 500 mm Frequency: 50 kHz
			Houston, TX Washburn Tunnel WT 9.16-1 West Side TAMU/TTI 9/2011

Figure N-37. Images of test site WT 9.16-1.

N-39

Washburn Tunnel, Houston, TX			Texas A&M Transportation Institute

Defects	Notes	Reinf. Detail	Vshear = 2710 m/s
Significant shallow debonding/delamination. Deep delamination approximately 13" deep (B-scan image).	Backsurface not discernible. Area tested because of debonding located via hammer sounding.	Hoop reinf: ~6.8" deep.	X-step: 110 mm Y-step: 110 mm Max Depth: 500 mm Frequency: 50 kHz
			Houston, TX Washburn Tunnel WT 9.16-1 West Side TAMU/TTI 9/2011

B-Scan

C-Scan

Volume-Scan

Figure N-38. UST images of test site WT 9.16-1.

Washburn Tunnel, Houston, TX			Texas A&M Transportation Institute

Defects	Notes	Reinf. Detail	Vshear = 2710 m/s
Significant shallow and deep debonding/delamination. Delamination as deep as approximately 18" deep (B-scan image).	Backsurface not discernible. Area tested because of debonding located via hammer sounding.	Hoop reinf: ~4.8"-5.2" deep @ 12.2 on center. Longitudinal reinf: below hoop reinforcement.	X-step: 110 mm Y-step: 110 mm Max Depth: 500 mm Frequency: 50 kHz
			Houston, TX Washburn Tunnel WT 9.16-2 West Side TAMU/TTI 9/2011

Figure N-39. Images of test site WT 9.16-2.

Washburn Tunnel, Houston, TX

Defects	Notes	Reinf. Detail	
Significant shallow and deep debonding/delamination. Delamination as deep as approximately 18" deep (B-scan image).	Backsurface not discernible. Area tested because of debonding located via hammer sounding.	Hoop reinf: ~4.8"-5.2" deep @ 12.2 on center. Longitudinal reinf: below hoop reinforcement.	Vshear = 2710 m/s X-step: 110 mm Y-step: 110 mm Max Depth: 500 mm Frequency: 50 kHz
			Houston, TX Washburn Tunnel WT 9.16-2 West Side TAMU/TTI 9/2011

Hoop reinforcement

Delamination at reinforcement

Region below tile debonding

B-Scans

Shallow debonding

C-Scans

Volume-Scan

Figure N-40. UST images of test site WT 9.16-2.

Washburn Tunnel, Houston, TX			Texas A&M Transportation Institute
Defects	Notes	Reinf. Detail	Vshear = 2710 m/s
Significant delaminations/debonding throughout. Delaminations as deep as 10.7" below surface.	Backsurface not discernible. Area tested because of debonding located via hammer sounding.	Hoop reinf: ~4.9" deep @ 13.4" on center. Longitudinal reinf: below hoop reinforcement.	X-step: 110 mm Y-step: 110 mm Max Depth: 500 mm Frequency: 50 kHz
			Houston, TX Washburn Tunnel WT 9.16-3 West Side TAMU/TTI 9/2011

Figure N-41. Images of test site WT 9.16-3.

Washburn Tunnel, Houston, TX			Texas A&M Transportation Institute

Defects	Notes	Reinf. Detail	Vshear = 2710 m/s
Significant delaminations/debonding throughout. Delaminations as deep as 10.7" below surface.	Backsurface not discernible. Area tested because of debonding located via hammer sounding.	Hoop reinf: ~4.9" deep @ 13.4" on center. Longitudinal reinf: below hoop reinforcement.	X-step: 110 mm Y-step: 110 mm Max Depth: 500 mm Frequency: 50 kHz
			Houston, TX Washburn Tunnel WT 9.16-3 West Side TAMU/TTI 9/2011

Delaminations

Hoop reinforcement

B-Scans

C-Scans

Shallow debonding

Volume-Scan

Figure N-42. UST images of test site WT 9.16-3.

Washburn Tunnel, Houston, TX			Texas A&M Transportation Institute
Defects	Notes	Reinf. Detail	Vshear = 2710 m/s
Significant delaminations/debonding throughout. Possible delaminations 11.7" deep.	Backsurface not discernible. Area tested because of debonding located via hammer sounding.	Hoop reinf: ~4.7" deep @ 11.7" on center. Longitudinal reinf: below hoop reinforcement.	X-step: 110 mm Y-step: 110 mm Max Depth: 500 mm Frequency: 50 kHz
			Houston, TX Washburn Tunnel WT 9.16-4 West Side TAMU/TTI 9/2011

Figure N-43. Images of test site WT 9.16-4.

| Washburn Tunnel, Houston, TX | | | Texas A&M Transportation Institute |

Defects	Notes	Reinf. Detail	Vshear = 2710 m/s
Significant delaminations/debonding throughout. Possible delaminations 11.7" deep.	Backsurface not discernible. Area tested because of debonding located via hammer sounding.	Hoop reinf: ~4.7" deep @ 11.7" on center. Longitudinal reinf: below hoop reinforcement.	X-step: 110 mm Y-step: 110 mm Max Depth: 500 mm Frequency: 50 kHz
			Houston, TX Washburn Tunnel WT 9.16-4 West Side TAMU/TTI 9/2011

Figure N-44. UST images of test site WT 9.16-4.

| | Interstate 20, Ft. Worth, TX | | Texas A&M Transportation Institute |

Defects	Notes	Reinf. Detail	Vshear = 2770 m/s
Significant delamination on both sides of surface crack, ranging from 4.2"-5.0" from top surface.	Top layer of pavement 10.2" below surface. Area tested because of transverse surface cracking. Pavement depth confirmed by 2 cores, both indicating 10.2" thickness and one indicating 5.0" reinf.	Longitudinal reinf.: ~4.6"- 5.0" deep @ 5.6" on center. No transverse reinforcement located in this area.	X-step: 150 mm Y-step: 50 mm Max Depth: 500 mm Frequency: 50 kHz
			Ft. Worth, TX I-20 IH20 9.27-1 MP 426 + 0.5, RM 2871 TAMU/TTI 9/2011

Figure N-45. Images of test site IH20 9.27-1.

N-47

Interstate 20, Ft. Worth, TX			Texas A&M Transportation Institute

Defects	Notes	Reinf. Detail	Vshear = 2770 m/s
Significant delamination on both sides of surface crack, ranging from 4.2"-5.0" from top surface.	Top layer of pavement 10.2" below surface. Area tested because of transverse surface cracking. Pavement depth confirmed by 2 cores, both indicating 10.2" thickness and one indicating 5.0" reinf.	Longitudinal reinf.: ~4.6"- 5.0" deep @ 5.6" on center. No transverse reinforcement located in this area.	X-step: 150 mm
			Y-step: 50 mm
			Max Depth: 500 mm
			Frequency: 50 kHz
			Ft. Worth, TX
			I-20
			IH20 9.27-1
			MP 426 + 0.5, RM 2871
			TAMU/TTI 9/2011

Delamination

Top layer interface

Longitudinal reinforcement

B-Scans

C-Scan

Delamination

Volume-Scan

Figure N-46. UST images of test site IH20 9.27-1.

Interstate 20, Ft. Worth, TX			Texas A&M Transportation Institute

Defects	Notes	Reinf. Detail	Vshear = 2770 m/s
Significant delamination on both sides of surface crack, ranging from 4.5"-5.3" from top surface.	Top layer of pavement 10.4" below surface. Area tested because of transverse surface cracking. Pavement depth confirmed by 2 cores, indicating 9.4"-10.4" thickness.	Longitudinal reinf.: ~4.5"- 5.2" deep @ 7.1" on center. No transverse reinforcement located in this area.	X-step: 150 mm Y-step: 50 mm Max Depth: 500 mm Frequency: 50 kHz Ft. Worth, TX I-20 IH20 9.27-2 MP 426 + 0.5, RM 2871 TAMU/TTI 9/2011

Figure N-47. Images of test site IH20 9.27-2.

N-49

Interstate 20, Ft. Worth, TX			Texas A&M Transportation Institute

Defects	Notes	Reinf. Detail	Vshear = 2770 m/s
Significant delamination on both sides of surface crack, ranging from 4.5"-5.3" from top surface.	Top layer of pavement 10.4" below surface. Area tested because of transverse surface cracking. Pavement depth confirmed by 2 cores, indicating 9.4"-10.4" thickness.	Longitudinal reinf.: ~4.5"- 5.2" deep @ 7.1" on center. No transverse reinforcement located in this area.	X-step: 150 mm Y-step: 50 mm Max Depth: 500 mm Frequency: 50 kHz Ft. Worth, TX I-20 IH20 9.27-2 MP 426 + 0.5, RM 2871 TAMU/TTI 9/2011

B-scan

Volume-Scan

Delamination

Top layer interface

Top layer interface

Longitudinal reinforcement

B-Scan

C-Scan

Figure N-48. UST images of test site IH20 9.27-2.

Interstate 20, Ft. Worth, TX			Texas A&M Transportation Institute
Defects	Notes	Reinf. Detail	Vshear = 2770 m/s
Significant delamination on both sides of surface crack, ranging from 4.6"-5.1" from top surface.	Top layer of pavement approximately 10.2" below surface. Area tested because of transverse surface cracking. Pavement depth confirmed by 2 cores, indicating 10.2" thickness.	Longitudinal reinf.: ~4.8"- 5.0" deep @ 7.2" on center. No transverse reinforcement located in this area.	X-step: 150 mm Y-step: 50 mm Max Depth: 500 mm Frequency: 50 kHz Ft. Worth, TX I-20 IH20 9.27-3 MP 426 + 0.5, RM 2871 TAMU/TTI 9/2011

Figure N-49. Images of test site IH20 9.27-3.

N-51

| Interstate 20, Ft. Worth, TX | | | Texas A&M Transportation Institute |

Defects	Notes	Reinf. Detail	Vshear = 2770 m/s
Significant delamination on both sides of surface crack, ranging from 4.6"-5.1" from top surface.	Top layer of pavement approximately 10.2" below surface. Area tested because of transverse surface cracking. Pavement depth confirmed by 2 cores, indicating 10.2" thickness.	Longitudinal reinf.: ~4.8"- 5.0" deep @ 7.2" on center. No transverse reinforcement located in this area.	X-step: 150 mm Y-step: 50 mm Max Depth: 500 mm Frequency: 50 kHz Ft. Worth, TX I-20 IH20 9.27-3 MP 426 + 0.5, RM 2871 TAMU/TTI 9/2011

Top layer interface

Delamination

B-scan

Longitudinal reinforcement

B-Scan

C-Scan

Delamination

Volume-Scan

Figure N-50. UST images of test site IH20 9.27-3.

N-52

Interstate 20, Ft. Worth, TX			Texas A&M Transportation Institute
Defects	Notes	Reinf. Detail	Vshear = 2770 m/s
Significant delamination on both sides of surface crack, approximately 5.0" from top surface.	Top layer of pavement approximately 10.1" below surface. Area tested because of transverse surface cracking. No cores taken in this location.	Longitudinal reinf.: ~4.6"- 5.2" deep @ 7.0" on center. No transverse reinforcement located in this area.	X-step: 150 mm
			Y-step: 50 mm
			Max Depth: 500 mm
			Frequency: 50 kHz
			Ft. Worth, TX I-20 IH20 9.27-5 MP 426 + 0.5, RM 2871 TAMU/TTI 9/2011

Figure N-51. Images of test site IH20 9.27-5.

Interstate 20, Ft. Worth, TX			Texas A&M Transportation Institute

Defects	Notes	Reinf. Detail	Vshear = 2770 m/s
Significant delamination on both sides of surface crack, approximately 5.0" from top surface.	Top layer of pavement approximately 10.1" below surface. Area tested because of transverse surface cracking. No cores taken in this location.	Longitudinal reinf.: ~4.6"- 5.2" deep @ 7.0" on center. No transverse reinforcement located in this area.	X-step: 150 mm Y-step: 50 mm Max Depth: 500 mm Frequency: 50 kHz
			Ft. Worth, TX I-20 IH20 9.27-5 MP 426 + 0.5, RM 2871 TAMU/TTI 9/2011

Figure N-52. UST images of test site IH20 9.27-5.

George Bush International Airport, Houston,		Texas A&M Transportation Institute	
Defects	Notes	Reinf. Detail	Vshear = 2885 m/s
Significant debonding at at runway/subbase (7.6"-8.1" deep) and verified by coring. Possible further debonding in deeper layers (26.9" and 37.7" deep).	Top layer of pavement approximately 7.6"-8.1" below surface; second layer 26.9" below surface; third layer 37.7" below surface.Area tested because of surface cracking and hammer sounding revealing possible debonding. Image is of typical runway segment.	None.	X-step: 200 mm
			Y-step: 100 mm
			Max Depth: 1000 mm
			Frequency: 50 kHz
			Houston, TX
			IAH
			IAH 6.9-1
			Sta 83+00 T/W WA E
			TAMU/TTI 6/2011

Figure N-53. Images of test site IAH 6.9-1.

George Bush International Airport, Houston,			**Texas A&M Transportation Institute**

Defects	Notes	Reinf. Detail	
Significant debonding at at runway/subbase (7.6"-8.1" deep) and verified by coring. Possible further debonding in deeper layers (26.9" and 37.7" deep).	Top layer of pavement approximately 7.6"-8.1" below surface; second layer 26.9" below surface; third layer 37.7" below surface. Area tested because of surface cracking and hammer sounding revealing possible debonding. Image is of typical runway segment.	None.	Vshear = 2885 m/s X-step: 200 mm Y-step: 100 mm Max Depth: 1000 mm Frequency: 50 kHz
			Houston, TX IAH IAH 6.9-1 Sta 83+00 T/W WA E TAMU/TTI 6/2011

Figure N-54. UST images of test site IAH 6.9-1.

George Bush International Airport, Houston,			Texas A&M Transportation Institute

Defects	Notes	Reinf. Detail	Vshear = 2885 m/s
Significant debonding at at runway/subbase (7.1" deep) and verified by coring. Possible further debonding in deeper layers (25.6" and 37.5" deep).	Top layer of pavement approximately 7.1" below surface; second layer 25.6" below surface; third layer 37.5" below surface. Area tested because of surface cracking and hammer sounding revealing possible delaminations. Image is of typical runway segment.	None.	X-step: 200 mm Y-step: 100 mm Max Depth: 1000 mm Frequency: 50 kHz
			Houston, TX IAH IAH 6.9-2 Sta 82+75 T/W WA E TAMU/TTI 6/2011

Figure N-55. Images of test site IAH 6.9-2.

George Bush International Airport, Houston,		Texas A&M Transportation Institute	
Defects	Notes	Reinf. Detail	Vshear = 2885 m/s
Significant debonding at at runway/subbase (7.1" deep) and verified by coring. Possible further debonding in deeper layers (25.6" and 37.5" deep).	Top layer of pavement approximately 7.1" below surface; second layer 25.6" below surface; third layer 37.5" below surface. Area tested because of surface cracking and hammer sounding revealing possible delaminations. Image is of typical runway segment.	None.	X-step: 200 mm Y-step: 100 mm Max Depth: 1000 mm Frequency: 50 kHz
			Houston, TX IAH IAH 6.9-2 Sta 82+75 T/W WA E TAMU/TTI 6/2011

B-Scans
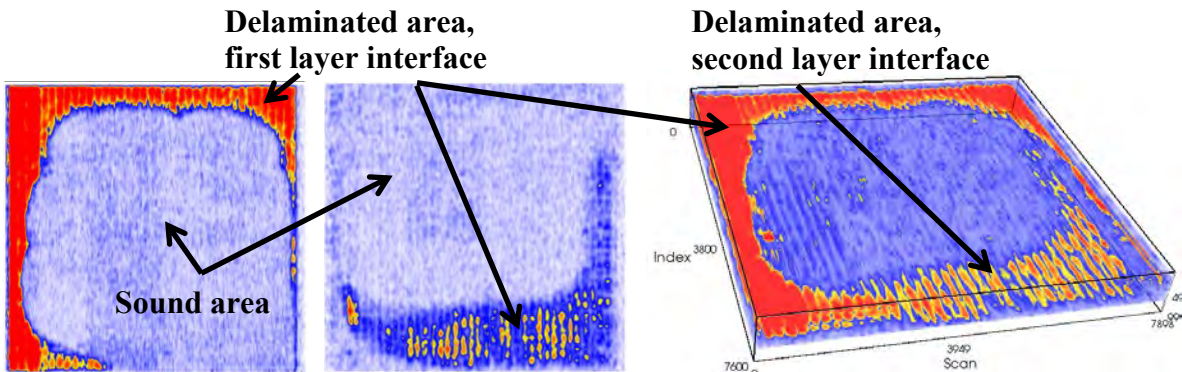
C-Scans   **Volume-Scan**

Figure N-56. UST images of test site IAH 6.9-2.

APPENDIX O
EVALUATION OF TILED TUNNEL LININGS USING ACOUSTIC SOUNDING

INTRODUCTION

This appendix describes the progress of a particular nondestructive testing (NDT) technique known as acoustic sounding and outlines how this system will work within the framework of the second Strategic Highway Research Program (SHRP2) Project R06(G), "High-Speed Nondestructive Testing Methods for Mapping Voids, Debonding, Delaminations, Moisture, and Other Defects Behind or Within Tunnel Linings."

This system requires further development to be efficiently implemented for tile debonding in tunnel linings. The technique summarized here has shown to be a promising technique capable of quickly determining the stage of tile debonding in tunnel linings in an unbiased manner. This appendix will discuss how the system will be used in inspection procedures and will provide an idea of the end product. Evaluations of public tunnels and a series of test specimens have been conducted and the preliminary results are given.

ACOUSTIC SOUNDING TECHNIQUE

When debonding occurs on tiled surfaces, hammer sounding by ear or by microphone can readily differentiate bonded from debonded tile. This is determined by the characteristic lower-frequency pinging that occurs on debonded areas relative to fully bonded tiles. The goal of the system devised here is to provide a quick and efficient way for inspectors to characterize the condition of tile bonding in a less subjective method.

Technical Needs

In general, debonded tile can occur for two reasons: improper installation or external influences. Improper installation commonly includes:

- Improper use of bonding agent (mixing ratios, wrong type, etc.).
- Improper tile spacing.
- Excessive open time.
- Low standard of workmanship (i.e., not backbuttering the tile).

External influences can include:

- Environmental conditions (such as thermal expansion).
- Excessive tunnel lining forces (damaged lining due to voids, cracks, delamination, debonding).

In either case, debonding of the tile can occur and pose danger to the public. Many NDT techniques are used in this SHRP2 project to determine the onset of damage behind the tiled wall lining prior to tile debonding, but there is a need to quickly and efficiently determine regions of tile that need immediate attention after this debonding occurs.

Research Approach

The system under development is to be used with a laptop computer capable of recording audio signals and installed with a version of MATLAB, along with an impact source (preferably a ball-peen hammer). As the centers of tile are lightly tapped with the hammer, the laptop's internal microphone records the audio signal. MATLAB software performs a Fast Fourier Transform (FFT) to the data set and uses pattern recognition techniques to monitor the fundamental frequencies of flexural vibration for each individual tile. The modes of vibration frequencies in a voided tile can be predicted using acoustic theory for a rectangular plate with simply supported edges (Rossing and Fletcher 2003):

$$f_{mn} = 0.453 c_L h \left[(\frac{m+1}{L_x})^2 + (\frac{n+1}{L_y})^2 \right]$$

where c_L is the longitudinal wave speed, h is the thickness of the tile, m and n are the integers describing the current mode of excitation ($m = n = 0$ for the fundamental frequency of flexural vibration), and L_x and L_y are the respective side lengths of the tile. It has been observed that the vibration frequencies increase as the voided section of tile decreases (Liu et al. 2011). Therefore, it is theoretically possible to relate the fundamental frequency to the approximate area of debonding.

This technique can be incorporated into a program that assigns a color scale to the frequency spectrum of a tile wall under inspection. It is envisioned that the final result can operate in two methods. The first method is for near-real-time inspection. In this mode of operation, a threshold frequency from an expected frequency band representing sound concrete is established and used to make a pass-fail decision telling the user whether the tile is most likely bonded or debonded. The second method is intended to be used in mapping a large region of tile, and the final result is a map of the tiles showing the levels of expected bond. Similar to the first mode of operation, the user will select a section of tile representing a fully bonded state for the program to determine the fundamental frequencies associated with bonded sections. The user will then tap each tile in a predetermined order. For instance, the section might consist of an area 13 tiles high and 40 tiles wide. The program will prompt the user to select the layout desired, and after tapping each tile in the given order, the program will output a plot showing the frequency spectrum.
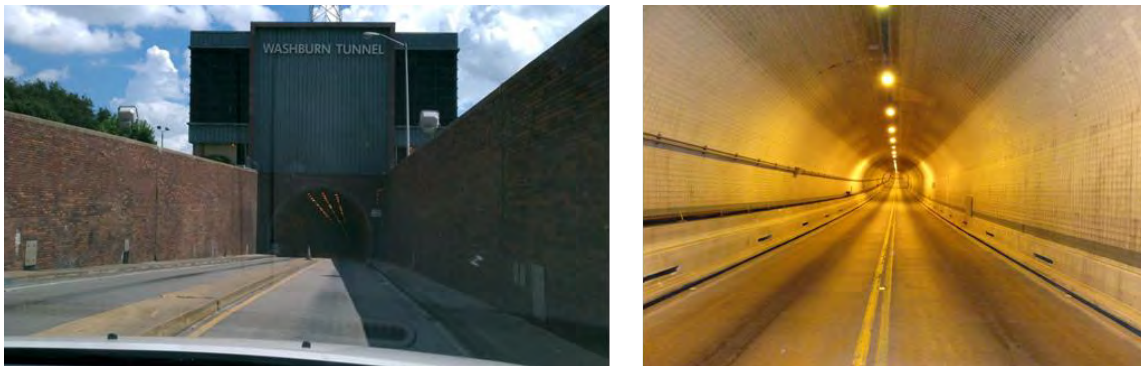
Figure O-1. Washburn Tunnel: exterior (left) and interior view (right).

FIELD APPLICATION—WASHBURN TUNNEL

This technique was used for a proof test in the Washburn Tunnel in Houston, Texas. The Washburn Tunnel (Figure O-1) is the only underwater vehicle tunnel in operation in Texas and was completed in 1950. It carries a federal road beneath the Houston Ship Channel joining two Houston suburbs.
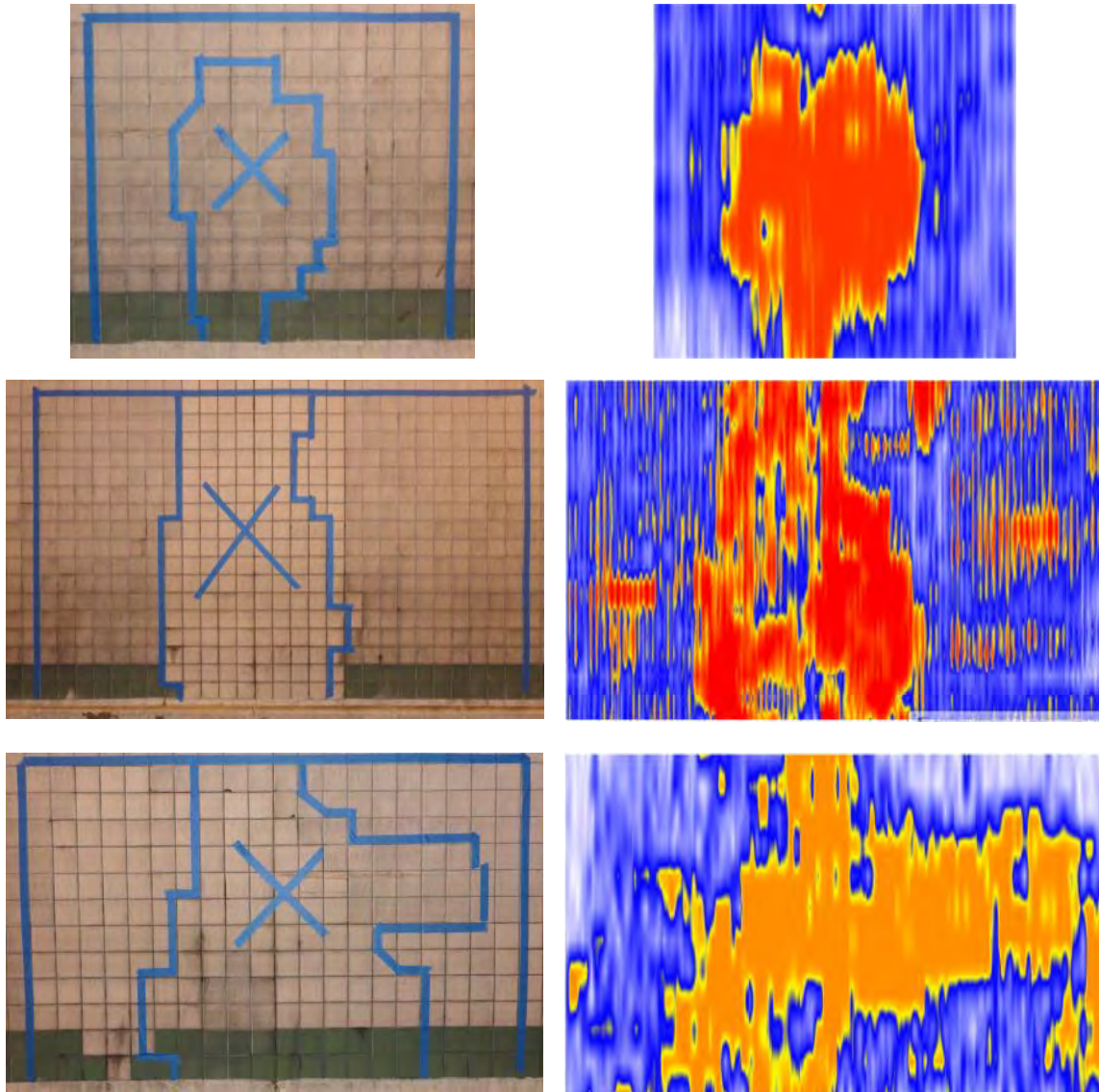
Figure O-2. Debonded regions of tile (left) paired with the associated UST C-scans (right).

The tunnel was constructed via the immersed tube method, with sections joined together in a prepared trench, 26 m (85 ft) below water. The entire inner wall is tiled with 110 x 110 mm (4.3 x 4.3 inch) ceramic tiles. Like many underwater tunnels with tiled walls, this one is experiencing debonding of tile in various areas. Three sections of tile that contained debonded regions (as determined by an inspector performing hammer sounding by ear) were chosen. The regions, shown on the left side of Figure O-2, are outlined with blue painter's tape. The debonded section (determined by human ear) is also outlined with blue painter's tape with an "x" on the debonded section. On the right side of Figure O-2, scans made via ultrasonic tomography (UST) are shown with each of the three regions. The ultrasonic tomography technique and its specific application to the Washburn Tunnel can be read in the companion report "Evaluation of Tunnel Linings Using Ultrasonic Tomography." The depths of the C-scans (or plan views) in Figure O-2 range from 16-103 mm (0.63-4.1 inches). One of the areas investigated (Figure O-2, middle) was evaluated using a rudimentary version of the acoustic sounding technique, as is shown in Figure O-3. This example shows a strong correlation between hammer sounding by ear and the automated version.
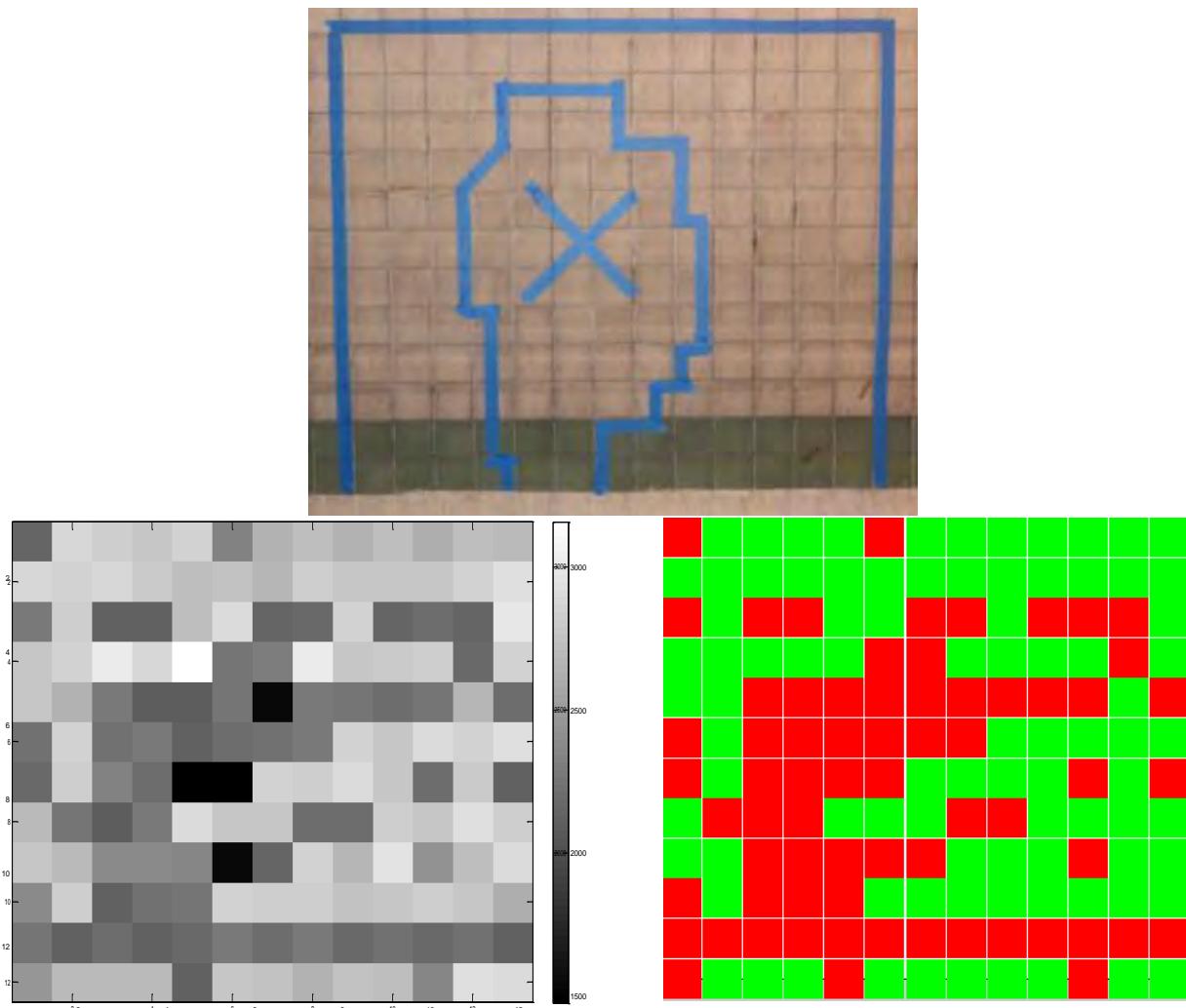
Figure O-3. Debonded regions of tile (top) paired with the acoustic sounding results (bottom).

In Figure O-3, the bottom left plot depicts the tiles color coded in grayscale, with the higher frequencies (predicting a fully bonded state) as white and the lower frequencies (predicting a debonded state) as black. As previously discussed, the lower frequencies observed should theoretically correspond to larger voided areas behind the tile. The bottom right plot in Figure O-3 shows the output with a pass-fail algorithm denoting tiles that fall below the expected fully bonded state (red is expected debonded state, green is expected fully bonded state).

CONCLUSIONS

This automated sounding technique is still under development, as many factors influence the peak frequencies observed in the frequency spectrum from a single tile tap, including the size of the void, whether or not the hammer tap is directly in the center of the tile, and multiple mode interference. Preliminary results indicate that this technique, although basic in its approach, will offer the tunnel inspector a quick, efficient, and inexpensive technique that provides sufficient information for repair procedures or further investigation.

REFERENCES

Liu, S., F. Tong, B. Luk, and K. Liu. Fuzzy Pattern Recognition of Impact Acoustic Signals for Nondestructive Evaluation. *Sensors and Actuators: A. Physical,* Vol. 167, No. 2, 2011, pp. 588-593.

Rossing, T., and N. Fletcher. *Principles of Vibration and Sound*, 2nd ed. Springer, New York, 2003.

APPENDIX P
FIELD TESTING WITH THE PORTABLE SEISMIC PAVEMENT ANALYZER (PSPA) IN THE UNITED STATES

INTRODUCTION

A survey of several tunnels linings was carried out with a Portable Seismic Property Analyzer (PSPA) within the framework of the SHRP2 Project R06G on "Mapping Voids, Debonding, Delamination, Moisture, and Other Defects behind or within Tunnel Linings." The main objectives of that research project are:

- To identify promising NDT technologies for evaluating the condition of various types of tunnel linings
- To evaluate the applicability, accuracy, precision, repeatability, ease of use, testing duration, and costs of the identified technologies;
- To conduct the required development in hardware or software for promising techniques; and
- To validate the selected technologies

Two tunnels in Colorado and one tunnel in Virginia were involved in this study. The Eisenhower-Johnson Memorial Tunnel in Colorado was investigated on October 3 and 4, 2011 and the Hanging Lake Tunnel in Colorado was assessed on October 5 and 6, 2011. Finally, the evaluation of the Chesapeake Channel Tunnel in Virginia was performed on October 11 through 12, 2011. The scope of UTEP study was to evaluate the performance of the PSPA in locating defects behind or within tunnel linings. This appendix describes the tests executed and the obtained results.

DESCRIPTION OF PSPA AND TESTING METHODS

PSPA is a portable device that can perform two tests (impact echo [IE] and ultrasonic surface wave [USW]) simultaneously. The PSPA consists of two receivers and a source packaged into a handheld portable device. The near and far receiver spacing from the source are 4 and 10 inches, respectively. The impact duration (contact time) is about 60 µs, and the data acquisition system has a sampling frequency of 390 kHz. The advantage of combining these two methods in a single device is that once the test is performed, the variations in the modulus (an indication of the quality of concrete) and return resonance frequency (an indication of the full thickness or depth of delamination) of a slab can be assessed concurrently. The following sections discuss the principles of the two seismic methods, along with interpretation approaches.

Impact Echo Method

The IE method is one of the most commonly used NDT methods in detecting delamination in concrete (Carino et al. 1986). This method is based on impacting a plate-like object such as a tunnel lining with an impactor that generates stress waves at frequencies of up to 20 to 30 kHz and collecting signals by a receiver (Figure P-1a). By using a fast Fourier transform (FFT) algorithm, the recorded time domain signal is converted into a frequency domain function (amplitude spectrum) and the peak frequency is monitored. For an intact point on a slab or an

intact portion of a slab, the thickness (h) is then determined from the compression wave velocity (V_p) and the return frequency (f):

$$h = \alpha \frac{V_p}{2f} \qquad \text{(P-1)}$$

where α is about 0.96 for concrete slabs.

For a deep and relatively small delaminated location in a concrete slab, the return frequency may shift to a higher frequency corresponding to the depth of the delamination. As shown in Figure P-1b, a shallow or a deep but extensive and severe delaminated area is usually manifested by a low peak frequency, indicating that little or no energy propagates toward the bottom of the deck and a flexural mode dominates the frequency response. In this case, Eq. (P-1) is not applicable to measure the depth of delamination since it is influenced by several factors.

(a) IE method
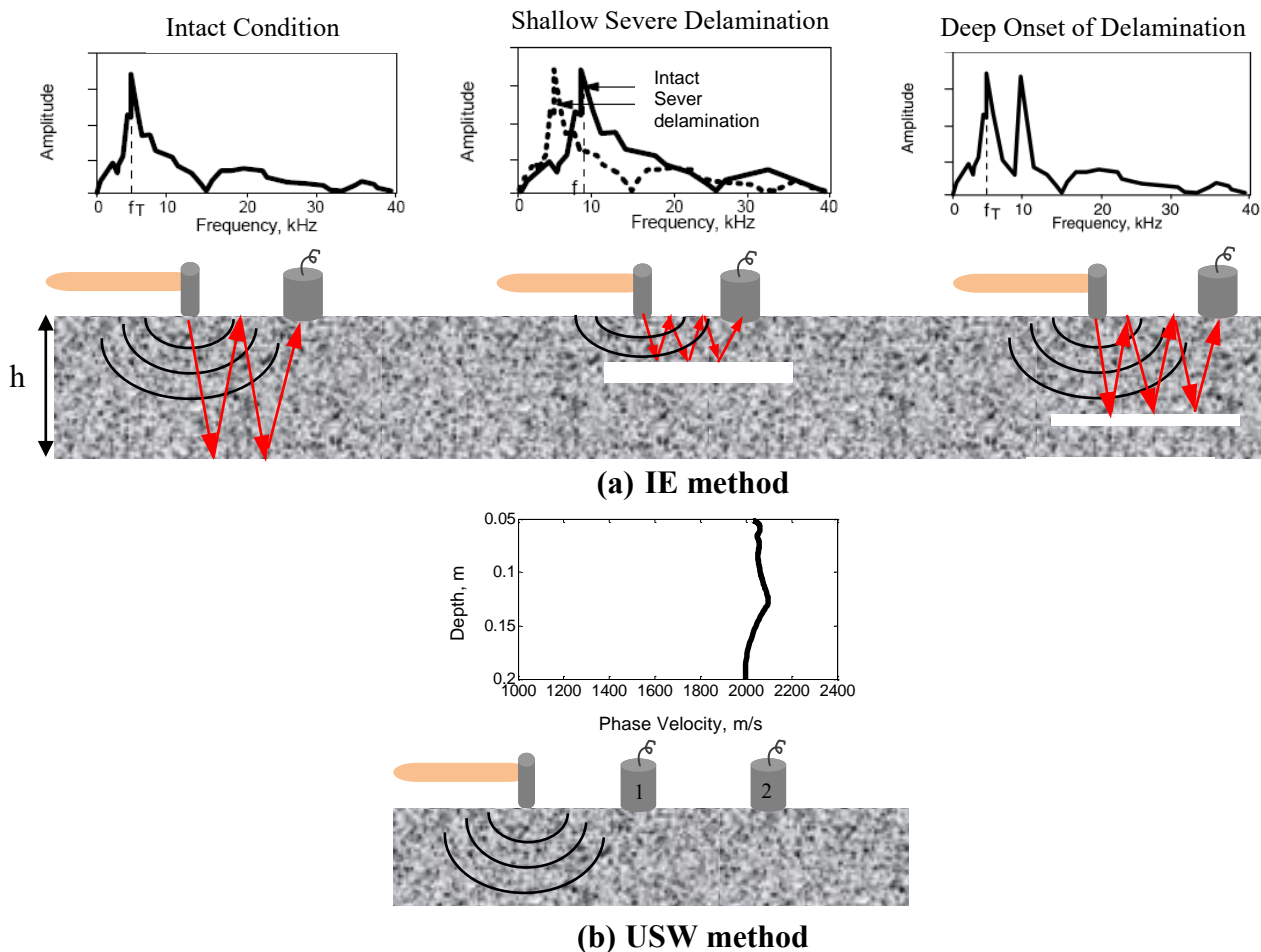
(b) USW method

Figure P-1. Schematic illustration of the test methods (Gucunski and Maher 1998).

Ultrasonic Surface Waves Method

The USW method is used to estimate the average velocity of propagation of surface waves in a medium, based on the time at which different types of energy arrive at each sensor (Figure P-1b). The velocity of propagation, V_R, is typically determined by dividing the distance between two receivers, ΔX, by the difference in the arrival time of a specific wave, Δt. Knowing the wave

velocity, the modulus can be determined from shear modulus, G, through Poisson's ratio (ν) using:

$$E = 2(1+\nu)G \qquad \text{(P-2)}$$

Shear modulus can be determined from shear wave velocity, V_S, using:

$$G = \frac{\gamma}{g}V_S^{\ 2} \qquad \text{(P-3)}$$

The modulus from surface wave velocity, V_R, first converted to shear wave velocity can be determined by:

$$V_S = V_R(1.13 - 0.16\nu) \qquad \text{(P-4)}$$

In the USW method, the variation in velocity with wavelength is measured to generate a so-called dispersion curve. For a uniform or intact concrete slab, the dispersion curve shows more or less a constant velocity within the wavelengths nor greater than the thickness of the slab. When a delamination or void is present in a concrete slab or the concrete is deteriorated, the average surface wave velocity (or modulus) becomes less than the actual one due to the interference caused by the defect. In this case, the velocity or modulus obtained may be called an apparent velocity or modulus.

DESCRIPTION OF SITES

The three tunnels were visited in this study as described below.

Eisenhower Tunnel

An outside view of the Eisenhower Tunnel is shown in Figure P-2. The tunnel was originally designed as a twin bore tunnel—Eisenhower Memorial Bore and Edwin C. Johnson. This two-bore tunnel is located approximately 60 mi west of Denver, CO, on Interstate 70. The tunnel is about 1.7 mi long, and the plenum is up to 18 ft high, with a nominally 2-ft-thick liner. Some sections of the ventilation plenum were investigated in this study.

Hanging Lake Tunnel

Hanging Lake Tunnel also consists of two bores and is located approximately 10 mi east of Glenwood Springs, CO, on Interstate 70. The tunnel is about 0.7 mi long, and the ventilation plenum is 7 ft high, with a nominally 15-inch-thick liner, as shown in Figure P-3. Some sections of the plenum were evaluated.

Chesapeake Bay Tunnel

This one-bore subsea tunnel is part of a 17-mi-long bridge-tunnel crossing Chesapeake Bay, VA, on US Highway 13. The tunnel is about 1 mi long with a nominally 2-ft-thick liner. An outside view of the tunnel is shown in Figure P-4. A section of about 2600 ft of the ventilation plenum and a section of 200 ft on the wall of the roadway were involved in this study.

DATA COLLECTION PROCESS

In the Eisenhower Tunnel, data were collected point by point, mostly at every 5 ft, along a line in each selected section. The selection was based on the detected anomalies with infrared thermography. In the Hanging Lake Tunnel, besides the line testing, data were collected along a test grid. The selection of test sections was based on visual inspection and previous investigation of the tunnel.

Figure P-2. Outside view of Eisenhower Tunnel.

Figure P-3. Outside view of Hanging Lake Tunnel.
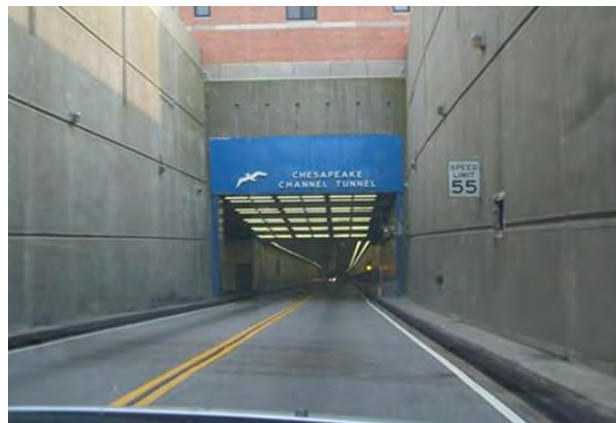
Figure P-4. Outside view of Chesapeake Bay Tunnel.

In the Chesapeake Bay Tunnel, both the ventilation plenum and roadway wall were evaluated with non-destructive testing (NDT). All tests including those with PSPA in this study were conducted at or within a number of spots or areas. The selection was based on the distribution of major anomalies with a dielectric constant. The testing schedules and locations for the tunnels are presented in Table P-1. Table P-2 lists the selected areas on the plenum ceiling of the Chesapeake Bay Tunnel, which include three spots in an area and 10 selected anomaly areas characterized by a high dielectric constant (greater than 15 as compared with 4.5 for typical dry concrete) and, for most of them, by cracking with more or less water dropping.

Table P-1. Testing schedules and locations of the tunnels.

Tunnel	Eisenhower Tunnel		Hanging Lake Tunnel		Chesapeake Bay Tunnel	
Location	Dillon, CO		Glenwood Springs, CO		Cape Charles, VA	
Date	Oct. 3	Oct. 4	Oct. 5	Oct. 6	Oct. 11	Oct. 12
Direction	eastbound	westbound	eastbound	eastbound	plenum	plenum and wall
Section Tested	8 to 13	148 to 166	57 to 61	57	Not Applicable	
Number of Blocks (Areas) Tested	60	190	50	2	7	14
Number of Points Tested	57	151	42	42	46	52

Table P-2. Approximate locations of the areas tested with PSPA in the plenum of the Chesapeake Bay Tunnel.

Area	Intact	Defective									
Location	470+50 to 470+75	473 + 56	474 + 27	477 + 60	478 + 85	481 + 76	486 + 67	486 + 81	491 + 25	493 + 15	496 + 25

Eisenhower Tunnel

In the Eisenhower Tunnel, each bore was investigated in one day. Six 50-ft-long sections (from section 8 to section 13) were tested on October 3 in the eastbound bore. About 19 sections (from section 148 to section 166) were investigated on October 4 in the westbound bore. The selection of sections was based on visual inspection and a preliminary infrared testing. In both bores, the investigation was mostly performed every 5 ft at the center of each block. Several extra points were tested around the cracked and delaminated areas. It took about 10 min for each 50-ft section to be tested. The rest of the time was allotted to documenting the data collection information and taking some pictures. The main challenge while using the PSPA device was the dirt on the wall that caused an occasional slip of the device during testing. Therefore, some points had to be tested several times to get a clear signal.

Hanging Lake Tunnel

In the Hanging Lake Tunnel, five 50-ft-long sections (from section 57 to section 61) were investigated on October 5 in the westbound bore. Similar to the Eisenhower Tunnel, the selection of sections was based on visual inspection and the severity of visible cracks. The data were collected at the center of each block plus around the cracks and delaminated areas. In addition to 10 min of testing for each block, extra time was allotted to documenting the data collection information and taking pictures. On October 6, two blocks in section 57 were tested in more detail with denser measurements. These two blocks were investigated through seven horizontal and six vertical lines (see Figure P-5). It took about 2 h to test the two blocks. The main challenge while using the PSPA was the areas with large curvature, which caused the device and the surface to not have full contact in some places.

Chesapeake Bay Tunnel

Since this tunnel has been previously evaluated by other NDT methods, the focus of this study was on a number of areas or spots on the plenum and the roadway wall where the high dielectric constants were measured. Forty-six points within seven areas on the ceiling of the plenum were evaluated on October 11. Thirty-eight points within six areas on the ceiling of the plenum and 14 points at 11 spots on the wall of the roadway were evaluated on October 12. All tests were stopped at midnight of that day since the traffic lane had to be reopened due to foggy weather.

TEST RESULTS

Since the impact echo (IE) and ultrasonic surface wave (USW) methods used in this study are point inspection methods, it is more effective to visualize the results using a contour map than to evaluate them individually. However, typical IE and USW results for an intact area and defective area are shown for each tunnel.

Eisenhower Tunnel

IE Method

The amplitude spectra for an intact point and two defective points along with the photograph taken through visual inspection are shown in Figure P-6. As compared to the intact point, either lower or higher peak frequencies control the response at defective points, as discussed above. Based on an average compression wave velocity of 13,800 ft/s measured for the concrete and Eq. (P-1), a nominal frequency of around 3.5 kHz approximately corresponds to the thickness of the liner (2 ft), whereas the frequency of 6.8 kHz for the shallow delamination approximately corresponds to a thickness of 1 ft. The response from the severely delaminated area corresponds to the flexural mode of vibration.

Figures P-7a and P-7b show the spectral B-scan of the IE results along several blocks in the eastbound and westbound bores, respectively. At some points, a frequency of about 3 to 3.5 kHz governs the response, which indicates the thickness of the liner. On the remaining areas, either a low- or high-frequency amplitude governs the response. The low-frequency flexural mode is due to a shallow or a deep but extensive delamination. Therefore, its peak frequency does not

correspond to any thickness measurement, and the depth of defect can be estimated from a USW B-scan. On the other hand, the high-frequency response could be attributed to the onset of delamination. In this case, the depth of delamination is estimated from Eq. (P-1) and confirmed with the USW B-scan. In the presence of a crack, data analysis is more complicated. Multiple frequencies are present in the response when a crack is between the source and receiver in an IE B-scan, and the crack is recognized through high average moduli in the USW B-scan.

(a) The actual photograph
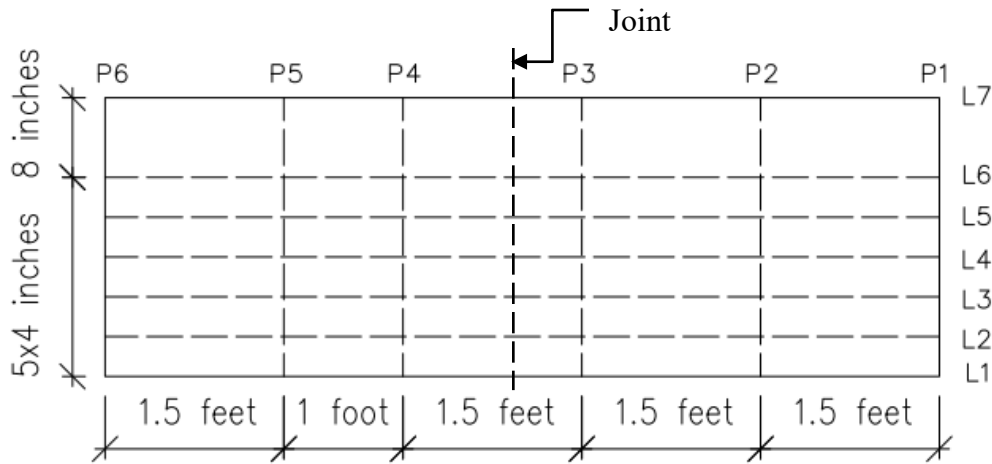
(b) Plan of the tested blocks

Figure P-5. The tested blocks with denser grid measurement in Hanging Lake Tunnel.

(a) Good condition

(b) Poor condition
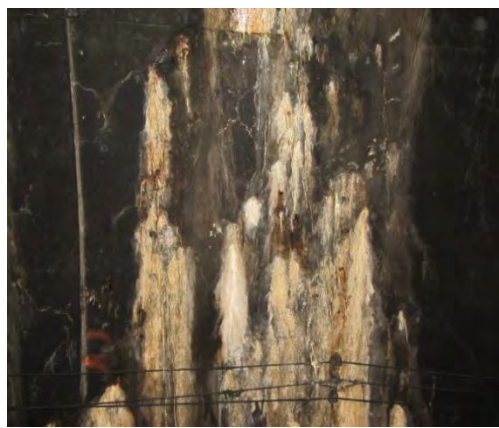
(c) Severe condition
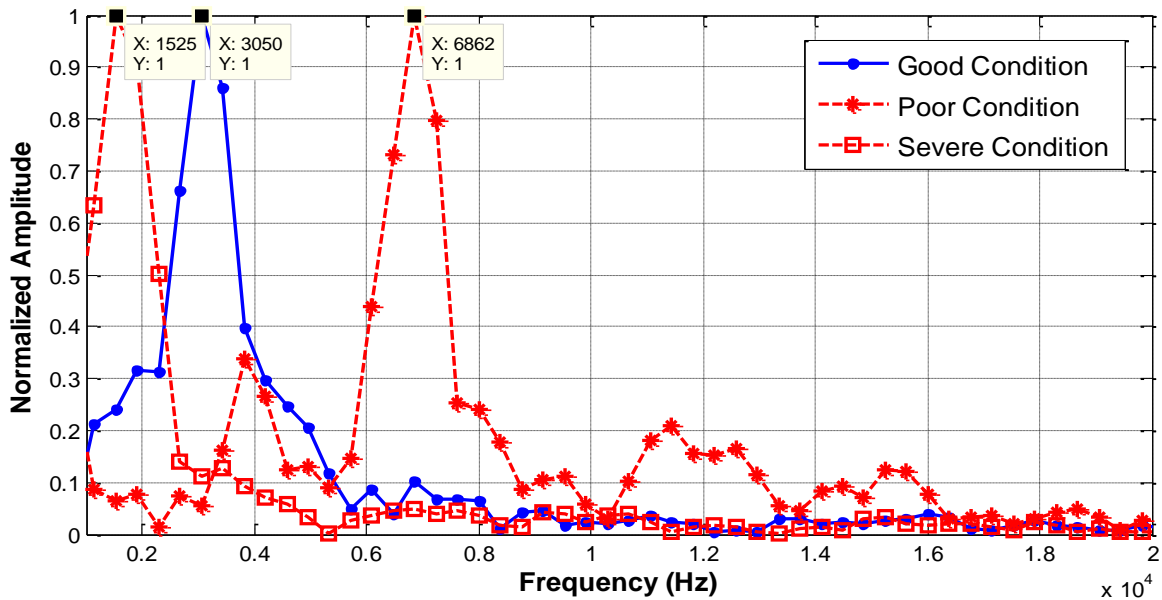
(d) Representative amplitude spectrum for intact and defective points

Figure P-6. Amplitude spectra along with actual photograph for intact and defective points in Eisenhower Tunnel.
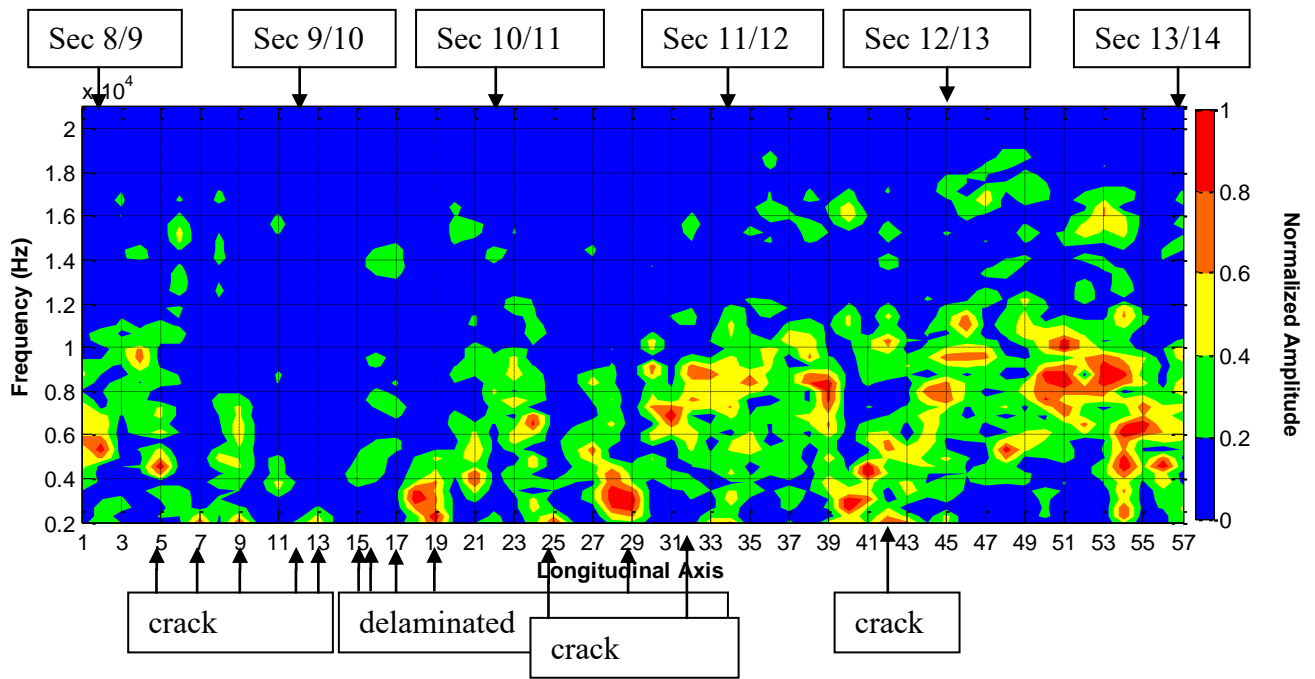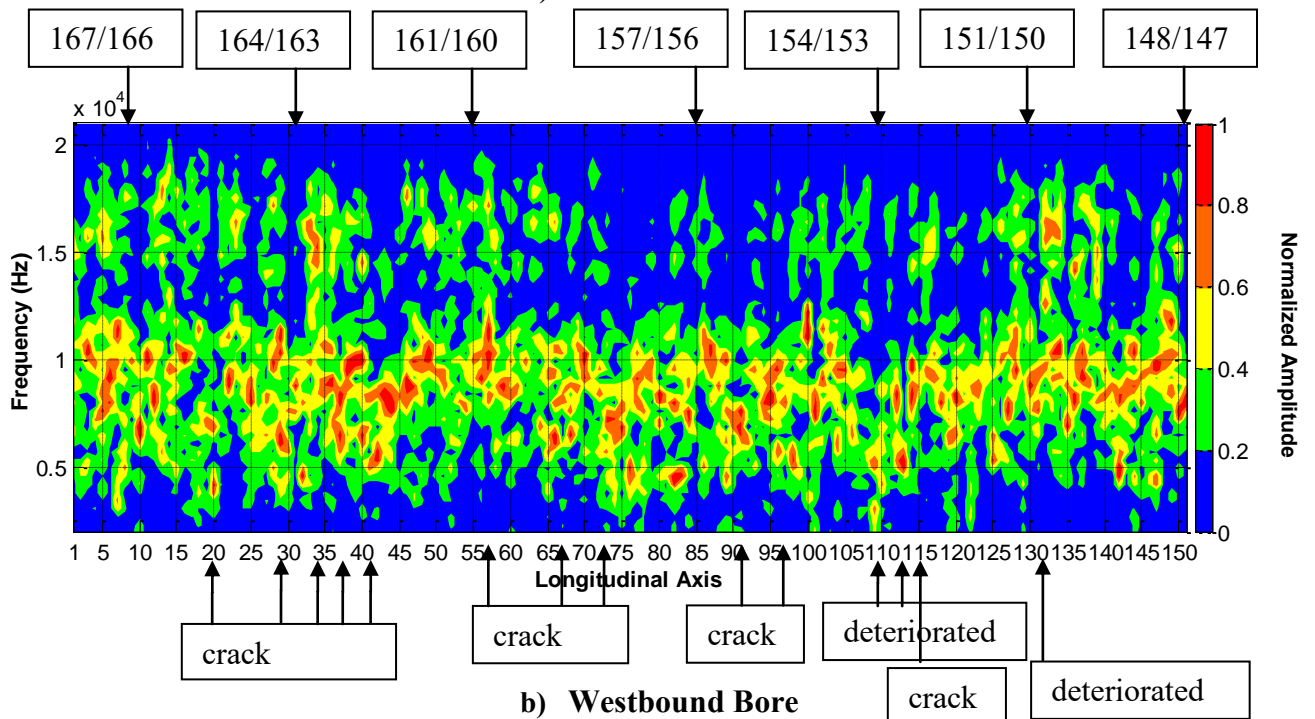
a) **Eastbound Bore**

b) **Westbound Bore**
Figure P-7. IE spectral B-scan along Eisenhower Tunnel.

USW Method

Figure P-8 shows a typical USW dispersion curve for an intact area and a defective point along with their actual photograph. The dispersion curve shifts to lower moduli where severe flaws are present.

The cross-sections of variation in modulus with wavelength, which can be viewed qualitatively as a scaled variation in modulus with depth, are shown in Figure P-9 for the eastbound and westbound bores. The problematic areas manifest themselves as areas with lower average moduli.

(a) Intact location   **b) Defective location**
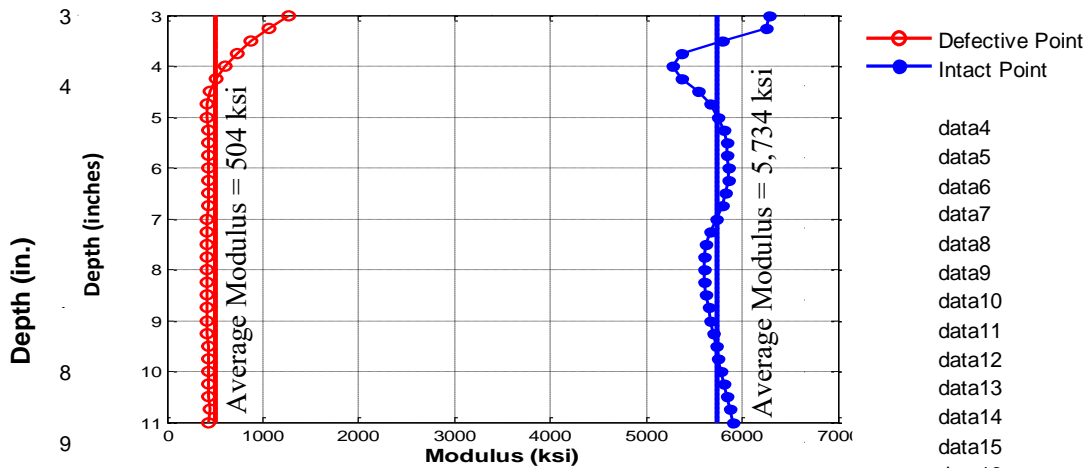
(c) Representative dispersion curve for intact and defective

Figure P-8. Representative dispersion curve along with the actual photographs of intact and defective points in Eisenhower Tunnel.

a) **Eastbound Bore**

b) **Westbound Bore**
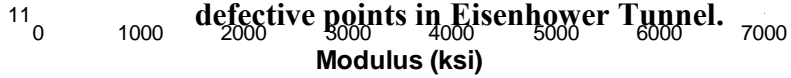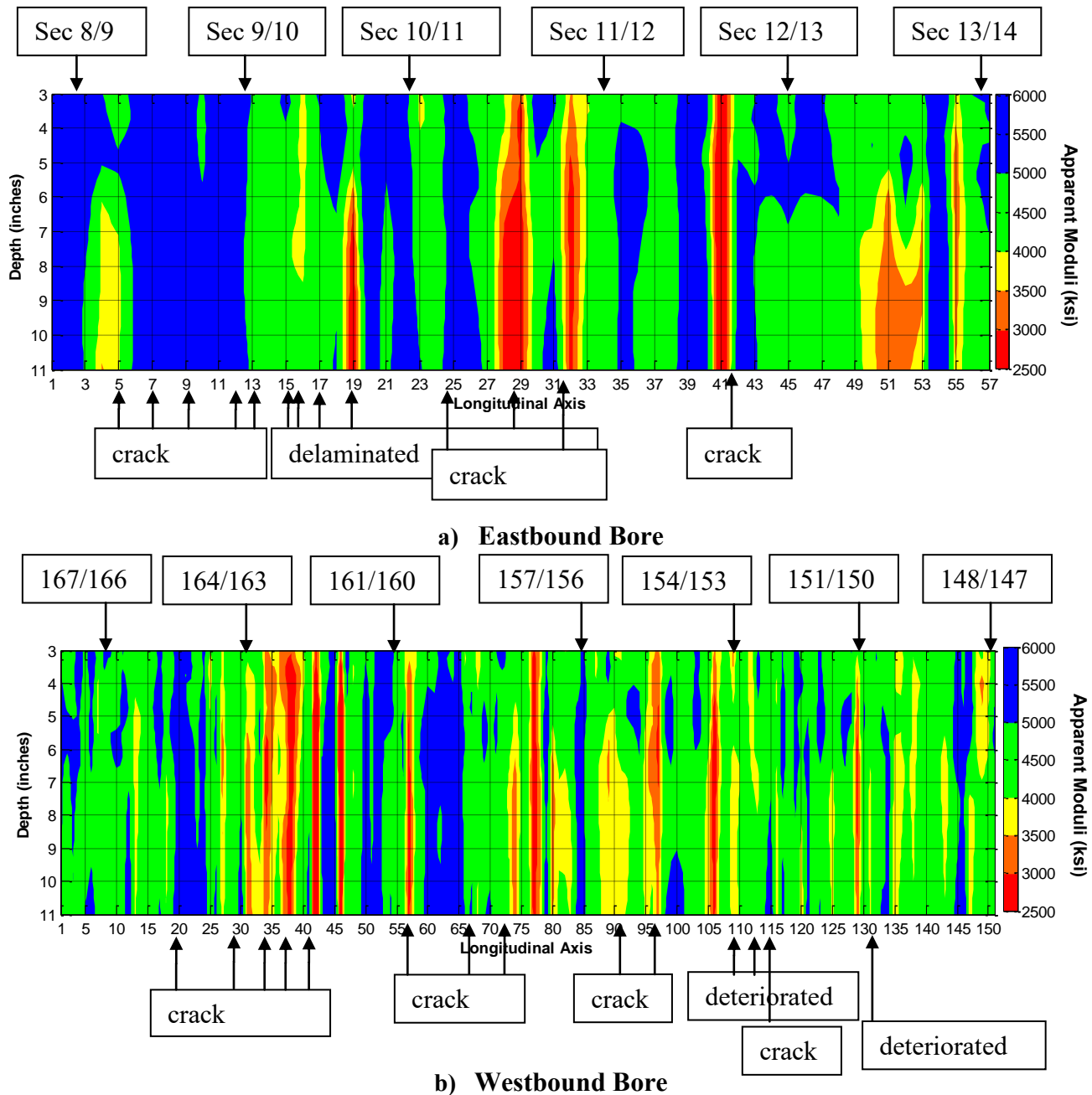
Figure P-9. Variation of modulus with depth along Eisenhower Tunnel.

Combining the IE and USW results builds confidence in the interpretation of the location and depth of the problematic areas. In other words, the combined tests allow for a better delineation between shallow/deep and initial/extensive defects. For instance, a low-frequency dominant frequency in the IE results in Figures P-7a and P-7b is an indication of a shallow or a very deep and extensive delamination, and the depth could be estimated from USW B-scans (Figures P-9a and P-9b). The areas with high-frequency dominant amplitudes (around 16 kHz) in Figures P-7a and P-7b are deep delamination, with the depth of the delamination around 5 inches (according to Eq. (P-1)). At several points in Figures P-9a and P-9b, the manifestation of defect starts at 6 inches. On the majority of testing areas, multiple frequencies control the response in the IE B-scans indicating the presence of cracks. Comparable results are obtained from the USW

B-scans. When the crack is between the source and first receiver, the USW modulus is typically greater than normal because of the travel path of the wave. Similarly, when the crack is between the two sensors, the reported USW modulus is lower than normal. The results for these points agree well with the actual condition that was documented during visual inspection.

Hanging Lake Tunnel

IE Method

The actual condition of liners at the time of testing is shown in Figures P-10a and P-10b. The amplitude spectra for selected intact and defective points are also shown in Figure P-10c. Based on an average compression wave velocity of about 14,000 ft/s measured for the concrete, the dominant frequency corresponding to the tunnel thickness (15 inches) is around 5.4 kHz. As compared to the intact point, higher peak frequencies mostly control the response at the defective points.

(a) Intact location   **(b) Defective location**
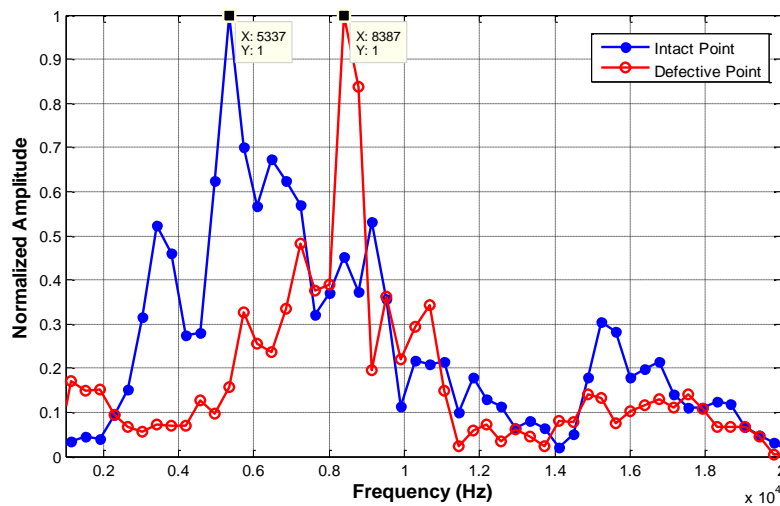
(c) Representative amplitude spectrum for intact and defective points

Figure P-10. The amplitude spectra along with the actual photograph for intact and defective points in Hanging Lake Tunnel.

Figure P-11 shows the spectral B-scan of the IE results along several blocks in the westbound bore. At some points, a frequency of 5.4 kHz dominates the response, which indicates the intact areas. On the remaining areas, mostly high frequency governs the response, which is an indication of deep (but not extensive) delamination or crack. A better delineation between delamination and crack can be obtained through the USW B-scan.

Figure P-12 presents the contour map of the peak frequency on the defined test grid. As mentioned earlier, the thickness frequency is around 5.4 kHz. The threshold in color index is set based on the dominant frequency on intact areas. The frequencies lower than 4 kHz and higher than 8 kHz are considered as the dominant low and high frequency, respectively. The spectral B-scan of the IE results along line 2 is shown in Figure P-13. The red stripe around 5.4 kHz corresponds to the tunnel thickness and indicates echo mode. The rest of the spectral B-scans of IE results are shown in Appendix P1.
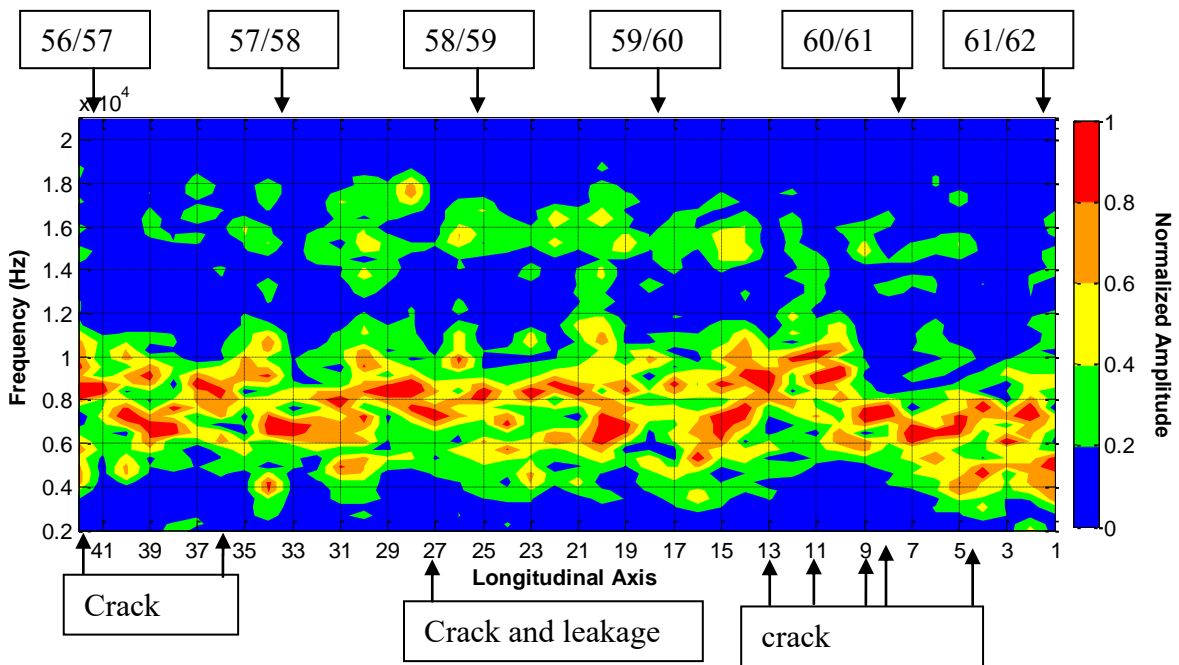
Figure P-11. IE spectral B-scan along Hanging Lake Tunnel.
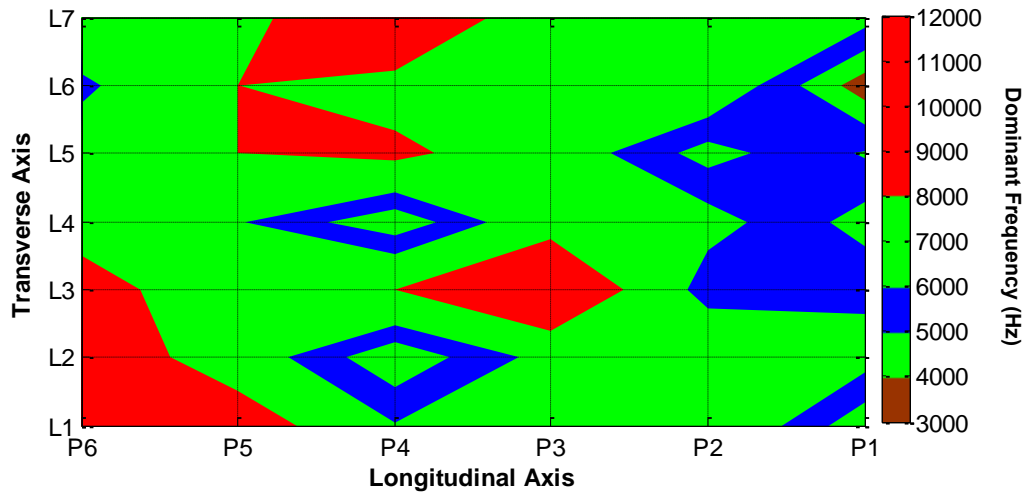
Figure P-12. Planar variation of the dominant frequency on the meshed block in Hanging Lake Tunnel.
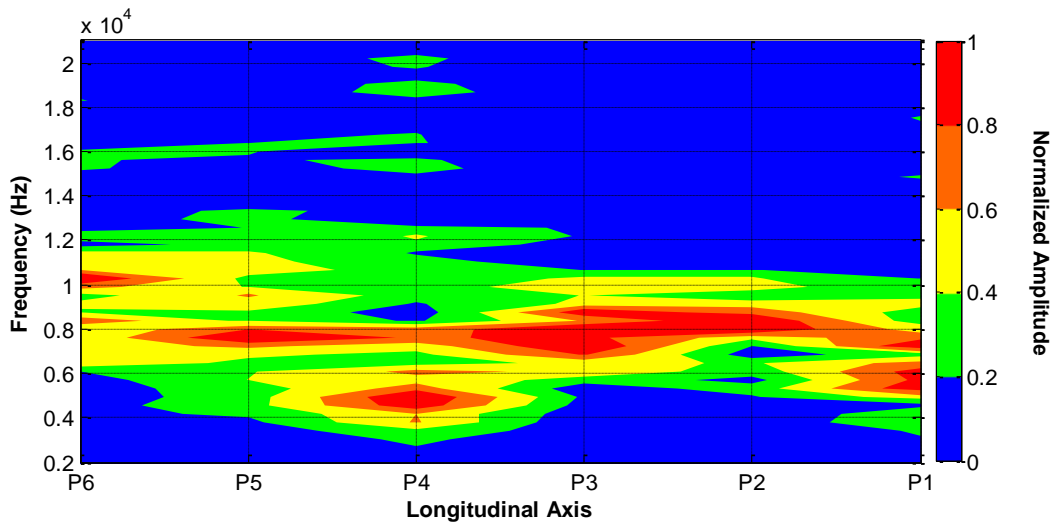
Figure P-13. IE spectral B-scan along L2 on the meshed block in Hanging Lake Tunnel.

USW Method

Figure P-14 compares typical USW dispersion curves from an intact area and a defective area along with their actual conditions, as was documented during visual inspection. In defective areas, the dispersion curve shifts to lower moduli.

The variation in modulus with wavelength (or depth) along several blocks of the eastbound bore of the Hanging Lake Tunnel is shown in Figure P-15. The problematic areas are marked with red, which indicate a lower modulus. The IE B-scan (Figure P-11) and the USW B-scan (Figure P-15) result in similar defect maps (both for location and depth). The points with multiple peak frequencies in Figure P-11 are recognizable in Figure P-15 through a low modulus starting at the surface (indication of crack). Other defective points that manifest themselves by high frequency (between 15 and 17 kHz) in the IE B-scan might be delamination at the depth of 5

to 5.5 inches (calculated based on Eq. (P-1)). Similarly, the indication of lower moduli starts at a depth of around 5 inches in the USW B-scan at those points.

The planar contour map of the variations of the average modulus on the meshed blocks is presented in Figure P-16. The defective areas manifest themselves as the areas with lower moduli and are marked in red.

Another form of representing the USW outcomes is through a line scan, which is shown in Figure P-17 for line 2. The depths of suspected delamination areas could be approximated through the B-scan. The line scans from the remaining lines are presented in Appendix P1. As shown in Figure P-17, the defective areas manifest themselves as areas with lower average moduli.

The planar variations in modulus, obtained by the USW method at two different depths, are shown in Figure P-18. All planar variations of modulus are presented in Appendix P1.

(a) Intact location   **(b) Defective location**
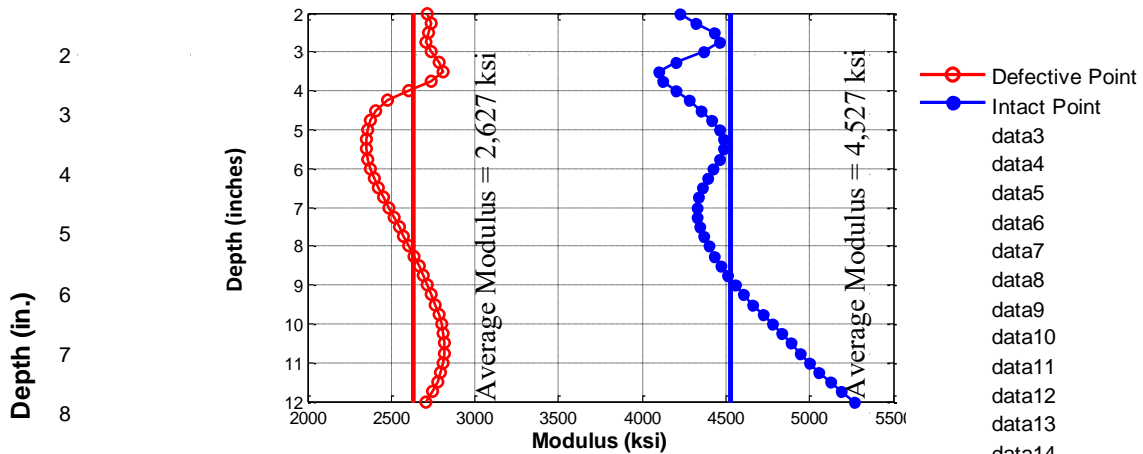
(c) Representative dispersion curve for intact and defecti

Figure P-14. Representative dispersion curve along with the actual p **act and defective points in Hanging Lake Tunnel.**
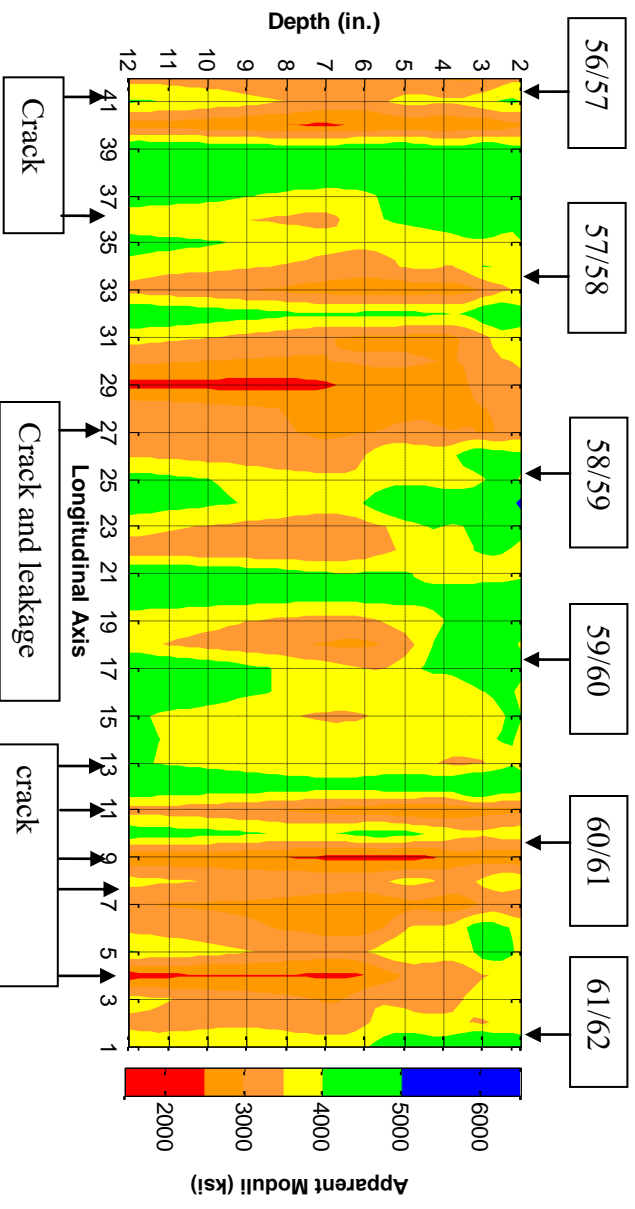
Figure P-15. Variation of apparent modulus with depth along Hanging Lake Tunnel.
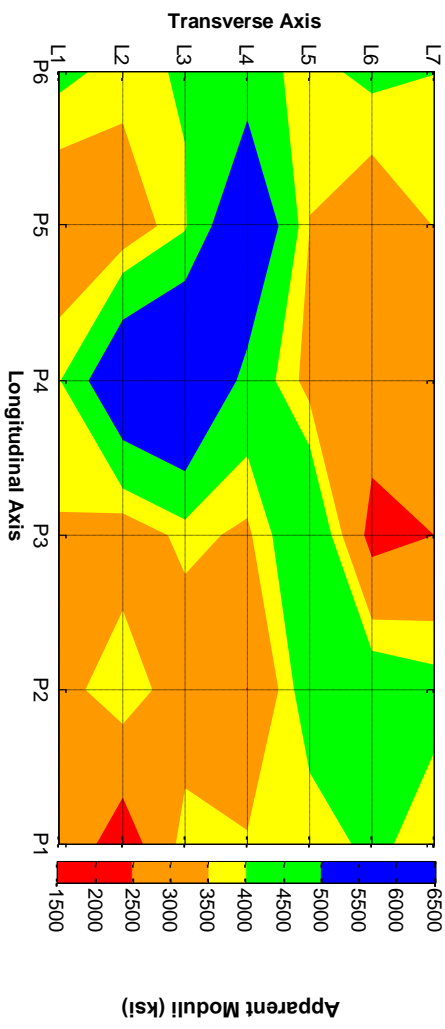
Figure P-16. Planar variation of the average apparent modulus on the meshed block in Hanging Lake Tunnel.
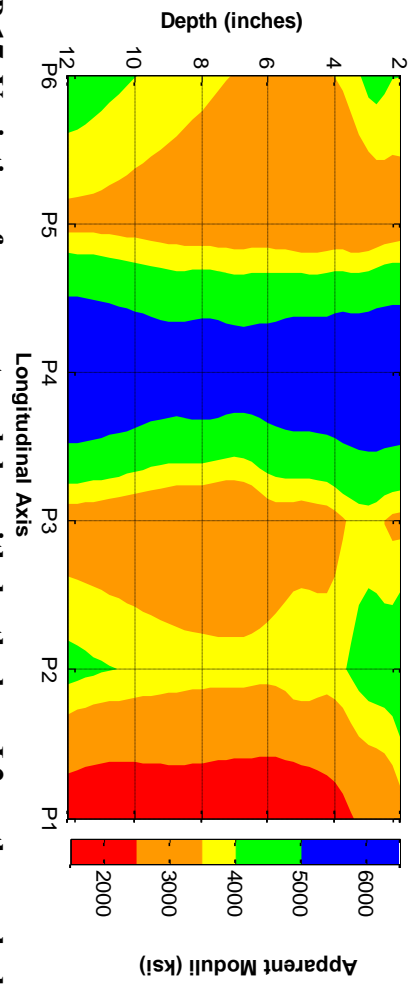
Figure P-17. Variation of apparent modulus with depth along L2 on the meshed block in Hanging Lake Tunnel.

P-16
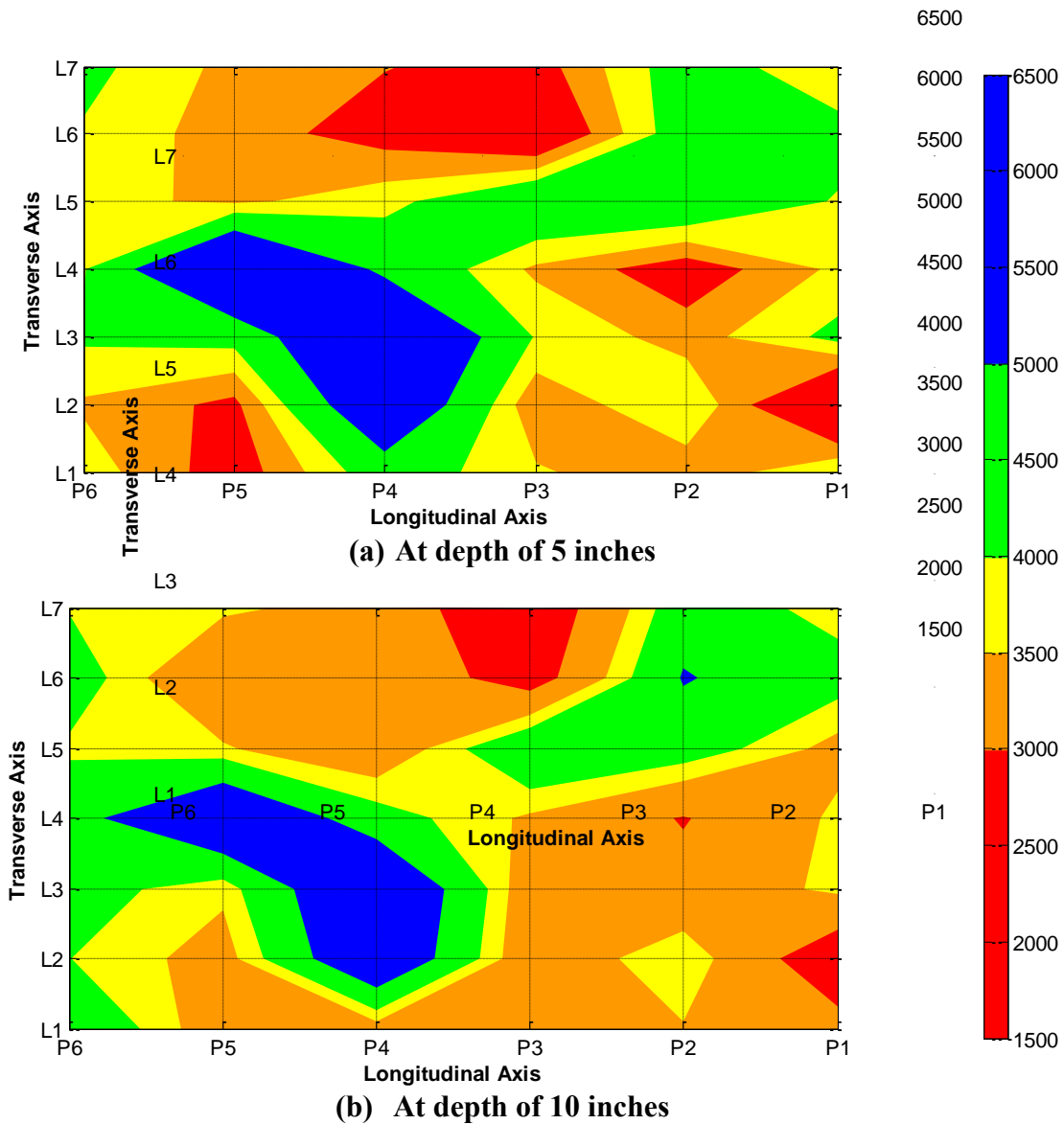
Figure P-18. Planar variation of apparent modulus at different depths of the meshed block in Hanging Lake Tunnel.

Chesapeake Bay Tunnel

Ceiling of Plenum

Figure P-19 shows the result from the IE and USW analyses of the data collected in the intact areas where no cracks or other surface damages were observed and with low dielectric constants (significantly less than 10).

(a) B-scans of amplitude spectrum   (b) B-scan of apparent modulus
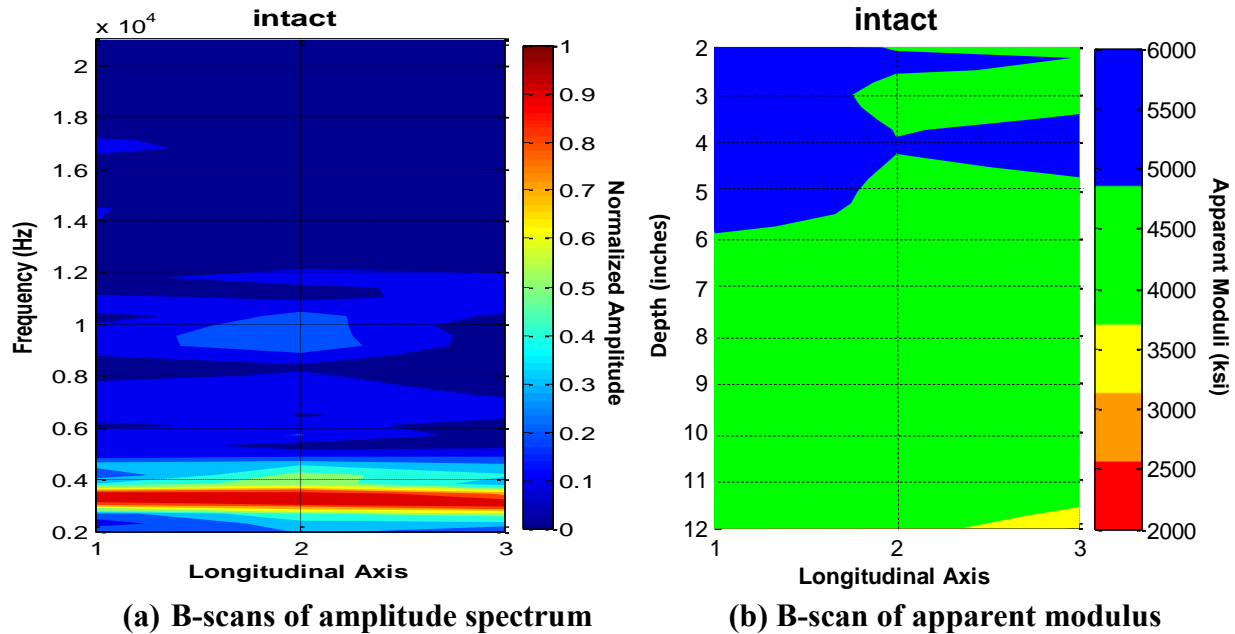
Figure P-19. PSPA results in an intact area on plenum ceiling in Chesapeake Bay Tunnel.

The data used in Figure P-19 were actually from three separated intact spots within a distance of about 20 ft. Since they have the similar feature, the results are represented together. As shown in Figure P-19a, a clear and almost constant peak frequency of about 3 kHz represents the thickness echo of the concrete liner. This frequency results in a thickness of 2 ft for the concrete liner with an average compressive velocity of 13,800 ft/s as per Eq. (P-1). On the other hand, Figure P-19b indicates that the concrete liner at these spots is quite uniform with an average modulus of more than 4000 ksi up to 12-inch penetration. The very high modulus values (indicated in blue in Figure P-19b) may reflect the high-velocity surface conditions.

The results from the PSPA tests for the 10 defective areas are shown in Figures P-20 through P-29. In general, the IE method exhibited higher peak frequencies compared to the thickness frequency, and the USW method showed lower moduli compared to the modulus of normal concrete at those defective areas or spots. For instance, in areas 477+60, 481+76, and 486+81, higher peak frequencies dominated the responses at several points in the IE B-scans. The calculated depths of delamination (by Eq. (P-1)) agreed well with the depths of delamination in the USW B-scans. The anomalies or defects mainly distributed along the transverse cracks on the plenum ceiling. Some exceptions happened, such as in areas 473+56 and 491+25, where the IE and USW analyses were not consistent. This can be attributed to the edge effect near the crack and placement of the PSPA sensor unit relative to the crack. When the crack is between the source and first receiver, the USW modulus is typically greater than normal because of the travel path of the wave. However, when the crack is between the two sensors, the reported USW modulus is lower than normal. The interpretation of the existence of the crack agrees well with the actual condition that was documented during visual inspection.

Apparent Moduli (ksi)

(b) B-scan of apparent modulus

Normalized Amplitude
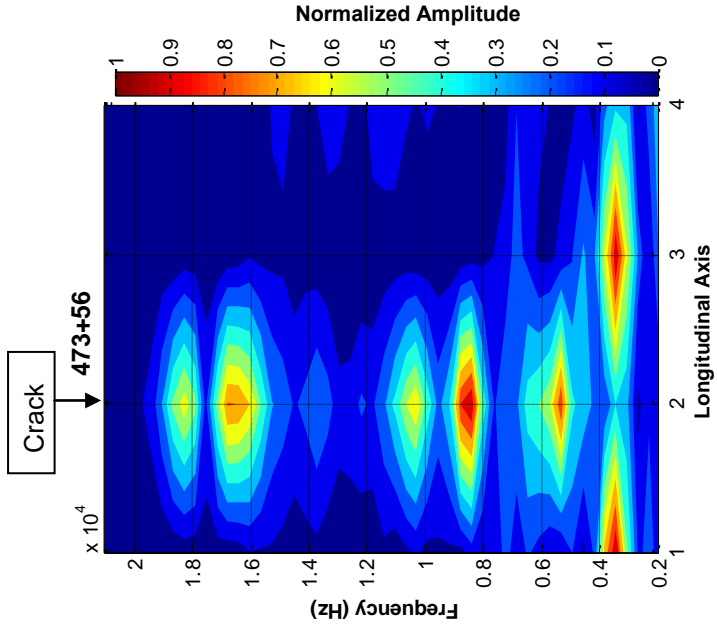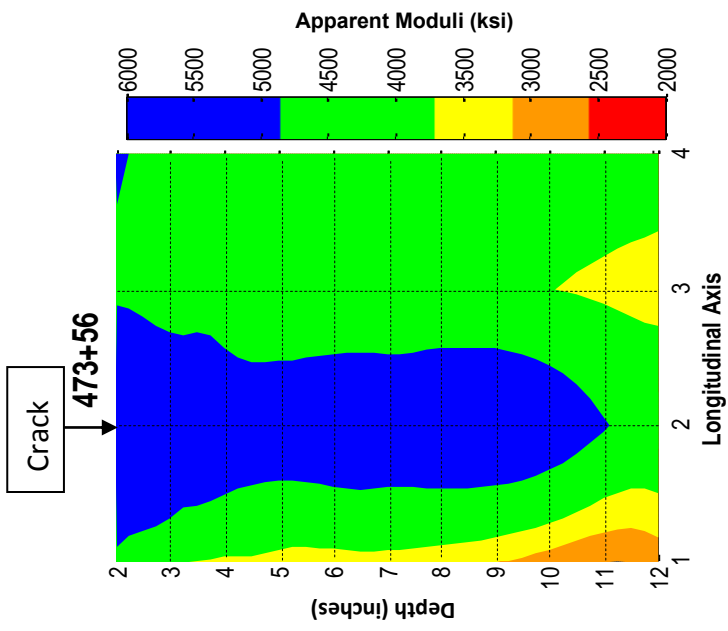
(a) B-scans of amplitude spectrum

Figure P-20. PSPA results on plenum ceiling in area of 473+56 in Chesapeake Bay Tunnel.
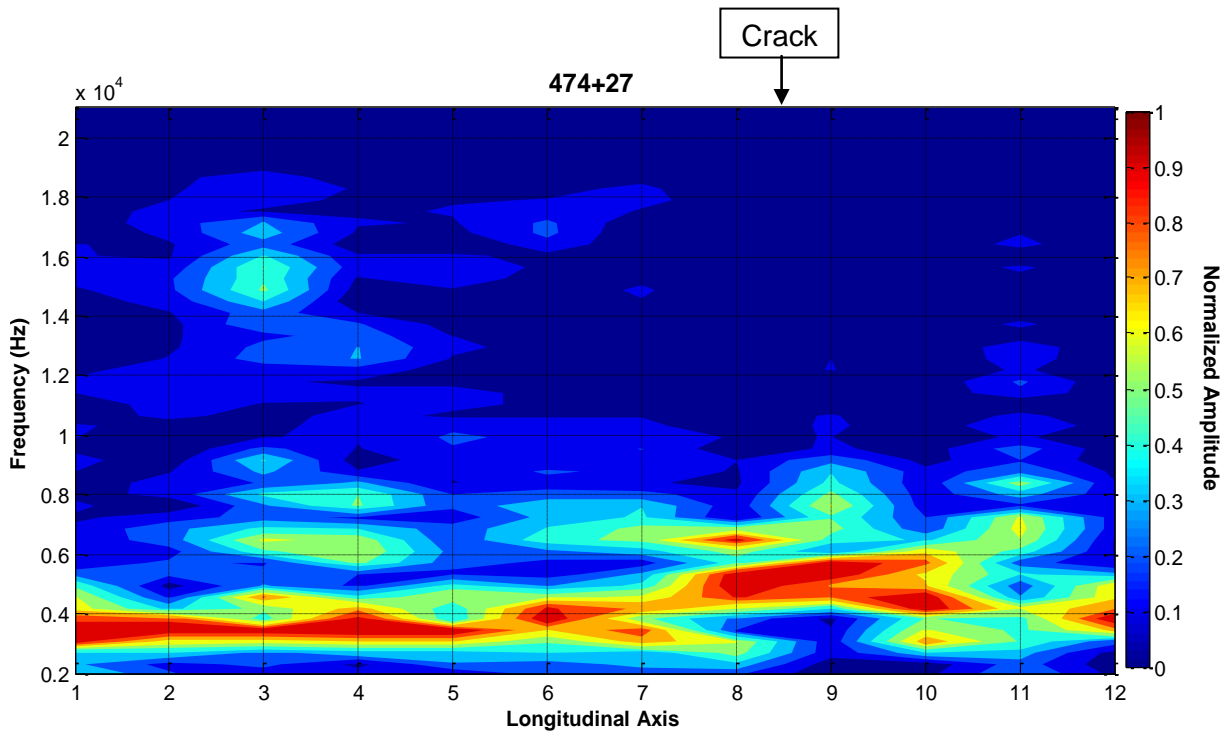
(a) B-scans of amplitude spectrum
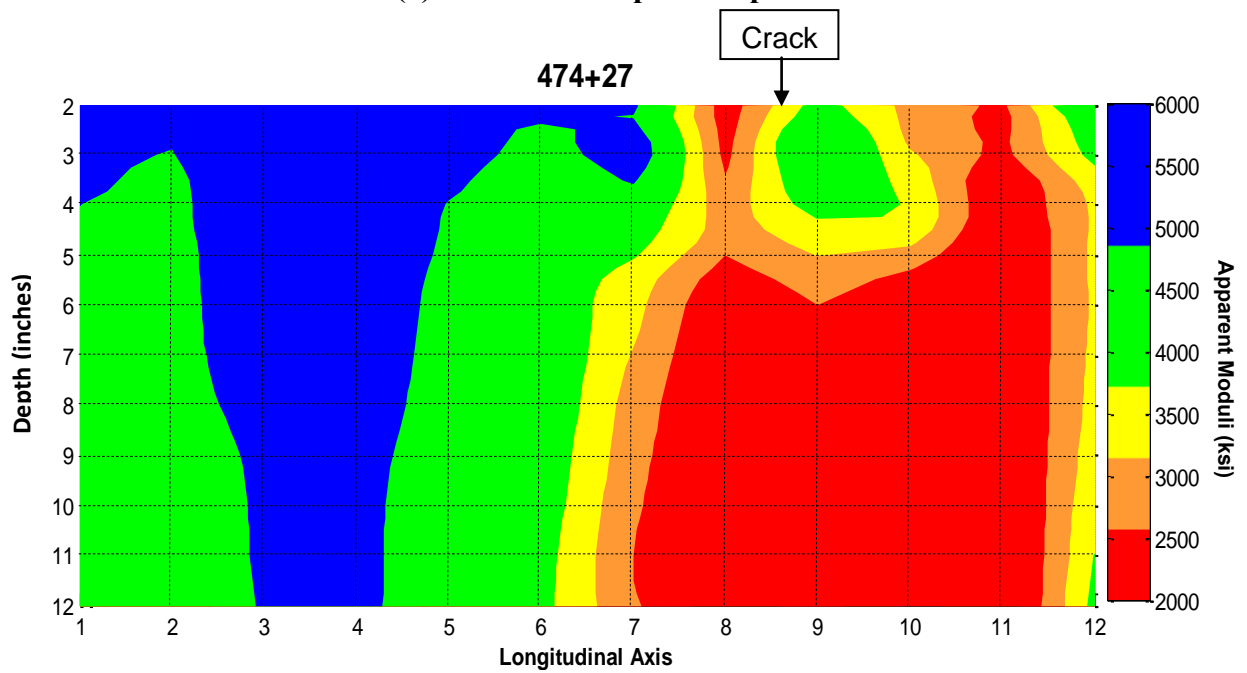
(b) B-scan of apparent modulus

Figure P-21. PSPA results on plenum ceiling in area of 474+27 in Chesapeake Bay Tunnel.

Normalized Amplitude

(a) B-scans of amplitude spectrum
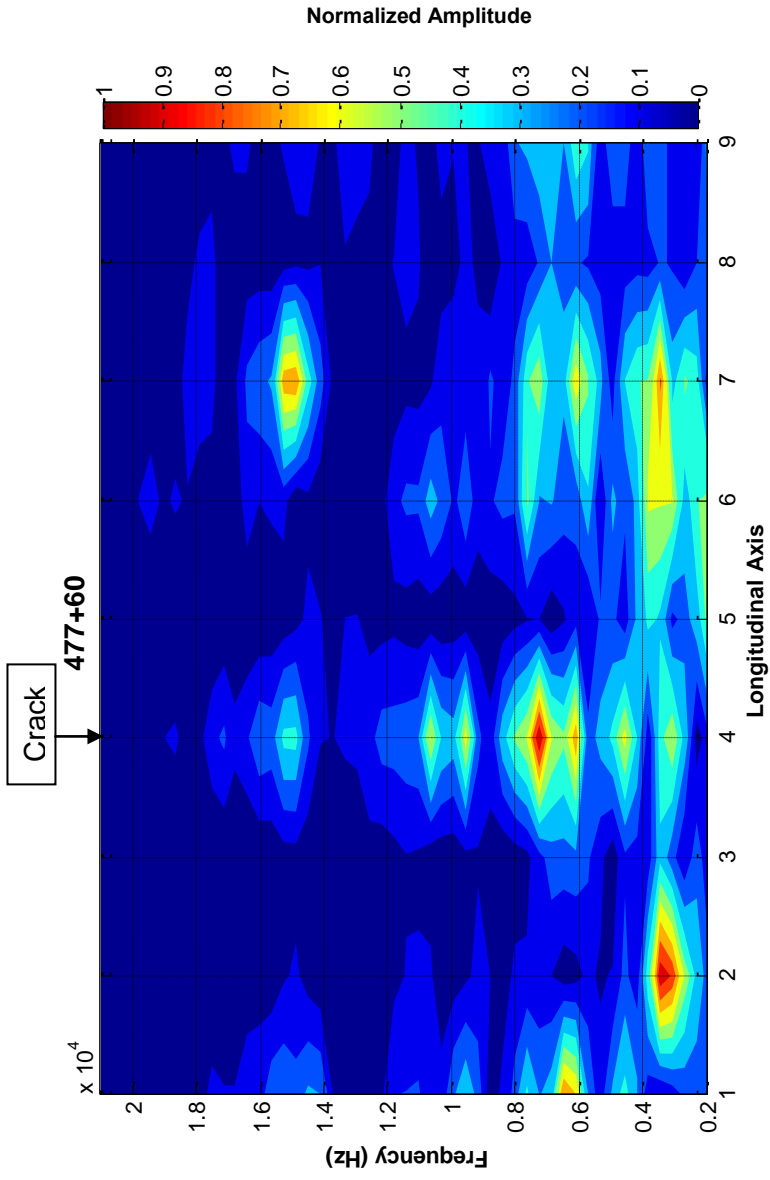
Apparent Moduli (ksi)
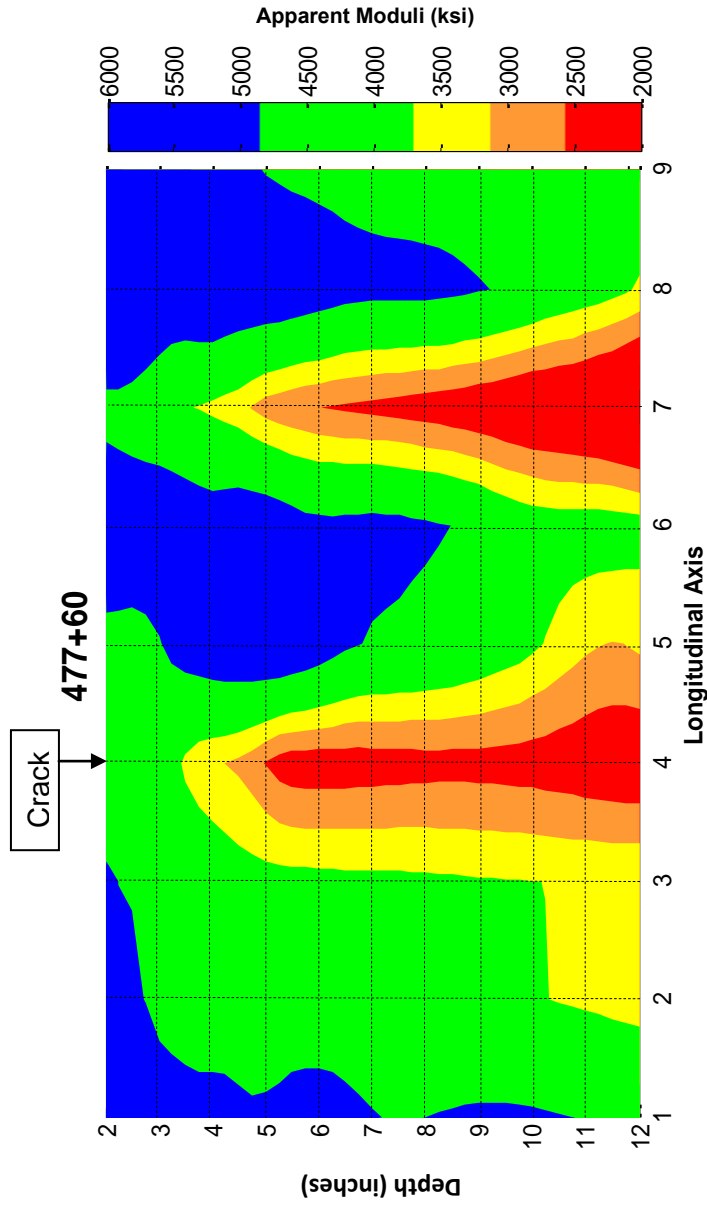
(b) B-scan of apparent modulus

Figure P-22. PSPA results on plenum ceiling in area of 477+60 in Chesapeake Bay Tunnel.

P-21
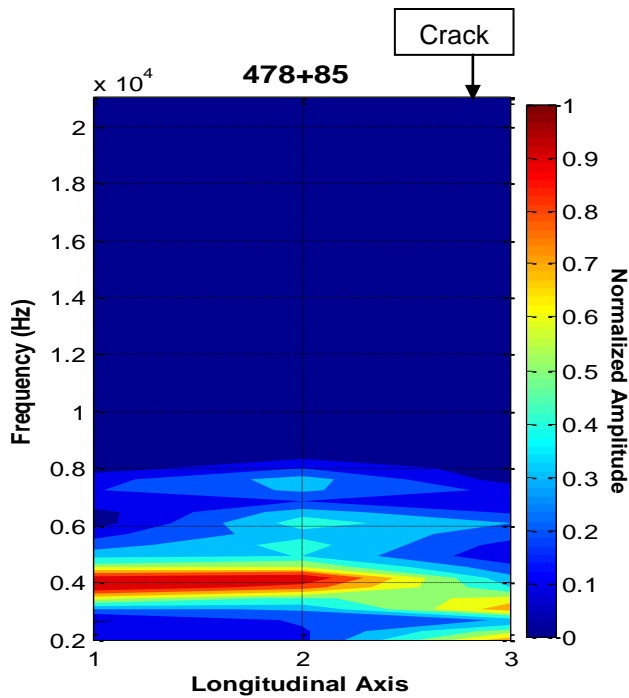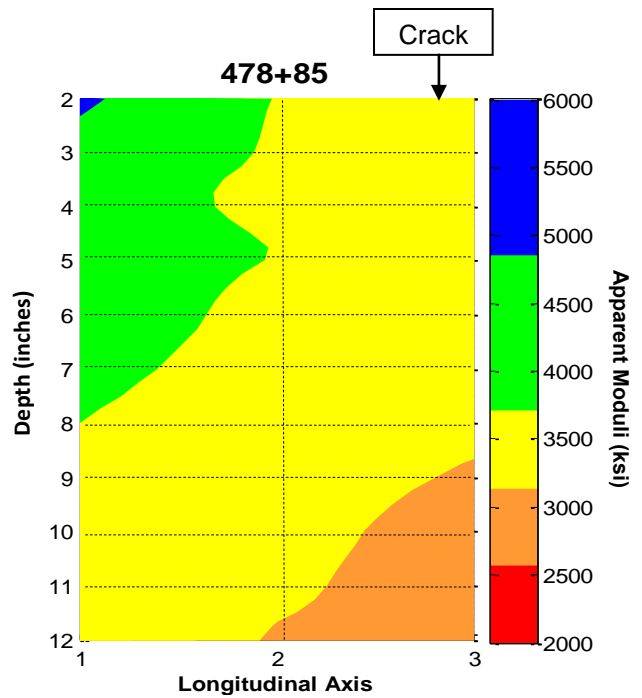
(a) B-scans of amplitude spectrum   (b) B-scan of apparent modulus

Figure P-23. PSPA results on plenum ceiling in area of 478+85 in Chesapeake Bay Tunnel.
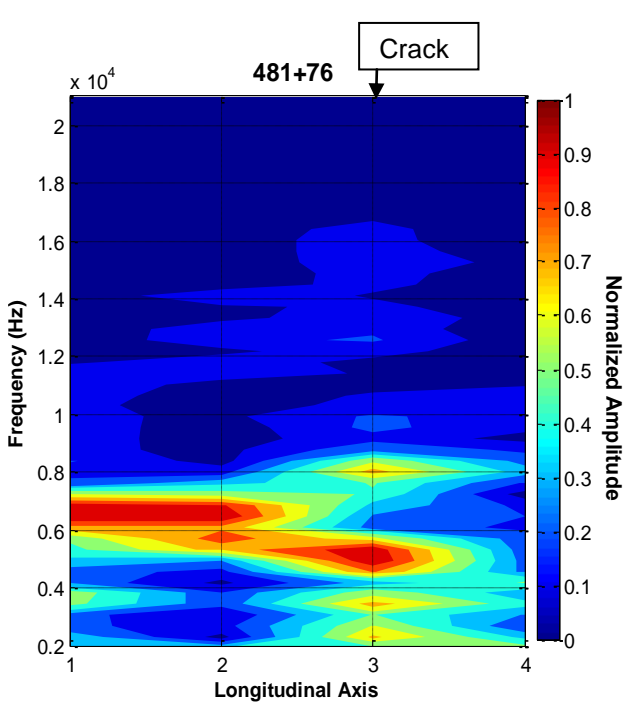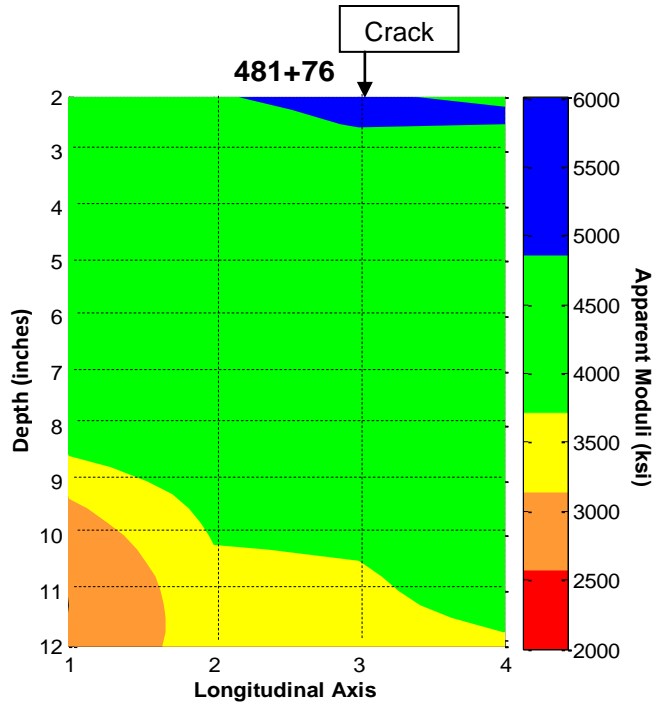
(a) B-scans of amplitude spectrum   (b) B-scan of apparent modulus

Figure P-24. PSPA results on plenum ceiling in area of 481+76 in Chesapeake Bay Tunnel.
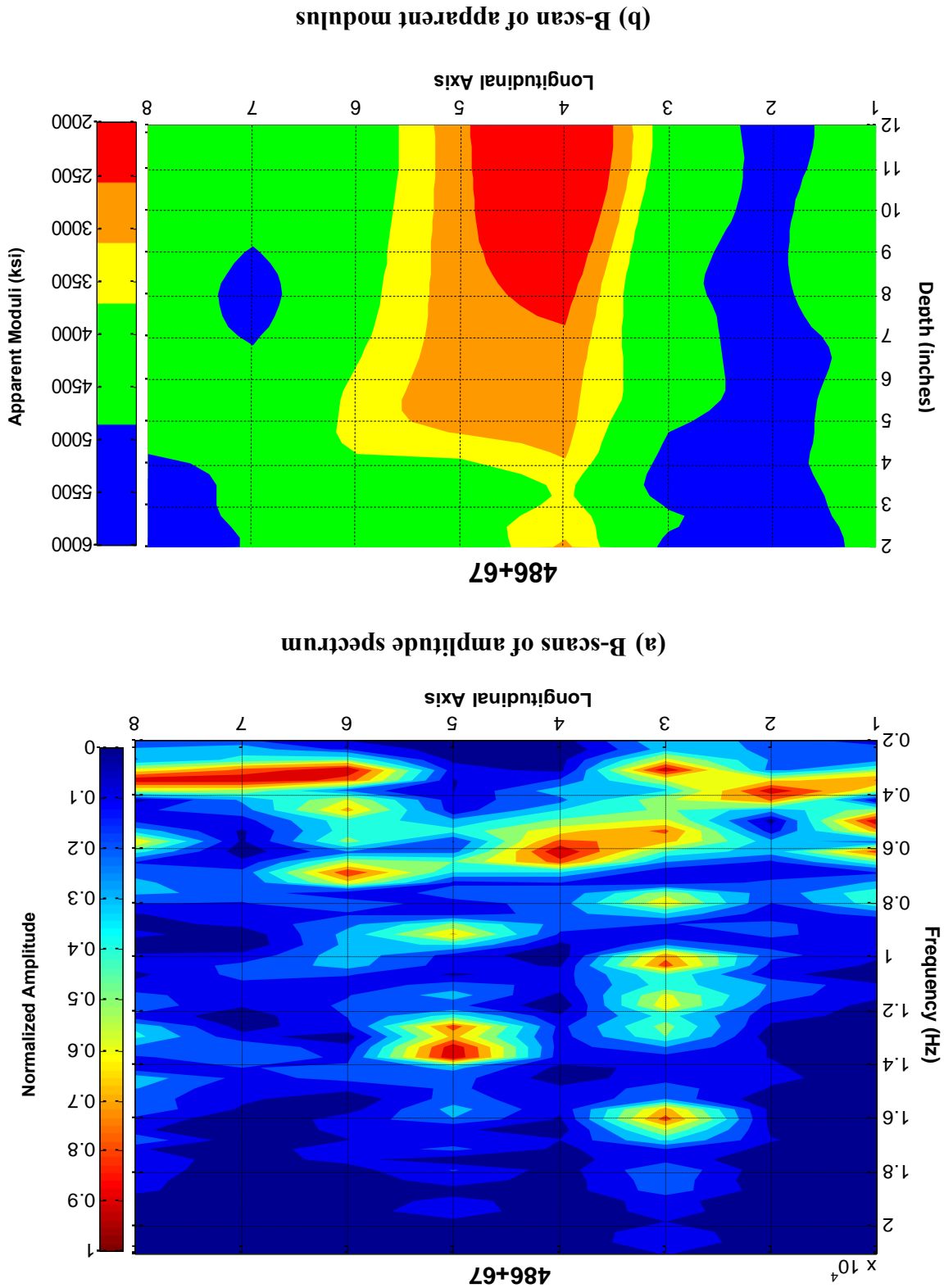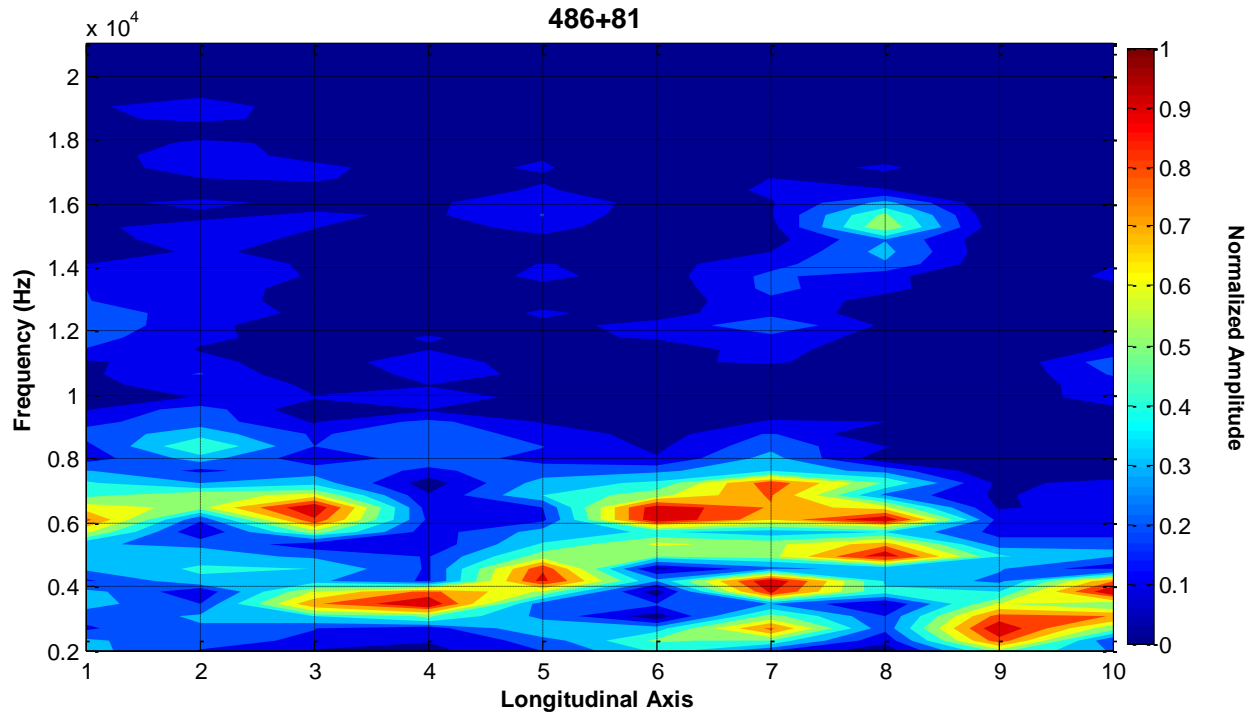
(a) B-scans of amplitude spectrum
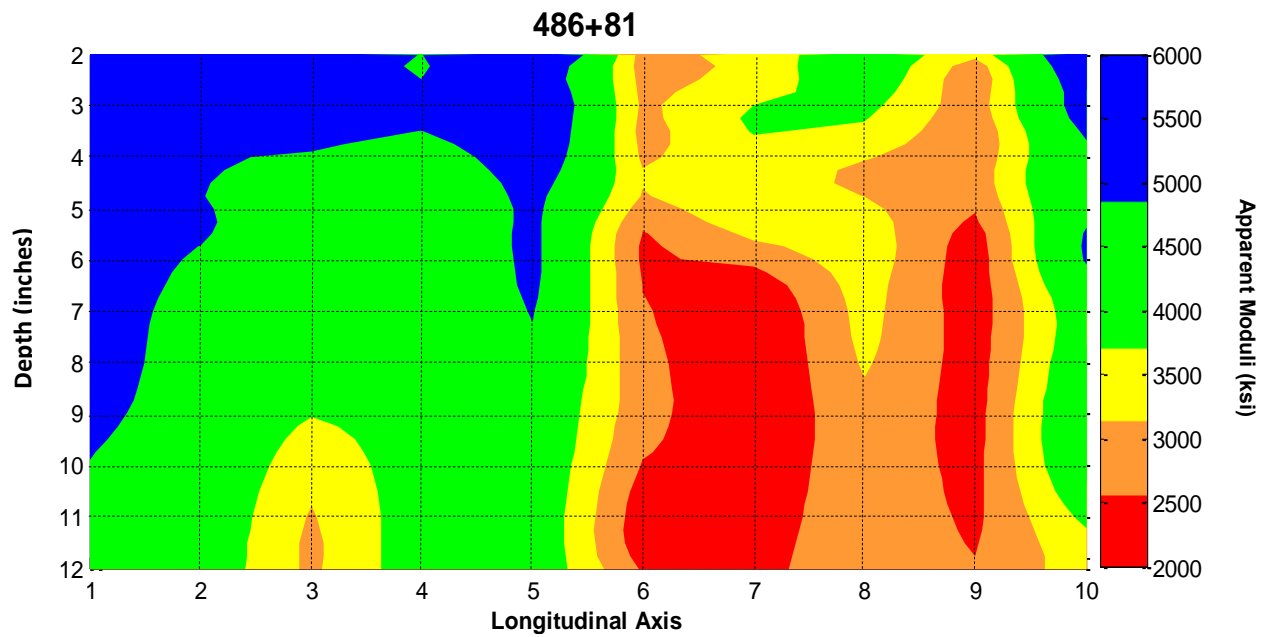
(b) B-scan of apparent modulus

Figure P-26. PSPA results on plenum ceiling in area of 486+81 in Chesapeake Bay Tunnel.
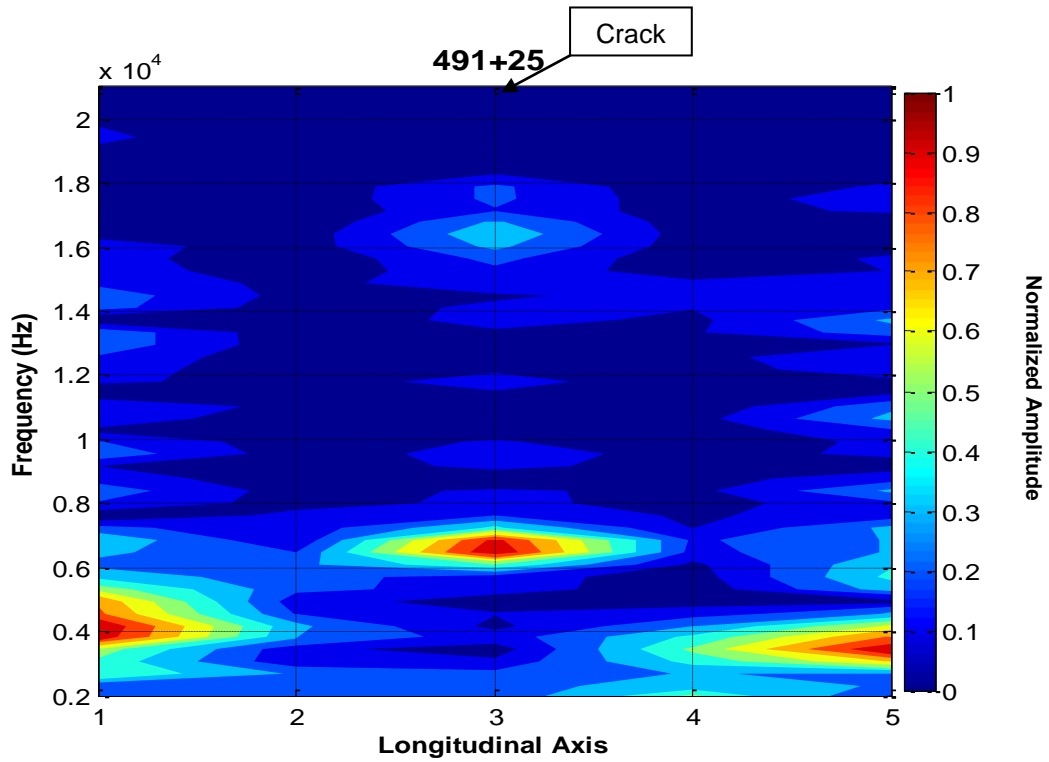
(a) B-scans of amplitude spectrum
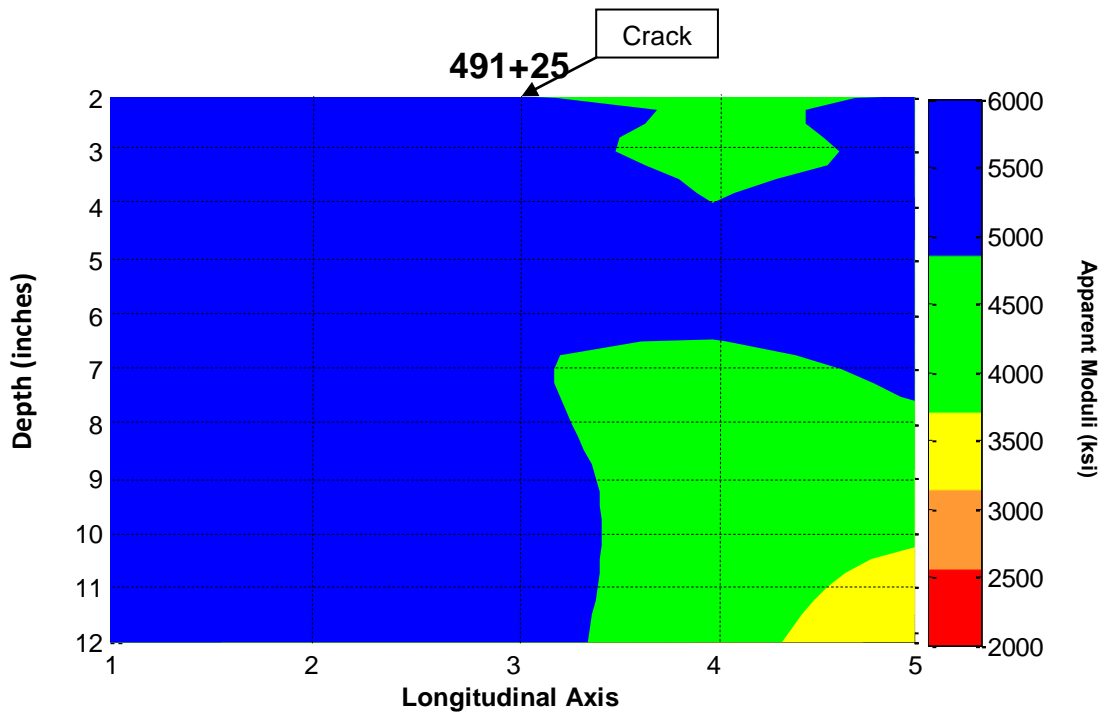
(b) B-scan of apparent modulus

Figure P-27. PSPA results on plenum ceiling in area of 491+25 in Chesapeake Bay Tunnel.

(a) B-scans of amplitude spectrum   (b) B-scan of apparent modulus
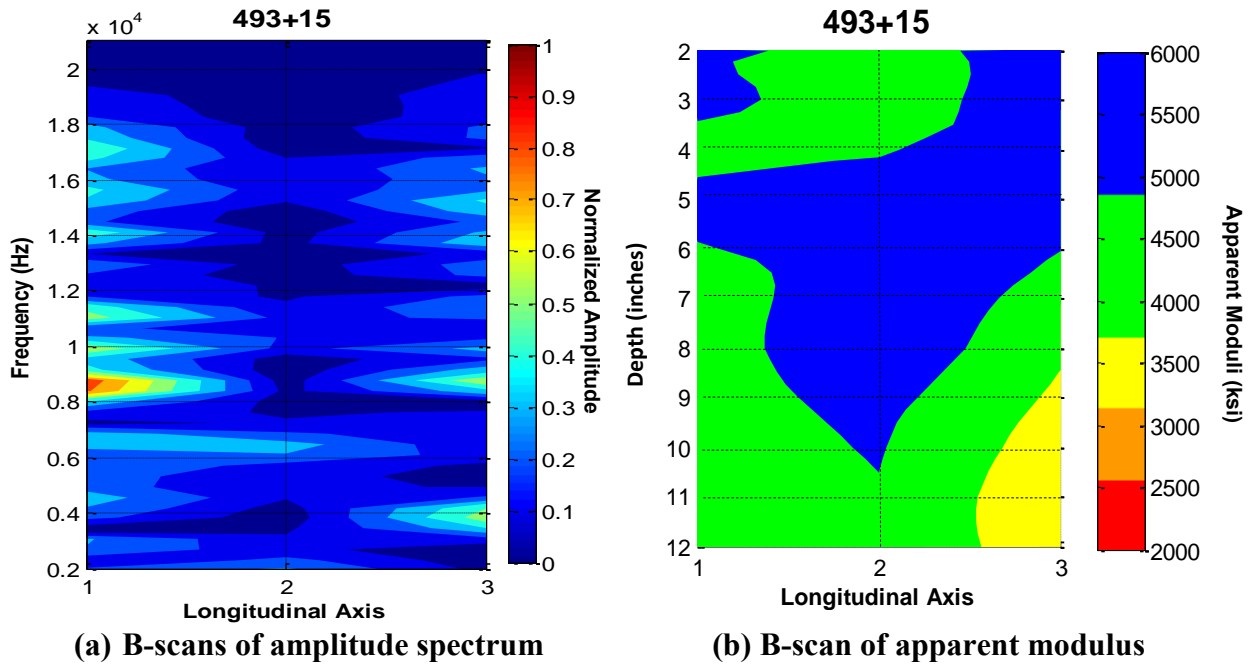
Figure P-28. PSPA results on plenum ceiling in area of 493+15 in Chesapeake Bay Tunnel.

(a) B-scans of amplitude spectrum   (b) B-scan of apparent modulus
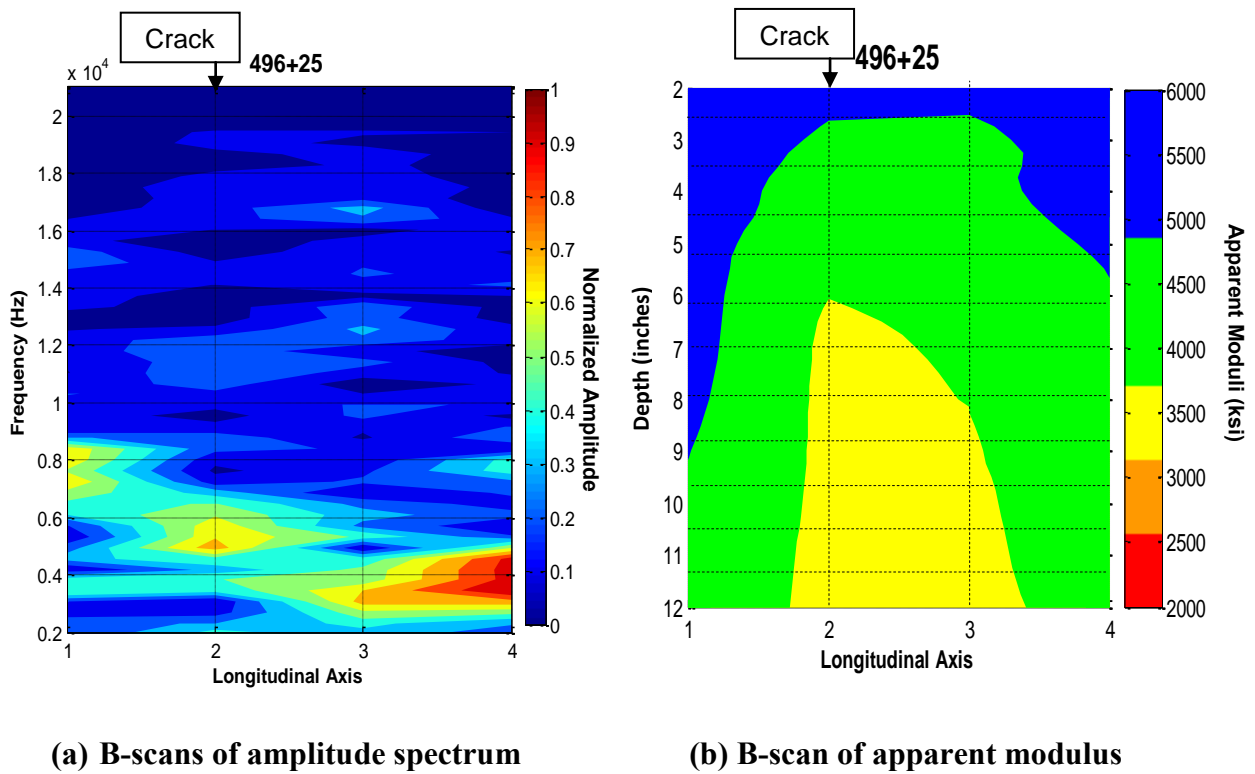
Figure P-29. PSPA results on plenum ceiling in area of 496+25 in Chesapeake Bay Tunnel.

Wall of the Roadway

Tests with the PSPA on the wall of the roadway covered a distance of approximately 150 ft from station 485+6 to station 486+54 with uneven intervals, following the blue marks on the wall. Results are shown in Figure P-30. Test points 9 to 12 were actually restricted in a very small area of about 2 ft by 2 ft. This small area was characterized by an extremely low modulus and higher IE peak frequencies compared to the thickness frequency of the liner, indicating that a severe delamination or void was just behind the tile of the wall.
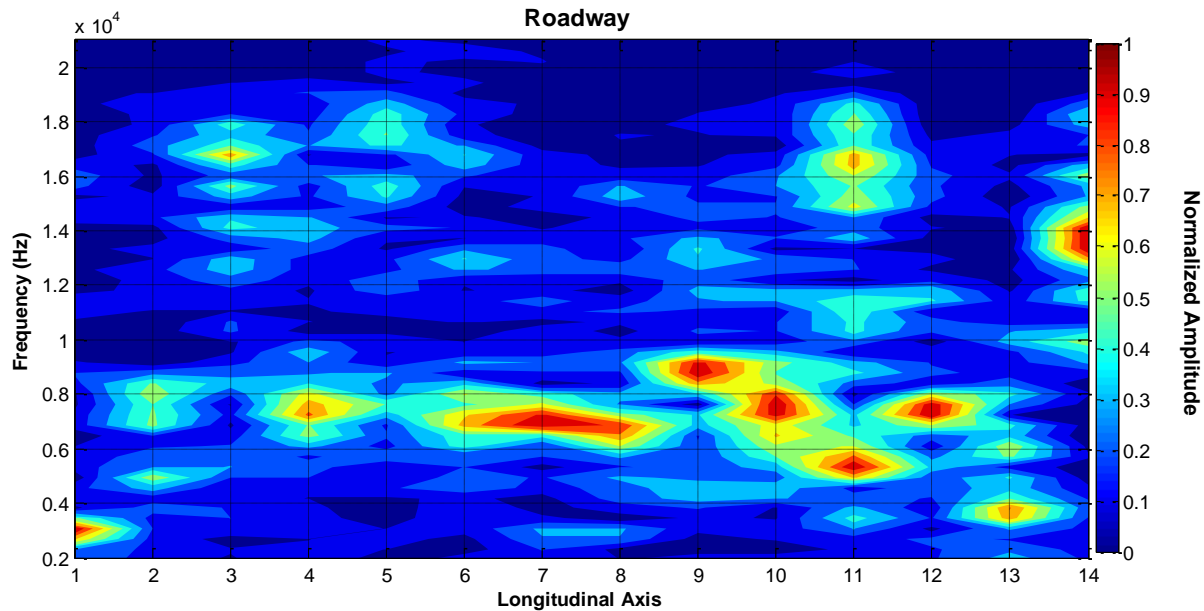
(a) B-scans of amplitude spectrum
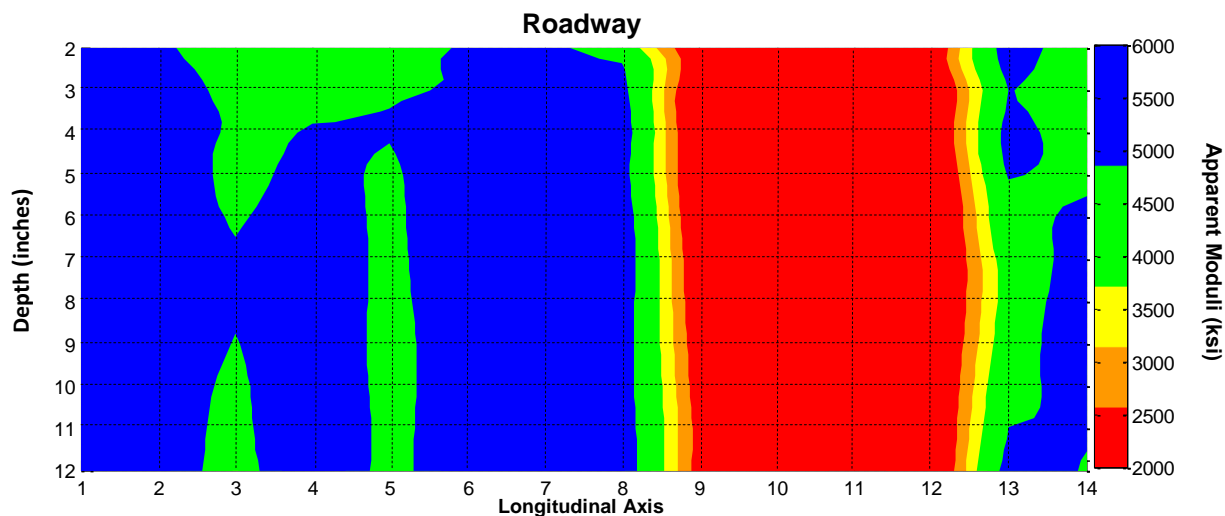
(a) B-scan of apparent modulus

Figure P-30. PSPA results on the wall of the roadway in Chesapeake Bay Tunnel.

APPENDIX P1
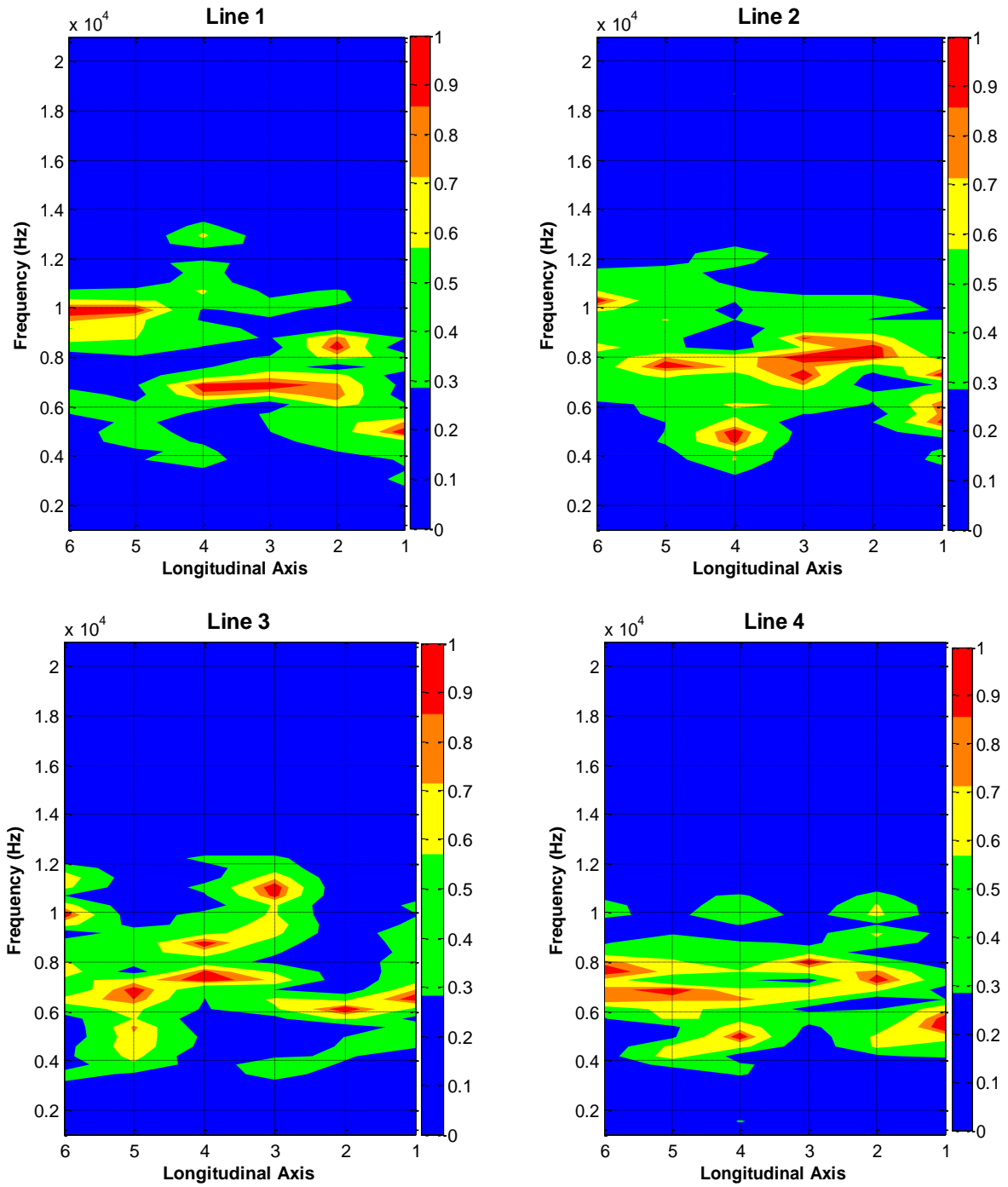
Figure P1-1. IE Spectral B-Scan on the Meshed Blocks in Hanging Lake Tunnel.
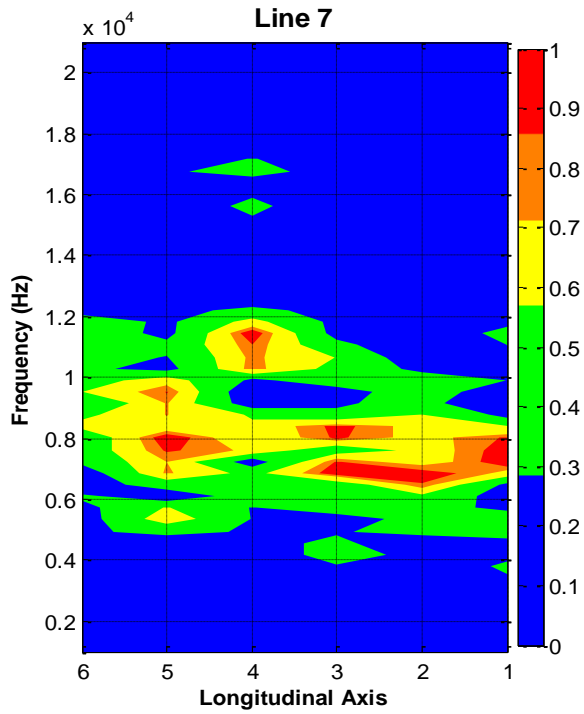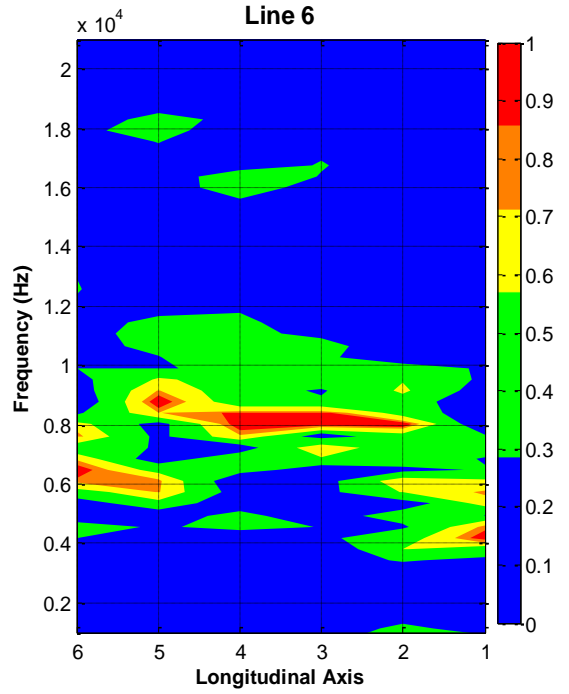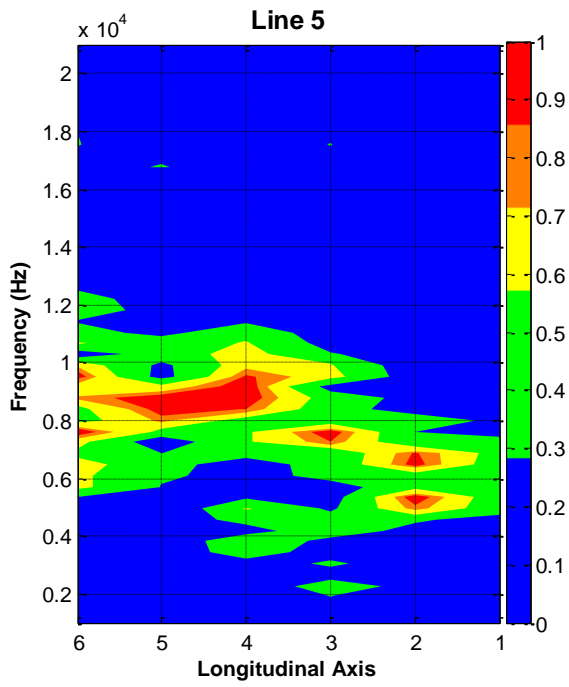
Figure P1-1. IE Spectral B-Scan on the Meshed Blocks in Hanging Lake Tunnel (Cont'd).
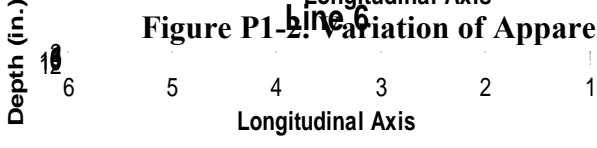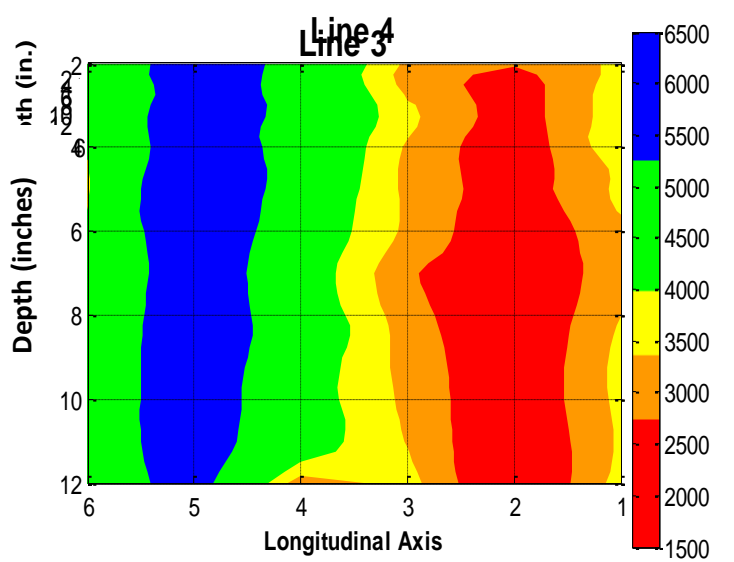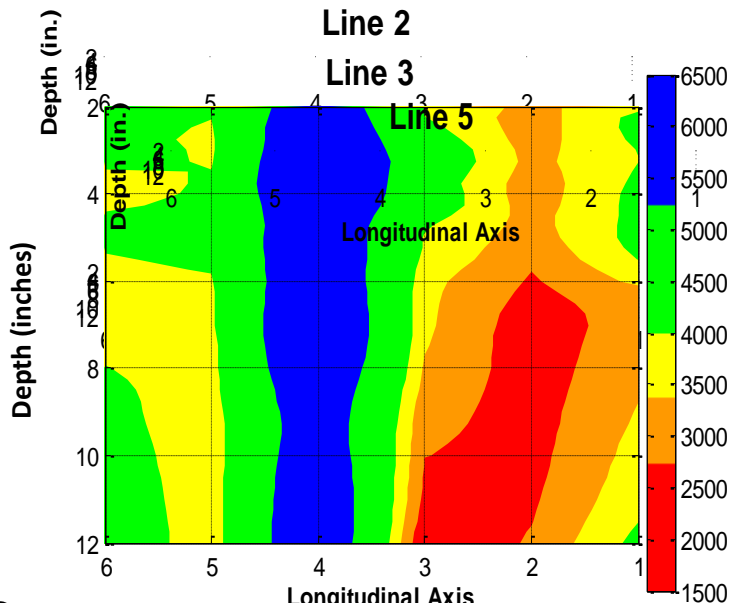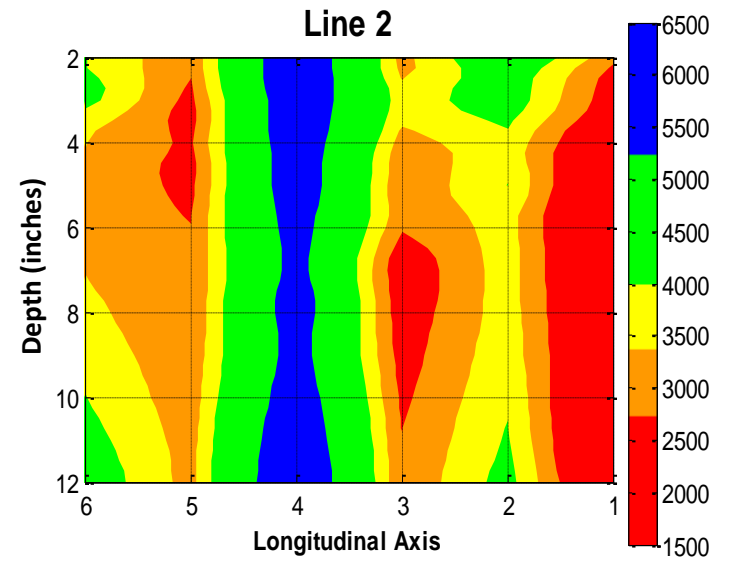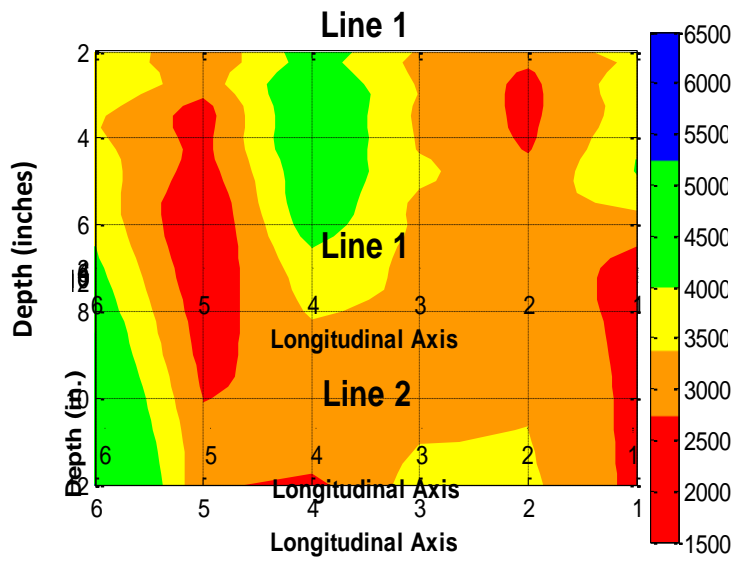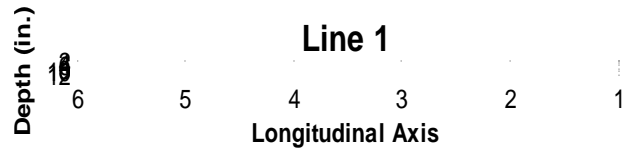
Figure P1-2. Variation of Apparent Modulus with Depth on the Meshed Block in Hanging Lake Tunnel.
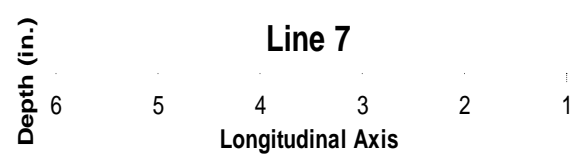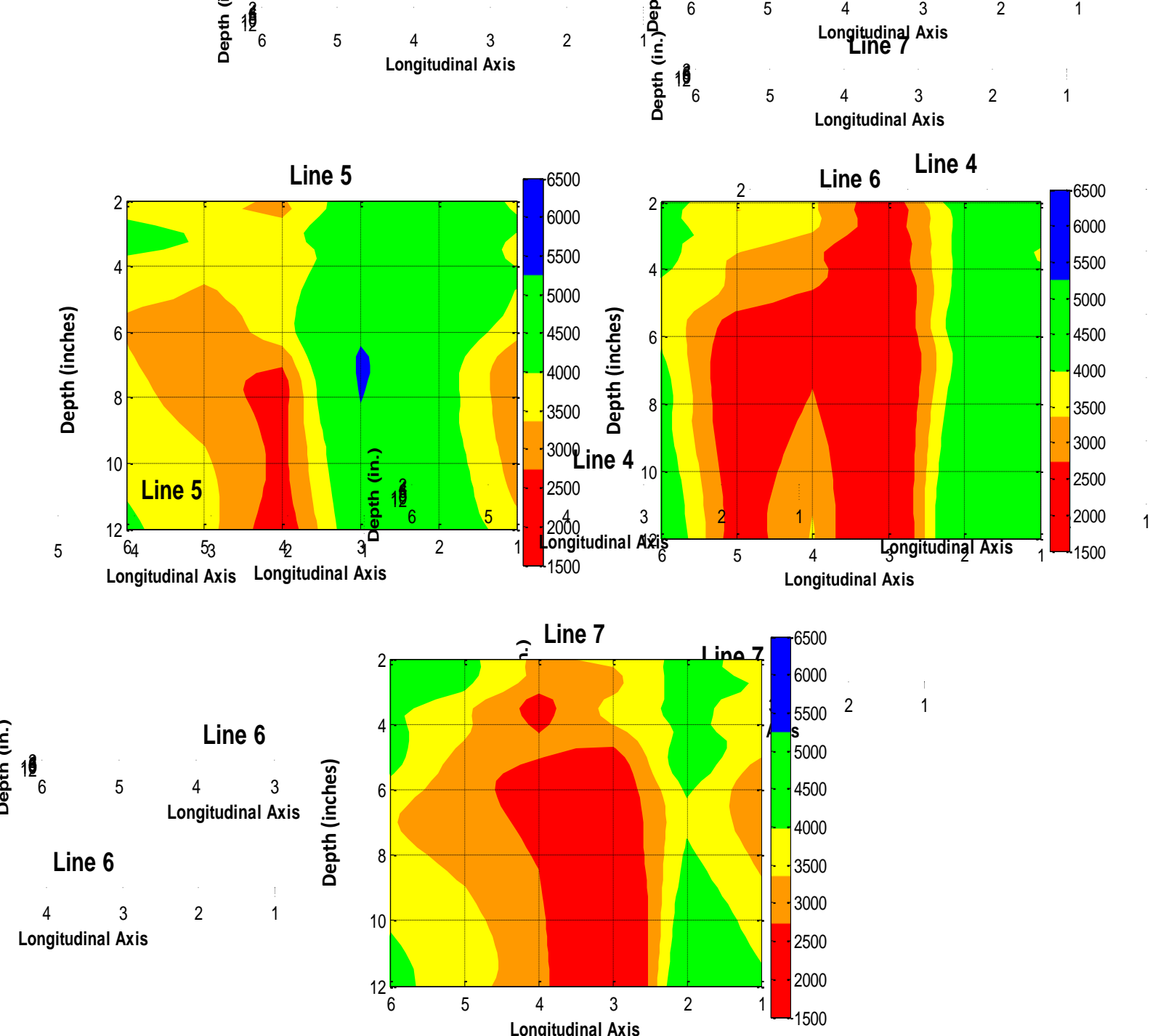
Figure P1-2. Variation of Apparent Modulus with Depth on the Meshed Block in Hanging Lake Tunnel (Cont'd).
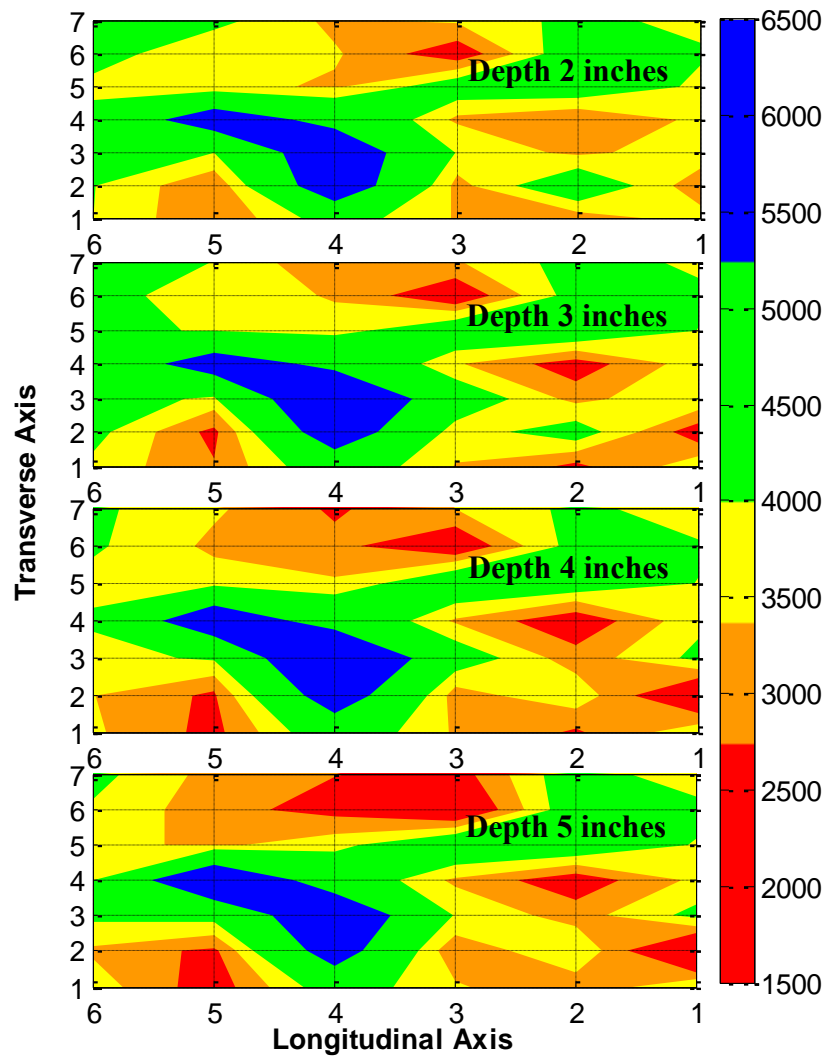
Figure P1-3. Planar Variation of Apparent Modulus at Different Depths for the Meshed Block in Hanging Lake Tunnel.
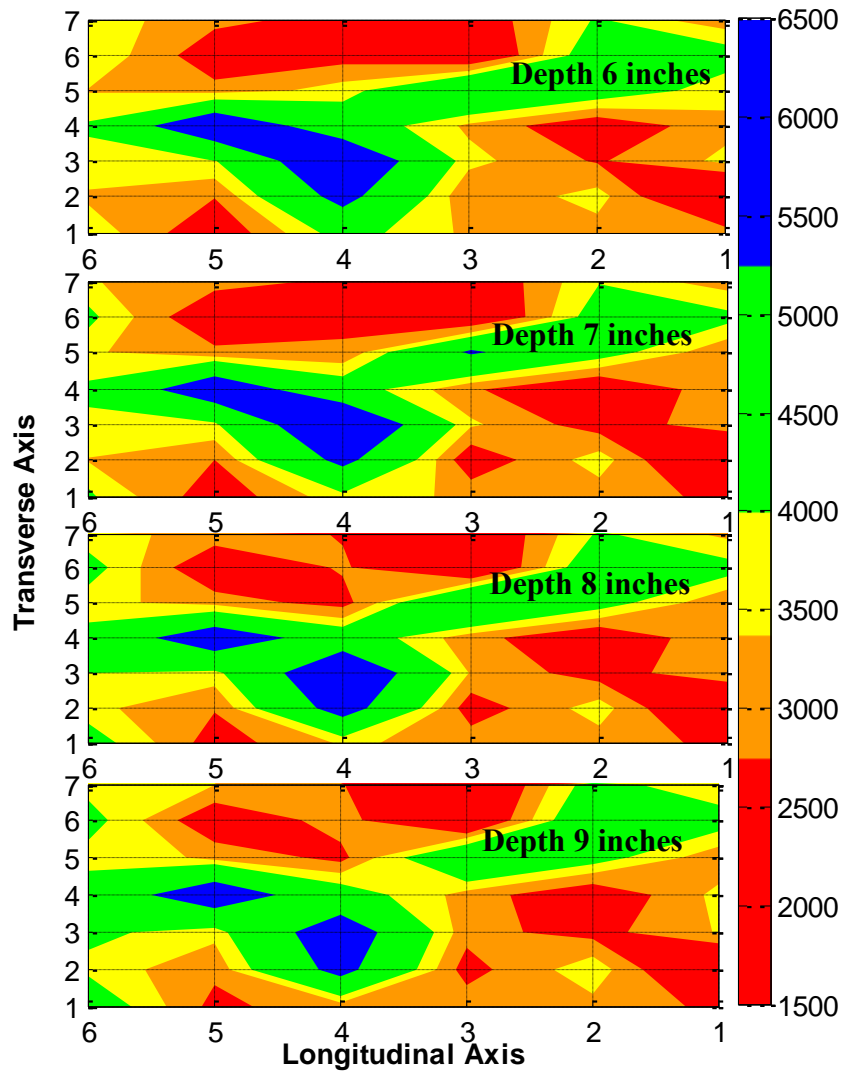
Figure P1-3. Planar Variation of Apparent Modulus at Different Depths for the Meshed Block in Hanging Lake Tunnel (Cont'd).
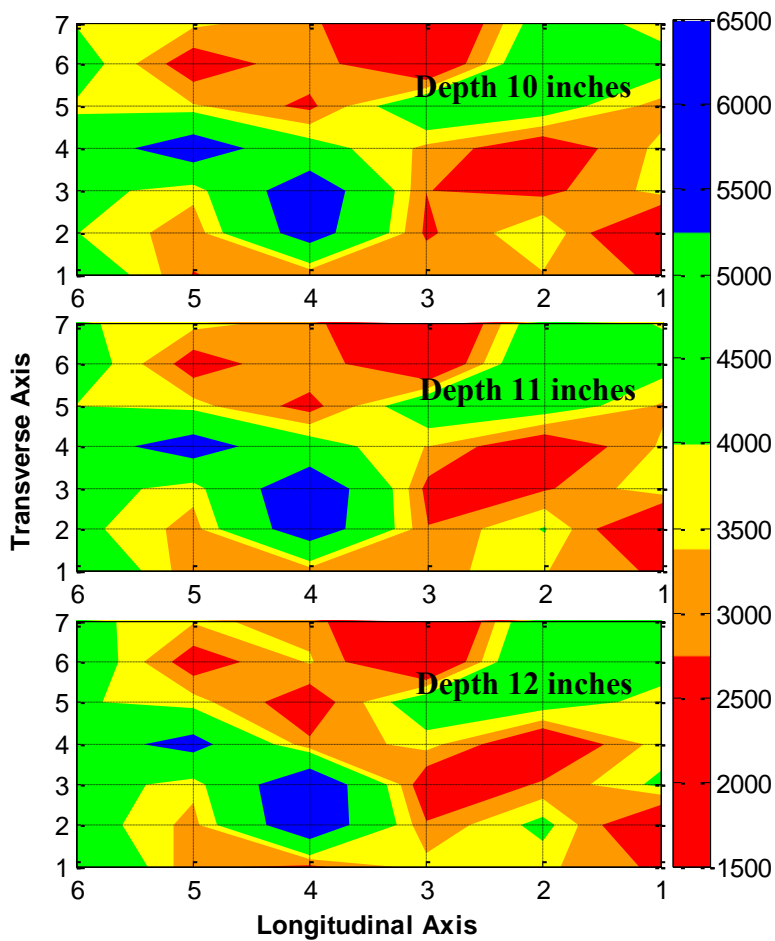
Figure P1-3. Planar Variation of Apparent Modulus at Different Depths for the Meshed Block in Hanging Lake Tunnel (Cont'd).

APPENDIX Q
AUTOMATED IN-DEPTH SCANNING OF TUNNEL LINING BY BAM

TESTING PROGRAM

Field testing was carried out between October 3, 2011, and October 12, 2011, in three tunnels in the United States: two in Colorado (Eisenhower Memorial Tunnel and Hanging Lake Tunnel) and one in Virginia (Chesapeake Bay Bridge-Tunnel). In each tunnel, selected areas were tested using three nondestructive testing (NDT) techniques: ground penetrating radar (GPR), ultrasonic echo (US), and impact echo (IE). The allocated testing time in each tunnel was limited. The number and location of the test areas were selected based on either pre-analysis (mostly thermography) or the existence of visual distress. The on-site working conditions were also taken into account. Table Q-1 provides the details of the test program including the number and size of test areas in each tunnel as well as the testing methods.

Table Q-1. Overview of BAM field-testing program in October 2011.

Code	Tunnel	Location	Date	Technique	Size in inch	Spacing in inch	Notes
EH1	Eisenhower	Seg3 Block2-3	10/03/2011	US	40 x 40	1	
				IE	2 x 24	1	
EH2	Eisenhower	Seg11 Block1	10/04/2011	US	40 x 24	1	anomaly, reinforcement
				IE	40 x 24	1	
				GPR	40 x 24	2	anomaly, reinforcement
HL1	Hanging Lake	Seg 56/57	10/05/2011	US	48 x 24	1	anomaly
				IE	48 x 24	1	anomaly
				GPR	48 x 24	2	beam, dowels, reinforce.
HL2	Hanging Lake	Seg 57	10/05/2011	US	48 x 24	1	crack, reinforcement
				IE	48 x 24	1	backwall?
				GPR	48 x 24	2	crack, reinforcement
HL3	Hanging Lake	Seg 57/58	10/06/2011	US	48 x 24	1	reinforcement
				IE	48 x 24	1	
				GPR	48 x 24	2	joint, dowels
CPB1	Chesapeake Bay Bridge Tunnel	St.No.474+27	10/11/2011	US	48 x 24	1	anomaly, backwall, reinforce.
				IE	46 x 24	1	anomaly, backwall
				GPR	48 x 24	2	reinforcement
CPB2	Chesapeake Bay Tunnel	St.No.481-76	10/12/2011	US	40 x 24	1	backwall, anomaly, reinforce.
				IE	40 x 24	1	backwall, anomaly
				GPR	40 x 24	2	reinforcement
CPB3	Chesapeake Bay Tunnel	St.No486-67	10/12/2011	US	48 x 24	1	anomaly, backwall, reinforce.
				IE	48 x 24	1	backwall, anomaly
				GPR	48 x 24	2	reinforcement
CPB4	Chesapeake Bay Tunnel	St.No.487	10/12/2011	US	48 x 36	1	condition of tile bonding
				IE	4 x 36	1	
				GPR	48 x 36	2	reinforcement

TUNNEL DESCRIPTION

Eisenhower Memorial Tunnel

The Eisenhower Tunnel is located approximately 60 miles west of Denver, Colorado, on Interstate 70 and is a part of the Colorado Department of Transportation. It is the highest vehicular tunnel in the world, located, on average, at an elevation of 11,112 ft. It is 1.693 mi long and runs through a mountain within the Arapaho National Forest. Figure Q-1 shows a construction information bulletin from the tunnel side, Figure Q-2 is a picture of the tunnel at present time and one of its supply air ducts where measurements took place. Construction started in March 1968 and was completed in March 1973. The information about this tunnel was obtained from the Colorado Department of Transportation Website (DOT, 2011).
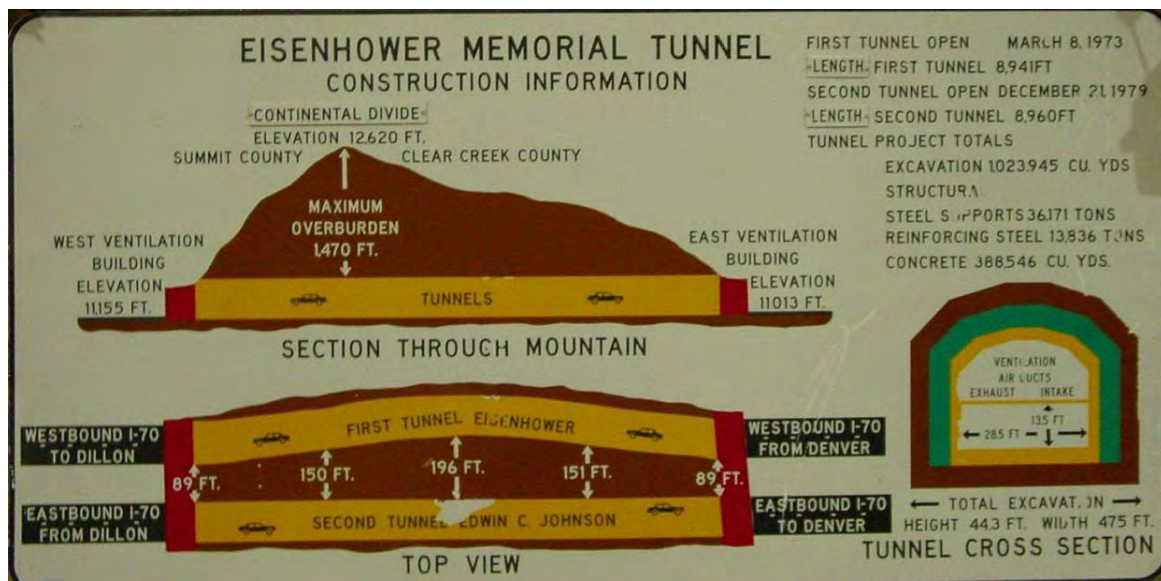
Figure Q-1. Construction information, Eisenhower Memorial Tunnel [1].

(a)   (b)

Figure Q-2. Entrance to the Eisenhower tunnel (a) and the interior of the supply air duct, where measurements took place (b).

Hanging Lake Tunnel

The Hanging Lake Tunnel stretches over 4000 ft through a mountain bordering the Glenwood Canyon in Colorado as part of I-70. The most noteworthy feature of this tunnel is

the direct change of I-70 from bridge to tunnel (Figure Q-3). Construction started in 1980 and was completed in 1992. The entrance of the tunnel and the supply air duct are shown in Figure Q-3.

(a)   (b)
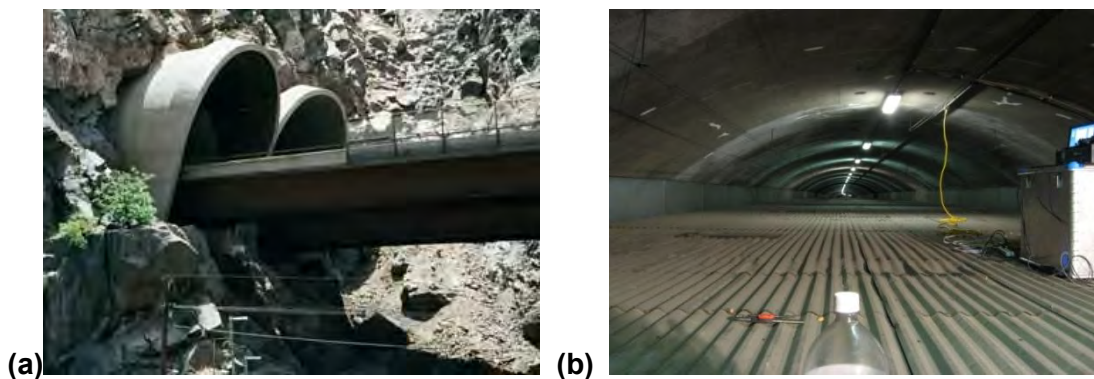
Figure Q-3. Hanging Lake Tunnel entrance (Salek, 2002) (a) and supply air duct, where measurements took place (b).

Chesapeake Bay Tunnel

The Chesapeake Bay Tunnel is a part of a bridge-tunnel construct connecting Virginia's eastern shore with its mainland. The tunnel itself is 1 mi long going under the Atlantic Ocean. Construction started in November 1960, and the first part was opened in April 1964. Figure Q-4 shows a bulletin from the side and a view of the supply air duct, where most measurements were taken.

(a)   (b)

Figure Q-3. Construction information on the Chesapeake Bay Bridge-Tunnel (a) and supply air duct where most measurements took place (b).

MEASUREMENT TECHNIQUES

The different measurement techniques used by BAM for this project can be mounted on an automated scanning device developed by BAM. This ZFP Scanner (Figure Q-5) (Zoega, et al., 2012) can be used on horizontal surfaces as well as vertical surfaces including overhead testing, even in narrow areas. The scanner is fixed to the surface using vacuum "feet" or plates. A choice of 1-inch grid spacing when running acoustic tests requiring contact allows a speed of operation of 11 ft^2/h (1 m²/h). With non-contact transducers such as air-coupled radar antenna, testing at a speed of 156 ft^2/h would be possible. The field of measurement can be up to 17.6 ft^2 (4.2 ft x 4.2 ft).

The advantage of the ZFP-Scanner lies in its easy and fast on-site assembly. It can be carried in a relatively light and small package. Its size allows the scanner to be transported in cars and carried through small openings to reach difficult-to-access areas such as the vents above tunnels. The commonly used equipment for NDT of structures, including GPR, US and IE devices, can be easily attached to the scanner for testing and detached after the completion of the measurements. The scanning and NDT data acquisition are controlled by a single notebook. This simplifies the control and reduces the equipment and weight of the measurement system.

(a)

(b)
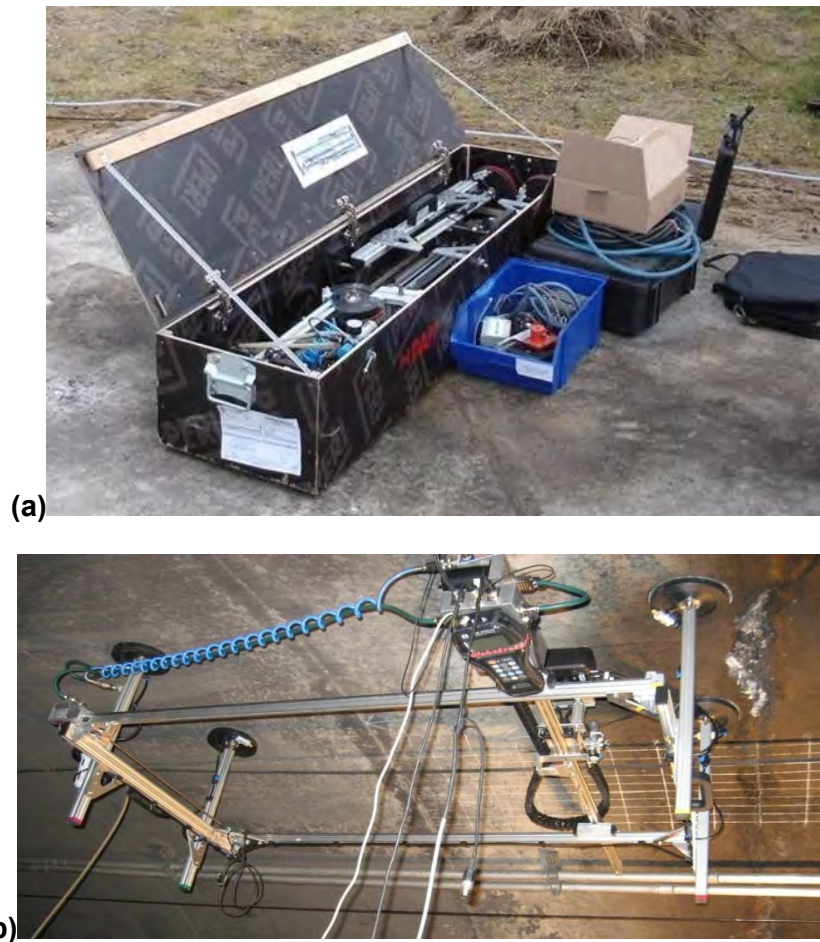
Figure Q-5. ZFP-Scanner packed in its custom-made box (a) and onsite in Chesapeake Bay Bridge Tunnel (b), with the ultrasonic echo transducer mounted on it.

The three NDT techniques and the typical data from each are briefly discussed below.

GPR

Basic Operation Principles

Ground-penetrating radar is a widely used subsurface scanning tool that was employed here to detect subsurface defects in tunnel linings. GPR sends discrete electromagnetic pulses into the structure and then captures the reflections from subsurface layer interfaces. Radar is an electromagnetic (EM) wave and therefore obeys the laws governing reflection and transmission of EM waves in layered media. At each interface within a structure, a part of the incident energy will be reflected and a part will be

transmitted. The ratio of reflected to transmitted energy depends on the electromagnetic contrast of the material on either side of the interface.

There are two main types of GPR equipment that are typically used for civil structure investigations. The high-speed air-coupled (AC) systems are capable of testing at high speeds of up to about 50 mph and can penetrate up to 24 inches in some materials. They are excellent tools for network-level data collection. The high-frequency ground-coupled (GC) GPR systems provide better depth penetration and high densities of readings and are excellent for project-level data collection and applications concerning locating steel and defects such as voids in concrete. Their limitation is that they must stay in close contact with the material under test, making the speed of data collection relatively slow (1 mph-5 mph).

GPR antennas can emit EM pulses of different frequencies. The choice of frequency depends on the required depth of penetration and depth resolution. In general, lower-frequency antennas have a better resolution in deeper depth. Higher-frequency antennas show better details of reflectors close to the surface but do not penetrate the test object as deep. Determining which antenna to use is therefore dependent on the task, the experience of the user, and other NDT methods used at the scene.

In this study, BAM used a ground-coupled GPR from Geophysical Survey Systems Inc. (GSSI), with a center frequency of about 1.5 GHz (see Figure Q-6).

Typical Results

Ground-coupled GPR has proved very useful in discovering reinforcements, dowels, surface cracks, moisture, and other intrusions. As shown in Figure Q-7, scanner testing on fine grids provides the opportunity to generate B-, D-, and C-Scans from the measurements. Reinforcement bars and dowels are best seen in C-Scans and recognized by their unusually high reflection amplitudes of positive phase (white strips) and linear geometries. Surface cracks are best seen in B- or D-Scans and recognized by near-surface hyperbolas. The term *anomaly* is hereinafter referred to as any unusual features detected in the radar scans. Anomalies are usually reflections of significant amplitude or extent, where reflections from the geometrical boundaries are not expected. For example, the area in the C-Scan exhibiting unusually high amplitudes with reverse phase is designated as an anomaly in Figure Q-7(d).

(a)   (b)
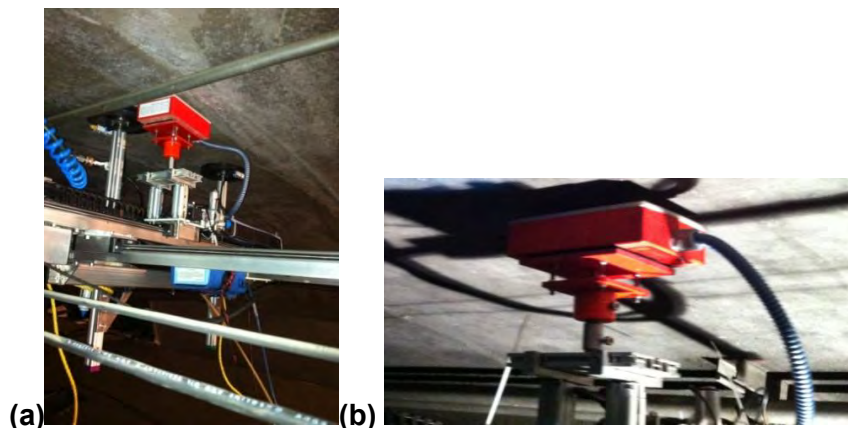
Figure Q-6. (a) The 1.5 GHz GC GPR antenna mounted on the scanning system, and (b) close-up view.
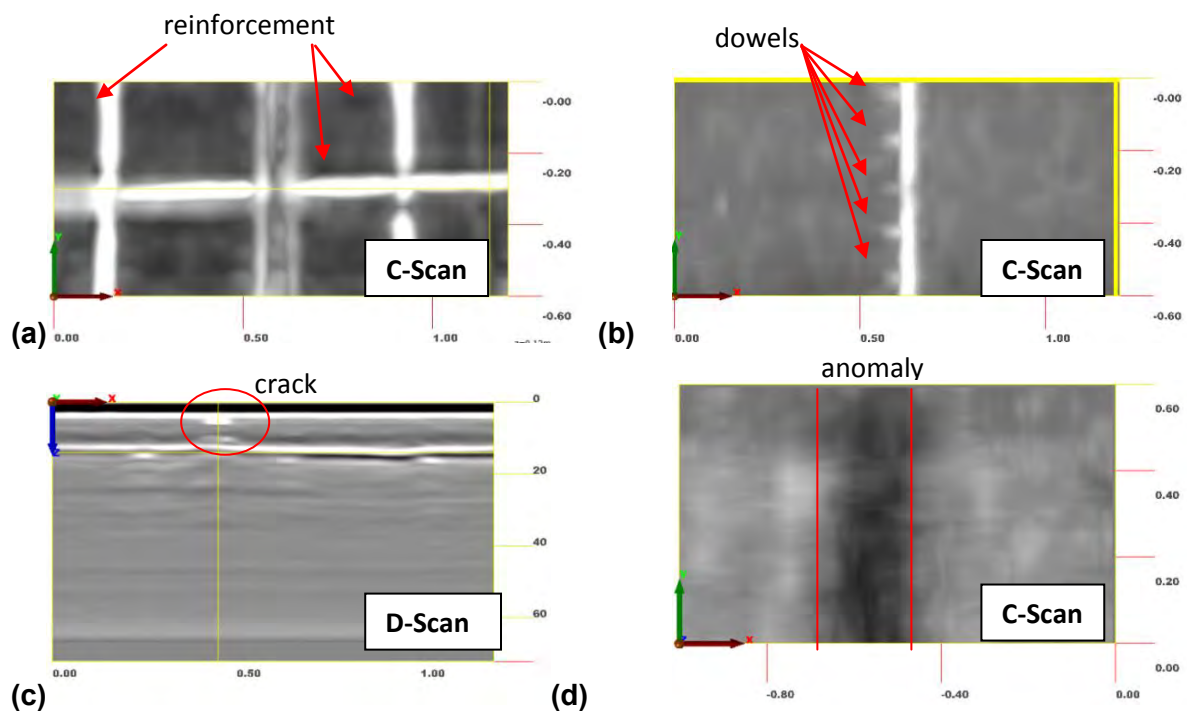
Figure Q-7. Typical radar scans illustrating (a) reinforcement, (b) dowels, (c) a surface crack, and (d) an anomaly.

Ultrasonic Echo

Basic Operation Principles

In this test, a single ultrasonic transducer is used to generate and detect ultrasonic waves in the structure. Ultrasonic is based on the measurement of propagation time to localize cracks, voids, deteriorations, and/or the thickness of a structure. The speed of ultrasonic pulses propagating through the structure is often correlated to material strength and thus a measure of material quality. Ultrasonic echo was employed here for the inspection of the tunnel lining to estimate the thickness of the lining and detect/locate defects and anomalies within the lining. In the absence of ground-truth data, the wave-speed of the lining material was either assumed or estimated from surface measurements. As such, the thickness of the tunnel lining as well as the depth of the reflectors could be only approximated. Ultrasonic data collection was done automatically using the previously described scanning system.

As data collection was conducted point-by-point following a pre-defined grid, the resulting signals (A-Scans) were processed and presented in real time as evolving B-, D-, and C-Scans. Figure Q-8 shows a typical A- and B-Scan obtained in one of the tunnels. The A-Scan shows the intensities of the reflections over time for each point of measurement. The evolution of the A-Scans along the profile can be seen in the B-Scan. Heterogeneities are recognized by their high reflection amplitudes. Knowing the wave propagation speed made it possible to estimate the depth of the reflector, which could be the tunnel lining backwall or defects. The collected data set could be further processed using the Synthetic Aperture Focusing Technique (SAFT) algorithm (Schickert, et al., 2003) to give a more clear image (higher Signal-to-noise ratio) of the internal structure of the test volume; see Figure Q-9).
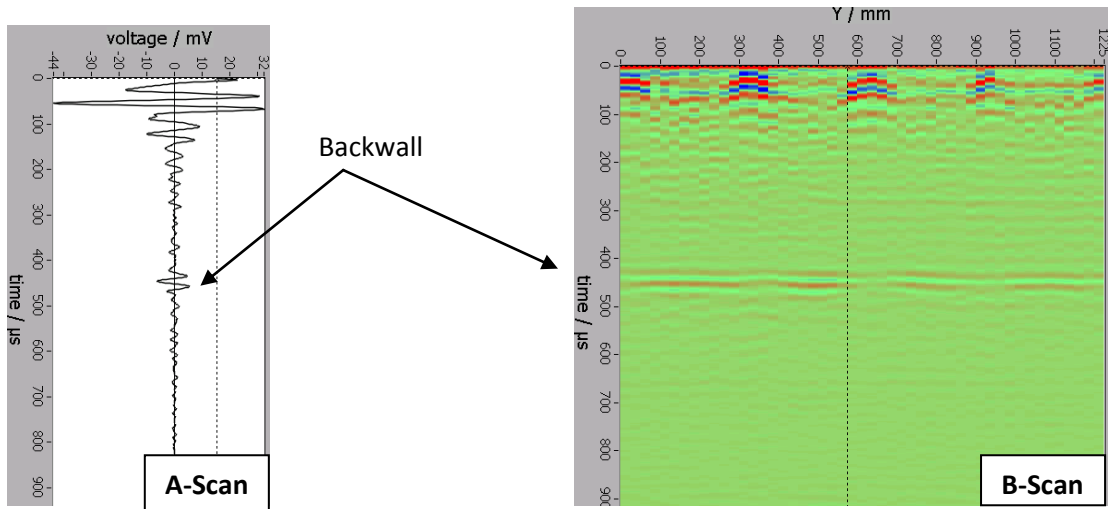
Figure Q-8. Typical A-Scan and B-Scan along the Chesapeake Bay Bridge-Tunnel lining.
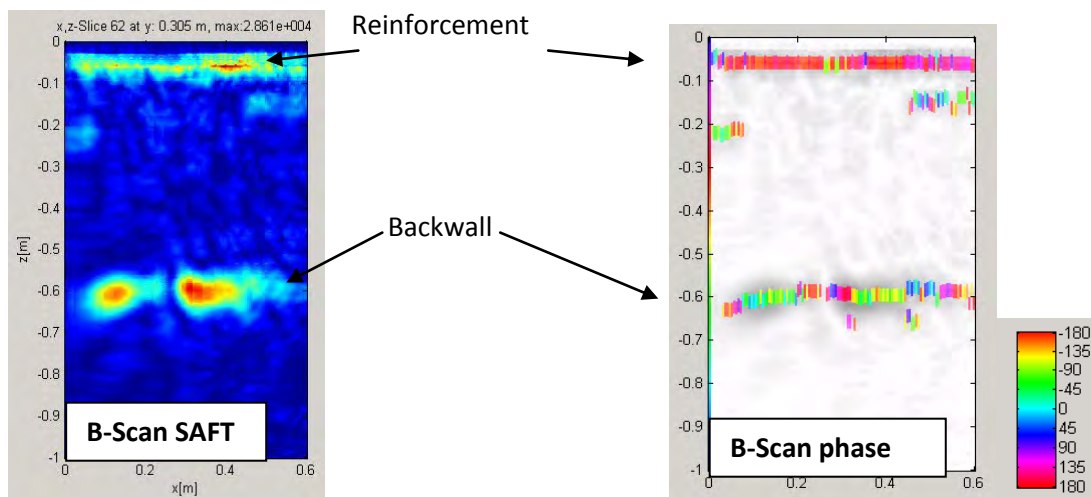
Figure Q-9. Post-processed ultrasonic data using SAFT including both amplitude and phase evaluation.

The phase diagram shows the change in phase of ultrasonic waves at the detected interfaces within the material. The color-coded local phase diagram helps distinguish between the reflections from steel objects and air interfaces. Relative to concrete, steel is of higher and air is of lower impedance. Therefore, the phase of the reflected waves at concrete-steel interfaces and concrete-air interfaces will be different. This can be seen in Figure Q-9 where a 180-degree phase shift (red color) is seen at the location of the rebars, while the backwall reflections do exhibit negative phase shifts of 0 to -100 degrees.

The advantage of ultrasonic testing lies in its potential to detect different types of defects such as voids, cracks, honeycombs, and delaminations directly or indirectly, in real time. It can further estimate the strength of the material and estimate the structure thickness. Conventional ultrasonic equipment is available and fairly inexpensive. The main limitation is the necessity of the transducers to be in contact with the surface of the structure, which slows down the speed of the automated scanning systems.

The ultrasonic equipment used by BAM was the A1220. It is a low-cost, multi-sensor, dry-contact, low-frequency, shear wave transducer developed by Acoustic Control Systems Ltd. (ACSYS) in cooperation with BAM. It includes 24 spring-mounted ultrasonic transducers of a nominal frequency of 50 kHz, out of which 12 serve as transducers and the other 12 as receivers. This construction ensures that a higher amount of ultrasonic energy is transmitted and the reflected and recorded signals can be averaged, thereby minimizing the scatter noise. The images in Figure Q-10 depict the A1220 being used as a handheld device and mounted on the ZFP Scanner. For post-processing the data (i.e., analysis, SAFT, and phase evaluation), two different programs were used: one program was developed at BAM by Rüdiger Feldmann and the other at the University of Kassel by Dr. Klaus Meyer.

(a)   **(b)**   **(c)**
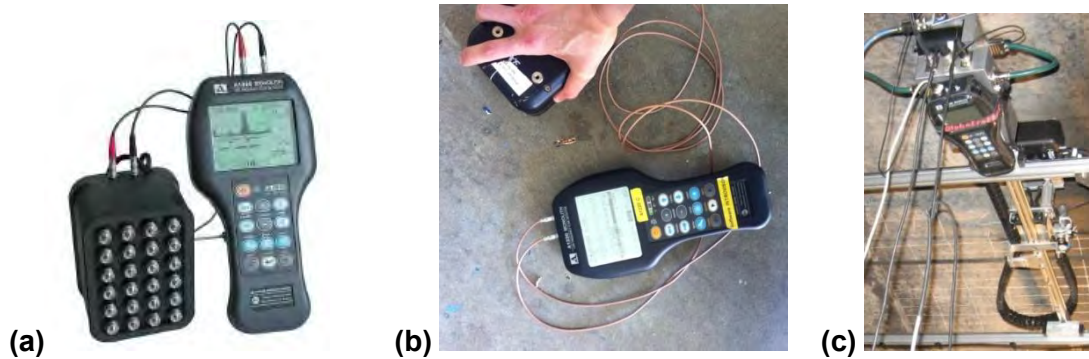
Figure Q-10. Ultrasonic A1220 from ACSYS (a) used for point measurements by hand (b) and used for profile measurements by an automated scanning device (c).

Typical Results

Ultrasonic echo was able to detect the backwall of tunnel linings directly, reinforcement directly, possible delamination directly and indirectly, surface cracks indirectly, and intrusions in an otherwise homogeneous volume directly (see Figure Q-11). The indirect detection of reflectors was possible by the "shadow effect," i.e., by recognizing a missing portion of an otherwise consistent element of the tunnel lining, such as backwall or reinforcement.
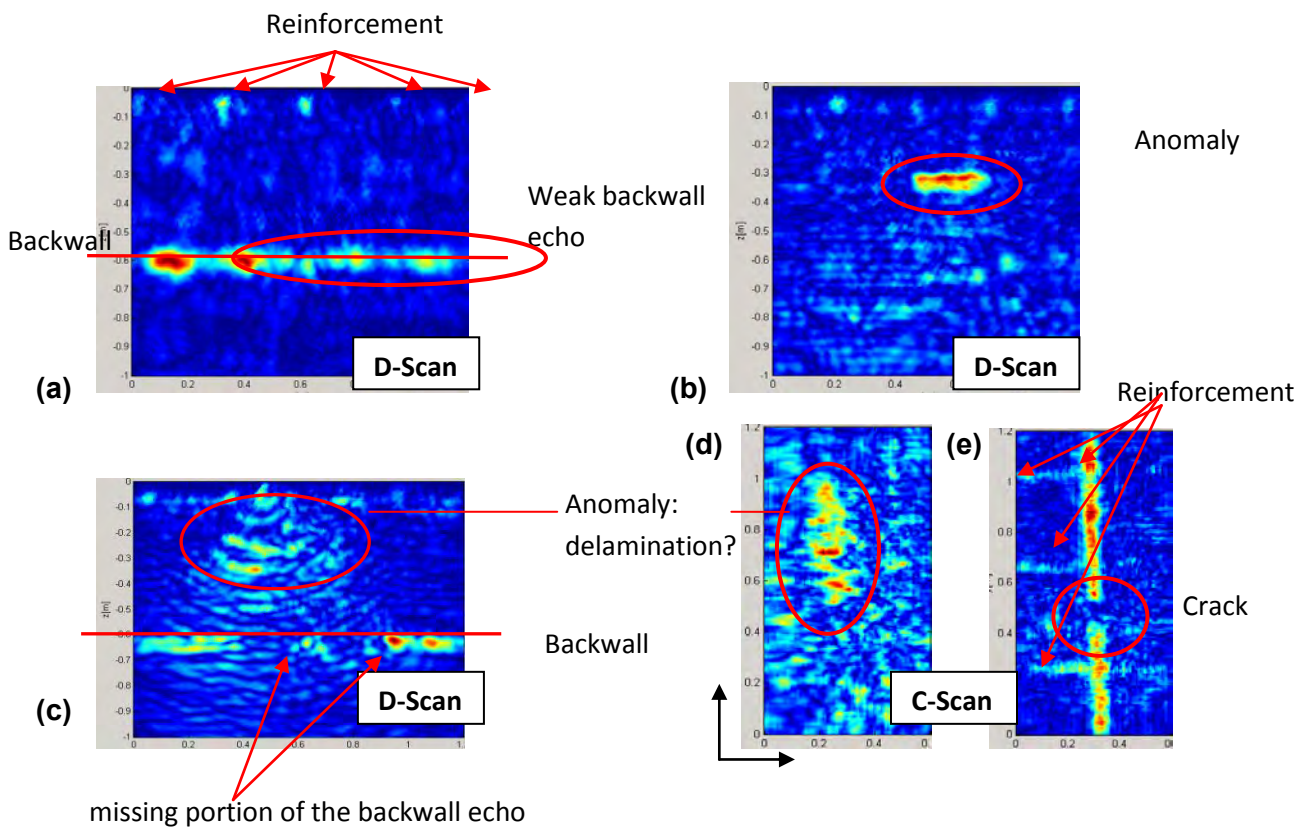
Figure Q-11. Typical ultrasonic echo results: (a) backwall and reinforcement in a D-Scan, (b) unknown detection of a reflector in a D-Scan, (c) direct detection of a delamination-like anomaly in a D-Scan, (d) direct detection of a delamination-like anomaly in a C-Scan, and (e) indirect detection of a surface crack considering the missing reinforcement in the C-Scan.

Impact Echo

Basic Principles of Operation

IE involves introducing a stress pulse into concrete, commonly by application of a mechanical impact on the surface of the structure. A broadband transducer located on the surface close to the impact source (usually at a distance of 2 inches to 4 inches) is used to record vertical deformations of the surface caused by the arrival of incident and reflected waves (or echoes). The response of solid or delaminated plates subjected to IE testing is distinctly different: thickness resonance vibrations in case of solid plates and plate-like flexural vibrations in the presence of shallow, severe delaminations (Shokouhi, 2005). Intermediate conditions will result in a response superimposing these two.

The time and frequency characteristics of the recorded response can be used to deduce the condition of the structure. Figure Q-12 shows two typical time signals (top) and frequency spectra, one corresponding to a supposedly sound area of a tunnel lining with the backwall as the only reflector with a frequency peak at 3.15 kHz, and the other on a supposedly delaminated area, where spectrum has multiple peaks. The peak in the frequency spectrum of the supposedly sound area is the resonance frequency of the tunnel lining depth. The dominant response of a severely delaminated deck to an impact is characterized by a low

frequency response because of oscillations of the upper delaminated portions of the deck. This response is almost always in the audible frequency range. Because it is significantly lower than the return frequency for the tunnel lining backwall, it produces an apparent reflector depth that is larger than the full thickness (Shokouhi, 2005).
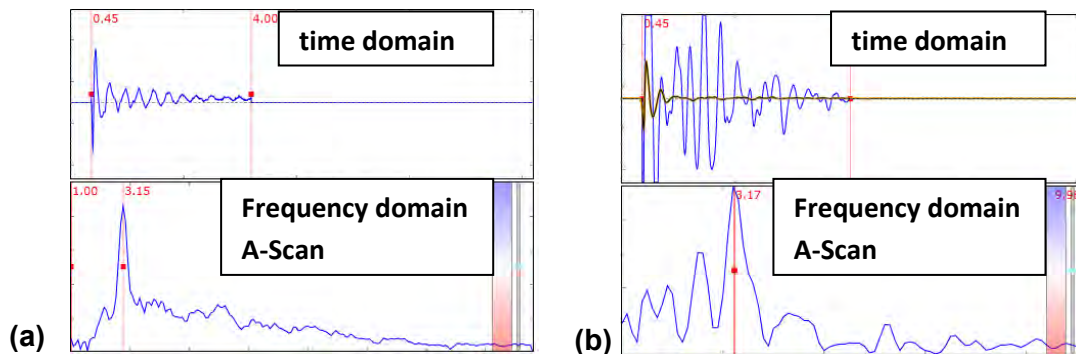
Figure Q-12. A sound area of a tunnel lining with a single frequency peak at 3.15 kHz (a) and a supposedly delaminated area with several low frequency peaks (b) from Chesapeake Bay Tunnel, Area 3.

When using automated scanning devices, the single point-by-point measurements along a profile add up to B- and D-Scans and C-Scans as time/frequency/depth slices (Figure Q-13).

Typical Results

IE is best known for thickness evaluation and delamination detection in plate-like structures. Depending on the mechanical source used, shallow or deep structures or defects may be investigated. Using IE, it is still possible to detect the backwall, even at delaminated areas, provided that the delaminations are not severe. Figure Q-12(a) shows an example of a sound tunnel lining with the backwall resonant single frequency peak at 3.4 kHz. Considering the P-wave velocity of about v_P in concrete ~4000 m/s, this amounts to a depth of about ~2 ft. Frequency-domain D-Scans along two selected test lines are shown in Figure Q-13. The D-Scan in Figure Q-13(a) was taken over a sound area, and the one in Figure Q-13(b) shows a D-Scan across a supposedly delaminated area.
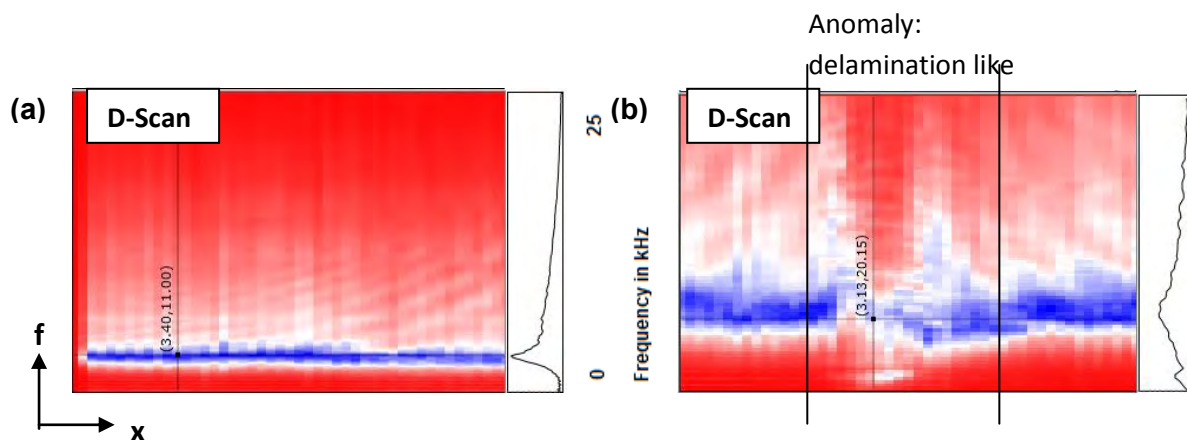
Figure Q-13. Frequency-domain D-Scans of a test line on a sound portion of a tunnel's lining with the backwall at 3.4 kHz (a) and on a supposedly delaminated area (b) of another tunnel's lining.

Q-11

MEASUREMENT RESULTS FOR EISENHOWER (EH) TUNNEL

Description of the Test Area

Measurements in the EH Tunnel were performed over two days: October 3, 2011, and October 4, 2011. The unusually high elevation of the EH Tunnel (11,112 ft) created a few challenges in the conduct of the measurements. ZFP Scanner is attached to the surface using four vacuum feet. Because of the high tunnel altitude, the compressor could not maintain the pressure necessary to create the vacuum under the feet. Two areas were examined. The first area was regarded as an equipment test. The second area was properly examined with all three NDT methods.

The second test area was located within Segment 11, Block 1 of the EH Tunnel and tested from east to west, starting in the lower right corner and then moving up and left. This test area is hereinafter referred to as EH2. As shown in Figure Q-14, the 40 inch x 24 inch test area was located 26 inches east of a joint between Segments 10 and 11 of the tunnel. The starting scanning point was located at the lower right corner of the scanner field. The scanner moved up and then left, in this case from east to west. The feet of the scanner slid down 0.5 inches during the testing (because of the difficulties in maintaining enough suction). Figure Q-15(a) shows the setup on the first area, and Figure Q-15(b) shows a cross-section of the tunnel photographed from an information bulletin with the two fields of testing marked on it. The grid spacing was 1 inch for US and IE tests and 2 inches for GPR. The position of the test apparatus and the feet of the scanner were marked with chalk. The lengths of the US, IE, and GPR transducers were parallel to the center line of the tunnel.
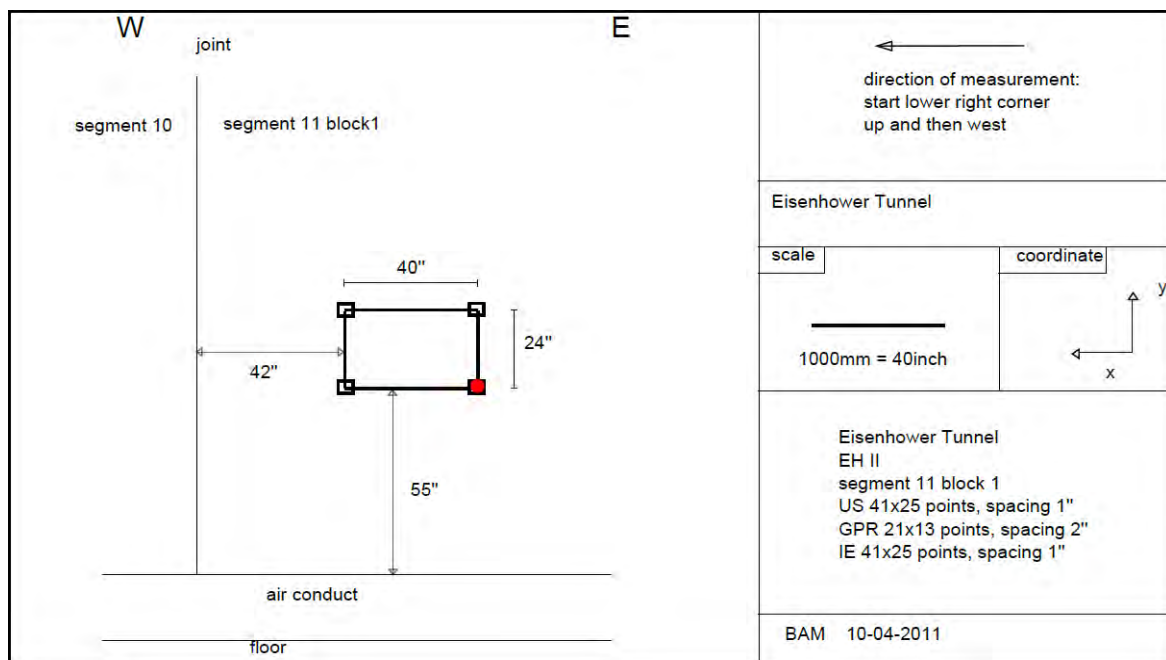
Figure Q-14. Sketch of Test Area EH2, located within Segment 11 Block 1.
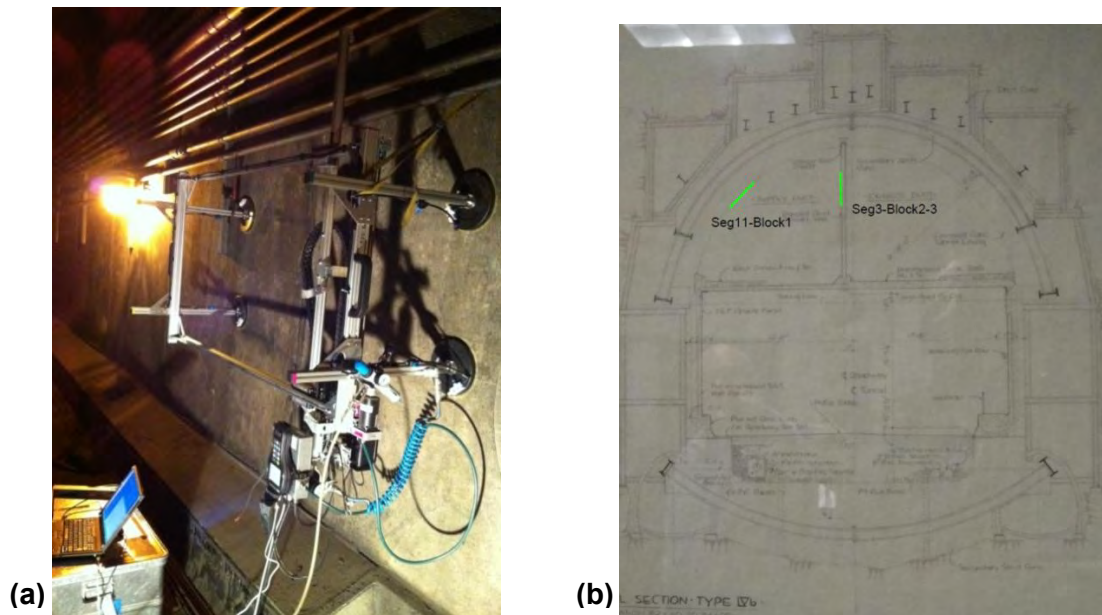
Figure Q-15. Test Area EH: (a) the test setup of the scanner on EH2 and (b) cross-section of the tunnel showing the locations of the two test areas.

The results obtained from each of the three tests performed are discussed below.

GPR Results

With the GSSI 1.5 GHz GPR antenna, the rebar mesh at a depth between 2 inches and 3 inches was clearly detected. Moreover, an anomaly (reflector of unknown origin) at 16 inches deep was detected. Based on the GPR results, the reinforcement bars within the test area along the y-direction were positioned regularly at 10-inch intervals: x = 8 inches, x = 18 inches, x = 28 inches, and x = 38 inches. The ones along the x-direction had a 10-inch distancing as well, located at y = 10 inches and y = 20 inches. The detected anomaly had a x-dimension of 10 inches extending from x = 18 inches to x = 28 inches and ran along the entire y-dimension of the test area. Figure Q-16 is a three-dimensional image of the volume with the slices (B-, C-, and D-Scans) positioned to reveal the anomaly and the reinforcing elements. Figure Q-17 shows a selection of the B-, D-, and C-Scans from EH2 including the detected reflectors: (a) is a D-Scan of the reinforcement bars in the y- and x- direction as well as the anomaly, (b) and (c) are B-Scans, and (d) and (e) are C-Scans showing the reinforcement bars and the anomaly at their respective depths.
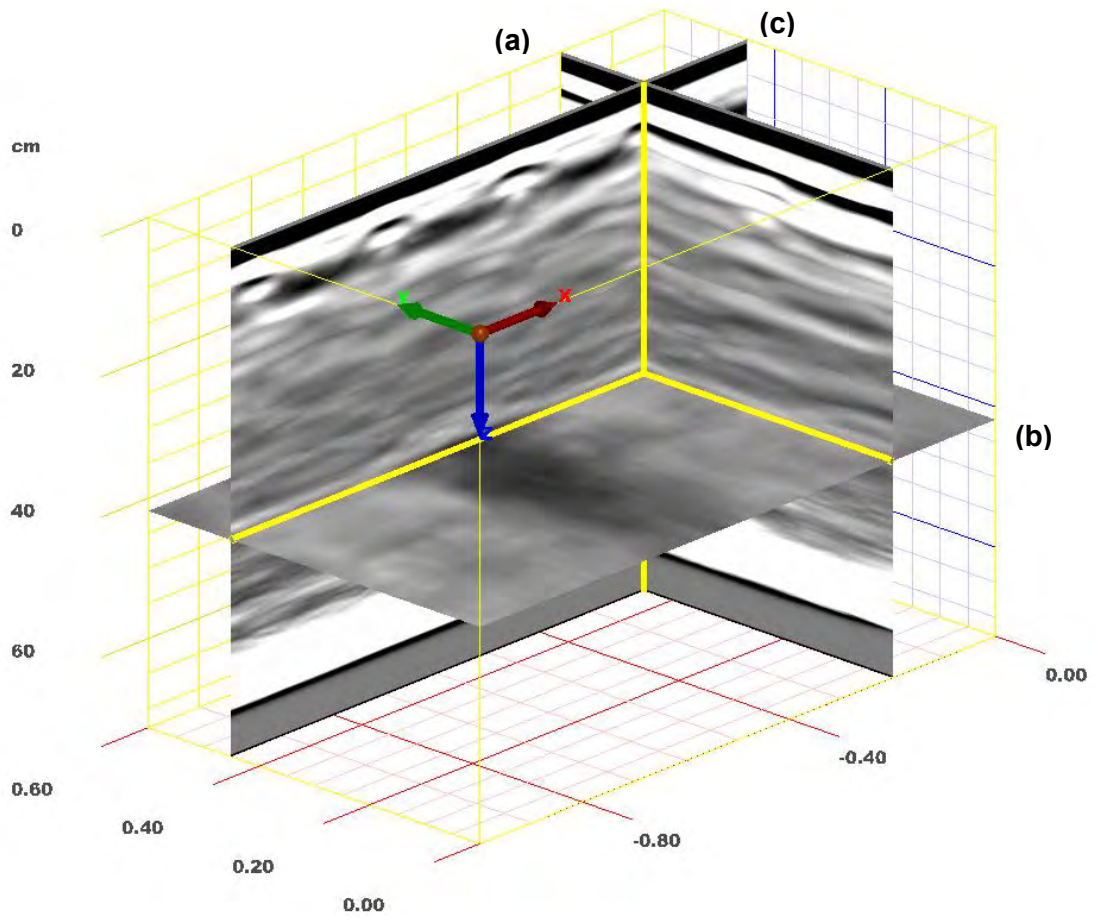
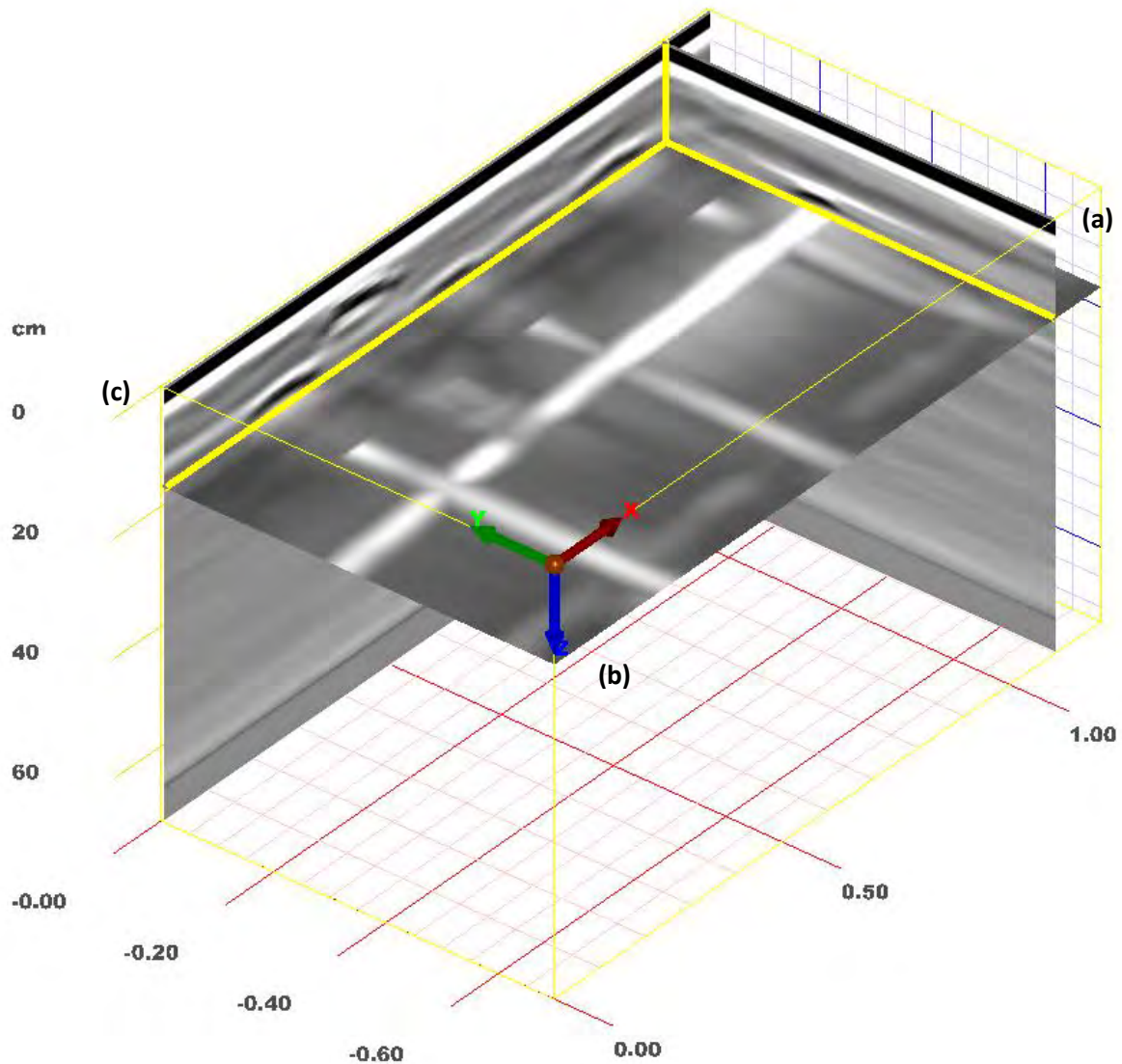**Figure Q-16. EH2, GPR: three-dimensional image of the volume positioned to reveal the anomaly, with the B-Scan (a) positioned at x = 8 inches, the C-Scan (b) at z = 16.8 inches, and the D-Scan (c) at y = 18 inches.**
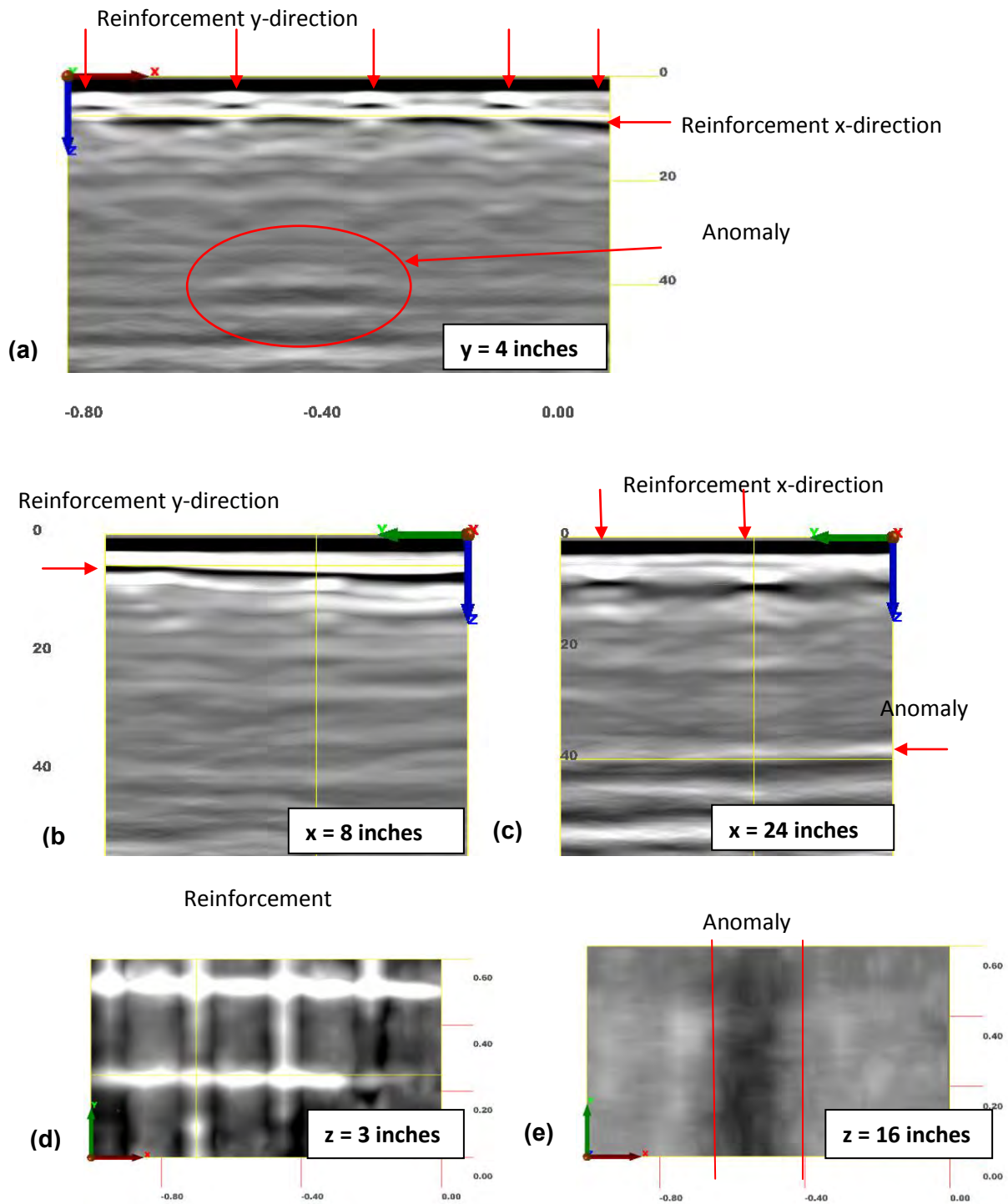
Figure Q-17. EH2, GPR: A collection of B-, D-, and C-Scans from the test area displaying the main GPR results.

Ultrasonic Echo Results

Using ultrasonic echo, reinforcements at a depth between z = 2 inches and z = 3 inches were detected. An anomaly (i.e., a reflector of an unknown origin) was also detected at an approximate depth of 16 inches. The reinforcement bars along the y-direction were 10 inches apart, located at x = 8 inches, x = 18 inches, x = 28 inches, and x = 38 inches. The bars along the x-direction were not very clear (due to the positioning and polarization of the probe), and thus could only be vaguely traced at y = 10 inches (Figure Q-18). Figure Q-19 is a three-dimensional image of the volume with the slices (B-, C-, and D-Scans) positioned to reveal the anomaly. The local phase at rebar reflections was, as expected, between 90 and 180 degrees (red color), indicating an impedance higher than the surrounding concrete. The anomaly was 10 inches in width and lay between x = 18 inches and x = 28 inches in the direction of x, as seen in Figure Q-20. It ran completely across the y-dimension of the test area. The local phase was negative, between 0 and -110 degrees (green, yellow), indicating an impedance lower than concrete.
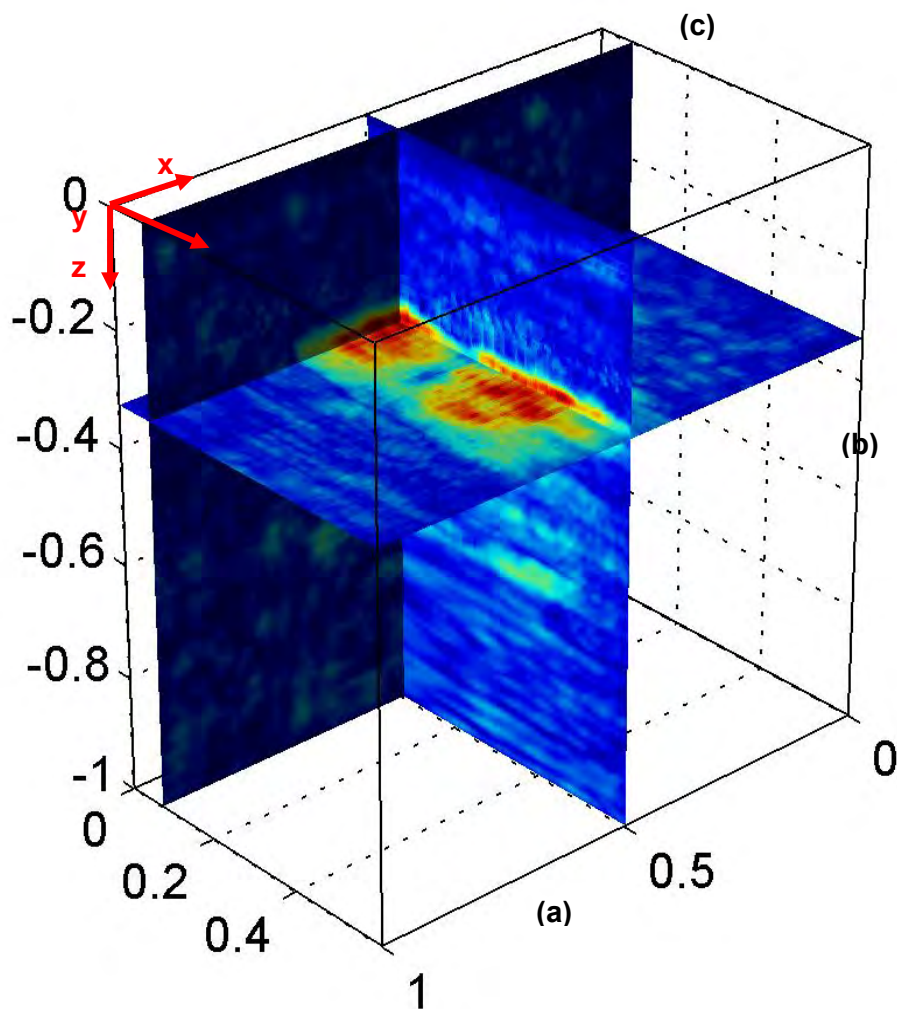
Figure Q-18. EH2, US: three-dimensional image of the volume positioned to reveal the anomaly, with the B-Scan (a) positioned at x = 19 inches, 6-inch width; the C-Scan (b) at z = 14 inches, 3-inch width; and the D-Scan (c) at y = 4 inches, 2-inch width.
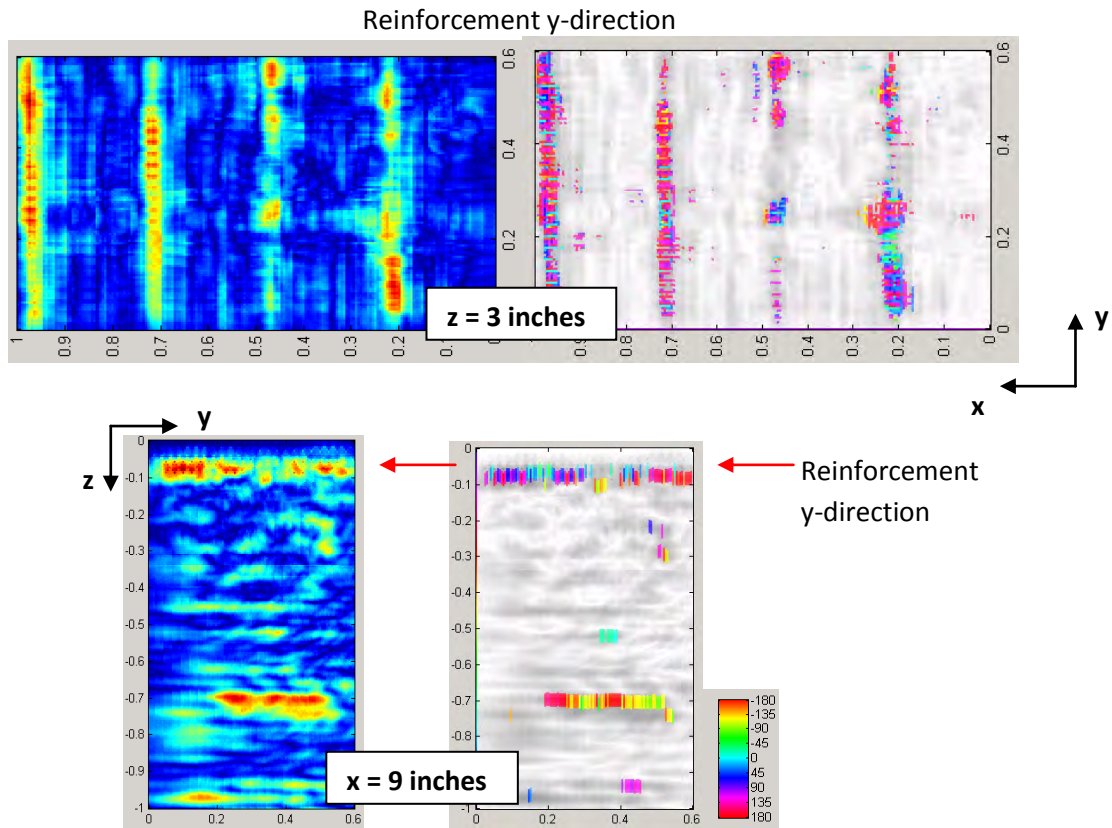
Figure Q-19. EH2, US: C- and B-Scan, displaying reinforcement. The reflector at 0.7 m could not be identified, as it showed up inconsistently.
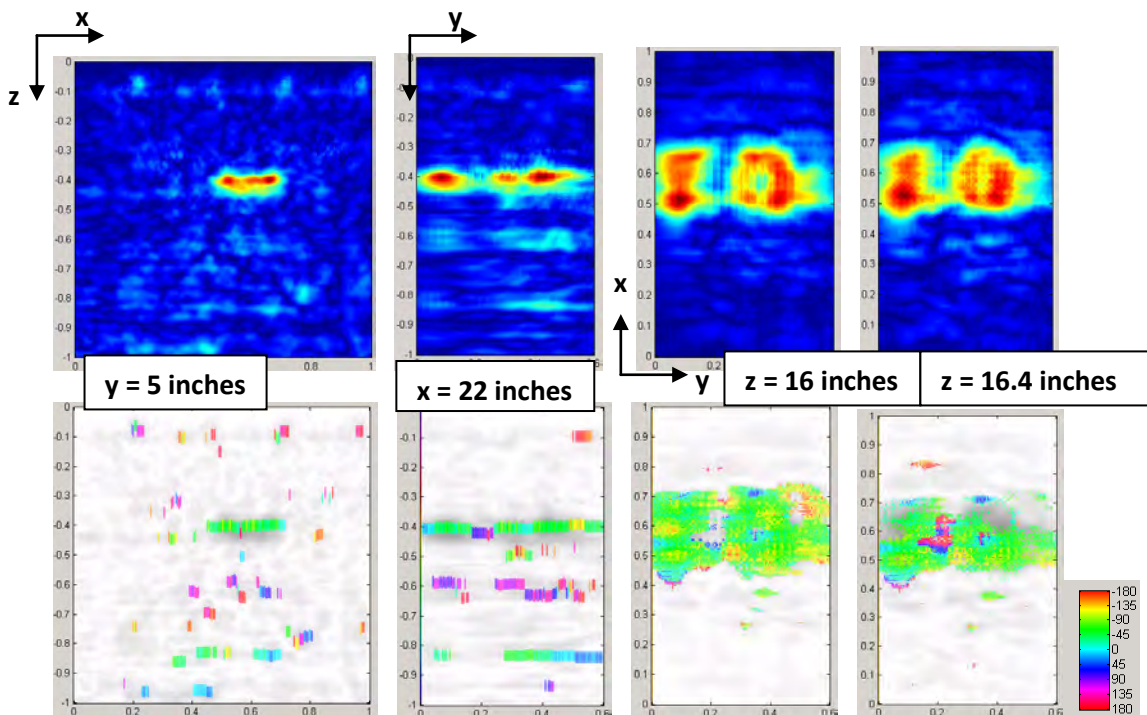
Figure Q-20. EH2, US: B-, C-, and D-Scans and the corresponding local phase diagram, displaying a reflector.

Q-17

Impact Echo Results

IE could not register either reinforcement or the anomaly detected by GPR and US. The frequency spectra did not have clear amplitude peaks but was rather a plateau of many overlapping peaks (Figure Q-21). IE could not yield any reliable information about the backwall of the tunnel lining. Assuming a shear wave velocity of 3400 m/s, the longitudinal wave velocity was approximately 5889 m/s.
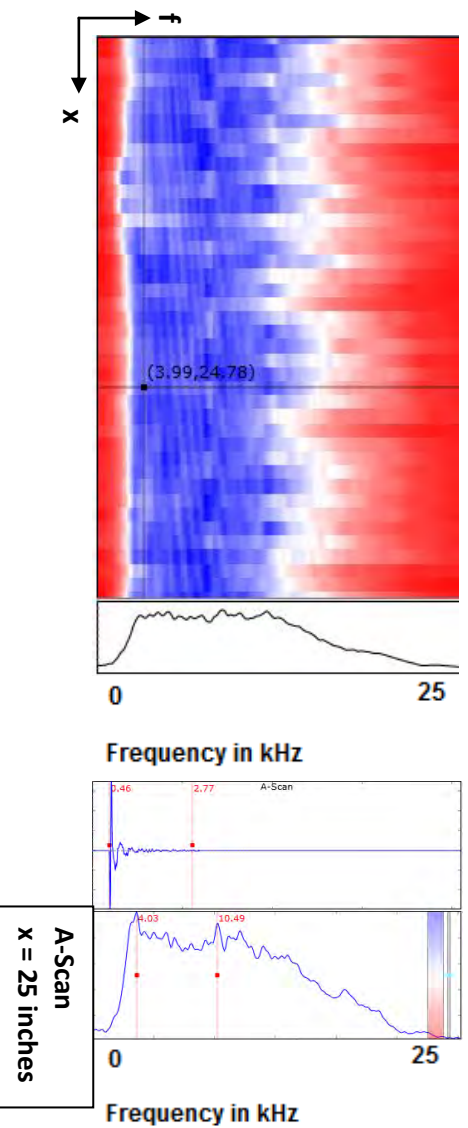
Figure Q-21. EH2, IE: A- and D-Scans. No information about the possible anomalies, reinforcements, or lining thickness could be drawn.

Comparison of Results

As expected, GPR proved to be the best tool in identifying and locating the reinforcement within the EH2 test volume. US could, on the other hand, locate the anomaly of unknown origin more clearly. The negative local phase of the amplitudes at the mysterious reflector led to the assumption that the anomaly would have a lesser impedance than the surrounding concrete. The fact that GPR registered that anomaly at a depth of 16 inches led to speculations about it having a higher impedance than the surrounding concrete. It is unlikely that wood or air voids in such a depth can be seen with a 1.5 GHz antenna as clearly as the anomaly seen in the radargrams.

One hypothesis is that the anomaly could be one of the steel beams shown in Figure Q-22. This assumption makes one wonder how the local phase normally associated to the reflections from wood or air appear. One theory is that the concrete around the metal beams may not be properly bonded to the steel anymore, leaving a thin layer of air between the two mediums. The local phase reflects the phase shift at the concrete-air interface rather than the steel underneath.

In general, both the GPR and US methods were effective in detecting reflectors within the Eisenhower Tunnel lining. A combination of the two result sets would provide the most detailed and reliable results. Both methods detected the reinforcement and an unknown anomaly. GPR was more effective in detecting the former, and US in detecting the latter. The backwall couldn't be seen with any of the employed techniques here.
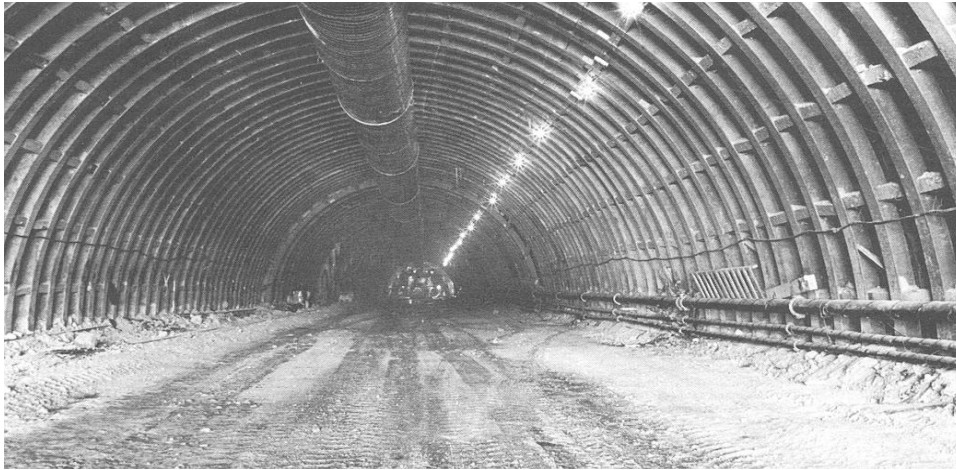
Figure Q-22. Photo of the construction of the Eisenhower Tunnel sometime between 1968 and 1973 (DOT, 2011). The steel beams could be the anomaly seen in the GPR and US data.

MEASUREMENT RESULTS FOR HANGING LAKE (HL) TUNNEL

Testing in the HL Tunnel took place on October 5, 2011, and October 6, 2011. As noted in Figure Q-23, three test areas were measured with GPR, US, and IE.

Test Area 1 (HL1)

Description of the Test Area

The first test area was situated in Section 56 of the tunnel and is hereinafter referred to as HL1. We did not find any referencing system for this tunnel. The test area was believed to be within Section 56 because 56/57 was marked with spray on the floor, looking south on the right-hand side of the test location (see Figure Q-23[a]). On the left-hand side, E16 was written. A repaired crack ran across the selected test area (see Figure Q-23[b]). As shown schematically in Figure Q-24, the 48 inch x 24 inch test area was located between two joints at a distance of 27 inches from the north joint and 56 inches from the south joint. The scanning started at the point closest to the center line. It then moved away from the center line and farther south, toward the tunnel entrance. The grid spacing was 1 inch for US and IE testing and 5 inches for GPR testing. The length (larger dimension) of the US, IE, and GPR transducer was parallel to the center line of the tunnel.

(a)   (b)

Figure Q-23. (a) Mark on the tunnel vent floor of HL1 used as a reference to identify the Sections). (b) The location of the repaired crack across the test field in relation to the scanner aperture.
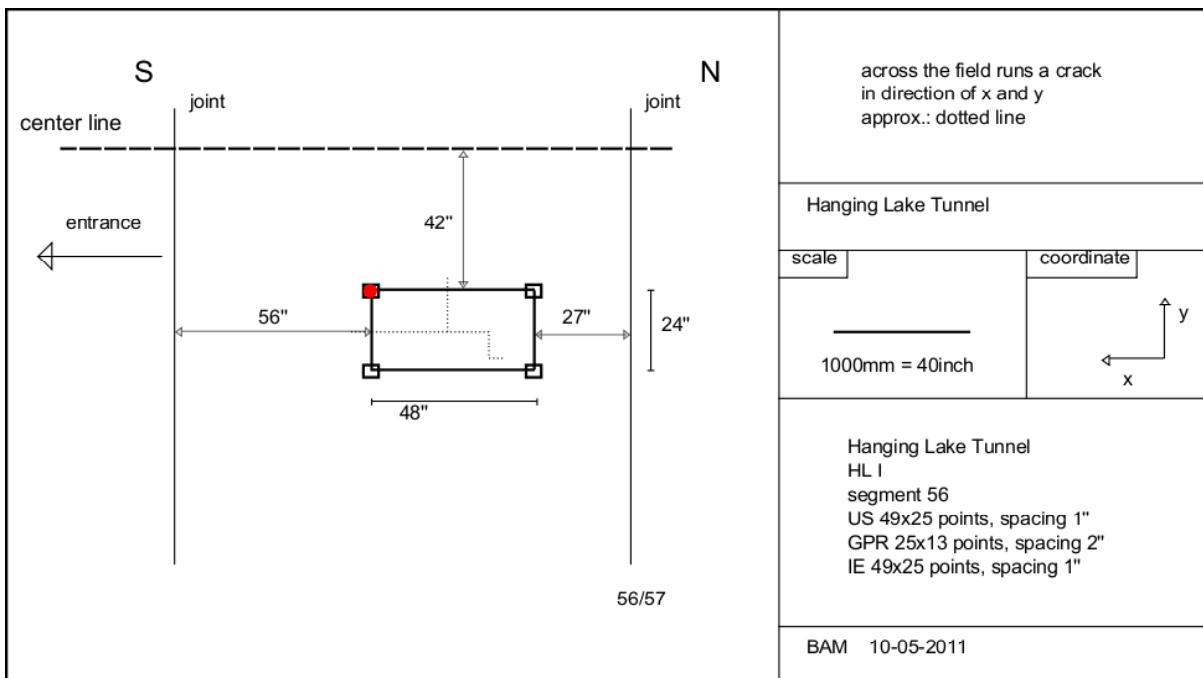
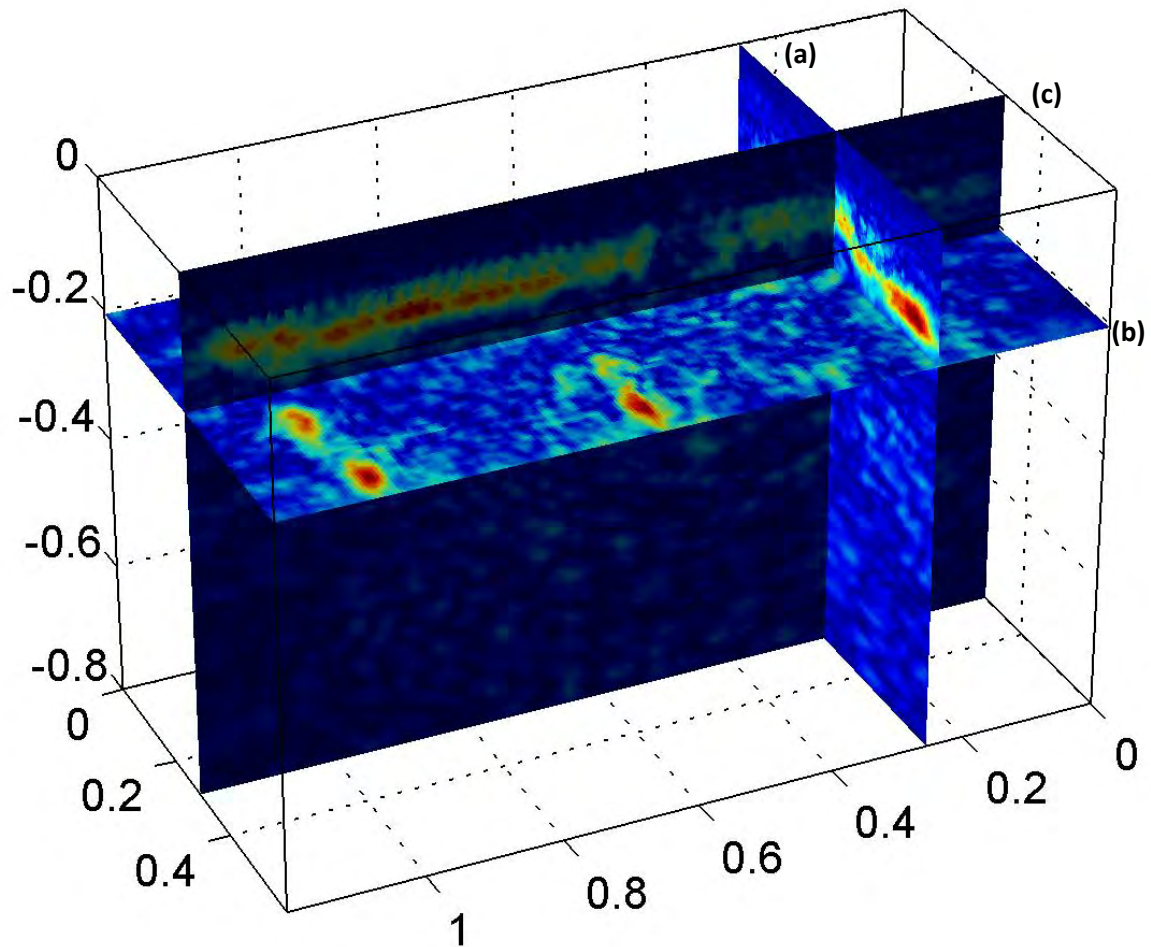**Figure Q-24. Sketch of the test area, HL1, Segment 56.**
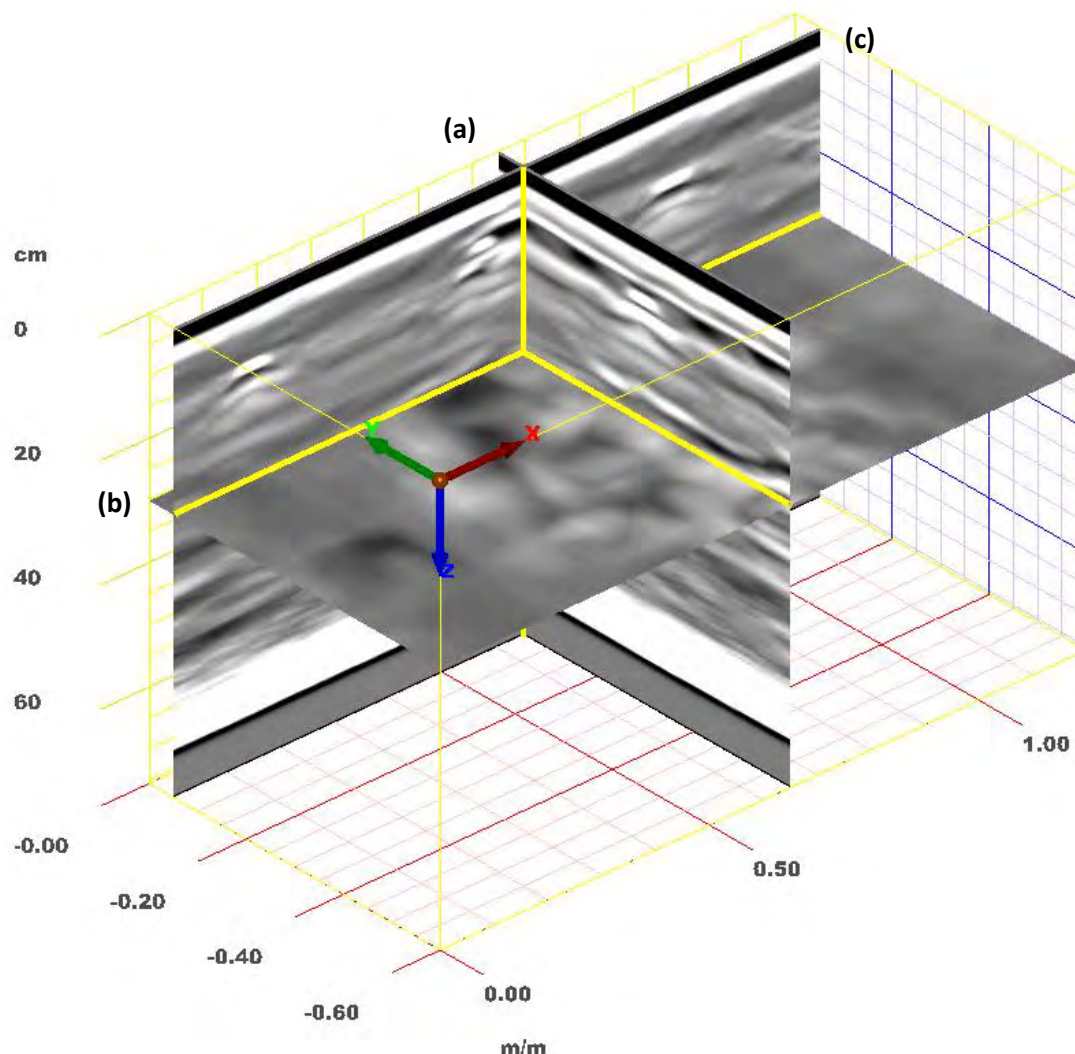
Figure Q-25. HL1, GPR: three-dimensional image of the volume positioned to reveal the anomaly and the reinforcing elements, with the B-Scan (a) positioned at x = 22 inches, the C-Scan (b) at z = 12 inches, and the D-Scan (c) at y = 1 inch.

Using the GSSI 1.5 GHz GPR antenna, the reinforcement mesh and other reinforcing elements (possibly dowels) at depths (z) between 1 inch and 6 inches could be detected, as well as an extended anomaly at z = 12 inches. Figure Q-26 is a three-dimensional image of the volume with the slices (B-, C-, and D-Scans) positioned to reveal the anomaly and the reinforcing elements. At a depth of 1 inch, rebar-like reflections at x = 24 inches were detected. At this depth, there were also reflections from a series of shorter elements (dowels) between the two rebar-like reflections. The shorter elements were regularly spaced and were oriented perpendicular to the rebar-like reflections. The C-Scan in Figure Q-26(c) shows the reinforcement mesh in both directions, with the bars along the y-direction at x = 6 inches and x = 38 inches. The D-Scans in Figure Q-27 and the B-Scan in Figure Q-28 show the third rebar, along the y-direction positioned at x = 22 inches, whose reflections couldn't be distinguished in the C-Scans due to the overlapping with the other reinforcing elements present. The depth of the rebars along the y-direction was between z = 5 inches and z = 6 inches.

Besides the reinforcing elements, at a depth of z = 5.5 inches, there was an anomaly from z = 12 inches down to z = 16 inches, which led to the rise of amplitudes over an area (Figure Q-26[d], Figure Q-27[c], Figure Q-28[b], and Figure Q-28[c]).

The backwall could not be seen in the GPR radargrams.
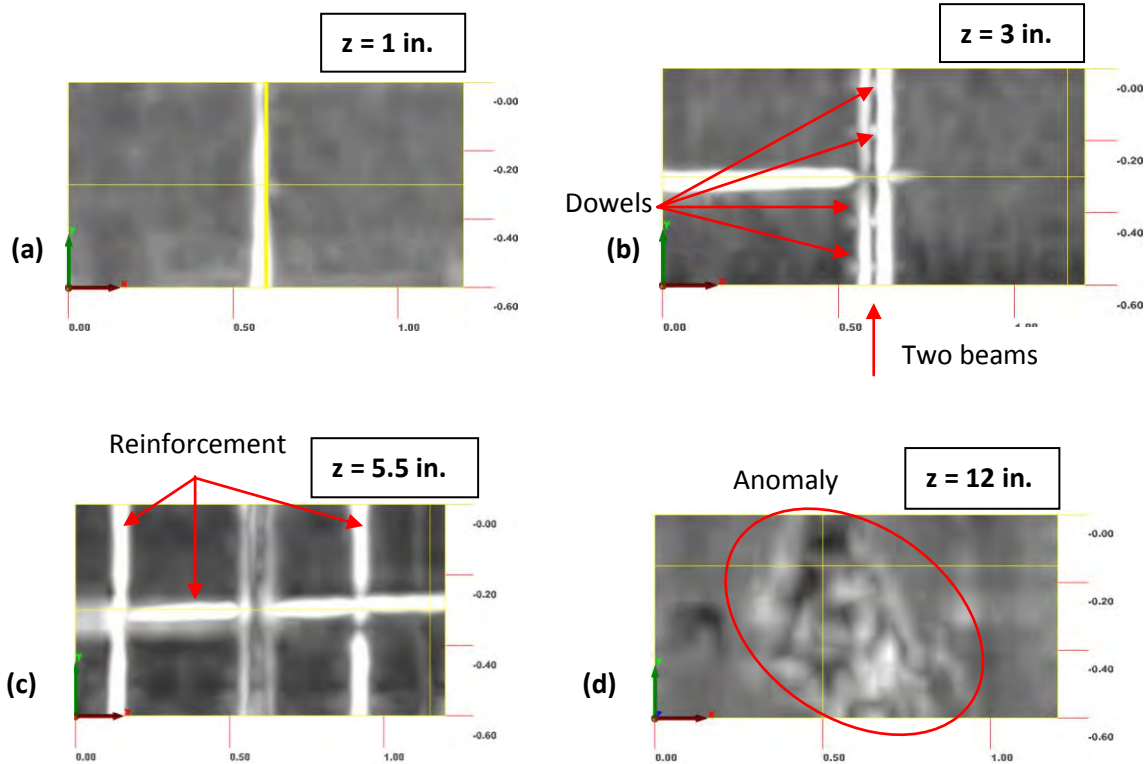
Figure Q-26. HL1, GPR: C-Scans with (a) rebar-like reflection, (b) reflections from two rebars appearing close to each other with dowel-like elements in between them along with the shallower part of a reinforcement bar in x-direction is seen at y = 12 inches, (c) the reinforcement mesh in both directions, and (d) the anomaly.
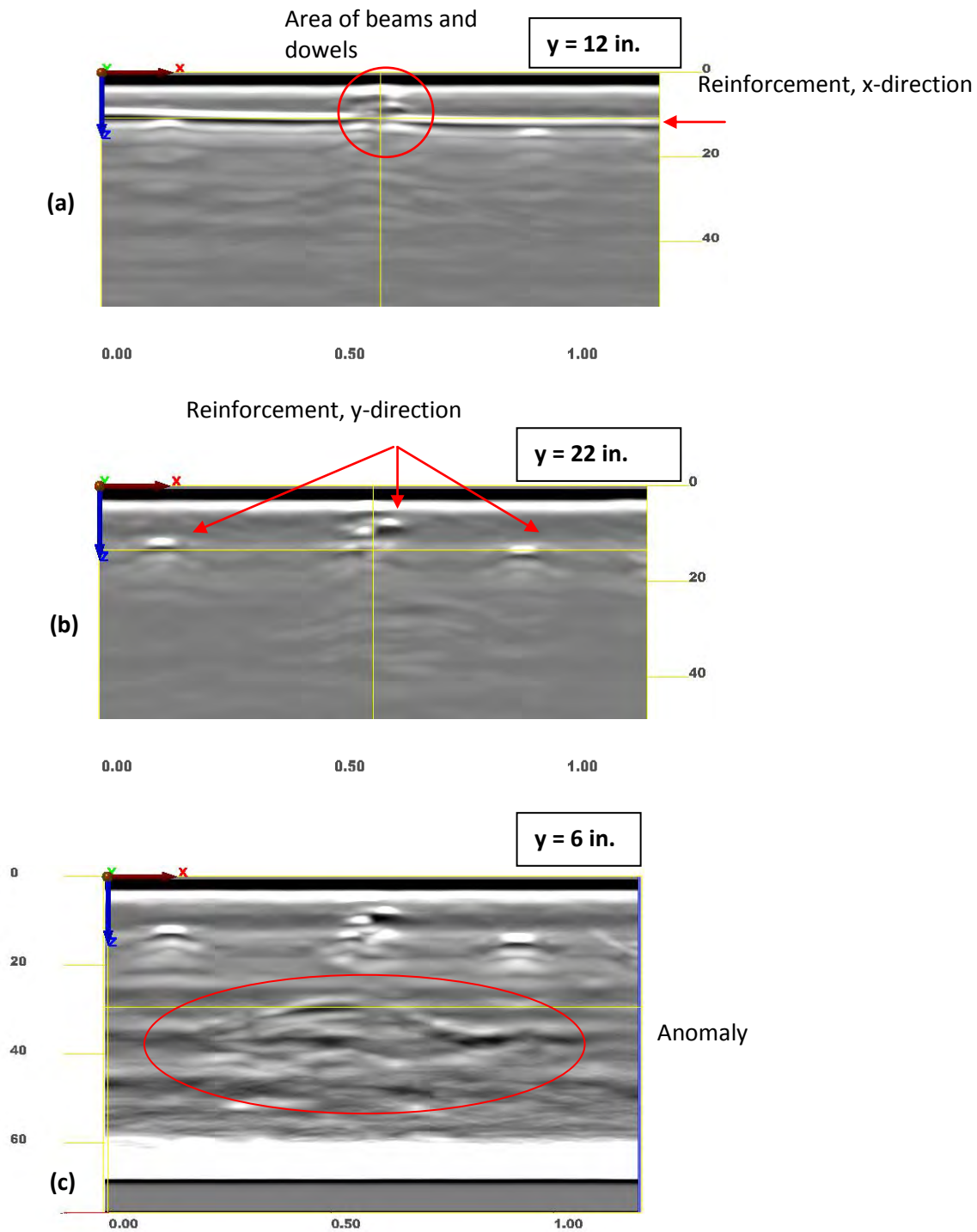
Figure Q-27. HL1, GPR: D-Scans. The area of the beams and dowels (a) as well as the reinforcement in x- and y-direction can be seen as a cut through. The reinforcement x-direction starts at z = 3 inches and leads down to z = 5 inches. The third reinforcement bar along y-direction at x = 22 inches is located beneath the other reinforcing elements at x = 24 inches (b), which makes it difficult to distinguish them in the C-Scan. Image (c) shows the anomaly starting from z = 12 inches and going down to z = 16 inches. The image has a higher gain used on it than the other images in order to visualize the anomaly.
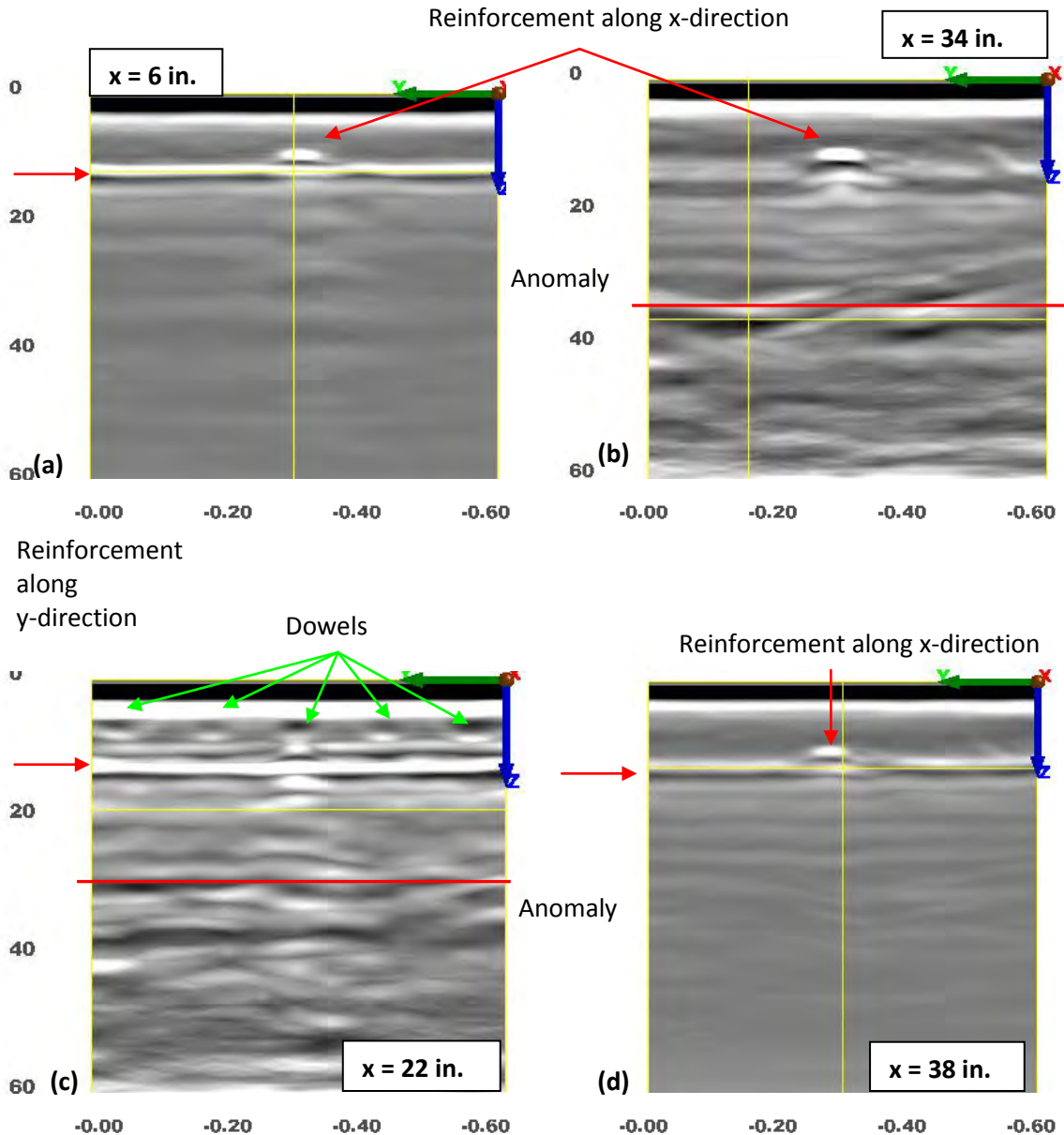
Figure Q-28. HL1, GPR: B-Scans. The first reinforcement bar along the y-direction at x = 6 inches (a). At x = 34 inches, the bar along the x-direction positioned at y = 12 inches (b) as well as the anomaly at z = 16 inches. is seen. The second bar along the y-direction at x = 22 inches, which is under the other reinforcing elements and the anomaly at z = 12 inches (c) and the third bar along the y-direction at x = 38 inches (d) are also shown.

Ultrasonic Echo Results

The reinforcement bars couldn't clearly be detected in ultrasonic results. There was no usable C-Scan at the depth of the reinforcement. No horizontal (the same depth) backwall could be identified. However, a deeper reflector plane (relative to the rebar mesh) of variable depth could be detected.

Figure Q-29 shows a D-Scan taken at y = 5 inches along with the corresponding phase diagram. The reinforcement was seen vaguely at depths between z = 4 inches to z = 6 inches. There was, however, an anomalous reflector of mostly negative phase shift at a depth between z = 12 inches and z = 16 inches.

Reinforcement, y-direction

z = 12 in.

z = 16 in.
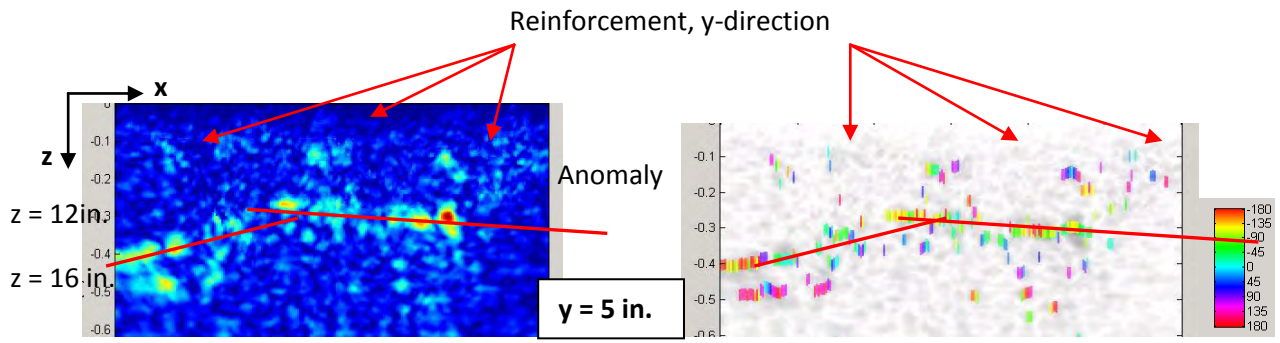
Anomaly

y = 5 in.

Figure Q-29. HL1, US: D-Scan at y = 5 inches. A curved anomalous reflector of mostly negative phase is detected between z = 12 inches and 16 inches.

The B-Scans at x = 6 inches and x = 23 inches are shown in Figure Q-30. Figure Q-31, a three-dimensional image of the volume, gives another view on the anomaly.

Anomaly

x = 6 in.

(a)

z = 16 in.

Reinforcement/beam

z = 5 in.

z = 12 in.

Anomaly

x = 23 in.

(b)
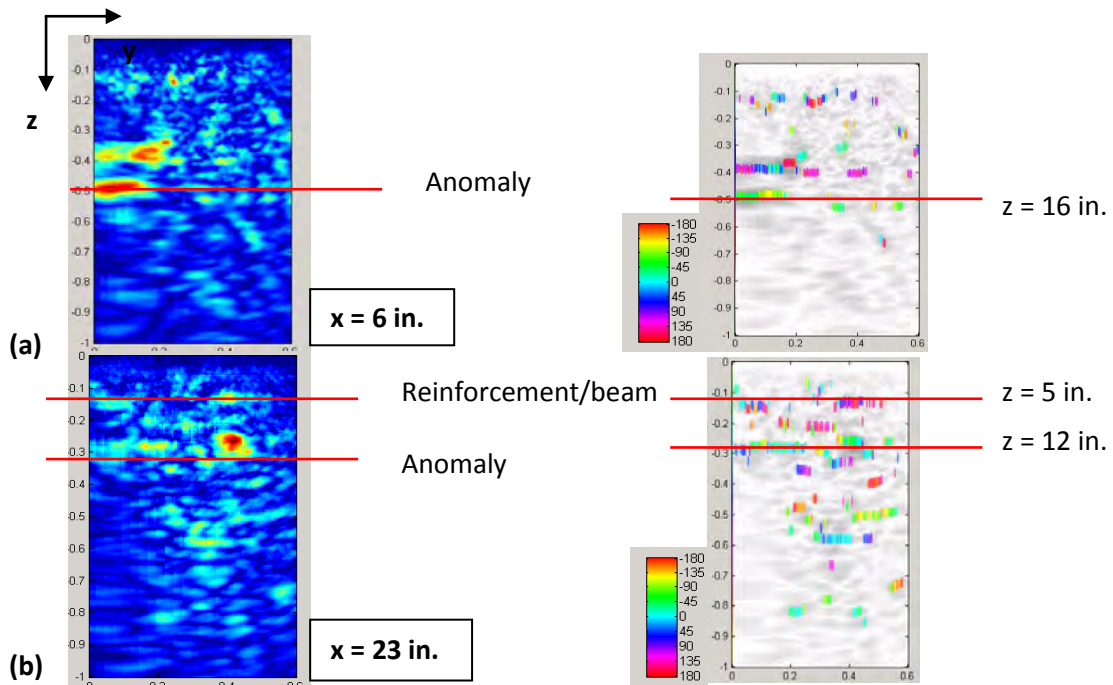
Figure Q-30. HL1, US: B-Scans to evaluate the extent of the anomaly. B-Scan crossing through the deeper reflector (a) and B-Scan crossing through the shallower anomaly (b).
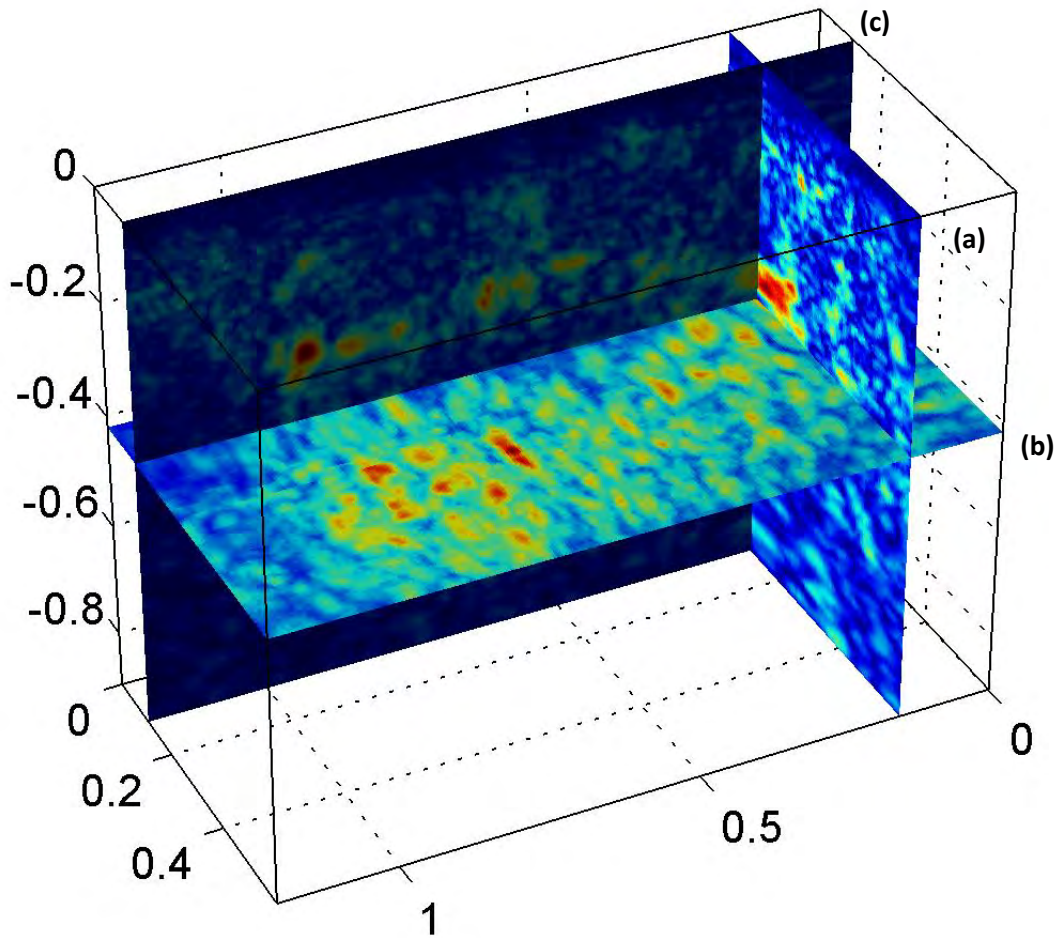
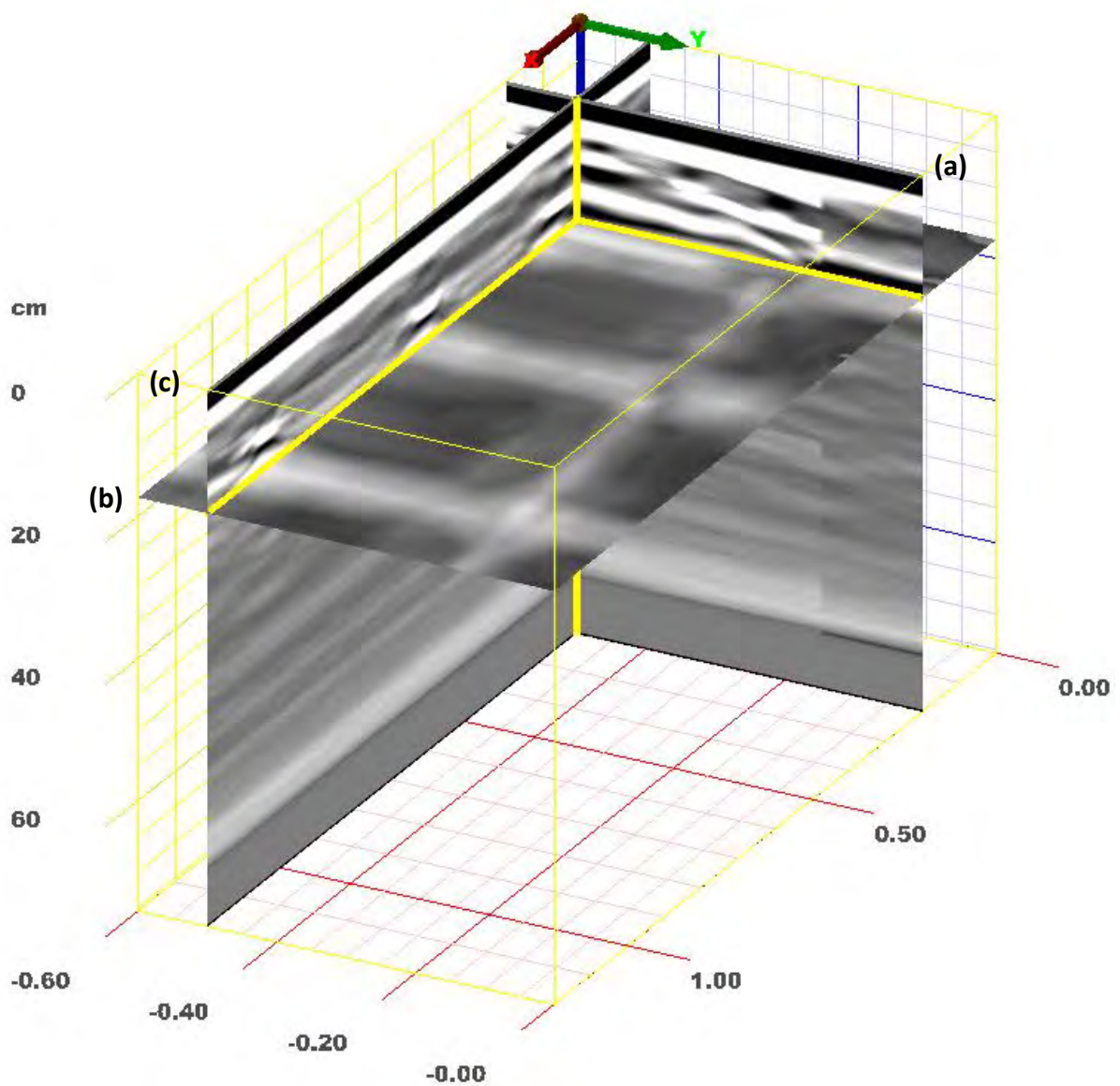**Figure Q-31. HL1, US: three-dimensional image of the volume positioned to reveal the anomaly, with the B-Scan (a) positioned at x = 6 inches, the C-Scan (b) at z = 21 inches, 4-inch width, and the D-Scan (c) at y = 6 inches.**

Impact Echo Results

The IE spectra contained peaks of frequencies much higher than the expected backwall resonance frequency.

Figure Q-32 is a D-Scan cut through the short side of the rectangular test area, therefore along the length. There were many frequency peaks within the frequency spectrum. The first peak of the individual spectra appeared at around 3700 Hz and 3400 Hz, corresponding to depths of z = 22 inches and z = 24 inches, respectively (assuming a longitudinal wave velocity of 4000 m/s). There was a recurring second peak at about 6700 Hz corresponding to a shallower reflector, at about z = 12 inches. Because the amplitude spectrum along the profile seemed rather scattered, no reliable conclusions about the nature of the reflector could be drawn.
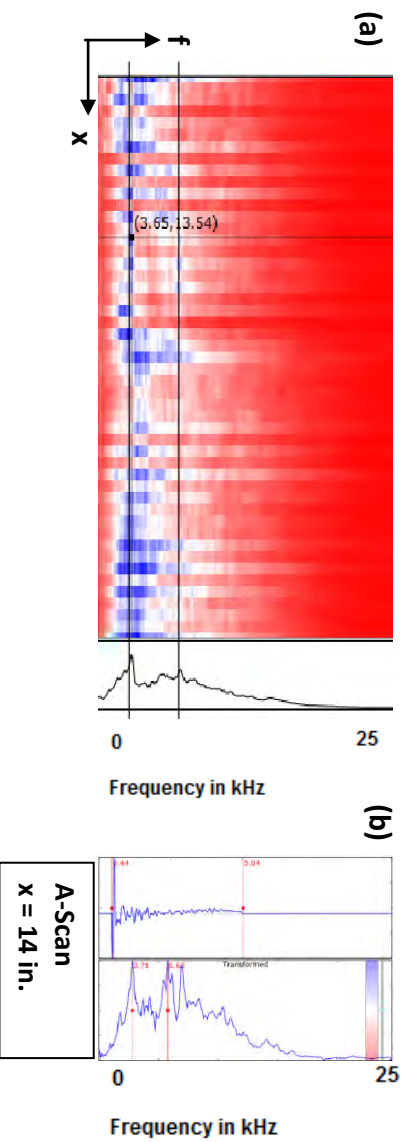
Figure Q-32. HL1, IE: D-Scan (a) and A-Scan (b).

Comparison of Results

For this test area (HL1), GPR proved to be the only method to identify the reinforcement mesh and the reinforcing elements. The fine measurement grid and three-dimensional data collection allowed detection of reinforcing elements overlapping each other in some views. The US technique was on the other hand, able to detect a deeper anomaly and establishing that the anomaly under the test area is located at different depths. The phase diagram could provide some information about the possible nature of the anomaly, which appears to have a lower impedance relative to its surrounding concrete. IE spectra contained high frequency energy, but no reliable information could be extracted from either IE time histories or spectra.

Comparing the results reveals the need to employ at least two complementary NDT techniques to locate different reflectors within the tunnel lining. GPR is best for locating the metallic reflectors within the penetration range of the antenna. To locate reflectors of different acoustic impedance such as voids and delaminations, the acoustic wave methods should be used. There seem to be a change of structure in the middle of the test area; there are unusual dowel-like reinforcing elements around this location and there is an abrupt change in the depth of the detected anomaly in the ultrasonic results.

It should be noted that none of the utilized NDT techniques was able to reliably identify the extent of the tunnel lining. Obviously, the impedance contrast between the tunnel lining and the surrounding rock formations was not detectable. The backwall was located outside the penetration range of GPR and possibly the zone of influence of US. Moreover, the reflection and scattering effects due to the presence of reinforcement and anomalies weaken the propagating wave and limit its penetration depth.

Test Area 2

Description of the Test Area

The second test area at Hanging Lake Tunnel (HL2) took place in Segment 57 (segment number was assumed based on the marking on the ground as shown in Figure Q-23[a]). The 48 inch x 24 inch test area was located 52 inches north of the joint dividing segments 56 and 57. Its upper (toward the tunnel crest) edge was at a distance of about 100 inches to the center line. Figure Q-33 shows a sketch of HL2. An unrepaired crack ran across the test area, as shown in Figure Q-34(a). Figure Q-34(a) and (b) show the ZFP Scanner. The scanning started at the point closest to the center line, first moving down away from the

center line and then south toward the tunnel entrance. The grid spacing for both the US and IE tests was 1 inches and for GPR was 2 inches. The US, IE, and GPR transducers were mounted such that their length (large dimension) was parallel to the center line of the tunnel. One profile line of the GPR data was missing (at y = 20 cm, or 8 inches), which caused a discontinuity in the C-Scans and B-Scans. Consequently, there was no D-Scan available for y = 8 inches.
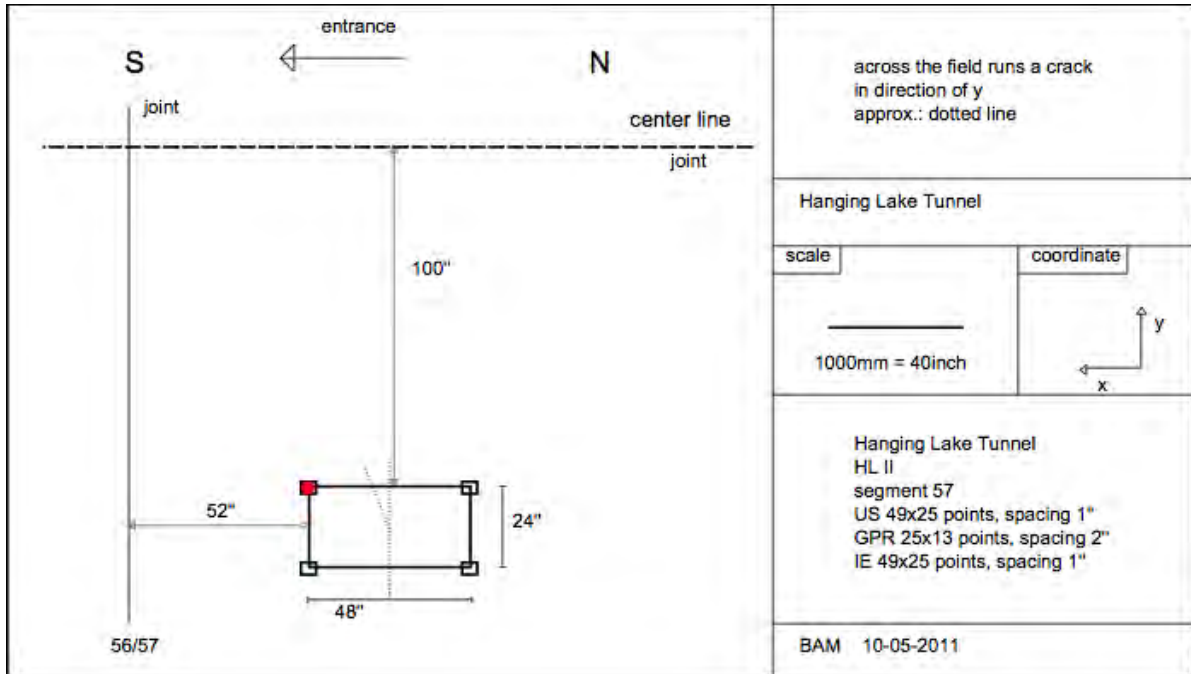
Figure Q-33. Sketch of Test Area HL2, Segment 57.

Figure Q-34. HL2: (a) crack running across the test area, (b) NDT scanner mounted on the tunnel ceiling, and (c) scanning of the test area.

GPR Results

Figure Q-35 is a three-dimensional image of the volume intended to give an overall view of the reinforcement.

Figure Q-35. HL2, GPR: three-dimensional image of the volume positioned to reveal the reinforcing elements, with the B-Scan (a) positioned at x = 44 inches, the C-Scan (b) at z = 6.5 inches, 3-inch width, and the D-Scan (c) at y = 0 inches.

In the C-Scan at a depth of z = 5 inches, a reinforcement bar in the general x-direction could be seen running across the test area roughly from y = 16 inches on the south side of the area to about y = 12 inches on the north side (Figure Q-36[b]). The D-Scan in Figure Q-36[c]) shows that this reinforcement bar ran above the bars perpendicular to it. Figure Q-36(a) is the B-Scan at x = 2 inches, where the bar at y = 16 inches was marked.

The C-Scan at z = 8 inches showed another, albeit weak, reinforcement bar along the x-axis, at about y = 24 inches (see Figure Q-37[b]). A D-Scan through the bar at y = 24 inches (c) and a B-Scan at x = 2 inches (a), with the weak reflection from the bar marked, are shown in Figure Q-37 as well.

The reinforcement bars in the y-direction at a depth of z = 6 inches are shown in Figure Q-38(b). Figure Q-38(c) shows the D-Scan at y = 24 inches with the reinforcements marked at a depth of 8 inches. The B-Scan (a) through the bar at x = 9 inches revealed that the bars did not run parallel to the surface but were bent from z = 6 inches down to z = 8 inches. This explained the weak reflections over half of the C-Scans at z = 6 inches.

Q-29
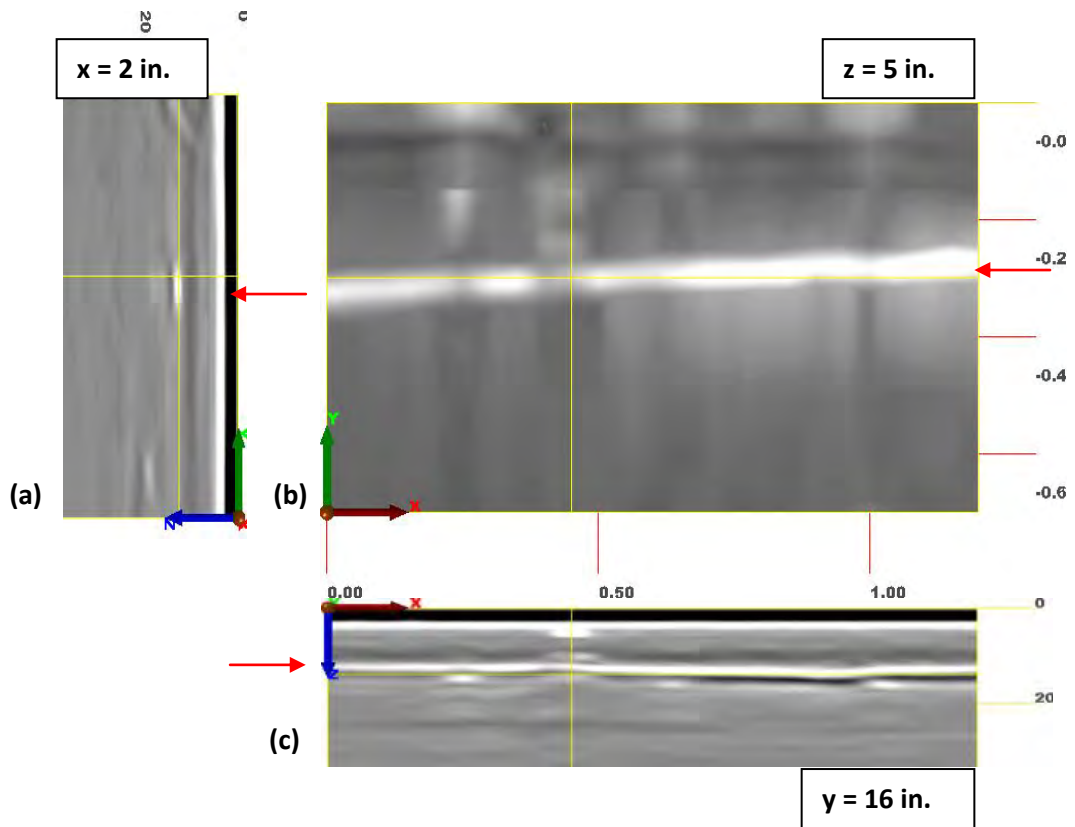
Figure Q-36. HL2, GPR: C-, D-, and B-Scans showing the first reinforcement bar along the x-direction at a depth of z = 5 inches.
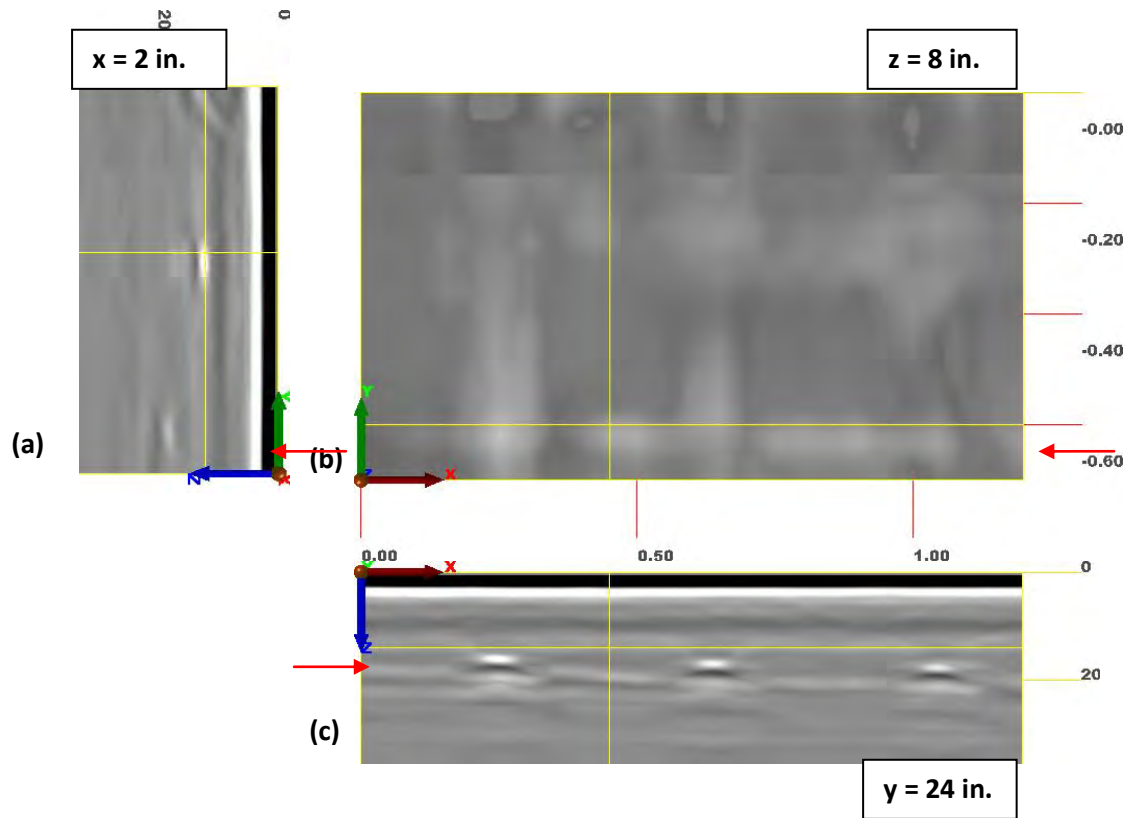
Figure Q-37. HL2, GPR: C-, D-, and B-Scans showing the second reinforcement bar in the x-direction at a depth of z = 8 inches.
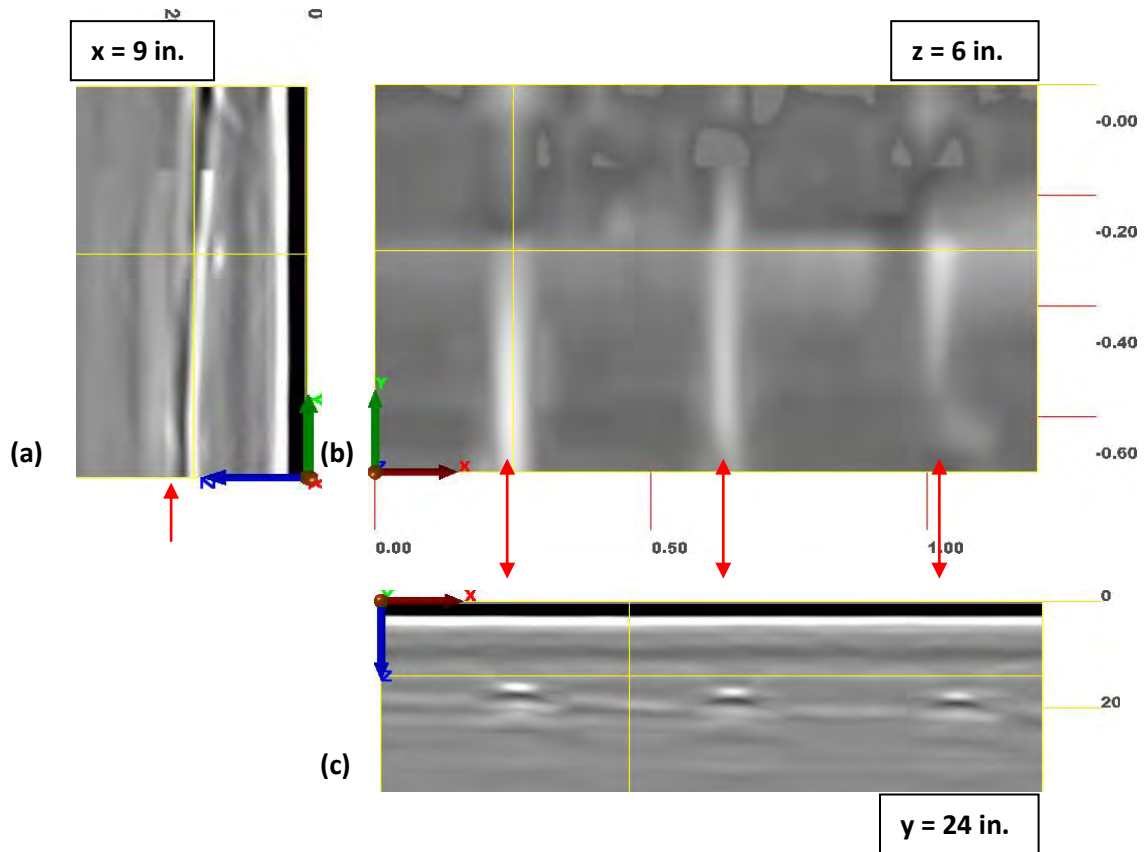
Figure Q-38. HL2, GPR: C-, D-, and B-Scans showing reinforcement bars in the y-direction at depths between 6 inches and 8 inches.

Figure Q-39 shows images resulting from the crack on the surface, which manifested itself by a changed impedance because of the intrusion of moisture into the very first layers of the lining. Image Figure Q-39(b) is a slice in the depth, this time at z = 3 inches. The circled area shows the reflection caused by moisture as a result of the crack on the surface. It ran in that depth until y = 12 inches (y = 30 cm). The upper part until y = 6 inches (y = 15 cm) doesn't seem to fit onto the lower part. The reason for this is a missing profile line caused by a failure during the measurements, which can't be reconstructed properly by the program. Image (c) shows the same reflector at a depth of z = 3 inches, which doesn't show up at the other D-Scans above, meaning it was local. The B-Scan at x = 19 inches (a) shows the extent of the reflector better: it was down to 3.4 inches deep and nearly 16 inches into the field of measurement.

x = 18 in.

z = 3 in.

(a)

(b)

(c)

y = 6 in.
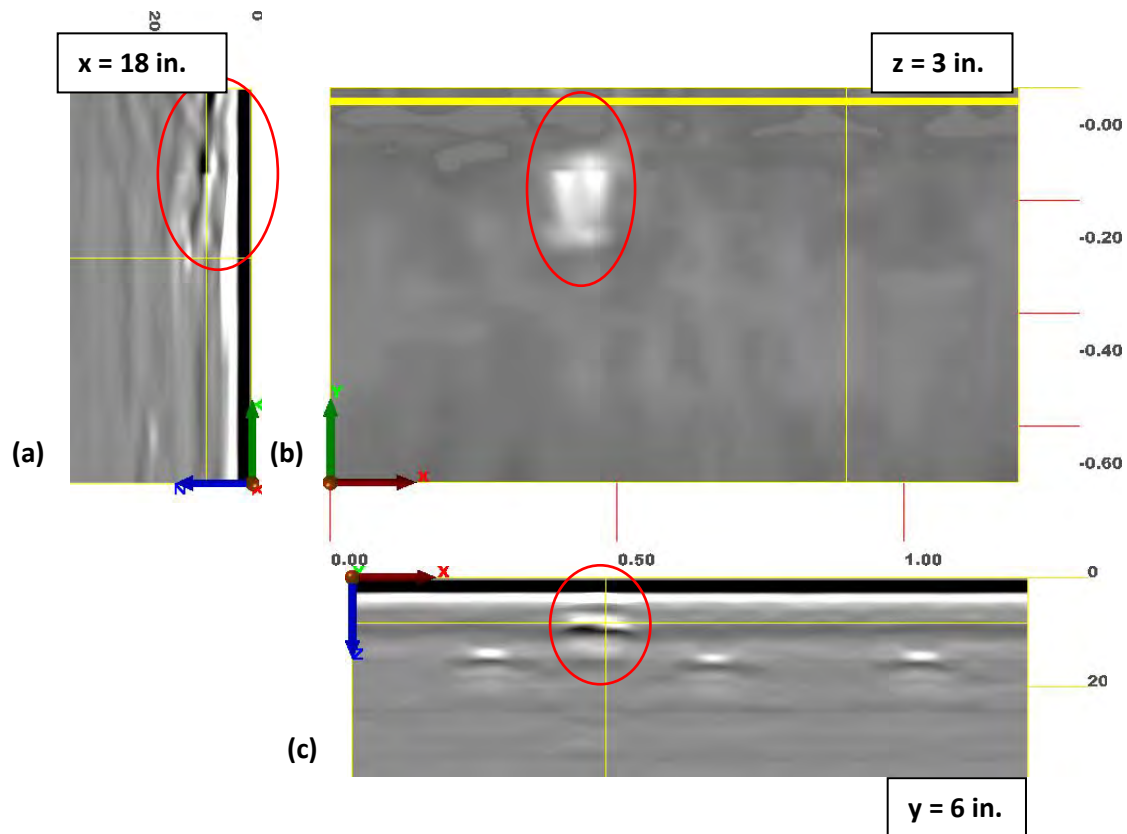
Figure Q-39. HL2, GPR: C-, D-, and B-Scans showing reflections caused by the presence of a surface crack.

Ultrasonic Echo

The reinforcement mesh could be clearly seen in the US C-Scan at a depth of $z = 6$ inches (Figure Q-40). The corresponding phase diagram is also included in this figure (b). As expected, the local phase of the reinforcement bars' reflections appeared mostly positive, which represented impedance higher than the surrounding concrete, i.e., steel.

Shadowed area due to crack

x

y

z = 6 in.

(a)

(b)
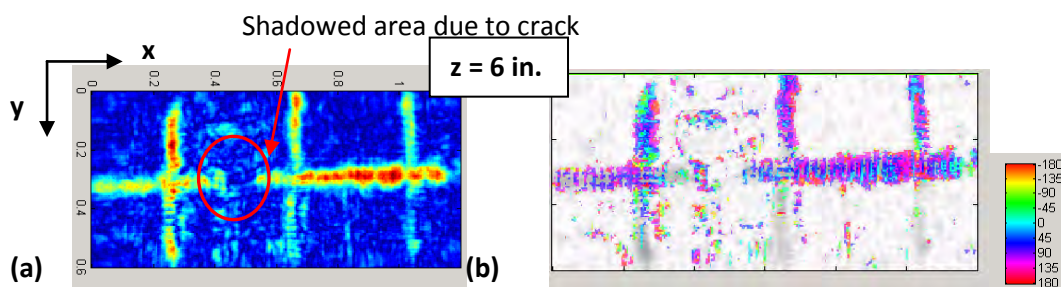
Figure Q-40. HL2, US: C-Scan at $z = 6$-inch amplitude (a) and the corresponding phase diagram (b). The missing part of the reinforcement bar is due to a surface crack within the test area.

The B-Scan (a) and D-Scans (b) in Figure Q-41 show the steel bars in both directions. The reinforcement bar along the x-axis at an approximate depth of $z = 8$ inches (Figure Q-41[c]) wouldn't be identified without prior knowledge of its existence through GPR data. The reinforcement bars in the y-direction were, however, easily detectable. The hole in the reinforcing bar reflections in Figure Q-40 and Figure Q-41(b) are due to the presence of

Q-33

moisture that intruded through the surface crack. It caused the US signal energy to be absorbed.

Figure Q-42 is a three-dimensional image of the volume intended to give an overall view of the reinforcement.
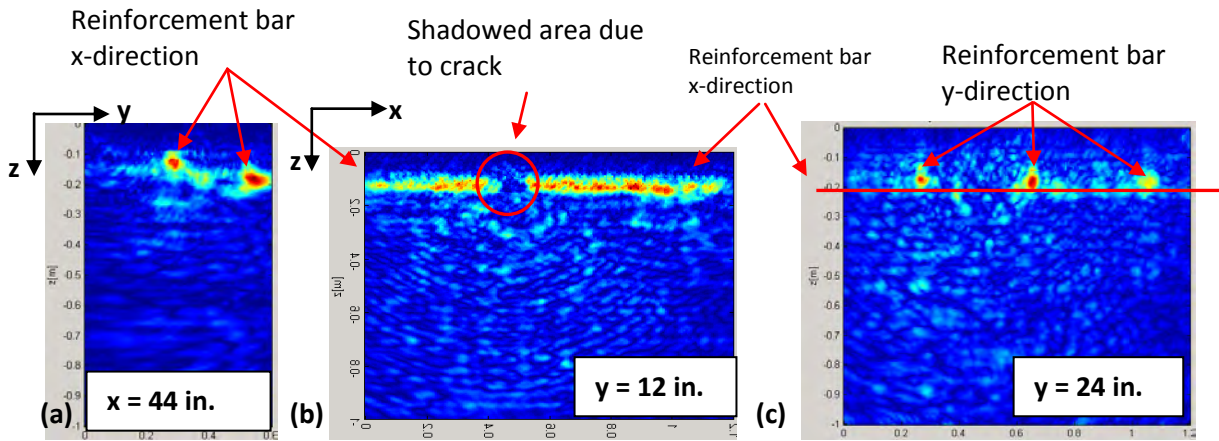
Figure Q-41. HL2, US: B-Scan (a) and D-Scans showing the reinforcement in the x- (a), (b) and y-directions (c). The reinforcement bar along the x-axis at z = 8 inches is very weak (c).

Figure Q-42. HL2, US: three-dimensional image of the volume positioned to reveal the reinforcing elements, with the B-Scan (a) positioned at x = 10.5 inches, the C-Scan (b) at z = 8 inches, and the D-Scan (c) at y = 12 inches. The missing reinforcement due to the crack is also seen in the D-Scan.

Impact Echo

Some of IE spectra showed a dominant frequency peak at about 3600 Hz, which equals a depth of z ~ 22 inches. However, in the B- and D-Scans, no clear backwall could be seen. Figure Q-43 shows a typical example of the obtained IE D-Scan (a) and A-Scan (b). The IE data for this test area yielded no reliable information about either the thickness of the lining or the presence of possible anomalies.

(a)

(b)

A-Scan
x = 17 in.

(3.54,16.75)

f

x

0   25

Frequency in kHz

Transformed

3.60 6.30
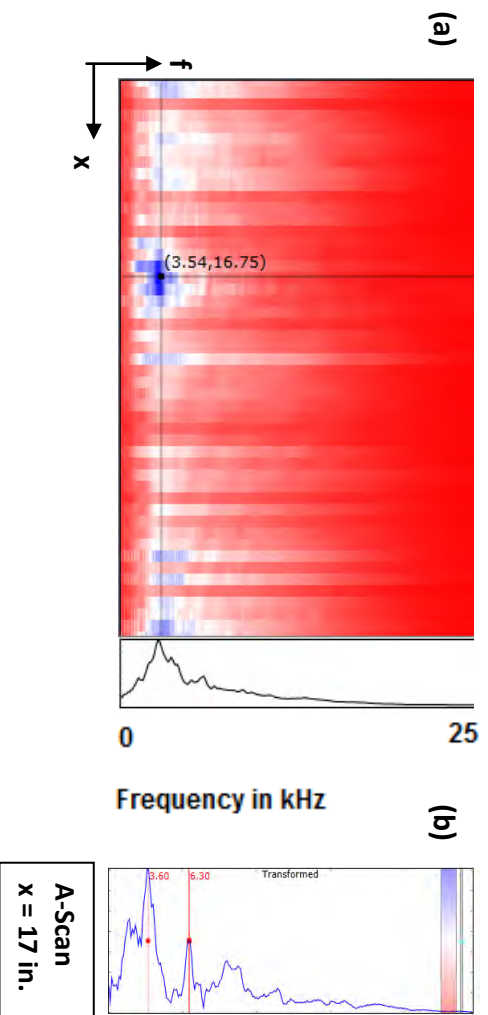
Figure Q-43. HL2, IE: D-Scan (a) and an A-Scan (b). The first frequency peak at 3600 Hz could be representing the backwall in a depth of z ~ 22 inches.

Comparison of Results

Reinforcement could be detected using both GPR and US, although GPR exhibited a clear advantage in detecting deep steel bars, which couldn't be reliably identified in US results. The surface crack was seen in the GPR data as a near-surface reflector, maybe due to moisture penetrating the tunnel lining through the crack, resulting in a change of the dielectric constant. The signature of this crack in the US data was a hole in the reflections from the reinforcement bars. Neither GPR nor US could give any indication of the thickness of the lining. IE spectra contained a repeated frequency peak at a frequency resonating at a depth of about z ~ 22 inches, which could possibly have been the backwall.

GPR proved to be the most effective NDT method to detect the reinforcement as well as the effects of a surface crack. Even the extent of the affected area could be detected, as the anomaly was directly influencing the data. The crack could be indirectly detected in the US results since the reflections from the reinforcements were shadowed by it. It is very curious that the thickness of the lining could not be detected by either method, as the tunnel is relatively recent. IE, on the other hand, could provide some hints about the thickness of the tunnel. It would be interesting to obtain ground-truth information on the lining thickness in order to verify the accuracy of the IE results.

Test Area 3

Description of the Test Area

The third test area at Hanging Lake Tunnel (HL3) was also near section 57/58 of the tunnel, which was marked as such with spray on the floor (Figure Q-44[a]). There was a small crack within the test area (Figure Q-44[b]). A transverse joint crossed through the test field, and the area was relatively close to the center line of the tunnel. The field had an area of 48 inches x 24 inches. The distance of the field to permanent features of the tunnel was not measured; therefore, the sketch in Figure Q-45 has no offsets marked. The grid spacing for US and IE was 1 inch, and for GPR was 2 inches. Figure Q-44(c) shows an image of the GPR, US, and IE Scanner on the test area. During the testing, the longer side (length) of the GPR, US, and IE transducers was set parallel to the center line of the tunnel.

(a)

(b)

(c)
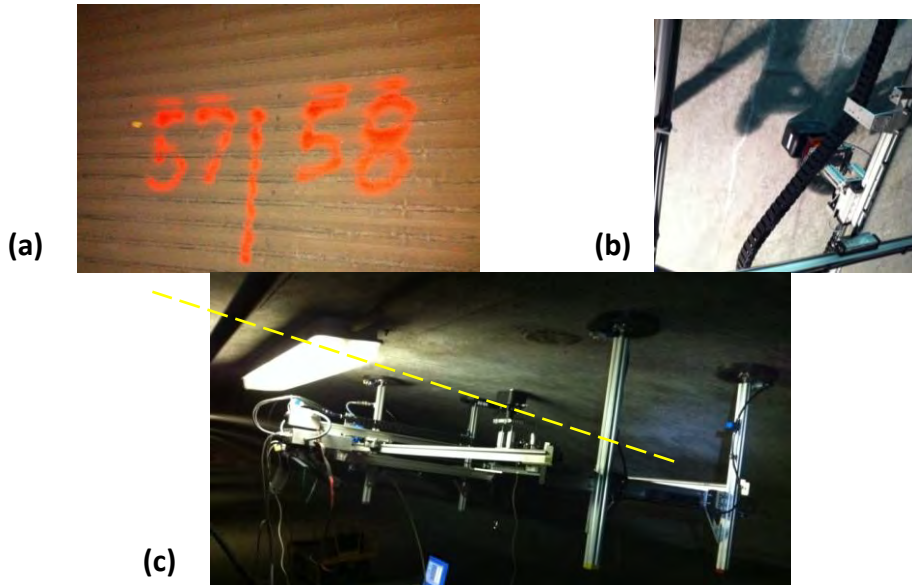
Figure Q-44. HL3 (a) section marking on the floor, (b) crack across the field, (c) ZFP Scanner.
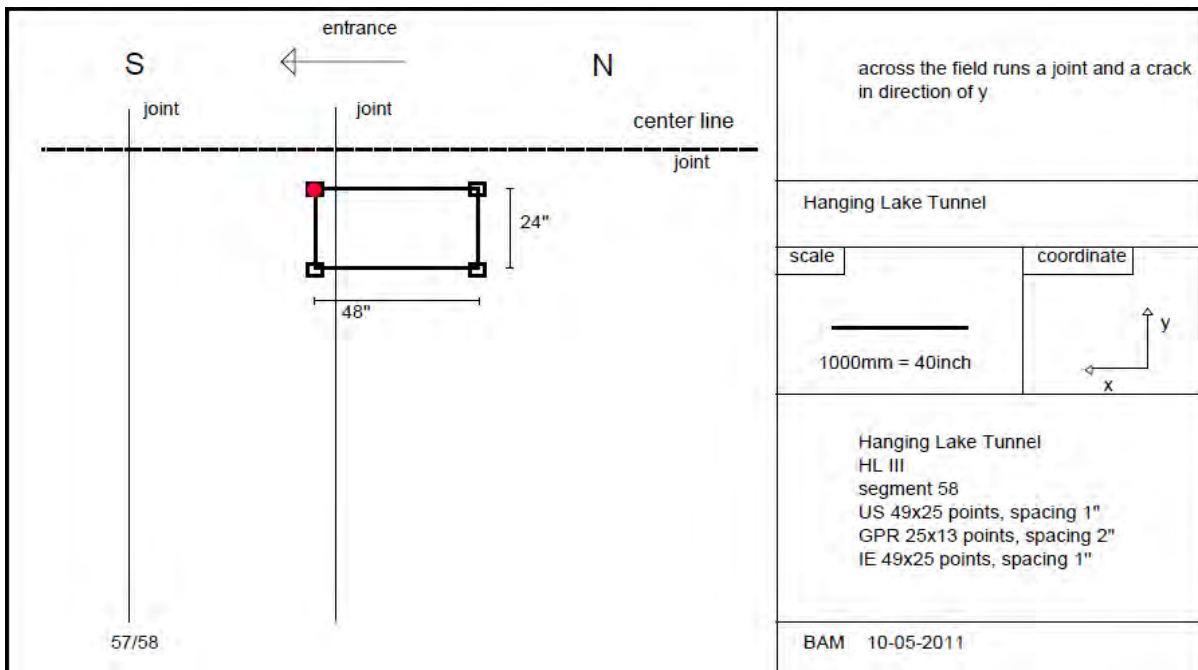
Q-45. Sketch of Test Area HL3, Segment 58, Hanging Lake Tunnel.

GPR Results

Figure Q-46 shows the reinforcement in the x-direction in B-, C-, and D-Scans. One bar is at the edge of the test area. The steel bars ran from around y = 8 inches to y = 6.5 inches at a depth of z = 5 inches and from around y = 24 inches to y = 22.5 inches at a depth of z = 4 inches. The transverse joint running across the test field was encircled on the radarscans. The reinforcement bars in the y-direction were positioned at x = 10 inches, x = 24 inches, and x = 42 inches, at a depth of z = 6 inches (Figure Q-47). The scans from the joint crossing the test field at x = 6 inches in z = 2 inches are shown in Figure Q-48. Dowel-like steel elements traversing the joint at z = 3 inches can be seen in the B- and D-Scans.

Q-37
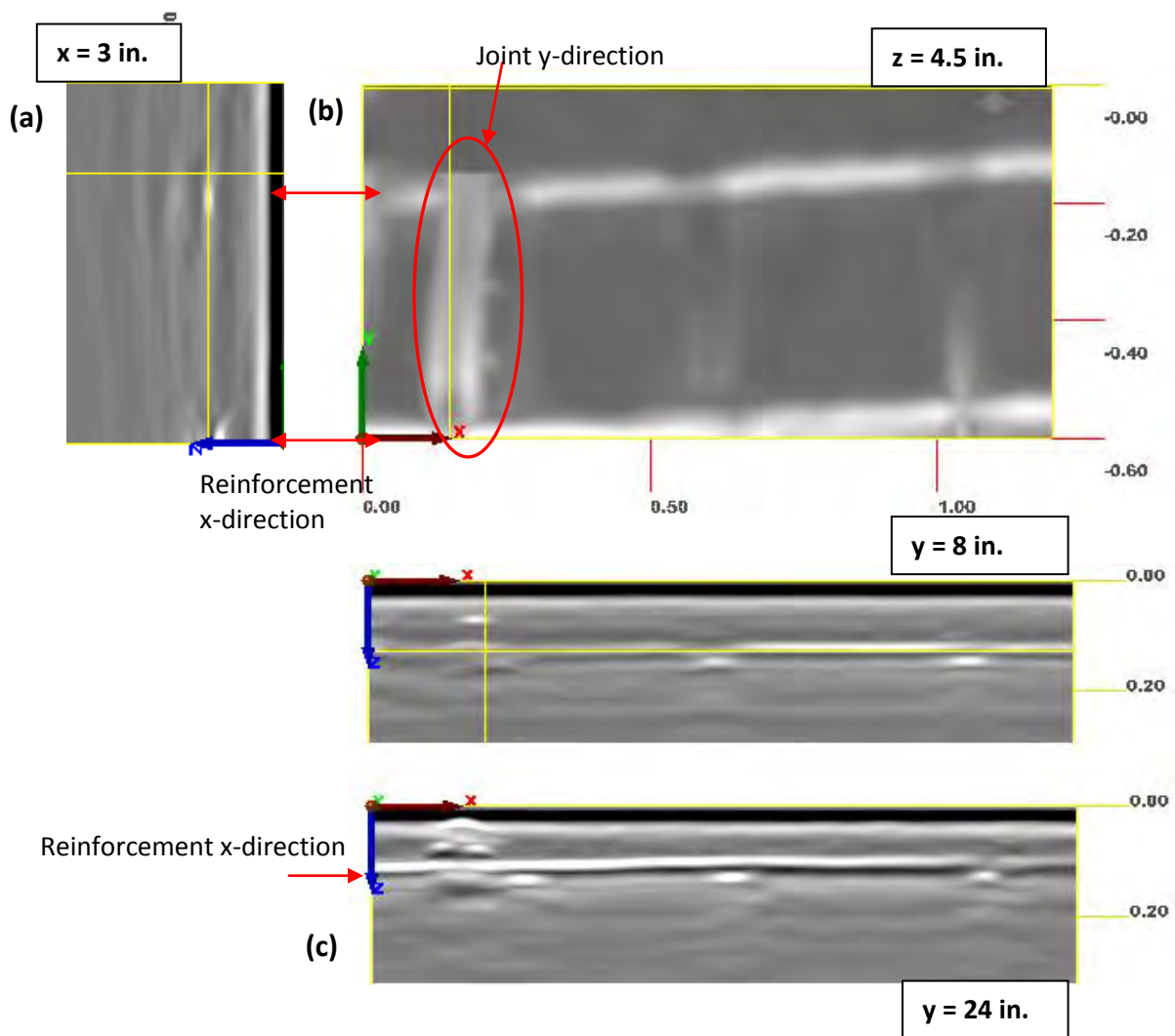
Figure Q-46. HL3, GPR: B-, C-, and D-Scan of reinforcement in x-direction running along a depth of z = 5 inches and z = 4 inches. B-Scan taken at x = 3 inches (a). C-Scan at z = 4.5 inches with a depth width of 1.5 inches (b). D-Scans taken from points y = 8 inches and y = 24 inches (c). The circled reflector is the joint.
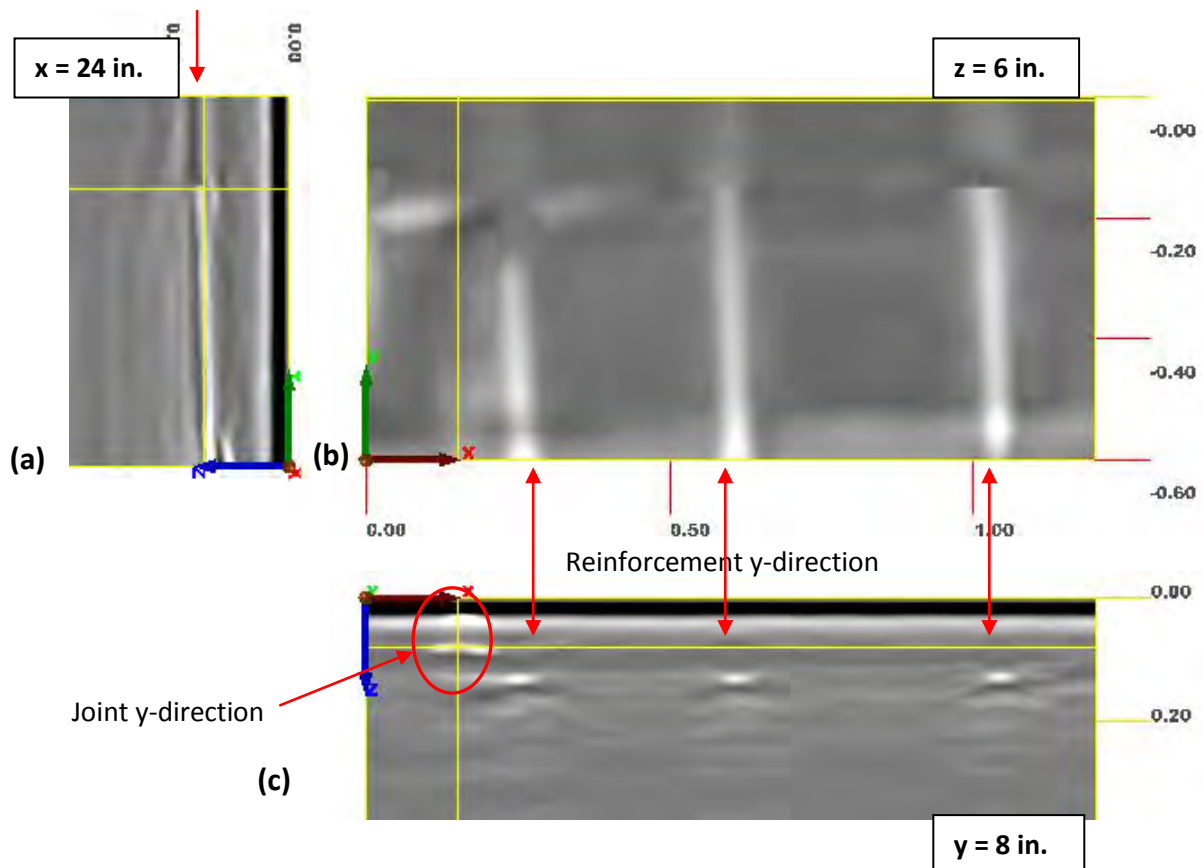
Figure Q-47. HL3, GPR: B-, C-, and D-Scans of reinforcement bars running along y-direction at a depth of z = 6 inches. B-Scan taken at x = 24 inches (a). C-Scan at z = 6 inches (b). D-Scan taken at y = 8 inches (c). The circled reflector is the joint.
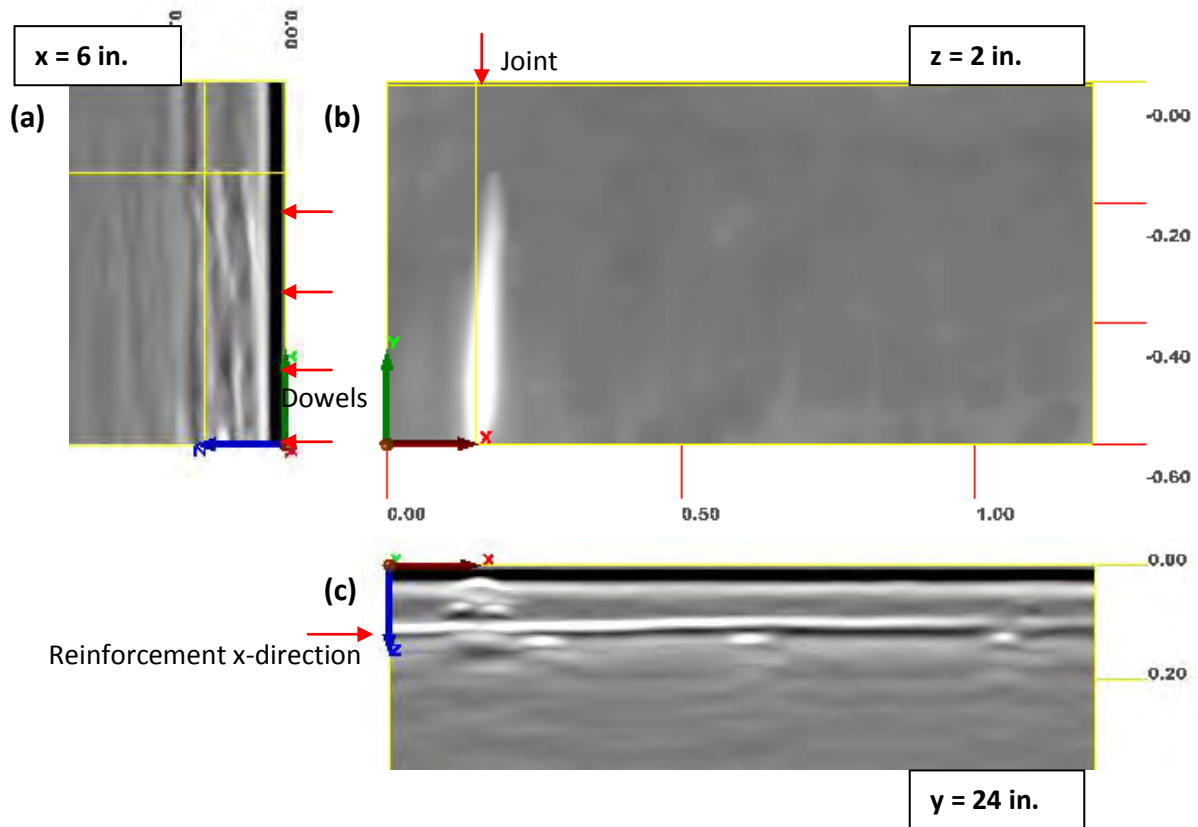
Figure Q-48. HL3, GPR: C-, D-, and B-Scans corresponding to the location of the joint at x = 6 inches.

The line scans at y = 0.45 cm (18 inches), y = 0.4 cm (16 inches), and y = 0.35 cm (14 inches) were missing.

Figure Q-49 is a three-dimensional image of the volume, intended to give an overall view of the reinforcing elements.

Figure Q-49. HL3, GPR: three-dimensional image of the volume positioned to reveal the reinforcing elements, with the B-Scan (a) positioned at x = 8 inches, the C-Scan (b) at z = 7 inches, 1-inch width, and the D-Scan (c) at y = 16 inches.

Ultrasonic Echo Results

The reinforcement running along both x- and y-directions at about z = 6 inches could be seen in the US results, although the rebars along the x-axis at y = 8 inches and y = 24 inches did not appear as clearly as the ones along the y-axis at x = 9 inches, x = 24 inches, and x = 40 inches (Figure Q-50). The joint couldn't be identified in the US results.
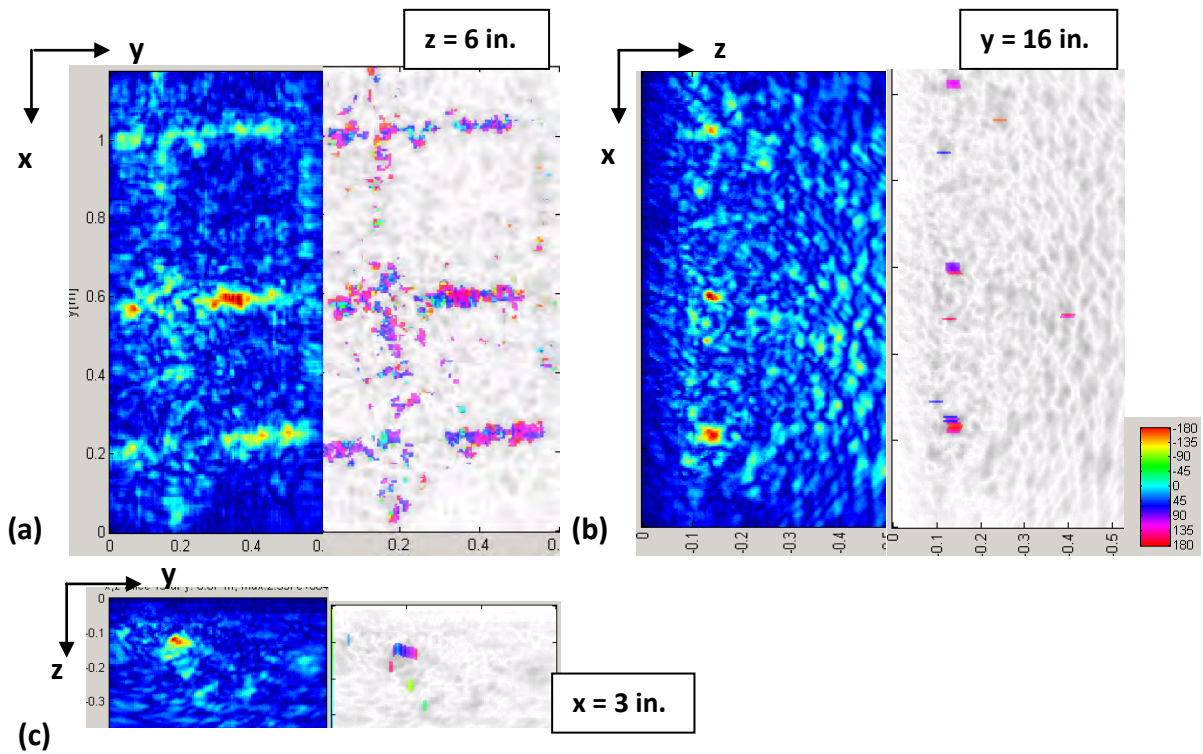
Figure Q-50. HL3, US: C-, D-, and B-Scan showing reinforcement bars running along x- and y-direction at a depth of z = 6 inches.

Impact Echo Results

There were no features resolved based on the IE results, as the frequency peaks were generally too broad to point to any particular resonating feature (Figure Q-51).
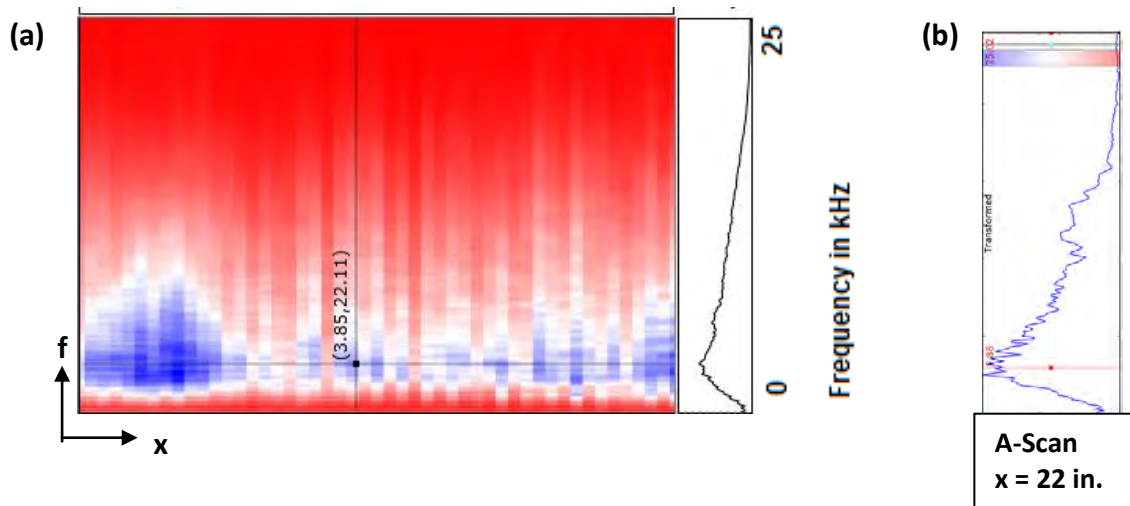
Figure Q-51. HL3, IE: A typical D-Scan (a) and A-Scan (b). There could be no clear frequency peaks identified, which could have represented a possible backwall or other reflectors.

Comparison of Results

Reinforcement could be detected with both GPR and US, but they were much clearer with GPR. The joint seen on the surface of the field could only be detected with GPR, as well as two beams. None of the NDT methods resolved the end of the tunnel lining.

MEASUREMENT RESULTS FOR CHESAPEAKE BAY (CPB) BRIDGE TUNNEL

Measurements in the Chesapeake Bay Tunnel were taken over two days: October 11, 2011, and October 12, 2011. Four test fields were tested, out of which three were located in the tunnel's exhaust air duct (shown in Figure Q-52) and one on the tiles of the wall of the tunnel itself.
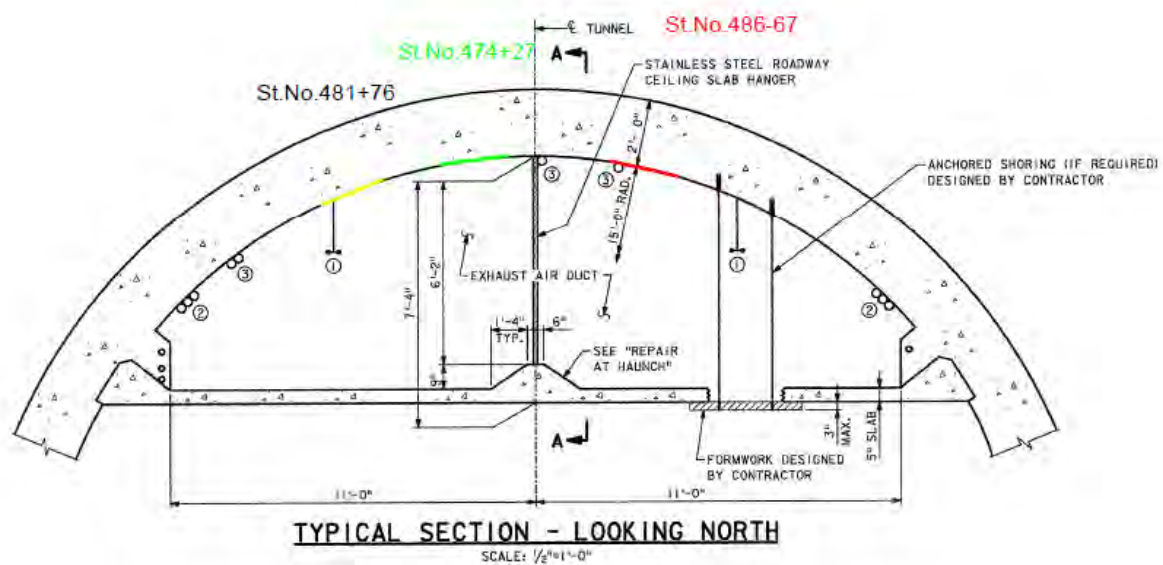
Figure Q-52. Cross-section of the exhaust air duct of the Chesapeake Bay Bridge Tunnel.

TEST AREA 1 (CPB1)

Description of the Test Area

The first test field (CPB1) was located at Sta. 474+27. A sketch of the field showing its positioning in the tunnel is shown in Figure Q-53. The 48 inch x 24 inch large test area started immediately above the pipe. A joint ran across the field, parallel to its shorter side, at one-fourth of its length. The center of the ZFP Scanner's feet were at 14 inches to the left of the joint marked Sta. 474+27 facing the tunnel wall and about 29 inches down from the joint running along the tunnel. When looking north, this joint was about 7 inches to the left of the vertical stands (center line). The tunnel's entrance is at Sta. 470 south end. The backwall has a nominal thickness of 24 inches according to the tunnel's blueprints and has a so-called steel skin.

The grid spacing for US and IE testing was set to 1 inch, for was 2 inches for GPR. During the testing, the GPR, US, and IE transducers were positioned such that their lengths were parallel to the center line of the tunnel.
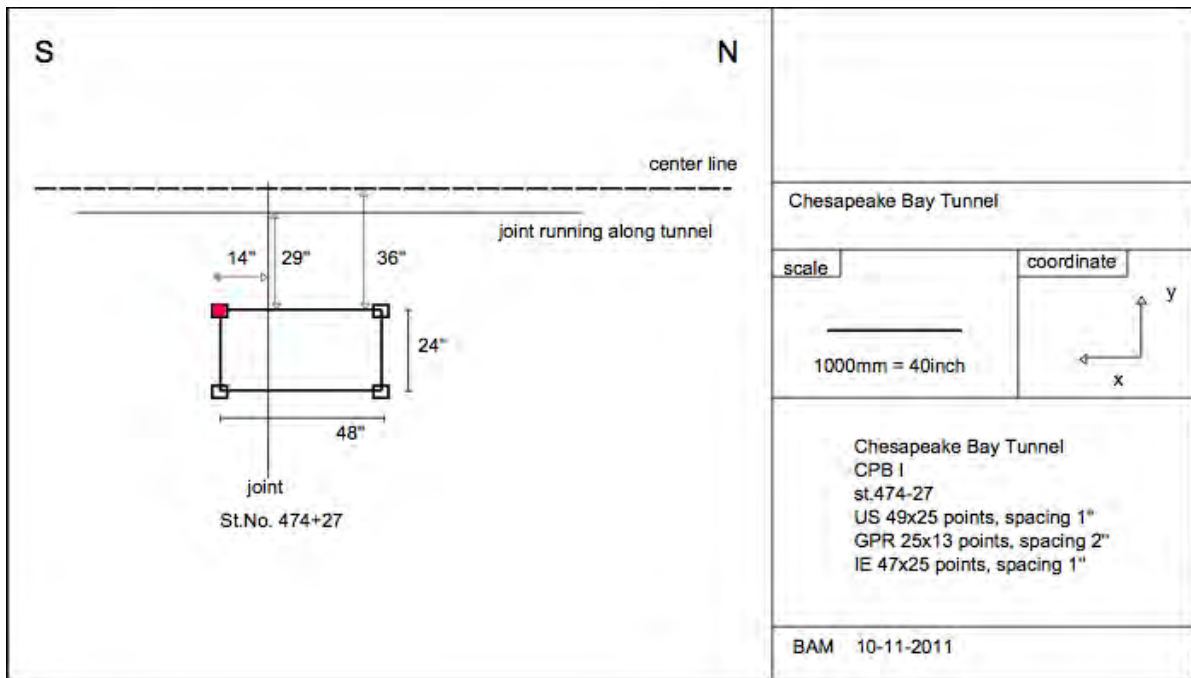
Figure Q-53. Sketch of Test Area CPB1, Sta. No. 474-27, Chesapeake Bay Bridge Tunnel.

GPR Results

Figure Q-54 gives an overview of the reinforcement within the volume.
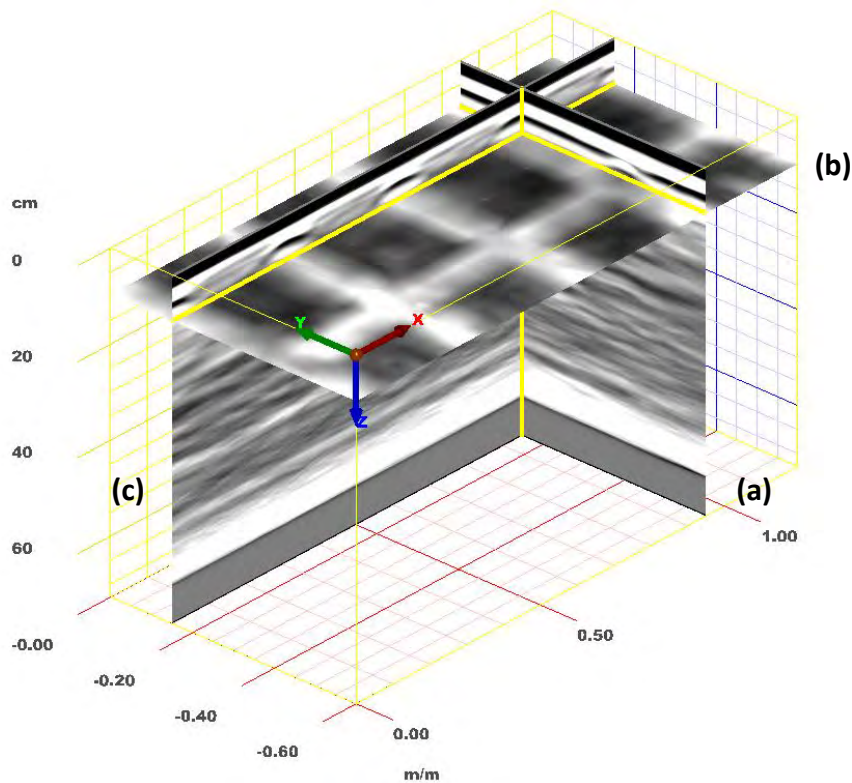
Figure Q-54. CPB1, GPR: three-dimensional image of the volume positioned to reveal the reinforcing elements, with the B-Scan (a) positioned at x = 38 inches, the C-Scan (b) at z = 4 inches, 1-inch width, and the D-Scan (c) at y = 6 inches.

The reinforcements in the y-direction at a depth of z = 1.5 inches and in the x-direction at a depth of z = 3 inches are depicted in the C-Scans of Figure Q-55. The transverse bars along the y-axis were detected at x = 0 inches (i.e., under one of the shorter sides of the test area), x = 12 inches, x = 24 inches, and x = 42 inches. The longitudinal reinforcement was detected at y = 16 inches.

Figure Q-56 includes two D-Scans at y = 22 inches and another one at y = 16 inches, which cuts through the longitudinal rebar appearing in Figure Q-55(b). A selection of B-Scans cutting through the transverse rebars at x = 24 inches and x = 42 inches is shown in Figure Q-57.

Reinforcement bars y-direction

Reinforcement bar x-direction

(a)

z = 1.5 in.

(b)
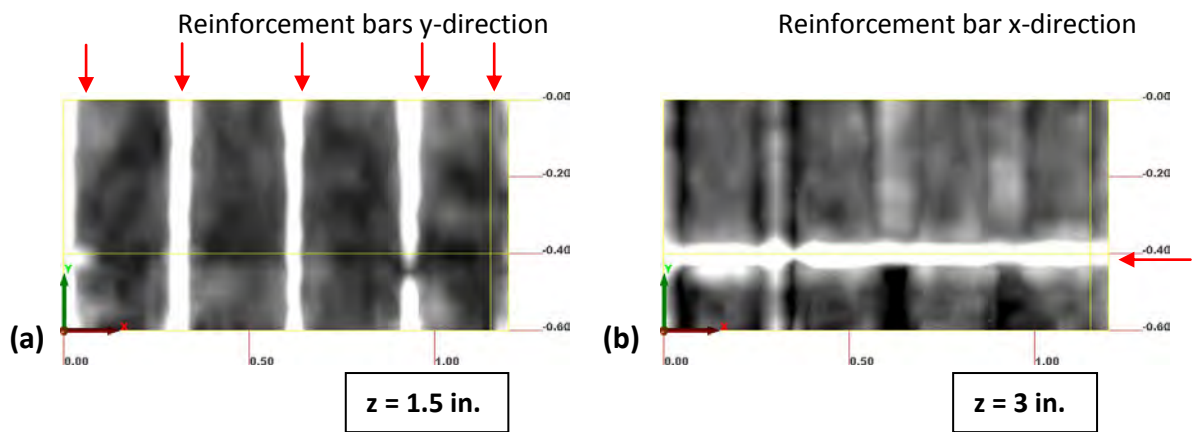
z = 3 in.

Figure Q-55. CPB1, GPR: C-Scans depicting the reinforcement bars (a) along the y-directions at z = 1.5 inches and (b) in the x-direction at a depth of about z = 3 inches.

Reinforcement bars y-direction

(a)

y = 22 in.

0.00   0.50   1.00

Reinforcement bar x-direction

(b)

0.00   0.50   1.00
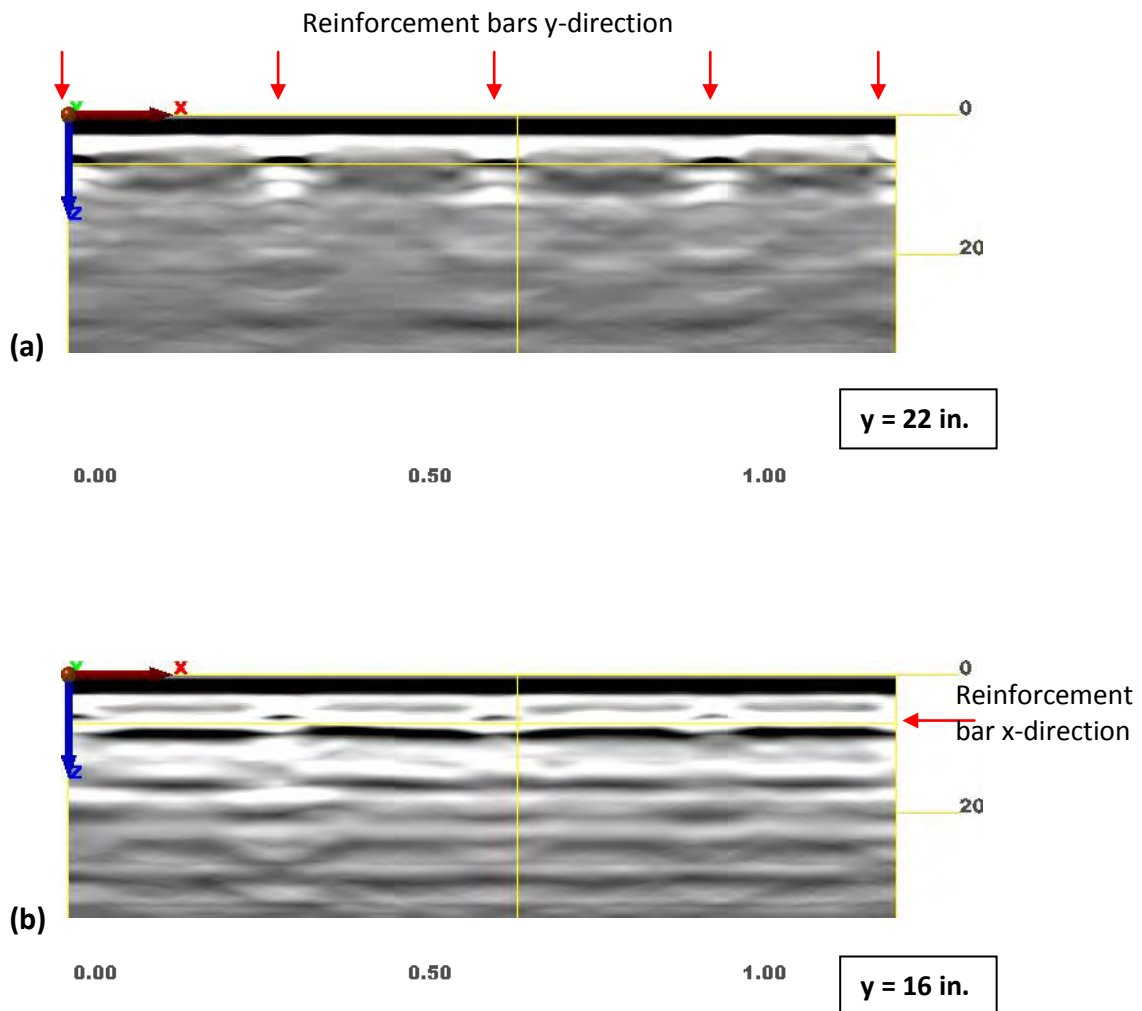
y = 16 in.

Figure Q-56. CPB1, GPR: D-Scans showing the reinforcement bars (a) along the y-direction at location y = 22 inches and (b) x-direction at location y = 16 inches.
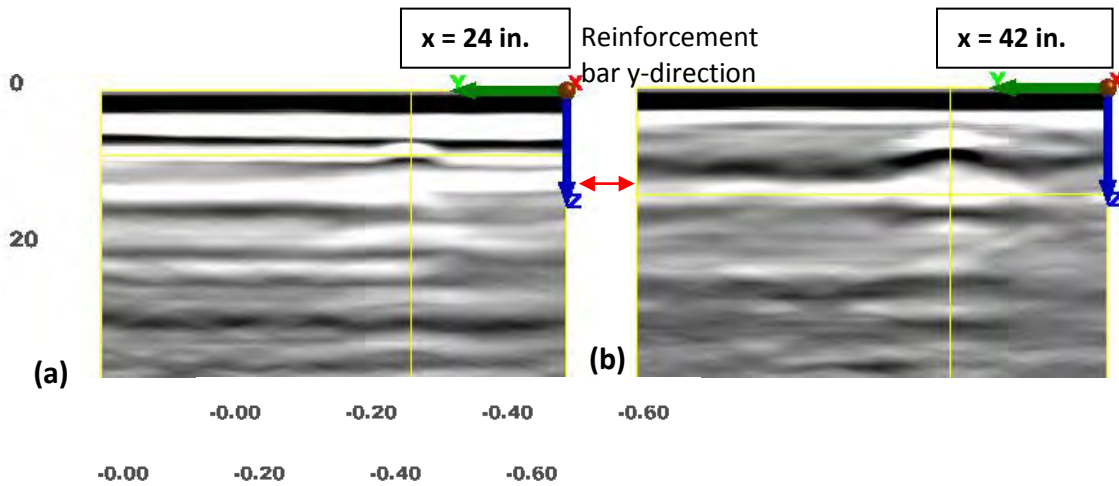
Figure Q-57. CPB1, GPR: B-Scans of transverse rebar (along the y-direction) taken at (a) x = 24 inches and (b) x = 42 inches.

Ultrasonic Echo Results

Transverse steel bars along the y-direction could be clearly detected and identified using the US technique as well (see the C-Scan of Figure Q-58 taken at z = 2 inches). The reflections from the longitudinal bar in the x-direction in the C-Scan were vaguely seen, although they could be more clearly seen in the later B-Scans. This repeating observation was due to the orientation of the US transducer, which made it more sensitive to transverse reinforcement (the polarization effect). When examining the C-Scans (Figure Q-59) at different depths, the steel skin of the tunnel at about z = 24 inches was detected. The shear wave velocity was adjusted to about 2710 m/s such that the backwall reflections occurred at the known depth of 24 inches. There was also a shallower anomaly at z = 15 inches spreading from x = 20 inches to x = 40 inches and y = 6 inches to y = 14 inches, detected both directly and indirectly through its shadowing of the skin reflections. The corresponding phase diagrams exhibited a positive phase for the reinforcement bars and steel skin and a mixture of positive and negative angles (inconclusive) for the anomaly.

Reinforcement bars y-direction
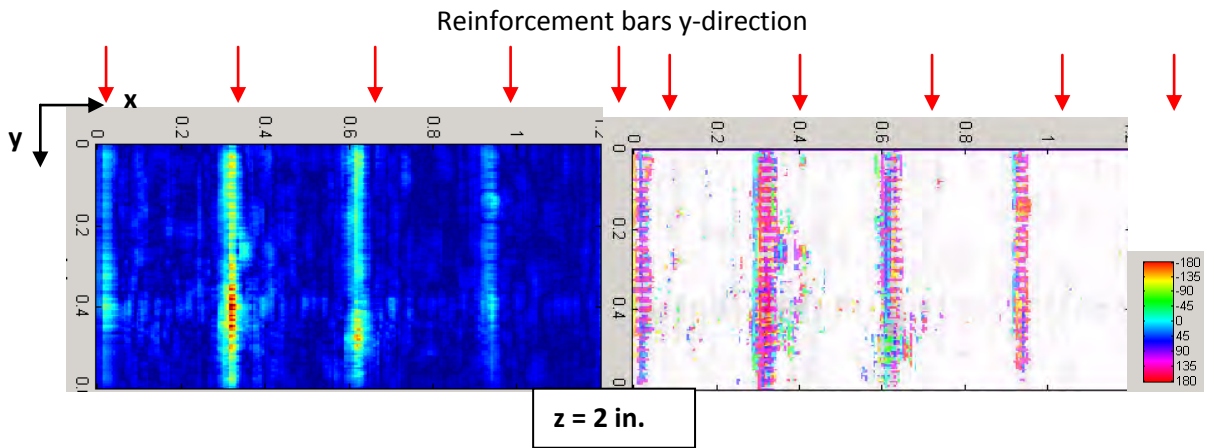
z = 2 in.

Figure Q-58. CPB1, US: C-Scan showing the transverse reinforcement in the y-direction at z = 2 inches.

(a)

z = 15 in.

(b)
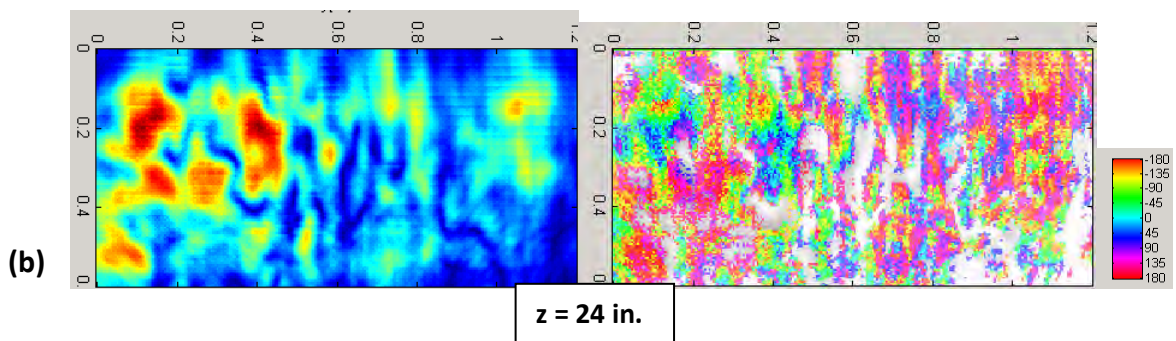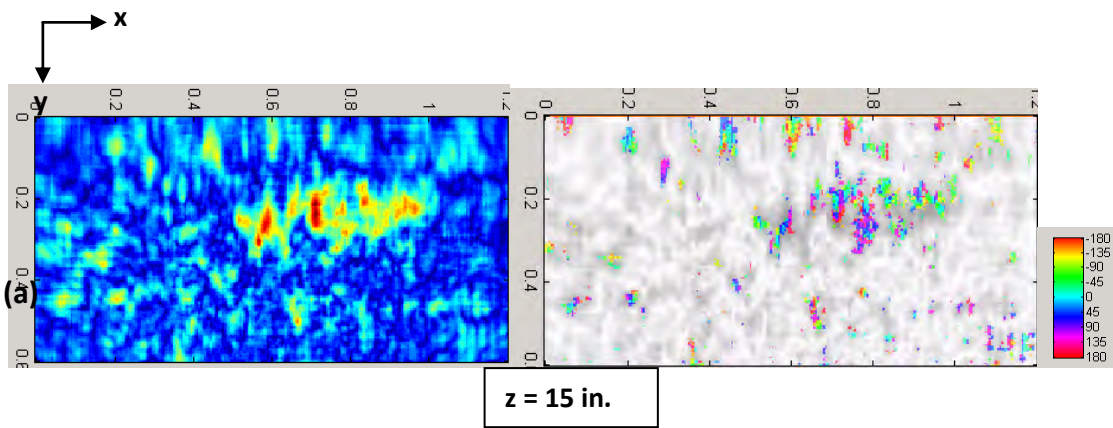
z = 24 in.

Figure Q-59. CPB1, US: C-Scans showing the reflection from an anomaly (a) and the tunnel skin (b).

Looking at the D-Scan at y = 12 inches (Figure Q-60), the rebars and the backwall at z = 24 inches are clearly seen. At this location, about half of the backwall (with x > 24 inches) exhibited weakened or even missing reflections. The phase evaluation offered more information about why the backwall reflections appeared weaker: at a depth of around z = 16 inches existed a confined anomaly that shadowed the backwall reflection between x = 22 inches and x = 30 inches. This anomaly was the same as seen in the C-Scan in Figure Q-59.

The B-Scans in Figure Q-61 were chosen to represent areas of the test volume with and without anomaly. The left image in Figure Q-61 is a B-Scan at x = 3 inches, where there is no anomaly. The backwall and reinforcement bar in x-direction (at y = 16 inches) can be clearly seen. The other B-Scan was obtained by cutting through the anomaly at x = 28 inches. The backwall is missing between y = 8 inches and y = 12 inches and some reflections from about z = 13 inches downwards can be seen. The corresponding phase diagrams are not conclusive.

Figure Q-62 is a three-dimensional image of the volume, showing the backwall and anomaly.

y = 12 in.
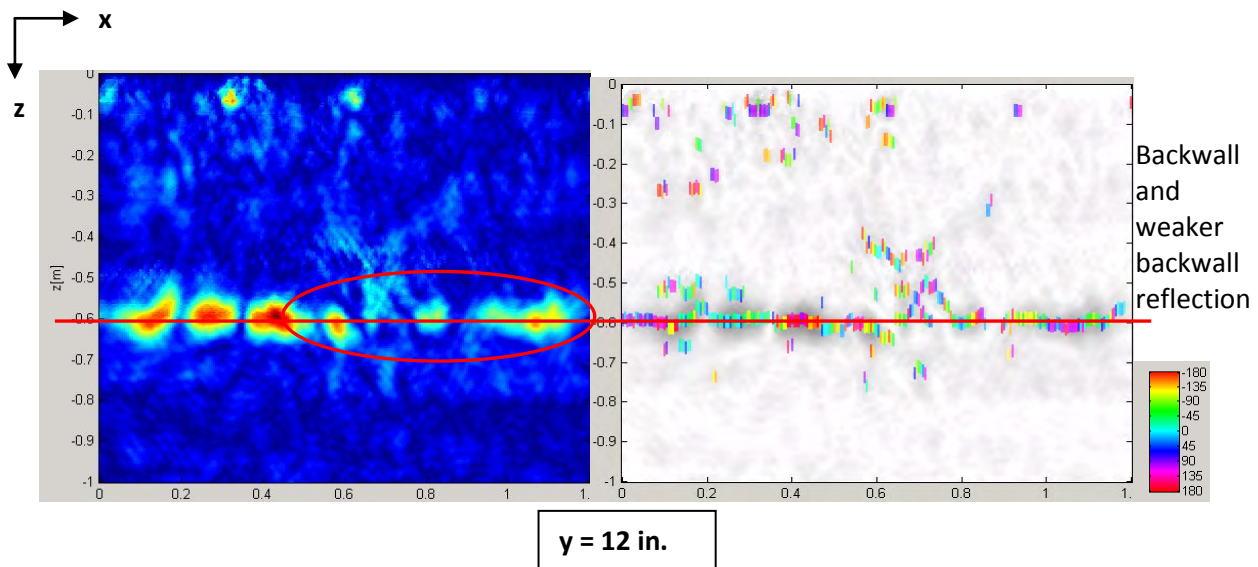
Figure Q-60. CPB1, US: D-Scan showing the reinforcement, the tunnel skin. The weakened reflection from the backwall is marked on this figure.
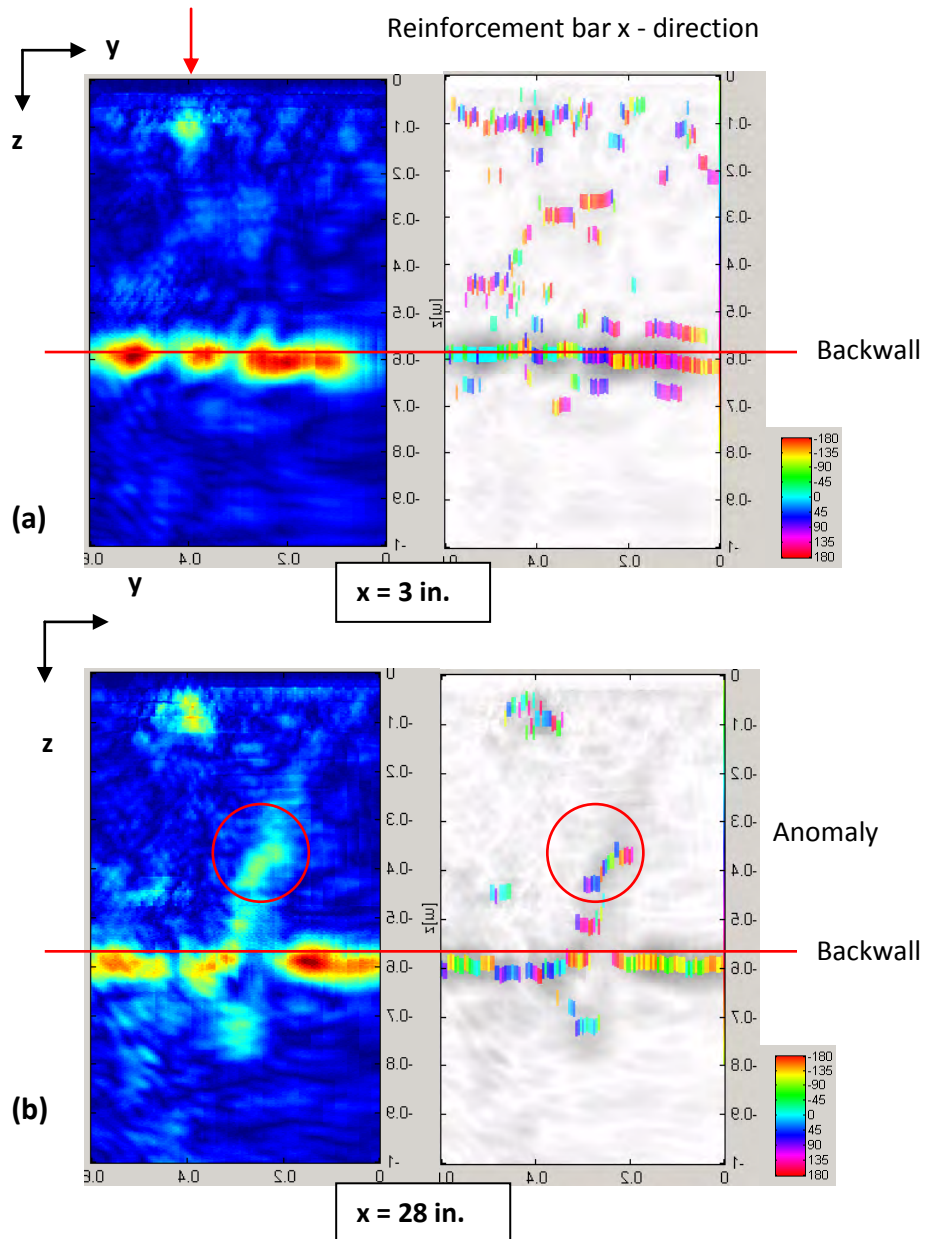
Figure Q-61. CPB1, US: B-Scan showing the longitudinal reinforcement bar (along x-direction) and the backwall, where no anomaly was detected (a), and where an anomaly was detected (b).
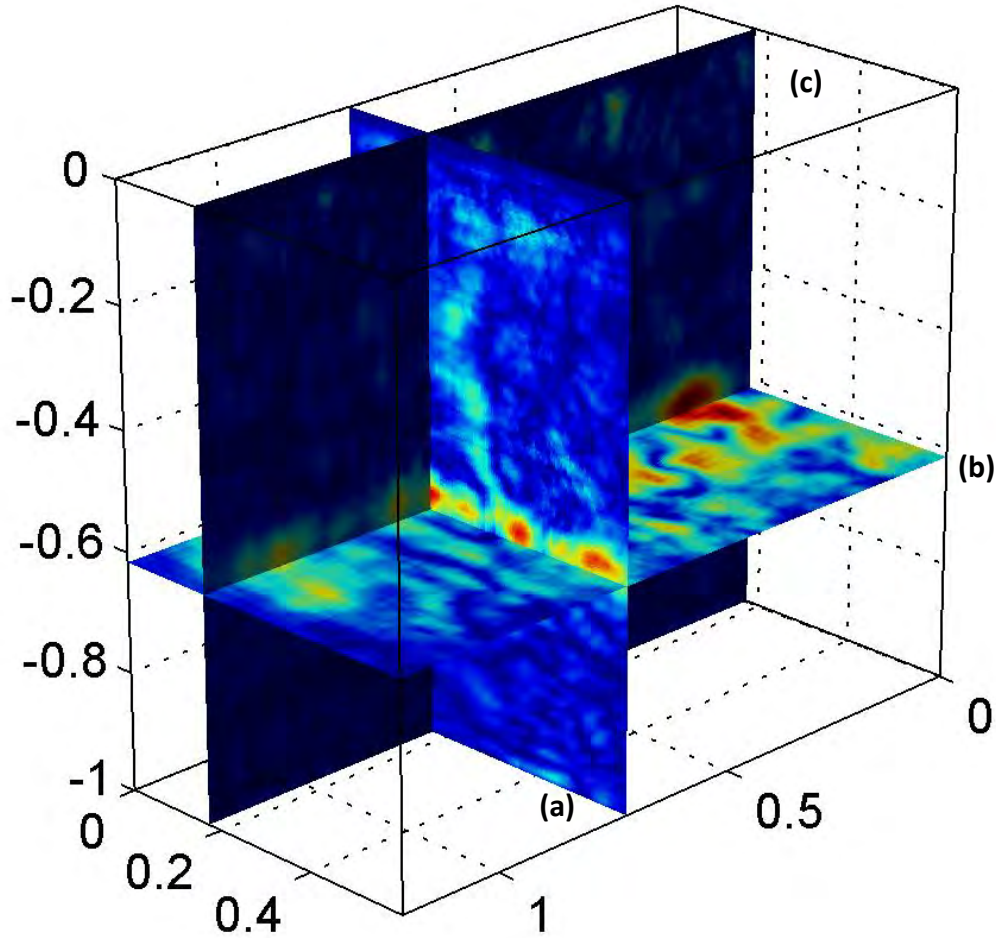
Figure Q-62. CPB1, US: three-dimensional image of the volume positioned to reveal the backwall and the anomaly, with the B-Scan (a) positioned at x = 29 inches, the C-Scan (b) at z = 24 inches, and the D-Scan (c) at y = 7 inches.

Impact Echo Results

The IE spectra contained a clear thickness resonance frequency peak at a frequency between 3600 Hz and 3400 Hz, representing a thickness of about z = 22 inches to z = 24 inches, assuming a longitudinal wave velocity of 4000 m/s. Figure Q-63 shows the selected B-Scan (a) and D-Scan (b) of the test volume along with a representative A-Scan and frequency spectrum. The amplitudes of the backwall echo in the D-Scan between x = 27 inches x = 46 inches were weaker than in the area x < 27 inches, indicating the presents of an inhomogeneity between the sensor and the backwall absorbing the wave energy. The same was true for the B-Scan between y = 0 inches and y = 8 inches.
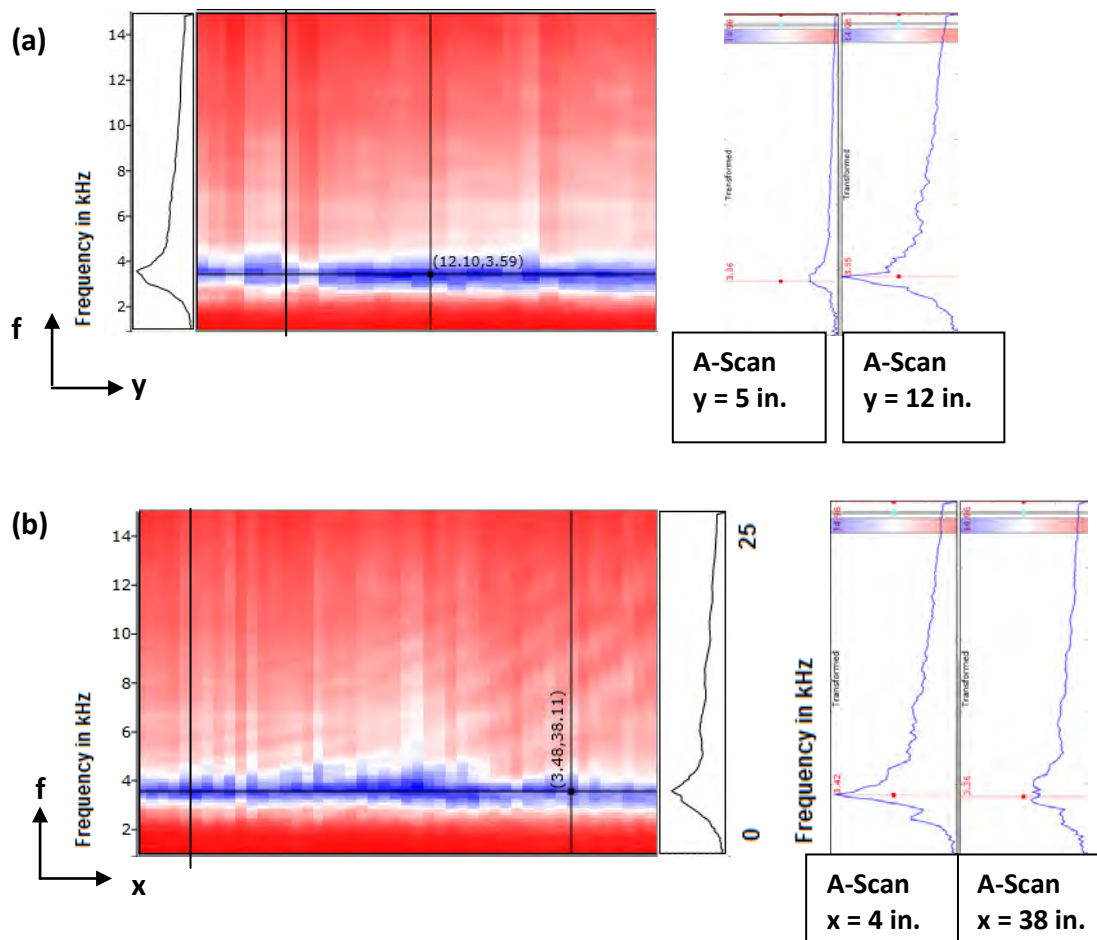
Figure Q-63. CPB1, IE: (a) B-Scan and (b) D-Scan of the profile lines along the y- and x-axes of the field coordinate system. Right: A-Scan. The frequency peaks represent the tunnel lining thickness. There are areas with weaker amplitudes, indicating a wave energy absorbing inhomogeneity.

Comparison of Results

While GPR proved to be the most reliable NDT method for detecting and identifying reinforcement bars, it couldn't detect a 15-inch-deep localized anomaly. The US technique, however, wasn't as clear in detecting the steel bars (due to the polarization effects) but indicated the presence of an anomaly, directly and indirectly (directly by evaluating the reflections from the anomaly and indirectly based on the weakened and even missing backwall echo).

Both US and IE could yield the thickness of the tunnel lining. Thanks to the phase diagrams, US results could even indicate that the impedance of the tunnel's skin was higher than that of the lining and, therefore, of steel. This could be verified by the tunnel's blueprint indicating the presence of a steel skin.

Considering the obtained data from all three employed NDT methods together, a more clear picture of the geometry and condition of the tunnel emerged.

Test Area 2

Description of the Test Area

The test area CPB2 was located on the west side of the tunnel, facing north. It was located south of the joint marked Sta. 481+76, and the entire area was on one single block. The 48 inch x 24 inch test area was oriented such that its length was parallel to the center line of the tunnel. The near and far shorter sides of the scanning aperture were 9 inches and 49 inches south of Sta. 481+76. The longer side was 47 inches away from the tunnel's center line, where the vertical stands were. Figure Q-64 provides a rough sketch of the test area and its positioning within the tunnel.

The grid-spacing for US and IE testing was set to 1 inch, and for GPR, it was 2 inches. The GPR, US, and IE transducers were oriented such that their lengths were parallel to the center line of the tunnel. Please note that the GPR measurements for this test area were shifted 1.5 inches in the x-direction compared to those from IE and US.
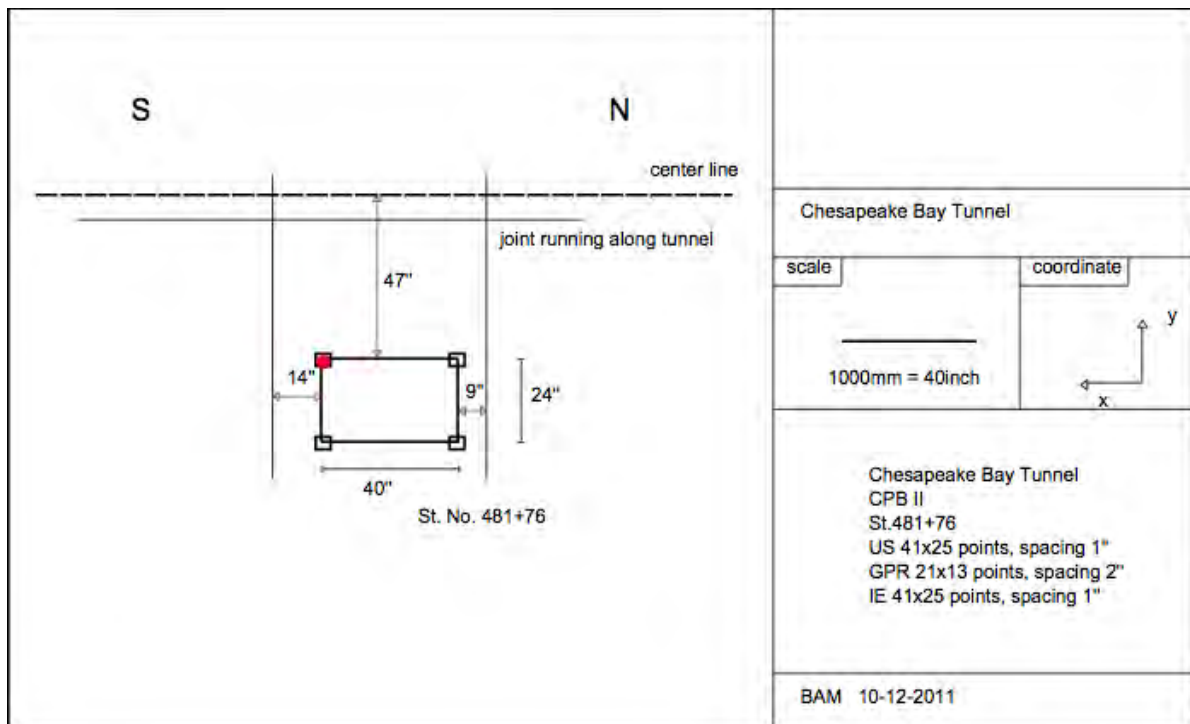
Figure Q-64. Sketch of Test Area CPB2 south of Sta. 481+76, Chesapeake Bay Tunnel.

GPR Results

Figure Q-65 is a three-dimensional image of the volume with the slices (B-, C-, and D-Scans) positioned to reveal the reinforcing elements.

Transverse reinforcement in the y-direction could be detected at a depth of $z = 2.5$ inches with the bars positioned at $x = 0$ inches, $x = 12$ inches, $x = 24$ inches, and $x = 36$ inches.. Two longitudinal steel rebars in the x-direction appeared 4 inches deep at $y = 8$ inches and $y = 24$ inches. The one at $y = 24$ inches ran out of the test field and was only partly visible.

Figure Q-66 provides C-Scans showing the reinforcement mesh at two different depths. D-Scans taken at y = 8 inches (a) and y = 24 inches (b) showed the rebars in the y-direction as well as one of the rebars in the x-direction (see Figure Q-67). One B-Scan at x = 12 inches cutting through one of the transverse rebars and a second one at x = 16 inches cutting between the transverse rebars, showing the longitudinal rebars, are shown in Figure Q-68.
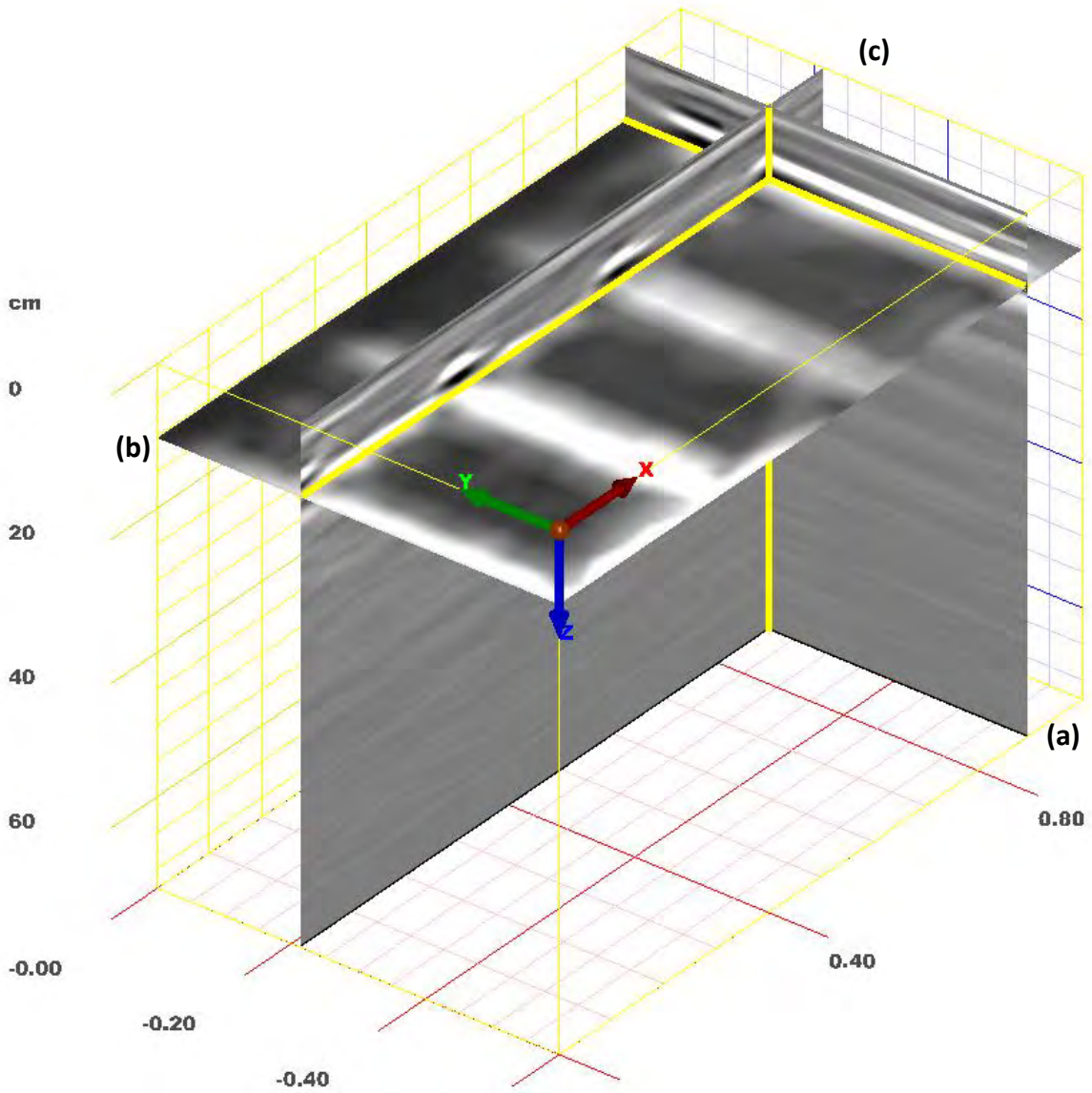
Figure Q-65. CPB2, GPR: three-dimensional image of the volume positioned to reveal the reinforcing elements, with the B-Scan (a) positioned at x = 36 inches, the C-Scan (b) at z = 4 inches, 4-inch width, and the D-Scan (c) at y = 8 inches.
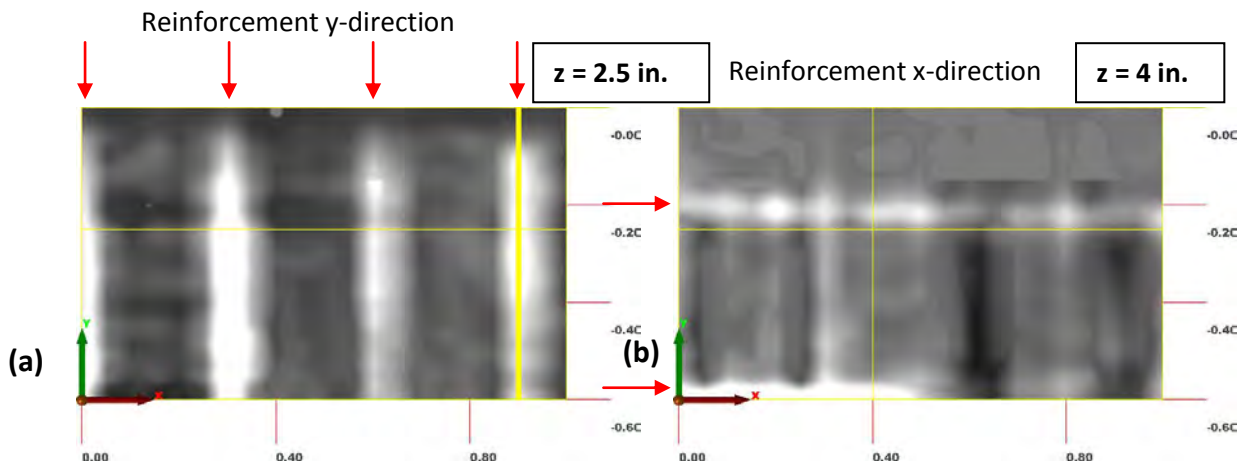
Figure Q-66. CPB2, GPR: C-Scans at z = 2.5 inches and z = 4 inches showing rebars in y-direction (a) and x-direction (b).
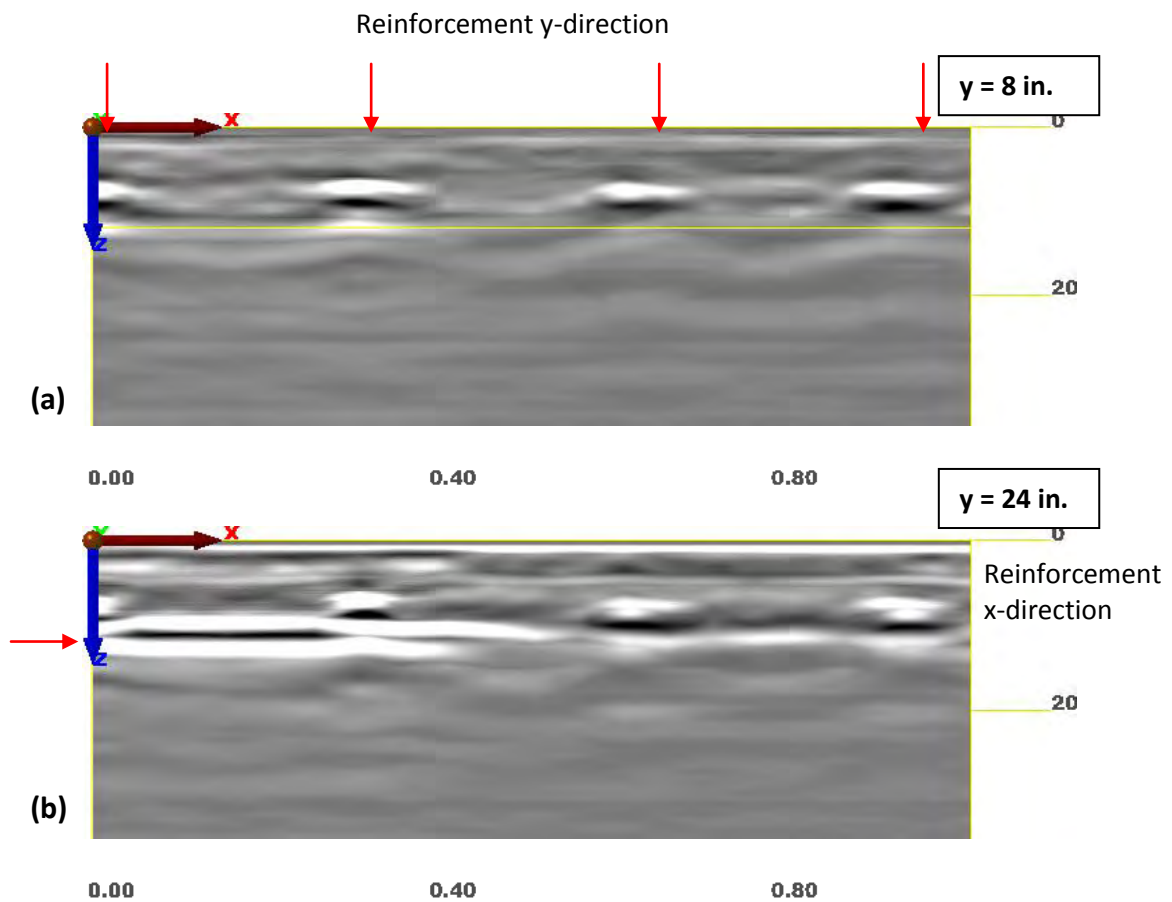
Figure Q-67. CPB2, GPR: D-Scans through the test volume at positions y = 8 inches and y = 24 inches showing the reinforcement in y-direction (a) and in x-direction (b).
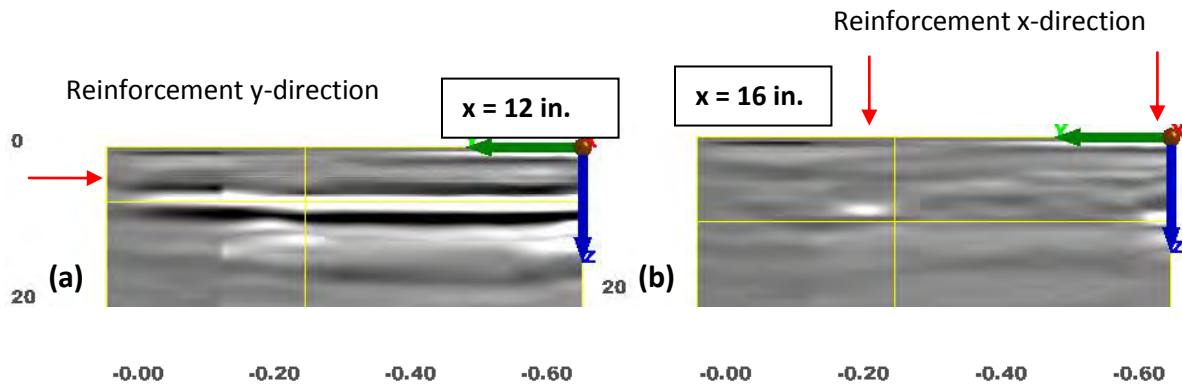
Figure Q-68. CPB2, GPR: B-Scans taken at x = 12 inches and x = 16 inches showing the rebars in y-direction (a) and in x-direction (b).

Ultrasonic Echo Results

Figure Q-69 shows a three-dimensional image of the volume focusing on the backwall and an anomaly shadowing it.

The reinforcement mesh wasn't very clear in the US C-Scans. The transverse bars along the y-axis were most clearly seen in the C-Scan at z = 2 inches (Figure Q-70[a]), and those along the x-axis, at z = 4 inches (Figure Q-70[b]).

Besides the reinforcements, an anomaly at z = 20 inches (Figure Q-71[a]) and the backwall at z = 28 inches (Figure Q-71[b]) could also be detected in the C-Scans. The anomaly had a phase shift between 45 degree and -45 degree (of lower acoustic impedance than concrete). The backwall exhibited a phase shift between -90 degree and -180 degree (of higher acoustic impedance than concrete). To analyze the US data, a transversal wave velocity of 2710 m/s was assumed (taken from the measurements at CPB1).

By examining D-Scans (Figure Q-72) and B-Scans (Figure Q-73), the extent of the anomaly could be approximated as running along the entire width of Test Field CPB2 (i.e., y-direction) but confined between x = 8 inches and x = 28 inches in the x-direction.
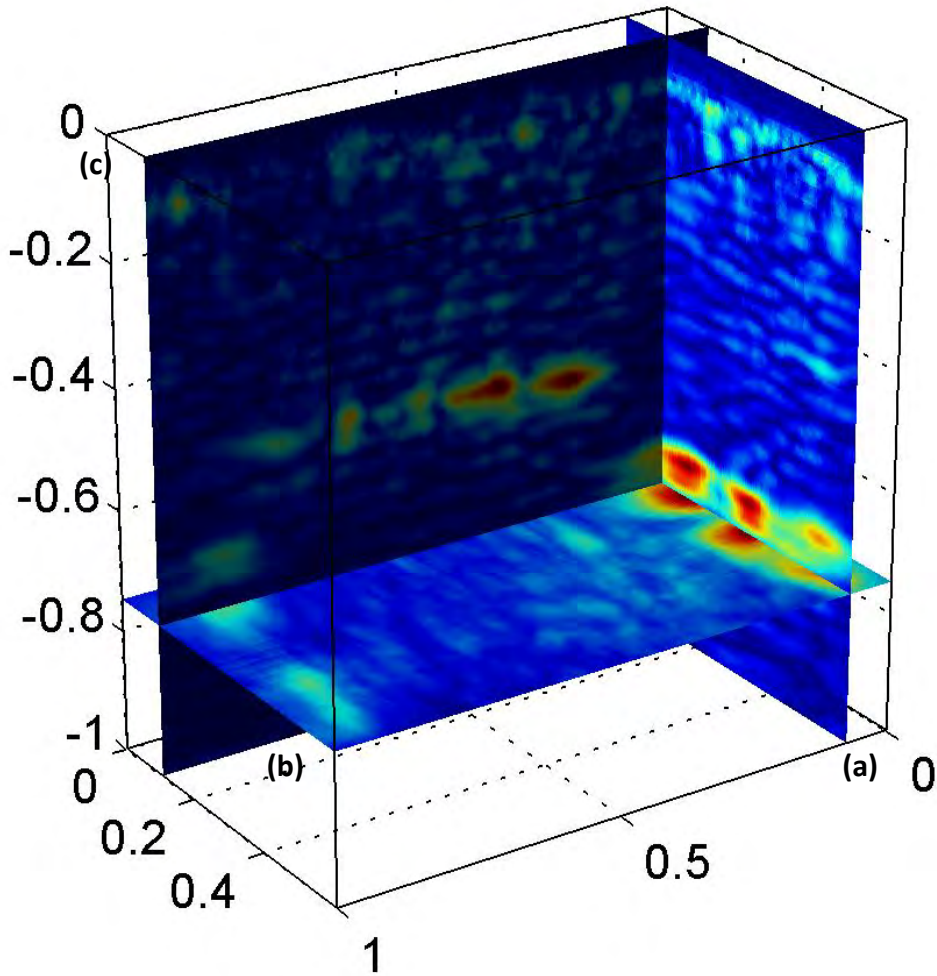
Figure Q-69. CPB2, US: three-dimensional image of the volume positioned to reveal the backwall and an anomaly, with the B-Scan (a) positioned at x = 3 inches, the C-Scan (b) at z = 25 inches, 5-inch width, and the D-Scan (c) at y = 4 inches.
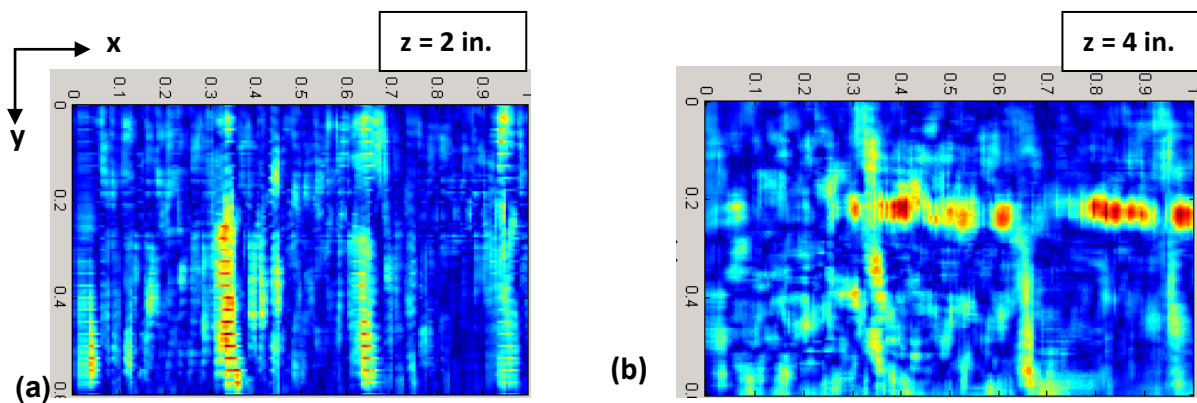
Figure Q-70. CPB2, US: C-Scans at z = 2 inches and z = 4 inches showing the reinforcement along (a) y- and (b) x-direction.
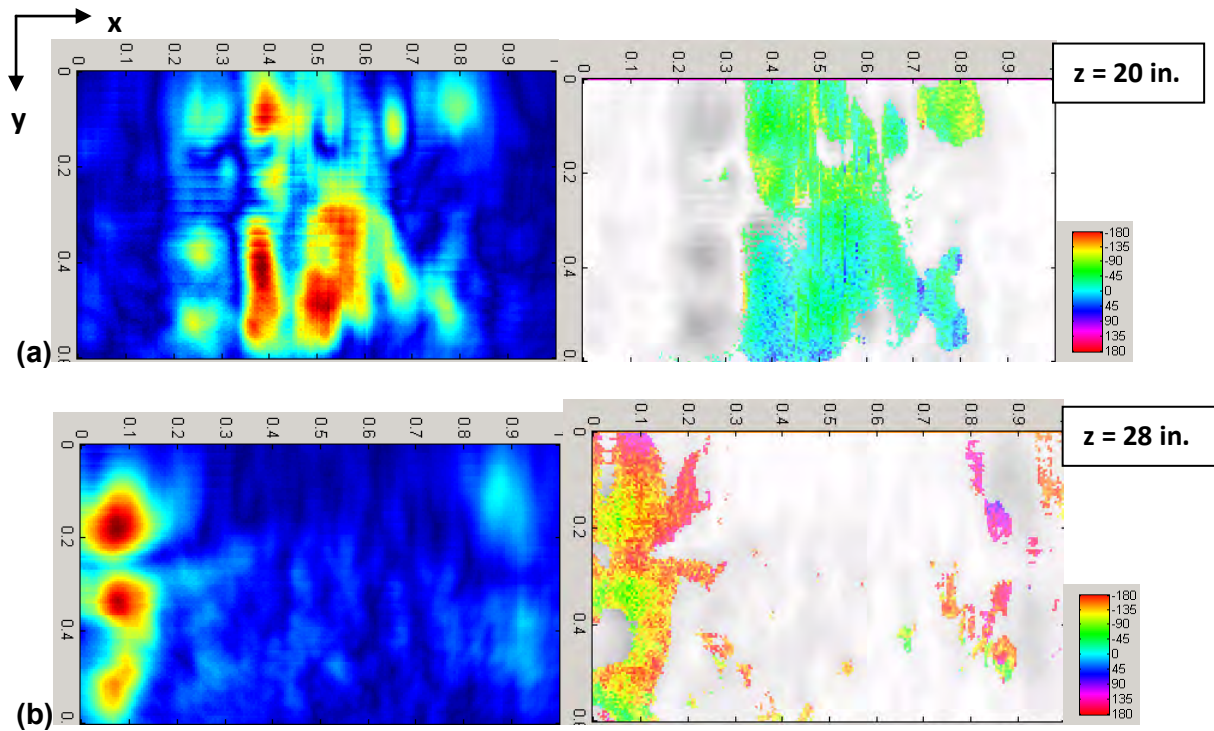
Figure Q-71. CPB2, US: C-Scans at different depths. (a) depth of the anomaly at 20 inches and (b) depth of the tunnel lining at 28 inches. Left: Image of the amplitudes. Right: Image of the corresponding phase.
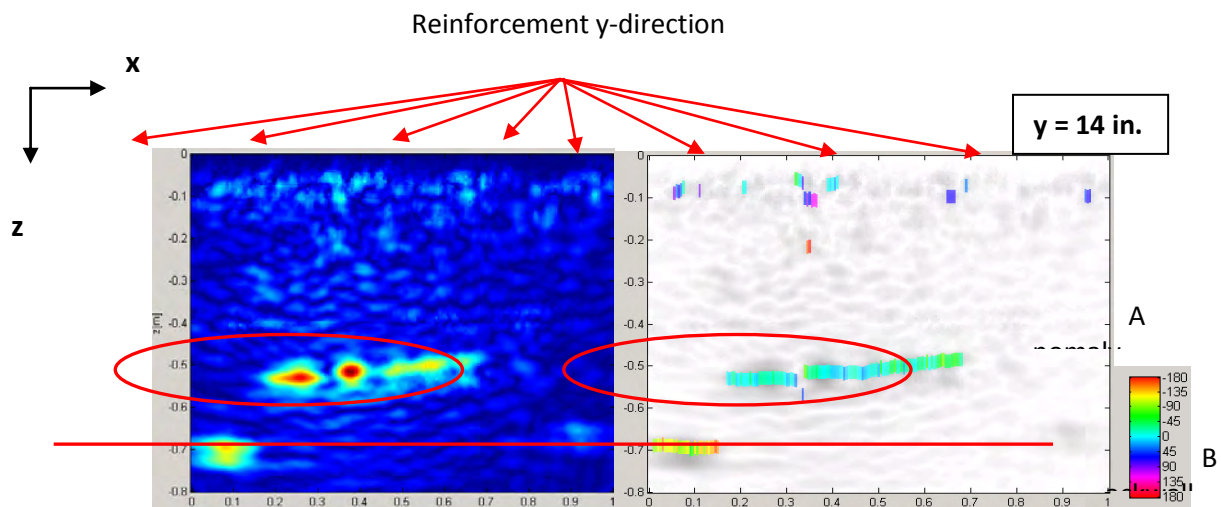
Figure Q-72. CPB2, US: D-Scan at y = 14 inches and its corresponding phase diagram.

Reinforcement x-direction
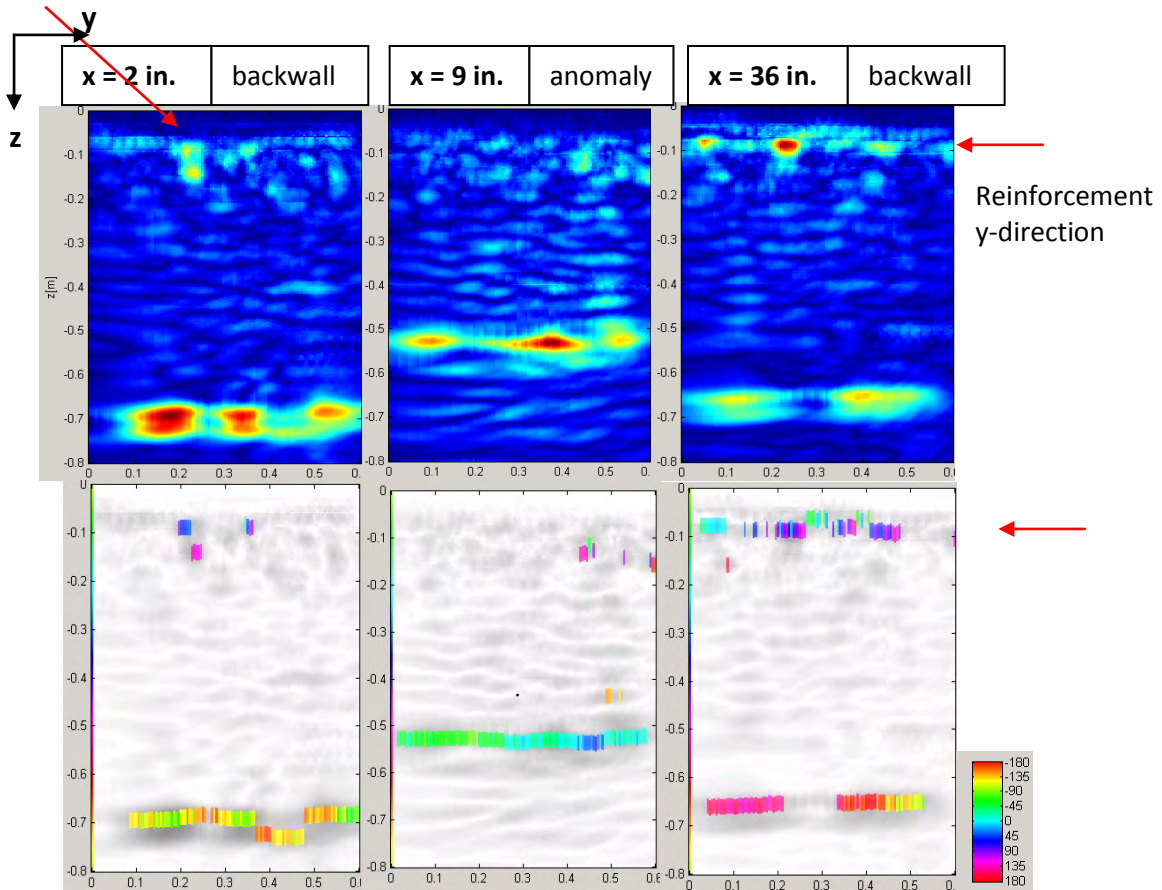
Figure Q-73. CPB2, US: B-Scans through the anomaly and backwall taken at x = 2 inches, x = 9 inches, and x = 36 inches.

Impact Echo Results

The IE spectra contained two distinct frequency peaks at about 2900 Hz and 4100 Hz (see spectral B-Scans of Figure Q-74) corresponding to the reflector depths of z = 27 inches (a) and z = 20 inches (b), respectively.
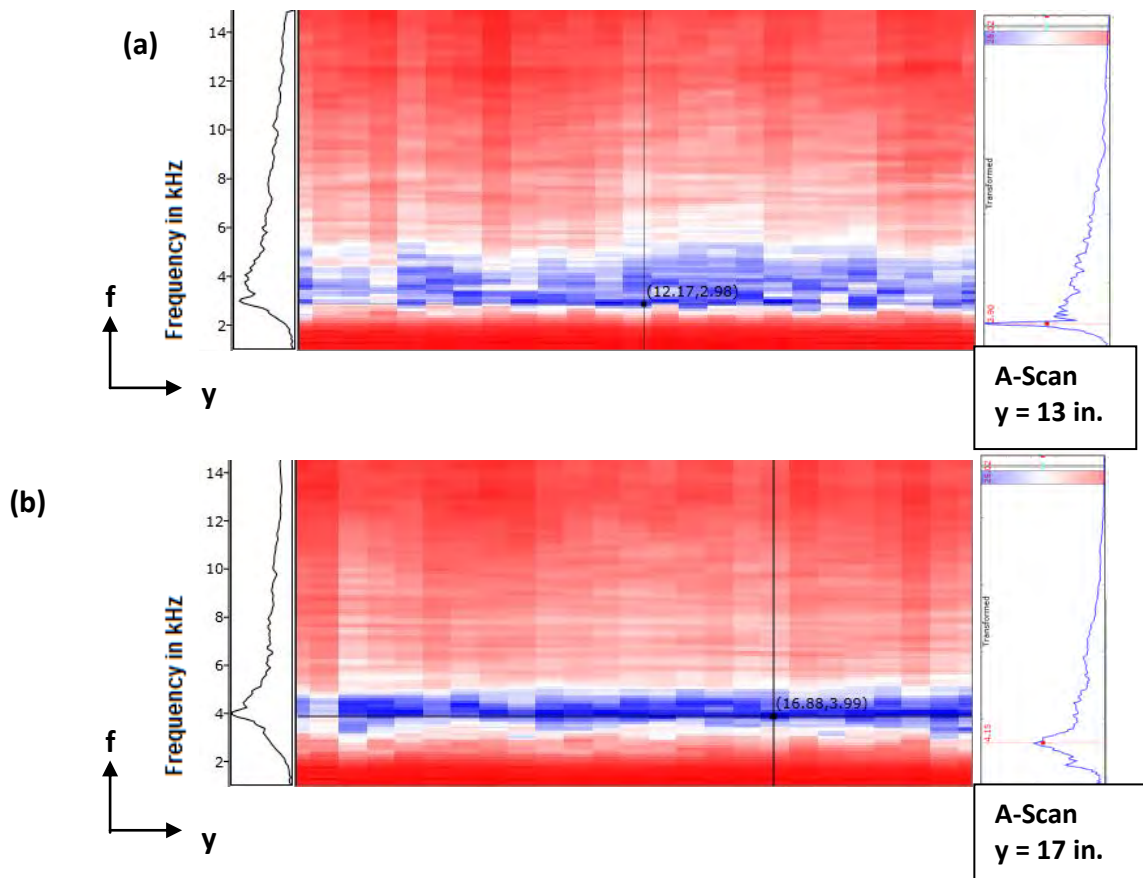
Figure Q-74. CPB2, IE: Spectral B-Scans taken at two different locations: (a) through the anomaly, and (b) through the backwall.

       The D-Scan in Figure Q-75 shows a clear shift in the frequency peak from 3000 Hz up to 3700 Hz, corresponding to the approximate depths of $z = 27$ inches (lining thickness) and $z = 21$ inches (anomaly).
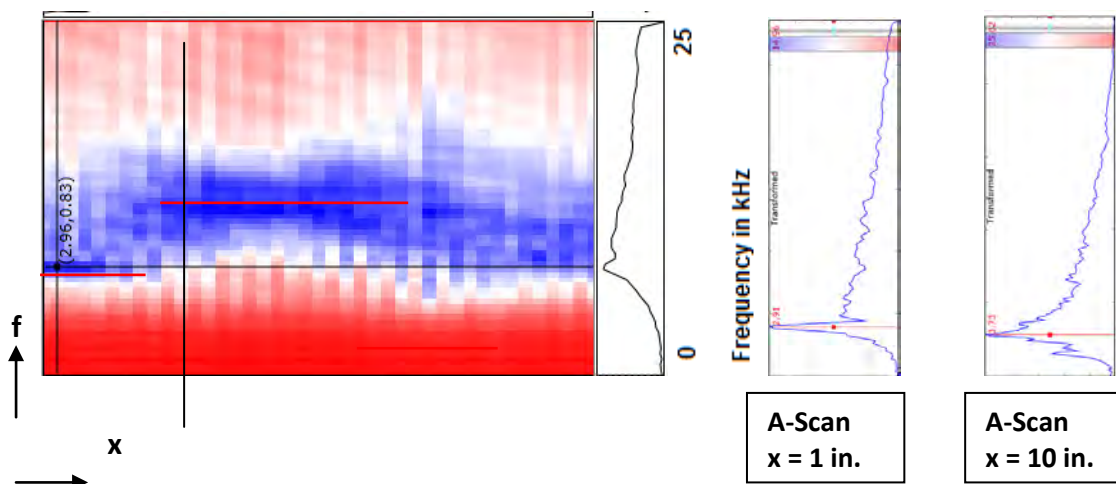
Figure Q-75. CPB2, IE: A Spectral D-Scan (along the x-axis) along with two selected spectral A-Scans representing different depths.

Comparison of Results

Steel reinforcement was best located with GPR. Two reflectors at two different depths were detected by both US and IE. Phase analysis of the US results showed different phase shifts at the reflectors: the phase shift at the shallower reflector (at 20 inches) indicated an impedance lower than concrete, while and the deeper reflector (at 28 inches) had an acoustic impedance higher than concrete. This higher impedance is typical of concrete-metal interfaces and leads to the assumption of it being the echo of the metal skin surrounding the tunnel, although the estimated depth of 28 inches does not match the nominal thickness of 24 inches. This could be a result of errors in the assumed concrete shear wave velocity used in estimating the reflector depths to analyze the US data of CPB2, as the shear wave velocity was assumed to be 2710 m/s (from CPB1).

The use of the GPR and at least one acoustic NDT method was necessary to analyze CPB2. GPR could reliably detect and identify the reinforcement bars. Both acoustic methods detected the echoes from an anomaly and the backwall. The accurate estimation of the reflector depth was possible only when the wave velocities at test locations were known. Neither US or IE could provide the wave velocity of the test medium without having ground-truth information. To measure the velocity profile in-situ, other methods such as high frequency Spectral Analysis of Surface Waves (SASW) or Multispectral Analysis of Surface Waves (MASW) could be employed.

Test Area 3

Description of the Test Area

As seen in the sketch in Figure Q-76, a joint near Sta. 486+67 ran almost in the middle across the test area, hereinafter referred to as CPB3. The area was on the east side of the tunnel, opposite the two other test fields: CPB1 and CPB2. The test area was 48 inches long and 24 inches wide, extending 22 inches and 26 inches to the south and north of the joint. The test field started at an offset of 24 inches from the center line of the tunnel.

The grid spacing for US and IE testing was 1 inch and for GPR testing was 2 inches. The length of the GPR, US, and IE transducers was parallel to the center line of the tunnel during the scanning.
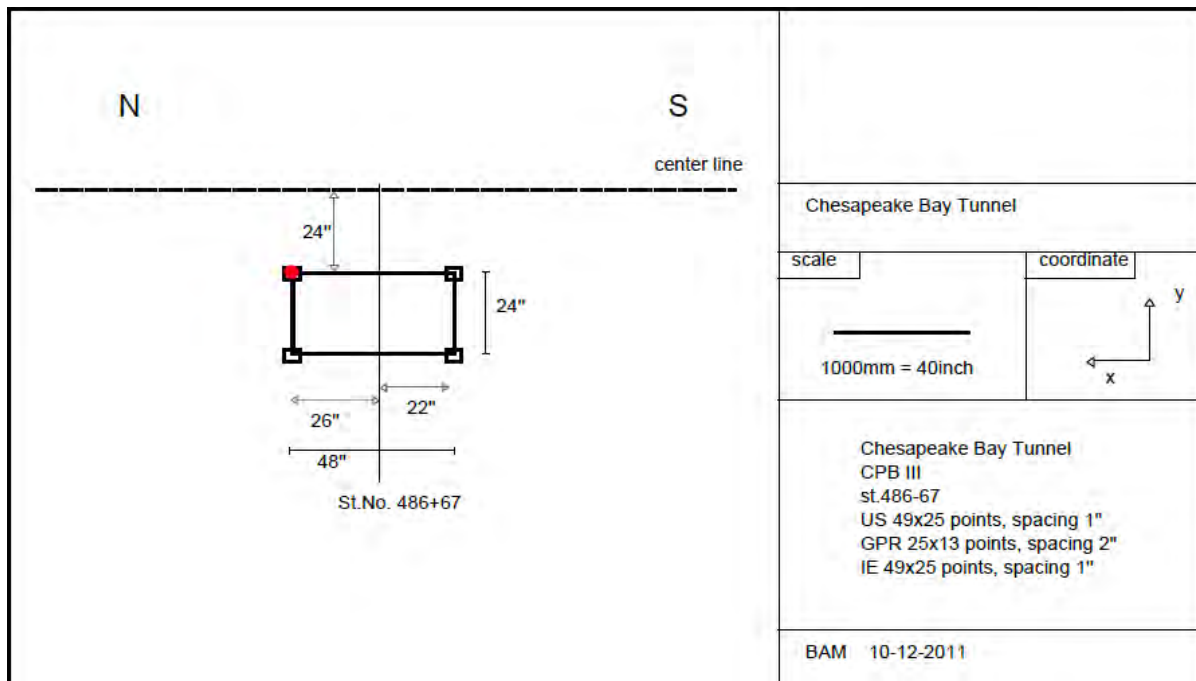
Figure Q-76. Sketch of CPB3, Sta. 486+67 Chesapeake Bay Tunnel

GPR Results

The reinforcement mesh could be easily seen in GPR C-Scans. The transverse rebars in the y-direction were spaced 12 inches from each other and were positioned at x = 2 inches, x = 14 inches, x = 26 inches, and x = 38 inches at a depth of z = 1.6 inches, as shown in Figure Q-77. The longitudinal ones in the x-direction were at y = 0 inches, y = 18 inches, and z = 3 inches deep (see Figure Q-77).
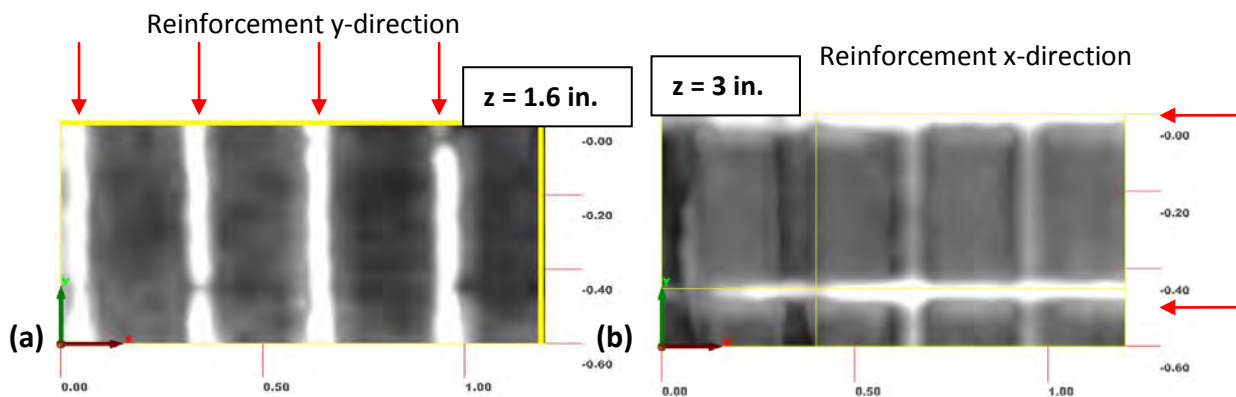
Figure Q-77. CPB2, GPR: C-Scans taken at (a) z = 1.6 inches showing reinforcement bars in y-direction, and (b) z = 3 inches showing the rebars in x-direction.

Q-62

The D-Scans taken at y = 22 inches and y = 18 inches (Figure Q-78) clearly showed that the rebars in the y-direction ran above those in the x-direction.
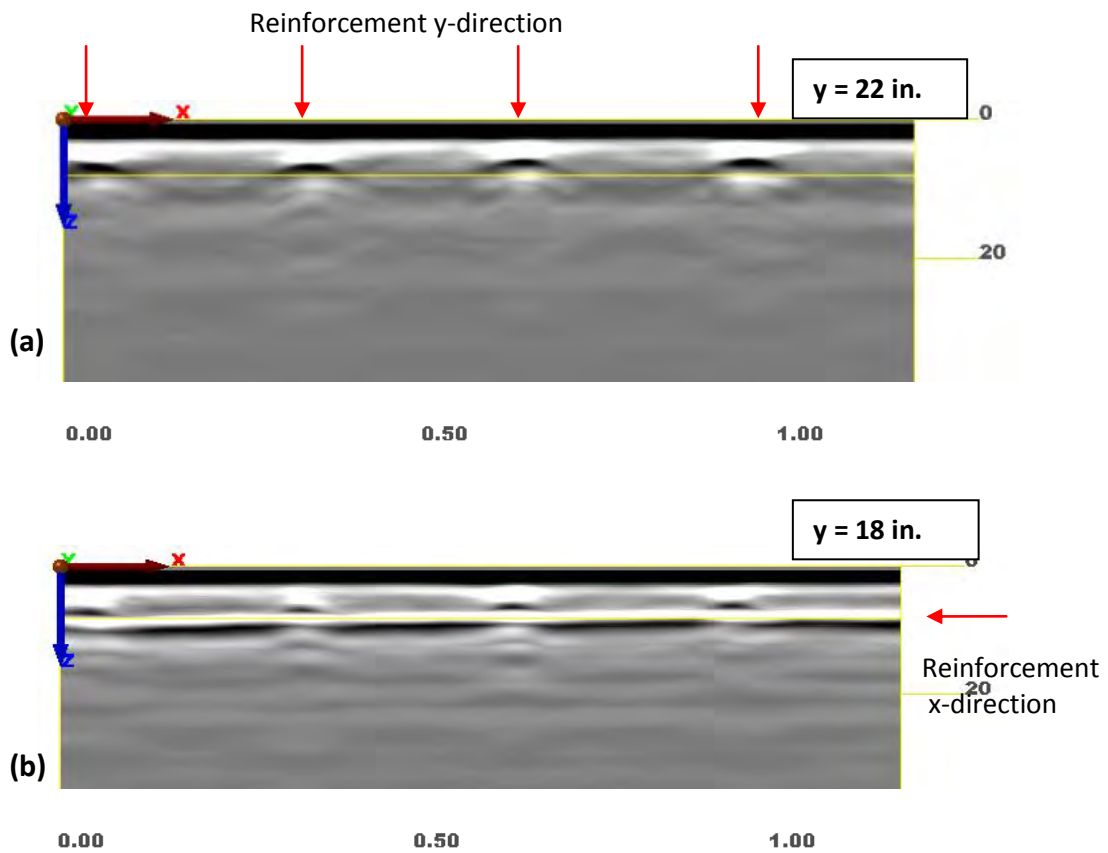
Figure Q-78. CPB3, GPR: D-Scans taken at y = 22 inches (a) and y = 18 inches (b) reveal reinforcement bars in both directions.

The B-Scan taken at x = 26 inches (seen in Figure Q-79) showed the cross section of one of the transverse rebars (along the y-direction). The one taken at x = 16 inches revealed only longitudinal rebars (along the x-direction).
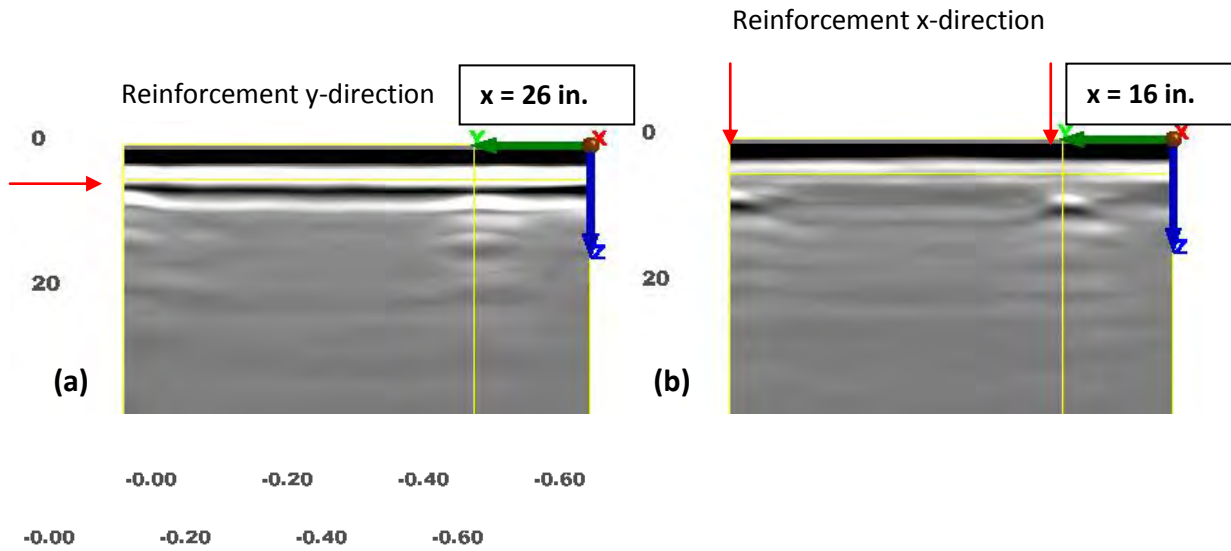
Figure Q-79. CPB3, GPR: B-Scans at x = 26 inches (a) and x = 16 inches (b) reveal the reinforcement rebars in both directions.

Figure Q-80 is a three-dimensional image of the volume as a summary of the reinforcing elements.
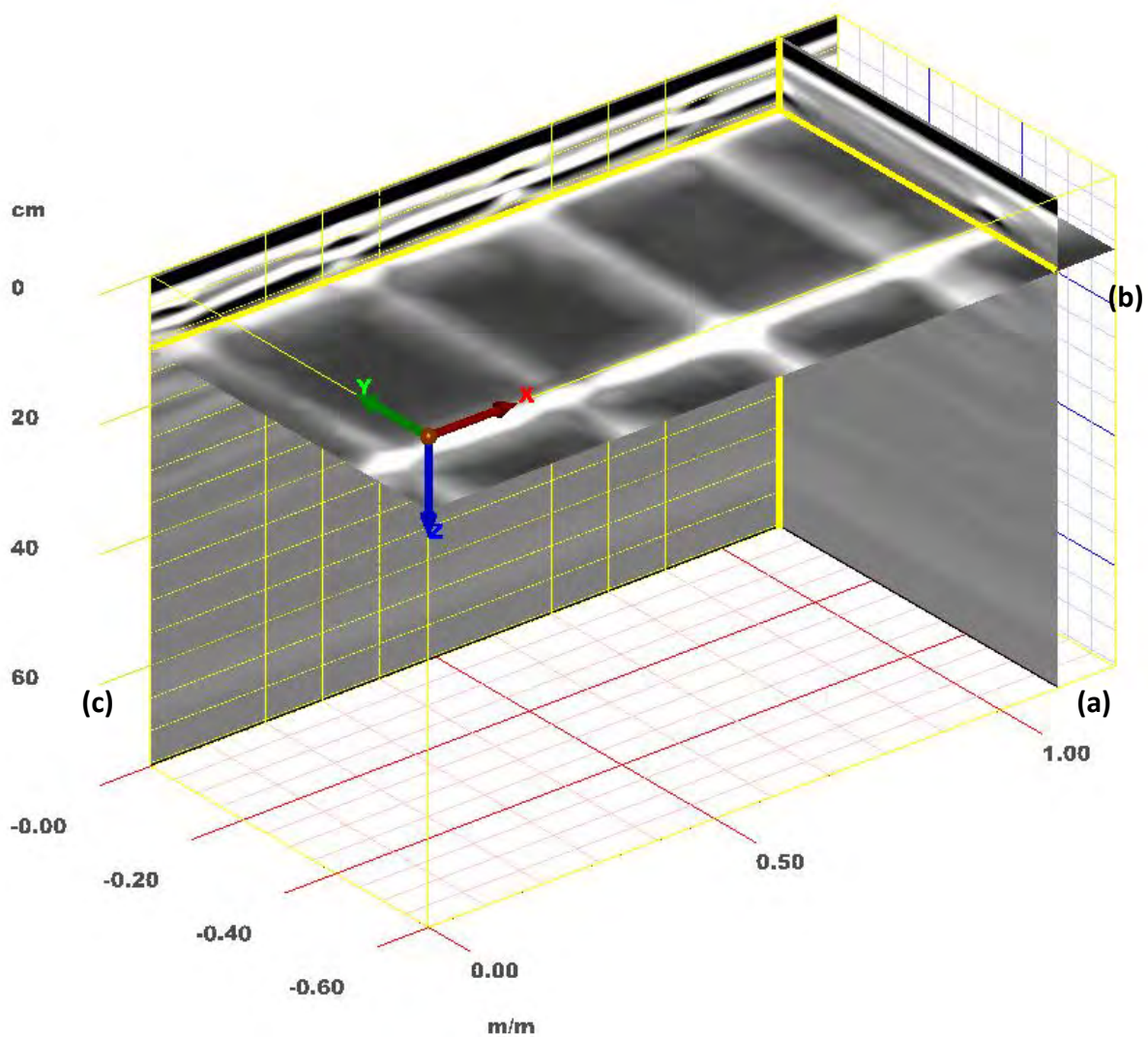
Figure Q-80. CPB3, GPR: three-dimensional image of the volume positioned to reveal reinforcement, with the B-Scan (a) positioned at x = 45 inches, the C-Scan (b) at z = 4.5 inches, 4-in. width, and the D-Scan (c) at y = 0 inches.

Ultrasonic Echo Results

Three of the four transverse reinforcement bars (in the y-direction) could be detected in the US C-Scan at z = 2 inches deep, at x = 2 inches, x = 14 inches, and x = 38 inches (Figure Q-81). There was an anomaly in the middle of the field starting at a depth of z = 2 inches. Examining deeper C-Scans confirmed the existence of an anomalous reflector (Figure Q-82). At a depth of about z = 25 inches (Figure Q-83), the backwall with a positive phase (indicating an impedance higher than the surrounding concrete) could be detected. Between x = 16 inches and x = 38 inches, the backwall echo was missing due to the shadowing effect of the earlier-described anomaly reflector. To analyze the US data of CPB3, the shear wave velocity 2710 m/s of CPB1 was assumed.
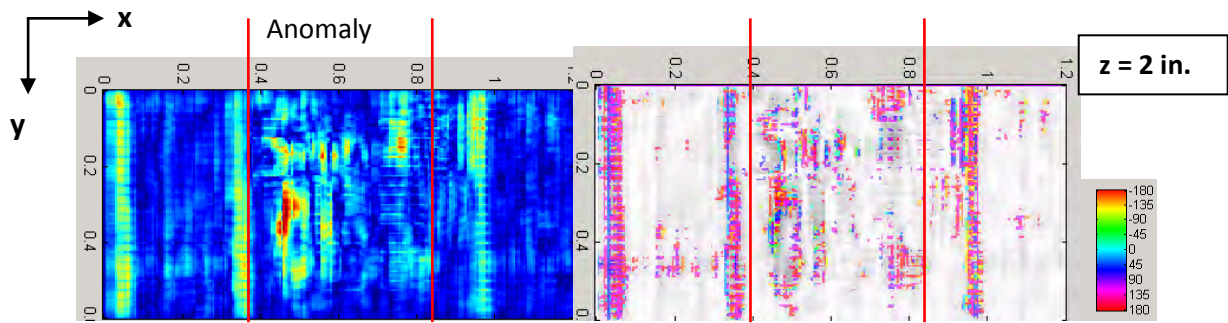
Figure Q-81. CPB3, US: C-Scan at z = 2 inches, showing reinforcement bars in y-direction as well as an anomaly between x = 16 inches and x = 38 inches (marked). Right: The corresponding phase diagram.
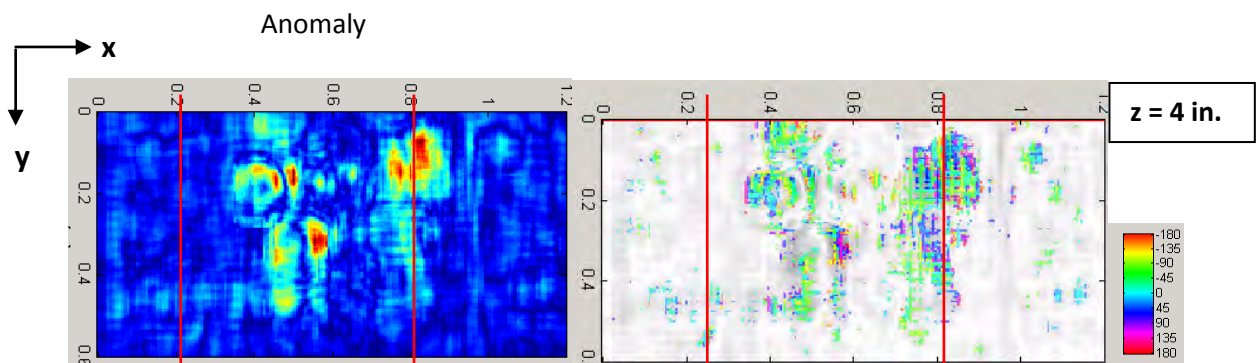
Figure Q-82. CPB3, US: C-Scan obtained at a depth of 4 inches. The reflector is confined between x = 14 inches and x = 36 inches.
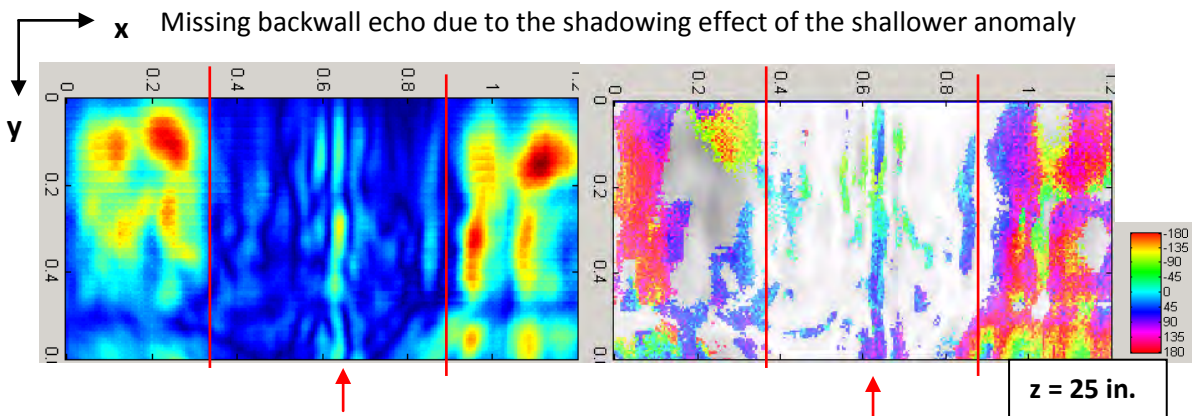
Figure Q-83. CPB3, US: C-Scan at z = 25 inches reveals the backwall echo. Between x = 16 inches and x = 36 inches, the echo is missing due to the presence of a shallower anomaly.

A D-Scan taken at y = 16 inches is shown in Figure Q-84. This view reveals multiple reflections from the anomaly at z = 6 inches, z = 10 inches, z = 15 inches, and z = 20 inches with changing phase. The backwall echo was missing because the anomaly shadows the

deeper reflectors. The multiple reflections with their changing phase gave indications of only one anomaly. However, this could not be verified.

There was also a linear reflector of unknown origin at x = 26 inches at the same depth as the backwall (marked with a question mark in both Figure Q-84 and Q-85). It should be noted that at x = 26 inches, the joint ran across the test field. As the reflector was not seen in the D-Scans produced by the raw data, it is likely that it was an artificial feature produced by the SAFT algorithm.
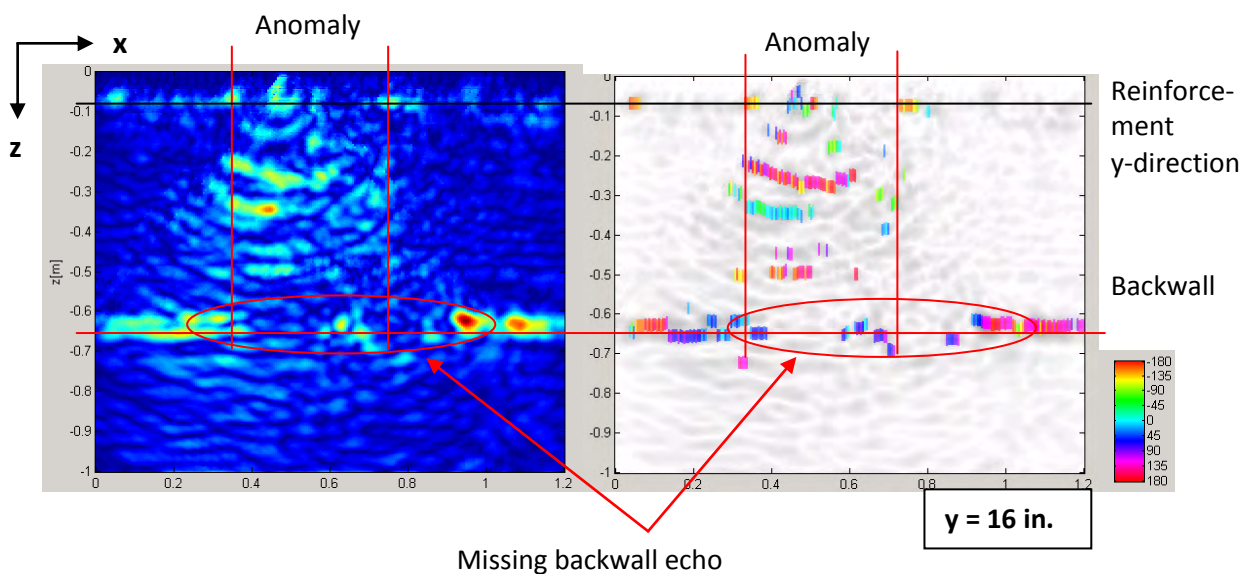
Figure Q-84. CPB3, US: D-Scan at y = 16 inches. The backwall can be seen where the anomaly doesn't shadow it. Reinforcement in y-direction is seen at z = 3 inches. A reflector of unknown origin is positioned at x = 26 inches at the backwall's depth.

The B-Scans did not provide additional information on the anomaly. As seen in Figure Q-85, the backwall of the tunnel lining could be clearly seen at z = 25 inches in the B-Scan taken at x = 1.5 inches. The transverse rebar in the y-direction was also clearly seen. In contrast, the B-Scan at x = 20 inches contained no backwall echoes, as expected from the D-Scan, but no further information about the anomaly itself.
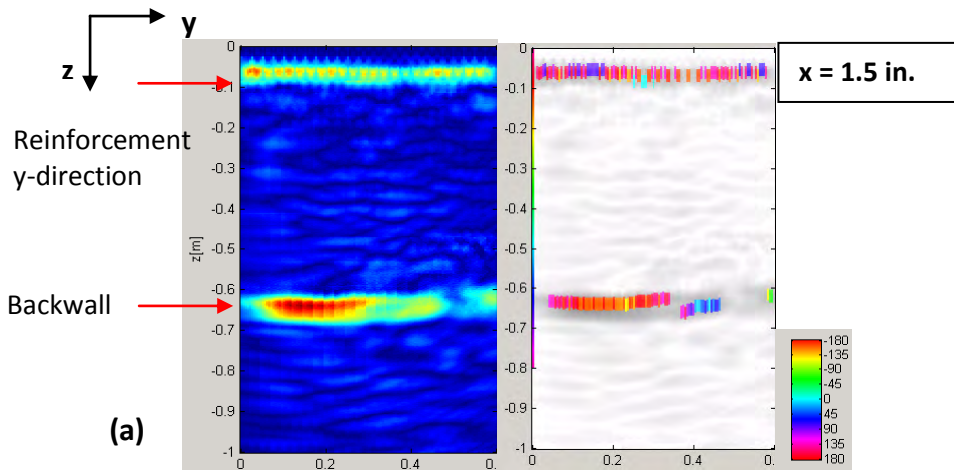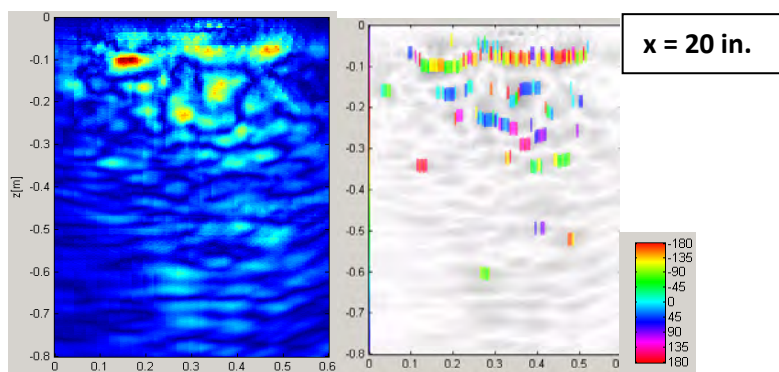
Figure Q-85. CPB3, US: B-Scans showing the backwall at z = 25 inches and reinforcement in y-direction (a) and through the anomaly that caused the backwall echo to disappear (b).

Figure Q-86 shows a three-dimensional image of the volume focusing on the backwall and its shadowed area, as well as the shallow anomaly.
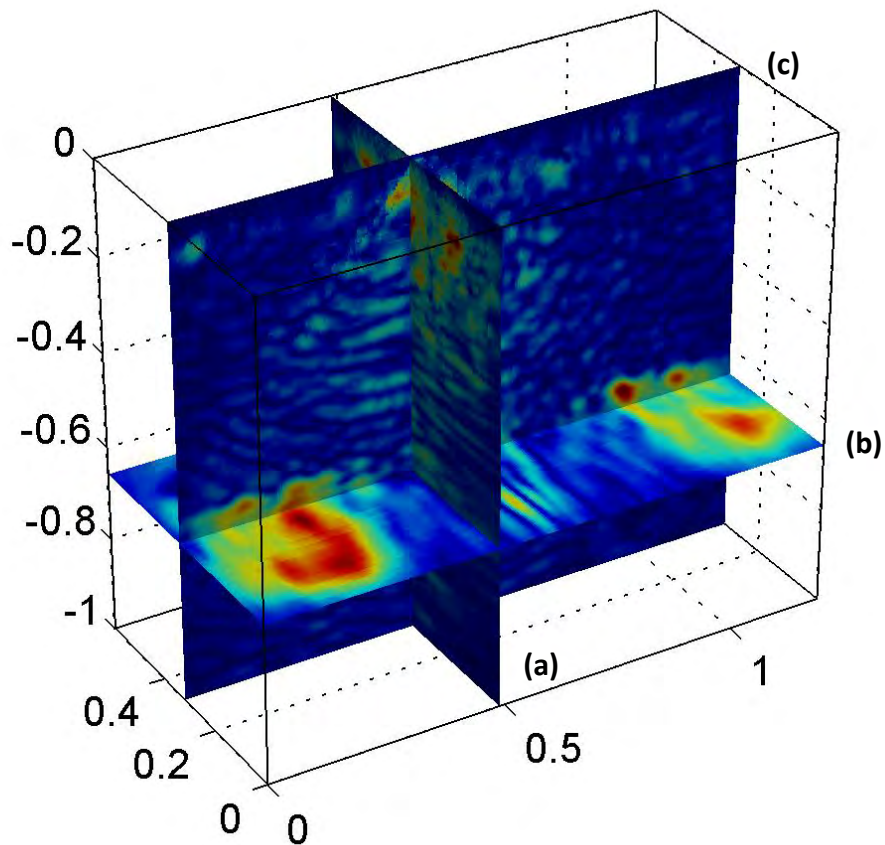
Figure Q-86. CPB3, US: three-dimensional image of the volume positioned to reveal the backwall and its shadowed area due to a shallow anomaly. With the B-Scan (a) positioned at x = 21 inches, the C-Scan (b) at z = 25 inches, and the D-Scan (c) at y = 12 inches.

Impact Echo Results

As seen in Figure Q-87, IE showed tunnel lining thickness resonance frequency except between x = 13 inches and x = 30 inches, where the echo was disturbed. The typical spectral and temporal A-Scans from the sound (x = 5.5 inches) and disturbed regions (x = 20 inches) are compared in the figure. While the sound spectrum contained one clearly dominant frequency, the disturbed spectrum contained multiple peaks, mostly of frequencies lower than that of the thickness resonance frequency. The thickness resonance frequency appeared at about 3200 Hz, corresponding to a depth of z = 25 inches.
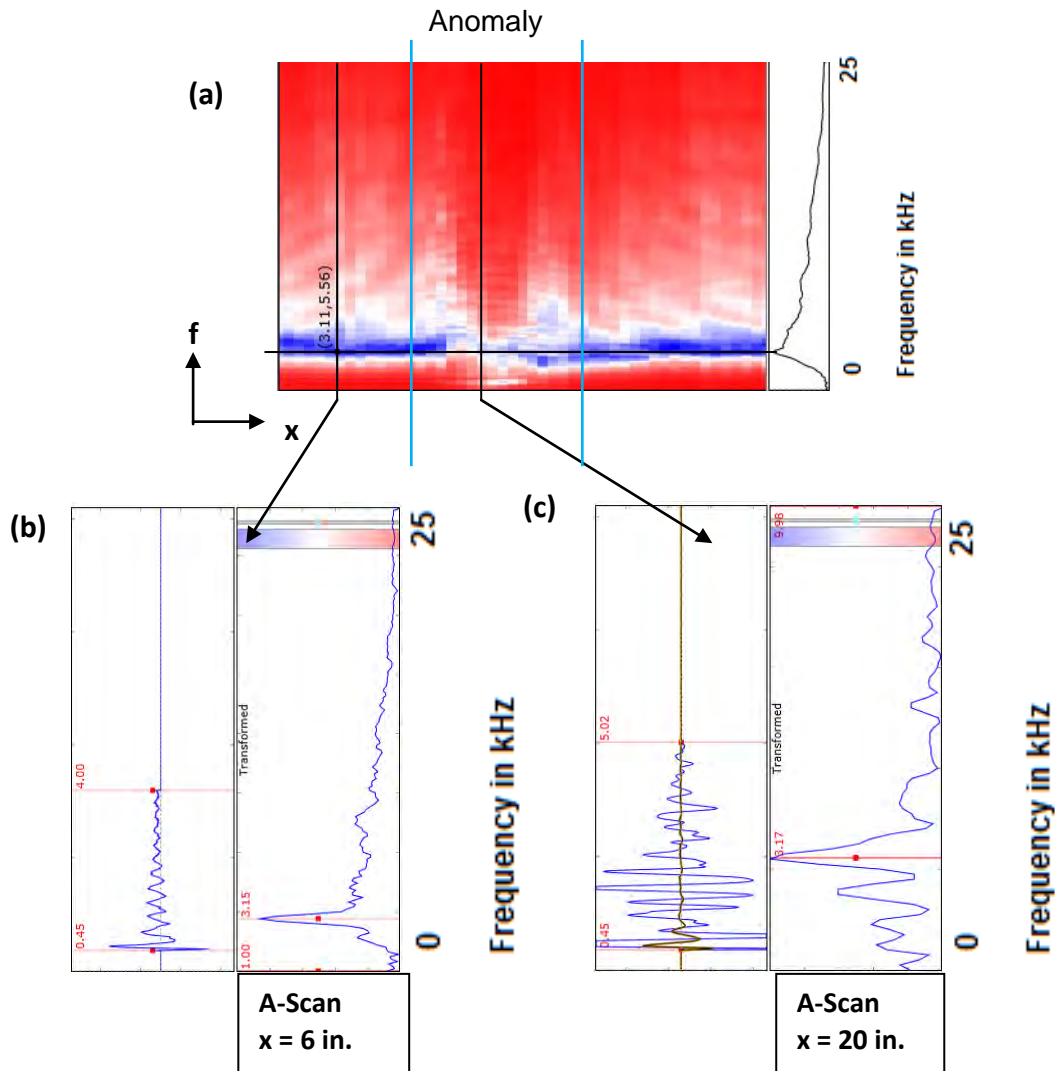
Figure Q-87. CPB3, IE: D-Scan of the volume (a) and selected A-Scans representing the echo from sound areas (b) and from areas with an anomaly (c).

Comparison of Results

GPR could provide a clear picture of the reinforcement bars in both directions, while US could only reveal the ones in the y-direction, except the one at x = 26 inches. This was due to the polarization effects due to the orientation of the US transducer. The US could, however, reveal the presence of a localized anomaly. That anomaly could not be detected using GPR. The anomaly appeared between x = 14 inches and x = 30 inches. US results indicated multiple reflections with changing phase shifts, suggesting a shallow delamination. The IE frequency spectra were disturbed at the location of the anomaly, containing frequency peaks of lower frequencies than that of the backwall echo, also indicating the presence of shallow delamination. However, the nature of the anomaly could not be confirmed. Both acoustic methods detected the backwall at approximately z = 25 inches.

Shallow reinforcements were best seen using GPR. Defects indicating a change of impedance from concrete to a material softer than the surrounding tunnel lining could be detected by the acoustic methods: US and IE. There were indications of a delamination-like anomaly. It was difficult to estimate the depth of the anomaly, as US analysis showed

multiple reflections of the defect within a cone broadening with depth. IE spectra contained peaks of lower frequencies, indicating a shallow reflector.

Test Field 4

Description of the Test Area

The last set of measurements at Chesapeake Bay Tunnel was taken inside the tunnel itself. The testing took place overnight, as traffic control measures were needed. Measurements were taken on tile-covered tunnel walls. The tiles were 2 inches x 2 inches.

The test area CPB4 was located between Sta. 486+28 and Sta. 487, close to the north end of the tunnel, where an anomaly was previously detected in SPACETEC thermal images. As seen in Figure Q-88, the scanner's feet were mounted on the wall near the joint. The test field was larger here, covering a 48 inch x 36 inch area. The spacing for US and IE was chosen as 1 inch, and that for GPR was 2 inches. During the testing, the GPR, US, and IE transducers were oriented such that their length was parallel to the center line of the tunnel. The measurement started in the lower right corner of the test field. The scanner moved upwards and then left (south). Figure Q-88 shows snapshots of the test area and measurement system.

Figure Q-88. CPB4 near Sta. 486+28.

GPR Results

Figure Q-89, a three-dimensional image, summarizes the reinforcing elements within the volume.
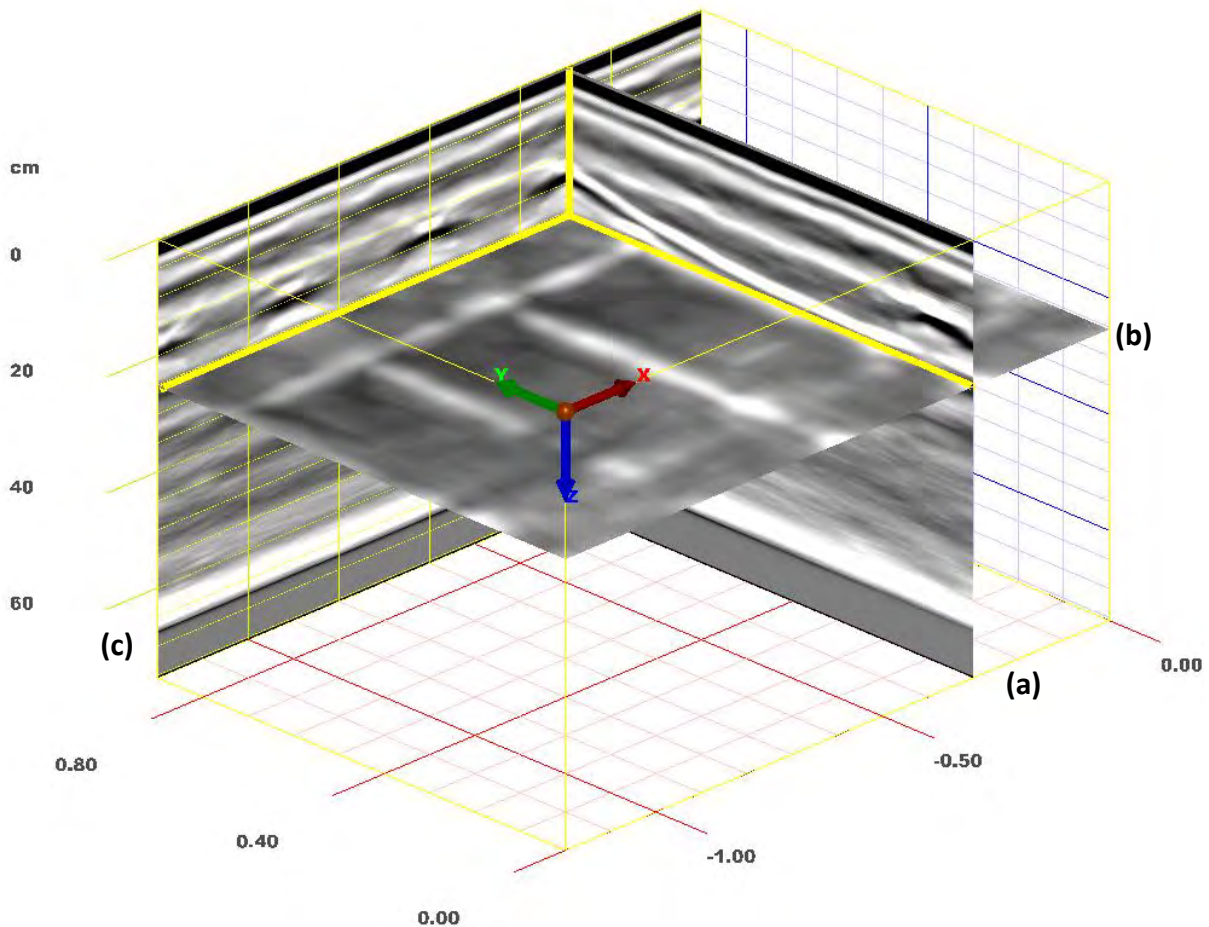
Figure Q-89. CPB4, GPR: three-dimensional image of the volume positioned to reveal the reinforcement, with the B-Scan (a) positioned at x = 11 inches, the C-Scan (b) at z = 10 inches, 4-in. width, and the D-Scan (c) at y = 4 inches.

Steel bars were found in both the x- and y-directions in GPR C-Scans. The bars in the y-direction appeared to be spaced 12 inches apart, at x = 0 inches, x = 12 inches, x = 24 inches, x = 36 inches, and x = 48 inches, running from 7 inches to 8 inches deep. The bars in the x-direction were at y = 4 inches, y = 12 inches, and y = 30 inches, at z = 6 inches, z = 10 inches, and z = 8 inches, respectively. Figure Q-90 includes several C-Scans at various depths.
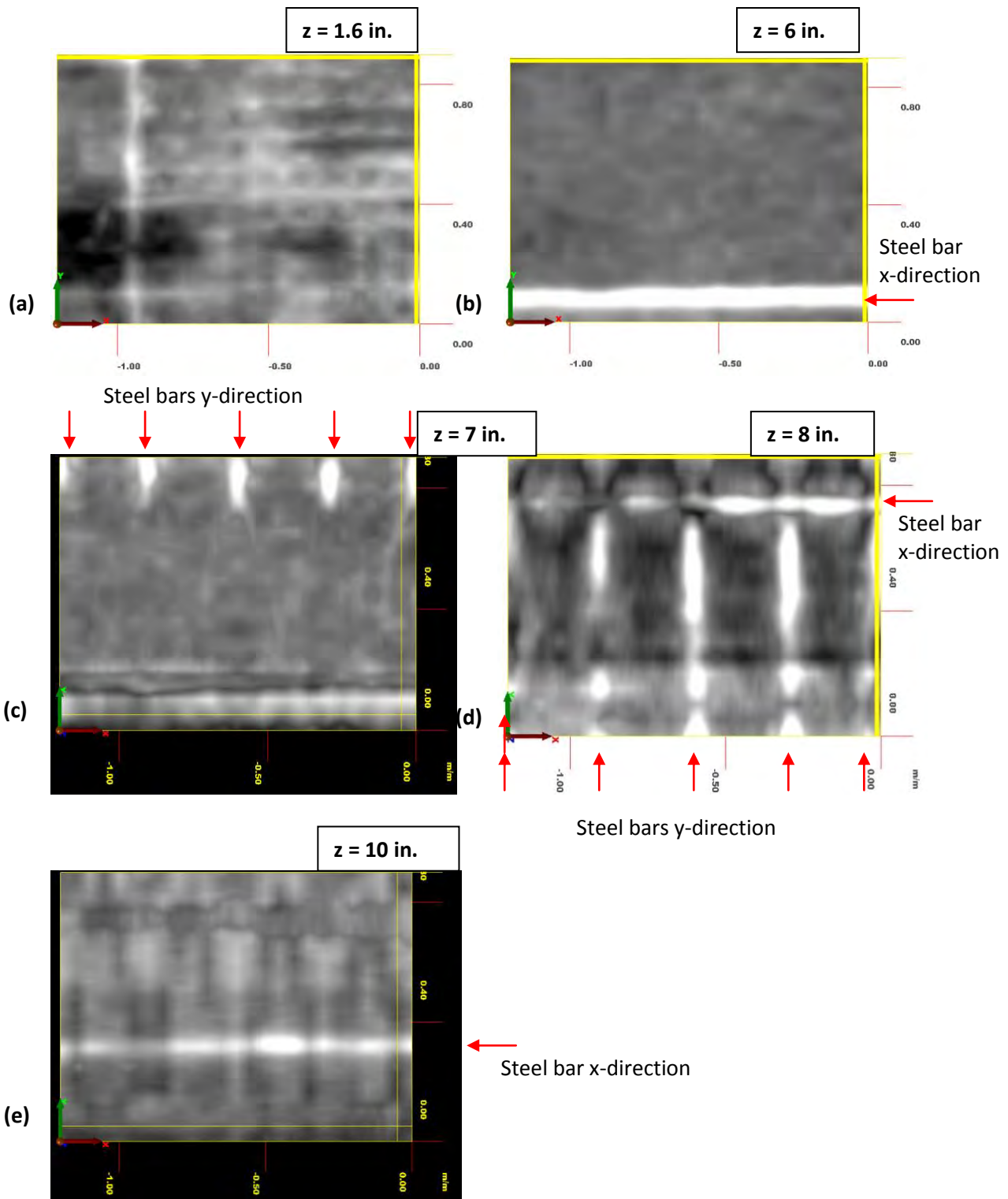
Figure Q-90. CPB4, GPR: C-Scans at different depths: (a) z = 1.6 inches, (b) z = 6 inches, (c) z = 7 inches, (d) z = 8 inches, and (e) z = 10 inches.

Two D-Scans taken at y = 2.5 inches and 12 inches are shown in Figure Q-91.
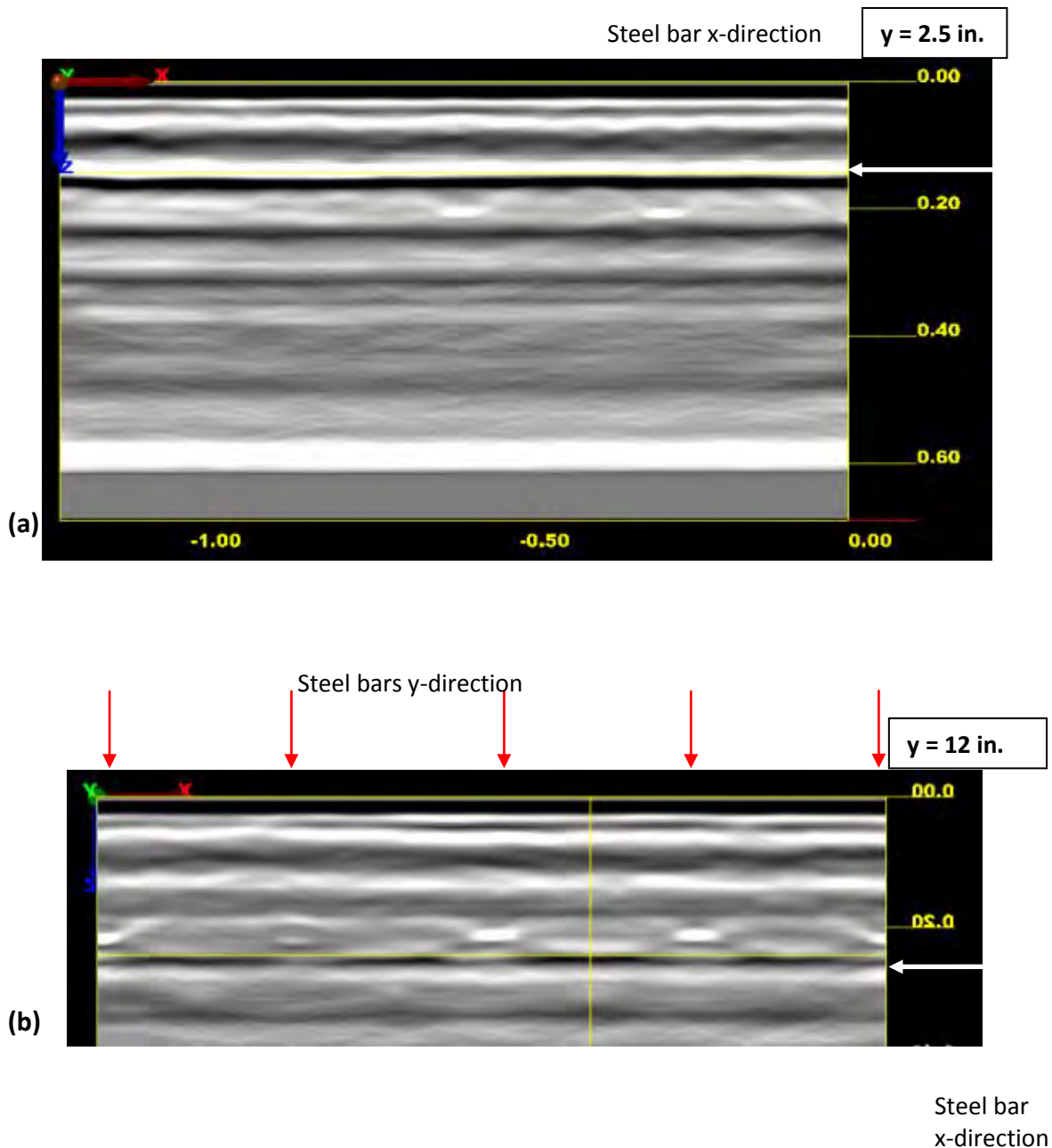
Figure Q-91. CPB4, GPR: D-Scans of steel bars along (a) x- and (b) y-directions. The rebars in x-direction run above and under the bars in y-direction.

Figure Q-92(a) is a B-Scan showing the rebars in the x-direction cut at x = 18 inches. Three rebars at different depths can be distinguished. Figure Q-92(b) is a B-Scan taken at x = 12 inches showing one bar in the y-direction. The rebar does not run parallel to the surface but is curved, which explains why the rebars are seen at different depths in the C-Scans. The rebar curves from z = 8 inches at x = 0 inches up to z = 6 inches at x = 36 inches. The rebars in the x-direction run above and under those in the y-direction.
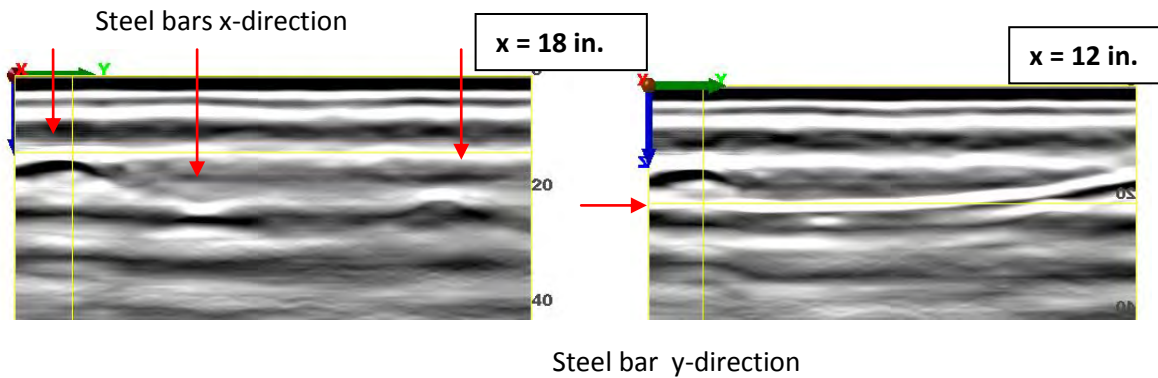
Figure Q-92. CPB4, GPR: B-Scans taken at (a) x = 18 inches and (b) x = 12 inches.

Ultrasonic Echo Results

The automatic scanning using US could provide no useful information about the condition of the lining at CPB4. It would have been possible to gain information about the bonding of the tiles by analyzing the individual A-Scans. However, the US transducer was too large (4 inches x 3 inches) compared to the size of the tiles (2 inches x 2 inches). The grid location and spacing had to be adjusted such that meaningful data (one A-Scan per tile) could be obtained. However, the measurements were interrupted due to an unforeseen weather condition, and no further measurements could be obtained.

Impact Echo Results

Because of intensifying foggy weather conditions, the testing during IE data collection was interrupted because the tunnel had to be fully opened to traffic. Therefore, only four scan lines were taken.

Our earlier manual measurements indicated that IE is able to evaluate the bonding between tiles and walls when A-Scans on individual tiles are analyzed. In the case of automated scanning, the analyzed signal is the average of 20 signals recorded close to the source. The dimension of the receiver is 4 inches x 3 inches, which covers the area of two tiles. Therefore, evaluating the condition of the bonding of one tile based on automatically collected A-Scans is not exact. The grid location and spacing had to be adjusted such that meaningful data (one A-Scan per tile) could be obtained. However, due to the interruption of the measurements, this was not possible.

Figure Q-93 illustrates one of the D-Scans along with two representative spectral and temporal A-Scans, showing signals/spectra from apparently debonded and bonded areas.
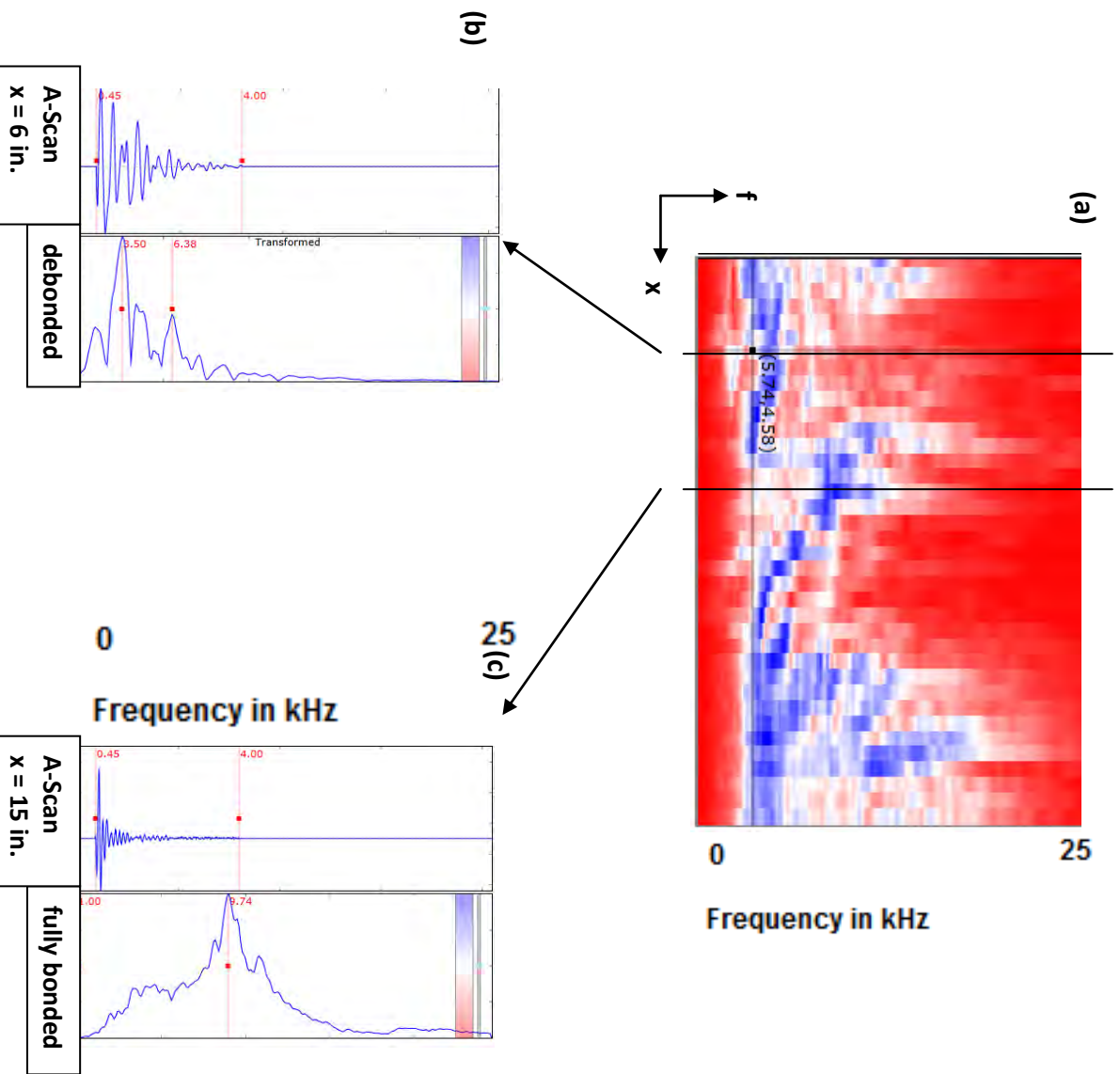
Figure Q-93. CPB4, IE: (a) D-Scan; (b) typical A-Scans for an area with seemingly debonded tiles; and (c) A-Scans for an area with seemingly bonded tiles.

Comparison of Results

GPR signals were not disturbed by the presence of the tiles and could image the reinforcement mesh behind the lining. The IE signals carried useful information about the bonding condition at tile-concrete interface and occasionally about the lining itself. The grid location and spacing had to be adjusted such that meaningful US data (one A-Scan per tile) could be obtained. However, the measurements had to be suddenly stopped.

REFERENCES

1. **DOT.** Colorado Department of Transportation. *http://www.coloradodot.info/travel/eisenhower-tunnel.* [Online] July 2011.

2. **Salek, Matthew E.** http://www.mesalek.com/colo/glenwood. *http://www.mesalek.com/colo/glenwood.* [Online] October 2002.

3. **Schickert, M., Krause, M. and Müller, W.** Ultrasonic Imaging of Concrete Elements Using Reconstruction by Synthetic Aperture Focusing technique. *ASCE Journal of Materials in Civil Engineering.* No. 3, 2003, Vol. 15.

4. **Shokouhi, Parisa.** Comprehensive evaluation of concrete bridge decks using impact echo. *PhD thesis.* New Brunswick, New Jersey: s.n., 2005.

5. **Zoega, Andreas, Feldmann, Rüdiger and Stoppel, Markus.** Praktische Anwendungen Zerstörungsfreier Prüfungen und Zukunftsaufgaben 23-24. February 2012. *Fachtagung Bauwerksdiagnose.* Berlin: BAM Berlin, 2012.

APPENDIX R
ESTIMATED DEPTHS FROM NONDESTRUCTIVE TESTING

Eisenhower Tunnel, CO (10/3/2011-10/4/2011)					
Segment 8 +17 ft, Eastbound					
Measured Characteristic	*1st Layer Reinforcement*	*Suspected Backwall*	*Suspected Delamination*	*Suspected Crack*	*Other Unknown*
UST Measured Depth	*4.2" (to center)*	*N/A*	*N/A*	*N/A*	*16.2"*
Segment 8 +22.5 ft, Eastbound					
Measured Characteristic	*1st Layer Reinforcement*	*Suspected Backwall*	*Suspected Delamination*	*Suspected Crack*	*Other Unknown*
UST Measured Depth	*3.7"-5.1" (to center)*	*N/A*	*N/A*	*N/A*	*17.2"*
Segment 10 +6.5 ft, Eastbound					
Measured Characteristic	*1st Layer Reinforcement*	*Suspected Backwall*	*Suspected Delamination*	*Suspected Crack*	*Other Unknown*
UST Measured Depth	*4.1" (to center)*	*N/A*	*N/A*	*N/A*	*16.1"*
Segment 11 + 3.4 ft, Eastbound					
Measured Characteristic	*1st Layer Reinforcement*	*Suspected Backwall*	*Suspected Delamination*	*Suspected Crack*	*Other Unknown*
BAM's GPR Measured Depth	*2'' - 3''*	*N/A*	*N/A*	*N/A*	*16''*
BAM's US Measured Depth	*2'' - 3''*	*N/A*	*N/A*	*N/A*	*16''*
BAM's IE Measured Depth	*N/A*	*N/A*	*N/A*	*N/A*	*N/A*

Hanging Lake Tunnel, CO (10/5/2011-10/6/2011)					
Segment 58 + unknown distance, Eastbound					
Measured Characteristic	*1st Layer Reinforcement*	*Suspected Backwall*	*Suspected Delamination*	*Suspected Crack*	*Other Unknown*
BAM's GPR Measured Depth	*4'' – 6''* *3''*	*N/A*	*N/A*	*N/A*	*N/A*
BAM's US Measured Depth	*6''*	*N/A*	*N/A*	*N/A*	*N/A*
BAM's IE Measured Depth	*N/A*	*N/A*	*N/A*	*N/A*	*N/A*
Segment 57 +4.2 ft, Eastbound					
Measured Characteristic	*1st Layer Reinforcement*	*Suspected Backwall*	*Suspected Delamination*	*Suspected Crack*	*Other Unknown*
BAM's GPR Measured Depth	*5'' - 8''*	*N/A*	*N/A*	*< 3''*	*N/A*
BAM's US Measured Depth	*6''*	*N/A*	*N/A*	*< 6''*	*N/A*
BAM's IE Measured Depth	*N/A*	*N/A*	*N/A*	*N/A*	*22''*
Segment 57 +3.4 ft, Eastbound					
Measured Characteristic	*1st Layer Reinforcement*	*Suspected Backwall*	*Suspected Delamination*	*Suspected Crack*	*Other Unknown*
UST Measured Depth	*4.6"-6.2" (to center)*	*27.6"*	*12.3"*	*Cracks extending to depth of delamination*	*N/A*
Segment 57 -2.2 ft, Eastbound					
Measured Characteristic	*1st Layer Reinforcement*	*Suspected Backwall*	*Suspected Delamination*	*Suspected Crack*	*Other Unknown*
BAM's GPR Measured Depth	*1'' – 6''* *3''*	*N/A*	*N/A*	*N/A*	*12'' – 16''*
BAM's US Measured Depth	*4'' – 6''*	*N/A*	*N/A*	*N/A*	*12'' – 16''*
BAM's IE Measured Depth	*N/A*	*22'' – 24''*	*N/A*	*N/A*	*12''*
Segment 54/55 Joint, Eastbound					
Measured Characteristic	*1st Layer Reinforcement*	*Suspected Backwall*	*Suspected Delamination*	*Suspected Crack*	*Other Unknown*
UST Measured Depth	*3.6" (to center)*	*N/A*	*N/A*	*N/A*	*Possible voids 9" deep*
Segment 49 -11 ft, Eastbound					
Measured Characteristic	*1st Layer Reinforcement*	*Suspected Backwall*	*Suspected Delamination*	*Suspected Crack*	*Other Unknown*
UST Measured Depth	*4.3-5.1" (to center)*	*29.6"-32.4"*	*N/A*	*N/A*	*N/A*

Segment 49 +6 ft, Eastbound					
Measured Characteristic	*1st Layer Reinforcement*	*Suspected Backwall*	*Suspected Delamination*	*Suspected Crack*	*Other Unknown*
UST Measured Depth	*3.7" (to center)*	*24.5"-29.6"*	*N/A*	*N/A*	*N/A*
Segment 55 -16 ft, Eastbound					
Measured Characteristic	*1st Layer Reinforcement*	*Suspected Backwall*	*Suspected Delamination*	*Suspected Crack*	*Other Unknown*
UST Measured Depth	*2.9"-5.1" (to center)*	*N/A*	*8"-20"*	*Cracks extending to depth of delamination*	*N/A*

Chesapeake Bay Tunnel, VA (10/11/2011-10/13/2011)					
Sta. 471 +80 ft, Southbound					
Measured Characteristic	*1st Layer Reinforcement*	*Suspected Backwall*	*Suspected Delamination*	*Suspected Crack*	*Other Unknown*
UST Measured Depth	*2.4"-4.4" (to center)*	*24.7"*	*N/A*	*N/A*	*N/A*
Sta. 473 +56 ft, Southbound					
Measured Characteristic	*1st Layer Reinforcement*	*Suspected Backwall*	*Suspected Delamination*	*Suspected Crack*	*Other Unknown*
UST Measured Depth	*2.3" (to center)*	*24.4"*	*N/A*	*N/A*	*N/A*
Sta. 474 -27, Southbound					
Measured Characteristic	*1st Layer Reinforcement*	*Suspected Backwall*	*Suspected Delamination*	*Suspected Crack*	*Other Unknown*
BAM's GPR Measured Depth	*1.5'' – 3''*	*N/A*	*N/A*	*N/A*	*N/A*
BAM's US Measured Depth	*2''*	*24''*	*N/A*	*N/A*	*15''*
BAM's IE Measured Depth	*N/A*	*22'' – 24''*	*N/A*	*N/A*	*indirectly*
Sta. 474 +27 ft, Southbound					
Measured Characteristic	*1st Layer Reinforcement*	*Suspected Backwall*	*Suspected Delamination*	*Suspected Crack*	*Other Unknown*
UST Measured Depth	*2.0"-2.6"" (to center)*	*24.1"*	*N/A*	*9.0"*	*Possible voids from surface to 9" deep in isolated area*
Sta. 481 +76, Southbound					
Measured Characteristic	*1st Layer Reinforcement*	*Suspected Backwall*	*Suspected Delamination*	*Suspected Crack*	*Other Unknown*
BAM's GPR Measured Depth	*2.5'' – 4''*	*N/A*	*N/A*	*N/A*	*N/A*
BAM's US Measured Depth	*2'' – 4''*	*28''*	*N/A*	*N/A*	*20''*
BAM's IE Measured Depth	*N/A*	*27''*	*N/A*	*N/A*	*20''*

Sta. 486 +67 ft, Northbound					
Measured Characteristic	*1st Layer Reinforcement*	*Suspected Backwall*	*Suspected Delamination*	*Suspected Crack*	*Other Unknown*
UST Measured Depth	*2.2" (to center)*	*24.1"-26.0"*	*19.2" and 2.2" in two locations*	*Cracks extending to depth of deepest delamination*	*N/A*
BAM's GPR Measured Depth	*1.6'' – 3''*	*N/A*	*N/A*	*N/A*	*N/A*
BAM's US Measured Depth	*2''*	*25''*	*N/A*	*N/A*	*2''*
BAM's IE Measured Depth	*N/A*	*25''*	*N/A*	*N/A*	*indirectly*
Sta. 486 +67 ft, Southbound					
Measured Characteristic	*1st Layer Reinforcement*	*Suspected Backwall*	*Suspected Delamination*	*Suspected Crack*	*Other Unknown*
UST Measured Depth	*2.0"-3.0" (to center)*	*24.3"-26.0"*	*N/A*	*8.6"*	*N/A*
Sta. 491 +25 ft, (Area extended from Southbound to Northbound)					
Measured Characteristic	*1st Layer Reinforcement*	*Suspected Backwall*	*Suspected Delamination*	*Suspected Crack*	*Other Unknown*
UST Measured Depth	*2.7"-3.2" (to center)*	*22.7"-25.9"*	*17.7"*	*9.8"*	*N/A*
Sta. 488 (Southbound Tile Lining)					
Measured Characteristic	*1st Layer Reinforcement*	*Suspected Backwall*	*Suspected Delamination*	*Suspected Crack*	*Other Unknown*
UST Measured Depth	*4.3"-7.7" (to center)*	*25.0"-30.0"*	*15.7"*	*N/A*	*N/A*
Sta. 486 -9 ft (Southbound Tile Lining)					
Measured Characteristic	*1st Layer Reinforcement*	*Suspected Backwall*	*Suspected Delamination*	*Suspected Crack*	*Other Unknown*
UST Measured Depth	*4.8"-9.4" (to center)*	*28.1"-31.0"*	*N/A*	*8.6"*	*N/A*
Between Sta. 486 + 28 and Sta. 487 (Southbound Tile Lining)					
Measured Characteristic	*1st Layer Reinforcement*	*Suspected Backwall*	*Suspected Delamination*	*Suspected Crack*	*Other Unknown*
BAM's GPR Measured Depth	*6'' – 10''*	*N/A*	*N/A*	*N/A*	*N/A*
BAM's US Measured Depth	*N/A*	*N/A*	*N/A*	*N/A*	*N/A*
BAM's IE Measured Depth	*N/A*	*N/A*	*N/A*	*N/A*	*Bonded and debonded tiles*

		Sta. 481 -76 ft, Southbound			
Measured Characteristic	*1st Layer Reinforcement*	*Suspected Backwall*	*Suspected Delamination*	*Suspected Crack*	*Other Unknown*
UST Measured Depth	*2.0-3.6" (to center)*	*26.6"-28.4*	*20.2"*	*N/A*	*N/A*

APPENDIX S
CONCRETE PERMEABILITY LABORATORY STUDY

INTRODUCTION

Ground penetrating radar (GPR) has been widely used for subsurface characterization by geologists, archeologists, and engineers. For civil engineering applications in pavements, GPR has been used to determine pavement/soil layer thickness and moisture content. The use of GPR in cementitious materials such as concrete, however, is still rather limited. Concrete is a widely used construction material made by combining cementitious materials with water, which forms a nanoporous network and binds aggregates together. The porous cementitious matrix contains hydration products, and water that exist in the bulk state in the macropores or, physically and chemically bound to the nanopores. The pore structure of cementitious materials controls mechanical properties, from compressive strength to other time-dependent mechanical behaviors such as creep.

Concrete structures suffer long-term deterioration from various environmental exposures. For example, in a cracked concrete tunnel lining surrounded by moist rocks, moisture will infiltrate through the crack and cause problems with the tunnel tiles. Permeability of concrete directly influences the durability of the concrete to withstand chemical attacks and is thus also of interest to engineers. The ability to determine the condition of the concrete and whether any anomalies exist in the structure without having to perform destructive testing will allow engineers to conduct inspections at a much lower cost. Normally, engineers have to destructively obtain concrete cores from the field to determine properties such as moisture content and permeability.

The characteristics of electromagnetic (EM) wave propagation in materials are dependent on many factors, one of which is the dielectric properties of the material. The interaction of EM waves in composite materials, such as cementitious materials, is inherently complex, due in part to the difference in electrical properties of constituents within a composite. The dielectric properties of materials directly affect the propagation of EM waves. To interpret output from GPR, a thorough understanding of the dielectric properties of the material is required. The solid constituents of porous materials usually have low relative permittivity. However, the porous matrix itself may contain various amounts of water, which greatly influences the dielectric properties in the bulk scale due to water's high relative permittivity.

The microstructure of cementitious materials is complicated, with length scales spanning many orders of magnitudes. This complexity, however, may be exploited to allow engineers to indirectly determine moisture content and pore size distribution from dielectric response, from which transport properties of cementitious materials may be inferred. Such understanding is required to develop moisture content and permeability correlation to dielectric response, and subsequently, development of non-destructive testing (NDT) using GPR for various types of concrete structures. In this research, the researchers sought to understand fundamental electrical properties of composite cementitious materials for EM waves at microwave frequencies through experimentation and modeling. The dependence of dielectric response of cementitious materials to pore structure and moisture content will be examined in this appendix.

BACKGROUND AND LITERATURE REVIEW

Materials that conduct charges poorly in the presence of an electric field are known as dielectrics. The charges do not move freely under an applied electric field. Instead, the charges polarize; they align with the field polarity, such as is found in the case of a parallel plate capacitor. The ability for the material to polarize is defined as the relative permittivity of the material. Relative permittivity is often referred to as dielectric constant in the literature. The term *complex permittivity* will be used in the rest of this appendix, which quantifies the *relative permittivity* ε_r as a function of the *dielectric response* of the different materials within the cementitious composite that may or may not contain an imaginary part. This will be explored in greater detail in the theory section.

The dielectric response of soils has long been a research interest in fields such as geophysics, geotechnical engineering, archeology, etc. Soils are porous mediums containing one or more fluids in their pore space. A model for soil moisture and its associated relative permittivity was developed by Wobschall [1]. Applications of GPR in civil engineering applications are well documented [2-8]. Comprehensive reviews on GPR were written by Saarenketo and Scullion [7] on pavements and Huisman et al. [9] on soil moisture content determination. Many previous researchers have determined composite dielectric response empirically (e.g., Topp et al. [10]). Other methods have also been developed for estimation of moisture content [2, 11], where the moisture content was determined by solving an inverse problem with GPR data. In cementitious materials, the dielectric response was studied by Miura et al. [12] at a wide range of frequencies in order to determine degree of hydration. Various mixture laws have been suggested to model the dielectric response of mixtures of sand, gravel, and water with known constituent properties [13] for use in cementitious materials, but the models were not validated with concrete or cement measurements.

For measurement of concrete permeability in the laboratory, rapid chloride ion permeability (ASTM C1202) is widely used, but the results can be significantly affected by differences in the pore-solution chemistry between different concrete samples. Jones and Grasley [14-16] developed dynamic pressurization and radial flow-through techniques for measurement of intrinsic concrete permeability with cylindrical samples. With this technique, however, cores have to be taken from an existing structure, and full saturation may be hard to achieve. Basheer and Nolan [17] developed in-situ air permeability measurement techniques. However, permeability obtained from the technique is highly dependent on internal relative humidity (RH), and only the surface permeability can be obtained.

For pavement engineering applications, GPR operates by measuring reflected EM waves from different layers due to impedance mismatch between the layers. The GPR has a transmitting antenna operating at a certain frequency and a receiving antenna that records the reflected waves in the time domain. Air-coupled GPR has an antenna that is situated at some distance from the pavement surface separated by air. It is commonly assumed that the layers are perfect dielectrics with no losses associated with propagation of the EM wave through the layers greatly simplify the analysis of pavement thickness and determination of dielectric constants. Such an assumption cannot be made in concrete materials since concrete has a non-negligible loss component in complex permittivity. The measured loss tangent for saturated concretes range from up to 0.5 between 200 MHz and 6 GHz. The theory section will outline the limitations of

time domain reflectometry methods (TDR) in determining the dielectric response of concrete materials.

Dielectric relaxation is the time/frequency dependent dissipation of EM wave energy in materials due to effects such as dipolar relaxation at the frequencies of interest in this research. At low frequencies, water molecules polarize almost instantaneously to an alternating electric field without any loss. Dielectric relaxation occurs at higher frequencies (~14 GHz) when the rotation of water molecule dipoles lag behind the alternating electric field, causing dissipation of electrical energy in the applied electric field through heat. Figure S-1 shows the complex permittivity of pure water and water containing conductive ionic species at a concentration commonly found in the pore solution of mature concrete [18].
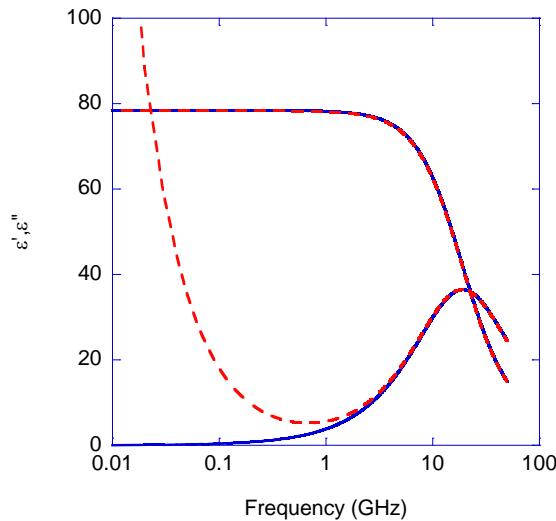
Figure S-1. Complex permittivity of water modeled after empirical equations in the work of Meissner and Wentz [19]. The abscissa is the frequency (GHz) in log scale, and the dielectric constants (real and imaginary) are on the ordinate. The dots indicate effect of minimal salt addition to complex permittivity of water, where at low frequencies a loss due to conduction is most apparent.

This literature review is not intended to be a comprehensive review of all of the completed work on the topic of dielectric relaxation. Research on dielectric relaxation on organic materials will likely be of little relevance to cementitious materials. Relevant work done on the dielectric relaxation constituents in cementitious materials, such as bulk water and water in confined spaces such as porous glass and soils, will be focused on in this literature review.

Dielectric relaxation of materials typically depends on frequency of the applied electric field and temperature, where lower temperature lowers the relaxation frequency. Jonscher [20] has written a thorough review on dielectric relaxation of solids. For more complex materials, a review on the concepts and measurement methods are described in the work of Feldman et al. [21]. While the properties of bulk water containing conducting species at various concentrations (i.e., seawater) have been extensively studied over a wide temperature and frequency range [19, 22-27], the behavior of water near interfaces is known to be drastically different [21, 28-32]. For confined water such as that found in nanoporous mediums, the physical and electrical properties

change dramatically. The dielectric response of water near interfaces can be found in a thorough review by Michot et al. [31]. A survey of loss mechanisms (both conduction and polarization) were given in the work of deLoor [33]. At current frequency range (> 50 MHz) of interest, mechanisms that affect losses include bound water relaxation, bulk water relaxation, and conduction. Clay materials contain structural water, and selected clays' dielectric properties were studied by Ishida et al. [34], where non-bound water, bound water, and interfacial polarization were identified as mechanisms for dielectric relaxation.

Other types of porous materials may possess a solid skeleton that resembles porous glass, which is not granular like most soils. Experimental work on dielectric relaxation in saturated porous media has been studied with controlled porous glass. Some of the work done on the characterization of water dynamics with porous glasses (e.g., Gutina et al. [28]) studied porous sodium borosilicate glass between 20 Hz-1 MHz at different temperatures, and a change in relaxation time due to water was observed between different pore sizes. The dynamics of water are hindered by the presence of interfaces. Such a shift in relaxation time was also observed in the work of Ryabov et al. [30] on porous glass.

Both early and mature age cement paste dielectric responses at microwave frequencies have been previously studied by the use of waveguide methods [35-38]. Previous studies on cement pastes have focused on the evolution of dielectric response of cement paste due to hydration [37]. For determination of moisture content and permeability, the microstructure of the cement paste must be considered. Consider a representative volume element of a hydrated cement paste, as shown in Figure S-2.
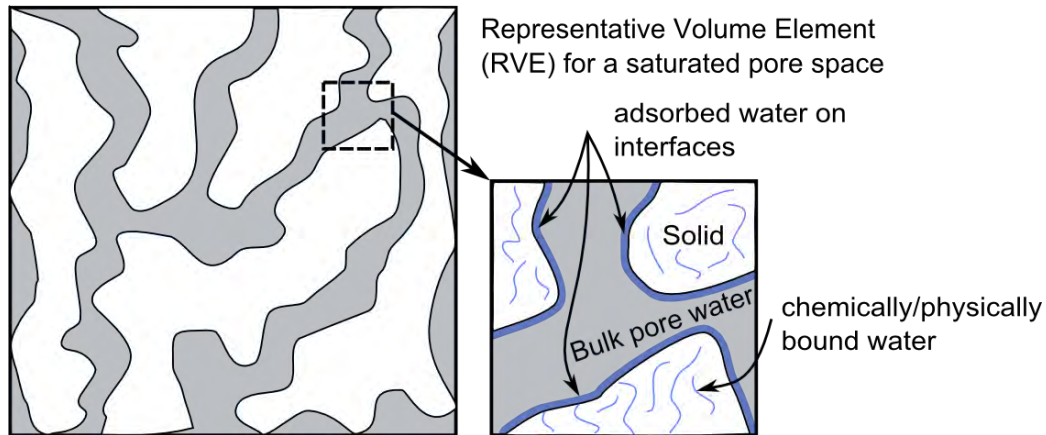
Figure S-2. Schematic of an arbitrary, fully saturated pore network. Water near and immediately adjacent to solids has different properties compared to that of the bulk water.

The solid matrix consists of calcium silica hydrates (CSHs), which contain physically bound water in nano-sized pores, and chemically bound water that is a part of the CSH structure. Capillary pores are filled with water containing various ions, and interfaces exist within the boundary between the bulk pore water and solid phases. In addition, interfaces are found within the CSH structure itself, often in very small length scales. Waters contained in these different length scales have different dielectric relaxation times, as demonstrated in pervious works on complex permittivity in other types of porous media.

THEORY

The interaction between matter and electromagnetic waves is described by Maxwell's equations [39]. For dielectrics, the constitutive equation of material response under the presence of an electric field is given as:

$$\hat{D} = \varepsilon_0 \hat{E} + \hat{P} \tag{1}$$

where $\hat{D}$ is the electric displacement field, ε_0 is the permittivity of free space, $\hat{E}$ is the electric field, and $\hat{P}$ is the polarization of the material as a function of the applied electric field. In a dielectric material under the presence of an electric field, the molecules in a dielectric material polarize by aligning along the applied field. At small field strengths, material behaves linearly at the presence of an electric field. The polarization $\hat{P}$ for linear materials is defined as:

$$\hat{P} = \chi_e \varepsilon_0 \hat{E} \tag{2}$$

where χ_e is the electric susceptibility of the material. Dielectric displacement can thus be written as:

$$\hat{D} = \varepsilon_0 (1 + \chi_e) \hat{E} = \varepsilon_0 \varepsilon_r \hat{E} \tag{3}$$

where ε_r is the relative permittivity of the material. In an isotropic, homogeneous material, ε_r is a scalar. Cementitious materials are assumed to be isotropic and homogeneous for this investigation due to the fact that the wavelength is 15 mm at 6 GHz assuming a refractive index of 3.2, which is much longer than any inhomogeneity found in cementitious materials. A perfect dielectric will have no dissipation of electrical energy. Materials experience dielectric dispersion/loss when polarization cannot follow an alternating electric field at certain frequencies. This time dependency of polarization can be written as:

$$\hat{P}(t) = \varepsilon_0 \int_{-\infty}^{t} \chi_e(t - t')\hat{E}(t')dt' \tag{4}$$

where $\hat{P}(t)$ is now a convolution of electric susceptibility (time-dependent) integral of a time-dependent electric field with reduced time t'. Dielectric displacement from Eq. (3) can then be written in the frequency domain by applying integral transform as:

$$\tilde{D}(\omega) = \varepsilon_r^*(\omega)\varepsilon_0 \tilde{E}(\omega) = \tilde{\varepsilon}(\omega)\tilde{E}(\omega) \tag{5}$$

where $\tilde{D}(\omega)$ is the dielectric displacement, $\tilde{\varepsilon}(\omega)$ is the absolute permittivity, $\tilde{E}(\omega)$ is the electric field, and $\varepsilon_r^*(\omega)$ is the complex permittivity in the frequency domain, respectively. $\varepsilon_r^*(\omega)$ has real and imaginary parts and is written as:

$$\varepsilon_r^{\,*}(\omega) = \varepsilon_r{}'(\omega) + \mathrm{i}\,\varepsilon_r{}''(\omega) \qquad\qquad (6)$$

where $\varepsilon_r{}'(\omega)$ is the real part of the complex permittivity, i is the imaginary number, and $\varepsilon_r{}''(\omega)$ is the imaginary part of the complex permittivity. The real part of complex permittivity indicates the ability for a material to polarize, thus storing charge. The imaginary part of complex permittivity describes losses in the electrical energy due to conduction and/or the lag in the polarization of molecules at certain frequencies (dipolar losses). Pure water, for instance, is a good insulator that has a fairly constant complex permittivity (real) up until the GHz range of frequency.

Consider a parallel plate capacitor where the charges accumulate on each side of the plates under an applied electric field, where the electrical energy is stored. When a dielectric material is inserted between the plates, the charges within the material polarize. Charges in a dielectric material require a finite amount of time to reorient to the direction of an applied electric field. At microwave frequencies, molecules such as water cannot align to the externally applied electric field. This delay causes dissipation in electrical energy. This relaxation time is normally many orders of magnitude larger than that observed in mechanical stress relaxation. For water, the relaxation time is in the order of picoseconds, whereas for viscoelastic materials such as polymeric materials, it is many orders of magnitude above picoseconds. This time-dependent response can be represented with empirical models such as the classical Debye model [40]. When discharged, the material returns to the non-polarized state over time, and the time required for relaxation is governed by the relaxation time. When an alternating field is applied to a material, the rate of polarization cannot follow the field at certain frequencies as a result of different mechanisms, causing dielectric relaxation.

Ground Penetrating Radar Theory of Operation

Consider a linearly polarized EM wave sent by a transmitting antenna (incident wave) down to the surface layer of concrete. A part of the EM wave is transmitted into the concrete from refraction, and the rest is reflected on the surface due to an impedance mismatch between the two layers with different refractive indices, which is a function of complex permittivity. Figure S-3 illustrates the propagation of the EM wave from an air-coupled system into concrete.
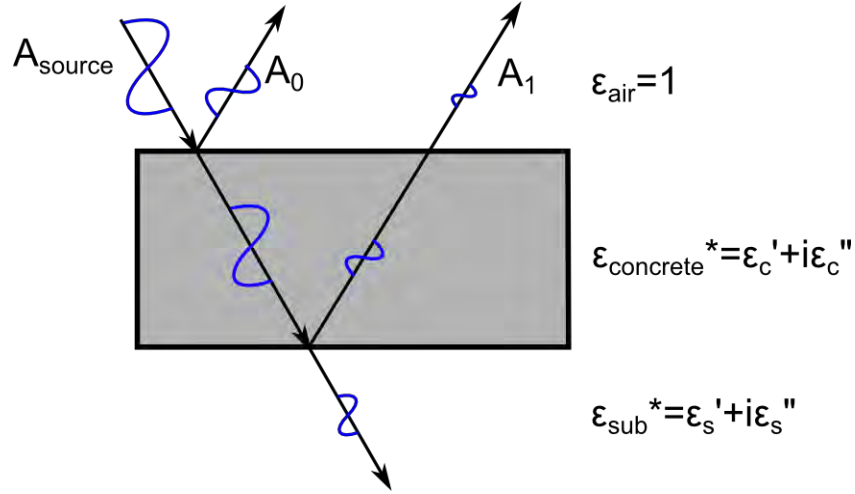
Figure S-3. GPR wave pulse reflection and refraction from concrete slab.

To simplify the analysis, several assumptions are made: there is no steel reinforcement in the concrete; the EM wave will entirely dissipate while traveling in the concrete, i.e., no reflection from the second interface or any reflection from the second interface is dissipated; there exists only two layers of air and concrete; the concrete has a uniform moisture profile, i.e., constant complex permittivity through depth; and the wave propagates perpendicular to the concrete layer. The EM wave propagating through a one-dimensional space (z) and time (t) is given as:

$$\hat{E}(z,t) = E_0 e^{-\alpha z} e^{i(\omega t - \beta z)} \tag{7}$$

where z is the location from the origin, t is the time, E_0 is half of the magnitude of the wave, α is the attenuation factor, and β is the phase coefficient. In a no-loss propagation medium such as air, α and β are given as:

$$\beta = \omega \sqrt{\mu \varepsilon_r} = \omega \sqrt{\mu_r \mu_0 \varepsilon_r} = \omega \sqrt{\mu_0} \tag{8}$$

where μ_0 is the magnetic permeability of free space in units in Newton Ampere^{-2}, and μ_r is the relative magnetic permeability of a material. For non-magnetic materials, $\mu_r = 1$. The ratio of the magnitude of the incident wave and reflected wave is the reflection coefficient given as:

$$\eta_{12} = \frac{n_1 - n_2}{n_1 + n_2} \tag{9}$$

where n is the refractive index of a particular layer, and the subscripts 1 and 2 denote the air and concrete layers (i.e., air and concrete), respectively. n is defined by:

$$n = \sqrt{\varepsilon_r \mu_r} \tag{10}$$

Since air and concrete are non-magnetic, and we assume that the bedrock layer is non-magnetic, the refractive indices are given as:

$$n_1 = \sqrt{\varepsilon_{r-air}} = 1 \tag{11}$$

$$n_2 = \sqrt{\varepsilon^*_{r-conc}(\omega)} = \sqrt{\varepsilon_r(\omega)' + i\varepsilon_r(\omega)''} \tag{12}$$

The reflection coefficient of a boundary for can thus be rewritten as:

$$\eta_{12} = \frac{1 - \sqrt{\varepsilon_r(\omega)' + i\varepsilon_r(\omega)''}}{1 + \sqrt{\varepsilon_r(\omega)' + i\varepsilon_r(\omega)''}} \tag{13}$$

Note that the reflection coefficient is complex due to the concrete layer having an imaginary part in complex permittivity. Since the GPR operates by measuring the time and magnitude of the reflected wave, the time and magnitude of the arriving wave pulse will change as a function of both the real and imaginary part of the complex permittivity. In short, the ratio of the magnitude of the incident and reflected wave represents the complex permittivity in imperfect dielectrics such as concrete. Using the magnitude of the incident and reflected wave to compute a complex permittivity with no-loss parts will lead to an overprediction of the real part of the relative complex permittivity.

In reality, if the EM wave does not entirely dissipate, the refracted wave through the concrete/air interface can be recorded in the time domain. Two phenomena occur during this time: attenuation of EM power and decrease in EM phase velocity in the reflected wave from the second interface. The assumption of perfect dielectric layers means that no attenuation occurs since the EM wave energy is stored and released as the EM wave propagates without losses from conductor or dipolar reorientation. The reflected wave in the concrete/bedrock layer due to an imperfect dielectric will therefore have a smaller magnitude. In the case where the waveform is not completely dissipated in the concrete, the ratio of the incident wave within the concrete and from the reflected wave on the concrete/bedrock surface cannot be used to compute the dielectric constant of the bedrock layer. Doing so will lead to an erroneous complex permittivity of the bedrock layer, and any determination of thickness will not be valid. In both cases, no information is given about the imaginary part of the concrete with TDR. If there exists a perfect conductor behind the concrete where the incident wave is completely reflected at the interface between the concrete and the conductor, the decrease in amplitude of the EM wave can be used to compute the imaginary part of the complex permittivity in the concrete.

Despite ample evidence of the dielectric relaxation of nanoporous, saturated media being strongly affected by the pore structure, the GPR systems evaluated in this research can only determine the magnitude of complex permittivity on the surface, and not the individual real and imaginary parts.

Modeling of Composite Complex Permittivity

As mentioned in previous sections, composite properties of the cement paste depend on the properties of the individual phases' complex permittivity. The problem of determining effective properties of a medium is the problem of homogenization of partial differential equations, which considers well-separated but different-length scales in order to obtain an effective tensor for the constitutive properties of the composite in the bulk scale. Homogenization requires knowledge of the microstructure and can be numerically intensive, and both of the aforementioned limitations are not considered in the scope of this research. Here, we instead seek the bounds and models of the effective tensors with known or inversely determined/backcalculated properties in each of the composite constituent phases, either to validate the experimental results in the case of composite viscoelastic properties of rubber-filled cement paste, or gain insights into relations between the microstructure of cement paste in relation to complex permittivity. Equations for composite complex permittivity bounds for two-phrase and three-phase materials will be presented.

The bounds for real-valued tensors were derived by Reuss-Voigt [41], and more restrictive bounds were derived by Hashin and Shtrikman [42] by solving for the composite constitutive property in an assembly of coated spheres, provided the spheres do not disturb the surrounding field and the constitutive property of the phases are positive and real. The bounds are subsequently derived using Hashin-Shtrikman's variational principles. All of these derivations assume that the externally applied stimulant/field is static in nature. In the literature, bounds were derived for conductivity tensors and various other constitutive properties, all of which are completely analogous to effective complex permittivity, and as such, the bounds can also be applied to effective complex permittivity problems.

As mentioned in the background section, relative permittivity can be complex. To find the bounds of a composite complex effective tensor, several researchers developed variational principles by transforming the frequency domain $\hat{D}$ and $\hat{E}$ (complex) into real equations. Lossy constituents represented by complex permittivity contain positive values for the imaginary part, and when the imaginary part of the composite is a positive definite, variational principles [43] can be applied. This method was used to derive bounds for a two-phase, complex bulk modulus. Analytic methods can also give tight bounds in the complex plane and were used by Bergman [44] to derive complex permittivity for a two-phase material. Finally, for a three-phase complex composite material, the field equation recursion method [45] was used to bound the composite complex permittivity.

Composite Constituents

Consider a case of a saturated cement paste. An illustration was shown previously in Figure S-2. The simplest case is a composite containing only water, with no geometrical effect on its dielectric properties, and solid. First, bounds for a two-phase composite with known dielectric properties for its constituents are developed and compared to experimental data. Then we examine the case of a three-phase composite where the geometrical effects on the dielectric properties of water are considered, namely a distinct separation between confined water and bulk water. The experimental data are compared to the bounds and an effective medium theory model, where the properties of the confined water are determined. Last, the moisture content in a

partially saturated case are modeled as a four-phase composite consisting of air, in addition to solid and water subject to various levels of geometric confinement. The complex permittivity of water used in the model is shown graphically in Figure S-1. The solid is assumed to be the oven-dried complex permittivity of the specimens ($\varepsilon_r = 6$), and the air has a relative permittivity of $\varepsilon_r = 1$.

Bounds on Complex Permittivity of a Two-Phase Composite

Before considering the more complicated cases, let us assume a completely saturated cementitious matrix with water and a hydrated cement matrix with relative complex permittivities of $\varepsilon^*_{bw}(\omega)$ and $\varepsilon^*_{cem}(\omega)$, respectively. Individual phases in the hydrated cement paste are not expected to have drastically different complex permittivities. In fact, most of the solid phases have high resistivity (negligible ohmic losses) *and* negligible dipolar losses, which makes the solid hydrated cement paste have a real relative permittivity only. Water within the pore space is assumed to behave like bulk water. Complex variables in terms of the complex permittivity of composite constituent phases and effective composite complex permittivity are defined as [44]:

$$s(\omega) \equiv \frac{\varepsilon^*_{cem}(\omega)}{\varepsilon^*_{cem}(\omega) - \varepsilon^*_{bw}(\omega)} \tag{14}$$

and

$$F(s(\omega)) \equiv \frac{\varepsilon^*_{cem}(\omega) - \varepsilon^*_{eff}(\omega)}{\varepsilon^*_{cem}(\omega)} \tag{15}$$

where $\varepsilon^*_{eff}(\omega)$ is the effective complex permittivity of the composite. For a two-phase isotropic composite with known volume fractions (from porosity) and complex permittivities, the bounds in $F(s)$ are derived with the analytic method and are given as:

$$F_1(\omega) = \frac{\phi(s(\omega) - s_0)}{s(\omega)(s(\omega) - s_0 - \frac{1}{d}(1 - \phi))} \tag{16}$$

and

$$F_2(\omega) = \frac{\phi(s(\omega) - s_0)}{(s(\omega) - s_0)(s(\omega) - \frac{1}{d}(1 - \phi)) - \frac{(d-1)}{d}(1 - \phi)(1 - s_0)} \tag{17}$$

where d is the dimension of the system (in this case, $d = 3$ for a three-dimensional system), s_0 is a variable that defines the bound, and ϕ is the porosity. For F_1, $0 < s_0 < \frac{(d-1)}{d}$ and for F_2,

$\dfrac{(d-1)}{d} < s_0 < 1$. Bounds on the effective composite permittivity can be found by solving Eq. (16) and Eq. (17) for $\varepsilon^*_{eff}(\omega)$.

Bounds on Complex Permittivity of a Three-Phase Composite

The complication arises when water under geometric confinement in nanoscale pores exhibits more drastically dynamic properties than bulk water, such that the dynamics of water molecules are hindered, as mentioned in the literature review. This geometrical confinement fact is well documented in the literature. With this consideration in mind, pore water in the cement paste is separated into two phases, and we define the additional phase as confined water, with an associated complex permittivity $\varepsilon^*_{cw}(\omega)$. The bounds are derived with the field recursion method described by Milton [45] and given as:

$$\cfrac{1}{\mathrm{Im}\left[\cfrac{\varepsilon_{cem}}{\varepsilon_{cem}-\varepsilon_{eff}}\right]} \leq \cfrac{\phi(1-p_{bw})}{\mathrm{Im}\left[\cfrac{\varepsilon_{cem}}{\varepsilon_{cem}-\varepsilon_{cw}(\omega)}\right]} + \cfrac{\phi p_{bw}}{\mathrm{Im}\left[\cfrac{\varepsilon_{cem}}{\varepsilon_{cem}-\varepsilon_{bw}(\omega)}\right]} \qquad (18)$$

$$\cfrac{1}{\mathrm{Im}\left[\cfrac{\varepsilon_{cw}(\omega)}{\varepsilon_{cw}(\omega)-\varepsilon_{eff}}\right]} \leq \cfrac{\phi p_{bw}}{\mathrm{Im}\left[\cfrac{\varepsilon_{cw}(\omega)}{\varepsilon_{cw}(\omega)-\varepsilon_{bw}(\omega)}\right]} + \cfrac{\phi}{\mathrm{Im}\left[\cfrac{\varepsilon_{cw}(\omega)}{\varepsilon_{cw}(\omega)-\varepsilon_{cem}}\right]} \qquad (19)$$

$$\varepsilon_{eff}(\omega) = f_1\varepsilon_{cw}(\omega) + f_2\varepsilon_{bw}(\omega) + f_3\varepsilon_{cem} - \cfrac{\left[f_1\cos(\theta)+f_2\sin(\theta)-f_3(\cos(\theta)+\sin(\theta))\right]^2}{\cfrac{\varepsilon_{cw}(\omega)}{f_1}\cos^2(\theta)+\cfrac{\varepsilon_{bw}(\omega)}{f_2}\sin^2(\theta)+\cfrac{\varepsilon_{cem}}{f_3}(\cos(\theta)+\sin(\theta))^2} \qquad (20)$$

where the parameter θ describes the bounds and varies from 0 to 2π, $f_1 = \phi(1-p_{bw})$, $f_2 = \phi p_{bw}$, $f_3 = \phi$, and p_{bw} is a new dimensionless variable that represents the volume fraction of bulk water within the water in the pore space. All of the relative permittivities of the individual components can be frequency dependent. The reader is directed to [45] for a thorough review of the theory and derivation of the bounds.

To utilize the derived bounds, cement pastes of different water/cement (w/c) ratios are first modeled with known porosities (invariant with frequency) and compared with the measurement results. For a two-phase system, the pore water in the cement paste is assumed to behave like bulk water, without any geometrical confinement effect. Then for a three-phase system, we extend the modeling of bounds along with an effective medium theory where the pore water is separated into two phases: bulk water and confined water. With the known complex permittivities of bulk water and cement paste, and the assumption that a certain percentage of confined water exists in the structure (from desorption isotherms), the properties of confined water can be fitted to the effective medium theory model and compared with the bounds of a three-phase material. Lastly, an effective medium model of four phases (solid, bound water,

confined water, and air) is used to develop collections for predicting moisture content versus complex permittivity and is compared to experimental results.

Effective Medium Model for Three- and Four-Phase Composites

In some cases, the bounds given in the previous sections are not useful for modeling purposes due to the bounds themselves being overly broad, such as the bounds given in the three-phase composite case. To model moisture content of hardened cement paste, the Bruggeman formula [46] is used assuming a three-dimensional space. It is assumed that interfacial polarization occurs at a much lower frequency (~1 MHz) and is neglected at this frequency range:

$$\sum_{i=1}^{m} f_i \frac{\varepsilon_i - \varepsilon_{eff}}{\varepsilon_i + 2\varepsilon_{eff}} = 0 \tag{21}$$

where m is the number of phases in the composite. For $m = 3$ (three-phase composite), Eq. (21) is written as:

$$f_1 \frac{\varepsilon_{bw} - \varepsilon_{eff}}{\varepsilon_{bw} + 2\varepsilon_{eff}} + f_2 \frac{\varepsilon_{cw} - \varepsilon_{eff}}{\varepsilon_{cw} + 2\varepsilon_{eff}} + f_3 \frac{\varepsilon_{cem} - \varepsilon_{eff}}{\varepsilon_{cem} + 2\varepsilon_{eff}} = 0 \tag{22}$$

For $m = 4$ (four-phase composite), Eq. (21) is written as:

$$f_1' \frac{\varepsilon_{bw} - \varepsilon_{eff}}{\varepsilon_{bw} + 2\varepsilon_{eff}} + f_2' \frac{\varepsilon_{cw} - \varepsilon_{eff}}{\varepsilon_{cw} + 2\varepsilon_{eff}} + f_3' \frac{\varepsilon_{cem} - \varepsilon_{eff}}{\varepsilon_{cem} + 2\varepsilon_{eff}} + f_4' \frac{\varepsilon_{air} - \varepsilon_{eff}}{\varepsilon_{air} + 2\varepsilon_{eff}} = 0 \tag{23}$$

f_i' is used to denote that the previously given formulations of f_i are different. S denotes the state of saturation of the pore space, where $f_1' = S\phi(1 - p_{bw})$, $f_2' = S\phi p_{bw}$, $f_3' = f_3 = \phi$, and $f_4' = \phi(1 - S)$. ε_{eff} in Eq. (22) and Eq. (23) can be solved analytically with different roots, and since the components of a complex ε_{eff} have to have positive values for both real and imaginary components, only the positive root is the valid solution. For a three-phase saturated cementitious composite system, the bound water complex permittivity ε_{cw} is determined from the saturated case by setting ε_{eff} equal to an experimentally determined value at a given frequency. To predict the response ε_{eff} as a function of saturation, ε_{eff} from Eq. (23) can be solved by using the ε_{cw} determined from a three-phase case.

EXPERIMENT

The desorption isotherm of specimens was determined with the mass loss method, where the specimens were placed in an RH-controlled chamber at constant temperature and the mass loss was recorded. Porosity was determined by completely drying the specimen in an oven. For relative and complex permittivity, the effective range of penetration of the percometer was determined. The operating frequency of the percometer was 40-50 MHz with the probe selected. The percometer operates on the principle of time domain reflectometry for determination of relative permittivity. For the determination of complex permittivity with respect to frequency, a coaxial dielectric probe was used. The method of operation for the coaxial dielectric probe was described in the work of Blackham and Pollard [47]. Dielectric measurements at frequencies between 200 MHz to 6 GHz were performed with a coaxial dielectric probe and vector network analyzer manufactured by HP (Agilent), model number 85070B and HP8753C, with the S-parameter test set, respectively. This method is hereinafter referred to as VNA. Previous testing indicated that the change in complex permittivity ceased after about 7 days with cement pastes from the same type of cement, regardless of w/c. Nevertheless, all specimens tested were mature (> 28 days).

Figure S-4. Determination of percometer penetration depth with cement paste cast on stainless steel at different thicknesses. The probe of the percometer uses a frequency of 40-50 MHz.

Materials

The following materials were used for fabrication of concrete specimens: ASTM Type I Portland cement, crushed limestone as coarse aggregate, and river sand as fine aggregate. The same type of cement was used in cement paste specimens.

Concrete

Specimens were made with embedded RH sensors for measurement of relative complex permittivity at the concrete surface with the percometer, and VNA 0.4, 0.5, and 0.6 w/c concrete specimens were fabricated. The specimen dimensions were 12 inches in diameter and approximately 6 inches tall. Plastic tubings were covered with a fibrous filter and inserted into a cylindrical tube normally used in construction, and concrete was cast around the tube. A plastic

petri dish cover was placed onto the center of the fresh concrete surface on the top. This ensured that the coaxial dielectric probe had a flat, smooth surface for measurement. The mix designs used are shown in Table S-1.

Table S-1. Mixture design for concrete specimens.

Mass per volume (kg/m^3)	Mixture A1	Mixture A2	Mixture A3
w/c	0.4	0.5	0.6
Water	210	210	210
Cement	525	420	350
Coarse Aggregate	907	907	907
Fine Aggregate	692	780	839

Specimens were covered for curing for 24 hr in a moist curing room prior to demolding. Specimens were wrapped on the bottom and the sides with tape to allow drying on the top surface of the specimen only. The specimens were then placed in a 100-percent RH moisture curing room for 28 days prior to testing. Specimens were placed in an air-conditioned laboratory for drying. Wires containing the RH sensors on one end were placed into the plastic tubes and sealed. RH and temperature were measured with a data logger, and data were downloaded from the logger periodically.
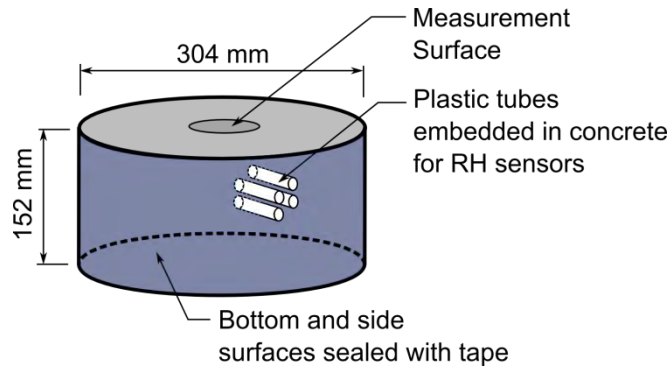
Figure S-5. Concrete specimen illustration. RH sensors on the end of wires were placed in the plastic tubes and sealed with rubber tape to prevent moisture from escaping into the surroundings.

Measurements were taken with the percometer periodically. The coaxial probe (from VNA) was placed in a holder and calibrated before testing. During testing, the specimen was moved underneath the probe. The probe was then placed in contact with the concrete with minimal movement to the cable to ensure accurate and repeatable measurements. The data were recorded with the software provided by the manufacturer on the computer. A total of four

readings were made on the measurement area/surface each time, and the averaged reading was reported.

Cement Paste

For the cement paste specimens, the mixing procedure followed procedures in ASTM C305-06. Two types of specimens were fabricated: one for testing with the VNA and the other for determination of penetration depth of the percometer. Fresh paste was placed into plastic petri dishes after mixing and covered to prevent moisture loss. Specimens with w/c ratios ranging from 0.4 to 0.6 w/c were fabricated at 0.1 w/c increments. Specimens were demolded at the earliest possible time and placed in deionized (DI) water to ensure saturation and to remove as many ions from the pore water as possible in order to remove effects due to conducting ionic species. All of the specimens were placed in saturated DI water to cure for at least 28 days. The permeability of the specimens were determined by the dynamic pressurization method [16] with solid cylindrical specimens. Each cement paste specimen was tested three times where the probe made contact on slightly different locations of the specimen surface, as illustrated in Figure S-6. Mass loss for 0.4, 0.5, and 0.6 w/c ratios was measured by pulverized, mature specimens for desorption isotherm determination.
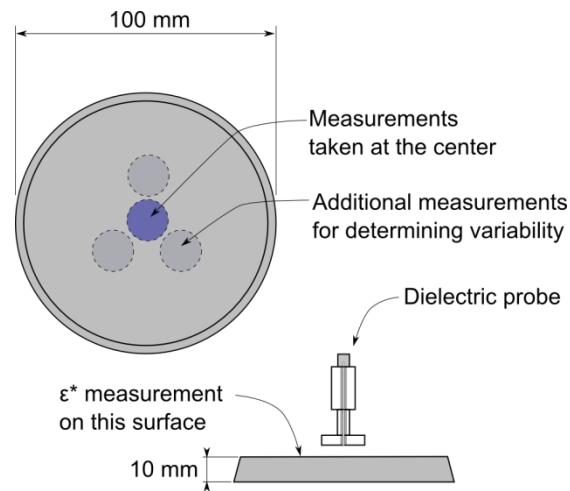
Figure S-6. Complex permittivity determination with dielectric probe. The small diameter side of the specimen (0.4 w/c) is also the bottom of the casting surface in petri dishes, providing a smooth surface for the probe.

After calibration, the specimen was placed on the bottom of the probe and the data were recorded. Four areas were tested near the center of the specimen. After testing the cement paste specimens at a saturated state, the specimens were placed in controlled RH chambers (saturated salt solution). Specimens were tested after 30 days from being placed in the chambers. For the percometer testing, 0.4 w/c paste was cast on a stainless steel plate. Readings were taken at different time intervals since the specimen was cast. The thickness ranged from 3 mm to 37 mm. The specimen was placed in a bucket partially filled with water for curing.

Porous Ceramics

Porous ceramic specimens were also purchased for testing. Porous ceramics were manufactured from ball clay, and the chemistry is proprietary. Permeability of specimens was provided by the manufacturer. A total of four specimens were purchased from the manufacturer for testing. Two were placed in DI water and vacuum saturated for 24 hr for testing with the VNA. The specimens had a diameter of 25.4 mm and a height of 10.26 mm. For desorption isotherm measurements, two specimens were saturated with DI water, and their mass loss was measured with a precision scale. The specimens had a diameter of 50.8 mm and a height of 7.14 mm.

EXPERIMENTAL RESULTS

Figure S-7 illustrates the data from the desorption isotherm of 0.4 w/c, 0.5 w/c, and 0.6 w/c. The cement with higher w/c tended to have a lower saturation level as a function of RH. The initial weight of the specimen (saturated surface dry) was obtained by determining the point at which the mass loss started to equilibrate by diffusion rather than evaporation of water on the specimen holder and specimen surface. Saturation was determined from the amount of free water in the specimens. At full saturation, S = 1, and when pores were completely emptied, S = 0. Pore sizes can be determined from sorption isotherms [48], and a sharp decrease in mass loss at higher RH levels indicates that more large pores are present, which is an indication of a high w/c ratio. For the concrete blocks, the measured RH is shown in Figure S-8.
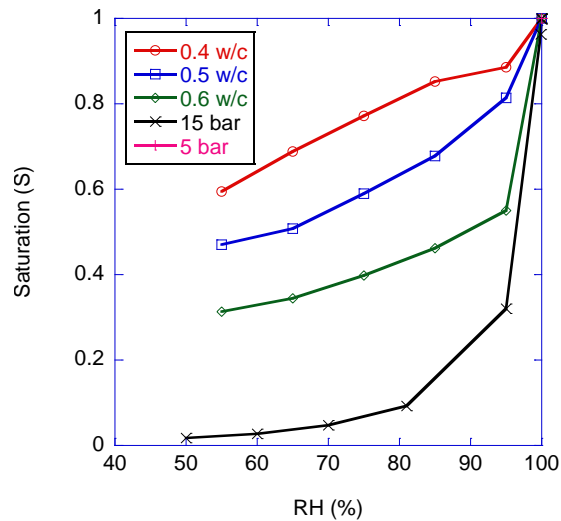
Figure S-7. Desorption isotherms from the cement paste specimens fabricated. As expected, larger pores were found in higher w/c ratio specimens.

RH in Concrete Specimens Versus Time

The measurements of internal RH in the concrete blocks along with the ambient RH are shown in Figure S-8. For the 0.4 and 0.6 w/c specimens, the abnormal fluctuations in the ambient RH were caused by a malfunctioning air conditioning system in the laboratory.
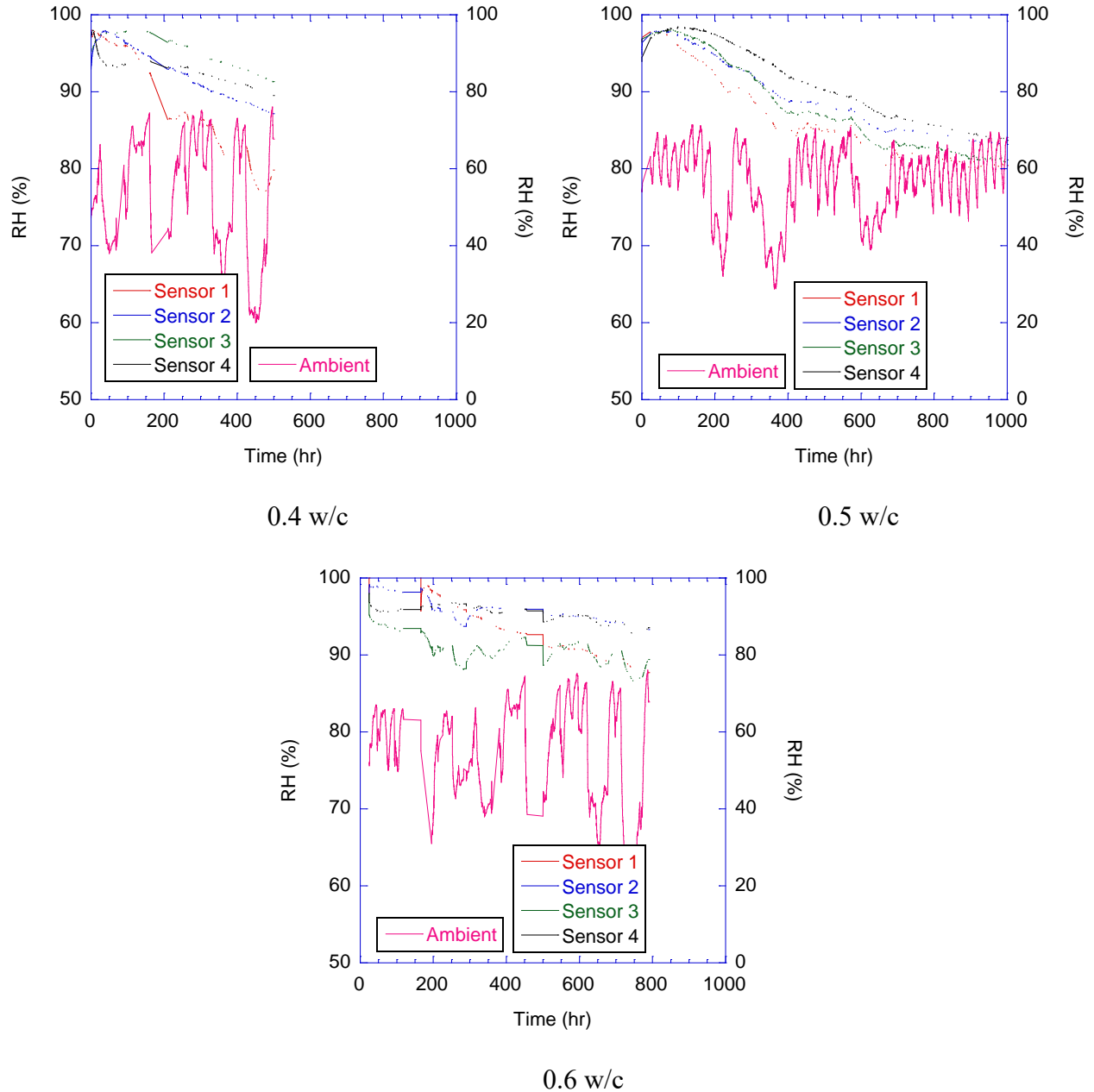
Figure S-8. Concrete RH measurements as a function of time. Note the difference in drying rate between the 0.4 and 0.5 w/c specimens. The 0.6 w/c specimens had water entrapped in the sensor tube, and readings were erroneous.

Even with the top sensors being situated only about 9 mm from the surface for all of the specimens tested, the RH level did not significantly decrease until about 100 hr after being placed in the laboratory. This indicated that the surface moisture content was significantly lower compared to the moisture content within the concrete. A moisture gradient was present in the concrete specimens.

Relative and Complex Permittivity of Concrete Specimens

It is noted from the manufacturer that the measured ε_r is reliable when the material conductivity is under a certain threshold. For the surface probe used in this research, < 2000 μS/cm is the recommended value. Values beyond that will affect the measurements. It is highly likely that the measured value from the percometer is actually the magnitude of the complex permittivity when the material is lossy. For the percometer measurements, the measured ε_r readings of concrete versus time elapsed since drying are shown in Figure S-9 and the readings of cement paste versus thickness of cement paste are shown in Figure S-10.
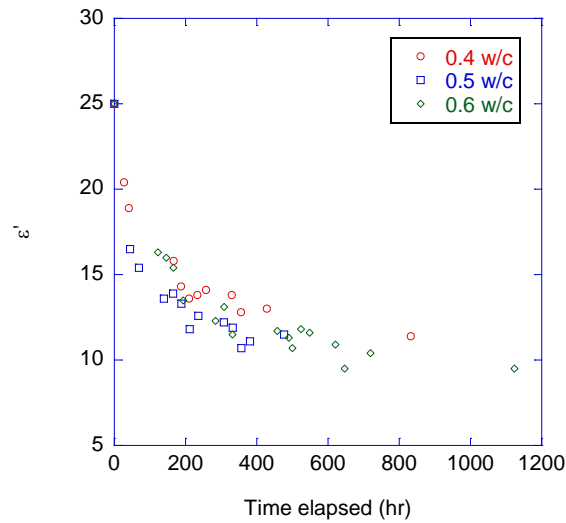
Figure S-9. Percometer readings on concrete specimens as a function of time. Note that despite the variation of ambient RH, the decrease in relative permittivity (possibly a complex reading) does not vary.
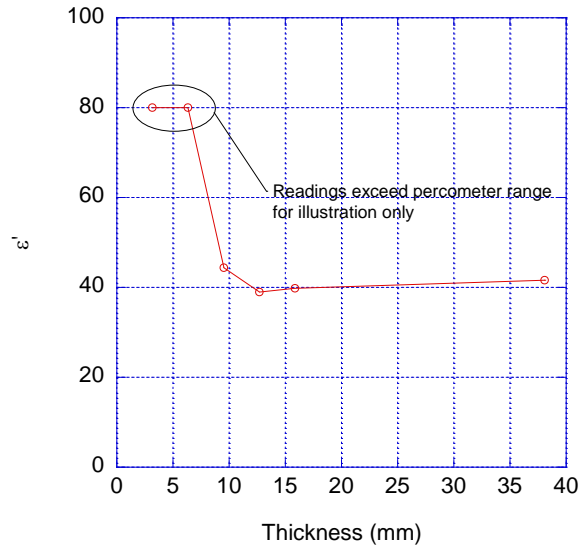
Figure S-10. Real part of permittivity as a function of cement paste specimen thickness.

The corresponding probe's range of readings for ε_r is between 1 and 40. When the range is exceeded, no reading is shown on the percometer, and it is represented by $\varepsilon_r = 80$ for comparison purposes. The range of penetration for a wet cement paste specimen is shown to be about 10-15 mm for cement paste. The complex permittivity is likely lower than that in the case of concrete, due to the presence of aggregates, and in partially saturated systems. In both of the cases mentioned, the depth of penetration will be higher.

The results from complex permittivity testing of concrete slabs with VNA are shown in Figure S-11 for the real part of complex permittivity and Figure S-12 for the imaginary part of complex permittivity. Very little difference between the magnitude and shape of complex permittivity was observed with respect to frequency. Even with known ambient moisture, the amount of moisture within the tested area (with respect to depth) was not known. The measured complex permittivity from VNA followed the same trend compared to measured relative permittivity from the percometer, which suggested that w/c and ambient RH fluctuation does not drastically affect the decrease in recorded relative permittivity.
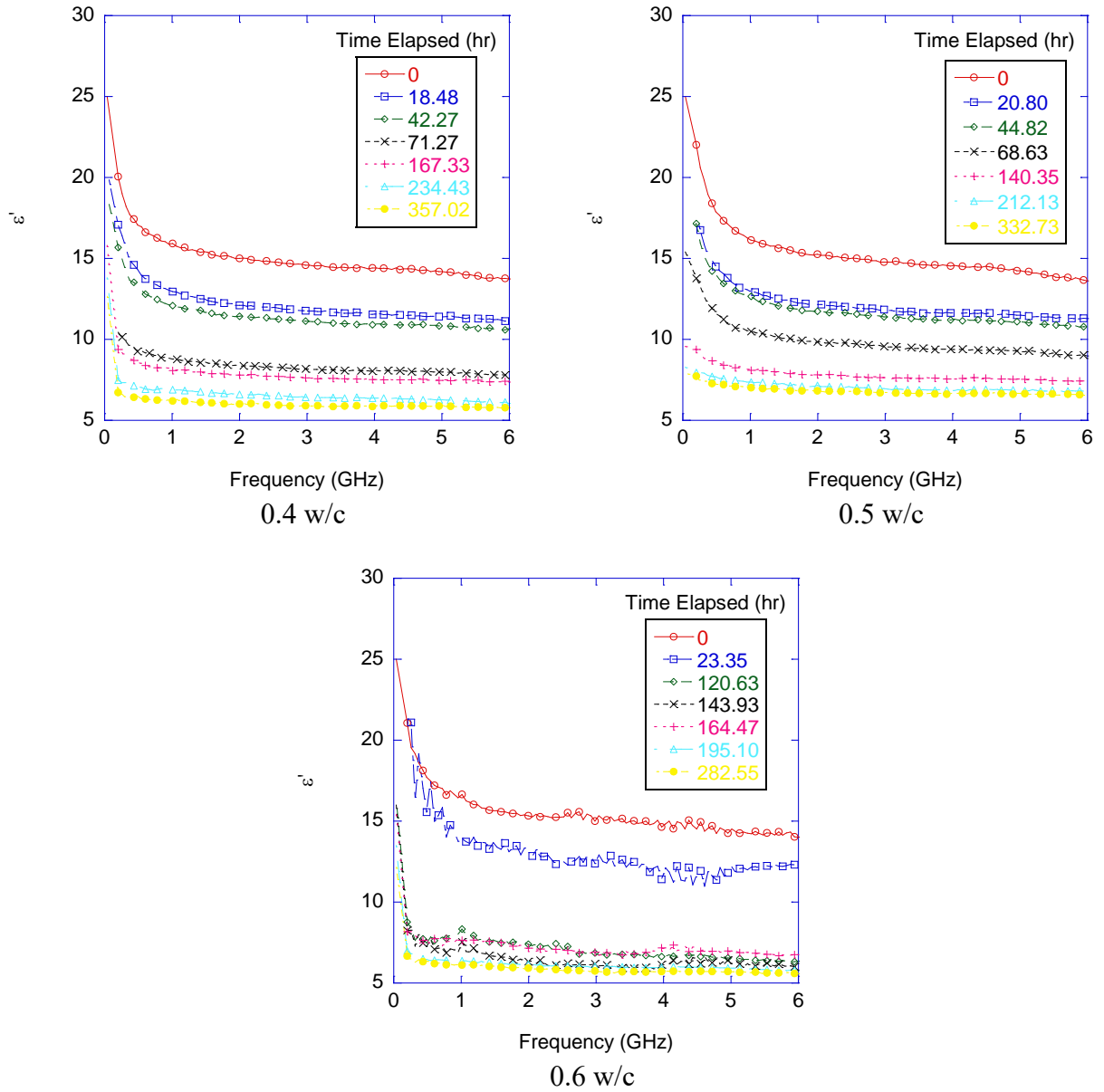
Figure S-11. Real part of complex permittivity from concrete specimens.
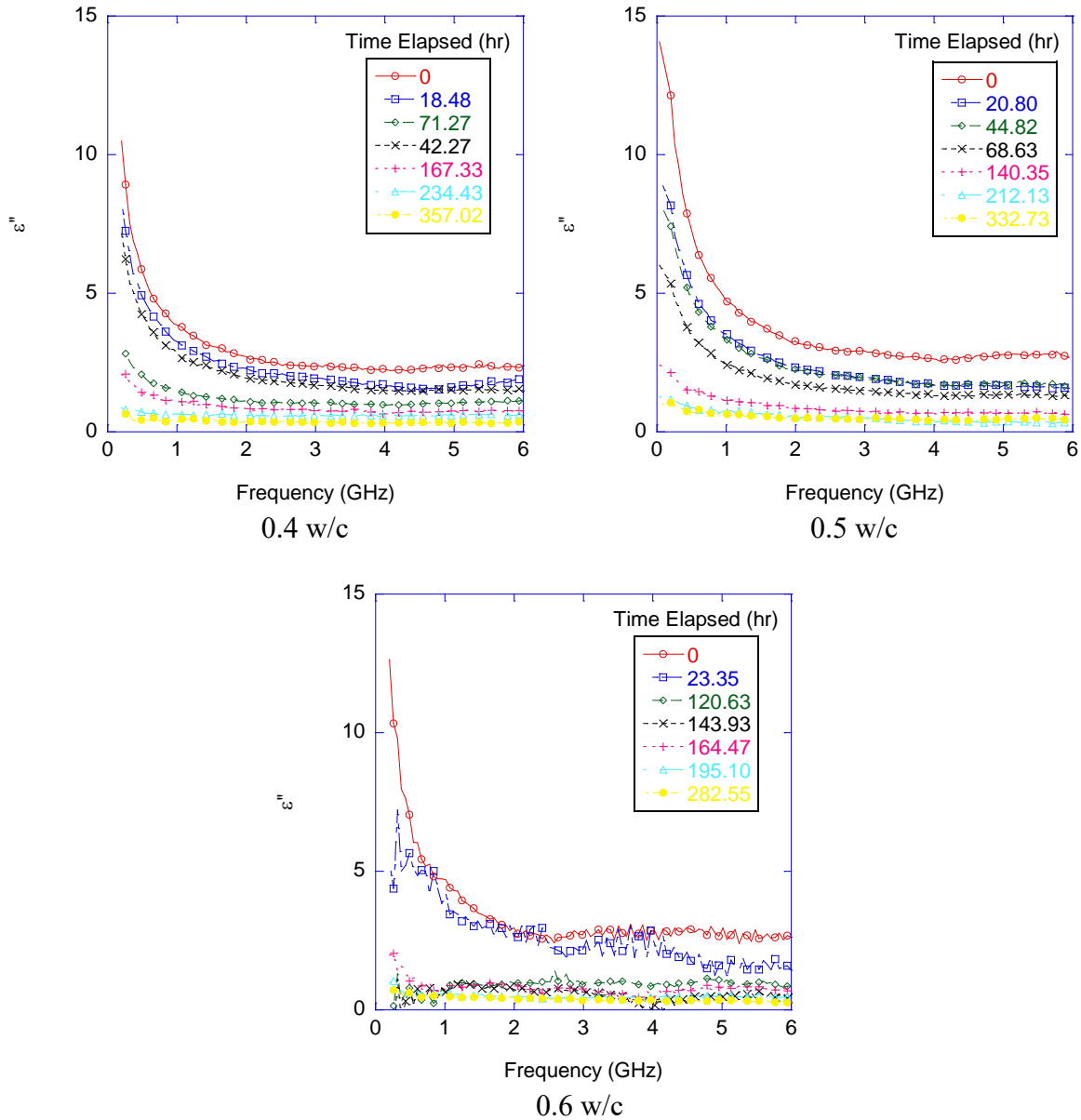
Figure S-12. Imaginary part of complex permittivity from concrete specimens.

Recall from Figure S-8 that the RH levels on the top sensors (~9 mm from the surface) did not drop until after about 100 hr. Yet drastic changes in complex permittivity were recorded for all of the specimens. Due to the fact that the coaxial dielectric probe had a permittivity-dependent sample size requirement from the manufacturer of the probe (4 mm for $\left|\varepsilon^*_r\right| = 25$, 9 mm for $\left|\varepsilon^*_r\right| = 5$), it is likely that the measured complex permittivity was primarily due only to the moisture content of the first few millimeters at the surface. It was hypothesized that after casting of the concrete specimens, the bleed water on the surfaces of the fresh concrete specimens would effectively increase the w/c of the concrete surface layer. The internal RH of the specimens also support this hypothesis, as the top sensors of the specimens stayed at a high RH level for an extended period of time, even though the top sensor was merely ~9 mm away from the surface

and drastic drops in magnitude of complex permittivity were recorded. This means that the recorded complex permittivity was most influenced by only the change in RH on the first few millimeters of the surface. The measurements from the concrete specimens thus only gave a qualitative measure of correlation between complex permittivity and moisture content.

Complex Permittivity of Cement Paste Specimens at Room Temperature

Since the measurement of concrete surface complex permittivity cannot be used to correlate RH level, moisture contents of cement paste specimens were conditioned to determine correlations between moisture content and complex permittivity. Figure S-13 and Figure S-14 show the complex permittivity of 0.4, 0.5, and 0.6 w/c specimens, respectively, at room temperature.

0.4 w/c

0.5 w/c

0.6 w/c
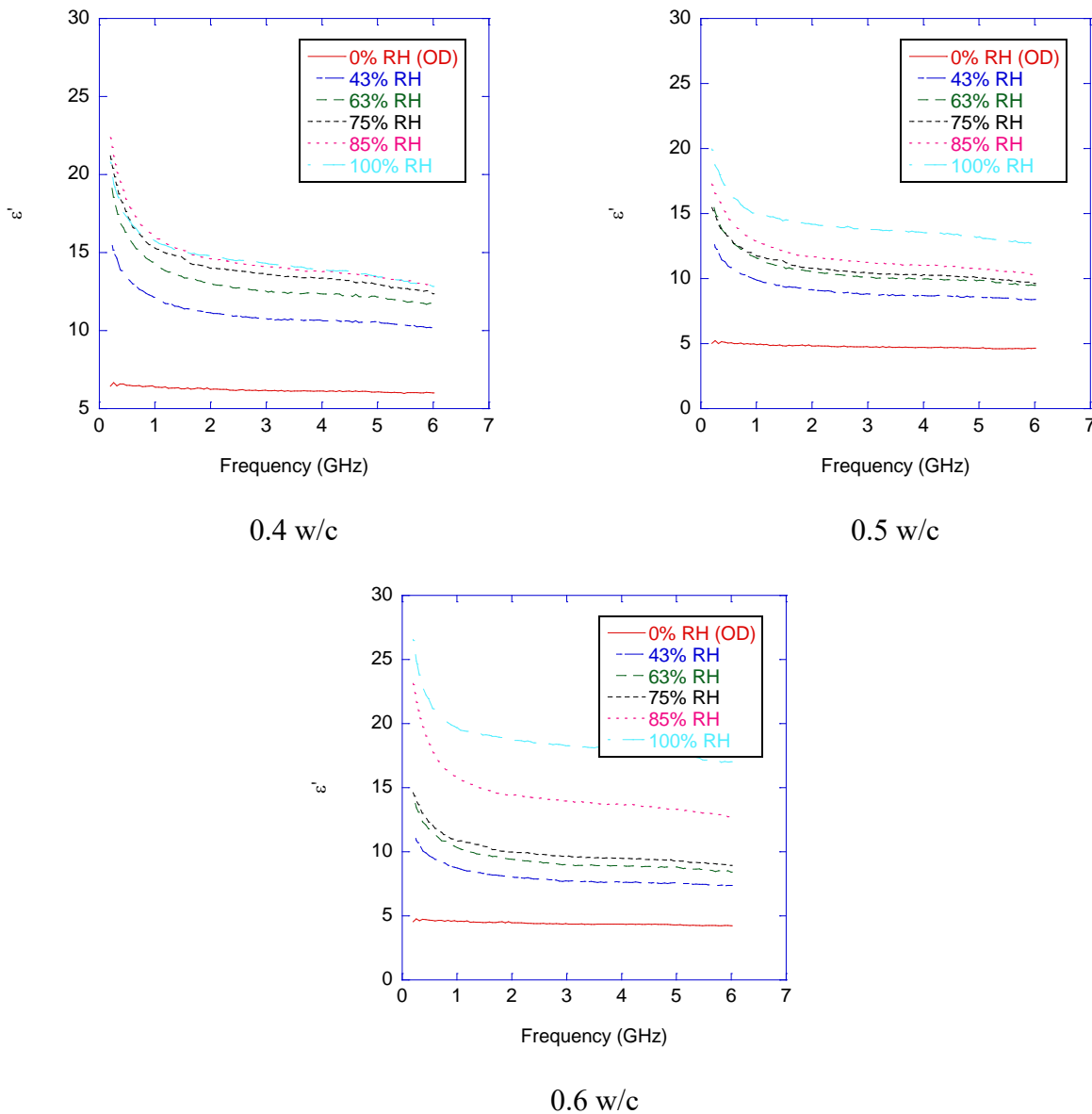
Figure S-13. Real part of complex permittivity for cement paste specimens.
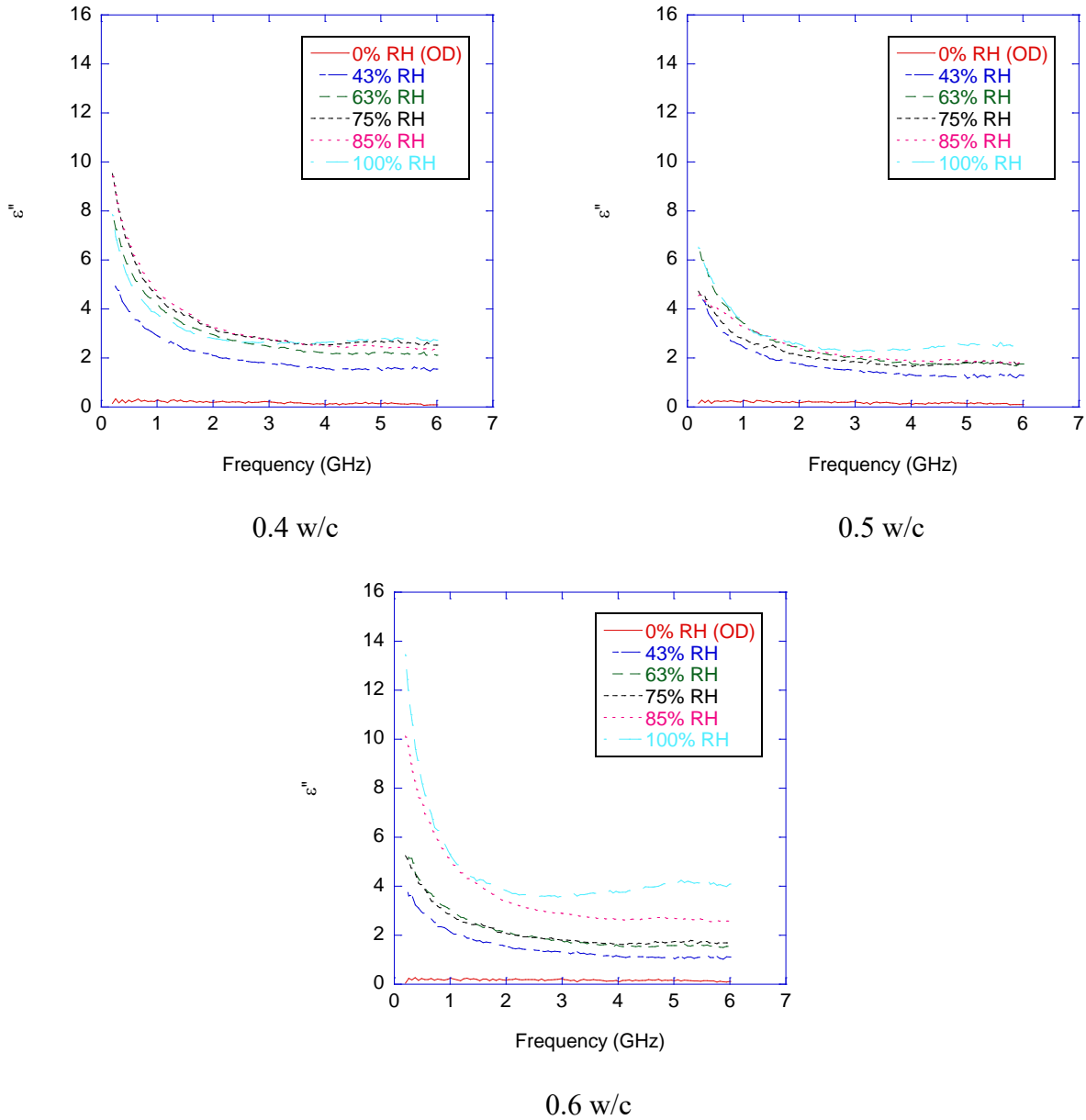
Figure S-14. Imaginary part of complex permittivity for cement paste specimens.

The differences in magnitude of the dielectric constants were noticed in all of the frequency ranges, which also scaled with the w/c ratio, i.e., a higher w/c resulted in a higher ε' and ε''. However, the loss part of permittivity appeared to be much less sensitive to change in moisture content, with the 0.6 w/c being the only exception. The real part of complex permittivity should be used to correlate moisture content with complex permittivity due to its high sensitivity to relatively small changes in moisture content. The saturation was obtained from converting RH by desorption isotherms, as shown in Figure S-7.

Complex Permittivity of Saturated Cement Pastes and Porous Ceramics at Different Temperatures

Porous ceramic discs were also tested with VNA to determine dependence of pore size distribution on the complex permittivity. The pore size distribution for the porous ceramic discs was expected to be a much narrower than that of cement paste. It was hypothesized that the narrow pore size distribution found in the ceramic discs would affect the dielectric dispersion in the confined water in the pore space, whereas in cement paste, a range of pore sizes would be found, and therefore a clear indication between water permeability and complex permittivity would not be observed in cement paste. Complex permittivity of porous materials containing water was previously studied, and it was noted that confined water has restricted dipole-dipole movement. This can be observed in the relaxation time of water at different temperatures, where the relaxation occurs at lower frequencies as temperature is lowered. To verify, measurements were made for water-saturated porous ceramics, and results are shown in Figure S-15.

a.   b.
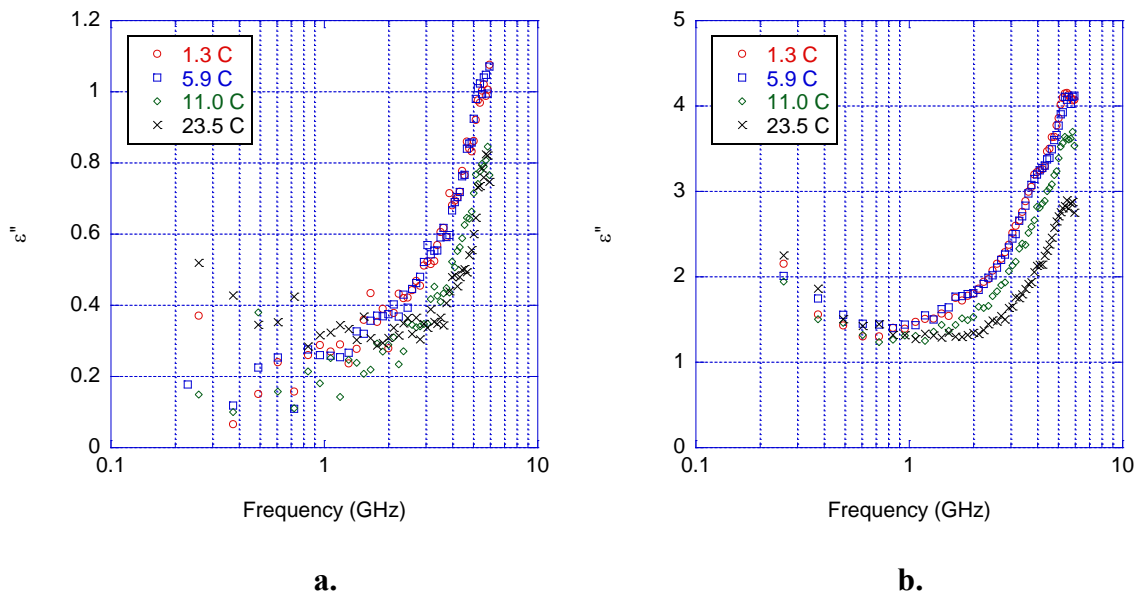
Figure S-15. Porous ceramic loss part of complex permittivity vs. temperature. Note that as temperature is lowered, relaxation due to the presence of water in the pore space starts to occur at a lower frequency.

For the imaginary part of complex permittivity, confined water did not seem to play a role in relaxation for the five-bar specimens due to the lack of a peak at the lower frequencies. For 15-bar specimens, a higher loss part was found at lower frequencies. Five-bar specimens had larger pores per volume (see desorption isotherm in Figure S-7). The complex permittivity with respect to frequency of porous ceramics was distinctly different from that observed in cement paste. For cement paste, the complex permittivity appeared to be well represented by an exponential decaying function with no bulk water relaxation component, whereas a distinct change in complex permittivity was observed due to bulk water relaxation in both porous ceramic specimens. For the 15-bar specimen with smaller pores, an exponential decay at the lower frequencies was observed, which is hypothesized to be due to the small amount of confined water in the porous ceramic, similar to that observed in the cement paste.

MODELING OF RELEVANT MATERIAL PROPERTIES WITH EXPERIMENTAL RESULTS

Complex Permittivity Bounds and Prediction with Effective Medium Theory

With known values of porosity for each of the materials, complex permittivity of bulk water and a measured value for the complex permittivity of the solid phase, Eq. (16) and (17) can be used to solve for the bounds of composite relative permittivity ε^*_{eff}. The bounds can then be plotted on the complex plane for comparison. Figure S-16 shows the difference between measured values at different frequencies vs. the complex permittivity predictions from a two-phase composite.

0.4 w/c

0.5 w/c

0.6 w/c
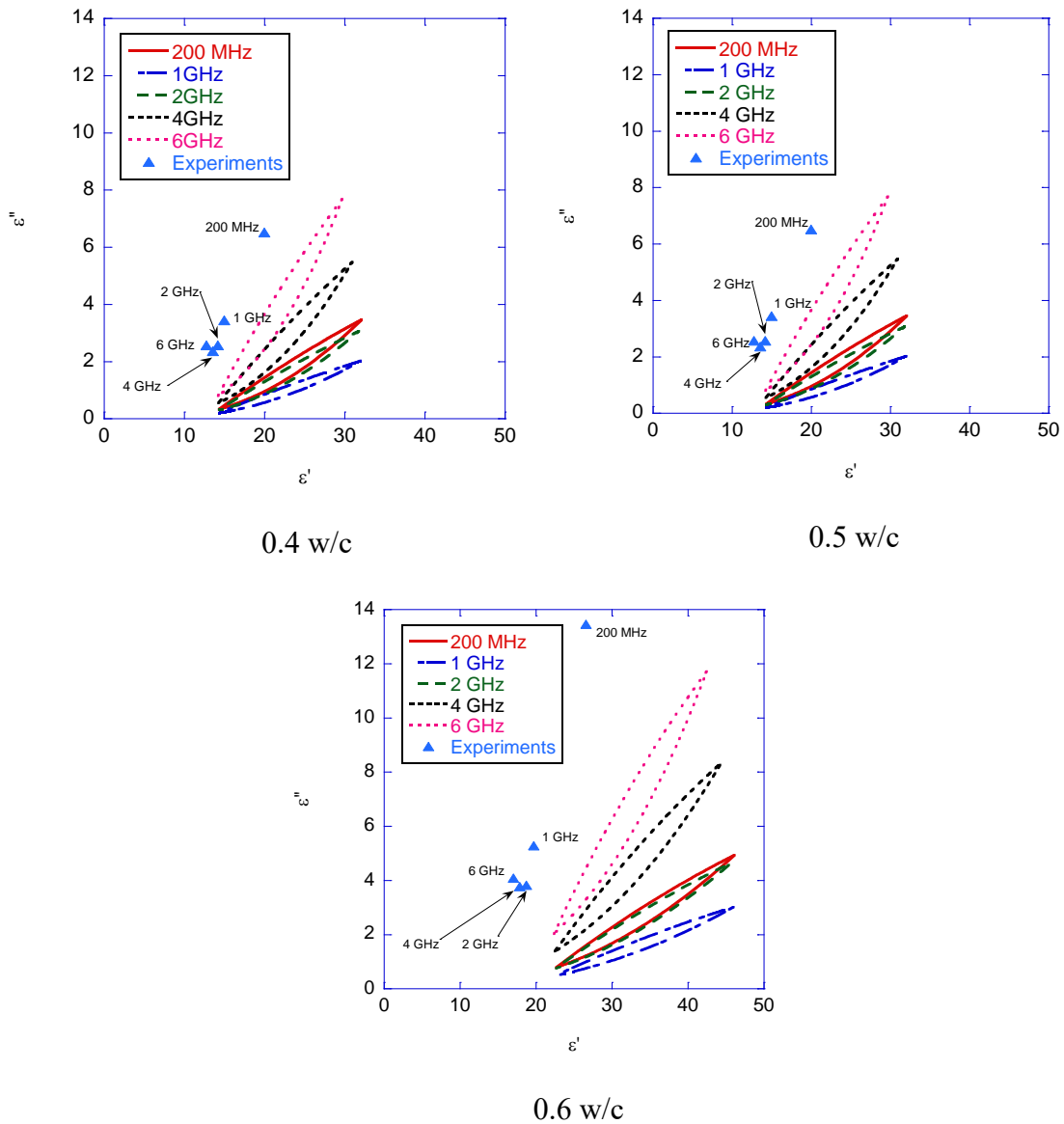
Figure S-16. Two-phase bounds of effective complex permittivity of cement paste vs. measured data.

The two-phase composite assumption, while able to produce restrictive bounds on the complex plane, was not able to predict value of the composite complex permittivity. The experimentally measured complex permittivity on the complex plane fell outside of the bounds from the model. Assuming the dielectric response of a saturated hardened cement paste as composite material containing only two phases made up of solids and bulk water was clearly not a valid assumption.

A three-phase composite bound and the effective medium theory (Eq.[22]) were used to determine the response of an additional phase of confined water by fitting the complex permittivity of bulk water to the experimentally determined value. The dielectric response of pore water was assumed to be described by two distinct phases of bulk and confined water, with different complex permittivity. The resulting bounds from Eq. (18), (19), and (20) are illustrated in Figure S-19 for a 0.4 w/c specimen at 1 GHz at room temperature.
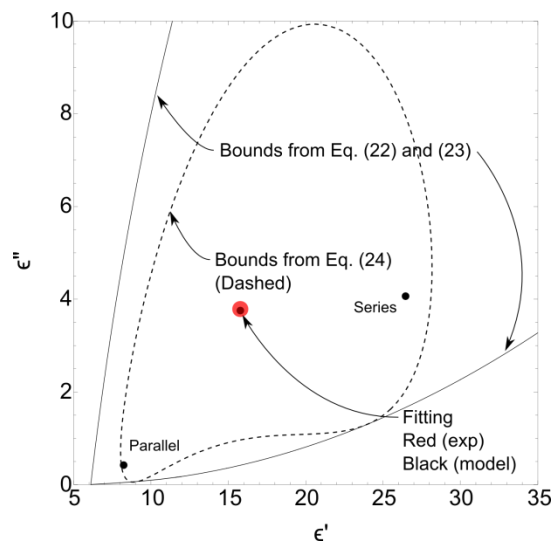
Figure S-17. Three-phase composite bounds of 0.4 w/c at 1 GHz. The red dot represents the experimentally obtained data plotted on the complex plane. The dashed line represents a bound from Eq. (20), whereas the solid lines represent the bounds from Eq. (19) and (20). The solid black dots represent the parallel and series model, with one of the solid black dots being the predicted composite complex permittivity from Eq. (22).

The bounds were obtained by fitting the experimental data point at each frequency (in the case of Figure S-17, at 1 GHz) by varying the properties of the confined water, which is a complex-valued quantity. The bounds shown in Figure S-17 are much wider than those shown in Figure S-16 due to the different method of derivation. The confined water was assumed to be a discrete phase, and its volume fraction was determined from the desorption isotherm. Water contained in < 20 nm pores was assumed to be confined water, and the volume fraction as a function of the total pore volume was used as a model parameter for the confined water. The complex permittivity of the confined water was determined by adjusting the real and imaginary components at each frequency and was fitted to the experimentally measured complex permittivity on the complex plane (i.e., Figure S-17, but at different frequencies). The modeled complex permittivity of the confined water as a function of frequency for each of the materials is shown in Figure S-18.
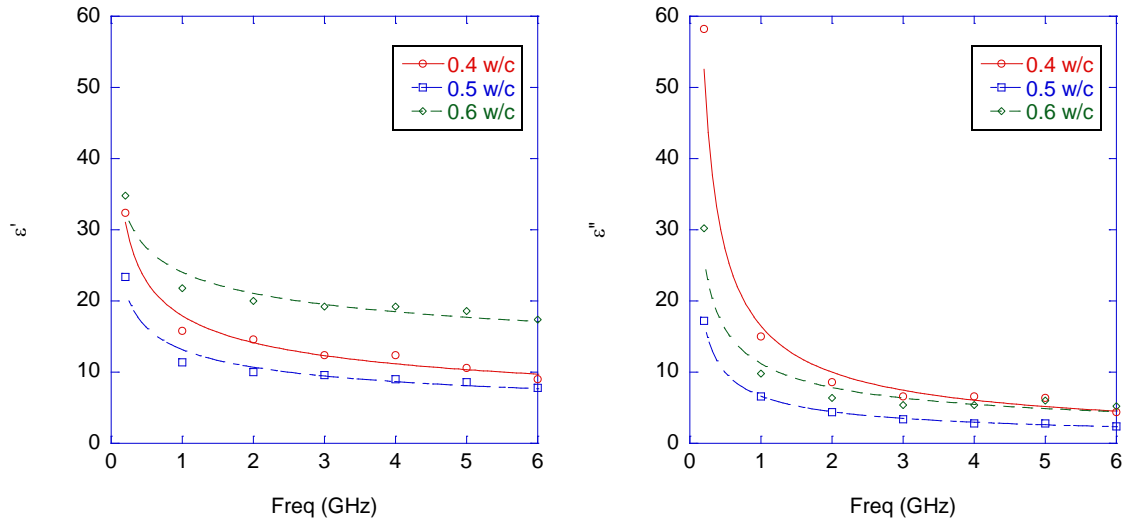
Figure S-18. Modeled confined water complex permittivity versus frequency.

The modeled real part of complex permittivity of confined water for 0.6 w/c specimens was significantly higher. It is hypothesized that the additional air bubbles introduced by mixing on a rotating shaft to prevent excessive bleeding of the specimen greatly increased the effective water content of the specimen when tested with the coaxial dielectric probe. Increasing the value of porosity ϕ used in modeling for 0.6 w/c reduced the real part of complex permittivity to a level comparable to 0.4 and 0.5 w/c. The most interesting finding from this three-phase composite model is that the predicted imaginary part of complex permittivity of confined water was significantly higher for a 0.4 w/c specimen than a 0.5 or 0.6 w/c specimen. This implies that the confined water cannot be assumed to be a discrete phase being independent on the microstructure and porosity.

Modeling of Cement Paste Moisture Content

Since the surface relative permittivity from GPR used in this research obtains the relative permittivity from reflected wave amplitudes, having the knowledge of complex permittivities at different moisture contents will allow engineers to determine moisture content from GPR readings. Figure S-19 shows the magnitude of complex permittivity of 0.4-0.6 w/c cement pastes at different moisture contents. The moisture content was converted from saturation since the porosity of the materials was previously determined. By plotting the associated moisture content for all of the materials (0.4, 0.5, and 0.6 w/c) at the two frequencies near the operating frequency of the air-coupled GPR, a linear relationship between volumetric moisture content and the real part of complex permittivity was observed. Figure S-13 and Figure S-14 show the different w/c vs. complex permittivity for specimens conditioned to different RH. Using the values of porosity at each different w/c, degree of saturation, S, can be readily converted to volumetric moisture content, MC. The correlation between laboratory measurements and MC and the model prediction from solving for the effective composite complex permittivity ε_{eff} with Eq. (23) are shown in Figure S-19.
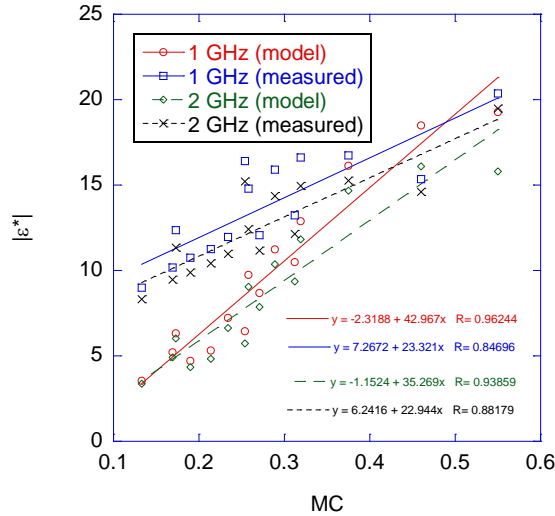
Figure S-19. Empirical fit and modeled magnitude of complex permittivity as a function of moisture content at 1 GHz and 2 GHz. The model used averaged ε_{cw}, and the points from all measurements (0.4-0.6 w/c) were plotted on the same graph.

The modeled response with Eq. (23) also uses an average value of complex permittivity of confined water, which could introduce significant error. The predictions made without using an averaged complex permittivity of confined water can be found in Figure S-20.
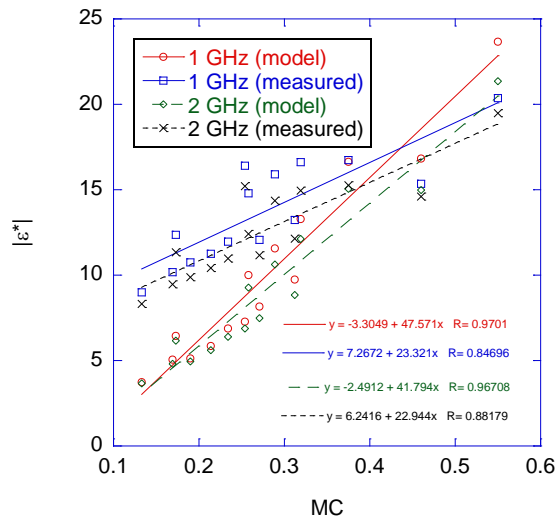
Figure S-20. Empirical fit and modeled magnitude of complex permittivity as a function of moisture content at 1 GHz and 2 GHz. The model used modeled ε_{cw} for each of the w/c ratio specimens, and the magnitude of the complex permittivity from all measurements was plotted on the same graph.

The modeled magnitude of complex permittivity slightly improved when the model used the corresponding ε_{cw} from each of the w/c ratios instead of an averaged value. The complex

permittivity from modeling was higher than the experimental values at lower RH. This could be attributed to the fact that even after 2 months of drying, the specimen dimension prevented the specimen from having a fully equilibrated moisture state through depth. It is also possible that the Bruggeman formula does not accurately represent the effective complex permittivity of cementitious materials. Nevertheless, it appears that the magnitude of the complex permittivity as a function of moisture content can be represented as a linear relation.

CONCLUSION

The dependence of complex permittivity on the moisture content of cementitious materials, including concrete and cement paste, was systematically evaluated by microwave dielectric spectroscopy and a percometer. The depth of penetration of the percometer was determined for a saturated cement paste, and the depth of penetration was expected to increase for partially saturated cement paste and concrete. The operator is cautioned that for concrete, the measured value of the real part of relative permittivity from the percometer will likely deviate from the actual value due to the effect of conducting ionic species on EM wave propagation and reflection. Multiphase composite models were used to validate experimental results on cement paste at various levels of saturation. The model was able to replicate the measured trends between moisture content and magnitude of complex permittivity, with deviations from the model attributed to the inability to control the internal RH of tested cement paste specimens in a reasonable amount of time.

The frequency dependent dissipation of EM waves in water in a bulk state and confined spaces, known as dielectric relaxation, has the potential to provide valuable parameters to the pore structure of a material, and transport properties such as permeability can be inferred from pore structures. Dielectric relaxation occurs when the polarization of charge within dielectric materials subjected to a time-dependent alternating electric field cannot follow the electric field due to frictional losses, and the EM wave energy in the propagating wave is dissipated.

Assessment of moisture content and permeability of cementitious materials by GPR has not been attempted in the past.

The properties of the confined water were used to estimate the percentage of confined water by fitting to the measured experimental values of a saturated 0.3 w/c paste. The permeability was estimated by considering the kozeny Carmen equation.

In the prior analysis, the EM wave is assumed to entirely dissipate. This includes the reflection between the next interface (i.e., concrete-subgrade) dissipating through the concrete layer before reaching the concrete/air interface.

Dielectric relaxation mechanisms of porous medium identified include bulk water relaxation, interfacial relaxation, and ionic relaxation. Bulk water relaxation is due to the rotation of water molecules in the bulk water, presumably not affected by interfaces. Interfacial polarization occurs when water molecules restrained in confined spaces relax at a different rate than those of bulk water. Ionic relaxation occurs at low frequencies.

REFERENCES

[1] D. Wobschall, A Theory of the Complex Dielectric Permittivity of Soil Containing Water: The Semidisperse Model, Geoscience Electronics, IEEE Transactions on, 15 (1977) 49-58.

[2] F.D. Amico, C. Guattari, A. Benedetto, GPR Signal processing in frequency domain using Artificial Neural Network for water content prediction in unsaturated subgrade, in: Ground Penetrating Radar (GPR), 2010 13th International Conference on, 2010, pp. 1-6.

[3] A. Benedetto, F. Benedetto, Remote Sensing of Soil Moisture Content by GPR Signal Processing in the Frequency Domain, Ieee Sens J, 11 (2011) 2432-2441.

[4] M. Charlton, Characterization of ground-penetrating radar (GPR) response in a variety of Earth materials under different moisture conditions, in: C. Nguyen (Ed.), SPIE, San Diego, CA, USA, 2001, pp. 288-299.

[5] W.L. Lai, W.F. Tsang, H. Fang, D. Xiao, Experimental determination of bulk dielectric properties and porosity of porous asphalt and soils using GPR and a cyclic moisture variation technique, Geophysics, 71 (2006) K93-K102.

[6] S. Laurens, J.P. Balayssac, J. Rhazi, G. Klysz, G. Arliguie, Non-destructive evaluation of concrete moisture by GPR: experimental study and direct modeling, Mater Struct, 38 (2005) 827-832.

[7] T. Saarenketo, T. Scullion, Road evaluation with ground penetrating radar, J Appl Geophys, 43 (2000) 119-138.

[8] M.N. Soutsos, J.H. Bungey, S.G. Millard, M.R. Shaw, A. Patterson, Dielectric properties of concrete and their influence on radar testing, Ndt&E Int, 34 (2001) 419-425.

[9] J.A. Huisman, S.S. Hubbard, J.D. Redman, A.P. Annan, Measuring Soil Water Content with Ground Penetrating Radar: A Review, Vadose Zone Journal, 2 (2003) 476-491.

[10] G.C. Topp, J.L. Davis, A.P. Annan, Electromagnetic Determination of Soil-Water Content—Measurements in Coaxial Transmission-Lines, Water Resour Res, 16 (1980) 574-582.

[11] K. Grote, S. Hubbard, Y. Rubin, Field-scale estimation of volumetric water content using ground-penetrating radar ground wave techniques, Water Resour Res, 39 (2003).

[12] N. Miura, N. Shinyashiki, S. Yagihara, M. Shiotsubo, Microwave dielectric study of water structure in the hydration process of cement paste, J Am Ceram Soc, 81 (1998) 213-216.

[13] U.B. Halabe, A. Sotoodehnia, K.R. Maser, E.A. Kausel, Modeling the Electromagnetic Properties of Concrete, Aci Mater J, 90 (1993) 552-563.

[14] C.A. Jones, Z.C. Grasley, Correlation of Radial Flow-Through and Hollow Cylinder Dynamic Pressurization Test for Measuring Permeability, Journal of Materials in Civil Engineering, 21 (2009) 594-600.

[15] C.A. Jones, Z.C. Grasley, Correlation of hollow and solid cylinder dynamic pressurization tests for measuring permeability, Cement and Concrete Research, 39 (2009) 345-352.

[16] C.A. Jones, Z.C. Grasley, Novel and Flexible Dual Permeability Measurement Device for Cementitious Materials, Aci Mater J, 106 (2009) 192-197.

[17] P.A.M. Basheer, E. Nolan, Near-surface moisture gradients and in situ permeation tests, Constr Build Mater, 15 (2001) 105-114.

[18] K.A. Snyder, X. Feng, B.D. Keen, T.O. Mason, Estimating the electrical conductivity of cement paste pore solutions from OH-, K+ and Na+ concentrations, Cement and Concrete Research, 33 (2003) 793-798.

[19] T. Meissner, F.J. Wentz, The complex dielectric constant of pure and sea water from microwave satellite observations, Ieee T Geosci Remote, 42 (2004) 1836-1849.

[20] A.K. Jonscher, Dielectric relaxation in solids, J Phys D Appl Phys, 32 (1999) R57-R70.

[21] Y. Feldman, A. Puzenko, Y. Ryabov, Dielectric Relaxation Phenomena in Complex Materials, in: Fractals, Diffusion, and Relaxation in Disordered Complex Systems, John Wiley & Sons, Inc., 2005, pp. 1-125.

[22] J.A. Lane, J.A. Saxton, Dielectric Dispersion in Pure Polar Liquids at Very High Radio Frequencies. III. The Effect of Electrolytes in Solution, Proceedings of the Royal Society of London Series A, Mathematical and Physical Sciences, 214 (1952) 531-545.

[23] W. Ho, W.F. Hall, Measurements of the Dielectric Properties of Seawater and NaCl Solutions at 2.65 GHz, J Geophys Res, 78 (1973) 6301-6315.

[24] H.J. Liebe, G.A. Hufford, T. Manabe, A Model for the Complex Permittivity of Water at Frequencies Below 1 Thz, Int J Infrared Milli, 12 (1991) 659-675.

[25] W. Ellison, A. Balana, G. Delbos, K. Lamkaouchi, L. Eymard, C. Guillou, C. Prigent, New permittivity measurements of seawater, Radio Sci, 33 (1998) 639-648.

[26] C. Guillou, W. Ellison, L. Eymard, K. Lamkaouchi, C. Prigent, G. Delbos, G. Balana, S.A. Boukabara, Impact of new permittivity measurements on sea surface emissivity modeling in microwaves, Radio Sci, 33 (1998) 649-667.

[27] J.R. Wang, A comparison of the MIR-estimated and model-calculated fresh water surface emissivities at 89, 150, and 220 GHz, Geoscience and Remote Sensing, IEEE Transactions on, 40 (2002) 1356-1365.

[28] Y. Feldman, A. Gutina, E. Axelrod, A. Puzenko, E. Rysiakiewicz-Pasek, N. Kozlovich, Dielectric relaxation of porous glasses, J Non-Cryst Solids, 235 (1998) 302-307.

[29] F. Kremer, A. Huwe, P. Behrens, W. Schwieger, Molecular dynamics in confining space: From the single molecule to the liquid state, Phys Rev Lett, 82 (1999) 2338-2341.

[30] Y. Feldman, Y. Ryabov, A. Gutina, V. Arkhipov, Dielectric relaxation of water absorbed in porous glass, J Phys Chem B, 105 (2001) 1845-1850.

[31] L.J. Michot, F. Villieras, M. Francois, I. Bihannic, M. Pelletier, J.M. Cases, Water organisation at the solid-aqueous solution interface, Cr Geosci, 334 (2002) 611-631.

[32] A. Spanoudaki, B. Albela, L. Bonneviot, M. Peyrard, The dynamics of water in nanoporous silica studied by dielectric spectroscopy, Eur Phys J E, 17 (2005) 21-27.

[33] G.P. deLoor, The Dielectric-Properties of Wet Materials, Ieee T Geosci Remote, 21 (1983) 364-369.

[34] T. Ishida, T. Makino, C.J. Wang, Dielectric-relaxation spectroscopy of kaolinite, montmorillonite, allophane, and imogolite under moist conditions, Clay Clay Miner, 48 (2000) 75-84.

[35] K. Gorur, M.K. Smit, F.H. Wittmann, Microwave Study of Hydrating Cement Paste at Early Age, Cement and Concrete Research, 12 (1982) 447-454.

[36] P. Gu, J.J. Beaudoin, Dielectric behaviour of hardened cement paste systems, J Mater Sci Lett, 15 (1996) 182-184.

[37] N.E. Hager, R.C. Domszy, Monitoring of cement hydration by broadband time-domain-reflectometry dielectric spectroscopy, J Appl Phys, 96 (2004) 5117-5128.

[38] F.H. Wittmann, F. Schlude, Microwave absorption of hardened cement paste, Cement and Concrete Research, 5 (1975) 63-71.

[39] J.C. Maxwell, W. Garnett, An elementary treatise on electricity, At the Clarendon Press, Oxford, 1881.

[40] P.J.W. Debye, The collected papers of Peter J. W. Debye, Interscience Publishers, New York, 1954.

[41] R. Hill, The elastic behaviour of a crystalline aggregate, Proceedings of the Physical Society Section A, 65 (1952) 349-354.

[42] Z. Hashin, S. Shtrikman, Variational approach to theory of elastic behaviour of multiphase materials, Journal of Mechanics and Physics of Solids, 11 (1963) 127-140.

[43] L.V. Gibiansky, G.W. Milton, On the Effective Viscoelastic Moduli of 2-Phase Media .1. Rigorous Bounds on the Complex Bulk Modulus, P Roy Soc Lond a Mat, 440 (1993) 163-188.

[44] D.J. Bergman, Rigorous Bounds for the Complex Dielectric-Constant of a 2-Component Composite, Ann Phys-New York, 138 (1982) 78-114.

[45] G.W. Milton, The theory of composites, Cambridge University Press, Cambridge; New York, 2002.

[46] D.A.G. Bruggeman, Berechnung verschiedener physikalischer Konstanten von heterogenen Substanzen. I. Dielektrizitätskonstanten und Leitfähigkeiten der Mischkörper aus isotropen Substanzen, Annalen der Physik, 416 (1935) 636-664.

[47] D.V. Blackham, R.D. Pollard, An improved technique for permittivity measurements using a coaxial probe, Ieee T Instrum Meas, 46 (1997) 1093-1099.

[48] S. Lowell, J.E. Shields, Powder surface area and porosity, 3rd ed., Chapman & Hall, London; New York, 1991.

APPENDIX T
RADAR SPECIFICATIONS FOR AIR-COUPLED GPR ANTENNAS

These specifications are based on the ground penetrating radar (GPR) reflection from a large metal plate. A typical metal plate reflection (MPF) is shown in the upper part of Figure T-1. The amplitude of reflection (i.e., volts) is measured from the maximum positive peak to the preceding negative. No filtering, averaging, or signal clean up, such as sky wave removal (and reflection subtraction), is allowed.

Performance specifications are as follows:

1. Noise-to-Signal Ratio Test: The antenna will be positioned at its recommended operating height (between 12 and 18 inches) above a minimum square foot (4' x 4') metal plate. The radar unit shall be turned on and allowed to operate for a 15-min warm-up period. After warm up, the unit shall be operated at maximum pulse rate, and fifty (50) radar waveform pulses shall be recorded. The recorded waveforms shall then be evaluated for noise-to-signal ratio. The noise-to-signal ratio is described by the following equation:

$$\frac{Noise\ Level\ (A_n)}{Signal\ Level\ (A_{mp})} \leq 0.05\ (5\%)$$

The signal level, A_{mp}, is defined as the average metal plate reflection amplitude as measured from the peak to the preceding minimum. The noise level, A_n, is defined as the worst-case maximum amplitude occurring between 1 and 10 ns after the surface echo. The noise level is measured from any positive peak to either the preceding or trailing negative, whichever is greater. The noise-to-signal ratio shall be less than or equal to 0.05 (5 percent).

2. Signal Stability Test: The same test configuration shall be used as described in the Noise-to-Signal Ratio Test. Fifty (50) traces shall be recorded at the minimum data rate of 25 traces per second. The signal stability shall be evaluated using the following equation:

T-1

$$\frac{A_{max} - A_{min}}{A_{AVG}} \leq 0.01(1\%)$$

where A_{max} is defined as the maximum amplitude for all 50 traces, A_{min} is defined as the minimum amplitude for all 50 traces, and A_{AVG} is defined as the average trace amplitude of all 50 traces.

The signal stability test results for the GPR shall be less than or equal to 1 percent.

3. Long-Term Signal Stability: The same test configuration shall be used as described in the Noise-to-Signal Ratio Test. The radar shall be switched on with no warm up and allowed to operate for 2 hours continuously. As a minimum, a single waveform shall be captured every 2 min, 60 in total. The amplitude of reflection shall be calculated and plotted against time. To check for signal drift, the time at which the metal plate reflection occurs shall be captured and plotted against time. For the system to be performing adequately, the amplitude should remain constant after a short warm-up period, and the system should have little or no drift.

The stability criterion is as follows:

$$\frac{A_{any} - A_{20}}{A_{20}} \leq 0.03\,(3\%)$$

where A_{20} is the amplitude measured at 20 min, and A_{any} is any amplitude measured after 20 min.

The drift criterion is as follows:

$$\frac{t_{any} - t_{20}}{t_{20}} \leq 0.05\,(5\%)$$

where t_{20} is the time when the peak metal plate reflection occurs at 20 min, and t_{any} is the time when the MPR occurs in any trace after 20 min.

4. Variations in Time Calibration Factor: The same test configuration shall be used as described in the Noise-to-Signal Ratio Test. Fifty(50) traces shall be collected, and the height of the antenna shall be measured. The test shall be repeated at two other heights. Typically, heights of approximately 12 inches, 16 inches, and 20 inches are used. The time delay from the end reflection at the tip of the antenna to the metal plate reflection shall be is measured for each trace, and their mean is time t_i (where the subscript represents height position at i). The difference between t_2 and t_1 represents the time to travel a fixed distance in air. For bistatic antennas, the travel distance must be calculated based on the system geometry. The factor C_1 is

calculated by dividing the distance by the time difference (e.g., inches per nanosecond). The factor C_2 represents the same between heights 2 and 3. The variation in time calibration factor is as shown below:

$$\frac{C_1 - C_2}{\text{Mean of } C_1 \text{ and } C_2} \leq 0.02 \, (2\%)$$

The variation in time calibration factor shall be less than or equal to 2 percent.

5. End Reflection Test: The same test configuration and results from the Noise-to-Signal Ratio Test shall be used. The amplitude of the end reflection directly preceding the metal plate reflection shall be measured. This is a measure of the adequacy of system tuning. The size of the end reflection shall be:

$$\frac{A_E}{A_{mp}} < 0.15 \, (15\%)$$

where A_E is the mean of the amplitude of end reflection defined as any peak occurring from 1 to 5 ns before the metal plate reflection, and A_{mp} is the mean of the amplitude of reflection from the metal plate.

The end reflection in the metal plate test shall be less than 15 percent of the amplitude of the metal plate reflection.

6. Symmetry of Metal Plate Reflection: The same test configuration as used in the Noise-to-Signal Ratio Test shall be used. Two different criteria have been established for symmetry, as described below:

6.1. The first criterion is that the time from the maximum negative peak following the surface reflection to the zero crossing point shall be measured. This time (t_f) is shown in Figure T-1. The required specification is:

$$t_f \leq 0.7ns$$

An example of metal plate reflections that pass and fail this specification are shown in Figure T-1.

6.2. The second criterion is based on the symmetry of the legs of the metal plate reflection. The amplitude is measured from the positive peak to both the preceding and trailing negative. The specification is:

$$A_{min}/A_{max} > .95 \, (95\%)$$

T-3

where A_{min} and A_{max} are the minimum and maximum metal plate reflections measured using the preceding or trailing negatives. The ratio should be at least 95 percent.

7. Concrete Penetration Test: The antenna shall be placed at its recommended operating height above a 6-inch-thick concrete block. The concrete block shall be non-reinforced, have a minimum age of 28 days, and have a minimum 3000 psi compressive strength. The block shall be 3 ft (36 inches) by 3 ft (36 inches) or greater to ensure that all the GPR energy enters the concrete. The concrete block shall be placed on top of a metal plate. Two hundred traces shall be recorded. The reflection amplitude from the top and bottom of the concrete block shall be measured. The Concrete Penetration Test is defined by the following equation:

$$\frac{A_{bottom}}{A_{top}} \geq 0.25\,(25\%)$$

where A_{top} is the mean of the measured return amplitude from the top of the concrete slab, and A_{bottom} is the mean of the measured return amplitude from the metal plate.

The concrete penetration test results for the GPR should be greater than or equal to 25 percent.
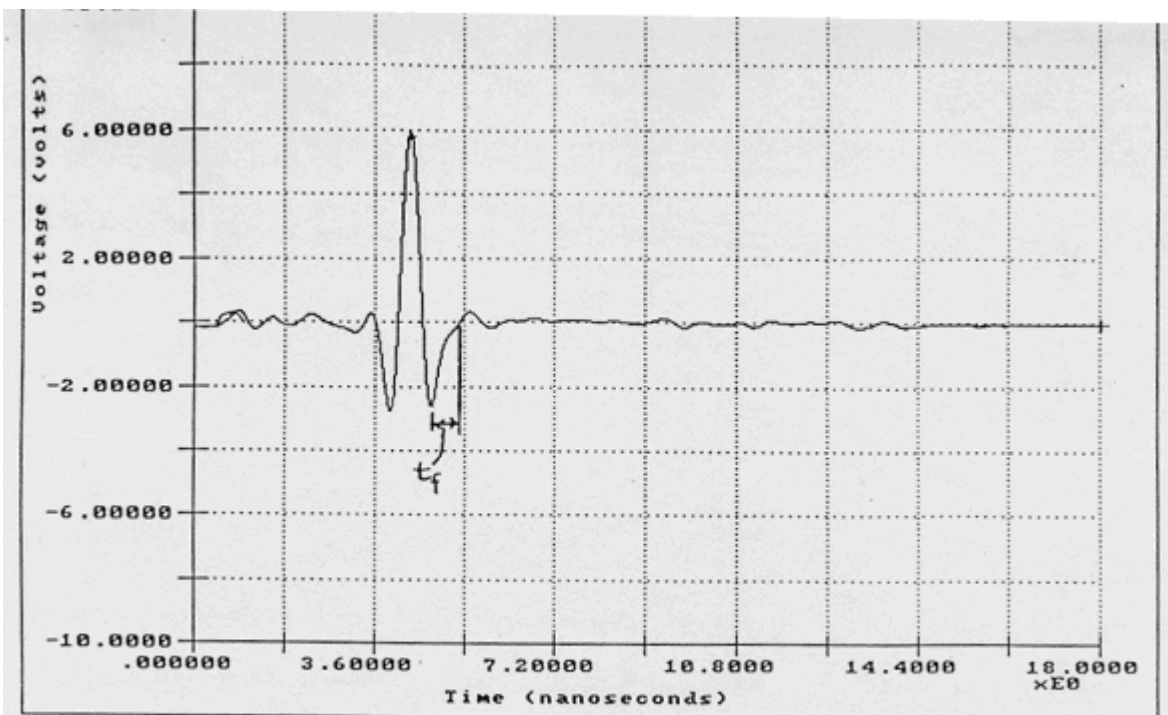
Acceptable Metal Plate Reflection
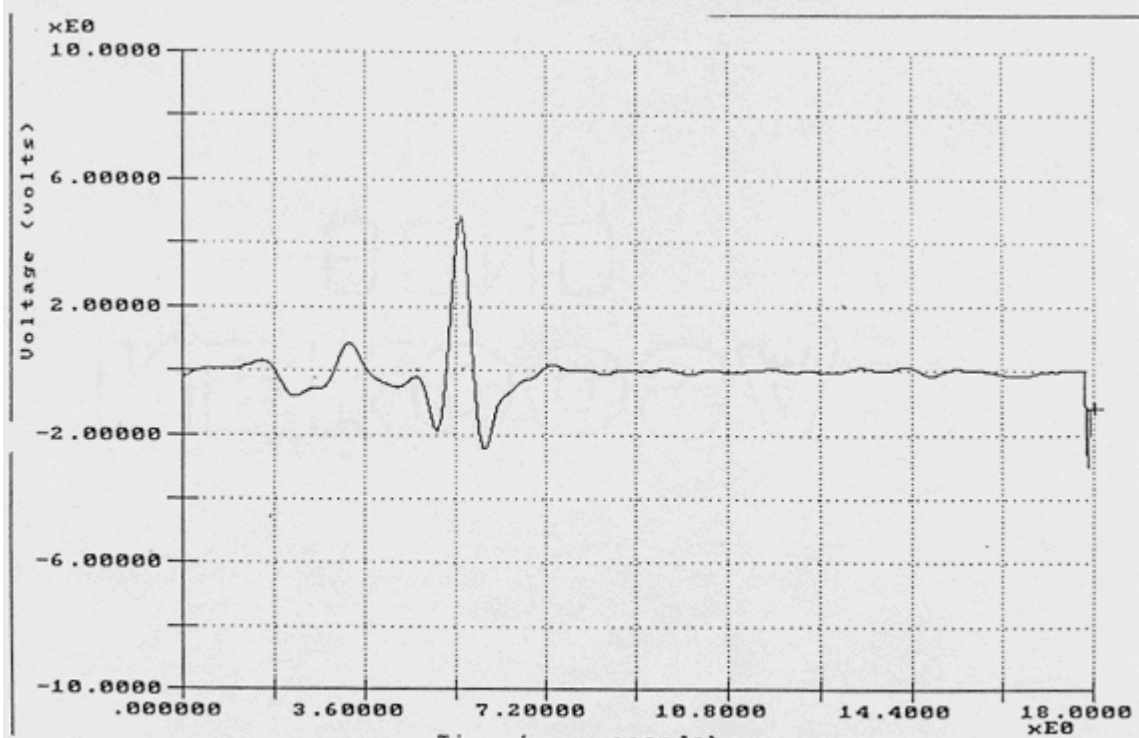
Unacceptable Metal Plate Reflection Fails Specification Tests 5 and 6.l

Figure T-1. Examples of acceptable and unacceptable metal plate reflections.

APPENDIX U
Evaluation of TEXAS A&M TRANSPORTATION INSTITUTE (TTI) SLABS WITH PORTABLE SEISMIC PROPERTY ANALYZER

INTRODUCTION

A survey of several concrete slabs was carried out with a Portable Seismic Property Analyzer (PSPA) within the framework of the second Strategic Highway Research Program (SHRP2) Project R06(G) on "Mapping Voids, Debonding, Delamination, Moisture, and Other Defects Behind or Within Tunnel Linings." The main objectives of that research project were:

- To identify promising nondestructive testing (NDT) technologies for evaluating the condition of various types of tunnel linings.
- To evaluate the applicability, accuracy, precision, repeatability, ease of use, testing duration, and costs of the identified technologies.
- To conduct the required development in hardware or software for promising techniques.
- To validate the selected technologies.

Eleven concrete slabs and 13 shotcrete slabs were involved in this study. The concrete slabs were evaluated on November 9 and 10, 2011, and the shotcrete slabs were assessed on November 10 and 11, 2011. The scope of this University of Texas at El Paso (UTEP) study was to evaluate the performance of the PSPA in locating defects inside concrete. The dimensions of the slabs and defects are more optimized toward the application of ground penetrating radar (GPR).

Given the desire of SHRP2 to develop user-friendly devices, the results presented here are as reported by the PSPA in the current state without further advanced analyses using an experienced expert analyst. The lessons learned are being incorporated in the new version of the PSPA under development.

DESCRIPTION OF PSPA AND TESTING METHODS

PSPA is a portable device that can perform two tests (impact echo [IE] and ultrasonic surface wave [USW]) simultaneously. The PSPA consists of two receivers and a source packaged into a handheld portable device. The near and far receiver spacing from the source are 4 and 10 inches, respectively. The impact duration (contact time) is about 60 μs, and the data acquisition system has a sampling frequency of 390 kHz. The advantage of combining these two methods in a single device is that once the test is performed, the variations in the modulus (an indication of the quality of concrete) and return resonance frequency (an indication of the full thickness or depth of delamination) of a slab can be assessed concurrently. The following sections discuss the principles of the two seismic methods, along with interpretation approaches.

Impact Echo Method

The IE method is one of the most commonly used NDT methods in detecting delamination in concrete (Carino et al. 1986). This method is based on impacting a plate-like object such as a tunnel lining with an impactor that generates stress waves at frequencies of up to 20 to 30 kHz and collecting signals by a receiver (Figure U-1a). By using a fast Fourier transform (FFT) algorithm, the recorded time domain signal is converted into a frequency domain function (amplitude spectrum) and the peak frequency is monitored. For an intact point on a slab or an intact portion of a slab, the thickness (h) is then determined from the compression wave velocity (V_p) and the return frequency (f):

$$h = \alpha \frac{V_p}{2f} \tag{U-1}$$

where α is about 0.96 for concrete slabs.

For a deep and relatively small delaminated location in a concrete slab, the return frequency may shift to a higher frequency corresponding to the depth of the delamination. As shown in Figure U-1b, a shallow or a deep but extensive and severe delaminated area is usually manifested by a low peak frequency, indicating that little or no energy propagates toward the bottom of the deck and a flexural mode dominates the frequency response. In this case, Eq. (U-1) is not applicable to measure the depth of delamination since it is influenced by several factors.

(a) IE method
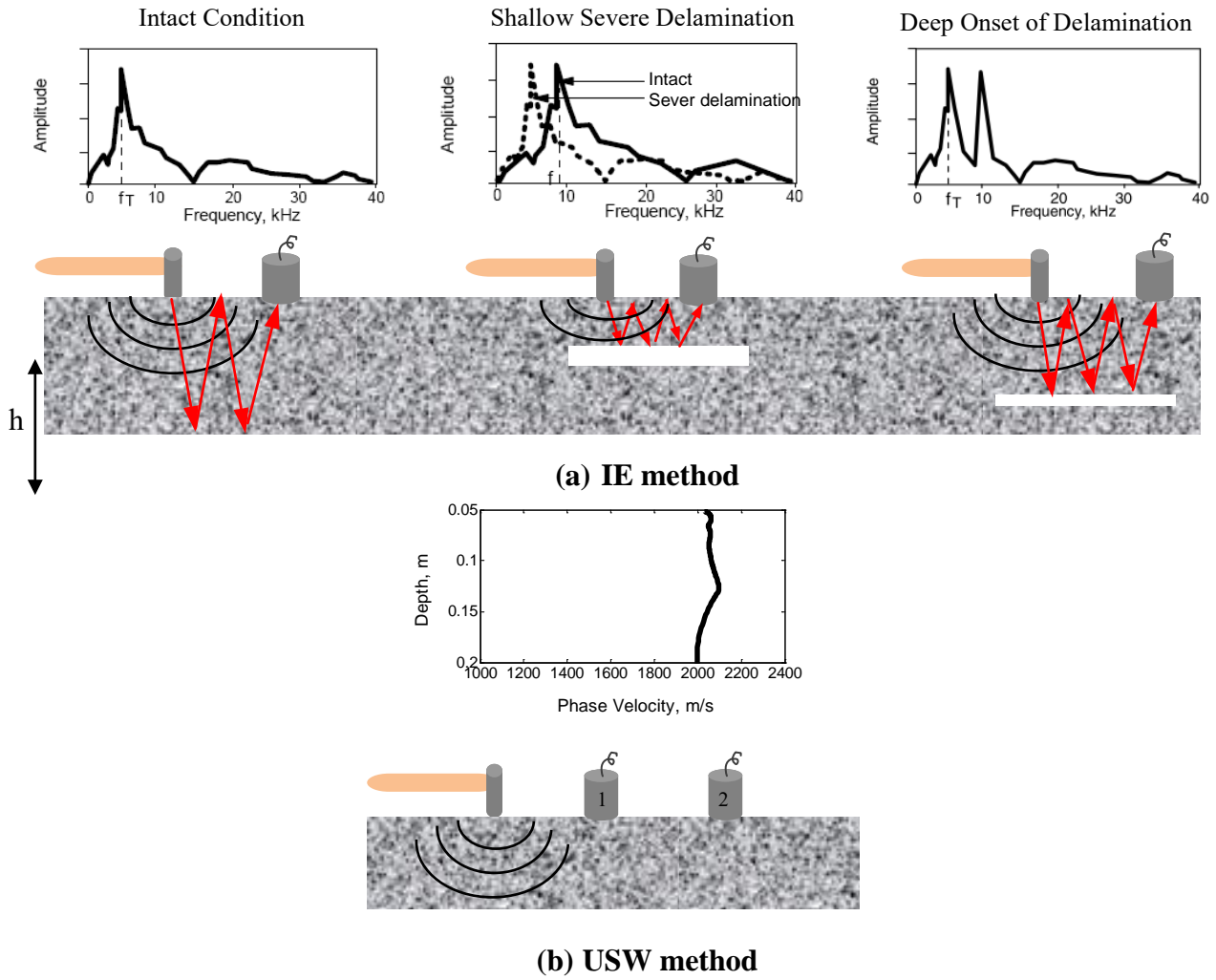
(b) USW method
Figure U-1. Schematic illustration of the test methods (Gucunski and Maher 1998).

Ultrasonic Surface Waves Method

The USW method is used to estimate the average velocity of propagation of surface waves in a medium, based on the time at which different types of energy arrive at each sensor (Figure U-1b). The velocity of propagation, V_R, is typically determined by dividing the distance between two receivers, ΔX, by the difference in the arrival time of a specific wave, Δt. Knowing the wave velocity, the modulus can be determined from shear modulus, G, through Poisson's ratio (v) using:

$$E = 2(1+v)G \qquad \text{(U-2)}$$

Shear modulus can be determined from shear wave velocity, V_S, using:

$$G = \frac{\gamma}{g}V_S^2 \qquad \text{(U-3)}$$

The modulus from surface wave velocity, V_R, first converted to shear wave velocity can be determined by:

$$V_S = V_R(1.13 - 0.16\nu) \qquad\qquad (U\text{-}4)$$

In the USW method, the variation in velocity with wavelength is measured to generate a so-called dispersion curve. For a uniform or intact concrete slab, the dispersion curve shows more or less a constant velocity within the wavelengths nor greater than the thickness of the slab. When a delamination or void is present in a concrete slab or the concrete is deteriorated, the average surface wave velocity (or modulus) becomes less than the actual one due to the interference caused by the defect. In this case, the velocity or modulus obtained may be called an apparent velocity or modulus.

DESCRIPTION OF SLABS

An overall view of the test slabs is shown in Figure U-2, and their characteristics are summarized in Table U-1. Two sets of slabs were tested in this study. Each slab was 6 ft by 6 ft in dimension. The first set of specimens included six intact concrete slabs with thicknesses of 12, 15, 18, and 24 inches, and three defective 15-inch-thick slabs with embedded 1 ft by 1 ft delaminated zones in the center of the slabs. The last three slabs contained defects at depths of 1, 2, and 3 inches from the top surface. Two other concrete slabs in this set were 15 inches thick with embedded air voids and water voids at a depth of 8 inches.

The second set of slabs was shotcrete slabs that included four intact slabs with thicknesses of 4, 6, 8, and 12 inches and five 12-inch-thick delaminated slabs. The 1 ft by 1 ft delaminated areas were embedded at the center of each slab at depths of 1, 2, 3, 4, and 8 inches from the top surface. Four other shotcrete slabs contained air voids and water voids with different sizes at different depths.

Figure U-2. Overall view of TTI slabs.

Table U-1. Characteristics of TTI slabs.

Slab Information		Thickness (inches)	Type of Defect	Size of Defect (ft x ft)	Depth of Defect (inches)
Concrete	Slab # 1	12	intact	N/A	N/A
	Slab # 2	18	intact	N/A	N/A
	Slab # 3	12	intact	N/A	N/A
	Slab # 4	24	intact	N/A	N/A
	Slab # 5	24	intact	N/A	N/A
	Slab # 6	15	intact	N/A	N/A
	Slab # 7	15	delamination	12 x 12	2
	Slab # 8	15	delamination	12 x 12	3
	Slab # 9	15	delamination	12 x 12	1
	Slab # 10	15	air void	12 x 12	8
	Slab # 11	15	water void	12 x 12	8
Shotcrete	Slab # 1	4	intact	N/A	N/A
	Slab # 2	6	intact	N/A	N/A
	Slab # 3	8	intact	N/A	N/A
	Slab # 4	12	air void	12 ⅛ x 9 ¾, 17 ¼ x 14 ¾*	7.5
	Slab # 5	12	water void	11 x 10 ½, 15 ¾ x 14 ½*	7.5
	Slab # 6	12	air void	12 ¼ x 12, 14 ¾ x 17 ⅛*	3
	Slab # 7	12	water void	10 ½ x 10 ½, 15 ½ x 14 ¼ *	3
	Slab # 8	12	delamination	12 x 12	8
	Slab # 9	12	delamination	12 x 12	4
	Slab # 10	12	delamination	12 x 12	3
	Slab # 11	12	delamination	12 x 12	2
	Slab # 12	12	delamination	12 x 12	1
	Slab # 13	12	intact	N/A	N/A

*The first set of numbers indicates the void, and the second set indicates the bag that encapsulates the void.

DATA COLLECTION PROCESS

The testing schemes of different slabs are shown in Figure U-3. Every intact slab was assessed through 11 testing lines equally spaced at 4 inches apart. On each line, 11 points were tested at every 4 inches. Therefore, 121 data points were collected for each intact slab (Figure U-3a). A similar scheme was used for the defective slabs except that data were collected at 143 points, as shown in Figure U-3b. It took about 1 hr to test each slab and about 30 min to interpret and develop the contour maps.

At each point, the PSPA source was placed on the grid point. For reporting the IE results, the coordinate was shifted 2 inches (half the distance between the source and Receiver 1). For the USW results, the coordinate was shifted 7 inches (half the distance between the two receivers and the source).

a) **Intact slabs**   b) **Defected slabs**
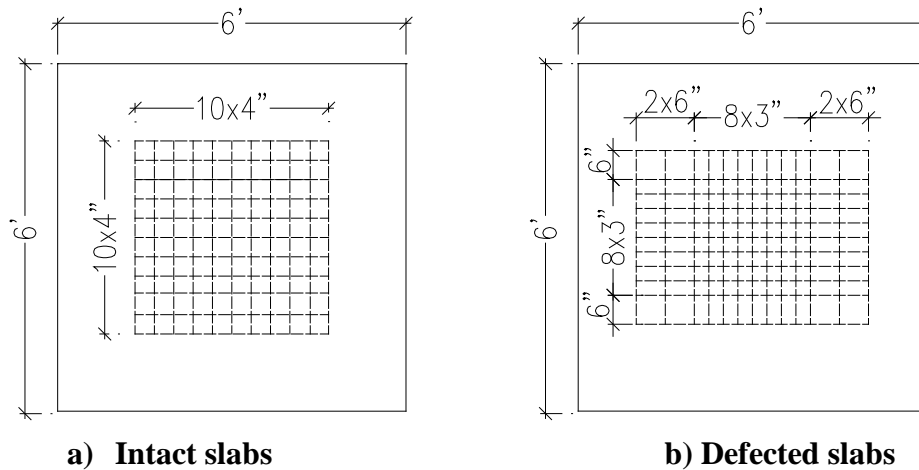
Figure U-3. Testing schemes of different slabs.

TEST RESULTS

A detailed description of the data reduction process was provided in a companion report related to testing in actual tunnels in Colorado and Virginia. As such, they are not repeated here.

Intact Concrete Slabs

Figure U-4 contains the results from Slab 1. Figure U-4a is a picture of the slab on the day of testing. The slab was visually uniform with a smooth finish.

The acquired waveforms from the two PSPA receivers at the center point of the slabs are shown in Figure U-4b. Due to the size of the specimens, reflections from the vertical boundaries are apparent in the later portions of the signals. The PSPA software contains appropriate filters to minimize the impact of these reflections as long as the PSPA is located at an adequate distance from the boundary.

Since the IE and USW methods used in this study are point inspection methods, it was more effective to visualize the results in contour maps rather than evaluate them individually. The contour map of the variations in the average modulus (from a depth of 2 inches to nominal thickness of the slab) from the USW tests is shown in Figure U-4c. The slab exhibited a fairly uniform modulus. The average modulus of the slab was 6400 ksi with a standard deviation of about 375 ksi. Similarly, the contour map of the dominant return frequency from the IE method, as shown in Figure U-4d, was also uniform.

Besides the planar contour maps, the USW and IE linescans (B-Scans) along the centerline are shown in Figure U-4. The USW B-Scan (Figure U-4e) is in the form of variation in modulus with wavelength, which can qualitatively be viewed as a scaled variation of modulus with depth. In this case, the variation in modulus with depth is small. The spectral B-Scan of the IE results (Figure U-4f) is in the form of variation of normalized amplitude with frequency. Throughout the width of the slab, a frequency of about 7.7 kHz (manifested as a red band) corresponds to the 12-inch thickness of the slab. The thickness reported from IE tests was 11.9 inches with a standard deviation of 0.8 inches.
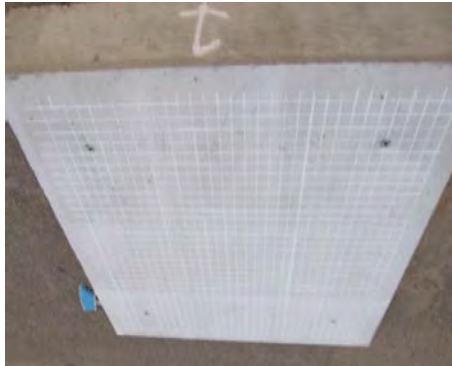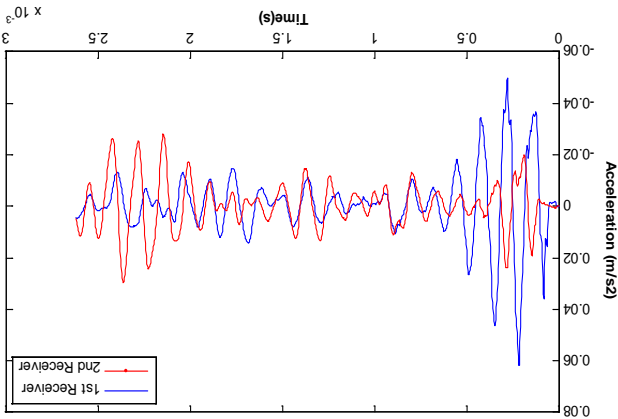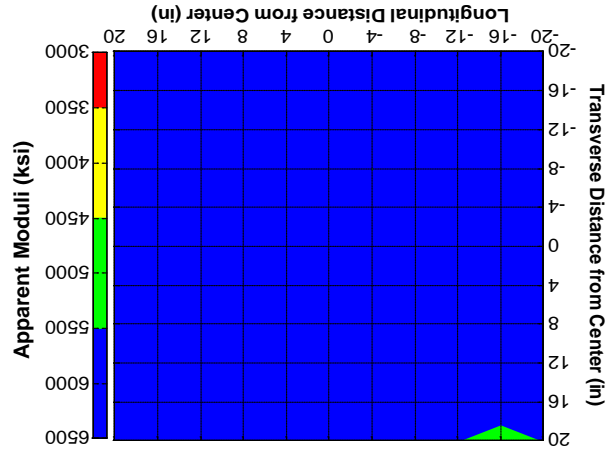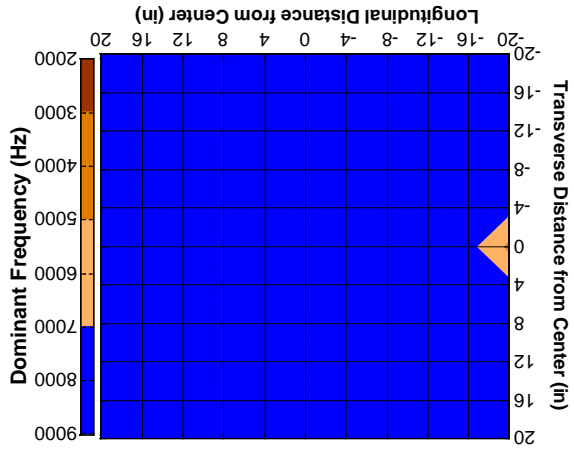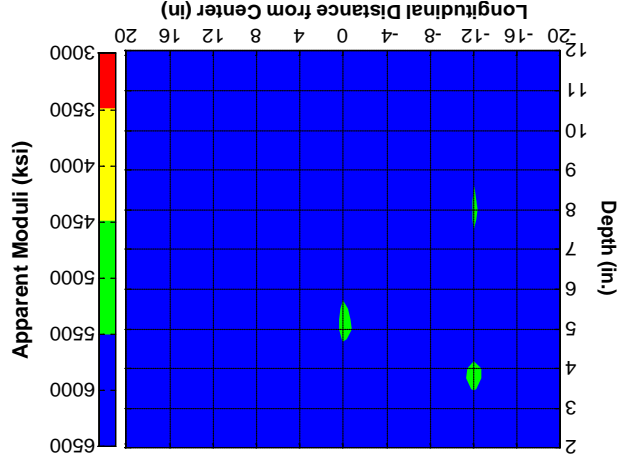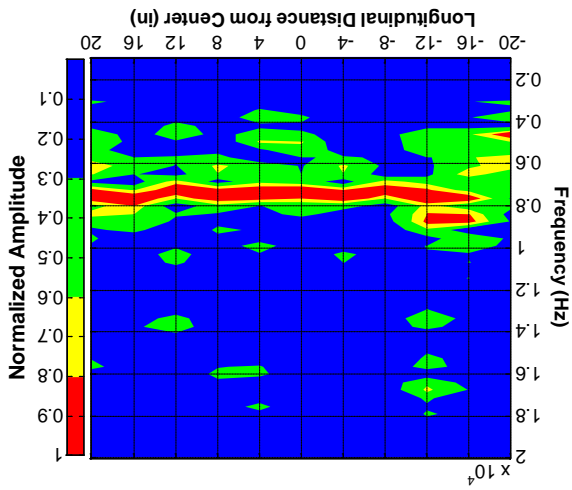
Figure U-4. Contour maps of the acquired results from USW and IE tests for concrete slab #1 (12-inch-thick intact slab).
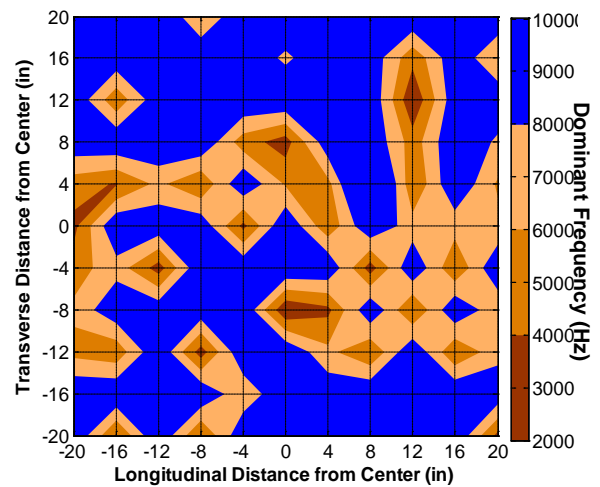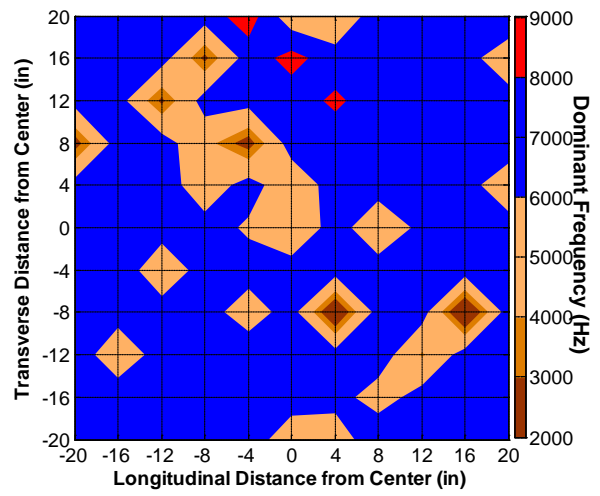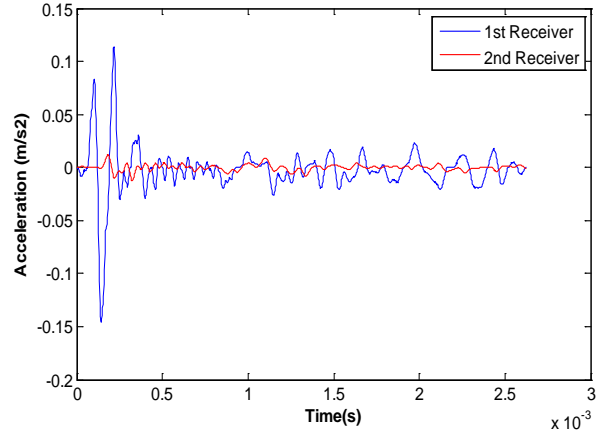
(f) IE Spectral B-Scan along center line

(e) USW B-Scan along center line

(d) Dominant frequency from IE

(c) Average modulus from USW

(b) Waveform obtained from PSPA at center point

(a) Slab #1

Similar results from the second intact slab, Slab 2, are shown in Figure U-5. This slab was 18 inches thick and contained two cracks. The interaction between the cracks and seismic wave propagation is rather complex. When the source-receiver array is parallel to the crack, the USW modulus variation and the IE response spectrum are marginally impacted in the current software. When the crack is between the source and first receiver, the USW modulus is typically greater than normal because of the travel path of the wave. Similarly, when the crack is between the two sensors, the reported USW modulus is lower than normal. To maintain the regularity of the testing program, we chose to carry out the tests on a rigid grid and not adjust the location of the sensors to avoid the cracks. As reflected in Figure U-5c, the PSPA sensors crossed the cracks only at a few points. For example, at a coordinate of -4 inches in Figure U-5e, the crack is propagating deep. The average modulus of this slab was about 5980 ksi with a standard deviation of about 533 ksi. The IE thickness was about 16.3 inches, but as shown in Figure U-5f, the return frequency was very consistent, and with one core, the thickness could be readily calibrated to the actual thickness.

Slab 3 (Figure U-6) was supposed to be similar to Slab 1. However, a portion of the slab was of lower quality than the rest with some isolated defects. As such, the average modulus was about 5997 ksi with a standard deviation of about 750 ksi. The average thickness was about 11.4 inches.

Slabs 4 and 5 were both 24 inches thick. The IE method as configured in the PSPA cannot detect the thickness in excess of 18 inches. As such, the detection of the slab thickness was not possible for these two slabs, as reflected in Figures U-7d and U-7f and Figures U-8d and U8f. However, the quality of the concrete, except in isolated points, was high with average moduli of 5900 ksi.

Finally, the 15-inch-thick intact Slab 6 yielded an average modulus of 6220 ksi with a thickness of 14.2 inches (see Figure U-9).

Delaminated Concrete Slabs

Slab 7 was similar to Slab 6 with a delamination embedded at a depth of 2 inches from the top surface. A comparison of the time records in Figures U-9b and U-10b clearly demonstrates the differences in the time records from an intact area and a delaminated area. With a few days of experience, the operator can readily detect the delamination by simply looking at the time signals. The delaminated area is clearly detectable in both the USW results and IE results in Figures U-10c through U-10f.

The same statements can be made for the results from Slabs 8 and 9 (Figures U-11 and U-12) where the delaminated zones were at nominal depths of 3 inches and 1 inch. By comparing the amplitudes of the waveforms in Figures U-10b, U-11b, and U-12b, one can roughly estimate that the delamination in Slab 7 is shallower than the one in Slab 8 but deeper than the defect in Slab 9. The delamination in Slab 8 is readily approximated in both the USW results and IE results in Figures U-11c and U-11d. It seems that the inserted delamination in Slabs 7 and 8 moved slightly in the construction phase.

One unexpected result was observed for Slab 9 where the presence of the delamination was obvious from the amplitude of time records and the USW results but not reflected in the IE interpretation. This simply occurred because of the high-pass filters applied to the IE results. The vibration frequency was so low that it was eliminated from the signal. In the design of the PSPA, the assumption has been that a 1-inch-deep delamination can be readily detected by tapping, and a device may not be needed during field testing.
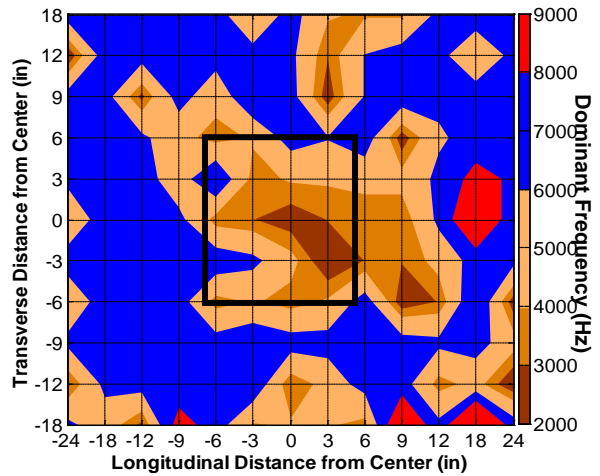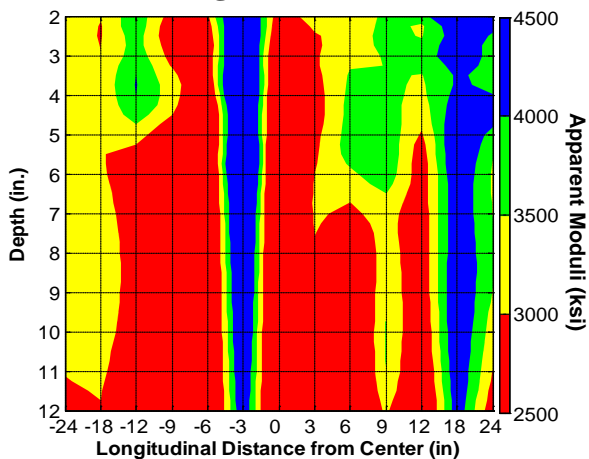
(a) Slab #2
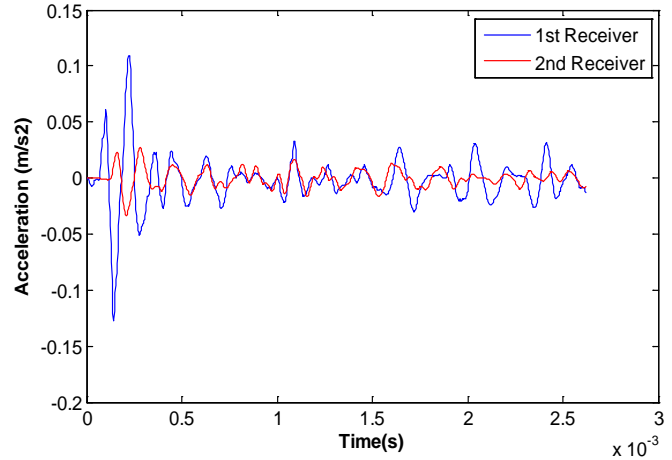
(b) Waveform obtained from PSPA at center point
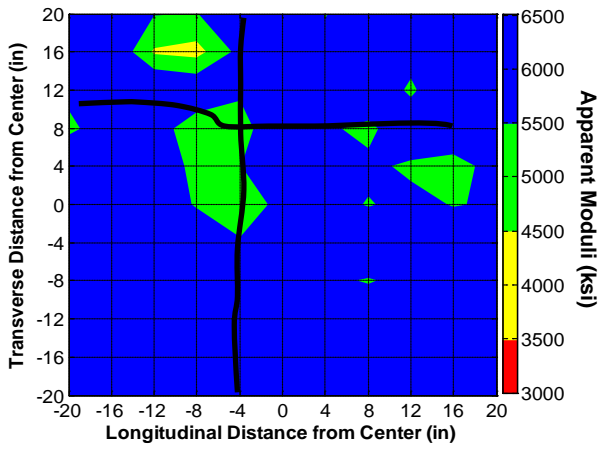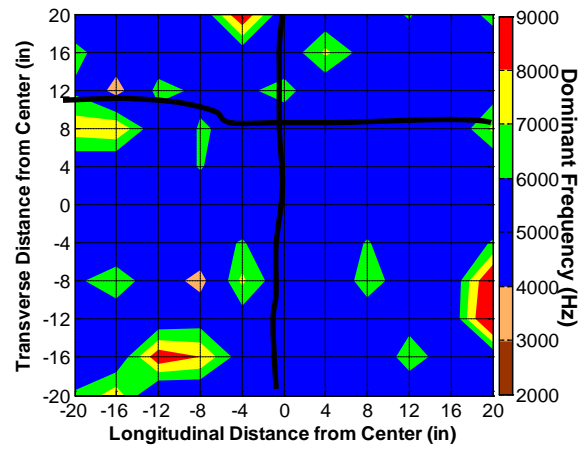
(c) Average modulus from USW

(d) Dominant frequency from IE
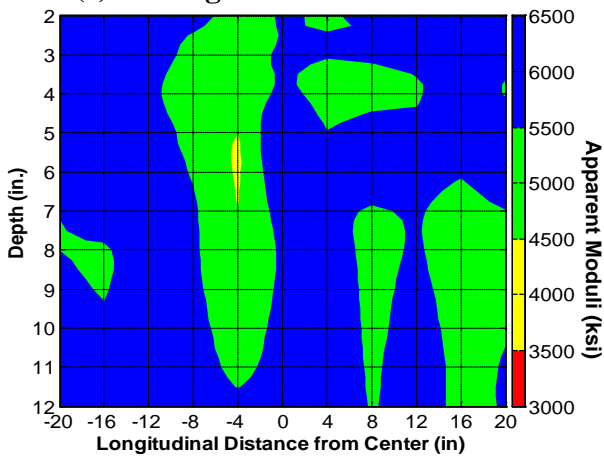
(e) USW B-Scan along center line
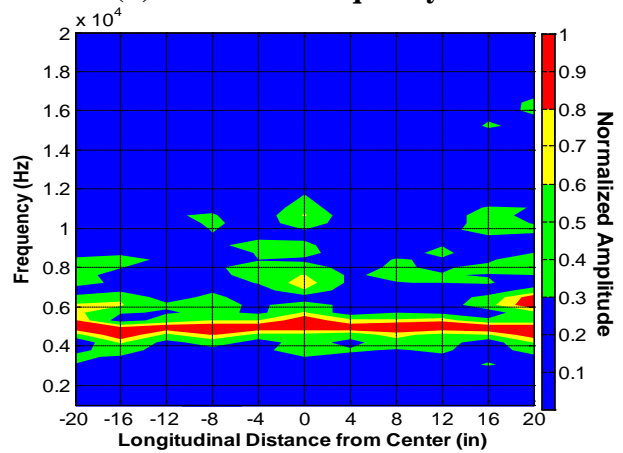
(f) IE Spectral B-Scan along center line

Figure U-5. Contour maps of the acquired results from USW and IE tests for concrete slab #2 (18-inch-thick intact slab).
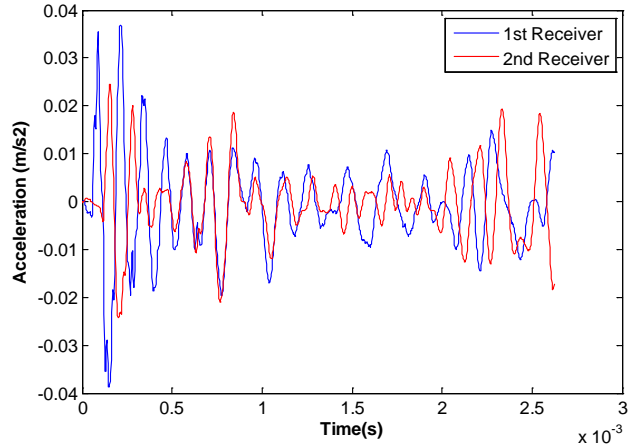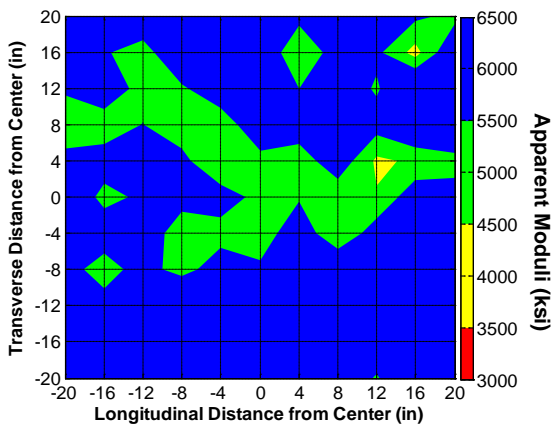
(a) Slab #3

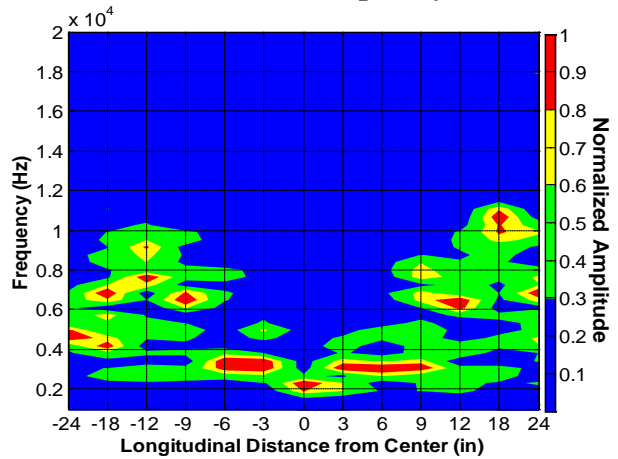(b) Waveform obtained from PSPA at center point

(c) Average modulus from USW
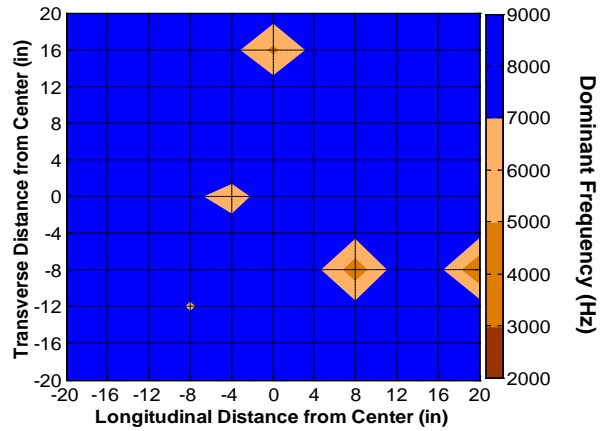
(d) Dominant frequency from IE
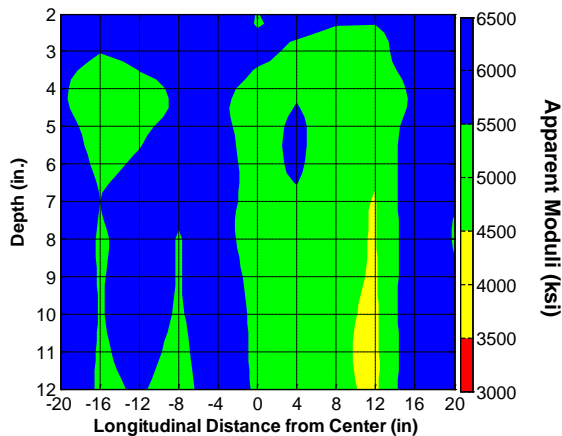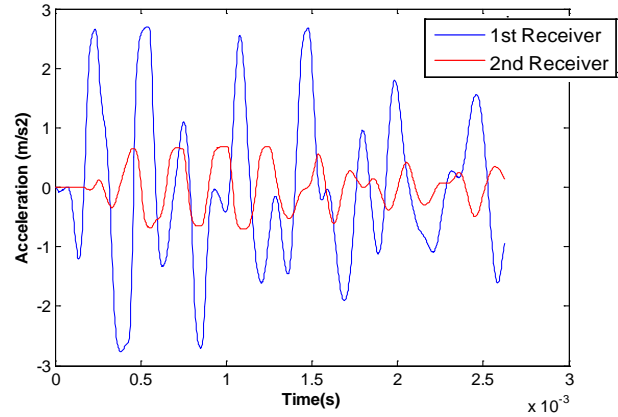

(e) USW B-Scan along center line
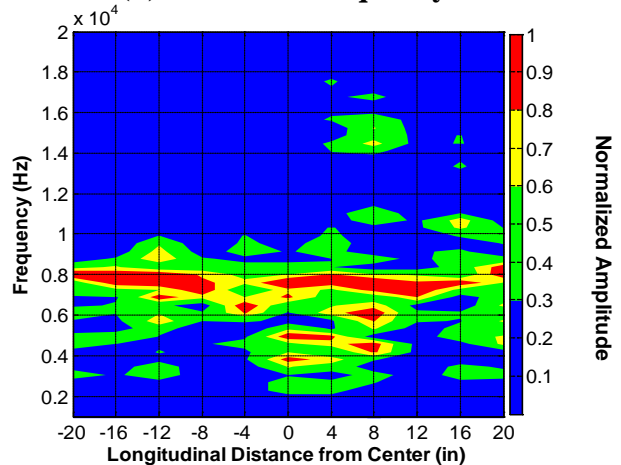
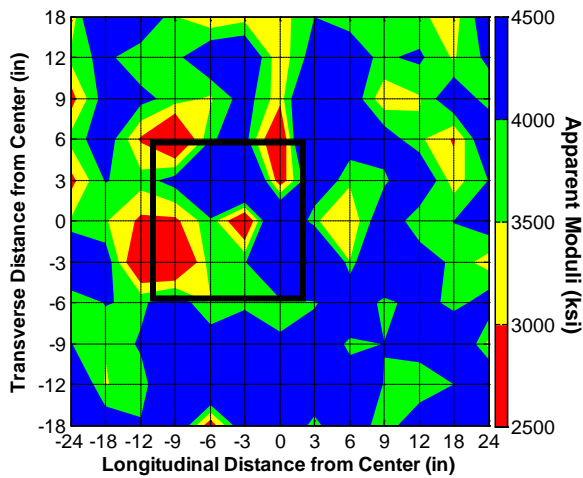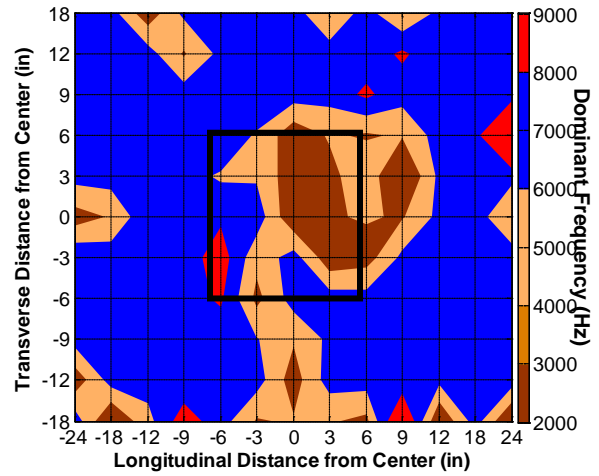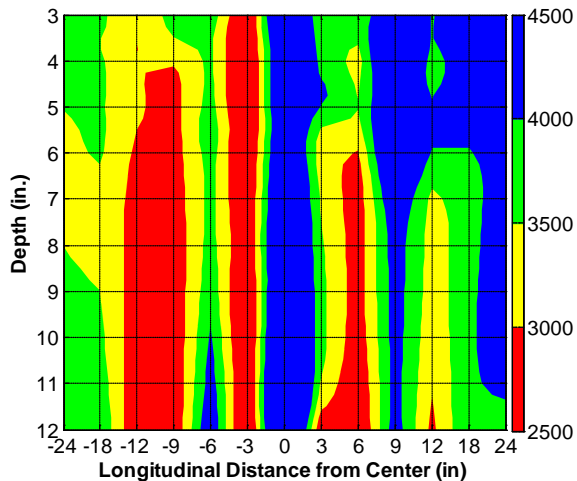(f) IE Spectral B-Scan along center line

Figure U-6. Contour maps of the acquired results from USW and IE tests for concrete slab #3 (12-inch-thick intact slab).

(a) Slab #4
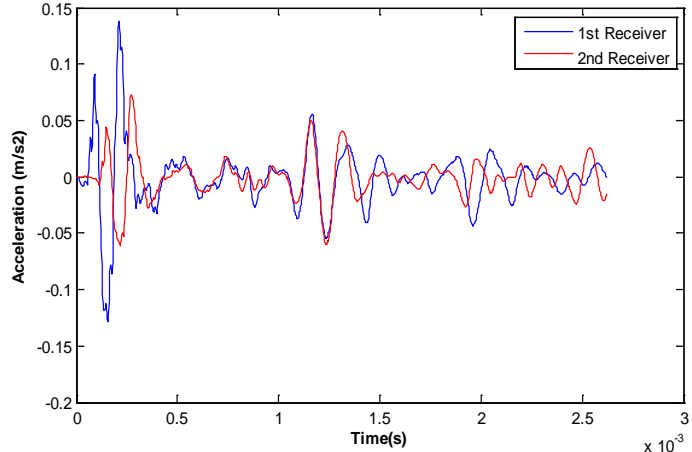
(b) Waveform obtained from PSPA at center point
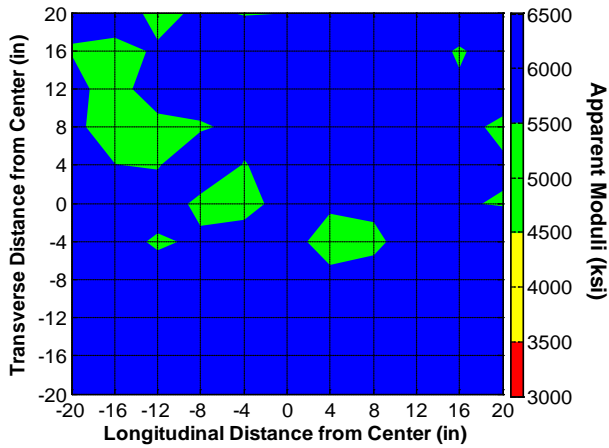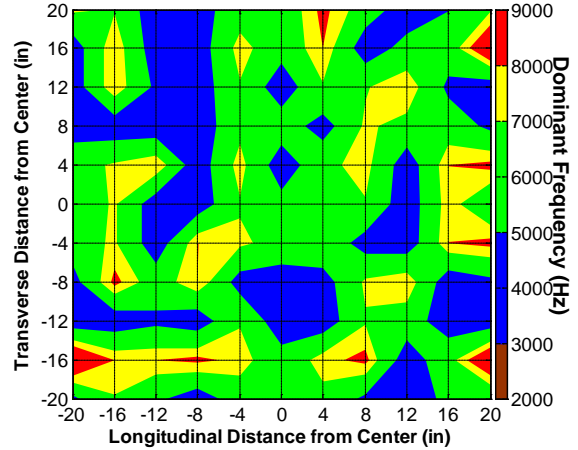
(c) Average modulus from USW

(d) Dominant frequency from IE
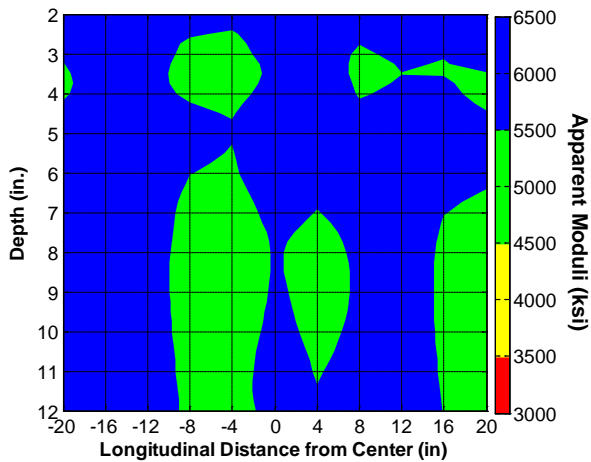
(e) USW B-Scan along center line
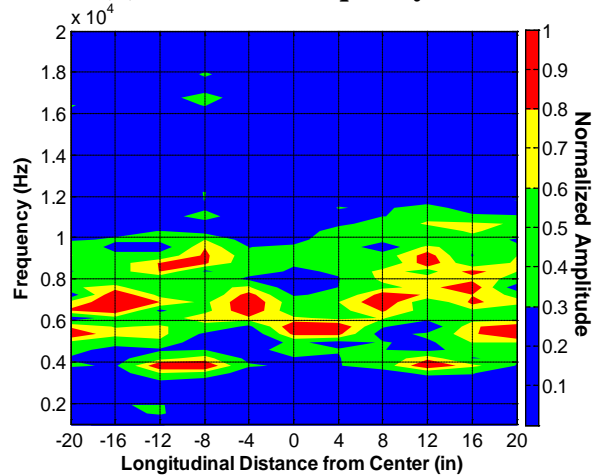
(f) IE Spectral B-Scan along center line

Figure U-7. Contour maps of the acquired results from USW and IE tests for concrete slab #4 (24-inch-thick intact slab).

(a) Slab #5
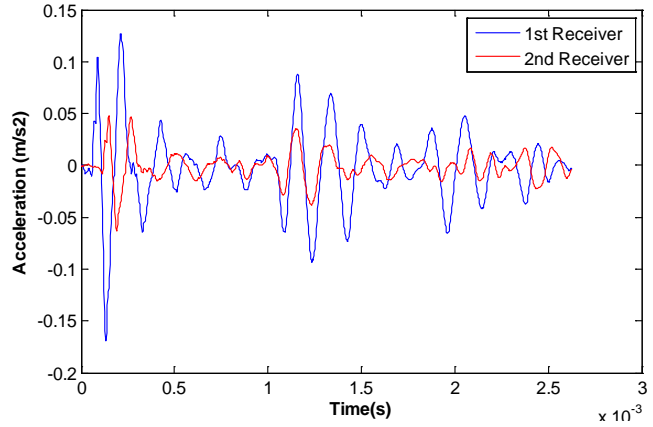
**(b) Waveform obtained from PSPA at center point**
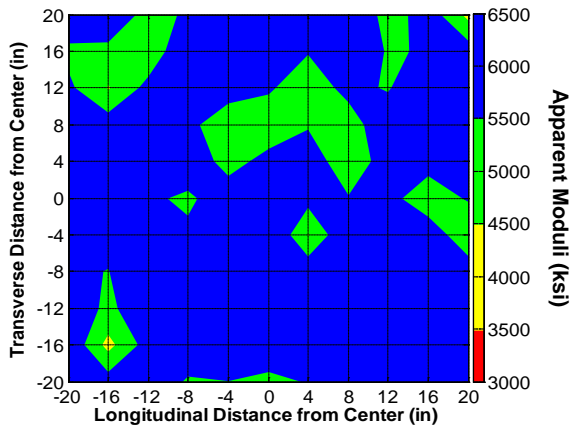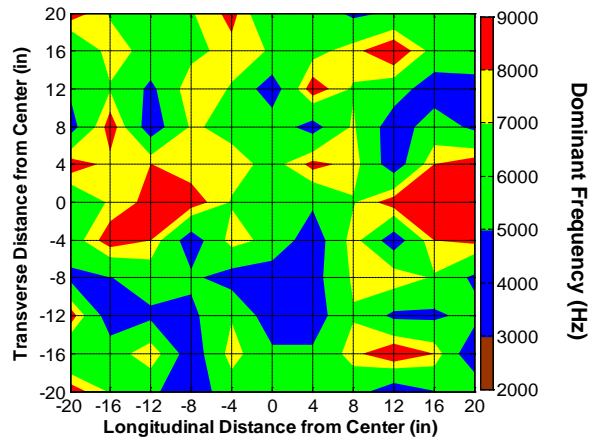
(c) Average modulus from USW

(d) Dominant frequency from IE
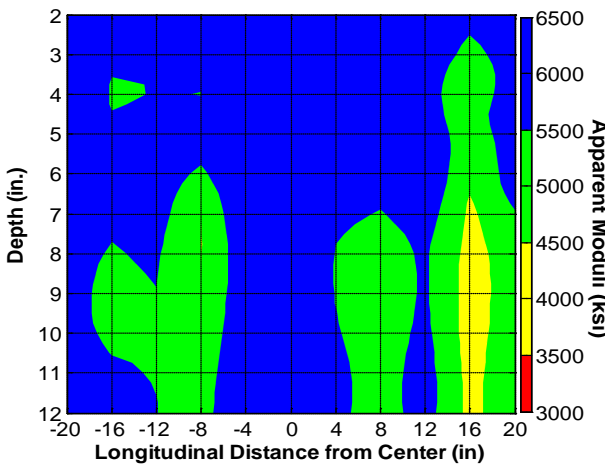
(e) USW B-Scan along center line
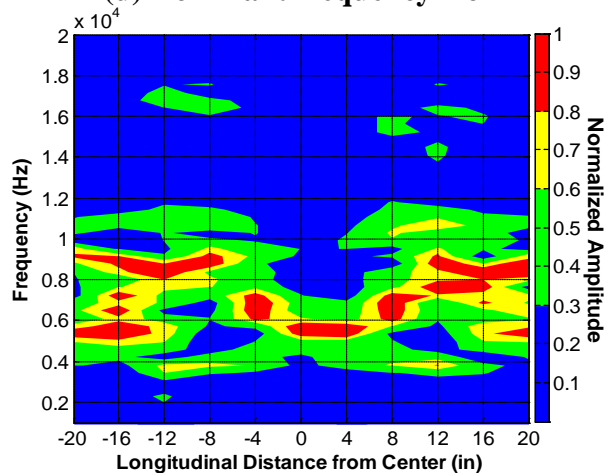
(f) IE Spectral B-Scan along center line

Figure U-8. Contour maps of the acquired results from USW and IE tests for concrete slab #5 (24-inch-thick intact slab).

(a) Slab #6
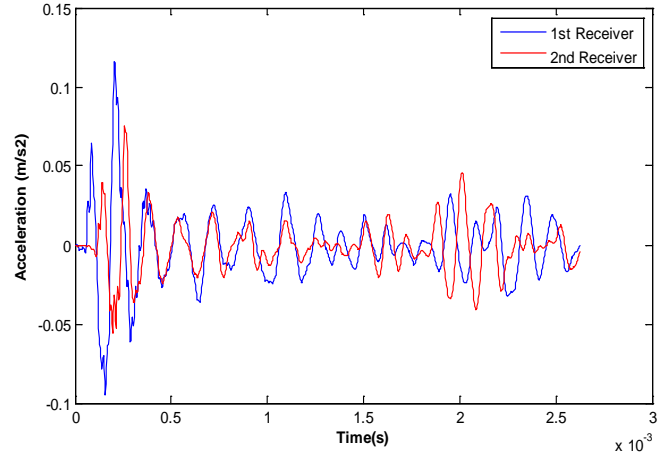
(b) Waveform obtained from PSPA at center point
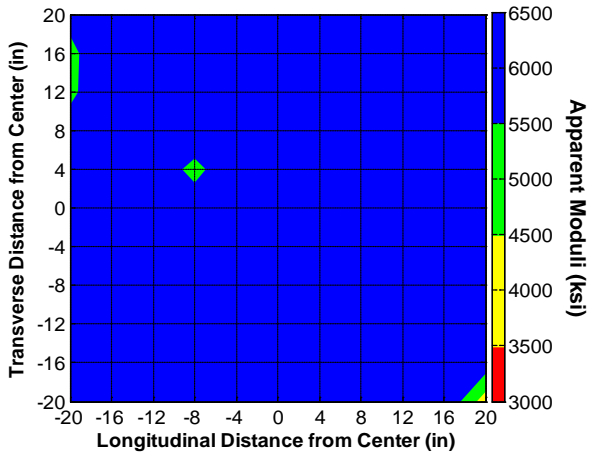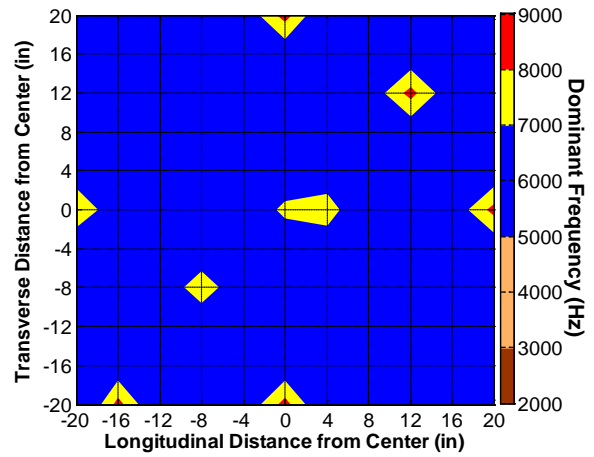
(c) Average modulus from USW

(d) Dominant frequency from IE
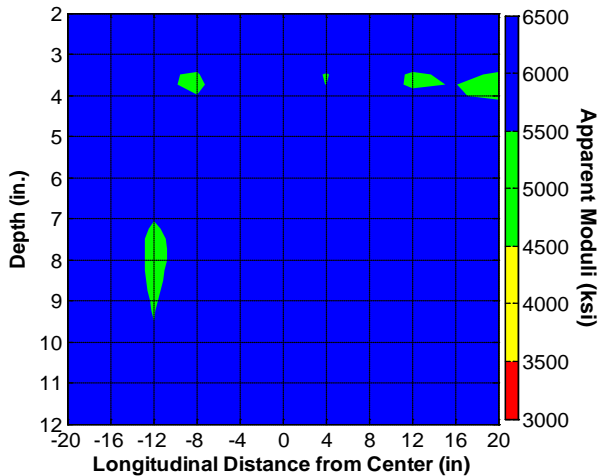
(e) USW B-Scan along center line
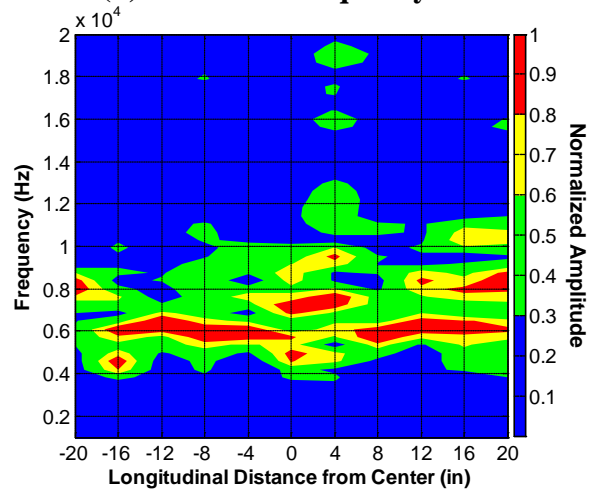
(f) IE Spectral B-Scan along center line

Figure U-9. Contour maps of the acquired results from USW and IE tests for concrete slab #6 (15-inch-thick intact slab).

(a) Slab #7
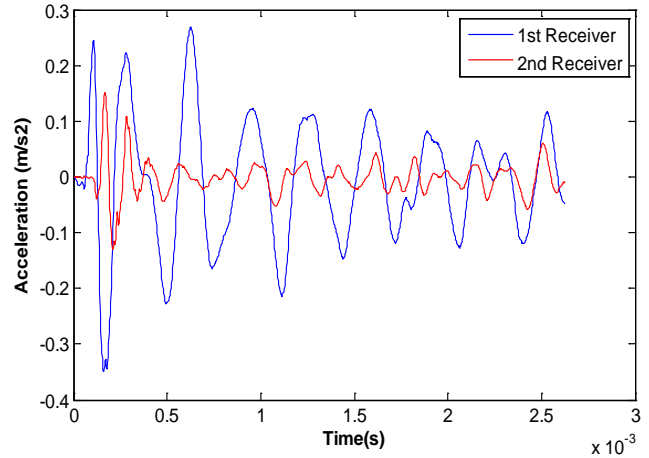
(b) Waveform obtained from PSPA at center point
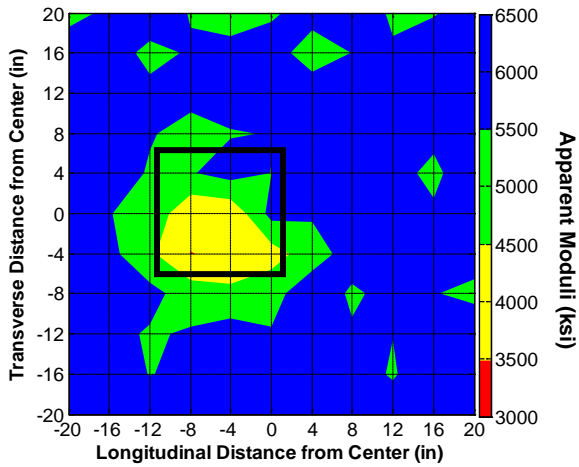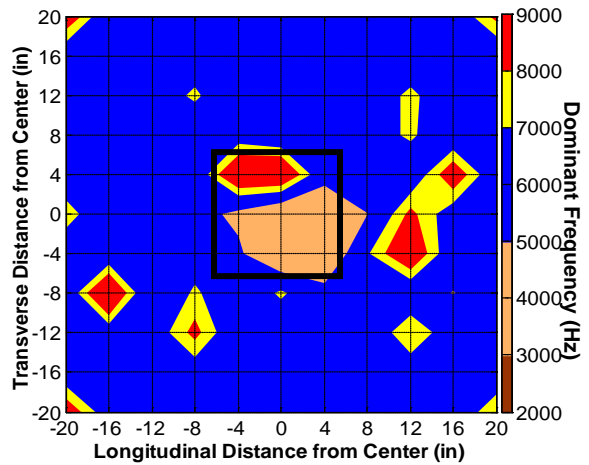
(c) Average modulus from USW

(d) Dominant frequency from IE
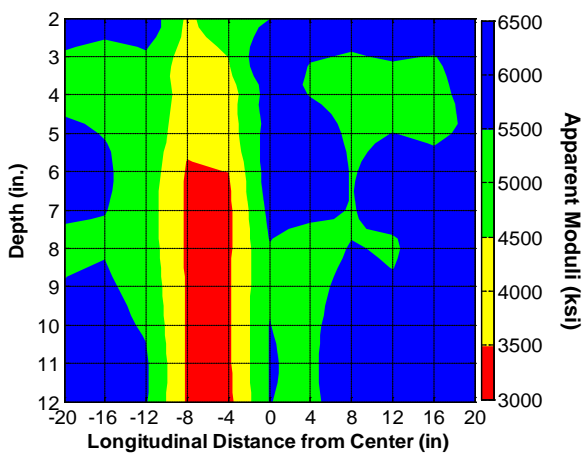
(e) USW B-Scan along center line
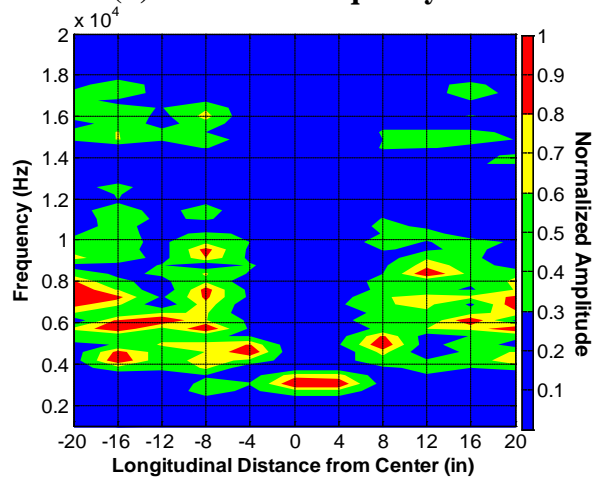
(f) IE Spectral B-Scan along center line

Figure U-10. Contour maps of the acquired results from USW and IE tests for concrete slab #7 (15-inch-thick delaminated at 2 inches).

(a) Slab #8
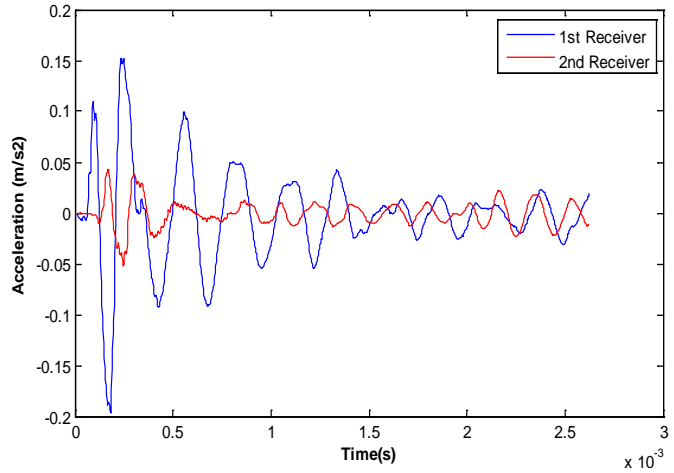
(b) Waveform obtained from PSPA at center point
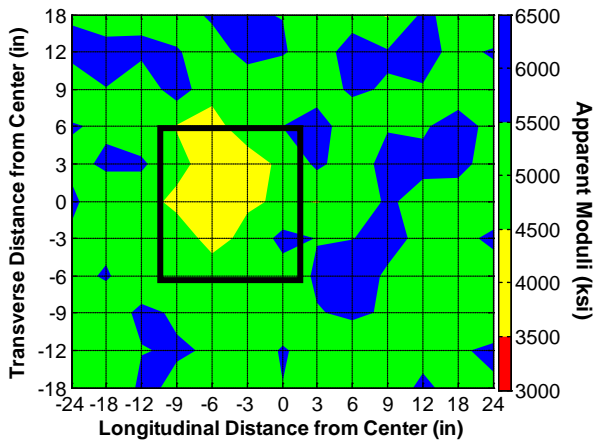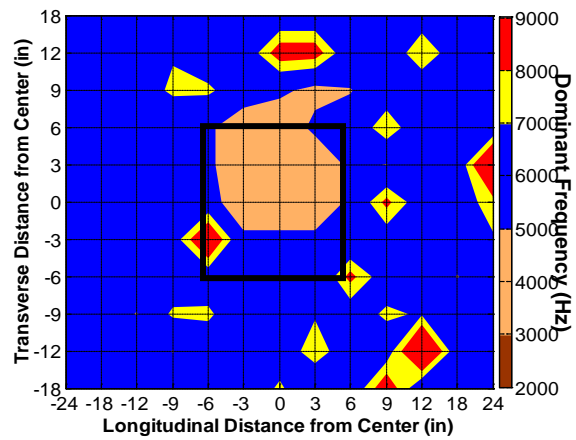
(c) Average modulus from USW

(d) Dominant frequency from IE
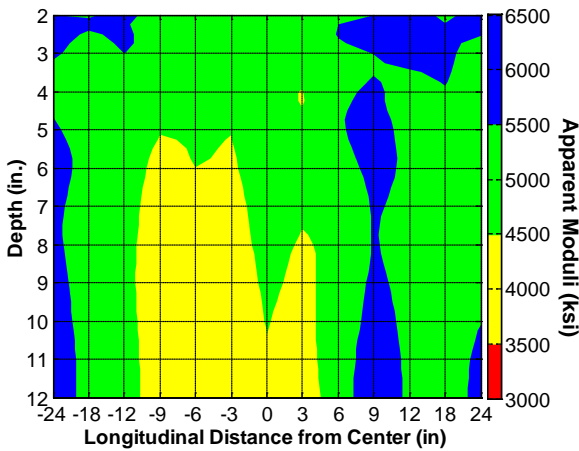
(e) USW B-Scan along center line
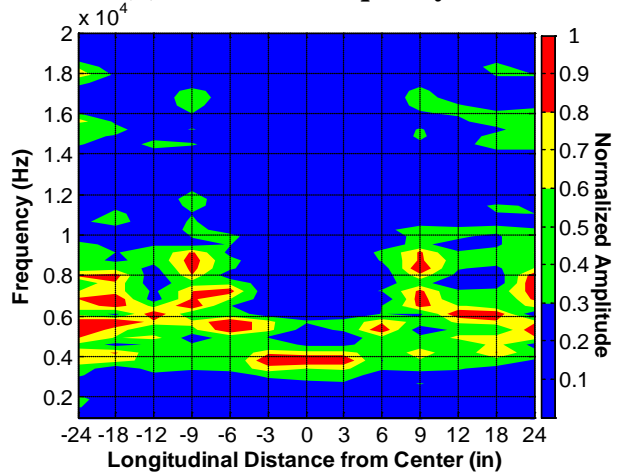
(f) IE Spectral B-Scan along center line

Figure U-11. Contour maps of the acquired results from USW and IE tests for concrete slab #8 (15-inch-thick delaminated at 3 inches).

(a) Slab #9
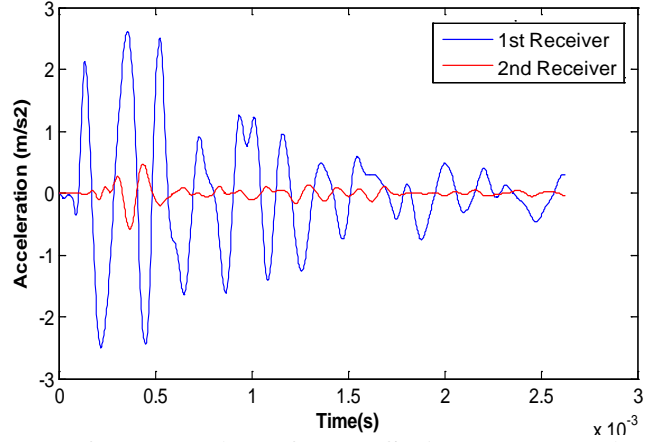
(b) Waveform obtained from PSPA at center point
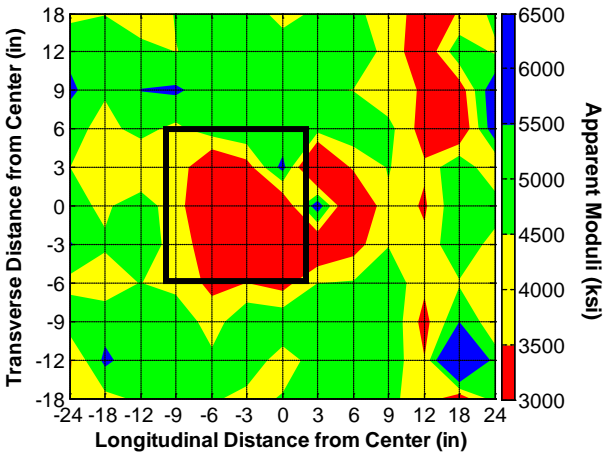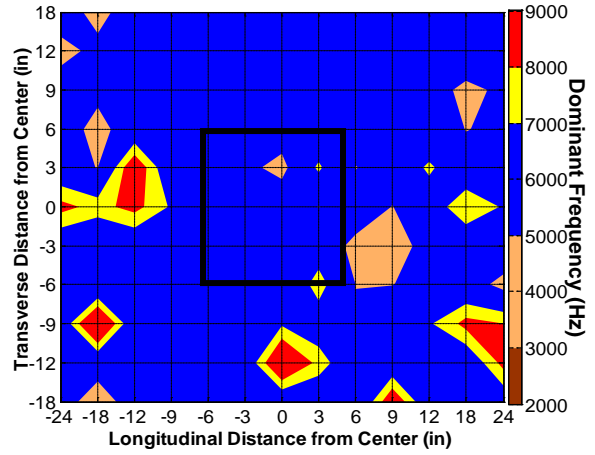
(c) Average modulus from USW

(d) Dominant frequency from IE
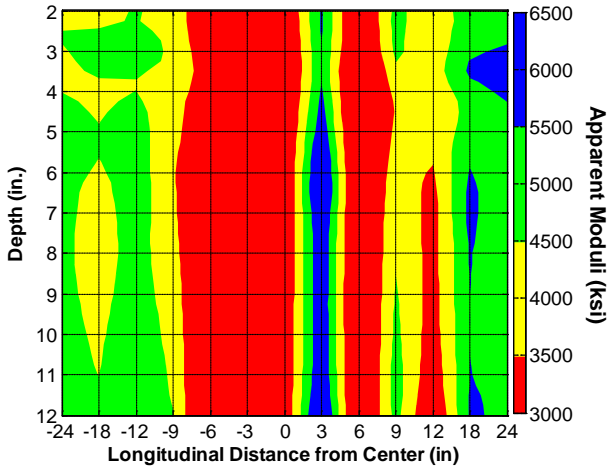
(e) USW B-Scan along center line
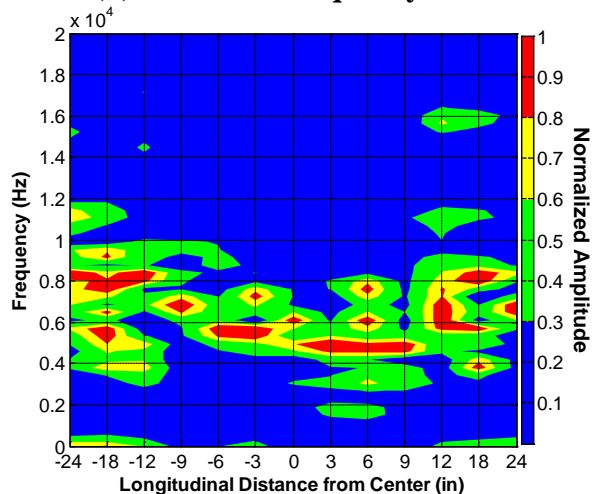
(f) IE Spectral B-Scan along center line

Figure U-12. Contour maps of the acquired results from USW and IE tests for concrete slab #9 (15-inch-thick delaminated at 1 inch).

Concrete Slabs with Voids

Slabs 10 and 11 (Figures U-13 and U-14) contained voids at a depth of 8 inches from the surface of the specimens. As reflected in Figure U-13, Slab 10 contained several surficial cracks. These cracks were reflected in the USW and IE results. The manifestation of the deep void was not readily detectable from the USW results. Based on the principles of wave propagation, the detection of voids with the USW became less effective as the depth of the defect increases. This occurred because surface waves propagated along a cylindrical front, and as such, they became less sensitive to horizontal discontinuities with depth. On the other hand, the air void was clearly mapped in a contour map of dominant frequency from the IE method (Figure U-13d). It seems that the void propagated beyond the boundaries intended. Similar results can be observed for the water-filled void in Figure U-14.

Intact Shotcrete Slabs

Due to its nature, shotcrete is quite variable in its properties. The results from four intact slabs with thicknesses of 4 inches, 6 inches, 8 inches, and 12 inches are shown in Figures U-15 through U-18, respectively. The thicknesses of the 4-inch and 6-inch slabs could not be ascertained with the IE method. However, the thickness of Slab 3 and 13 (thicknesses of 8 inches and 12 inches) was estimated as 9.8 inches and 13.1 inches, respectively, using the properties of concrete and dominant frequency. Unlike the concrete slabs, the reported thicknesses resulted in high standard deviations, making the IE method suitable for a rough estimation of the thickness of shotcrete.

The average and standard deviation of the modulus of each intact slab are shown in Table U-2. The average moduli varied significantly among the slabs, and the standard deviation increased (uniformity of construction decreased) as the shotcrete slab became thicker.

Delaminated Shotcrete Slabs

Five 12-inch-thick slabs (Slabs 8 through 12) were similar to Slab 13, except that they contained 1-ft-square delaminated zones at depths varying from 8 inches to 1 inch from the top surface. The results from these five slabs are shown in Figures U-19 through U-23. These slabs exhibited non-uniform finishes and contained micro-cracks (often) and macro-cracks in a few cases.

By simply comparing the waveforms in Figure U-19b through U-23b and time record in Figure U-18b (Slab 13), one can conclude that Slabs 8 through 12 were delaminated, and the higher amplitude in time records in Figures U-22b and U-23b is an indication of very shallow delamination. Therefore, the operator could roughly interpret time signals at the time of testing.

As reflected in Figure U-19c, USW was not as effective in estimating deep delamination as it was in locating shallower ones (Figure U-20c through U-23c). On the other hand, the delaminated zones were clearly detectable in the contour maps of the dominant return frequency from the IE method (Figure U-19d through U-23d). The size of detected delamination in Slab 11 was bigger than it was aimed to be.
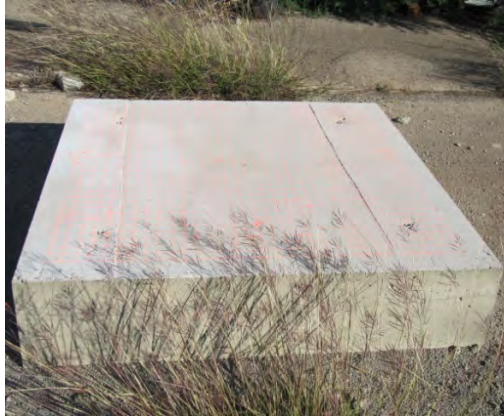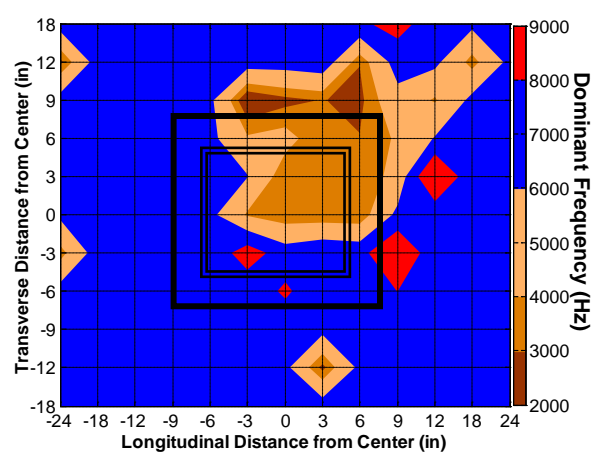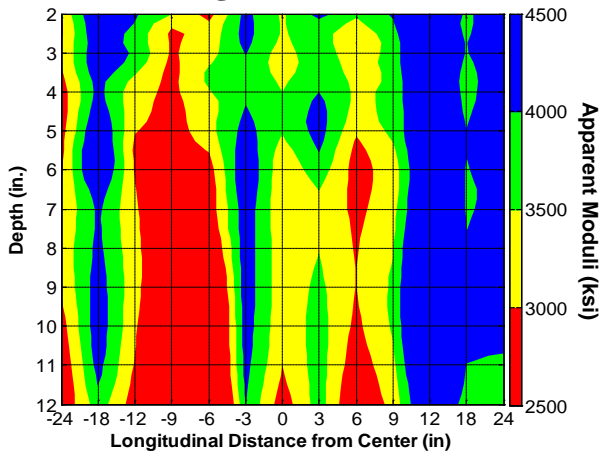
(a) Slab #10
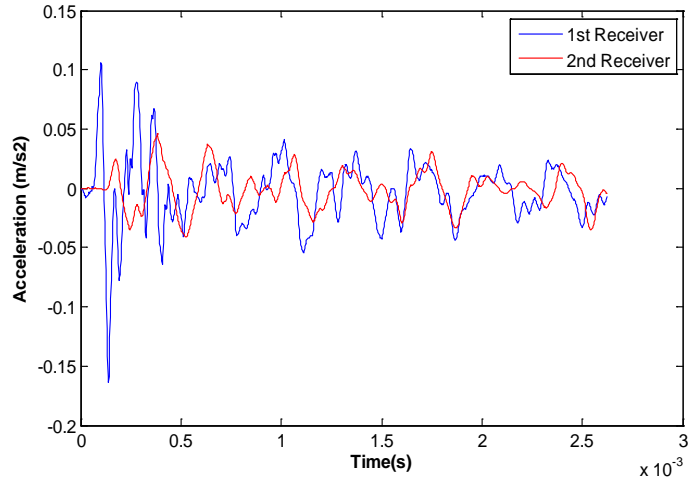
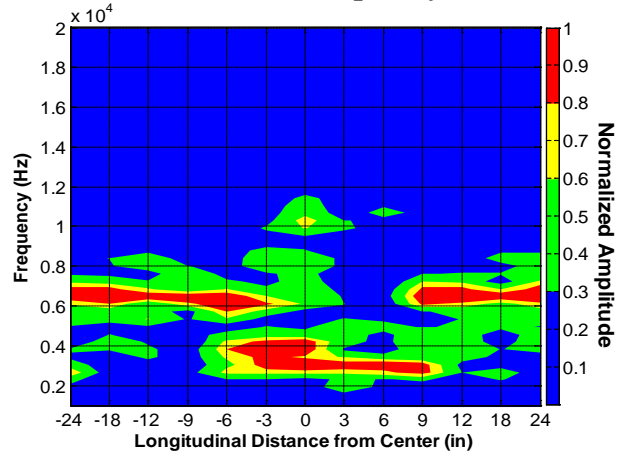(b) Waveform obtained from PSPA at center point
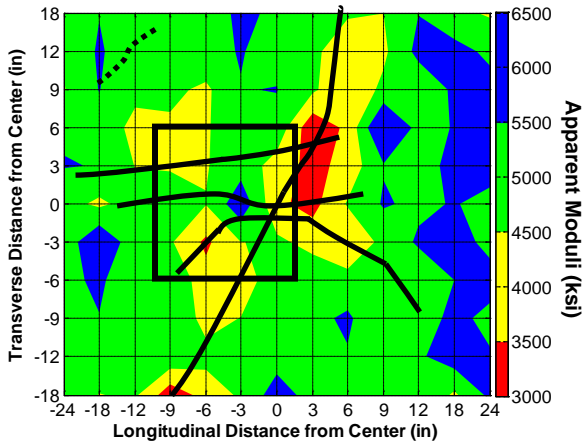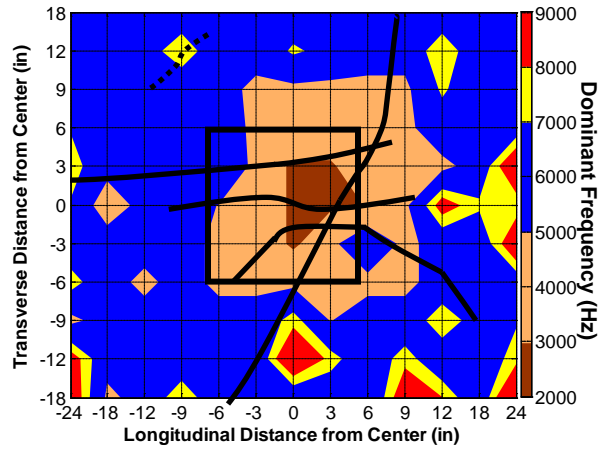
(c) Average modulus from USW

(d) Dominant frequency from IE
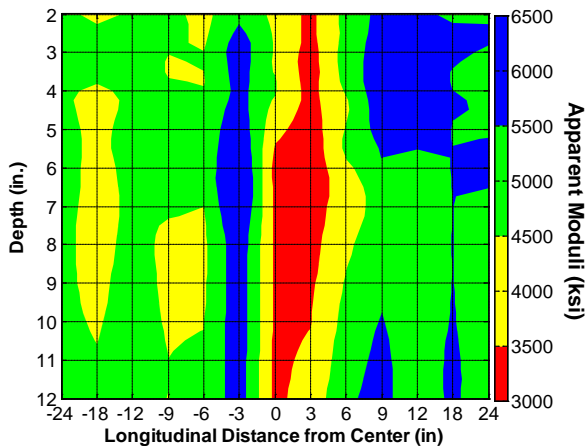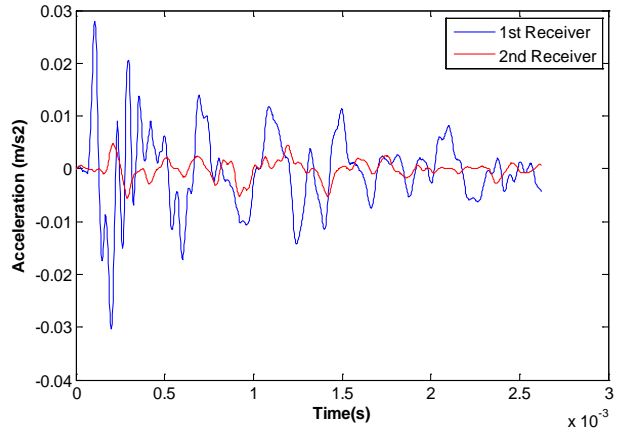

(e) USW B-Scan along center line
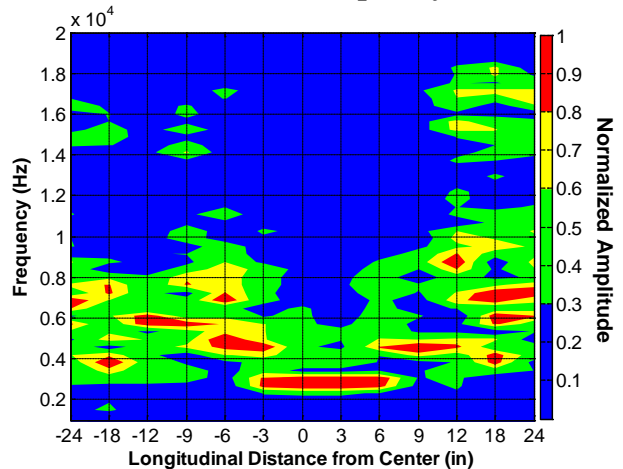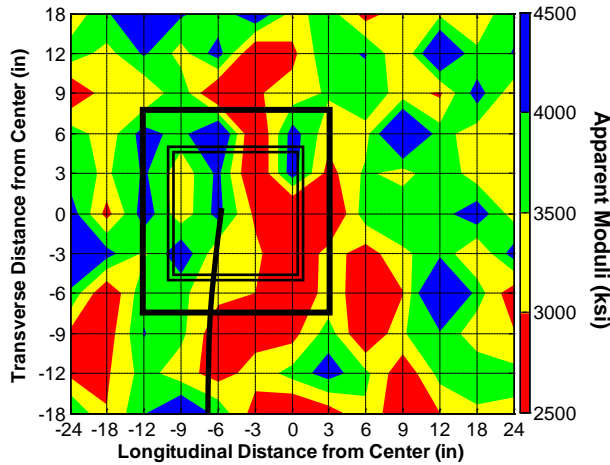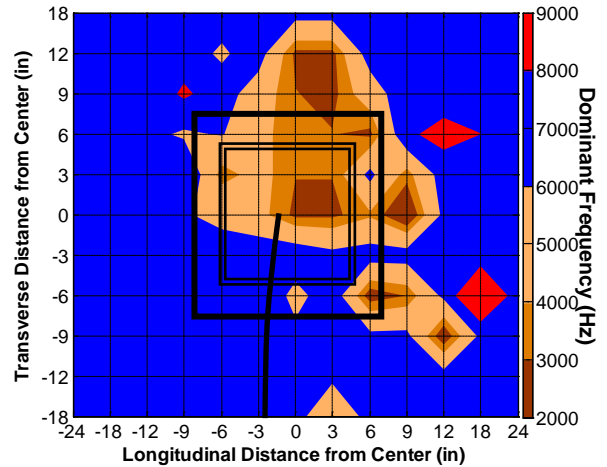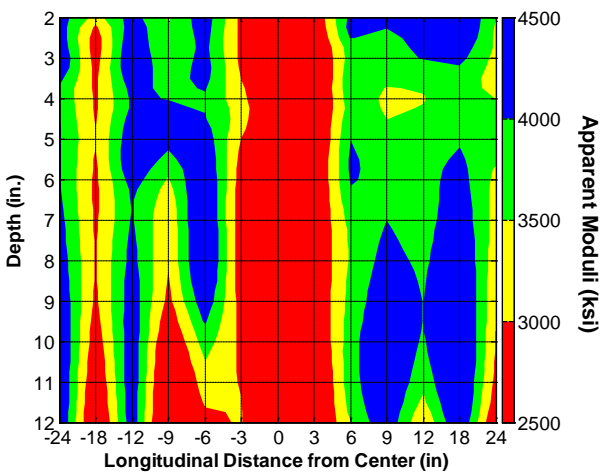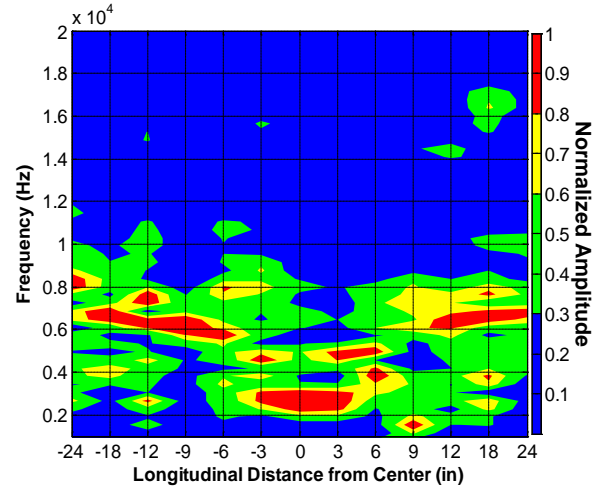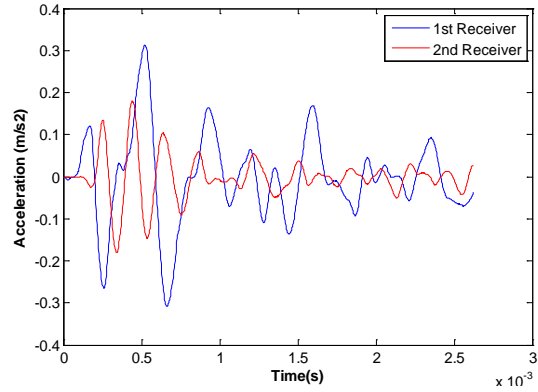

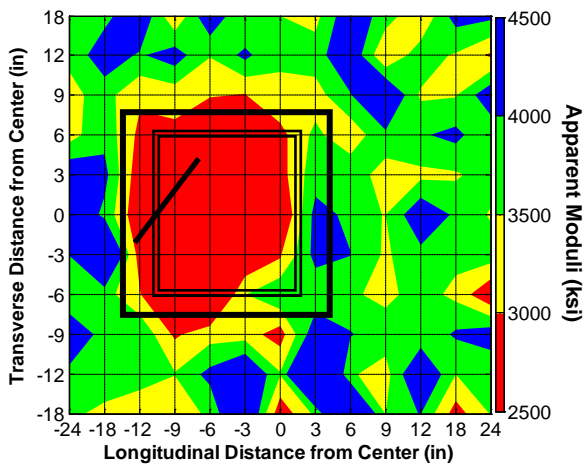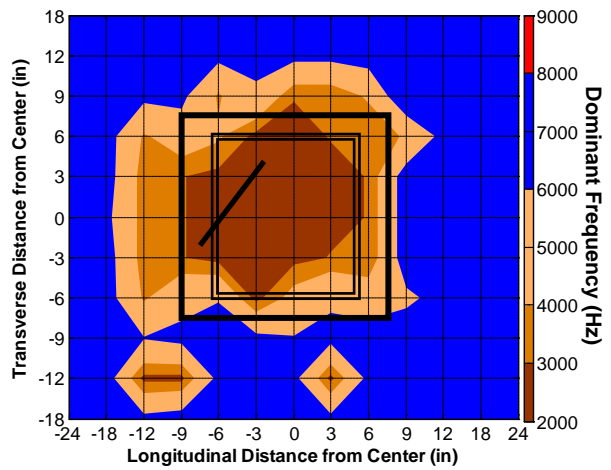(f) IE Spectral B-Scan along center line

Figure U-13. Contour maps of the acquired results from USW and IE tests for concrete slab #10 (15-inch-thick slab with air void at 8-inch depth).
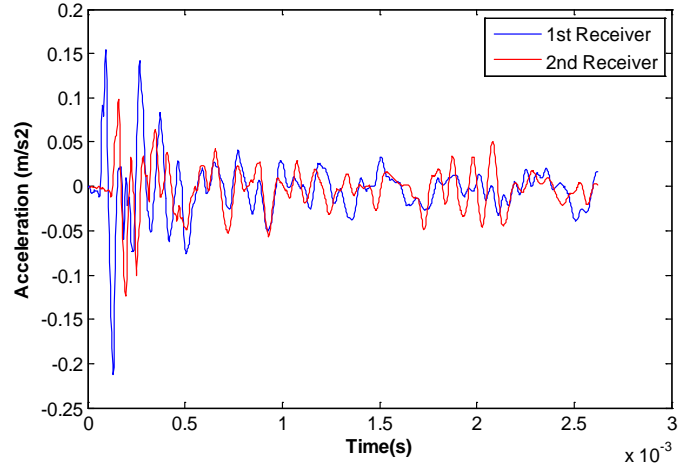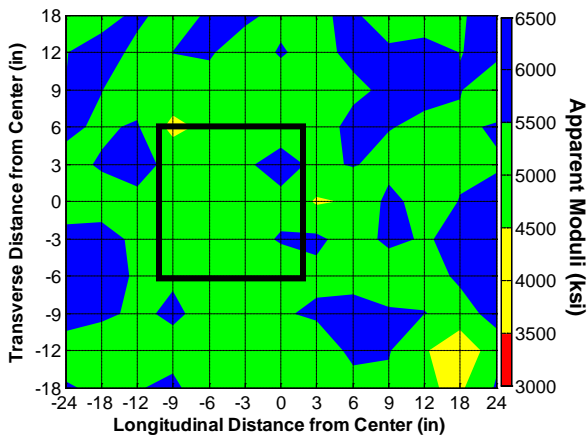
(a) Slab #11

(b) Waveform obtained from PSPA at center point

(c) Average modulus from USW
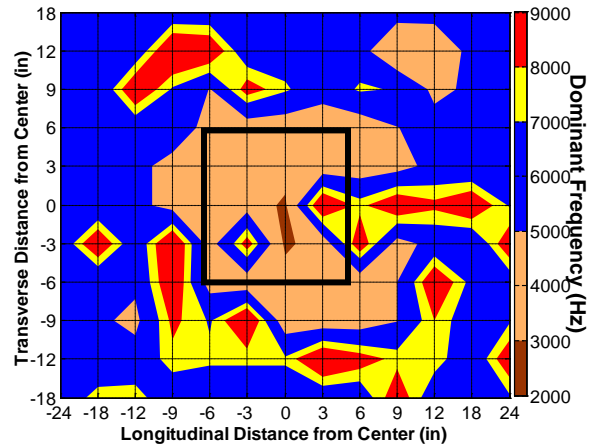
(d) Dominant frequency from IE
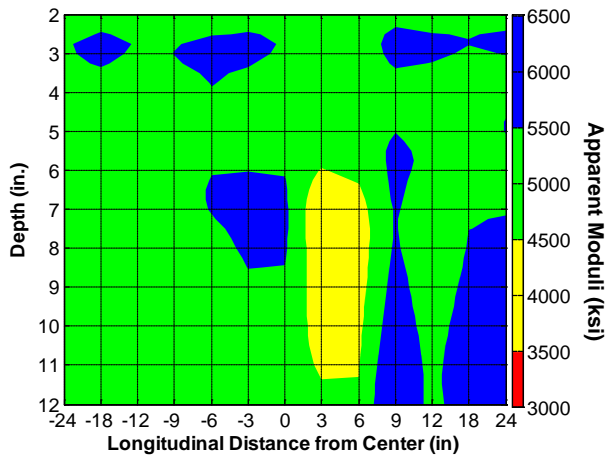
(e) USW B-Scan along center line
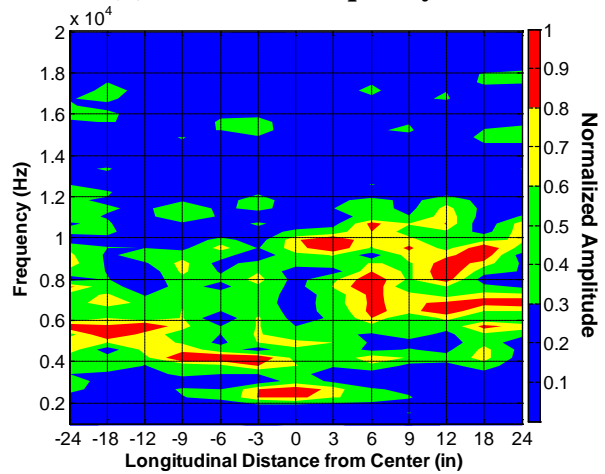
(f) IE Spectral B-Scan along center line

Figure U-14. Contour maps of the acquired results from USW and IE tests for concrete slab #11 (15-inch-thick slab with water void at 8-inch depth).
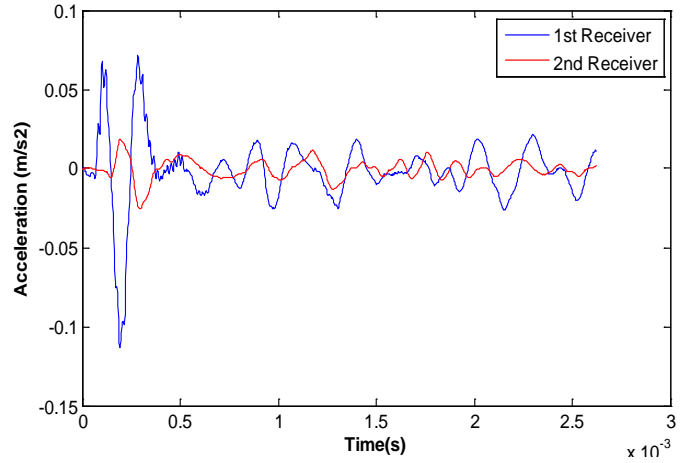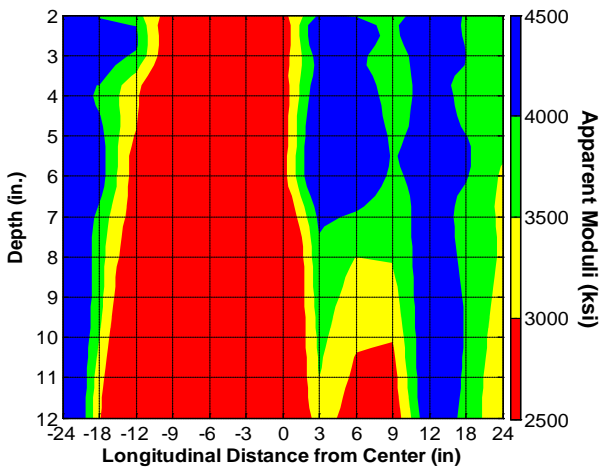
(a) Slab #1

(b) Waveform obtained from PSPA at center point
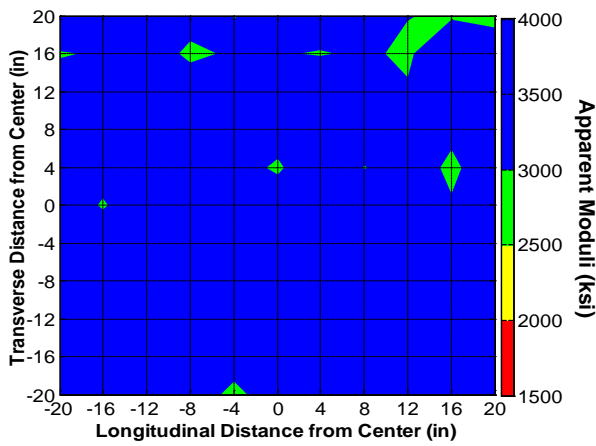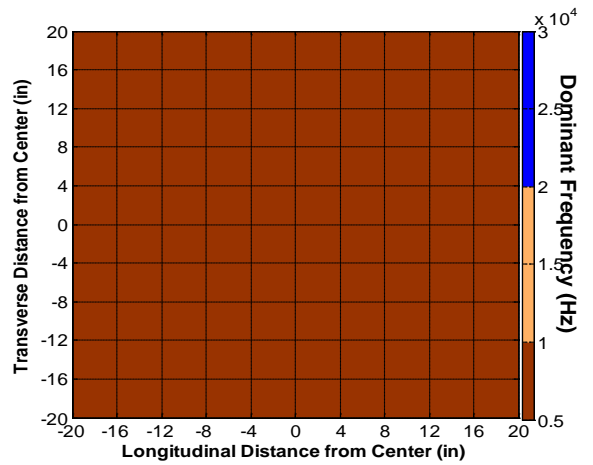
(c) Average modulus from USW

(d) Dominant frequency from IE
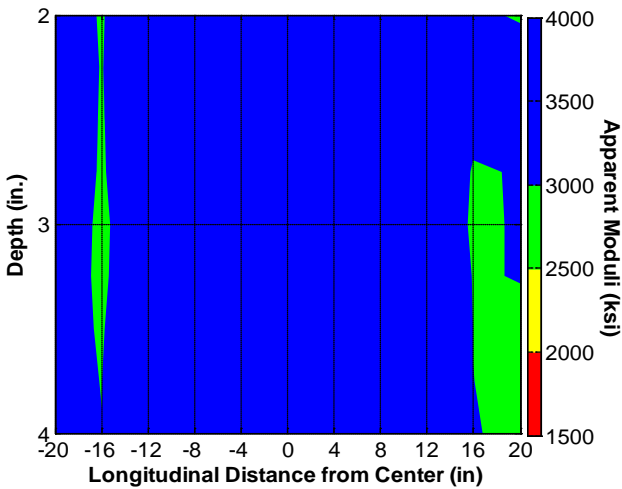
(e) USW B-Scan along center line
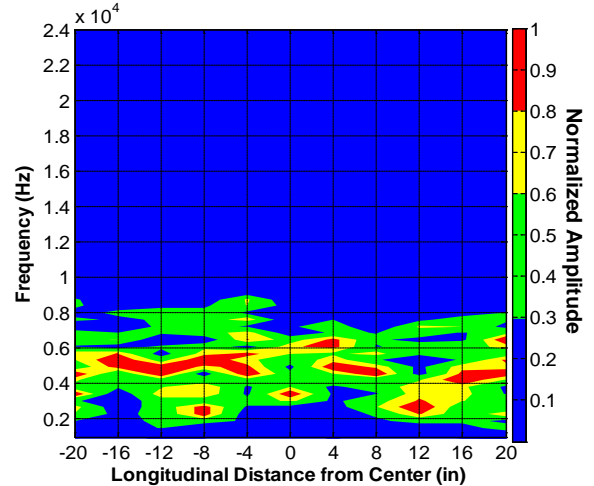
(f) IE Spectral B-Scan along center line

Figure U-15. Contour maps of the acquired results from USW and IE tests for shotcrete slab #1 (4-inch-thick intact slab).

(a) Slab #2
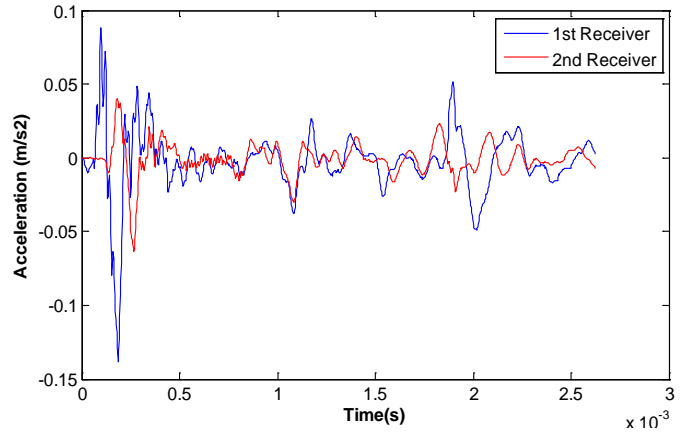
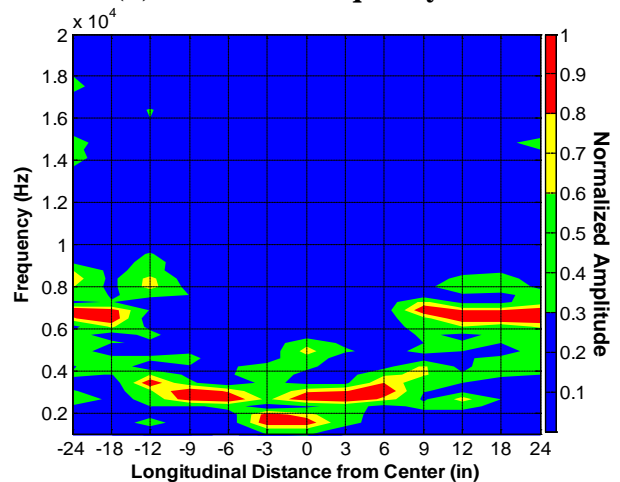**(b) Waveform obtained from PSPA at center point**
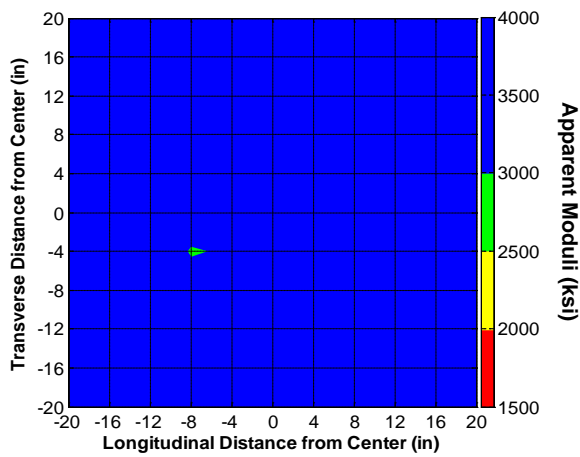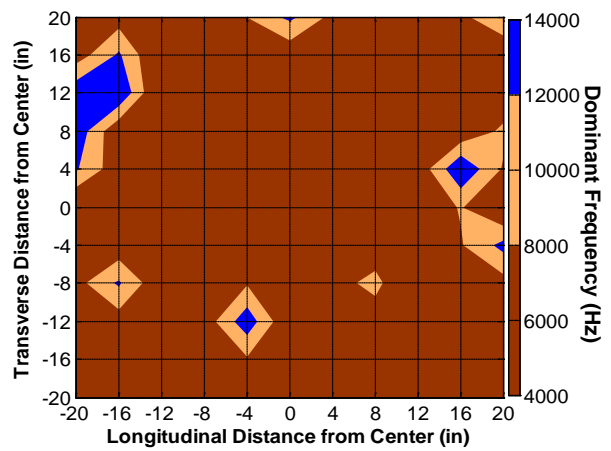
(c) Average modulus from USW

(d) Dominant frequency from IE
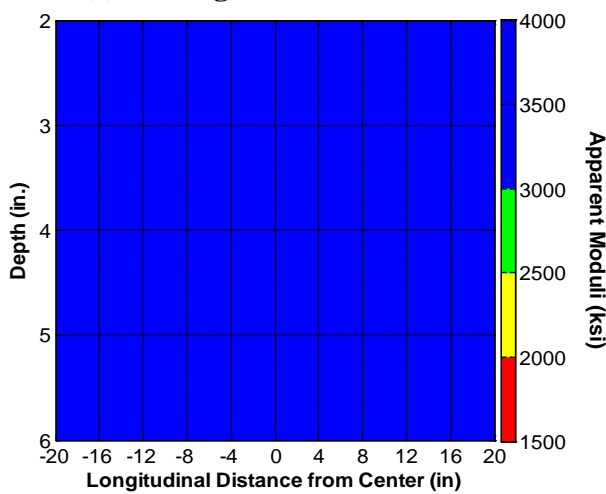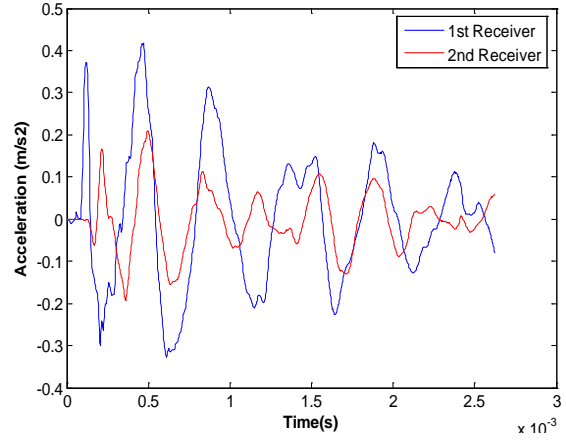

(e) USW B-Scan along center line
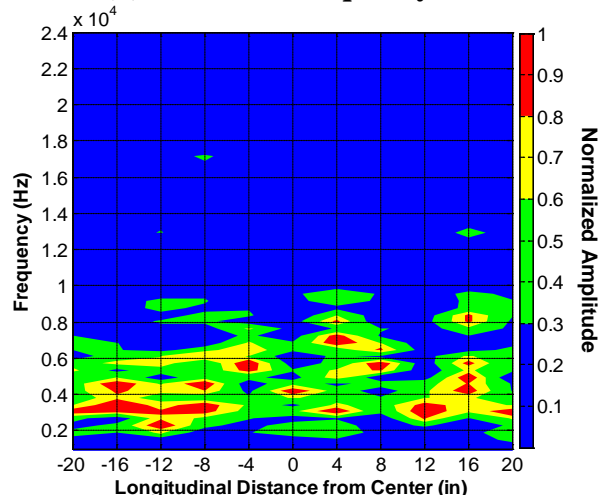
(f) IE Spectral B-Scan along center line

Figure U-16. Contour maps of the acquired results from USW and IE tests for shotcrete slab #2 (6-inch-thick intact slab).
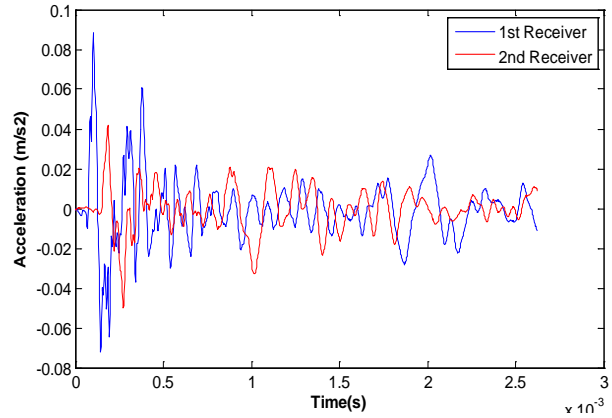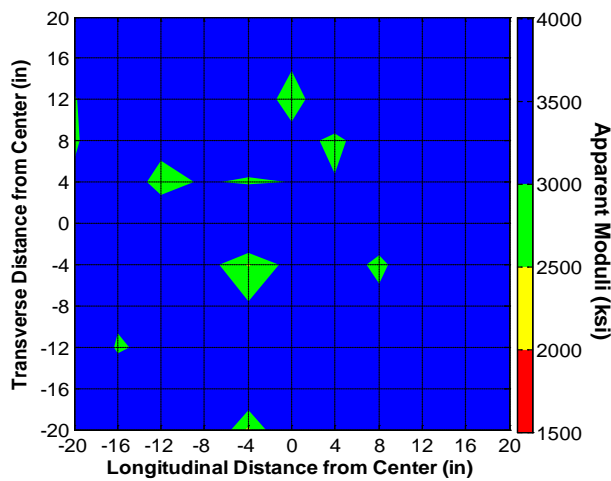
(a) Slab #3

(b) Waveform obtained from PSPA at center point

(c) Average modulus from USW

(d) Dominant frequency from IE
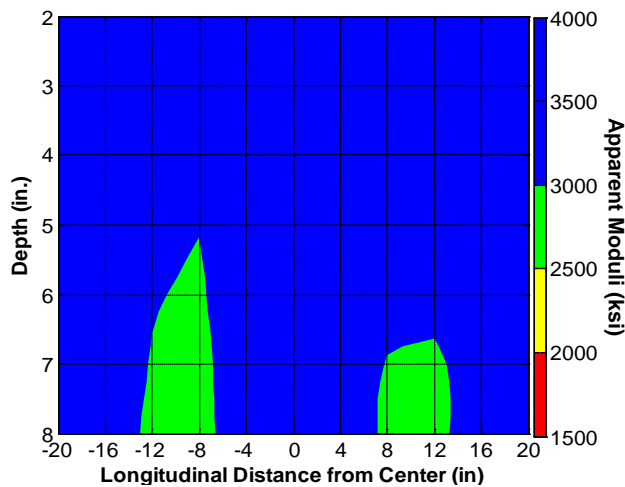
(e) USW B-Scan along center line
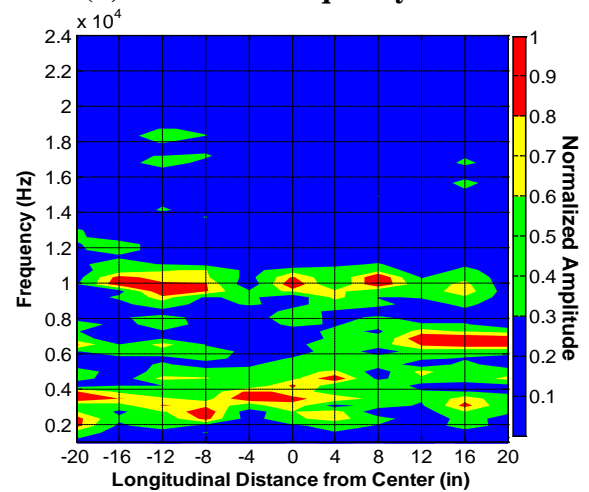
(f) IE Spectral B-Scan along center line

Figure U-17. Contour maps of the acquired results from USW and IE tests for shotcrete slab #3 (8-inch-thick intact slab).

(a) Slab #13
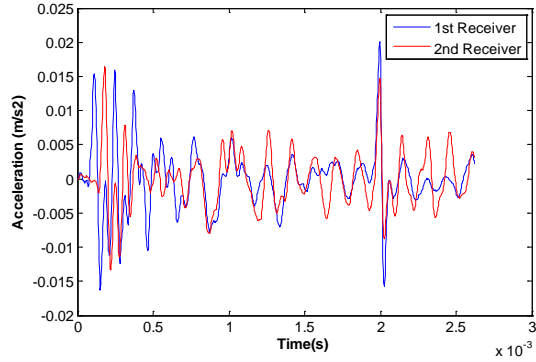
(b) Waveform obtained from PSPA at center point
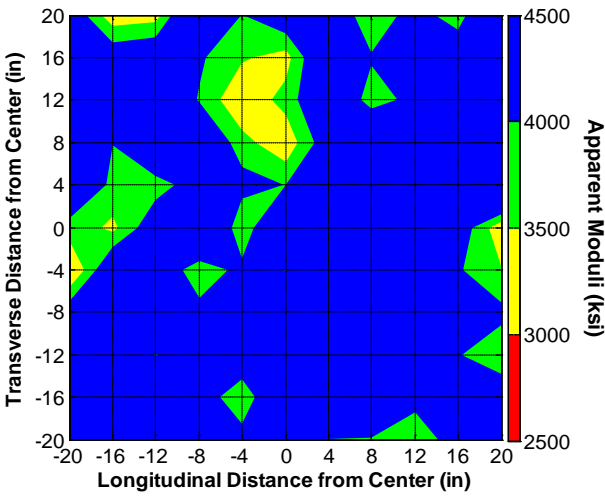
(c) Average modulus from USW

(d) Dominant frequency from IE
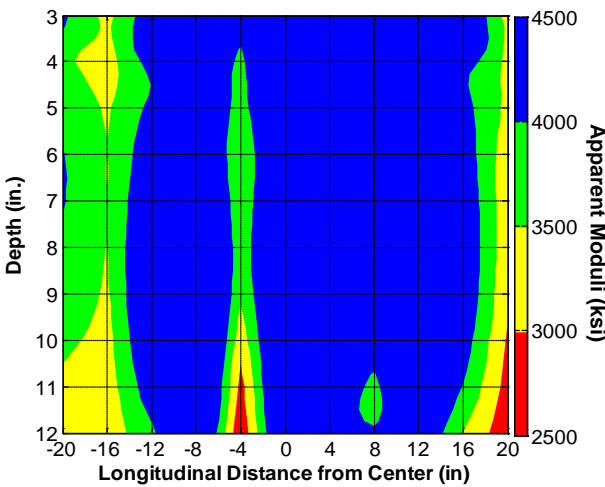
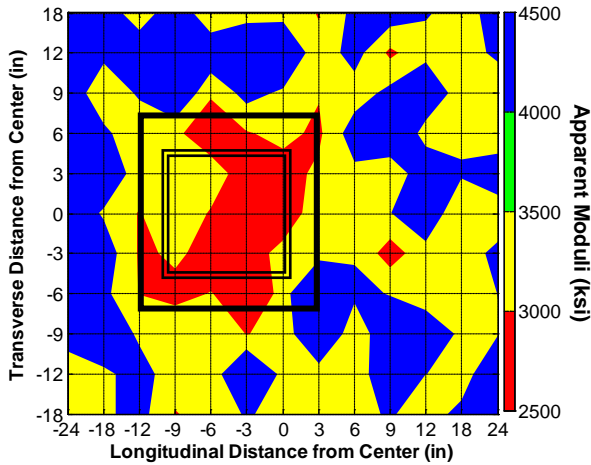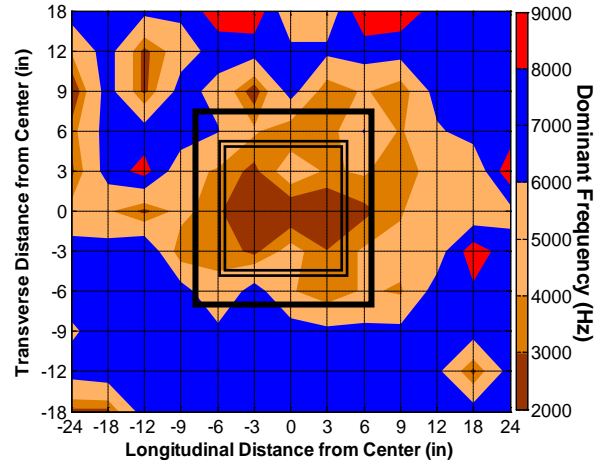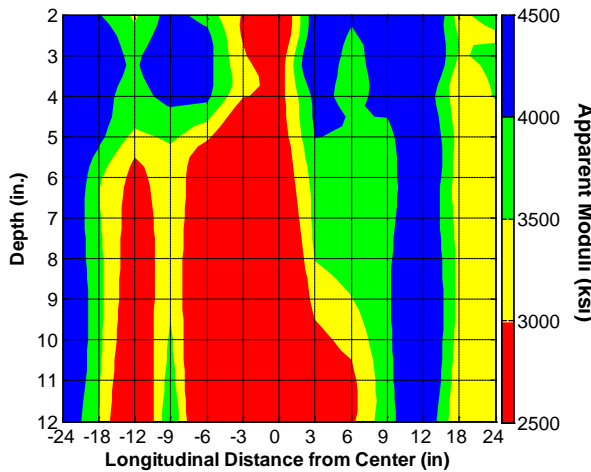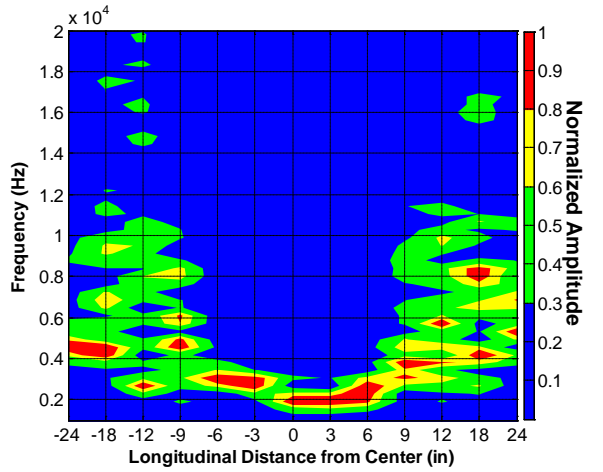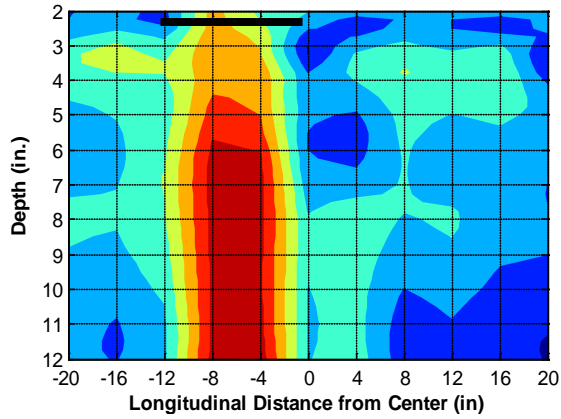(e) USW B-Scan along center line
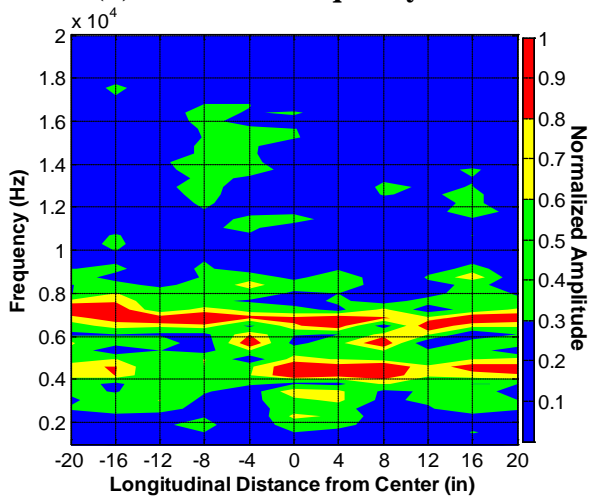
(f) IE Spectral B-Scan along center line

Figure U-18. Contour maps of the acquired results from USW and IE tests for shotcrete slab #13 (12-inch-thick intact slab).

Table U-2. Average and standard deviation of moduli of intact shotcrete slabs.

Slab	USW Modulus, ksi	
	Average	Standard Deviation
1	3460	386
2	4178	549
3	3607	506
13	4401	684

(a) Slab #8

(b) Waveform obtained from PSPA at center point
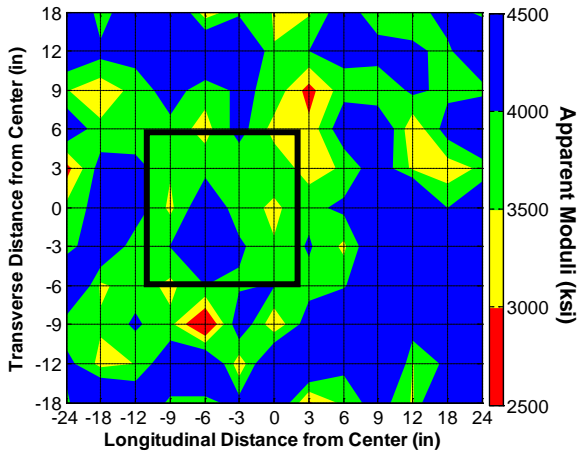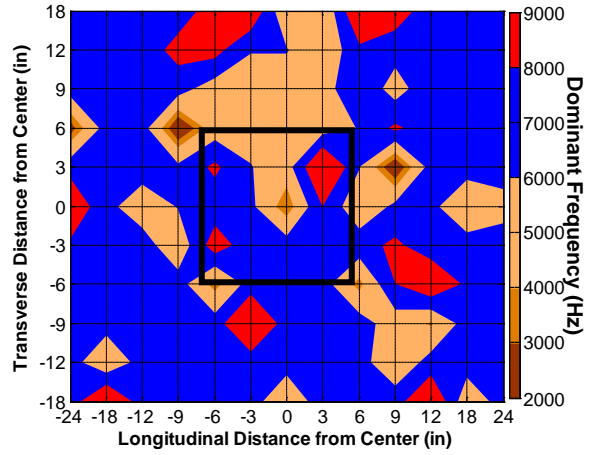
(c) Average modulus from USW

(d) Dominant frequency from IE
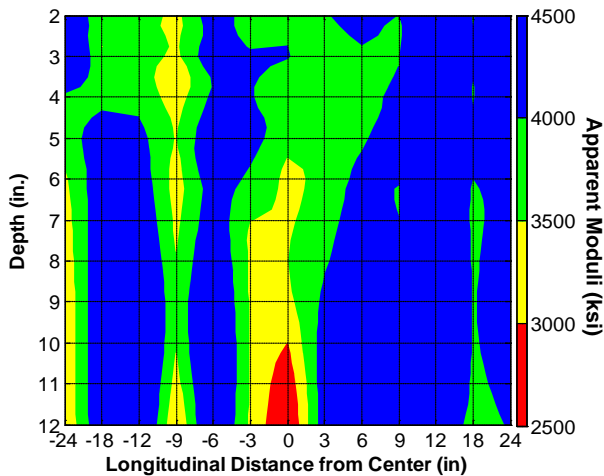
(e) USW B-Scan along center line
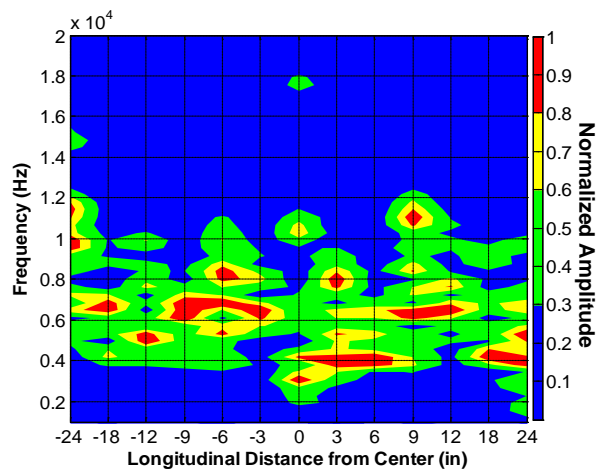
(f) IE Spectral B-Scan along center line

Figure U-19. Contour maps of the acquired results from USW and IE tests for shotcrete slab #8 (12-inch-thick delaminated at 8-inch depth).

(a) Slab #9
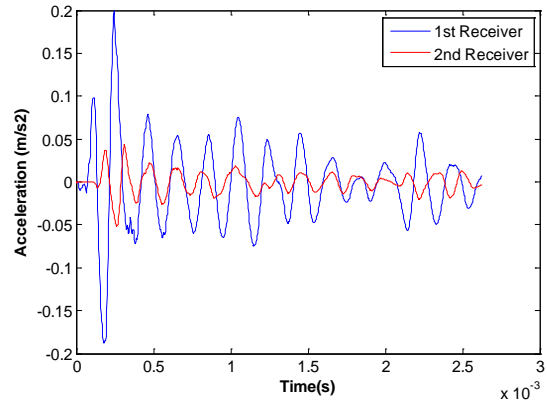
(b) Waveform obtained from PSPA at center point
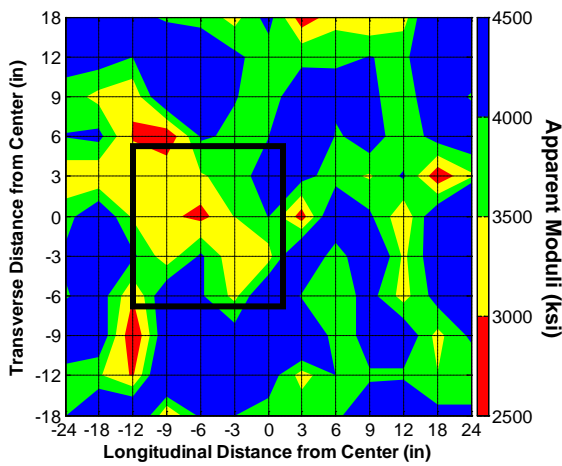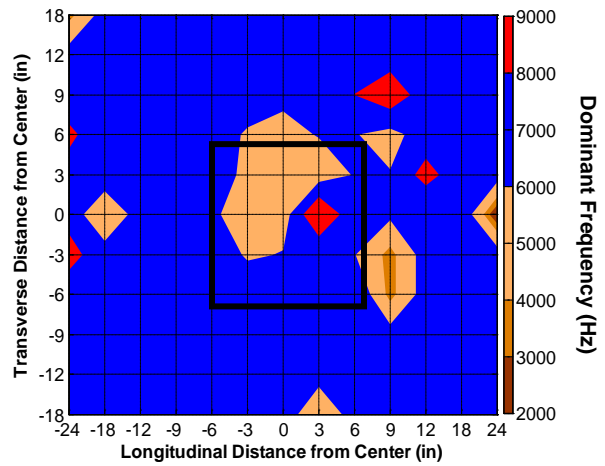
(c) Average modulus from USW

(d) Dominant frequency from IE
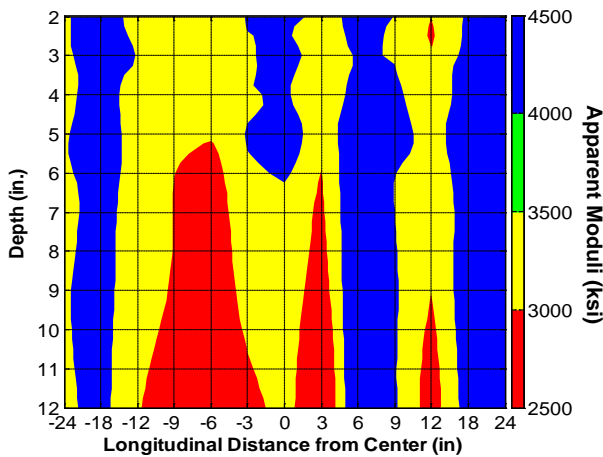
(e) USW B-Scan along center line
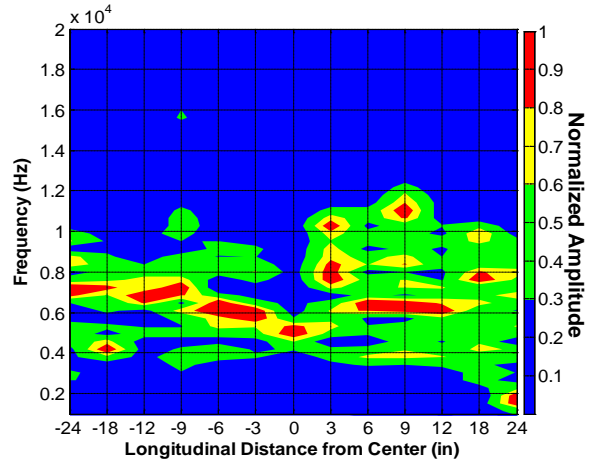
(f) IE Spectral B-Scan along center line

Figure U-20. Contour maps of the acquired results from USW and IE tests for shotcrete slab #9 (12-inch-thick delaminated at 4-inch depth).

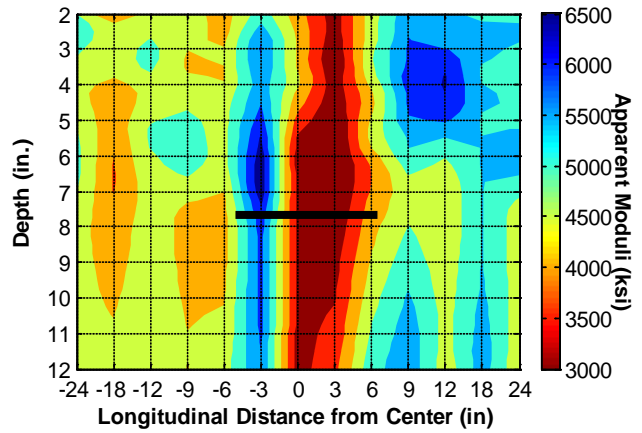**(a) Slab #10**
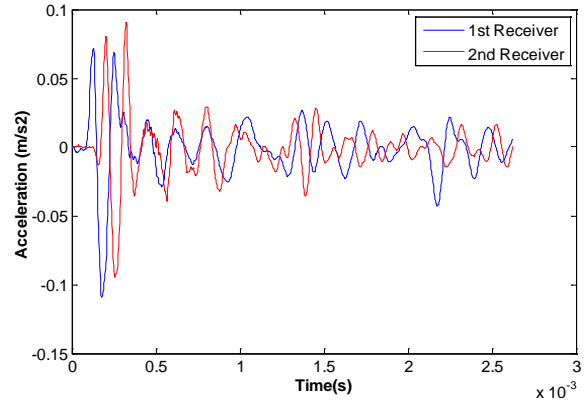
(b) Waveform obtained from PSPA at center point
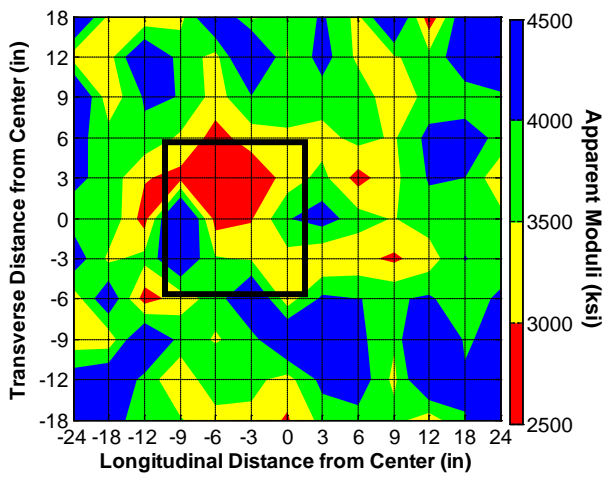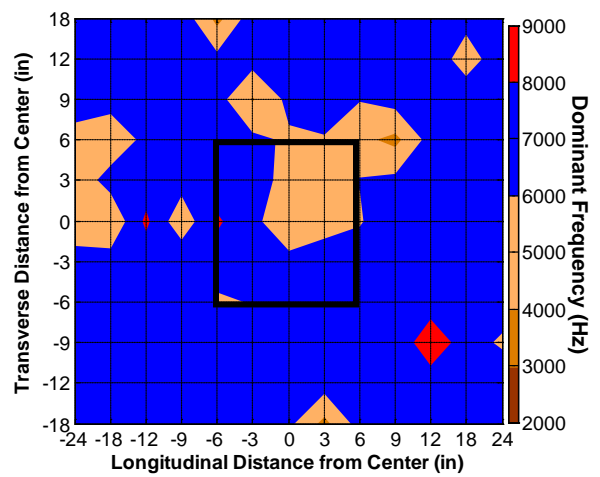
(c) Average modulus from USW

(d) Dominant frequency from IE
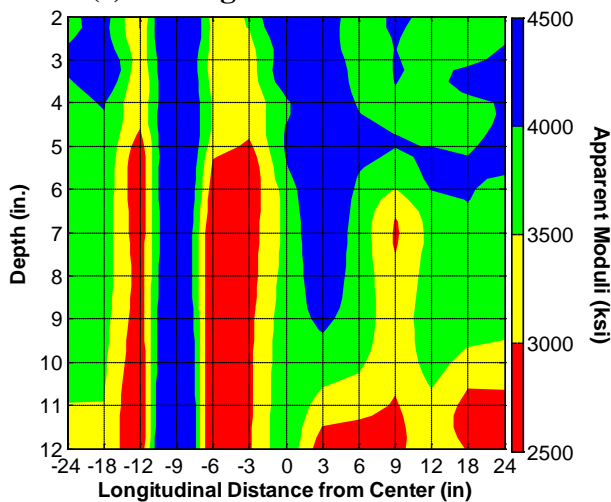
(e) USW B-Scan along center line
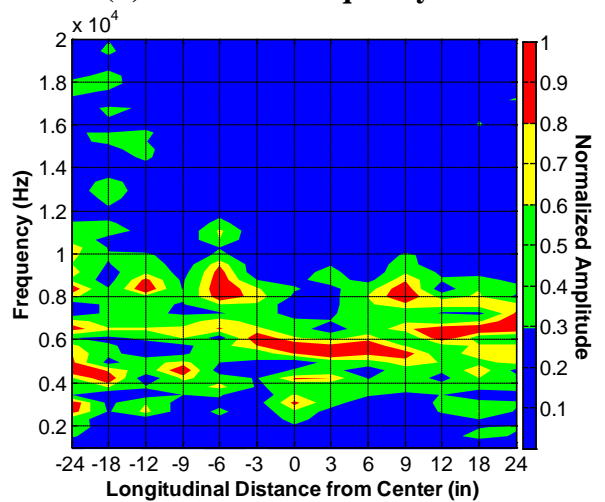
(f) IE Spectral B-Scan along center line

Figure U-21. Contour maps of the acquired results from USW and IE tests for shotcrete slab #10 (12-inch-thick delaminated at 3-inch depth).

(a) Slab #11
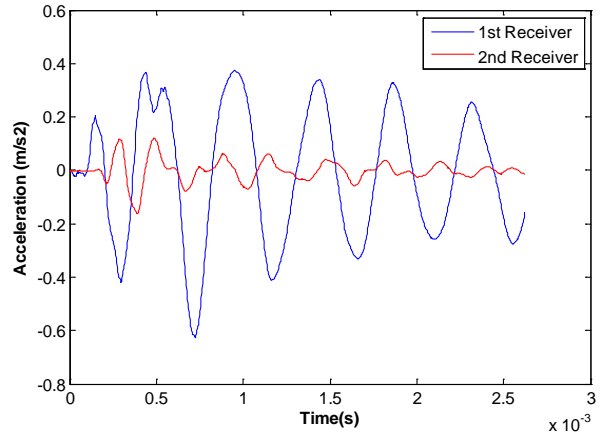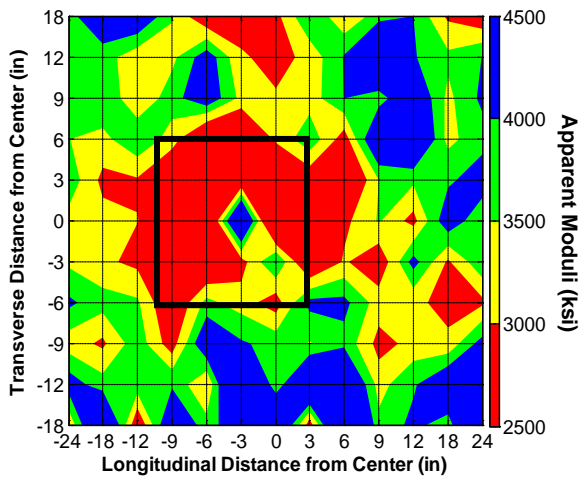
(b) Waveform obtained from PSPA at center point

(c) Average modulus from USW

(d) Dominant frequency from IE

USW B-Scan along center line

(f) IE Spectral B-Scan along center line

Figure U-22. Contour maps of the acquired results from USW and IE tests for shotcrete slab #11 (12-inch-thick delaminated at 2-inch depth).

(a) Slab #12

(b) Waveform obtained from PSPA at center point

(c) Average modulus from USW

(d) Dominant frequency from IE

(e) USW B-Scan along center line
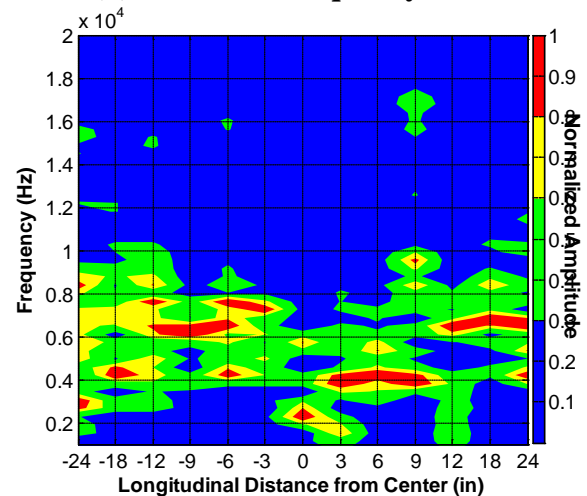
(f) IE Spectral B-Scan along center line

Figure U-23. Contour maps of the acquired results from USW and IE tests for shotcrete slab #12 (12-inch-thick delaminated at 1-inch depth).

Shotcrete Slabs with Voids

Slabs 4 through 7 contained different sizes of bags that simulated air-filled and water-filled voids at different depths. In Slabs 4 and 5, the voids were embedded at a depth of 7.5 inches and in Slabs 6 and 7 at a depth of 3 inches from the surface. Again, the time signals in Figure U-24b through U-27b are significantly different than the time records of a similar intact slab (Slab 13) in Figure U-18b.

As in the case of concrete slabs, the USW method lost it resolving power as the defects were placed deeper. As shown in Figures U-24c and U-25c, the deep voids were not as readily detectable from the USW results as for the shallower ones shown in Figures U-26c and U-27c. The deep and shallow voids were mapped in contour maps of the dominant frequency from the IE method (Figures U-24d through U-27d). It seems that the voids in Slabs 6 and 7 were bigger than intended, and they shifted when the slabs were constructed.

ESTIMATION OF DEPTH OF DEFECTS

One of the goals of this study was to estimate the depth of defects, especially the shallow ones (less than 4 inches). For severe defects like the ones installed in the TTI slabs, the flexural mode of vibration controls the responses obtained from the IE method. However, as demonstrated in two concurrent SHRP2 projects (R06A for concrete and R06D for hot-mix asphalt) the depth to defect can be estimated from the USW B-Scans. To demonstrate this concept, the USW B-Scans shown in Figures U-3f through U-27f for the defective concrete and shotcrete slabs were re-contoured, as seen in Figures U-28 and U-29. The re-contouring process was needed since, as reflected in Azari et al. (2012), the previous contour maps were optimized to accentuate the existence of the defects. The reported depths of defects are shown with a black solid line in Figures U-28 and U-29.

Given the limitation of the minimum depth of investigation of the PSPA as 2 inches, the depths of delamination were fairly accurate for Slabs 7, 8, and 9. Figures 28b and 28c indicate that the delaminated zone extended beyond the intended areas. As previously discussed, the predictive power of the USW method diminished with depth. As reflected in Figure U-28d, the quality of the concrete above the 8-inch-deep air void was quite low, manifesting as severe cracking on the slab surface (see Figure U-13). The manifestation of the water-filled void at the same depth in Slab 11 could be detected; however, once again the quality of the concrete above that void was lower than the intact areas. Similar results were obtained in the defective shotcrete slabs in Figure U-29. The depths of the defects could be quantitatively estimated from the new B-Scans only in an approximate fashion. However, the USW B-Scans provided information about the change in quality of concrete placed after the installation of the defects. That is why the indication of defect (lower modulus) in some of the slabs started a few inches above the top of the defects.

(a) Slab #4
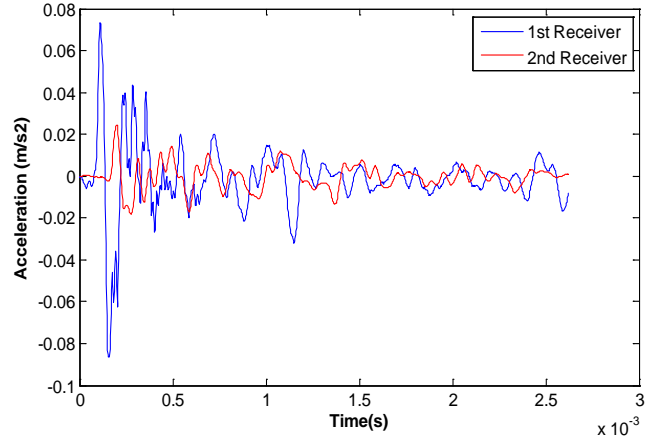
(b) Waveform obtained from PSPA at center point
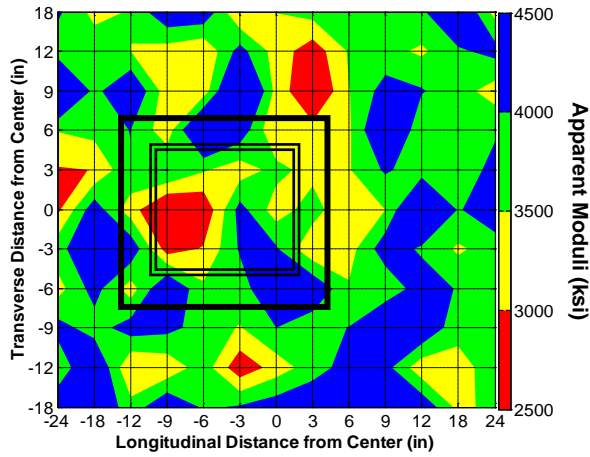
(c) Average modulus from USW

(d) Dominant frequency from IE

(e) USW B-Scan along center line

(f) IE Spectral B-Scan along center line

Figure U-24. Contour maps of the acquired results from USW and IE tests for shotcrete slab #4 (12-inch-thick slab with air void at 7.5-inch depth).

(a) Slab #5

(b) Waveform obtained from PSPA at center point

(c) Average modulus from USW

(d) Dominant frequency from IE

USW B-Scan along center line

(f) IE Spectral B-Scan along center line

Figure U-25. Contour maps of the acquired results from USW and IE tests for shotcrete slab #5 (12-inch-thick slab with water void at 7.5-inch depth).

(a) Slab #6

(b) Waveform obtained from PSPA at center point

(c) Average modulus from USW

(d) Dominant frequency from IE

(e) USW B-Scan along center line

(f) IE Spectral B-Scan along center line

Figure U-26. Contour maps of the acquired results from USW and IE tests for shotcrete slab #6 (12-inch-thick slab with air void at 3-inch depth).

(a) Slab #7

(b) Waveform obtained from PSPA at center point

(c) Average modulus from USW

(d) Dominant frequency from IE

(e) USW B-Scan along center line

(f) IE Spectral B-Scan along center line

Figure U-27. Contour maps of the acquired results from USW and IE tests for shotcrete slab #7 (12-inch-thick slab with water void at 3-inch depth).

(a) Slab #7
(delamination at 2-inch depth)
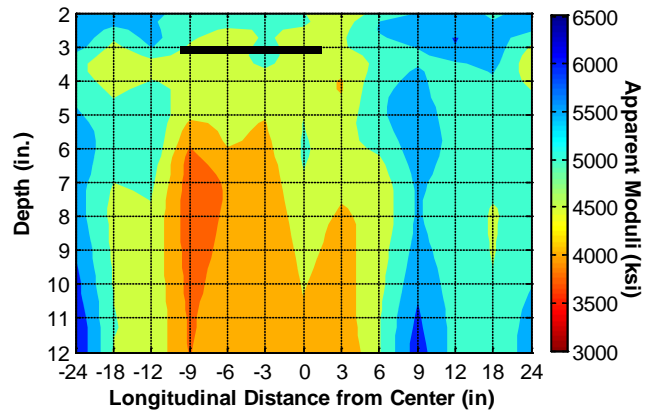
(b) Slab #8
(delamination at 3-inch depth)
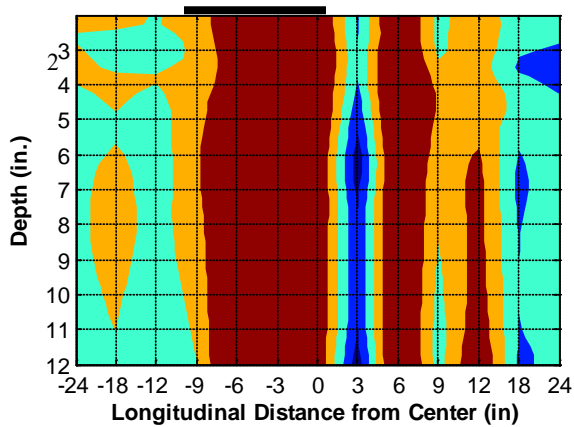
(c) Slab #9
(delamination at 1-inch depth)

(d) Slab #10
(air void at 8-inch depth with surficial cracks)
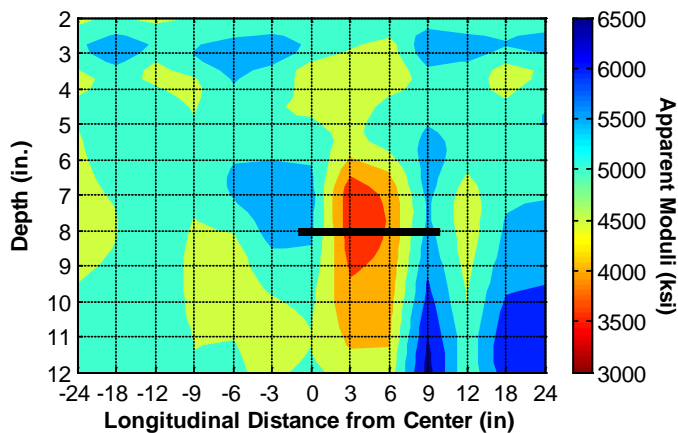
(e) Slab #11
(water void at 8-inch depth)

Figure U-28. USW B-Scan along center line for concrete slabs.
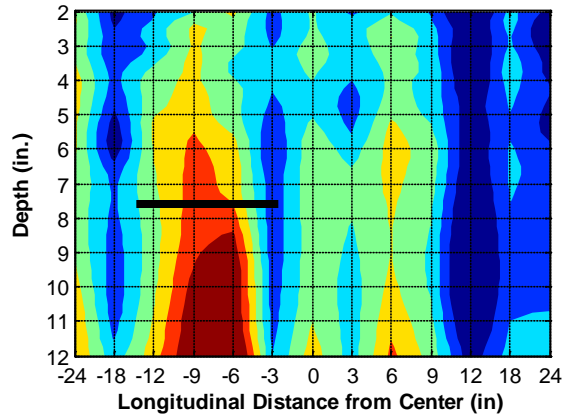
(a) Slab #4
(air void at 7.5-inch depth)
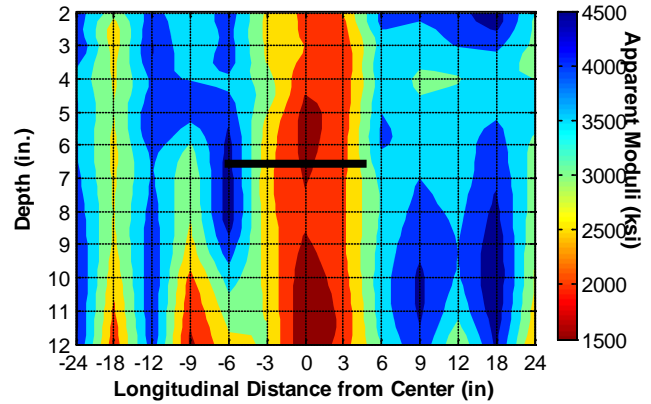
(b) Slab #5
(water void at 7.5-inch depth with surficial cracks)
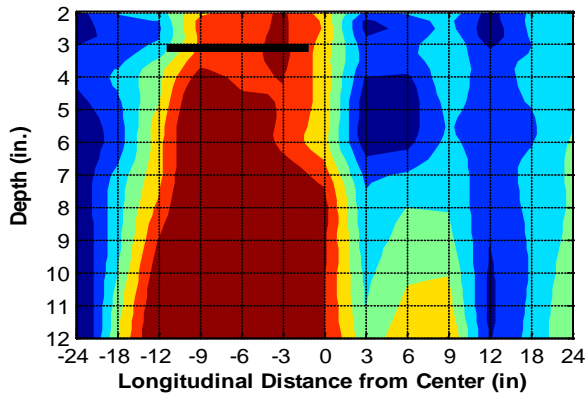
(c) Slab #6
(air void at 3-inch depth with surficial cracks)
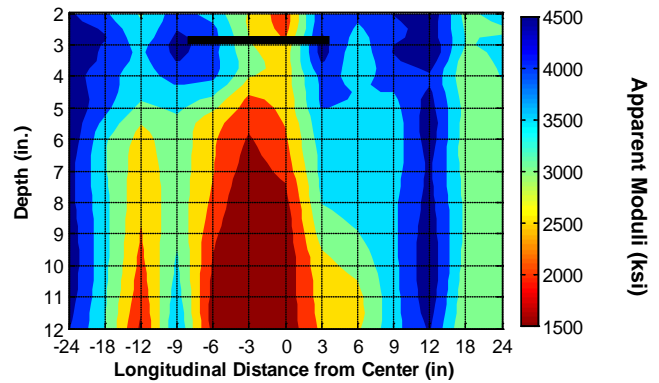
(d) Slab #7
(water void at 3-inch depth)
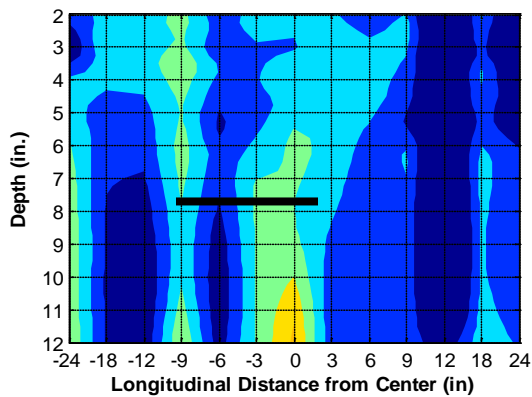
(e) Slab #8
(delamination at 8-inch depth)
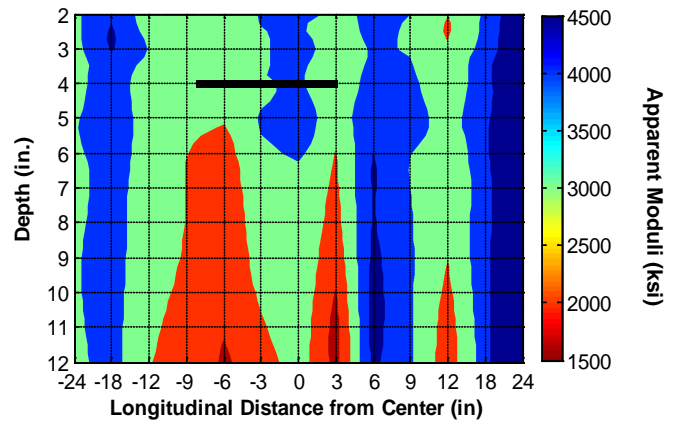
(f) Slab #9
(delamination at 4-inch depth)

Figure U-29. USW B-Scan along center line for shotcrete slabs.
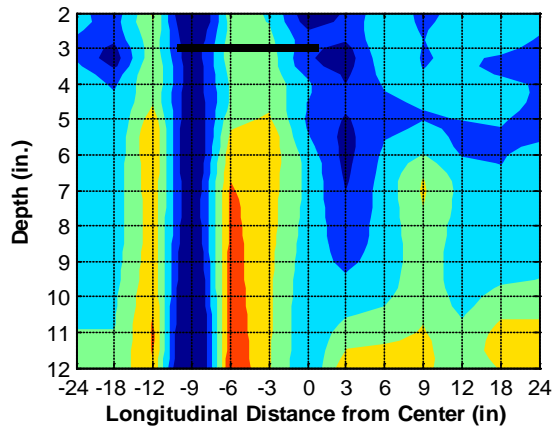
(g) Slab #10
(delamination at 3-inch depth)
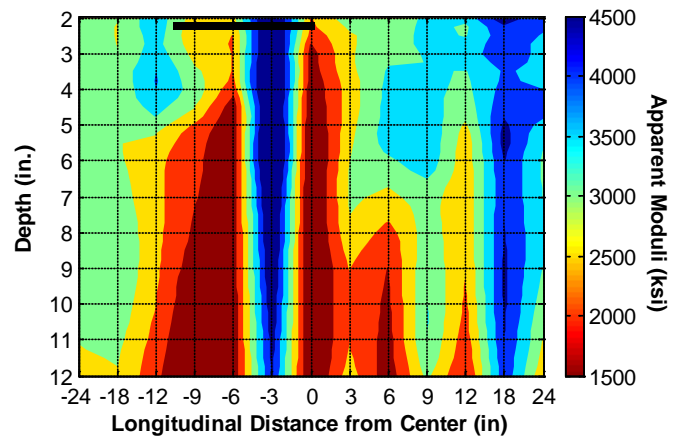
(h) Slab #11
(delamination at 2-inch depth)
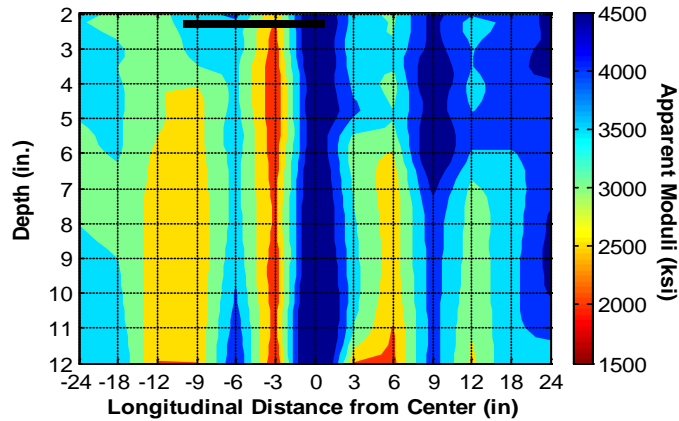
(i) Slab #12
(delamination at 3-inch depth)

Figure U-29. USW B-Scan along center line for shotcrete slabs (continued).

REFERENCES

Azari, H., D. Yuan, S. Nazarian, and N. Gucunski. Impact of Testing Configuration and Data Analysis Approach on Detection of Delamination in Concrete Bridge Deck with Sonic Methods. *Proceedings of the 91st Transportation Research Board (TRB) Annual Meeting (CD-ROM)*, Washington, DC, 2012.

Carino, N. J., M. Sansalone, and N. N. Hsu. A Point Source-Point Receiver, Pulse-Echo Technique for Flaw Detection in Concrete. *ACI Material Journal*, Vol. 83, No. 2, 1986, pp. 199-208.

Gucunski, N., and A. Maher. Bridge Deck Condition Monitoring by Impact Echo Method. *Proceedings of International Conference MATEST '98—Life Extension*, Brijuni, Croatia, 1998, pp. 39-45.

APPENDIX V
ANALYSIS OF SPACETEC DATA

Broken tiles on the interior of a tunnel (especially on the roof) are hazardous to vehicles passing through the tunnel at 55 mph. Routine tunnel maintenance measures include examination of tiles and detection and repair of loose tiles. The current state of practice is visual inspection and hammer tapping of the tiles. Prior to our field investigation, the Chesapeake Bay Bridge Tunnel (CBBT) owners had employed one engineer for 1 month to evaluate the bonding of the roof tiles with the hammer-sounding method. Broken and loose tiles were found and marked as such.

During the first round of field evaluation using the SPACETEC scanner in April 2011, a thermal anomaly (an isolated hot spot) around Sta. 483 that did not correspond to any known or marked loose tiles was detected in the field. Manual measurements using impact echo (IE) and ultrasonic echo (US) were carried out to investigate the bonding of tiles at the location of the thermal anomaly.

Both US and IE tests were conducted on the selected 8 tiles by 8 tiles grid covering the location of the detected anomaly. IE was carried out on an adjacent 4 by 4 tile grid. Measurements were taken on individual tiles and repeated three times. Data analysis was done in time domains, examining the time histories of the signal recorded on each tile. Frequency spectra as well as the short-time Fourier transform-based spectrograms were calculated and examined. The envelopes of the US signals depicting their attenuation rates were also calculated.

To showcase the data corresponding to the areas of good bonding and possible debonding, two rows of the 8 by 8 tile grid were selected to be presented here. Figures V.1 to V.3 provide the IE test results corresponding to the tiles on the sixth row (from the top) of the 8 by 8 tile grid illustrating the time histories, spectra and Short-Time Fourier Transform (STFT) spectrograms. The time signals in Figure V.1 attenuate rapidly (the impact energy propagates in the lining), and the frequency spectra are broadband with spectral energy centered around 50 kHz. Four records (one on the top left and three at the bottom left) depict additional frequency peaks of lower frequencies as well. Time and frequency features can be seen simultaneously in the spectrograms of Figure V.3. The above-described characteristics in time and frequency domains are indications of good bonding between the tested tiles and the underlying lining.
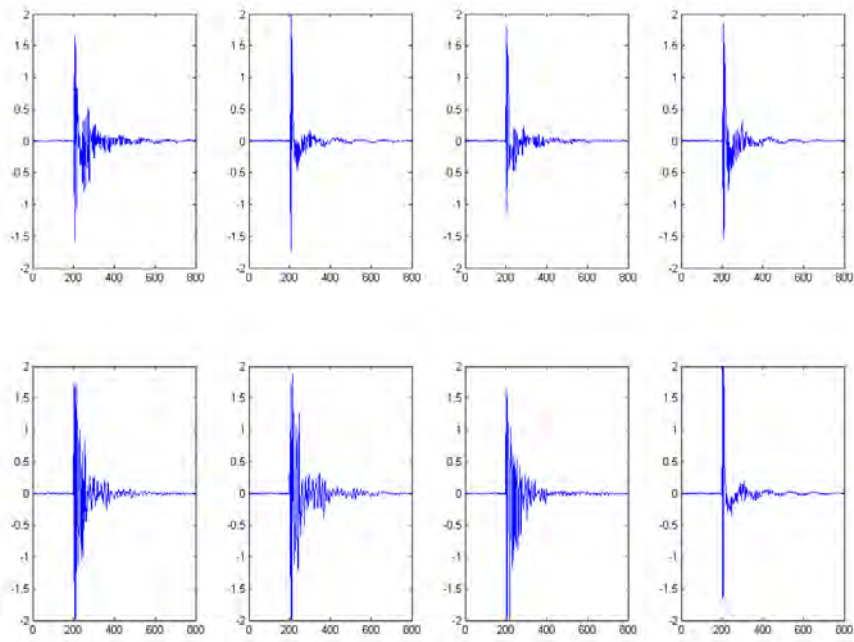
Figure V.1 Time histories of IE signals along the sixth row of the 8 by 8 tile grid at about Sta. 483 of the Chesapeake Bay Bridge Tunnel, where the thermal anomaly in SPACETEC data was detected.
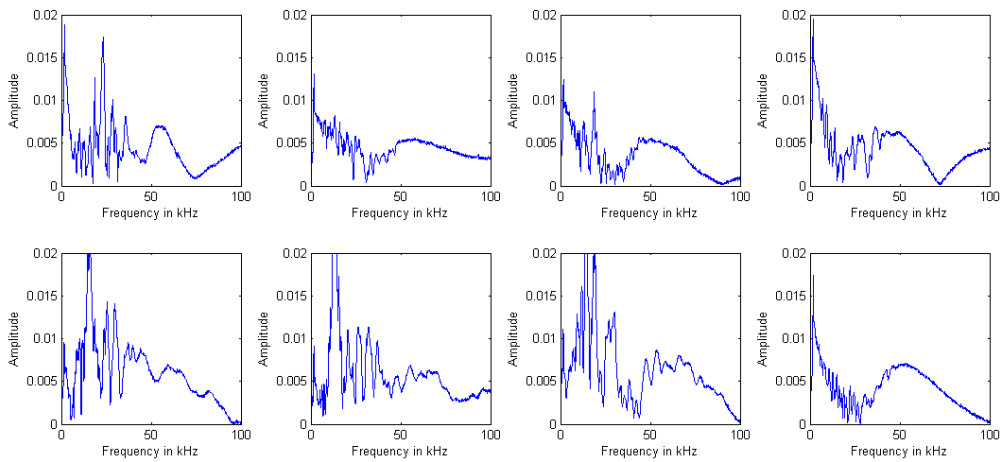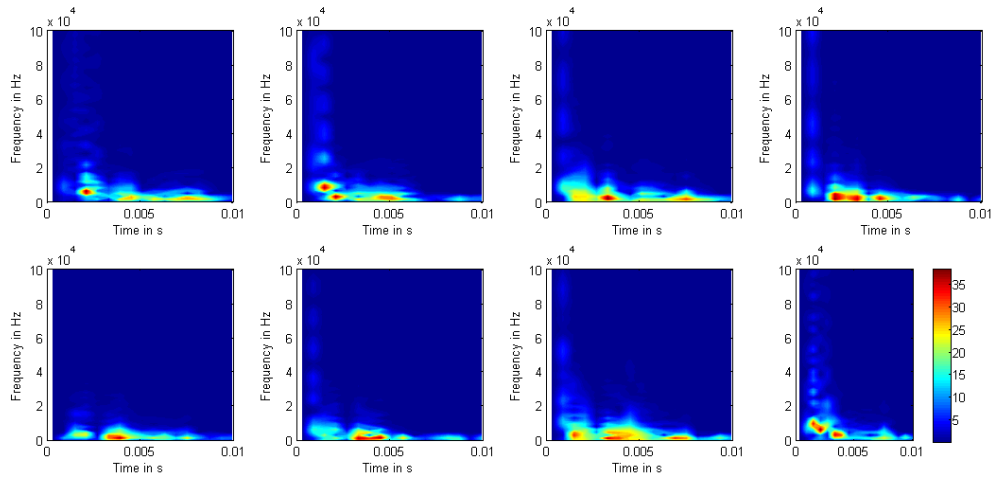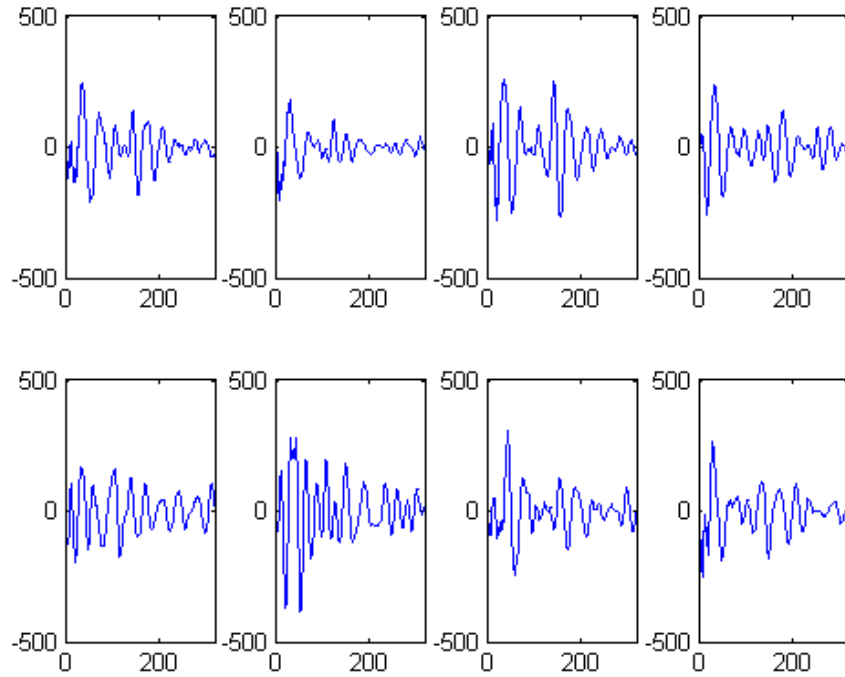

Figure V.2 Frequency spectra of IE signals along the sixth row of the 8 by 8 tile grid at about Sta. 483 of the Chesapeake Bay Bridge Tunnel, where the thermal anomaly in SPACETEC data was detected.
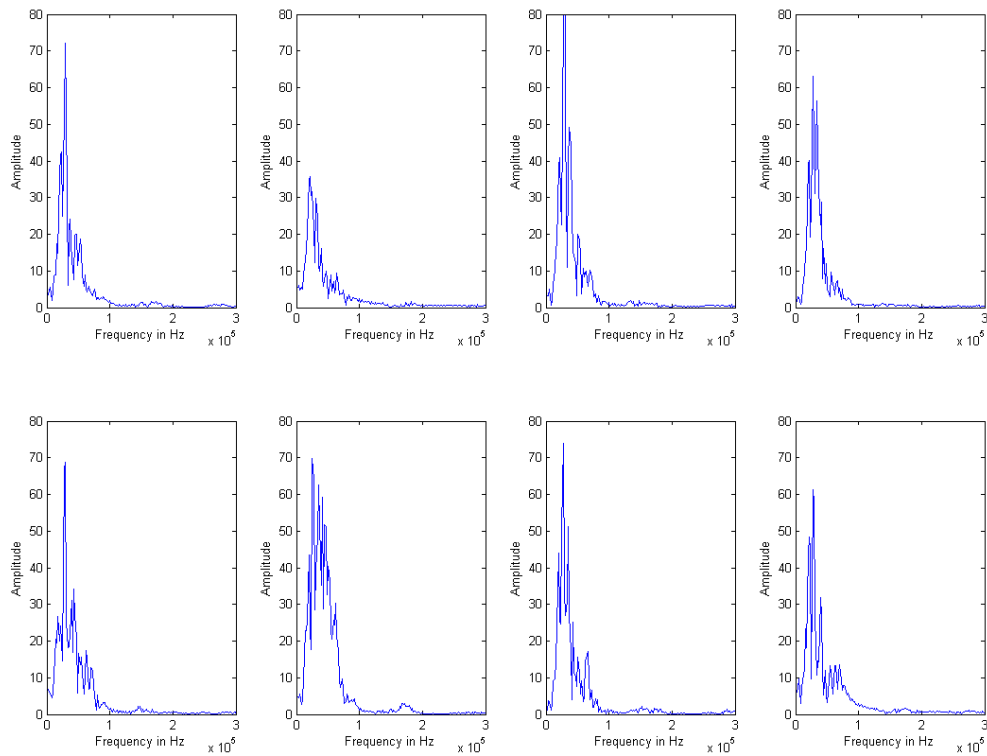
V.2
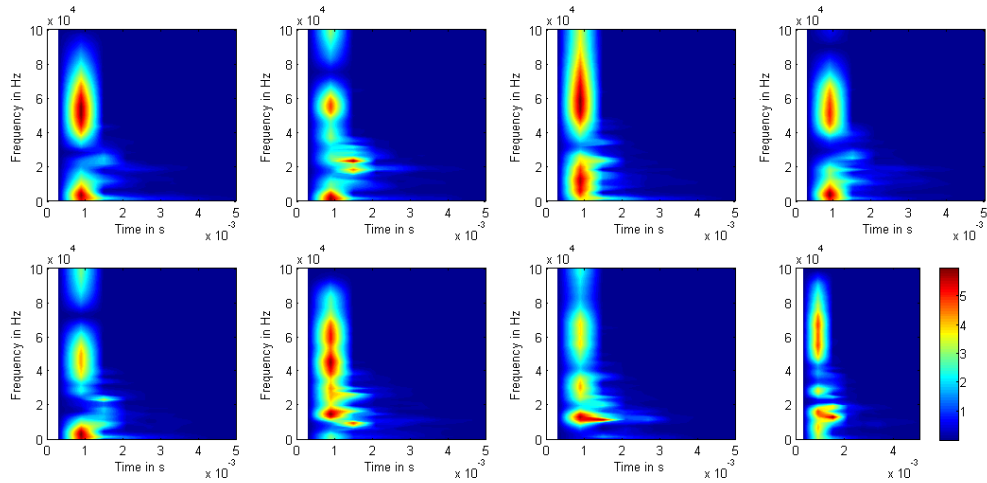
Figure V.3 STFT spectrograms of IE signals along the sixth row of the 8 by 8 tile grid at about Sta. 483 of the Chesapeake Bay Bridge Tunnel, where the thermal anomaly in SPACETEC data was detected.

Figures V.4 to V.6 provide the IE test results corresponding to the tiles on the third row (from the top) of the 8 by 8 tile grid, including the time histories, spectra, and spectrograms. In contrast to those shown in Figure V.1, the time signals of Figure V.4 show little or no attenuation. The frequency spectra contain multiple equally spaced frequency peaks. Both measured time and frequency features are expected for loose tiles, as the debonding from the tunnel lining leads to multiple reflections of the acoustic energy between the tile and the underlying lining.
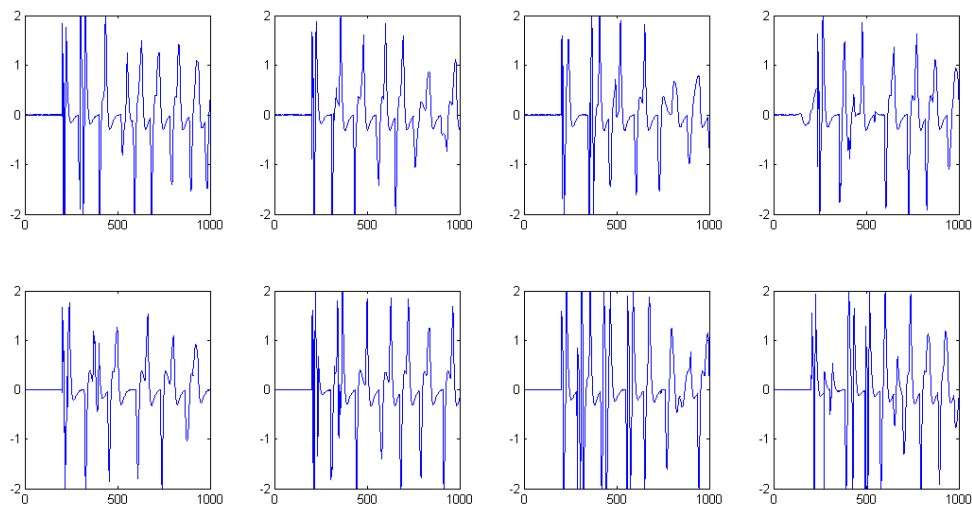
Figure V.4 Time histories of IE signals along the third row of the 8 by 8 tile grid at about Sta. 483 of the Chesapeake Bay Bridge Tunnel, where the thermal anomaly in SPACETEC data was detected.
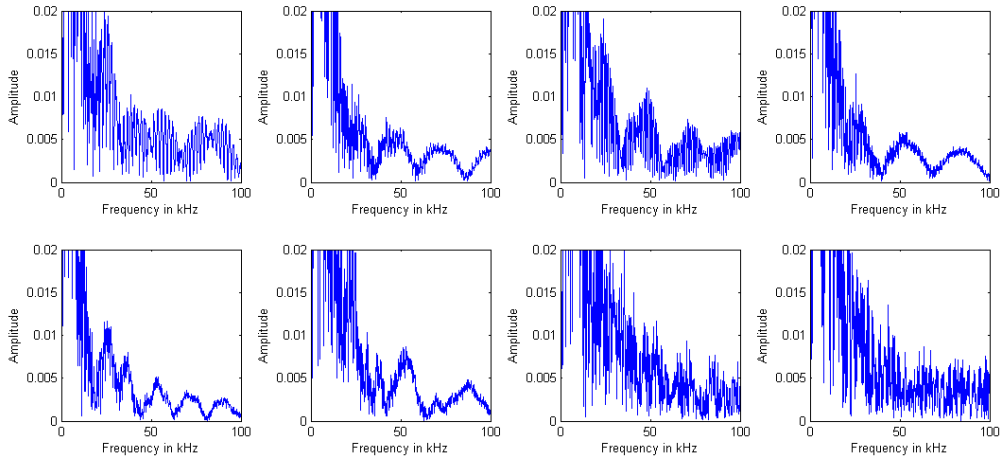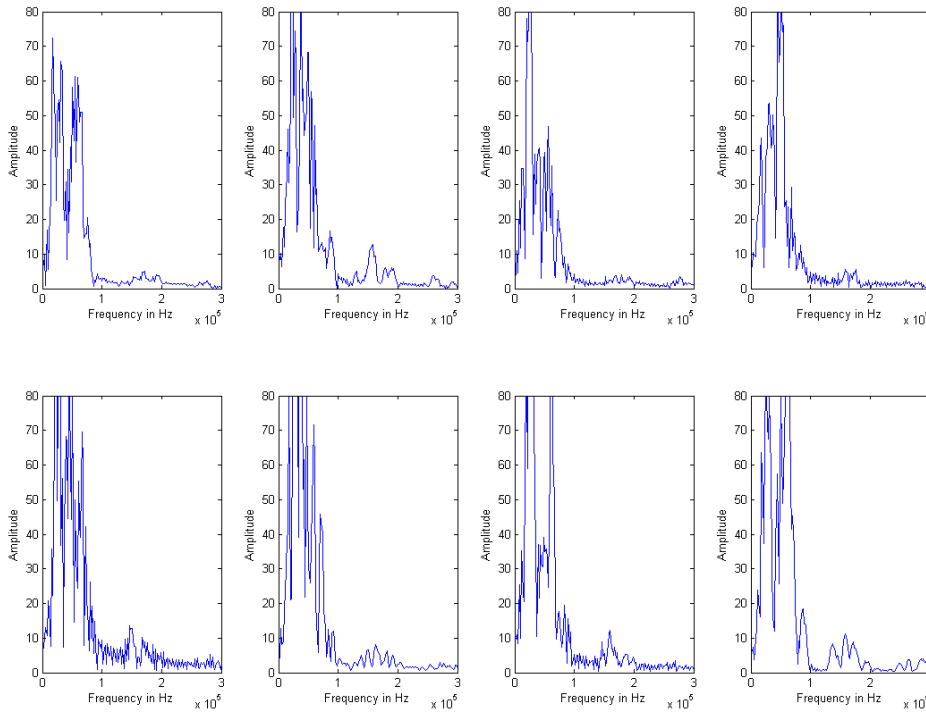
Figure V.5 Frequency spectra of IE signals along the third row of the 8 by 8 tile grid at about Sta. 483 of the Chesapeake Bay Bridge Tunnel, where the thermal anomaly in SPACETEC data was detected.

Figure V.6 STFT spectrograms of IE signals along the third row of the 8 by 8 tile grid at about Sta. 483 of the Chesapeake Bay Bridge Tunnel, where the thermal anomaly in SPACETEC data was detected.

The individual records obtained on each tile were analyzed in both time and frequency domains, and their assessed bonding conditions were color coded and superimposed on the thermal image in Figure V.7. In this figure, green indicates well-bonded tiles, while loose tiles are marked with orange to red spots. A comparison of the obtained results reveals that the tiles at the thermal anomaly detected by SPACETEC as a noticeable warm spot were diagnosed as debonded by IE measurements.
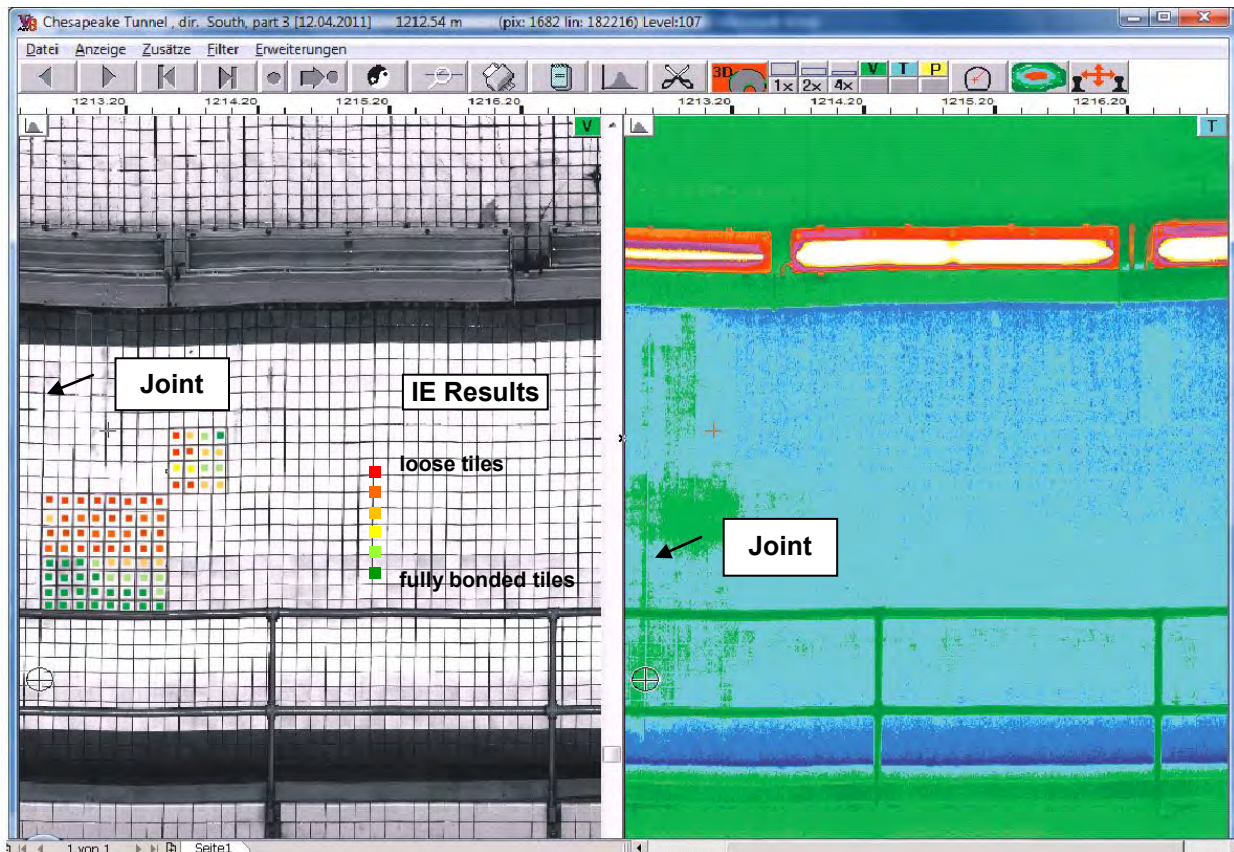
Figure V.7 Visual image (left) and thermal image (right) at about Sta. 483 of the Chesapeake Bay Bridge Tunnel. The bonding conditions of tiles around the location of the thermal anomaly (warm spot) evaluated based on IE measurements are color coded and superimposed on the thermal image.

US measurements were taken on the same 8 by 8 tile grid (8 by 8 grid only) as the one described for IE testing. The US time histories and spectra obtained on the sixth row of the tiles (from top) are shown in Figures V.8 and V.9, respectively. The US time histories and spectra obtained on the third row of the tiles (from top) are shown in Figures V.10 and V.11, respectively.

The characteristics of the ultrasonic echo signals were similar to those of the IE signals: when the tiles were loose, the time signals were less attenuated. The spectral energy in the frequency spectra on bonded tiles were centered around 50 kHz (which is about the center frequency of the transducer). The spectra obtained on presumably debonded tiles were broader, showing multiple peaks. US amplitudes were generally higher on debonded tiles. However, given the variability of the pressing pressure during hand measurements, no reliable correlation between the US amplitude and debonding condition could be concluded.

The individual US signals were analyzed, and their bonding conditions were color coded and superimposed on the thermal image of Figure V.12. Similar to the IE results, the manual US measurements indicated the presence of loose tiles where a thermal anomaly (warm spot) by SPACETEC was registered. It appears that loose tiles can be detected as thermal anomalies in SPACETEC thermal images.

Figure V.8 US time histories along the sixth row of the 8 by 8 tile grid at about Sta. 483 of the Chesapeake Bay Bridge Tunnel, where the thermal anomaly in SPACETEC data was detected.

Figure V.9 Frequency spectra of US signals along the sixth row of the 8 by 8 tile grid at about Sta. 483 of the Chesapeake Bay Bridge Tunnel, where the thermal anomaly in SPACETEC data was detected.
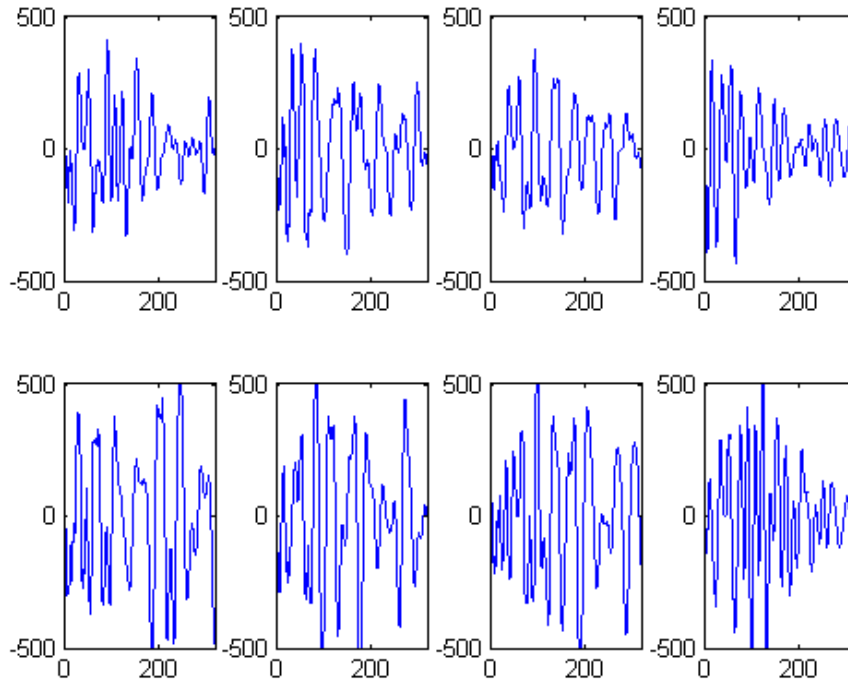
Figure V.10 US time histories along the third row of the 8 by 8 tile grid at about Sta. 483 of the Chesapeake Bay Bridge Tunnel, where the thermal anomaly in SPACETEC data was detected.

Figure V.11 Frequency spectra of US signals along the third row of the 8 by 8 tile grid at about Sta. 483 of the Chesapeake Bay Bridge Tunnel, where the thermal anomaly in SPACETEC data was detected.

V.7
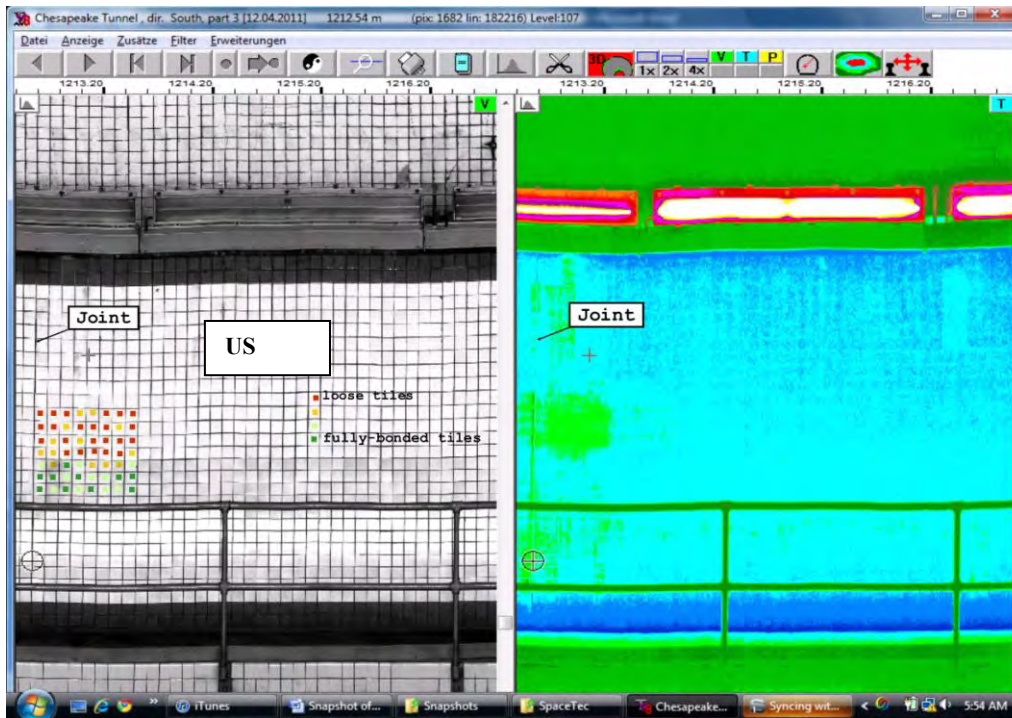
Figure V.12 Visual image (left) and thermal image (right) at about Sta. 483 of the Chesapeake Bay Bridge Tunnel. The bonding conditions of tiles around the location of the thermal anomaly (warm spot) evaluated based on US measurements are color coded and superimposed on the thermal image.

To further investigate this hypothesis, the thermal and visual images obtained from the Spacetec scanner along one direction were compared against the manual hammer-sounding maps provided to the research team by CBBT owners. An example of such comparisons obtained at about Sta. 475 is given in Figure V.13. Thermal anomalies (marked green) seemed to correspond well to the tiles deemed as loose (or debonded) during the hammer-sounding survey.
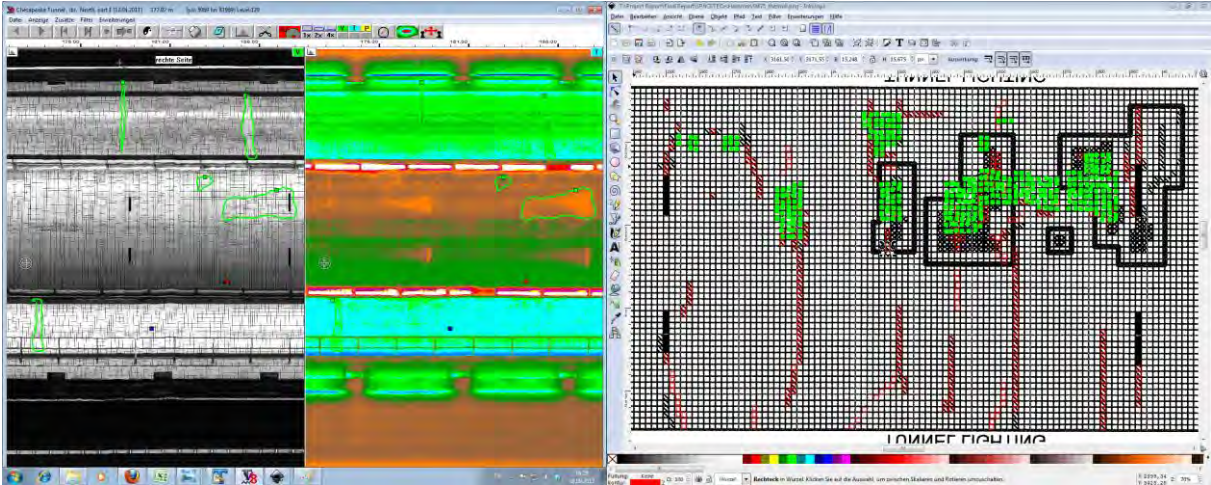
Figure V.13 A comparison of anomalies detected in SPACETEC thermal and visual images (left) against the results of the manual hammer-sounding survey conducted by tunnel owners (right) at about Sta. 475. The thermal anomalies are superimposed on the hammer-sounding map as green-colored tiles, while broken tiles seen on visual images are shown as red hatched areas.

A statistical analysis was performed to establish the sensitivity of thermal/visual imaging to the debonding of tiles on the tunnel ceiling, as detected by hammer sounding. Both thermal and visual images were used to find anomalies in Spacetec survey results. Data collected along one direction (SB) was used for this analysis. The sensitivity was calculated according to the following equation:

Sensitivity = TP / (TP+FN)   **(Equation V.1)**

where TP and FN stand for true positives and false negatives, respectively. Given the nature of data available, only could the sensitivity be estimated here. The hammer sounding results were assumed to give the "true" number and location of debonded tiles. That means anomalies detected by Spacetec, where no delaminated tiles were marked were considered as "false alarms".

Sensitivity was calculated separately for defect groups of various sizes (tile counts) as shown in Figure V.14 below. The overall sensitivity (independent of the defect size) was obtained as 0.71 or 71%. 97% of areas including more than 50 tiles could be detected, compared to 55% for areas covering less than 50 tiles. A visual comparison of thermal/visual anomalies versus the delaminated tiles is provided in Figures V.15 to V.37. In these figures, thermal anomalies are superimposed on hammer-sounding maps at various locations along the tunnel. Please note that the hammer sounding maps were flipped to facilitate the superposition.
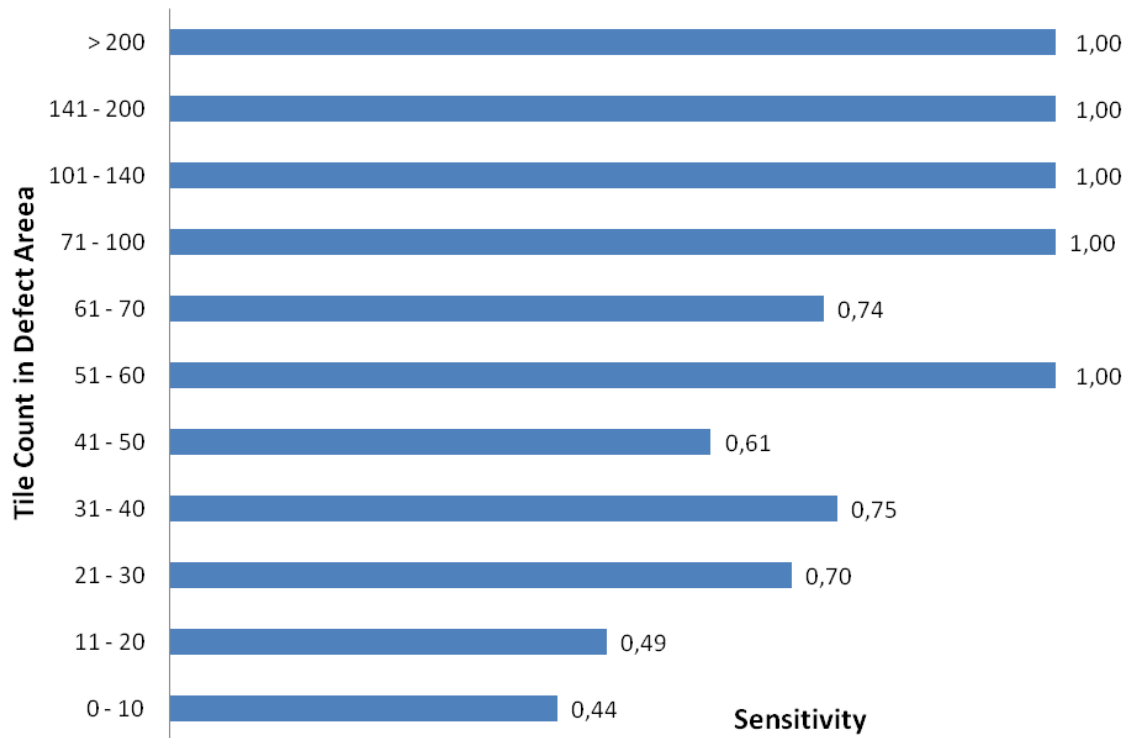
Figure V.14 Sensitivity of SPACETEC thermal and visual imaging to debonded tiles as detected by manual hammer-sounding. The sensitivity is calculated for defect areas of various sizes (tile count).

An additional analysis was performed to investigate why some of the debonded areas were not detected in Spacetec data. Very small debonded areas covering less than 20 tiles seem not to be always detectable in thermal images obtained during this particular survey. Reflection of light from the surface of tiles (at certain scanning angles) and the interference with the temperature gradient in front of the air vents were found to be the top two factors why larger debonded areas were not detected.

This analysis suggests that a combination of thermal and visual imaging offers a reliable alternative to the tedious practice of hammer sounding on individual tiles. The great advantage of such scanning operations becomes obvious considering the speed of the SPACETEC survey (about one hour at 1.5 km/h or 1 mph) in comparison to that of the tedious hammer sounding (one man-month).
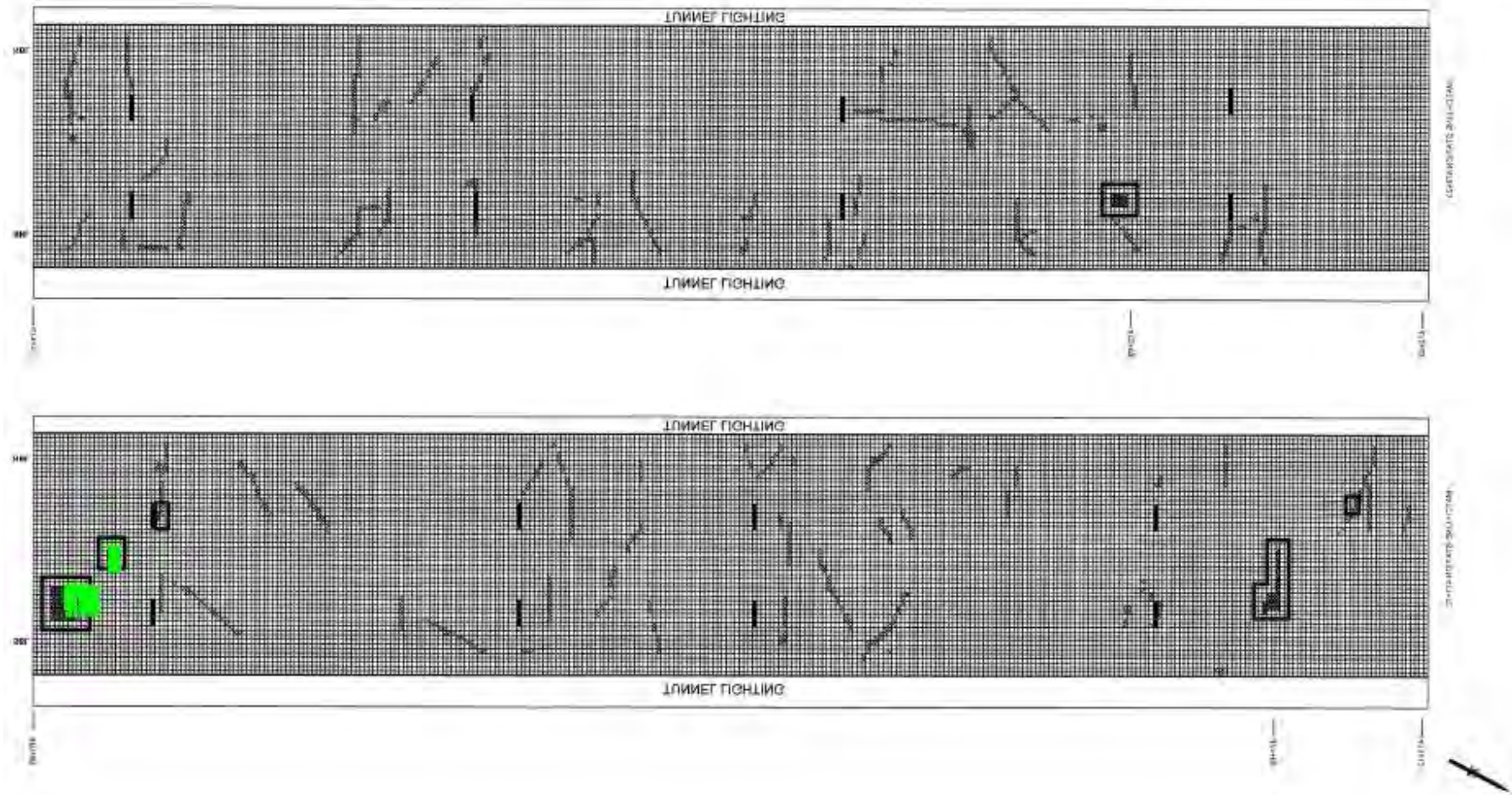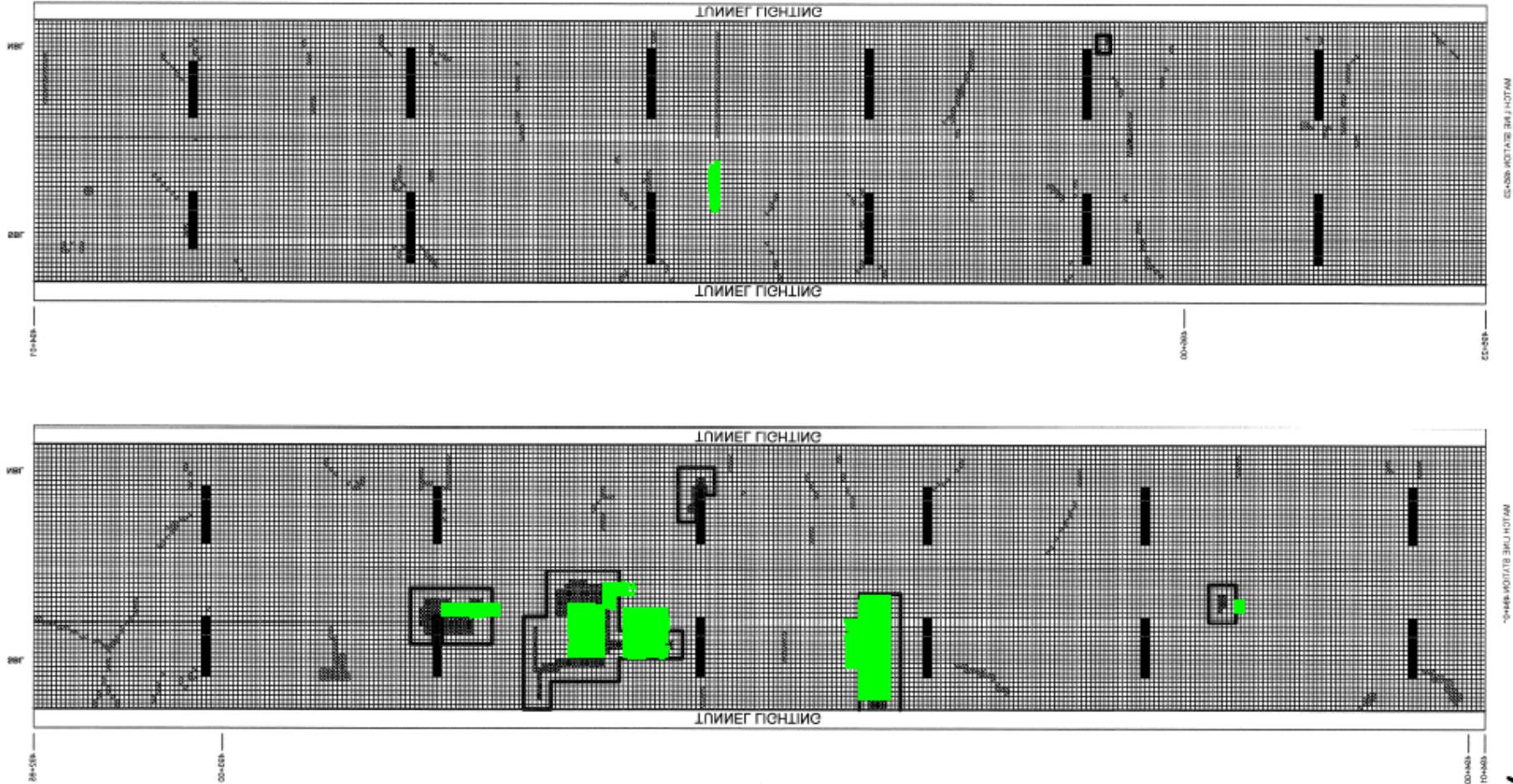
Figure V.15 Visual comparison of thermal anomalies and delaminated tiles (as detected by hammer sounding) between Sts. 470+00 and 472+23.
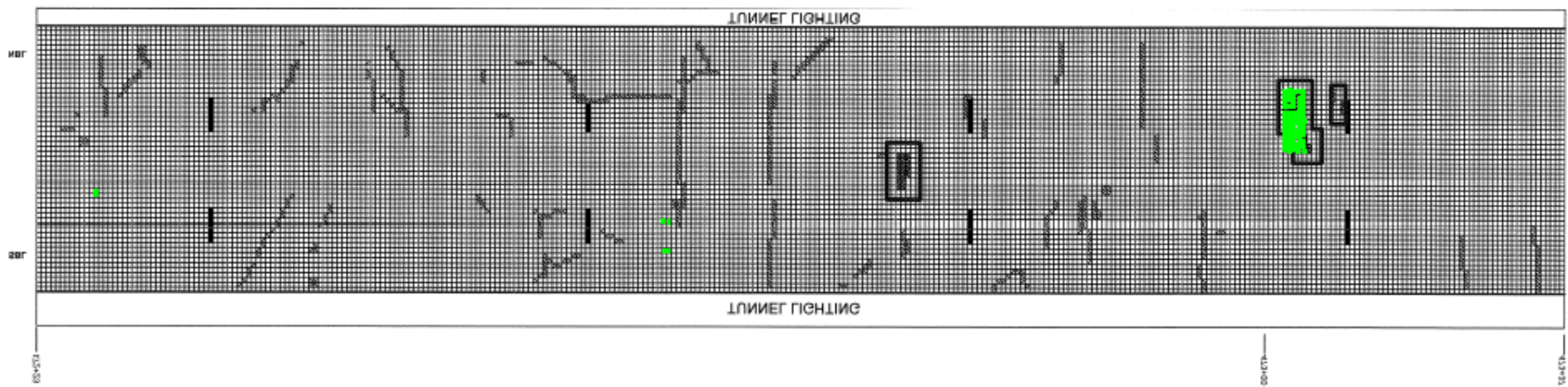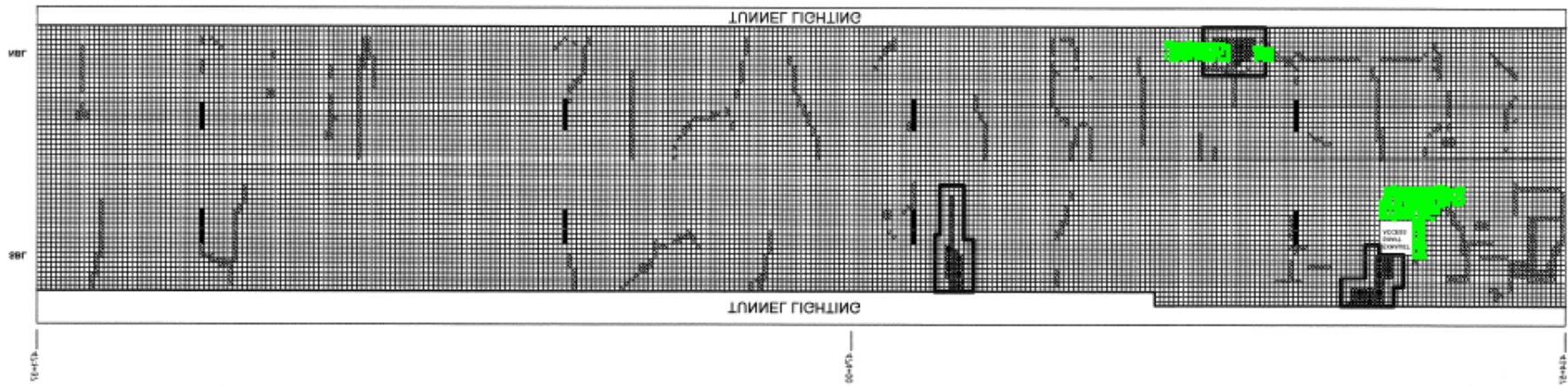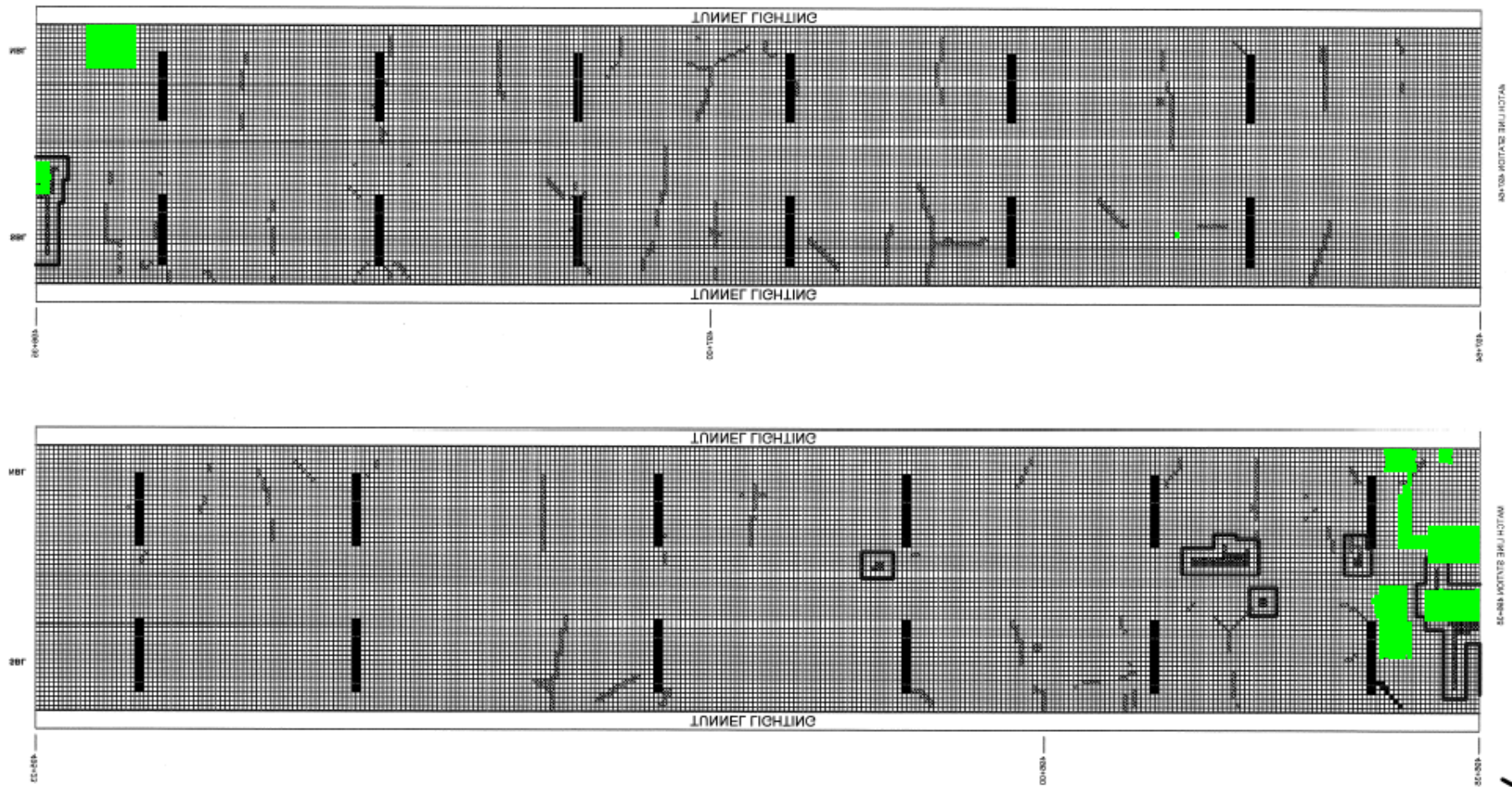
Figure V.16 Visual comparison of thermal anomalies and delaminated tiles (as detected by hammer sounding) between Sts. 472+23 and 474+57.
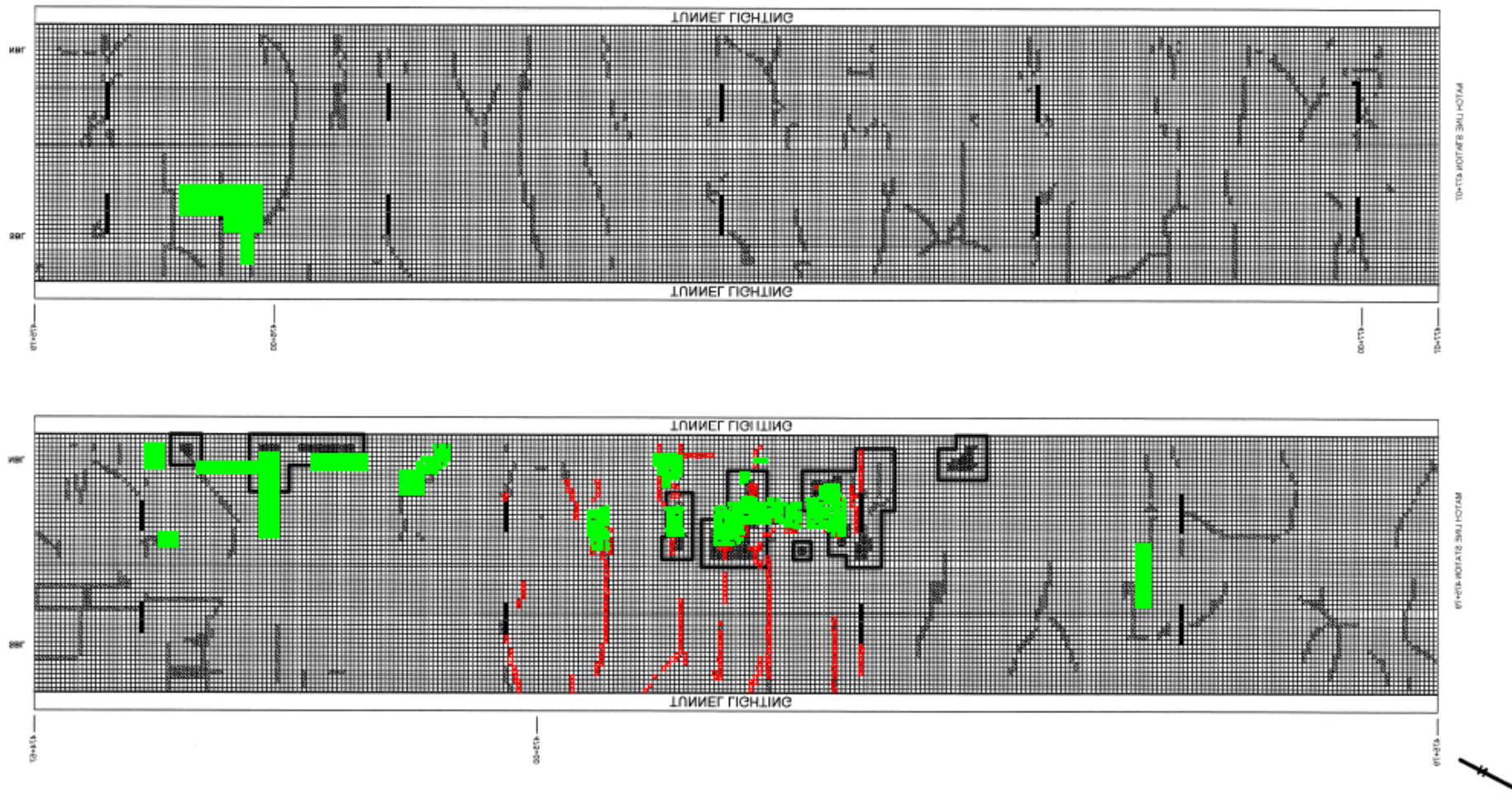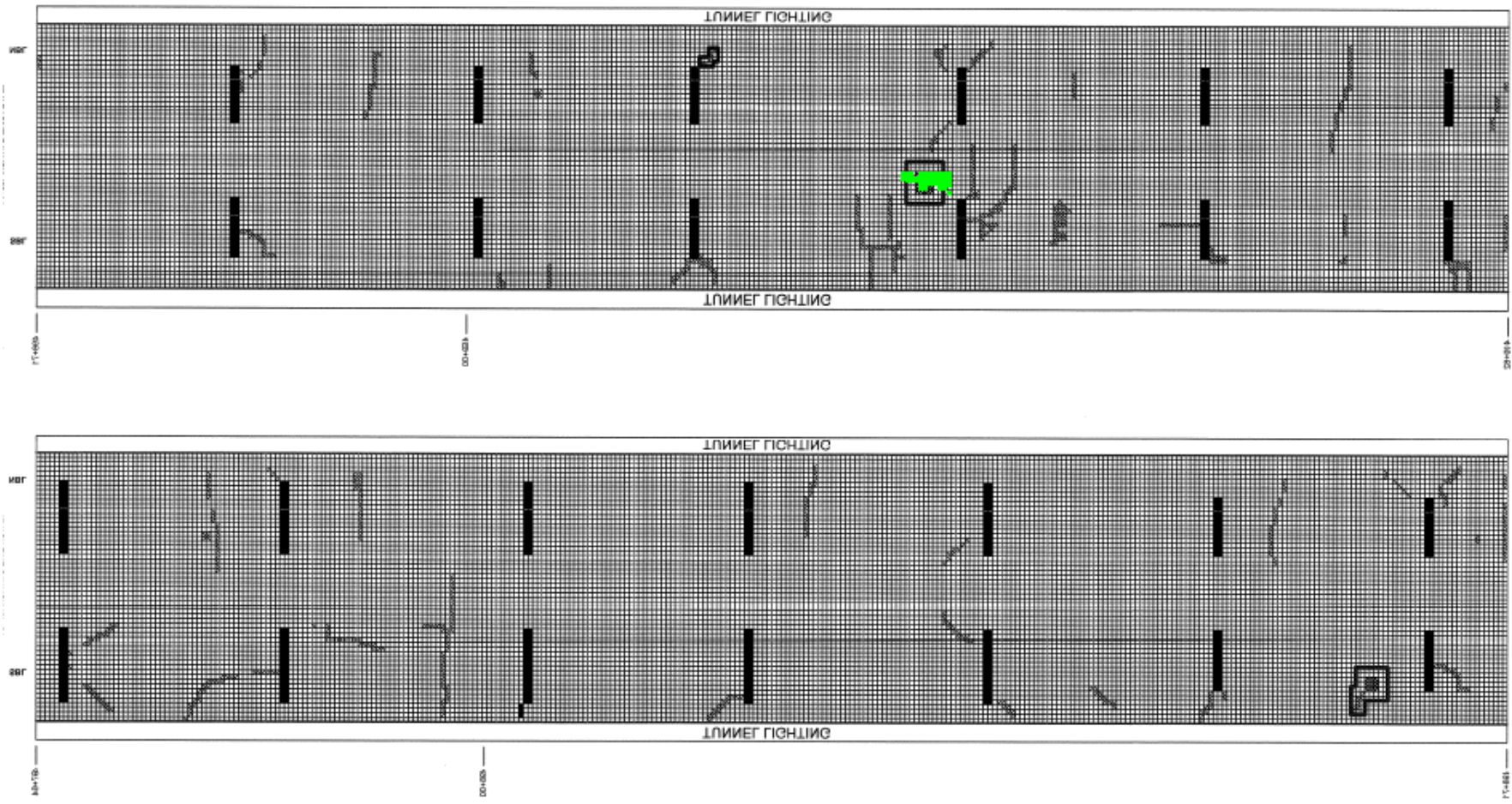
Figure V.17 Visual comparison of thermal anomalies and delaminated tiles (as detected by hammer sounding) between Sts. 474+57 and 477+07.
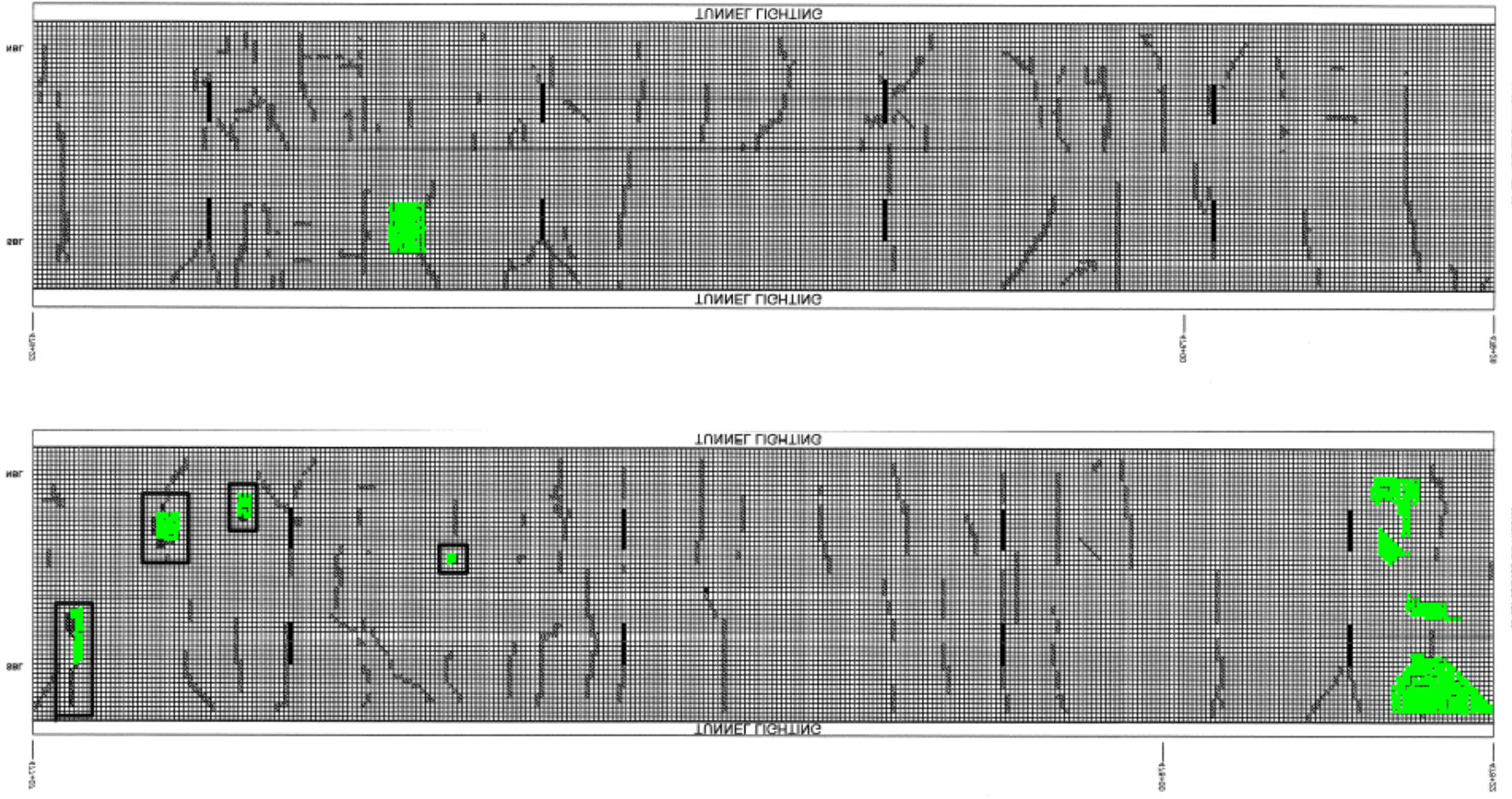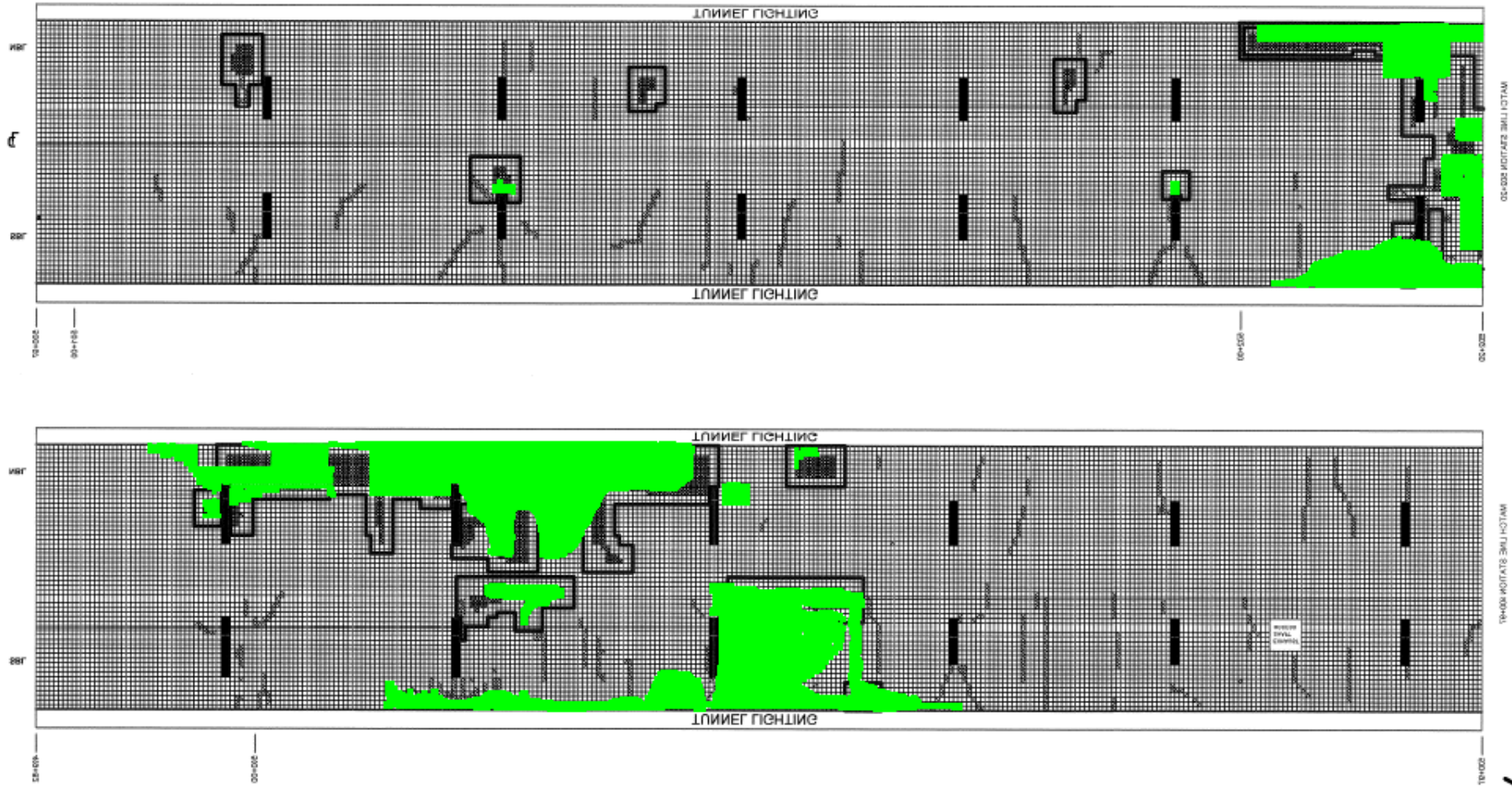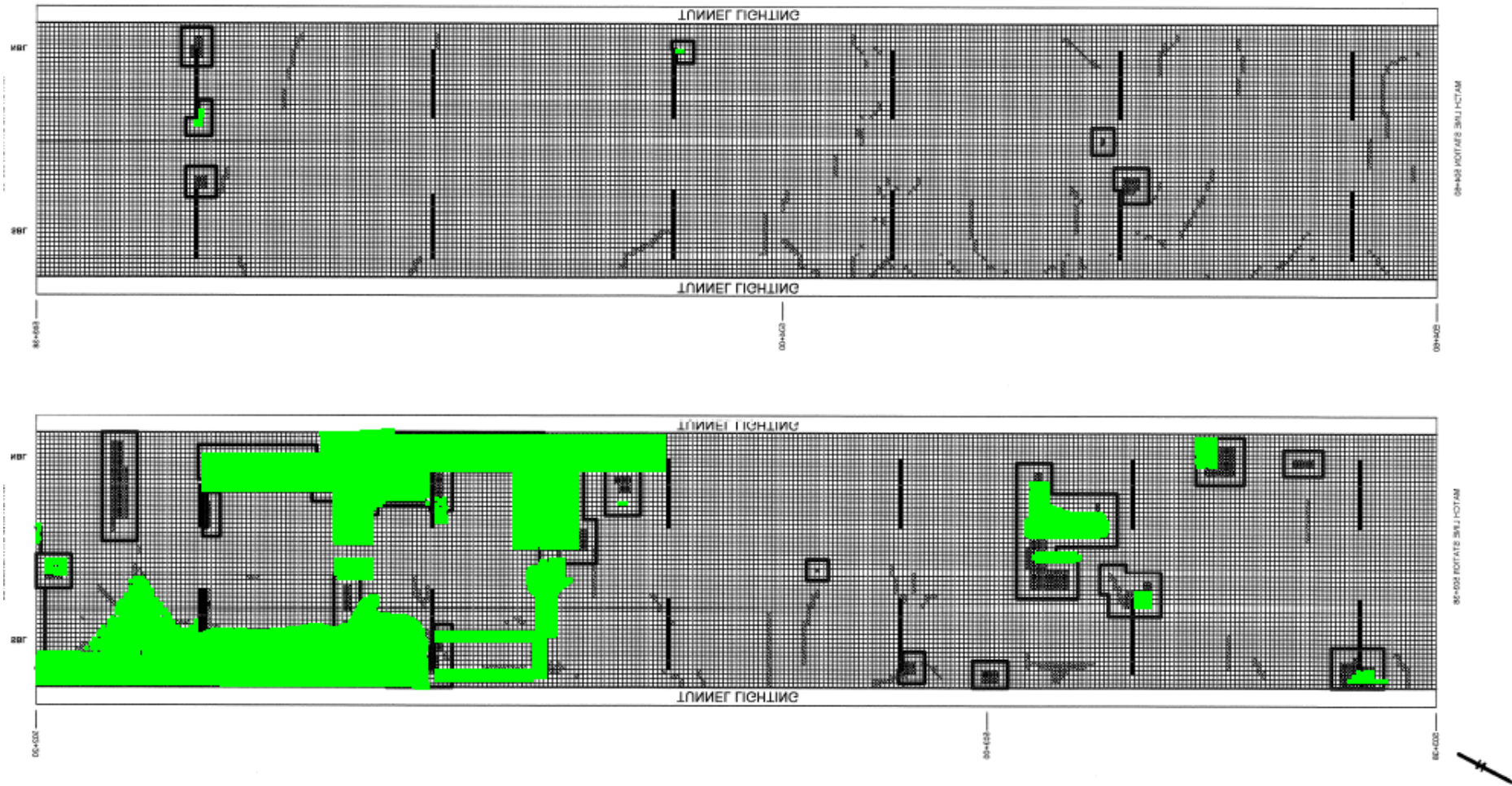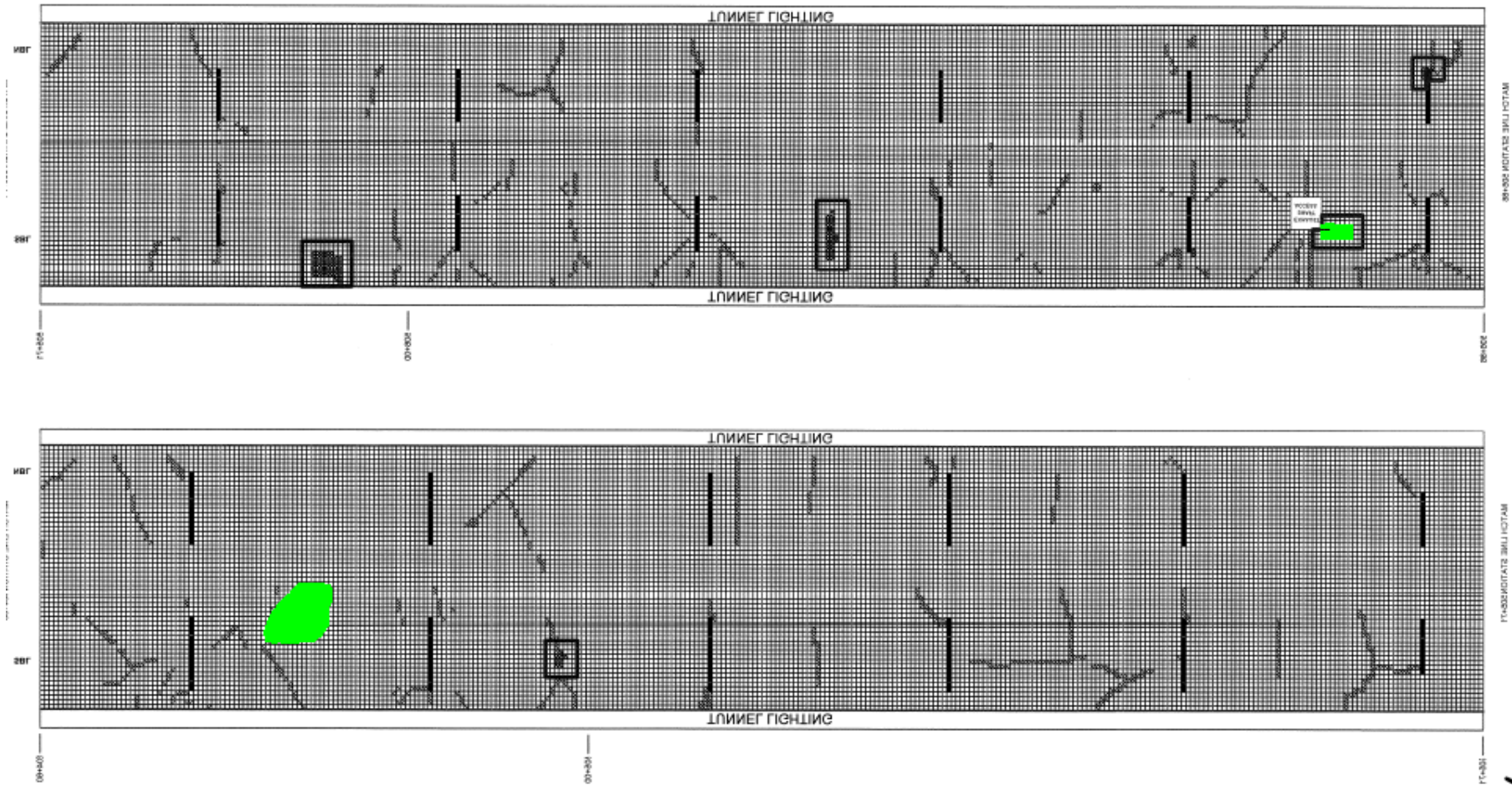
Figure V.18 Visual comparison of thermal anomalies and delaminated tiles (as detected by hammer sounding) between Sts. 477+07 and 479+28.
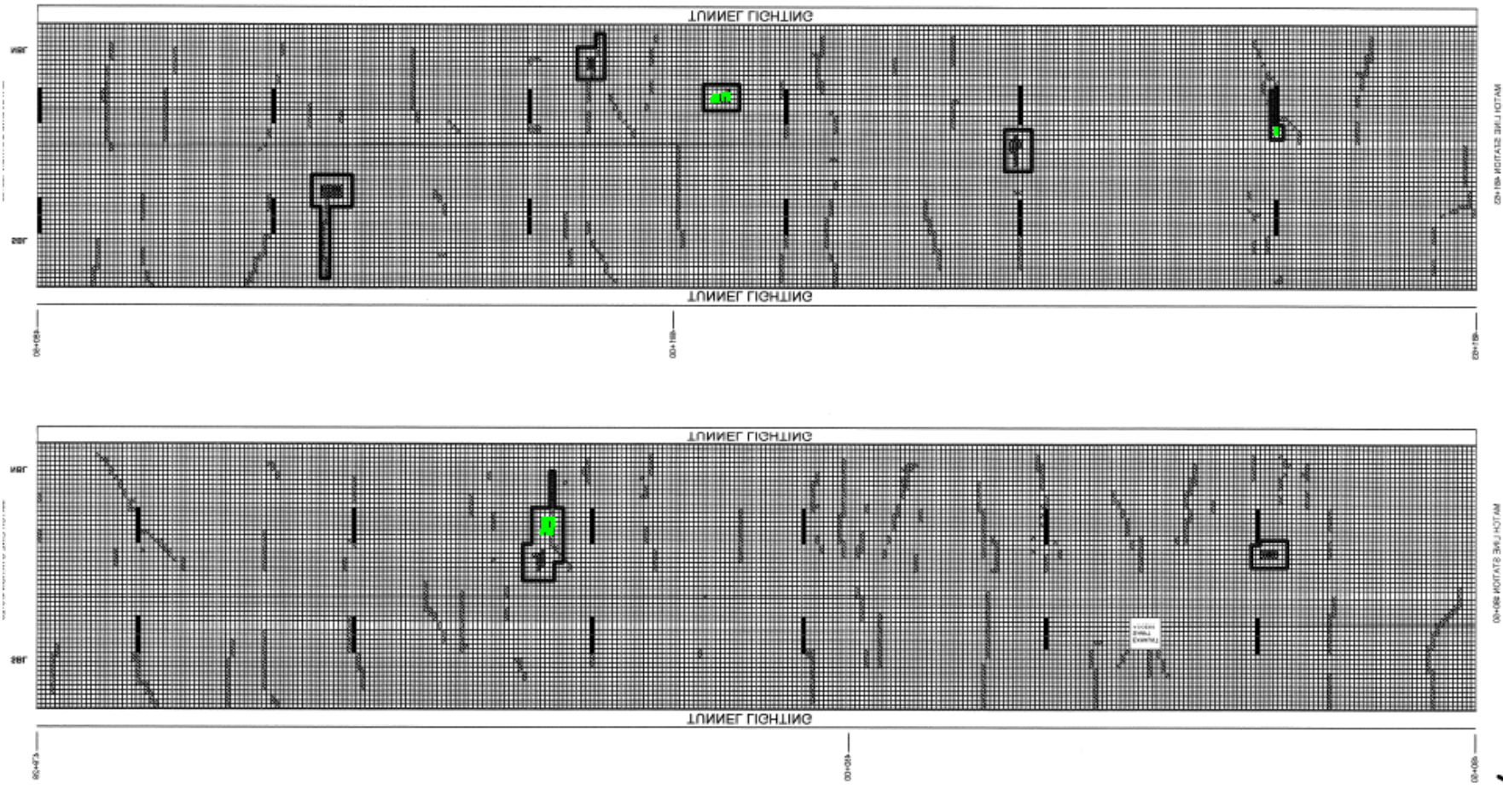
Figure V.19 Visual comparison of thermal anomalies and delaminated tiles (as detected by hammer sounding) between Sts. 479+28 and 481+63.
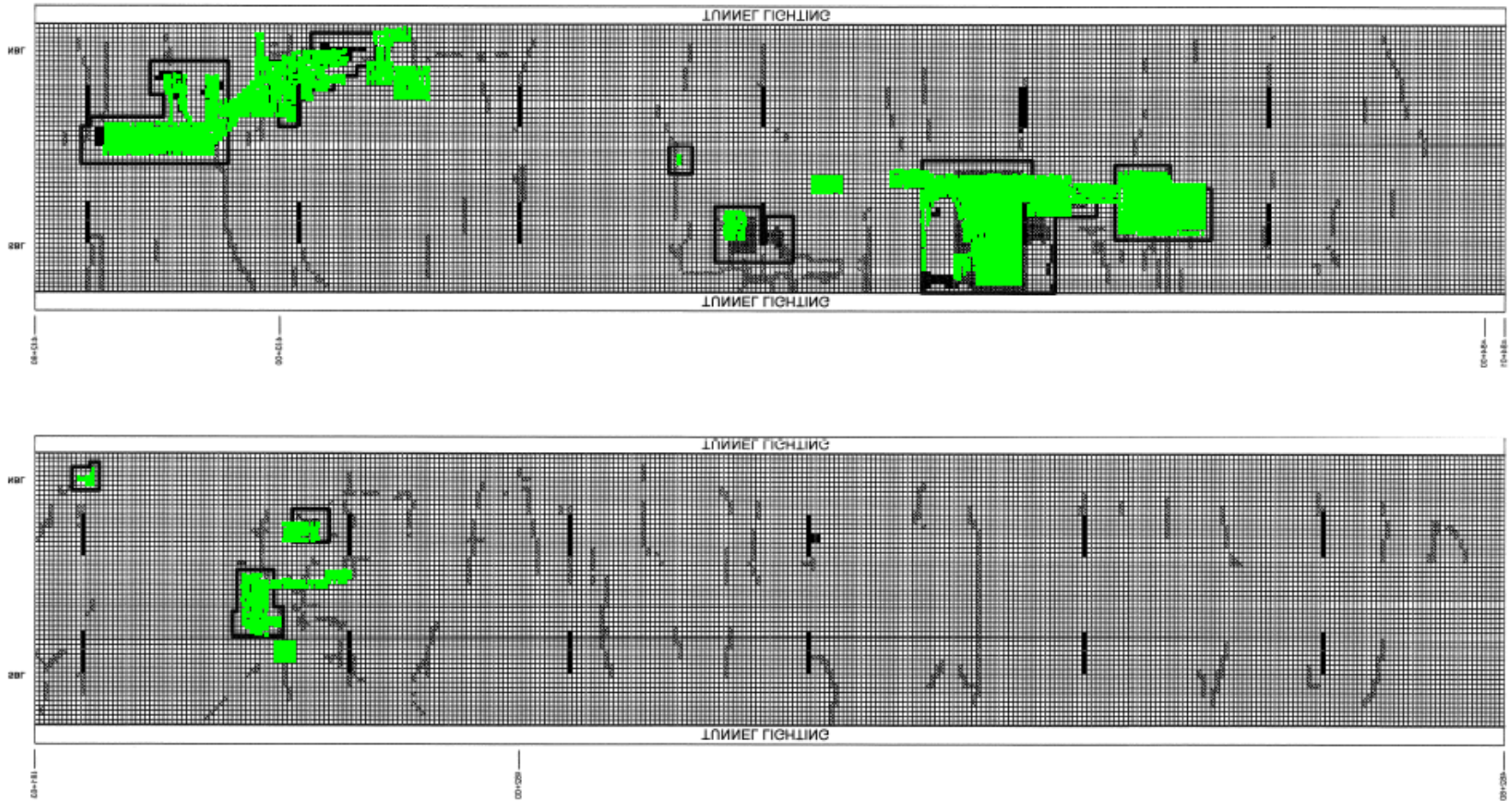
Figure V.20 Visual comparison of thermal anomalies and delaminated tiles (as detected by hammer sounding) between Sts. 481+63 and 484+01.
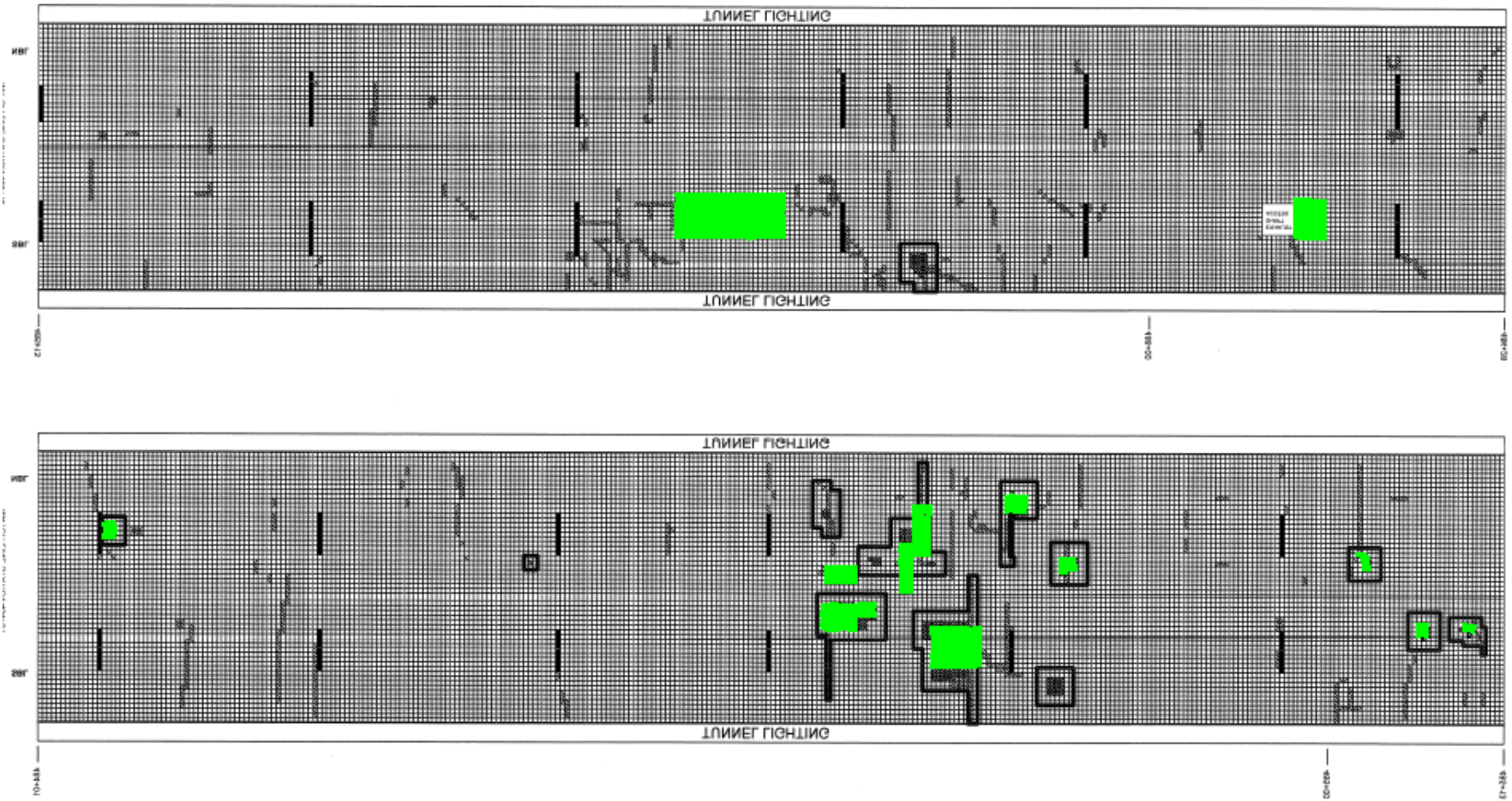
Figure V.21 Visual comparison of thermal anomalies and delaminated tiles (as detected by hammer sounding) between Sts. 484+01 and 486+28.
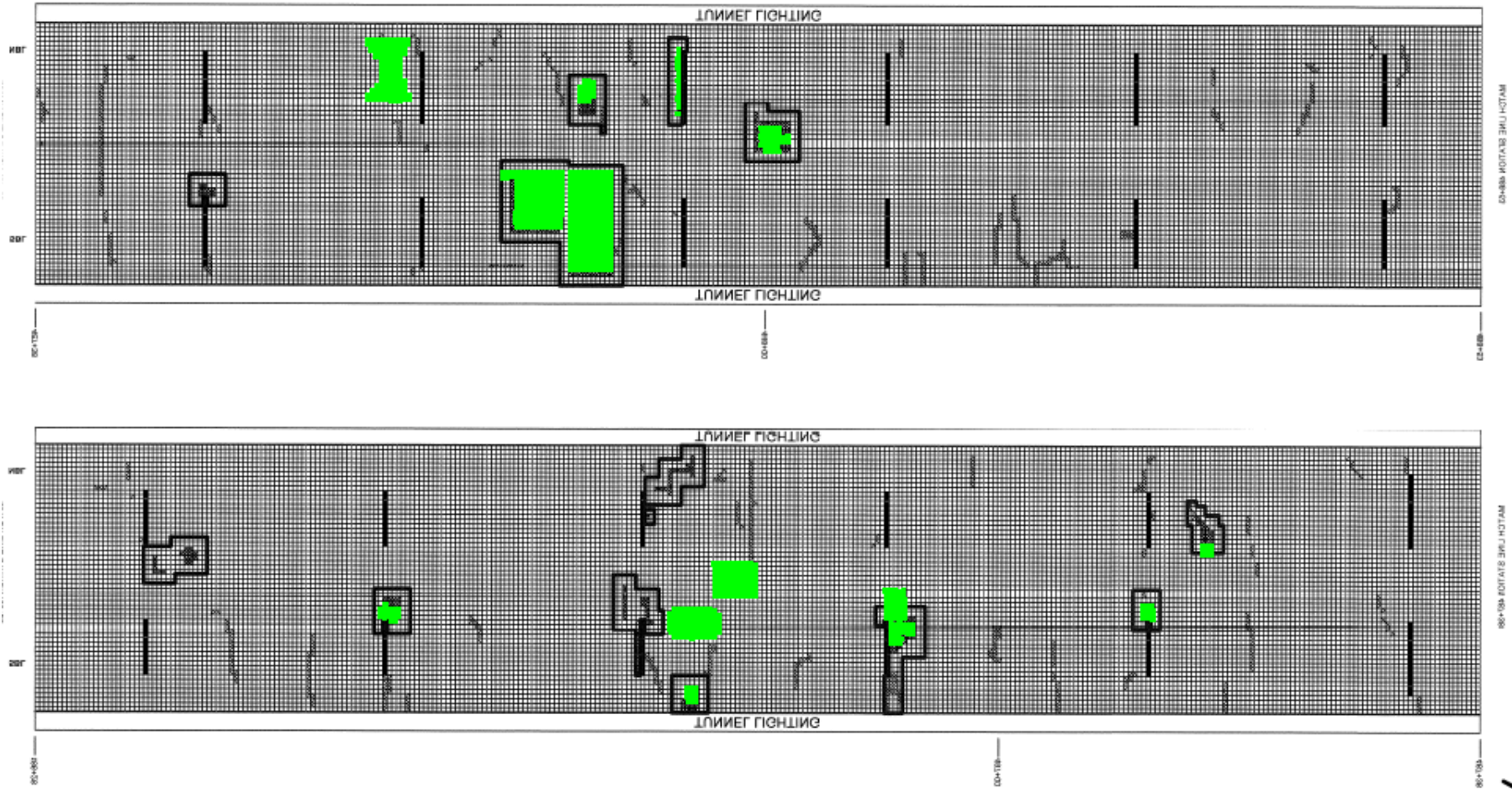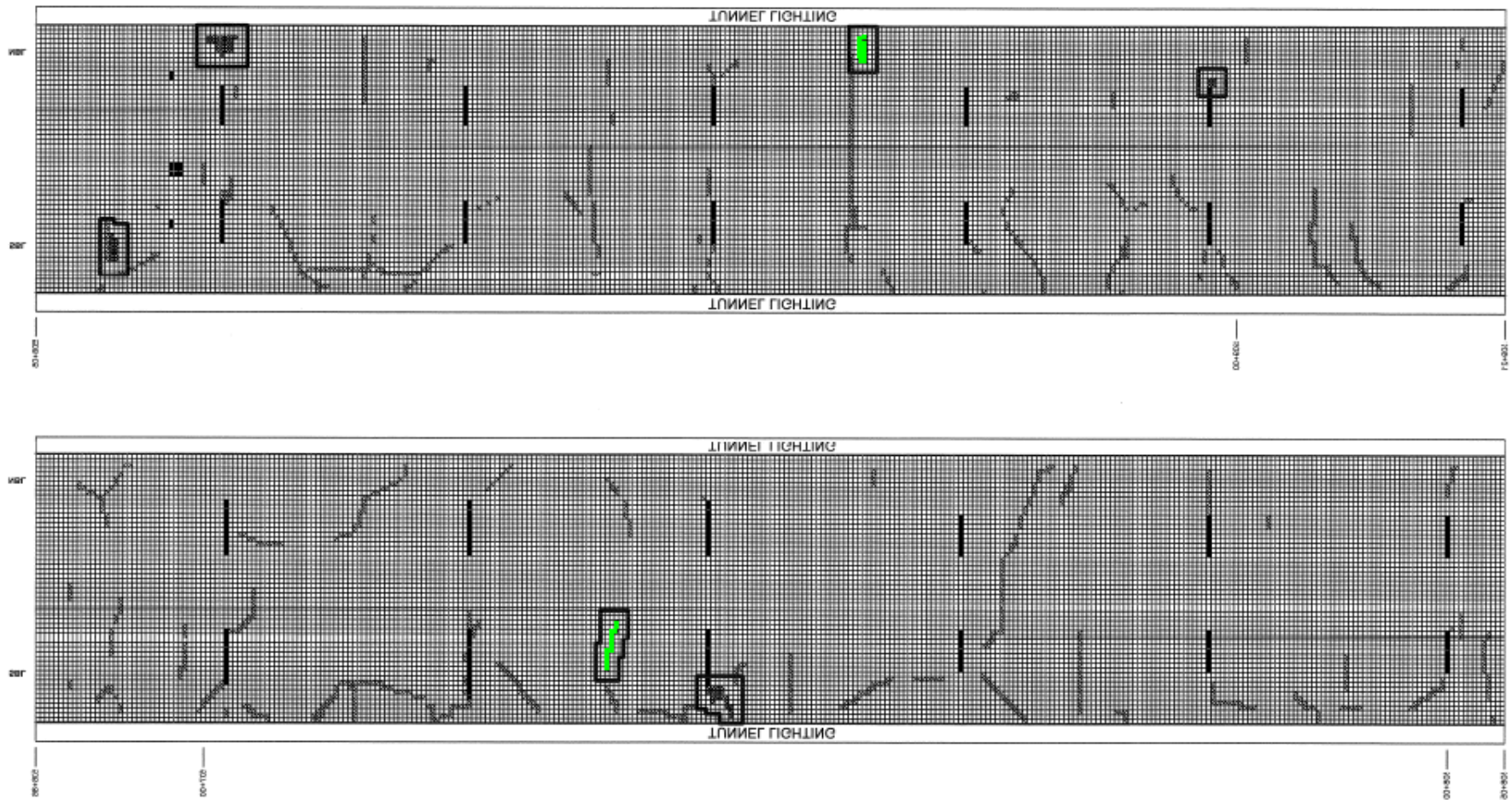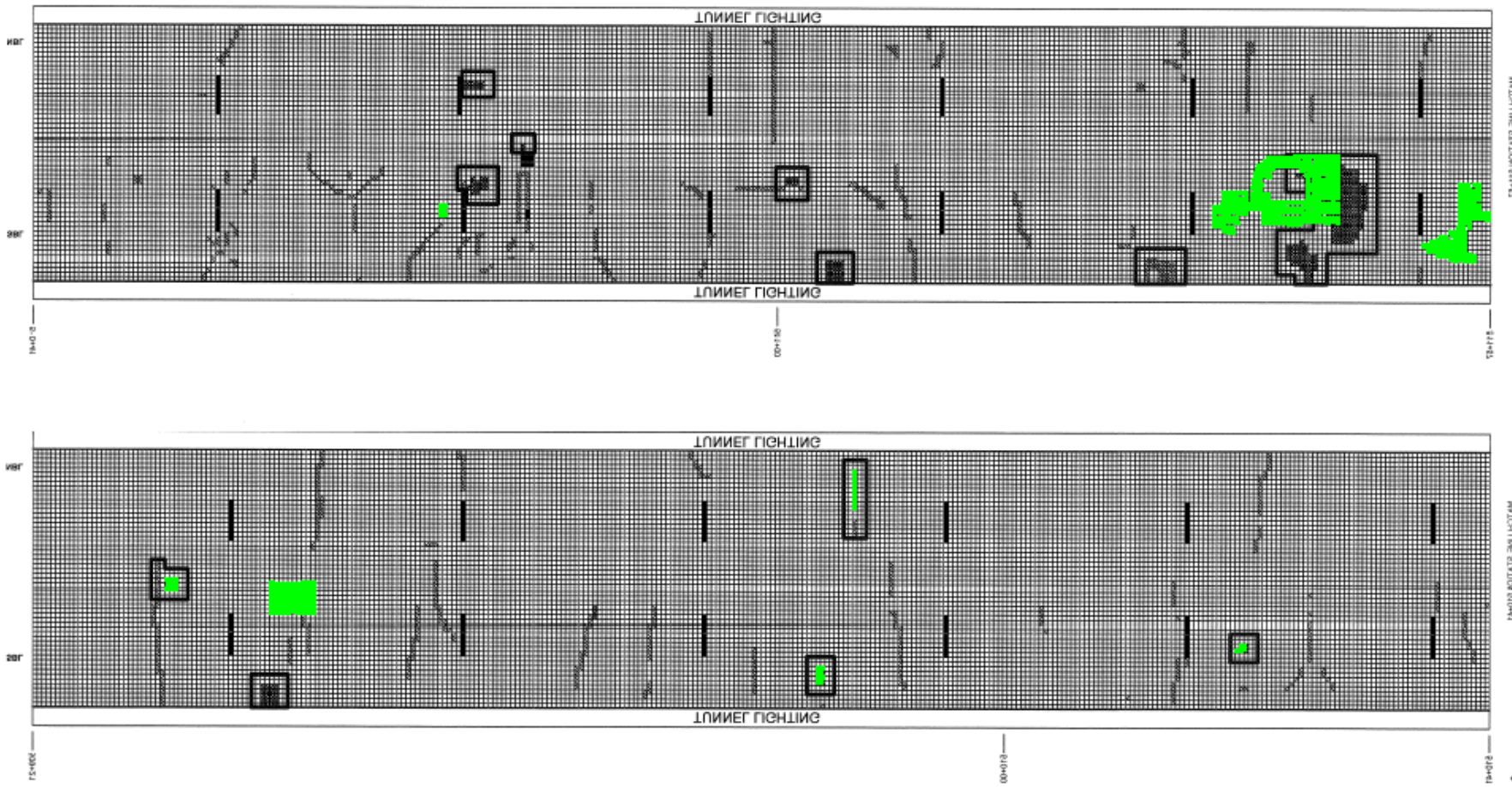
Figure V.22 Visual comparison of thermal anomalies and delaminated tiles (as detected by hammer sounding) between Sts. 486+28 and 488+53.
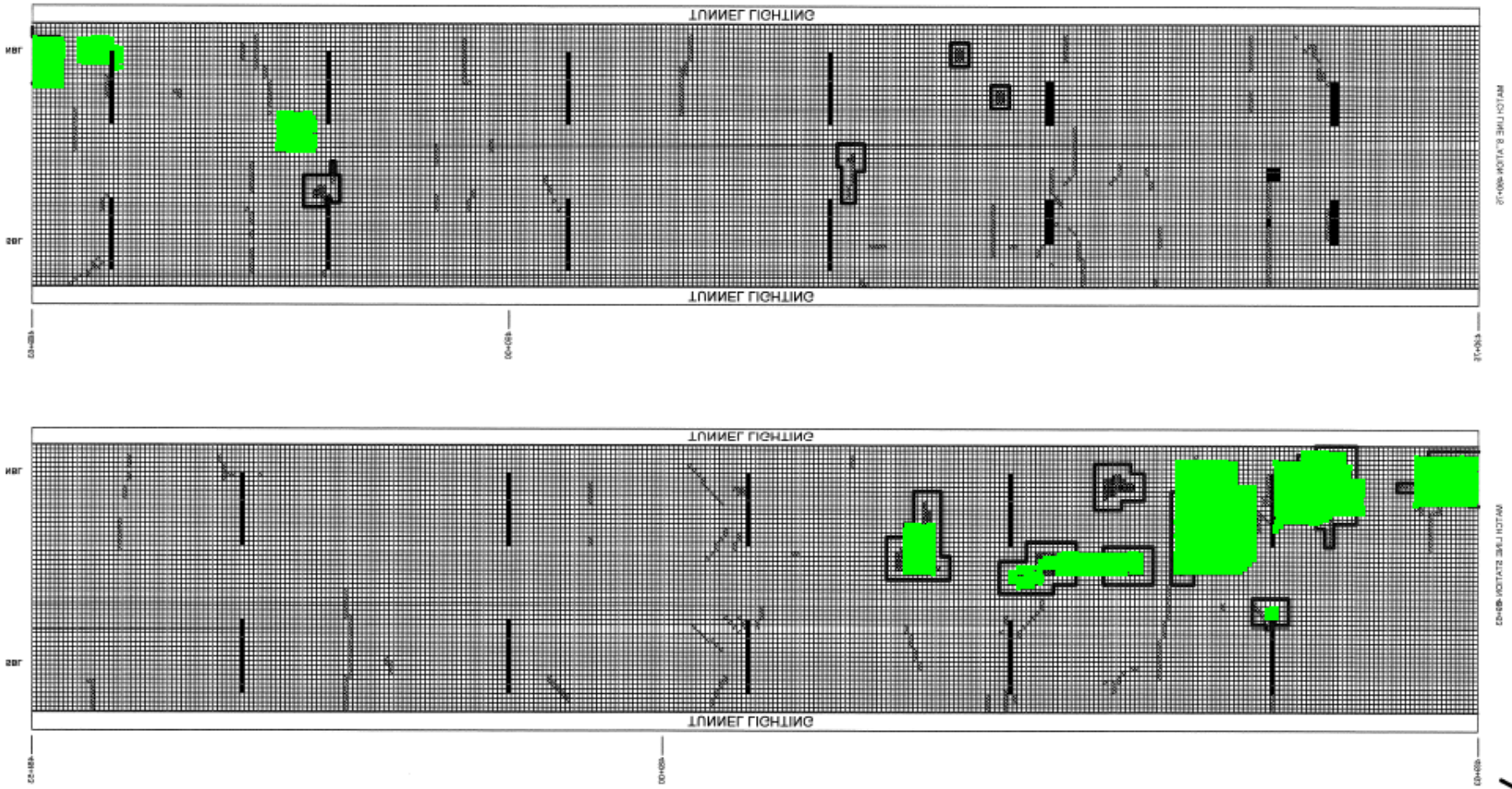
Figure V.23 Visual comparison of thermal anomalies and delaminated tiles (as detected by hammer sounding) between Sts. 488+53 and 490+75.

Figure V.24 Visual comparison of thermal anomalies and delaminated tiles (as detected by hammer sounding) between Sts. 490+75 and 492+85.

Figure V.25 Visual comparison of thermal anomalies and delaminated tiles (as detected by hammer sounding) between Sts. 492+85 and 495+23.

Figure V.26 Visual comparison of thermal anomalies and delaminated tiles (as detected by hammer sounding) between Sts. 495+23 and 497+64.
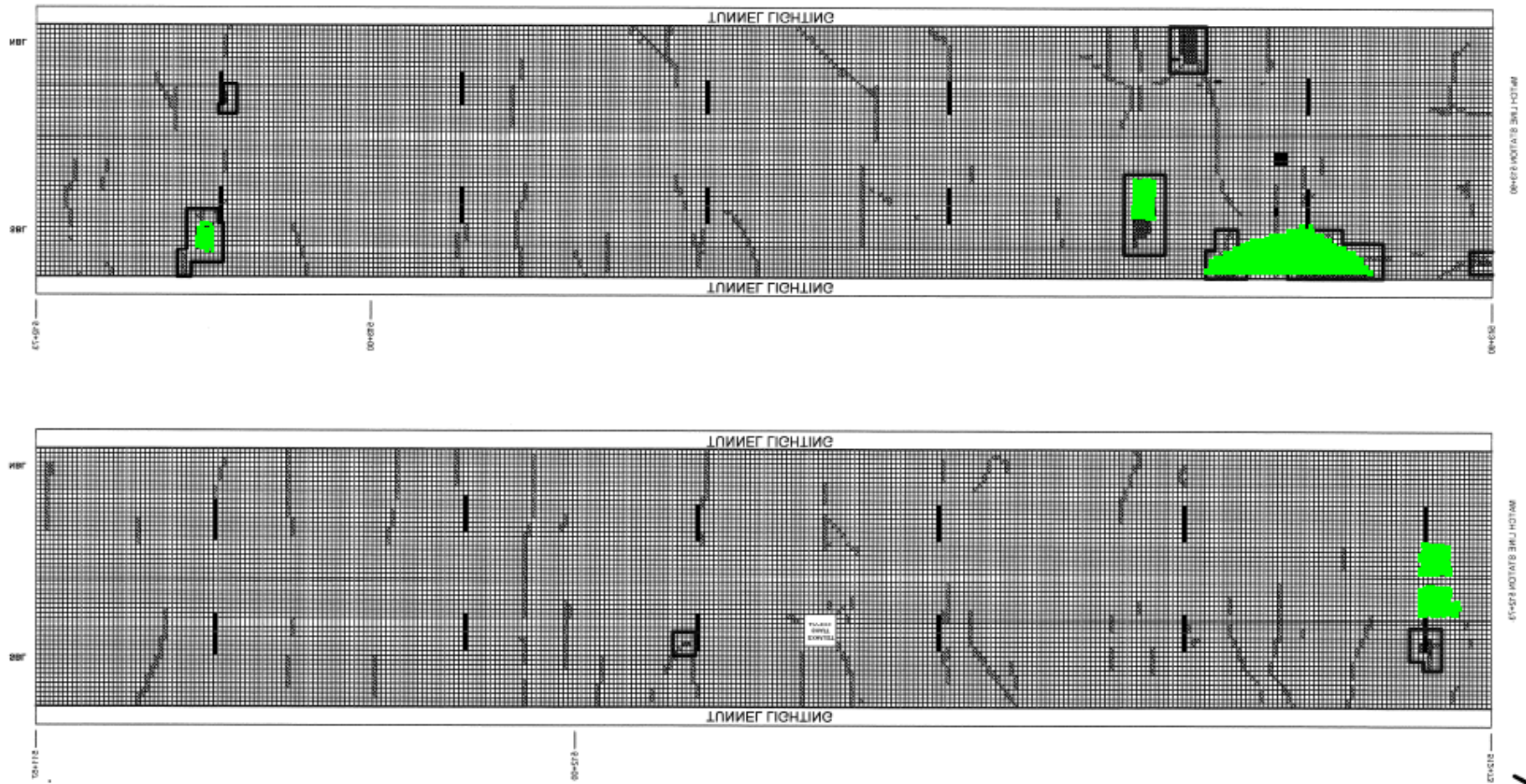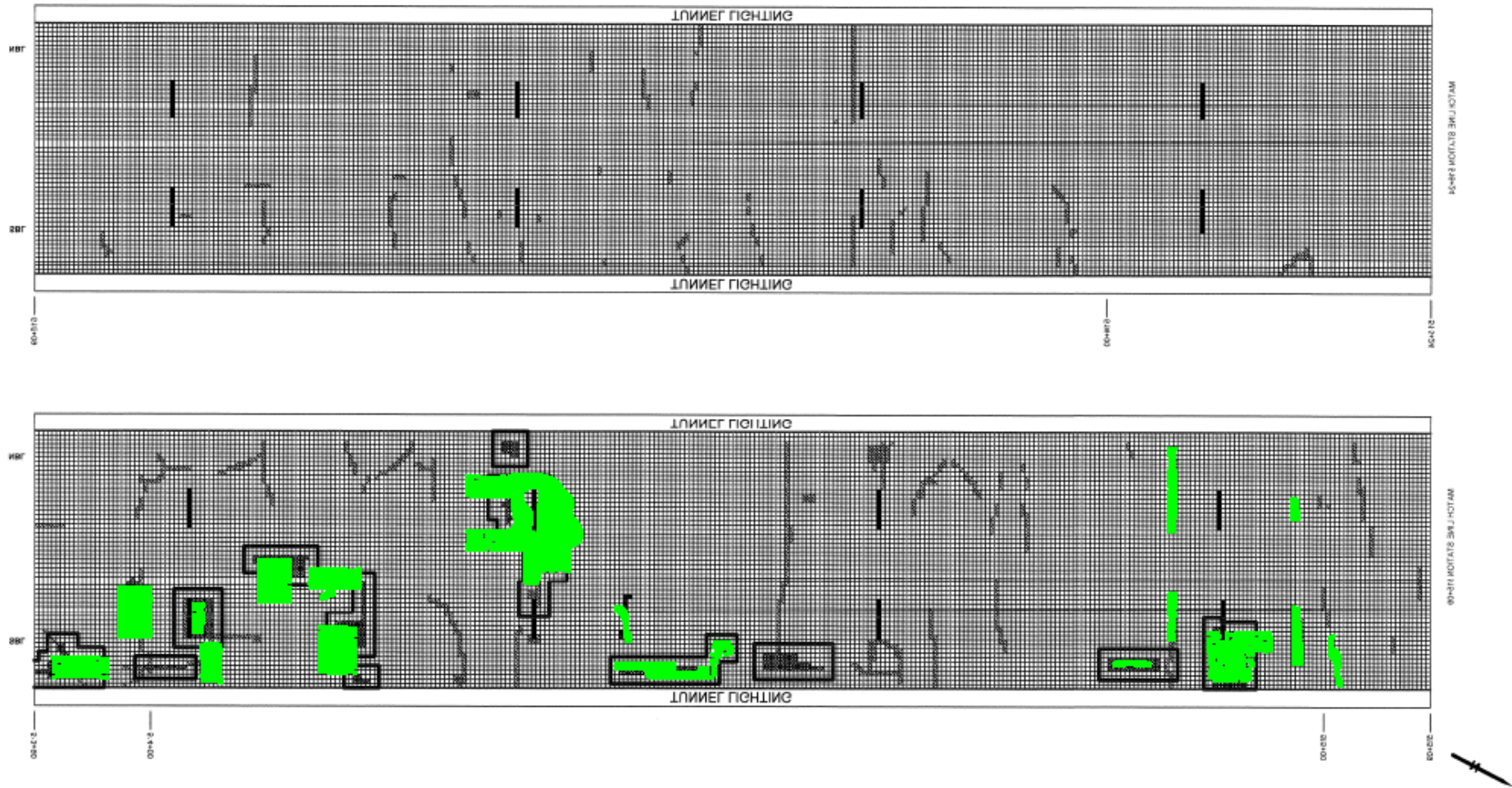
Figure V.27 Visual comparison of thermal anomalies and delaminated tiles (as detected by hammer sounding) between Sts. 497+64 and 499+82.

Figure V.28 Visual comparison of thermal anomalies and delaminated tiles (as detected by hammer sounding) between Sts. 499+82 and 502+20.

Figure V.29 Visual comparison of thermal anomalies and delaminated tiles (as detected by hammer sounding) between Sts. 502+20 and 504+60.

Figure V.30 Visual comparison of thermal anomalies and delaminated tiles (as detected by hammer sounding) between Sts. 504+60 and 506+86.
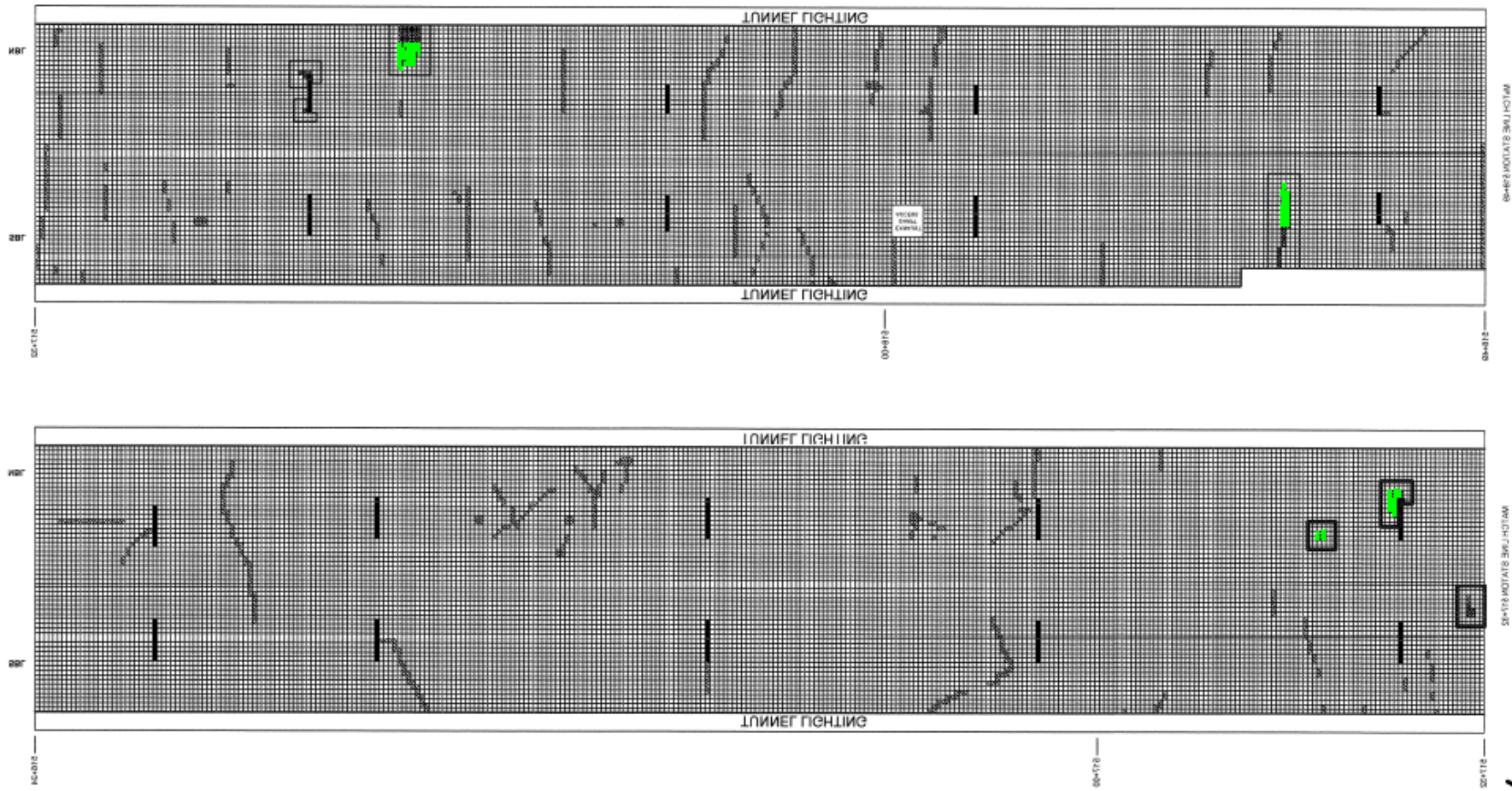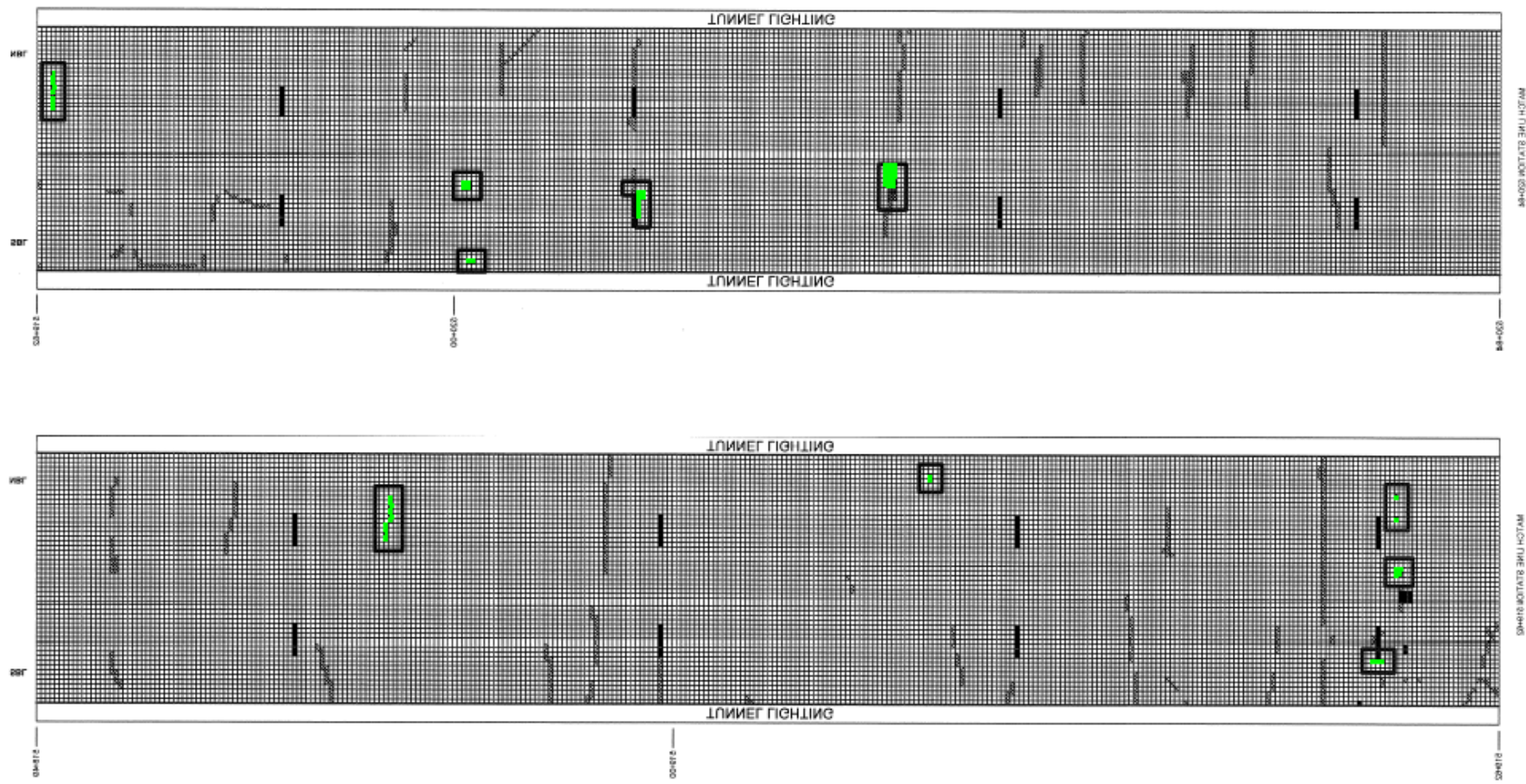
Figure V.31 Visual comparison of thermal anomalies and delaminated tiles (as detected by hammer sounding) between Sts. 506+86 and 509+21.
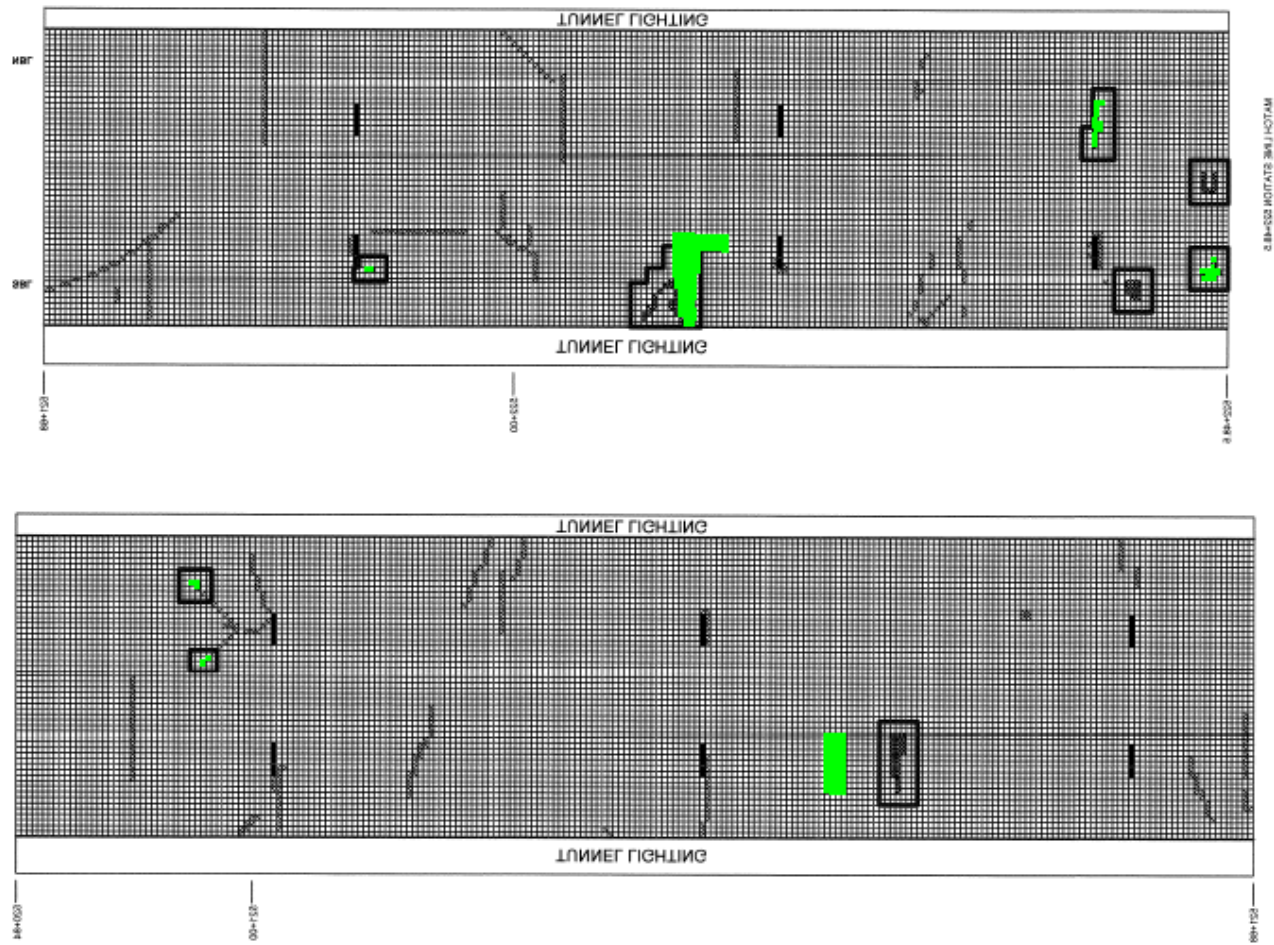
Figure V.32 Visual comparison of thermal anomalies and delaminated tiles (as detected by hammer sounding) between Sts. 509+21 and 511+57.

Figure V.33 Visual comparison of thermal anomalies and delaminated tiles (as detected by hammer sounding) between Sts. 511+57 and 513+90.

Figure V.34 Visual comparison of thermal anomalies and delaminated tiles (as detected by hammer sounding) between Sts. 513+90 and 516+24.

Figure V.35 Visual comparison of thermal anomalies and delaminated tiles (as detected by hammer sounding) between Sts. 516+24 and 518+49.

Figure V.36 Visual comparison of thermal anomalies and delaminated tiles (as detected by hammer sounding) between Sts. 518+49 and 520+84.

Figure V.37 Visual comparison of thermal anomalies and delaminated tiles (as detected by hammer sounding) between Sts. 520+84 and 522+48.5.

APPENDIX W
FINDINGS AND APPLICATIONS OF THE FEDERAL INSTITUTE FOR MATERIALS RESEARCH AND TESTING (BAM)

DETECTING DELAMINATIONS AND VOIDS

Delamination-like anomalies were detected at three test sites in two different tunnels. At Hanging Lake Tunnel, Segment 56 (BAM-HL1), ground penetrating radar (GPR) detected an anomaly at a depth of 12 inches. The GPR C-Scan (at a depth of 12 inches) and D-Scan are shown in Figures W.1 and W.2, respectively. The anomaly size was at its most (24 inches x 20 inches), as shown in Figure 3.1.
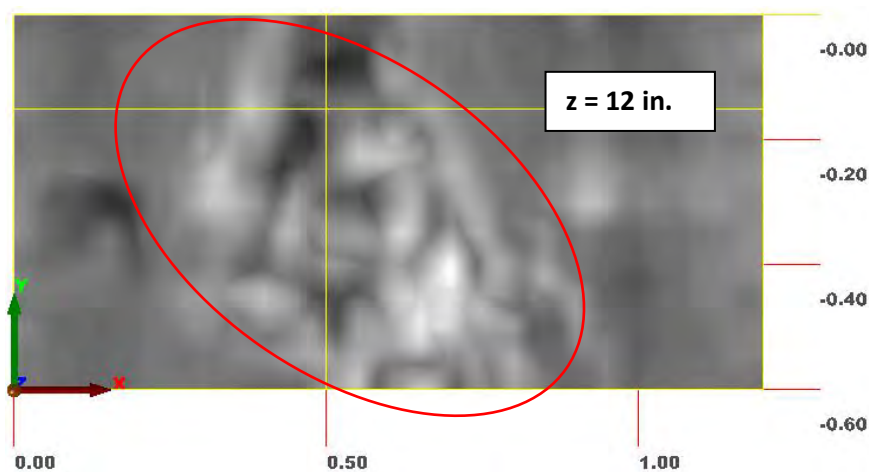
Figure W.1 BAM-HL1, GPR: C-Scan showing an anomaly at a depth of z = 12 inches. The encircled area is about 24 inches x 20 inches.
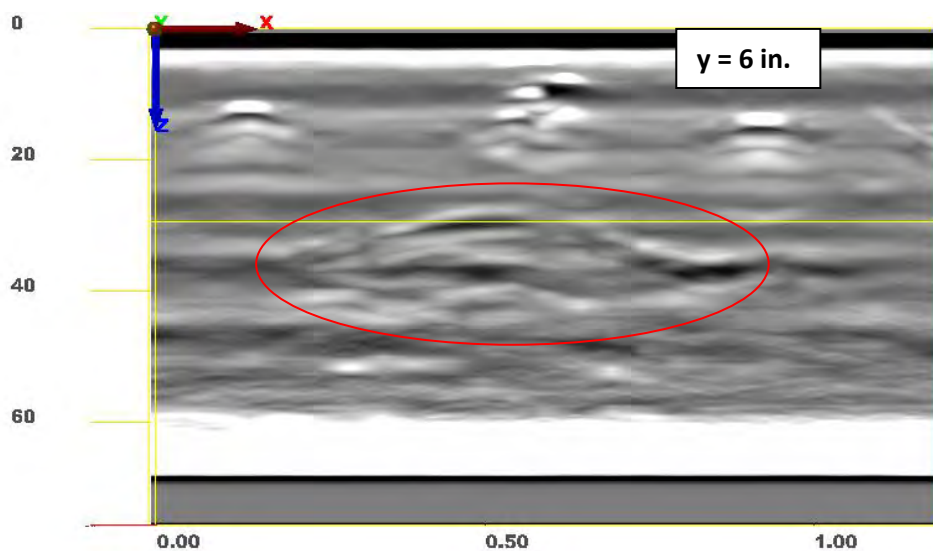

Figure W.2 BAM-HL1, GPR: D-Scan showing the extension of an anomaly from z = 12 inches to z = 16 inches. The slice was taken at y = 6 inches.

The same anomaly was detected in the ultrasonic echo (US) records as well, as shown in Figure W.3 (D-Scan taken at y = 5 inches) and Figure W.4 (B-Scans at x = 6 inches and x = 23 inches). Figure W.3 shows the anomalous reflector at a depth between z = 12 inches and

z = 16 inches. The phase evaluation of the anomalous reflector pointed to an acoustic impedance lower than that of concrete (similar to air-concrete interfaces). A three-dimensional view of ultrasonic data including the anomaly is shown in Figure W.5.
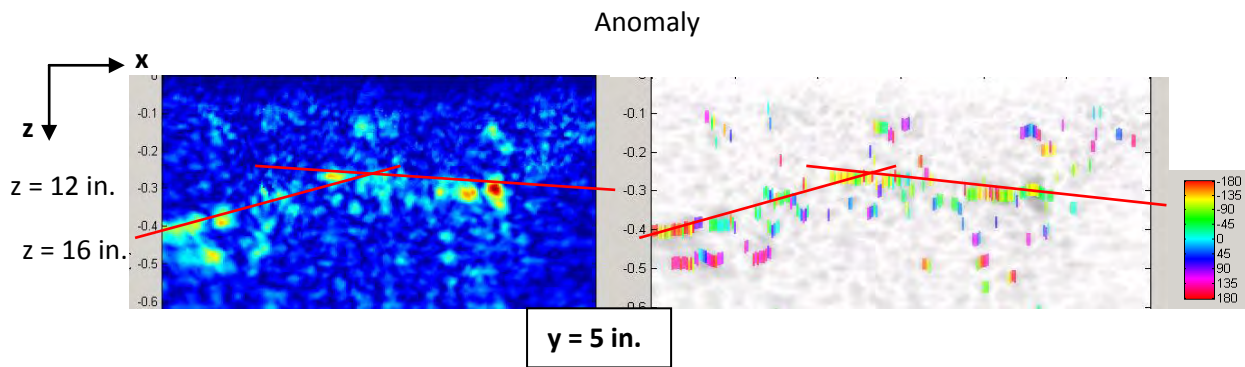

Figure W.3 BAM-HL1 US: D-Scan taken at y = 5 inches. A curved anomalous reflector of mostly negative phase was detected between z = 12 inches and 16 inches.
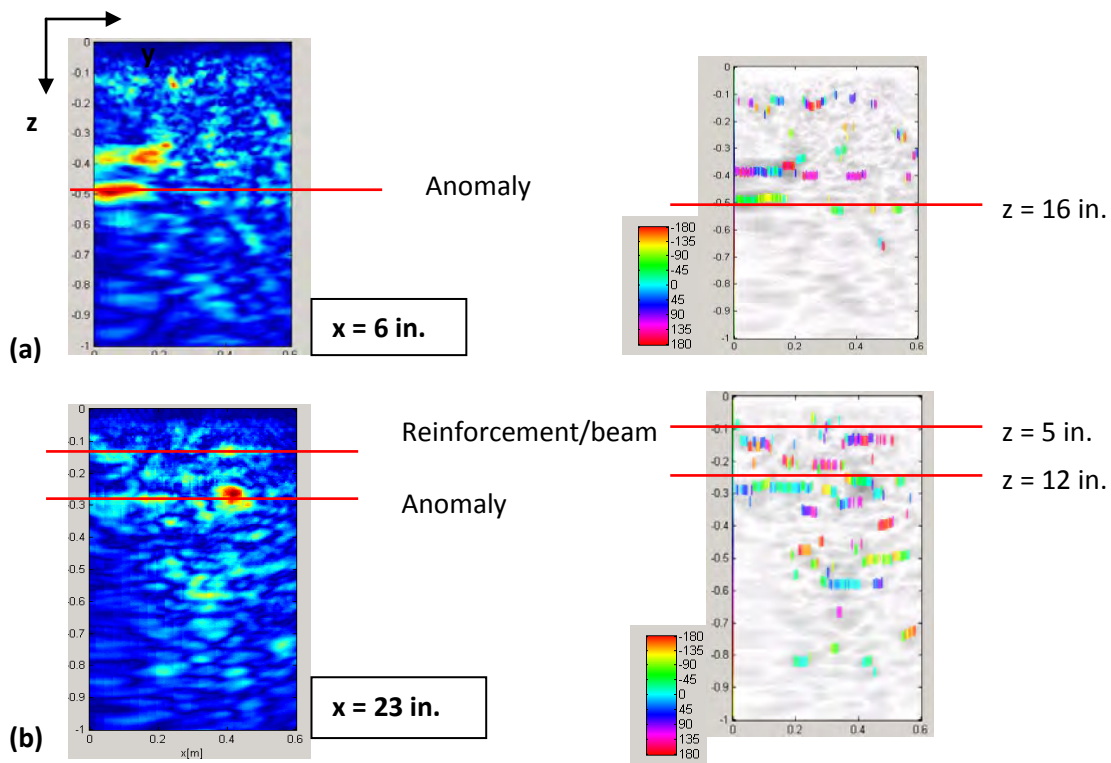

Figure W.4 BAM-HL1, US: B-Scans to evaluate the extent of the anomaly within the tunnel lining: (a) B-Scan crossing through the deeper part of the reflector, and (b) B-Scan crossing through the shallower part.
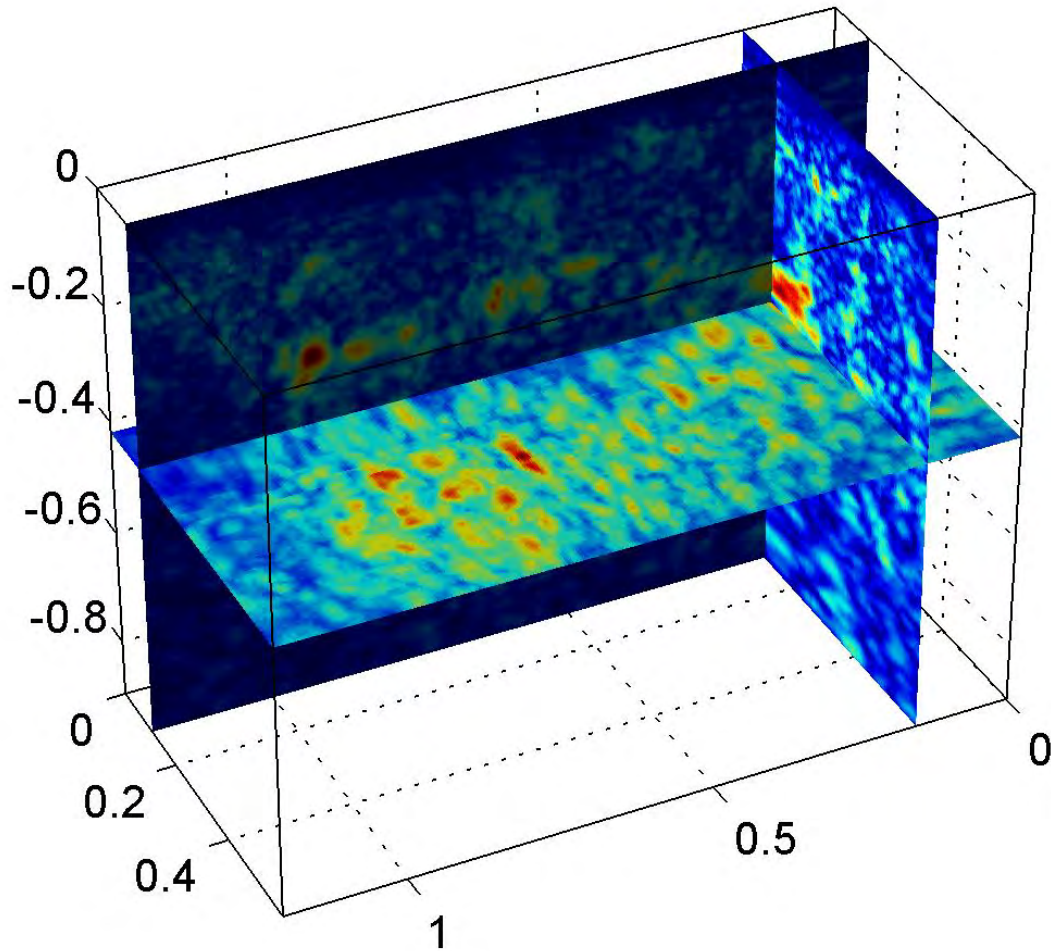
Figure W.5 BAM-HL1, US: three-dimensional image of the volume positioned to reveal the anomaly, with the B-Scan positioned at x = 6 inches, the C-Scan at z = 21 inches (4 inches thick), and the D-Scan at y = 6 inches.

Two other anomalies were found within the test areas of the Chesapeake Bay Bridge Tunnel. The first one at Sta. 474+27 (BAM-CPB1) was only detected with US. This anomaly was detected directly at z = 15 inches, spreading over about 20 inches, from x = 20 inches to x = 40 inches (Figure W.6[a]), and indirectly because of the suddenly weakened backwall reflection (Figure W.6[b]). The D- and B-Scans shown in Figure W.7 depict the location of the anomaly within the lining. The phase evaluation at detected reflections was not conclusive. Therefore, no reliable conclusions could be made about the nature of the anomaly.

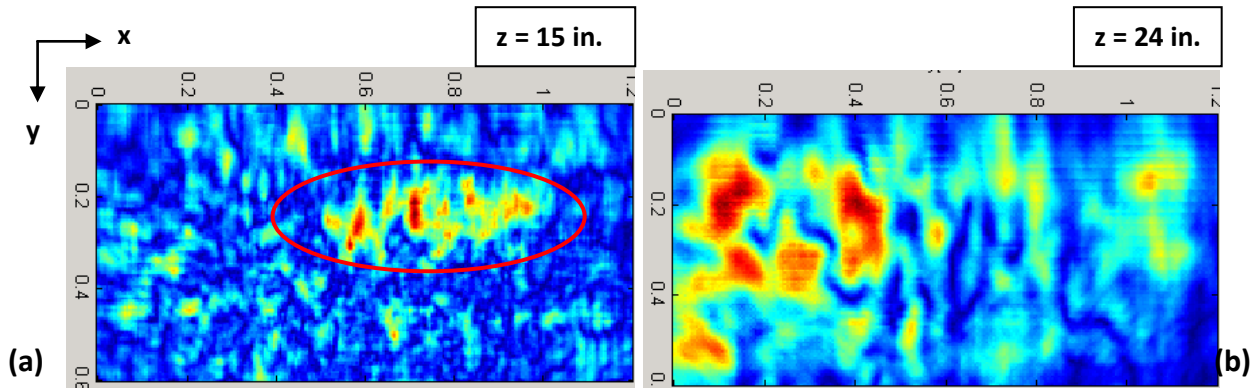The three-dimensional image in Figure W.8 illustrates the location of the anomaly within the test volume.

Figure W.6 BAM-CPB1, US: (a) C-Scans showing an anomaly directly at a depth of 15 inches, and (b) indirectly as a weakened backwall reflection.
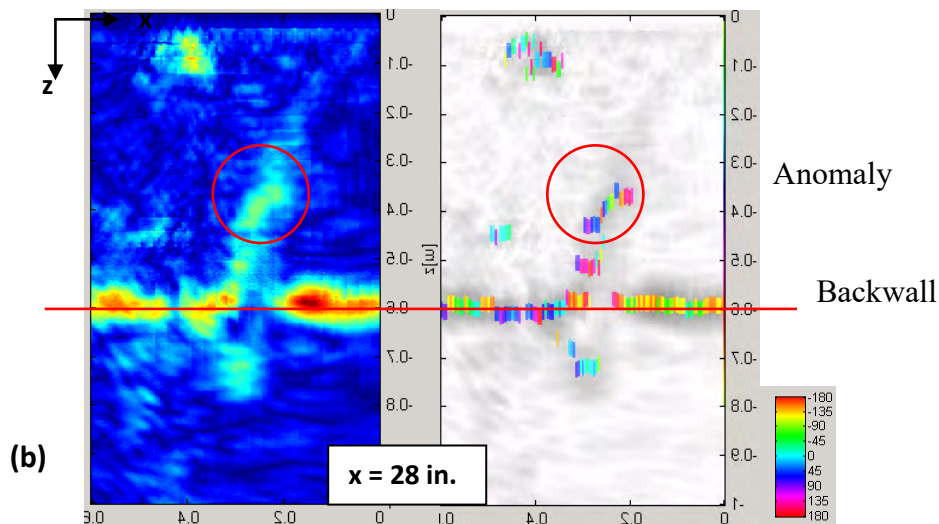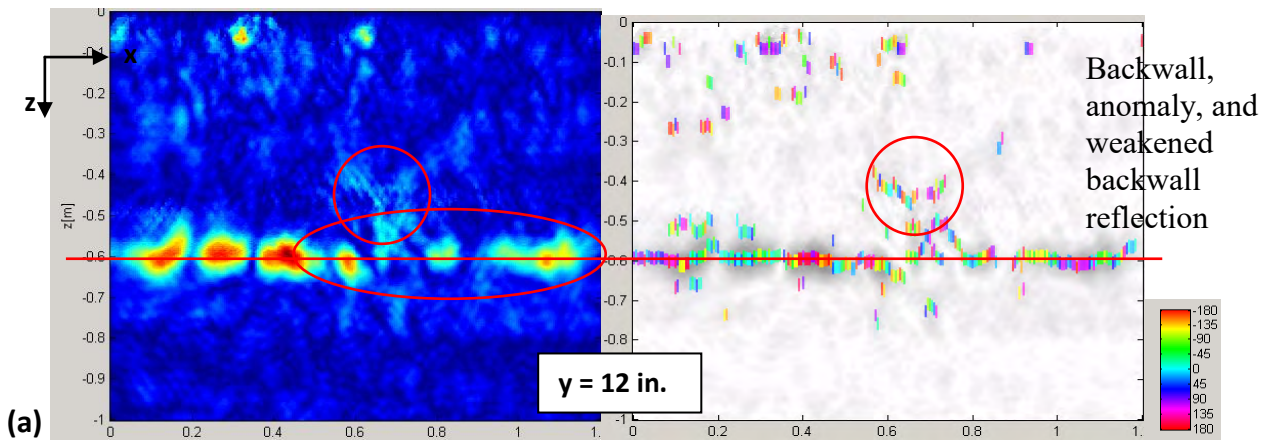

Figure W.7 BAM-CPB1, US: (a) D-Scan at y = 12 inches, and (b) B-Scan at x = 28 inches depicting the anomaly and weakened backwall reflection. No conclusive information could be drawn from the phase diagram.
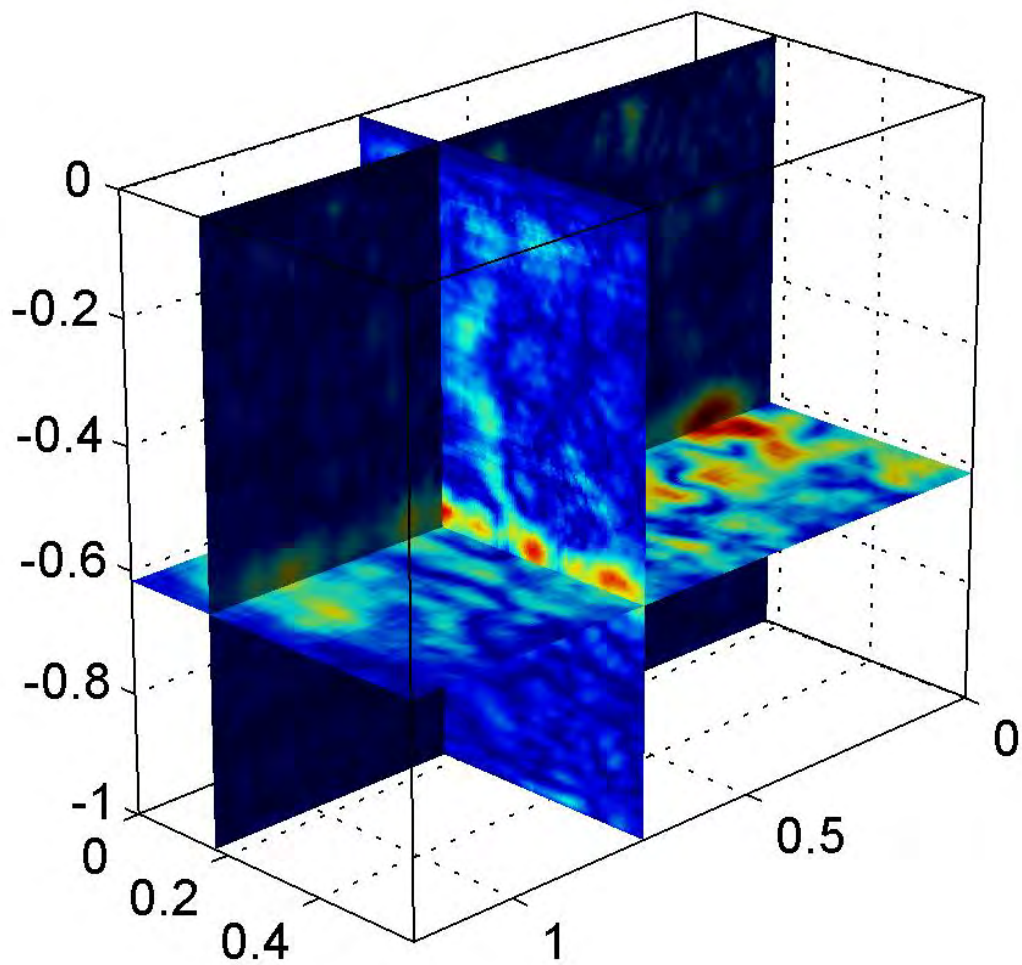
Figure W.8 BAM-CPB1, US: three-dimensional image of the volume positioned to reveal the backwall and the anomaly, with the B-Scan positioned at x = 29 inches, the C-Scan at z = 24 inches, and the D-Scan at y = 7 inches.

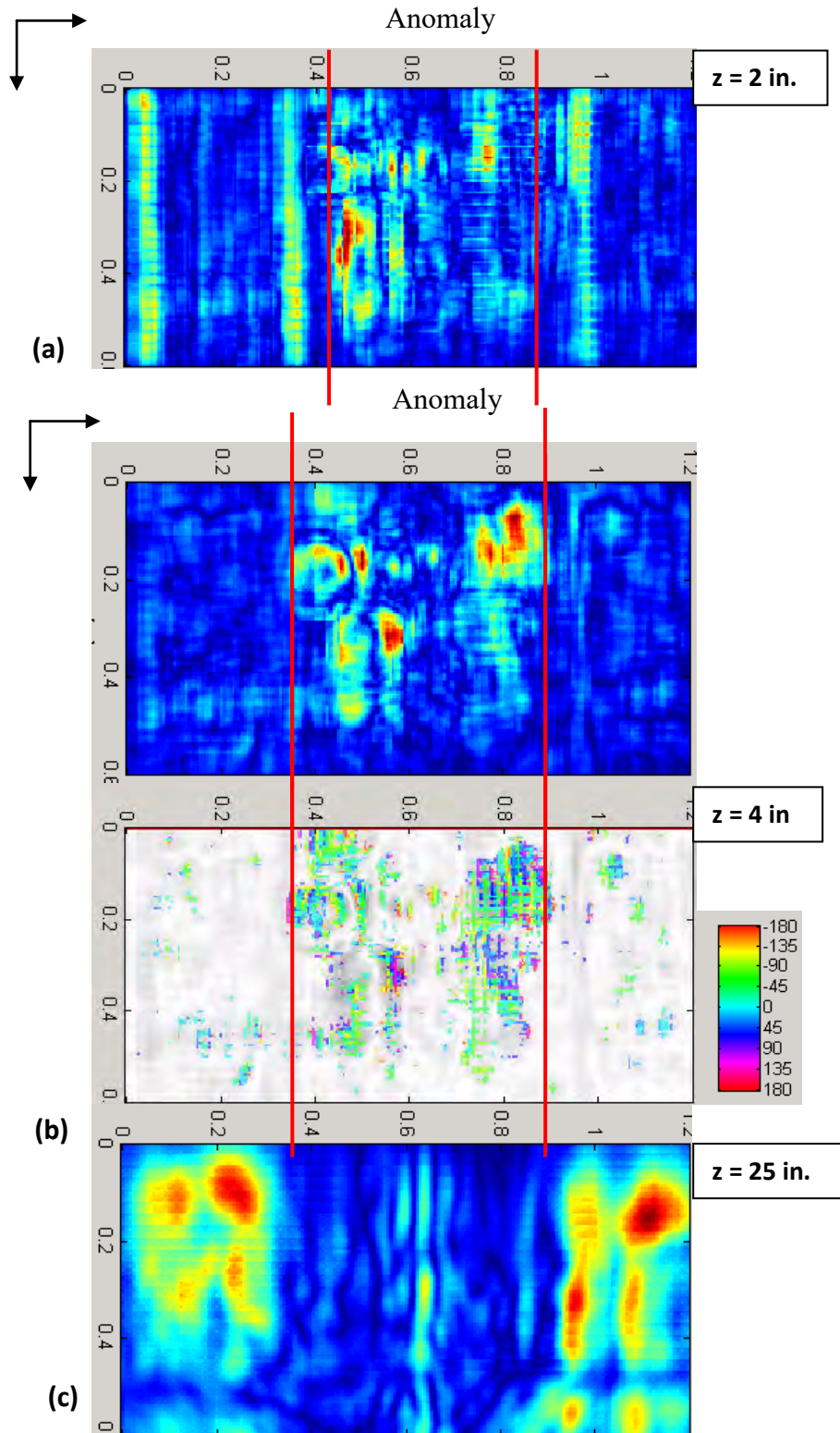Another anomaly at Sta. 486+67 (BAM-CPB3) was detected by both the US and impact echo (IE) techniques.

Figure W.9 BAM-CPB3, US: C-Scans of the showing the anomaly at (a) z = 2 inches, (b) z = 4 inches, and (c) the missing backwall echo at z = 25 inches.

In the US data, the anomaly manifested itself directly as an anomalous reflector at depths from z = 2 inches to z = 4 inches and indirectly as the missing backwall echo between x = 16 inches and x = 38 inches, as seen in Figure W.9. The phase evaluation indicated an acoustic impedance lower than that of the surrounding concrete.

D-Scans cutting through the length of the test area showed multiple reflectors in the volume above the missing backwall echoes at z = 6 inches, z = 10 inches, z = 15 inches, and z = 20 inches, with changing phases (Figure W.10). Multiple reflections with their phase jumping between negative and positive are typically indications of shallow delamination (Shokouhi, 2005).

The three-dimensional image of Figure W.12 illustrates the missing backwall echo and the anomalous reflections above it.
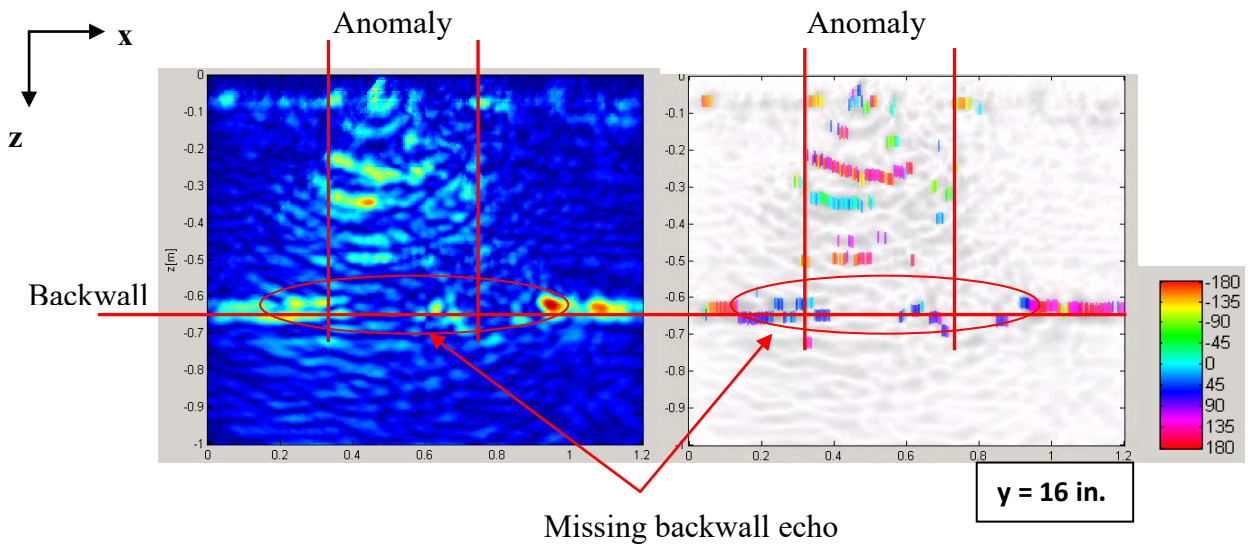

Figure W.10 BAM-CPB3, US: D-Scan at y = 16 inches showing multiple anomalous reflections with depth as well as the missing backwall echo. The phase values jumped between positive and negative, from reflection to reflection.
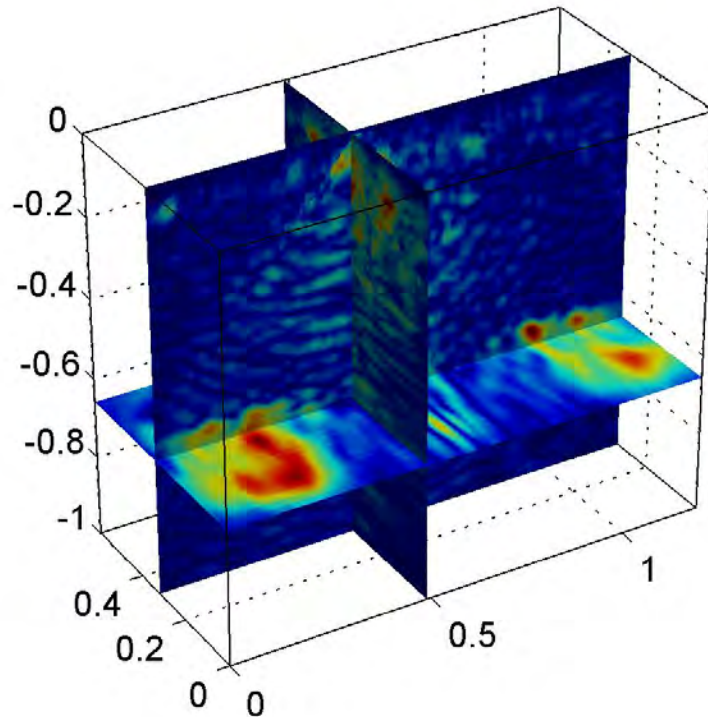
Figure W.11 BAM-CPB3, US: three-dimensional image of the volume positioned to reveal the backwall and its shadowed area due to the existence of an apparent shallow anomaly. The B-Scan is positioned at x = 21 inches, the C-Scan at z = 25 inches, and the D-Scan at y = 12 inches.

Figure W.12 presents a spectral D-Scan and two selected IE A-Scans (spectra). The tunnel lining thickness resonance frequency can be seen throughout the D-Scan, except between x = 13 inches and x = 30 inches, where the echo is disturbed. Two typical spectral and temporal A-Scans from the sound (x = 5.5 inches) and disturbed regions (x = 20 inches) are compared in this figure. While the sound spectrum contains one clearly dominant frequency, the disturbed spectrum contains multiple peaks, mostly of frequencies lower than that of thickness resonance frequency, indicating shallow delamination (2). The thickness resonance frequency appears at about 3.2 KHz, corresponding to a depth of about z = 25 inches.
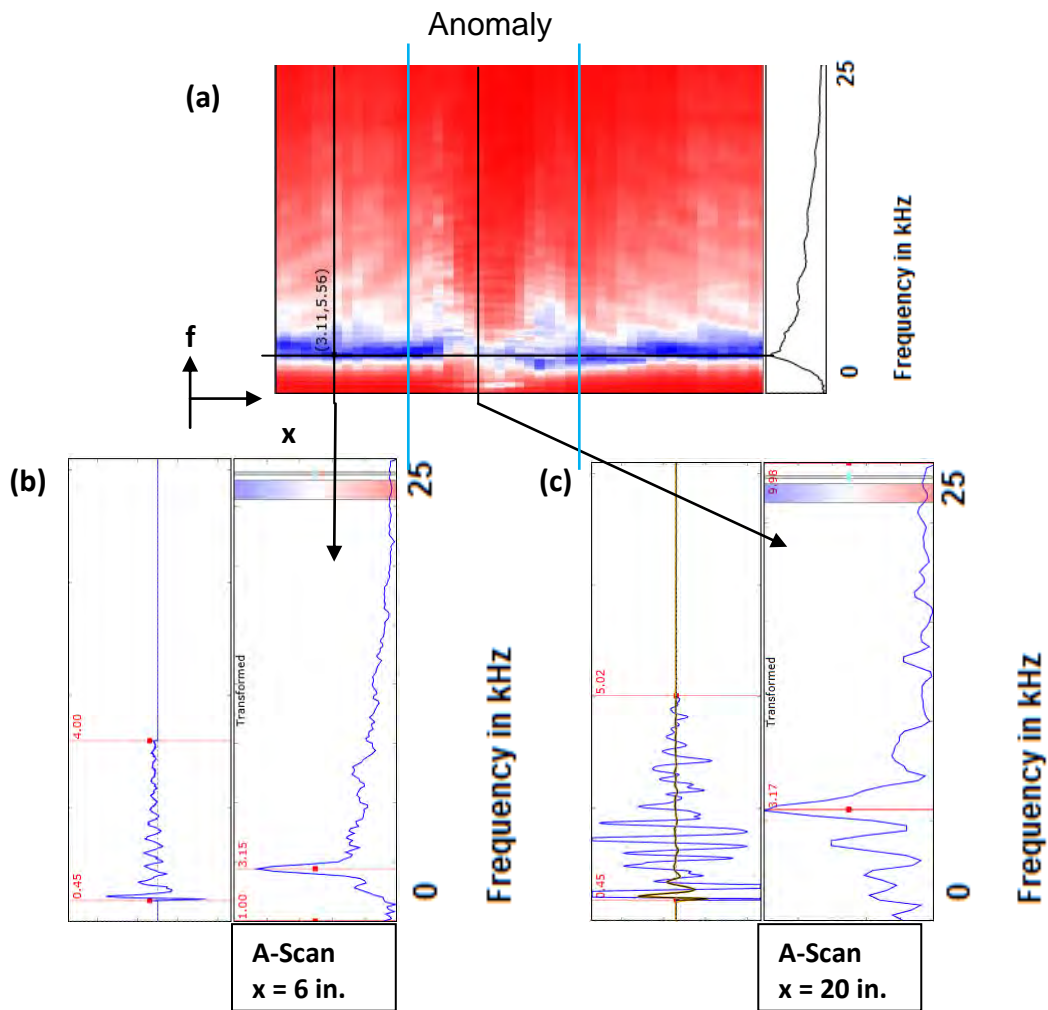
Figure W.12 BAM-CPB3, IE: D-Scan (a) and selected A-Scans representing the echo from a sound section (b) and from an area with an anomaly (c).

The three above discussed data sets were combined as shown in Figure W.14. Data combination was achieved by weighing and adding the three different data sets. Depth-varying weights were assigned to each data set to account for the different resolution and penetration depths associated with each method. A combined image of IE, US, and GPR data at y = 15 inches is shown in Figure W.13. The combined image provides a concise combined presentation of all the useful information provided by each method: the reinforcement from GPR and US, a reflector at z = 4 inches at x =32 inches from US, and the backwall from US and IE. In the area of missing US backwall echoes, the disturbed IE spectra are seen.
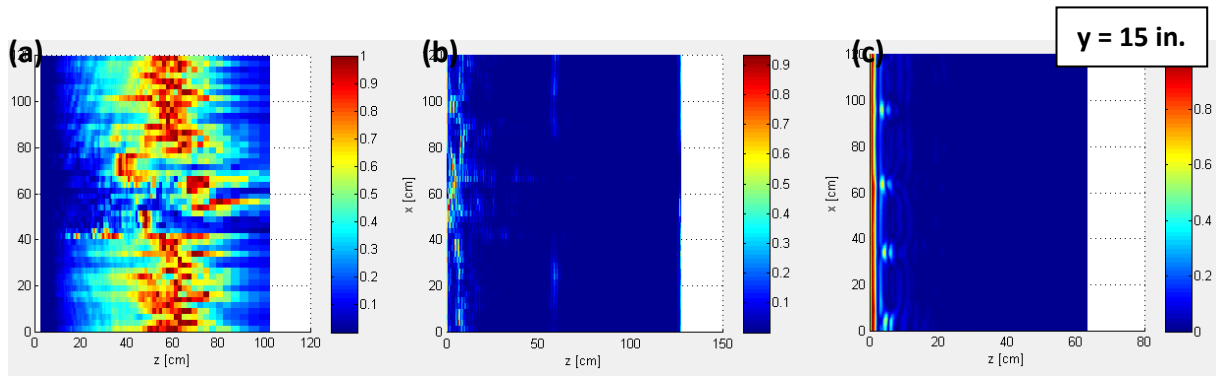
Figure W.13 BAM-CPB3, IE, US, GPR: individual D-Scans at y = 15 inches for each of the nondestructive testing (NDT) methods: (a) IE, (b) US, and (c) GPR.
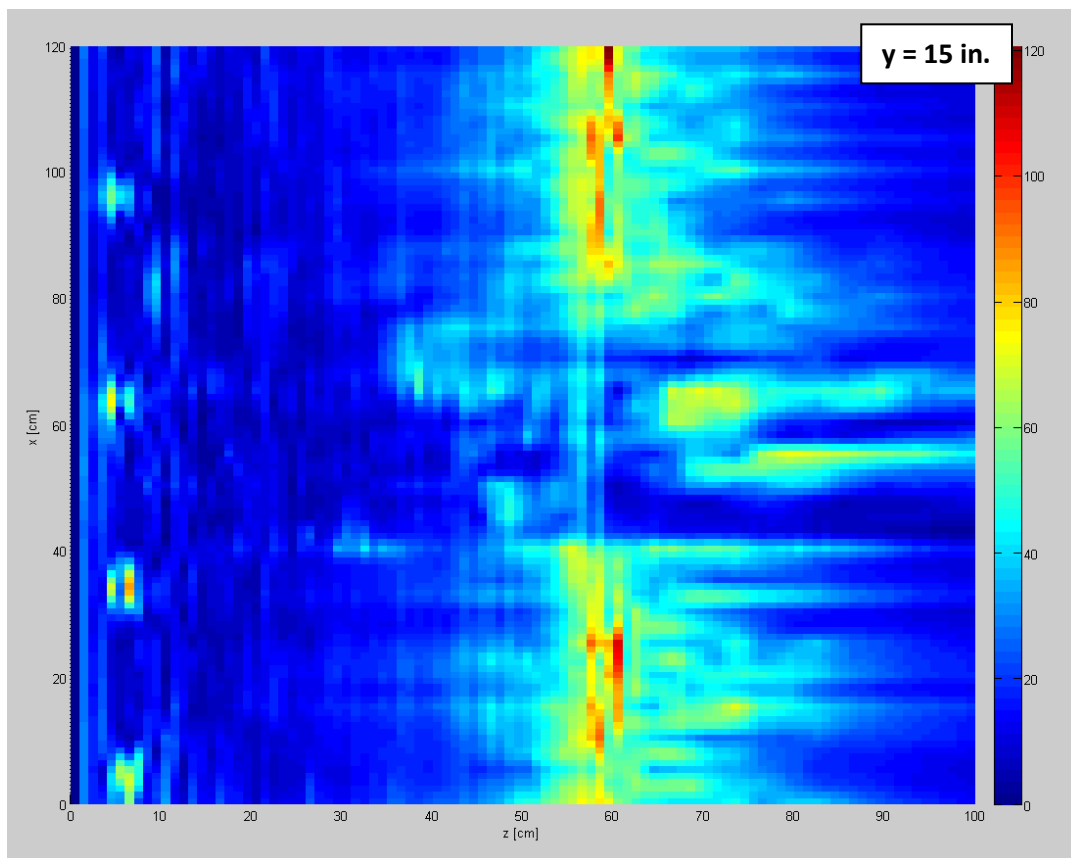

Figure W.14 BAM-CPB3: the combined IE-US-GPR D-Scan at y = 15 inches.

A surface crack was detected at one of the test fields at Hanging Lake Tunnel (Segment 57). In the GPR results, the crack manifested itself as a change in electromagnetic impedance, most likely because of the intrusion of moisture into the lining. Figure W.15 presents a collection of GPR B-, C-, and D-Scans with the cracked zone marked on each scan.

The circled areas mark the reflections at the location of the surface crack. The reason for the seeming mismatch of the first 6 inches in the C-Scan was a missing profile line caused by a failure during the measurements, which resulted in artifacts in the reconstructed images. Figure W.15(c) shows the reflector at a depth of z = 3 inches. The B-Scan at x = 19 inches (Figure W.15[a]) shows that the reflector extended down to a depth of 3.4 inches.
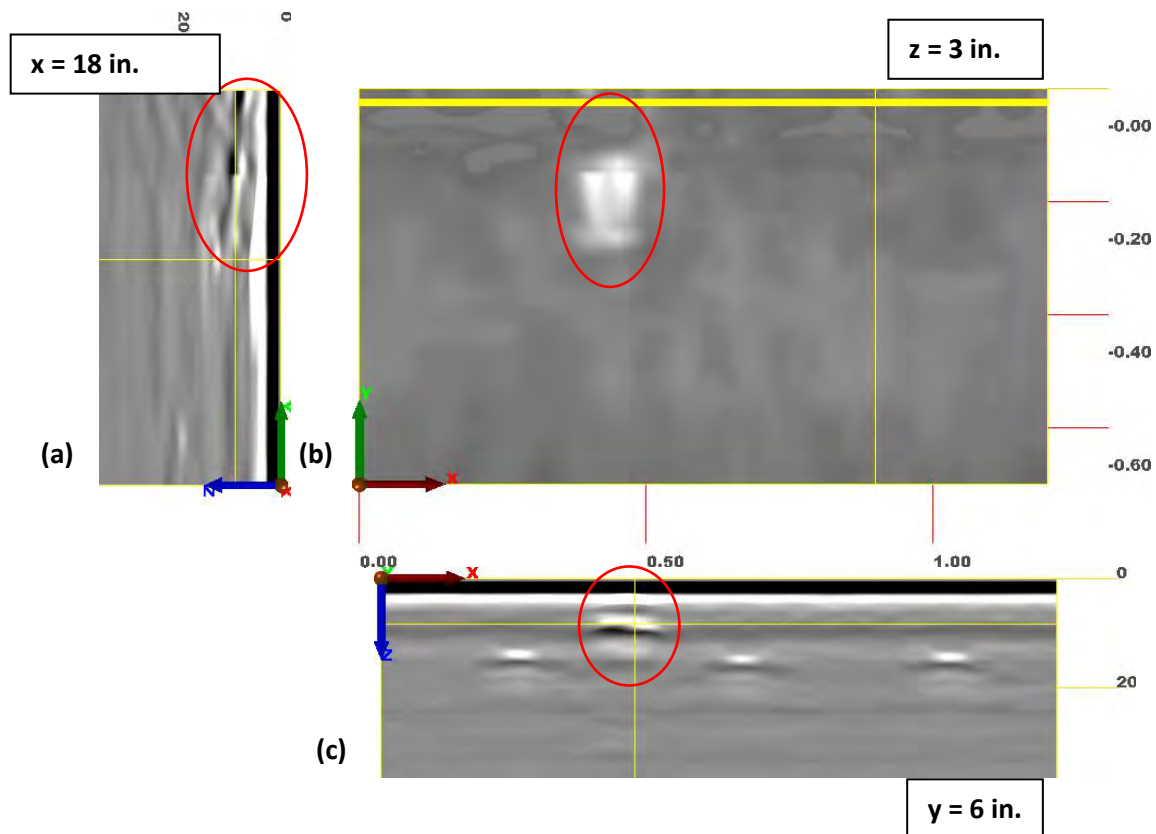
Figure W.15 BAM-HL2, GPR: C-, D-, and B-Scans showing reflections caused by the presence of a surface crack.

In the US data, the crack was indirectly detected, where a part of the longitudinal reinforcement was missing (Figure W.16). As US only detected the anomaly indirectly, the technique could not specify the depth of the crack or the dimension of the possible moisture intrusion.

z = 6 in.

Shadowed area due to surface crack

(a)

x = 44 in.

Shadowed area due to a surface crack

(b)

Figure W.16 BAM-HL2, US: (a) C-Scan at z = 6 inches, and (b) D-Scan at x = 44 inches showing the missing echoes of the longitudinal reinforcement due to the surface crack.

W.12

APPENDIX X
DIGITAL PHOTOGRAMMETRY

DATA ACQUISITION

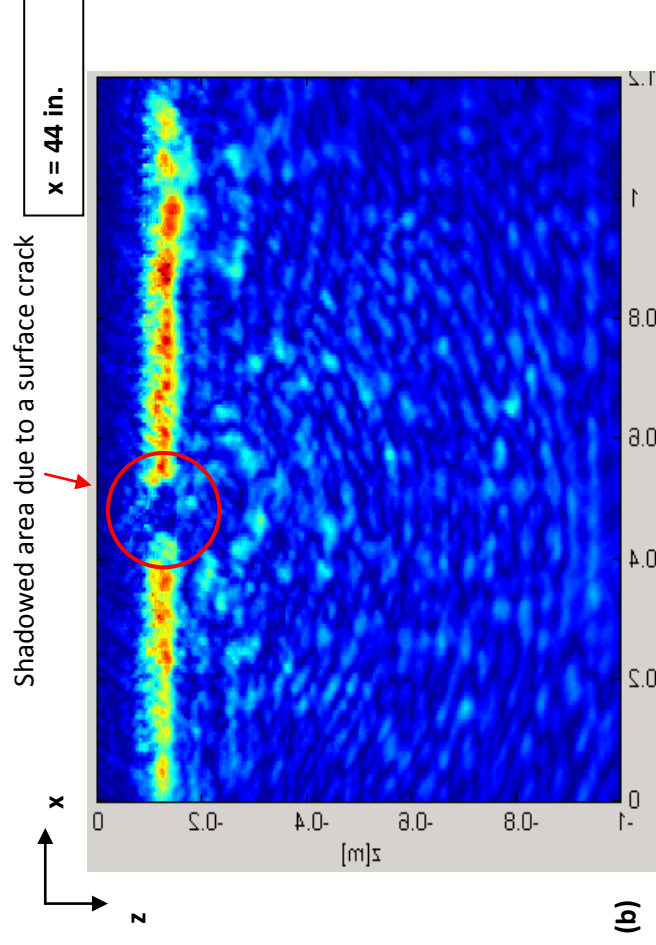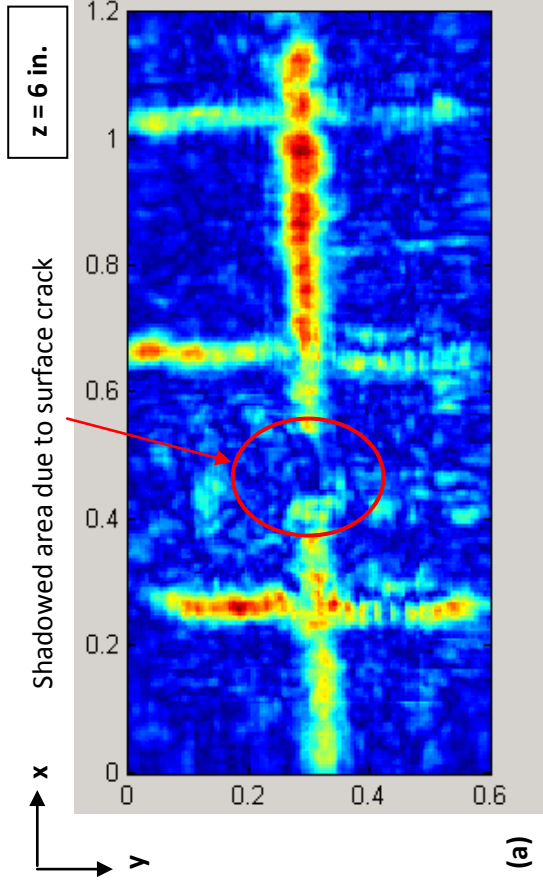The basic principles of photogrammetry are illustrated in Figure X-1: once a pair of photos is acquired, the same point, P, is identified on each photo, and the spatial coordinates of point P on the object (the ground in this case) are calculated by tracing two rays from the focal points Ol and Or of each photo, respectively, through the pixels that represent point P on each photo. A patch of an object surface is therefore reconstructed from each pair of photos: it is the patch portrayed by both photos. The reconstructed surface can then be either scaled or scaled and georeferenced in a reference system of interest.
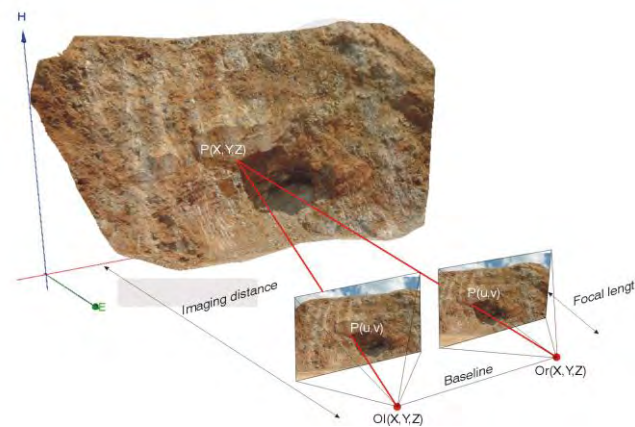

Figure X-1. Photogrammetry principles.

Since each point on the reconstructed surface comes from a known pixel, each pixel can be *exactly* attributed to the relevant point of the reconstructed surface. As a consequence, the reconstructed surface is *exactly* textured with high-definition photos, thus allowing for a reliable and realistic virtualization of the object under consideration. This means that when digitizing the trace of a lining crack by following the trace pixels on the textured surface, one is sure to identify the correct trace geometry on the underlying surface; this is not the case with laser scanner applications.

Once a three-dimensional model has been reconstructed, it can be scaled, or it can be scaled and georeferenced. A scaled model allows for crack, spalling, and visible moisture detection and measurement: crack length, aperture, location (relative to an arbitrary point); spalling area, depth, volume, and location; and moist area and location. Additionally, a scaled and georeferenced model allows for:

- Change detection, i.e., to determine changes in crack lengths and aperture, spalling extent (area and depth), and moist area.
- Determination of:
  - Crack orientation (very useful to ensure that the grouting holes actually intersect the crack).

o Wall displacements: convergence, tile delamination, concrete delamination, and ceiling or floor sagging.
o Overall tunnel displacement, e.g., in immersed tube tunnels, lifting caused by loss of ballast or sinking caused by debris discharge over the tunnel.

The speed of photo acquisition depends on the accuracy required, the minimum distance between the cameras and the tunnel lining, and whether the tunnel is accessible to vehicles or not. As part of this research, special technology has been developed in order to achieve the performance detailed in Table X-1.

Table X-1. Speed of photo acquisition.

Tunnel Type	Taking Pictures from	Taking Pictures of	Lane Closure Required	Accuracy Required*	Speed
2-Lane Road Enclosure	1 lane	Entire tunnel	1 lane from which pictures are taken	0.8 mm	1,200 ft/hr (360 m/hr)
2-Lane Road Enclosure	1 lane	Entire tunnel	1 lane from which pictures are taken	1 mm	2,400 ft/hr (720 m/hr)
2-Lane Road Enclosure	1 lane	Single wall (e.g., only tile panels)	1 lane from which pictures are taken	0.8 mm	2,000 ft/hr (600 m/hr)
2-Lane Road Enclosure	1 lane	Single wall (e.g., only tile panels)	1 lane from which pictures are taken	1 mm	3,300 ft/hr (1,000 m/hr)
Air Duct (20 ft, 6 m wide)	Center	Entire duct	No	0.6 mm	660 ft/hr (200 m/hr)
Air Duct (20 ft, 6 m wide)	Center	Entire duct	No	0.7 mm	1,000 ft/hr (300 m/hr)

* Accuracy refers to photogrammetric model only.

ACCURACY OF THE THREE-DIMENSIONAL MODEL AND INFORMATION PROVIDED TO CLIENT

An additional advantage of digital photogrammetry with respect to the laser scanner is that the bundle adjustment residual is provided at each common point P (Figure X-1), and then the root mean square (RMS) of the residuals is provided for each photo, and for the entire model. These data provide detailed local and global information on the accuracy of the model, which is not available in laser scanner applications.

The pixel size on the lining is chosen before entering the tunnel based on the desired accuracy. For example, Table X-2 refers to the two-lane Liberty Tunnel in Pennsylvania, which is about 20 ft wide; in this tunnel, photographs were taken from the left lane, and the maximum distance from cameras to the opposite wall was about 12 ft. The *a priori* calculated accuracy of the photogrammetric model was 0.8 mm; the chosen pixel size on the lining (farthest distance to the camera) was about 1 mm × 1 mm. For each picture actually taken in the field, Table X-2

provides the RMS of the residuals, which is always less than 0.3 pixels, i.e., 0.3 mm on the lining. The "Active Points" column refers to the number of common points between a given picture and all overlapping pictures.

Table X-2. Residuals and active points for pictures taken at Liberty Tunnel.

Names	RMS Error (Pixels)			Active Points
	X	Y	Total	
IMG_2272.JPG	0.116403	0.153484	0.192632	195
IMG_2273.JPG	0.117043	0.179321	0.214138	277
IMG_2274.JPG	0.131904	0.214972	0.252214	337
IMG_2275.JPG	0.145841	0.182533	0.233640	226
IMG_2276.JPG	0.119270	0.228402	0.257668	281
IMG_2277.JPG	0.082480	0.207591	0.223376	283
IMG_2278.JPG	0.098254	0.161682	0.189195	298
IMG_2279.JPG	0.114083	0.212339	0.241046	383
IMG_2280.JPG	0.135485	0.190771	0.233987	343
IMG_2281.JPG	0.123500	0.181342	0.219401	244
IMG_2282.JPG	0.132664	0.236927	0.271540	236
IMG_2283.JPG	0.107341	0.179687	0.209307	330
IMG_2284.JPG	0.109541	0.168065	0.200612	289
IMG_2285.JPG	0.153775	0.200796	0.252914	252
IMG_2286.JPG	0.176630	0.198991	0.266075	210
IMG_2287.JPG	0.164044	0.212679	0.268594	211
IMG_2288.JPG	0.117306	0.184640	0.218753	228
IMG_2289.JPG	0.097516	0.177364	0.202404	355
IMG_2290.JPG	0.097395	0.143055	0.173062	333
IMG_2291.JPG	0.114015	0.175516	0.209297	472
IMG_2292.JPG	0.113118	0.204120	0.233368	473
IMG_2293.JPG	0.133337	0.195348	0.236515	353
IMG_2294.JPG	0.110535	0.183812	0.214488	388
IMG_2295.JPG	0.112492	0.179191	0.211574	342
IMG_2296.JPG	0.109538	0.122035	0.163985	268
IMG_2297.JPG	0.111083	0.189163	0.219367	407
IMG_2298.JPG	0.122423	0.203170	0.237203	446
IMG_2299.JPG	0.114291	0.180656	0.213773	365
IMG_2300.JPG	0.117907	0.184573	0.219019	352
IMG_2301.JPG	0.119525	0.167282	0.205595	235

Residuals are also calculated on:

- **Scale bars (scaled models):** Table X-2 gives the residuals at the scale bars used at the Liberty Tunnel. The scale bar dimensions are provided with a National Institute of Standards and Technology (NIST)-traceable certificate of calibration. The residuals are better than 50 microns (0.002 in.).
- **Surveyed targets applied to the final lining (scaled and georeferenced models):** Table X-4 gives the residuals obtained on surveyed targets in the road enclosure of the Eisenhower-Johnson Tunnel in Colorado. The residuals in each direction are equal to about 0.5 mm (0.2 in.), and the overall, spatial residual is equal to 0.8 mm (0.03 in.). The overall accuracy (target survey and photogrammetric model) obtained in the divider wall at the Eisenhower-Johnson Tunnel was equal to 1 mm.

Table X-3. Residuals at scale bars used at Liberty Tunnel.

Scale Bar Name	First Point ID	Second Point ID	Distance (Meters)	Accuracy (Meters)	Residual (Meters)
Scale Bar 1	Point 1	Point 2	1.095956	0.000010	−0.000044
Scale Bar 2	Point 3	Point 4	1.096029	0.000010	0.000029

Table X-4. Residuals at scale bars used at Eisenhower Tunnel (road enclosure).

Control Point Names	Image Point Residuals			Control Point Residuals (Meters)		
	No. of Observations	X (Pixels)	Y (Pixels)	X	Y	Z
1	2	0.0067	0.0407	−0.0000	0.0004	−0.0006
2	2	0.0846	0.1426	0.0001	−0.0004	0.0006
3	2	0.1233	0.0489	0.0002	−0.0003	−0.0006
4	2	0.0458	0.1339	−0.0003	0.0003	0.0005
Control Point RMS				0.0002	0.0004	0.0006
Total				0.0008		

These results indicate that the following may be identified with confidence:

- Bulging caused by incipient spalling and tile delaminations.
- Subtle ceiling/floor movements that may indicate progressive failure of the support (e.g., roof collapse at the Central Artery Tunnel in Boston).
- Convergence of the tunnel walls.
- Overall tunnel displacement, e.g., in immersed tube tunnels, lifting caused by loss of ballast or sinking caused by debris discharge over the tunnel.

Figure X-2 through Figure X-13 provide an example of a three-dimensional model of a tunnel lining (Liberty Tunnel in Pennsylvania) and its use in identifying lining defects. (Figure X-3 through Figure X-8 show close-up views of the circled spalling event.) Figure X-14, Figure X-15, Table X-5, and Table X-6 exemplify the results provided to the client at the end of the photogrammetric survey in order to document existing cracks and spalling events.

Figure X-16 through Figure X-21 illustrate the three-dimensional model of the clean air supply duct at the Eisenhower-Johnson Tunnel. In this research, special lighting systems have been devised to evenly illuminate the lining even in dark situations, such as air ducts, and to ensure that the colors of the lining are reliably reproduced. The pipes attached to the divider wall have not been reproduced satisfactorily in three dimensions: this is due to the fact that pattern is needed in photogrammetry to find relative-only points, and steel pipes have very little, if any, pattern. In any case, one of the objectives of this application was to check the use of photogrammetry in surveying a divider wall with embedded steel hangers that cannot be examined by any nondestructive technique. Details of the divider walls are given in Figure X-17 and Figure X-18, and a global accuracy of 1 mm was achieved; this ensures that progressive yielding of a hanger (or hangers) may be detected if surveys of this kind are carried out systematically. Figure X-19 and Figure X-20 depict the model of the south wall as seen from the inside of the tunnel, where several cracks are evident. Some of the cracks have been digitized in Figure X-20: one is a typical construction (pour) joint, but the others are not, and their orientation allows one to infer the causes of distress in a specific area of the lining. Such inferences are very difficult to make while inspecting the tunnel and mapping the cracks by hand. Finally, Figure X-21 provides a detail of a cracked area of the lining.

The provided model and the quantities obtained are completely objective and defensible, and may be used at any time during the operational phases of the underground infrastructures.

Figure X-2. Three-dimensional model of Liberty Tunnel inbound tube by the ventilation shaft.

Figure X-3. Detail of spalling by the ventilation shaft.

Figure X-4. Foreshortened view of spalling by the ventilation shaft.

Figure X-5. Detail of exposed aggregate and rebar by the ventilation shaft.

Figure X-6. Backside view of spalling by the ventilation shaft to better appreciate spalling depth and extent.

Figure X-7. Closed polyline to determine area of spalling by the ventilation shaft.

Figure X-8. Information on spalling by the ventilation shaft: coordinates of center point and area.
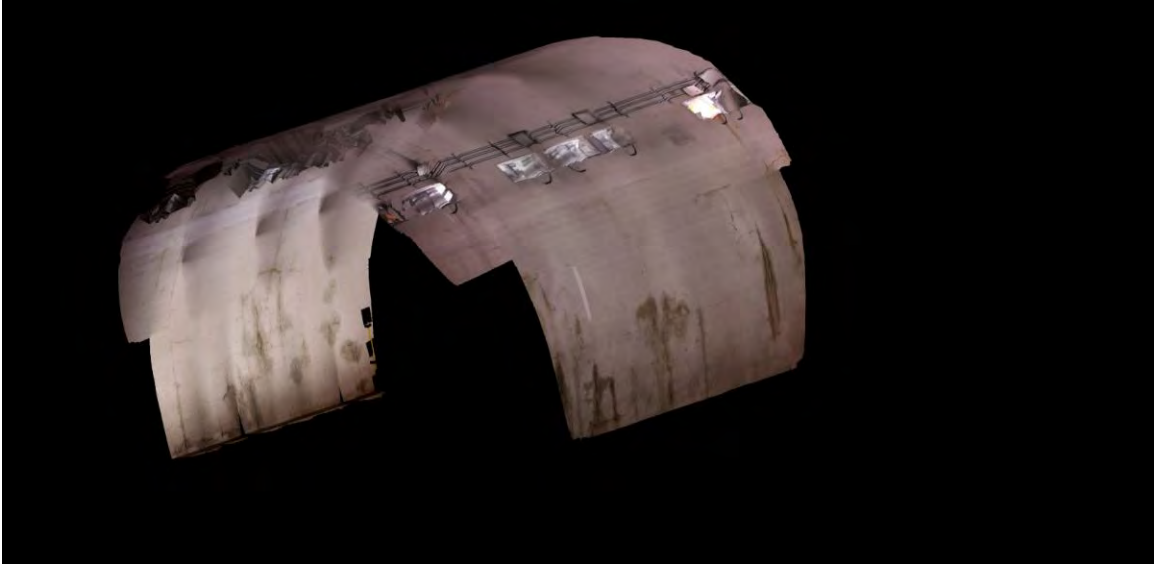
Figure X-9. Overall view of a tunnel stretch by the southern portal.
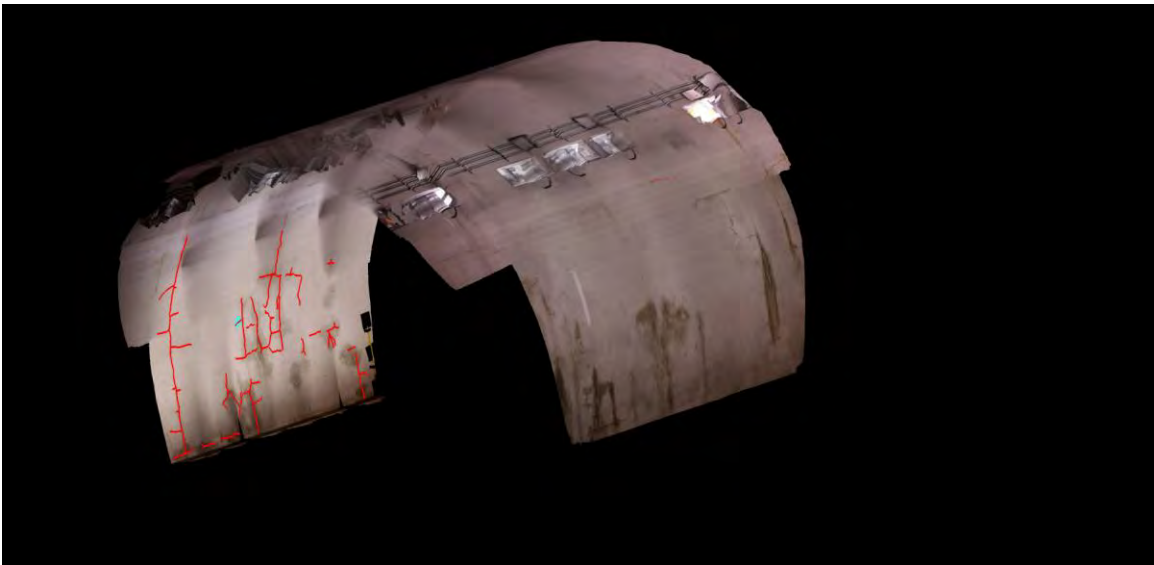
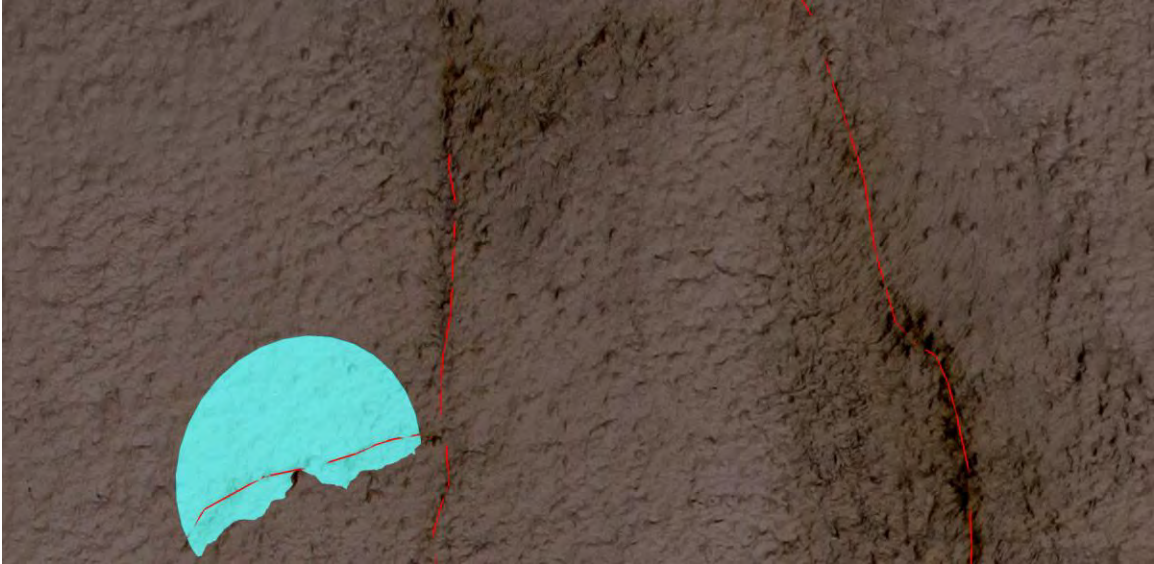**Figure X-10. Overall view of a tunnel stretch by the southern portal with digitized cracks on left wall.**

Figure X-11. Detail of digitized shotcrete cracks on left wall by the southern portal; also visible is a plane interpolated through the crack trace.

Figure X-12. Detail of shotcrete cracks on left wall by the southern portal with digitized cracks toggled off.

Figure X-13. Close-up view of shotcrete crack on left wall by the southern portal: detail of surface roughness.
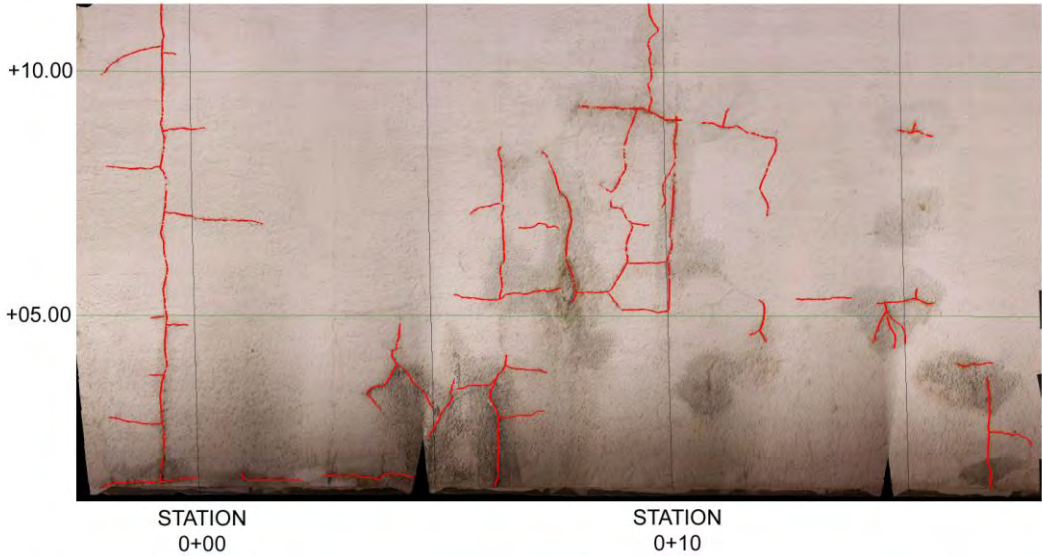

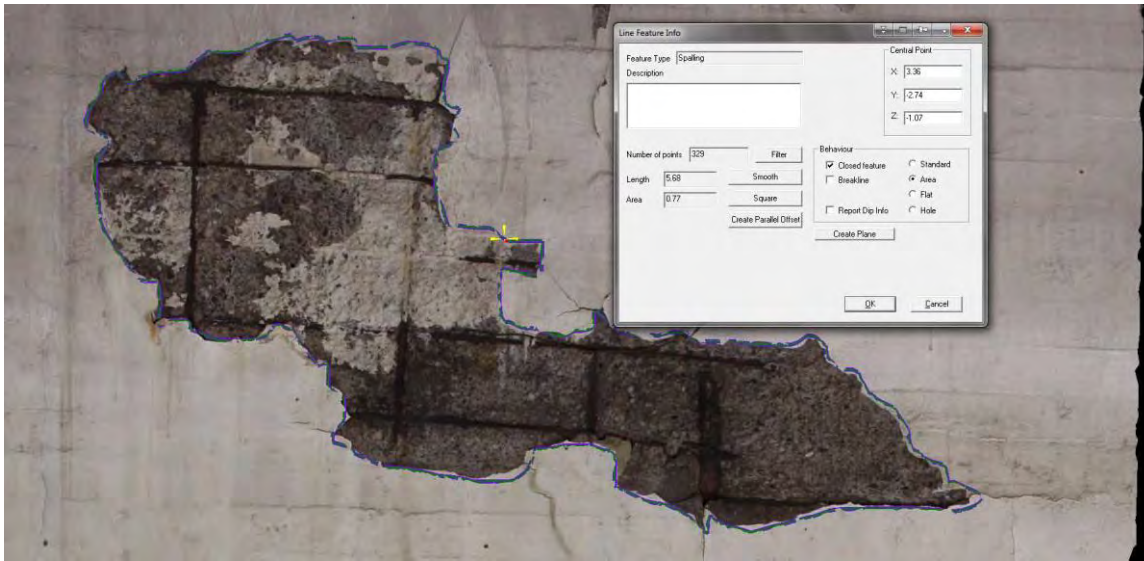**Figure X-14. Typical survey of existing cracks in a final lining.**

Figure X-15. Typical survey of a spalling event in a final lining.

Table X-5. Example of surveyed crack report for a final lining.

Center X (Feet)	Center Y (Feet)	Center Z (Feet)	Dipº	Directionº	Diameter (Feet)	Trace Length (Feet)
7.218	34.186	0.098	90.0	0.0	11.188	10.925
9.383	13.944	−0.886	89.9	176.0	12.238	12.041
9.974	13.222	−3.839	88.0	84.0	1.444	1.411

Table X-6. Example of surveyed spalling report for a final lining.

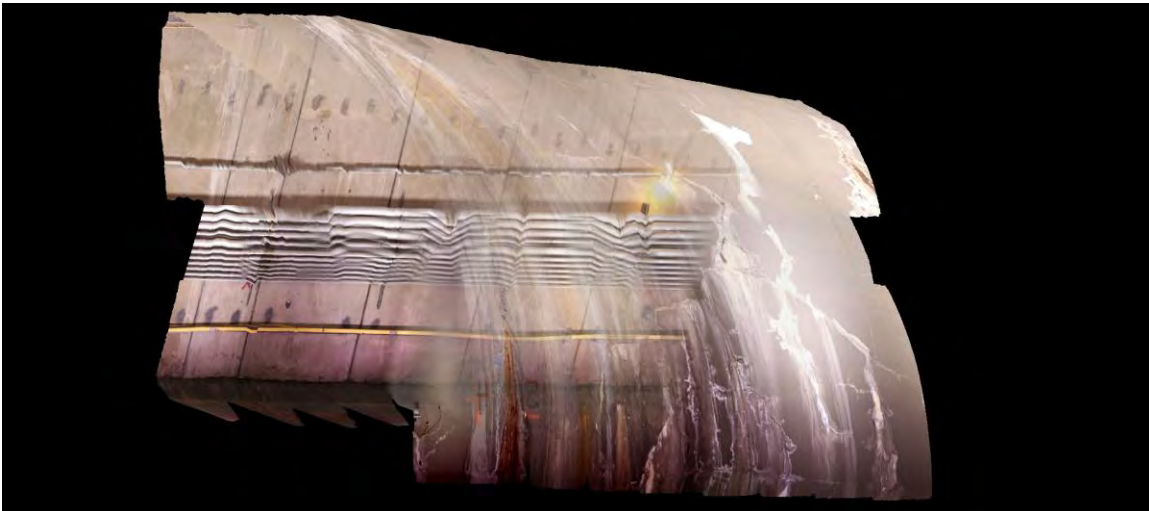| Center X (Feet)	Center Y (Feet)	Center Z (Feet)	Area	Depth (Inches)	Volume (Square Feet)	Exposed Rebars?
23.845	151.513	3.515	3.51	2.4	0.702	Y

Figure X-16. Eisenhower-Johnson Tunnel: clean air supply duct south-west ventilation building.
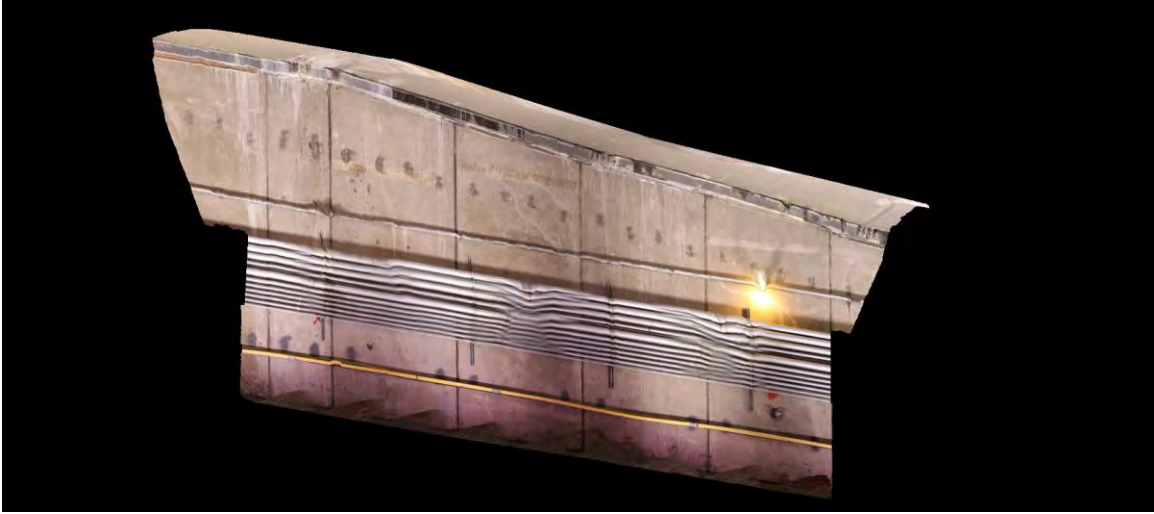
Figure X-17. Eisenhower-Johnson Tunnel: clean air supply duct south-west ventilation building: divider wall.
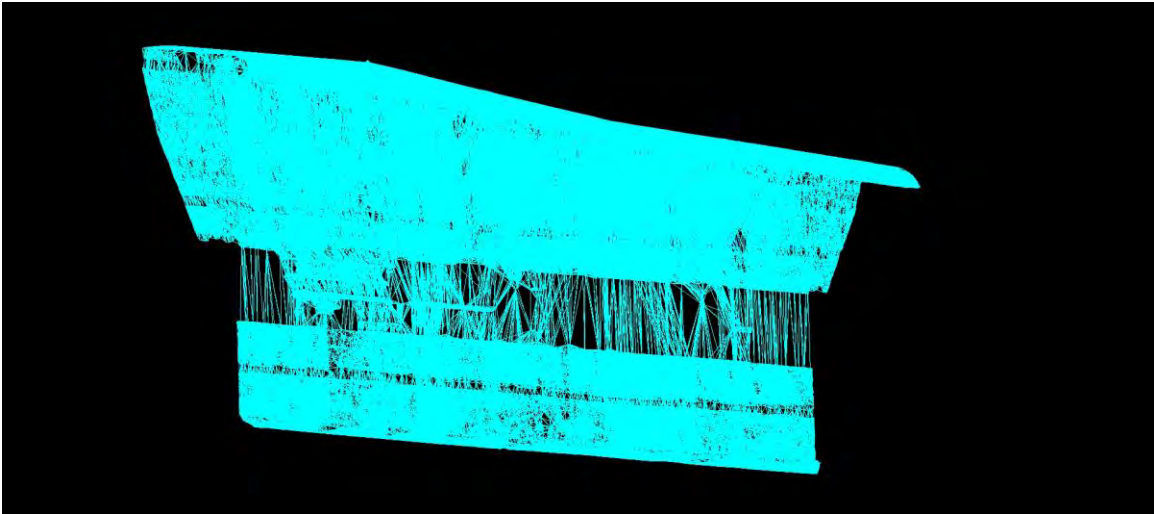

Figure X-18. Eisenhower-Johnson Tunnel: clean air supply duct south-west ventilation building: triangulated mesh of the divider wall.

Figure X-19. Eisenhower-Johnson Tunnel: clean air supply duct south-west ventilation building: view of the south lining wall from within the duct.
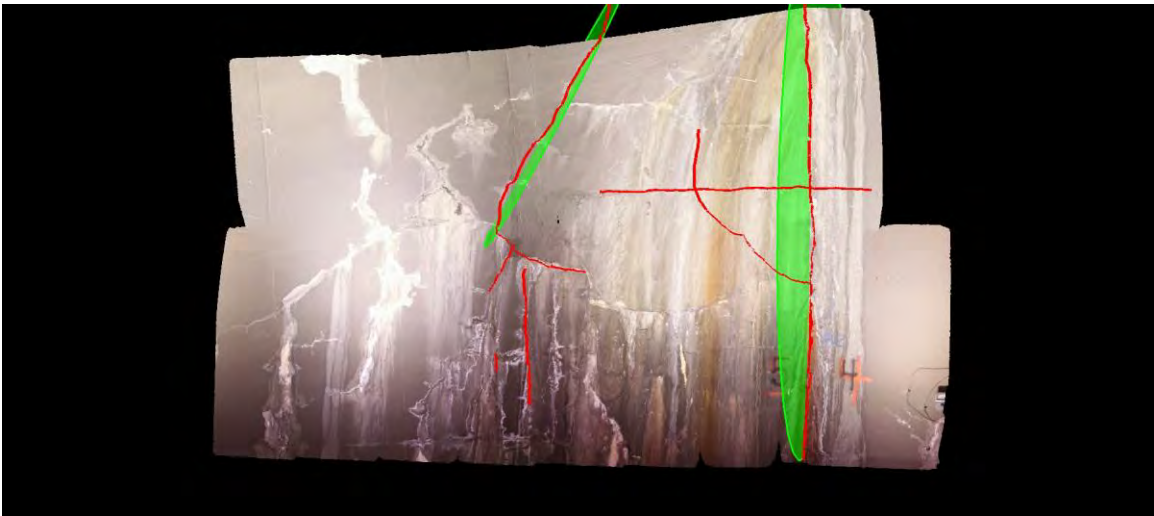

Figure X-20. Eisenhower-Johnson Tunnel: clean air supply duct south-west ventilation building: view of the south lining wall from within the duct with digitized features.

Figure X-21. Eisenhower-Johnson Tunnel: clean air supply duct south-west ventilation building: detail of the south lining wall from within the duct.